DESIGN OF A PERMANENT MAGNET AIR-TURBO GENERATOR

AND

OSCILLATION STUDIES IN MINIATURE SYNCHRONOUS MOTORS

BY

TAN GUAN HONG

A THESIS PRESENTED FOR THE DEGREE OF DOCTOR OF PHILOSOPHY IN THE DEPARTMENT OF ELECTRONIC AND ELECTRICAL ENGINEERING, THE UNIVERSITY OF SHEFFIELD

JANUARY, 1980

To

My

parents

and

wife

ACKNOWLEDGEMENTS

The investigation covered by this thesis was conducted in the Department of Electronic and Electrical Engineering, University of Sheffield.

The author wishes to thank Professor F.A. Benson for the laboratory, computing and workshop facilities, his supervisor Dr. T.S. Birch for his advice, guidance and encouragement throughout the course of the investigation, Dr. D. Howe for his interest in the work and in particular for allowing the author to use his finite element computer programs, and Dr. R. Brown for his assistance in the investigation.

Thanks are also due to all the technical and clerical staff, The Wolf Safety Lamp Company (Wm. Maurice) Limited, Sheffield, England for the award of a research studentship, and Messrs. J. Jackson and N. Bishop for their helpful advice.

CONTENTS

PART 1: Design of a Permanent Magnet Air-Turbo Generator

PART 1

SUMMARY

The work described in this part of the thesis is involved mainly with uprating a 55W air-turbine driven permanent magnet generator to 250W. It is shown that the electrical performance of the generator can be predicted from a simple equivalent circuit comprising an induced emf source with a series inductance and resistance. When matching the generator and turbine characteristics iron losses are included as an additional torque requirement.

Analysis has identified that the most important parameters which determine the rating of the generator are the stator flux linkage, stator inductance and number of pole pairs. Investigations have therefore centred around the calculation of these quantities. Previous design methods for calculating the parameters have been dependent on experimental data for particular magnet geometries. They are not sufficiently general to permit design calculations for magnets having radically different shapes or properties. Therefore the finite element method is used to predict the magnetic field distribution, from which the stator winding flux linkages and inductance, and the saliency torque, are predicted, an important parameter when matching the turbine and generator at starting. The finite element method offers significant advantages over analytical methods because it can account accurately for leakage flux, it can handle complex configurations of magnetic circuit and the directional properties of the magnet, and it allows different parts of the magnet to operate at different flux density levels.

The performance of the generator is predicted with reasonable accuracy.

Alternative rotors for the 250W generator have been designed and tested. Results have shown that the existing generator can be adapted to the 250W design simply by using a rare-earth magnet rotor, and selecting a suitable stator winding turns factor for matching the generator and bulb. Two methods of matching the load characteristics of the turbine, generator and bulb, to produce an acceptable system have been developed.

A simple electronic protection circuit has been designed to prevent the 250W generator from overspeeding in the event of bulb failure. Additionally it can limit over-voltages, caused by variations in the pressure of the air supply, which would otherwise decrease the life of the bulb.

LIST OF PRINCIPAL SYMBOLS

A	magnetic vector potential
A_a	effective area of end-winding reluctance
A_g	effective area of airgap path
A_m	cross-sectional area of magnet
A_{DE}	area of airgap path
A_{EF}	effective area of leakage reluctance
B	flux density
B_{DE}	useful flux density
B_{EF}	leakage flux density
B_g	airgap flux density
B_m	flux density at $(BH)_{max}$
B_{mag}	magnet flux density
B_r	remanent flux density
B_{stab}	stabilised flux density
B_x	flux density in x direction
B_y	flux density in y direction
$B_{\theta j}$	radial flux density
B_{rj}	tangential flux density
C	capacitor/gradient of turbine torque-speed curve
C_I	equivalent iron-loss constant
D	pressure constant/diameter of rotor
d_n	normal stress
d_t	tangential stress
E	open-circuit emf
e	element
F	force
f	supply frequency
G	gain of integrator
G_{xy}	gain of multiplier
G_{ac}	gain of a.c. filter
H	magnetic field strength
H_c	coercivity magnetic field strength
H_g	magnetic field strength across airgap
H_m	magnetic field strength at $(BH)_{max}$
H_{stab}	stabilised magnetic field strength
I	current/energy functional
J	current density
J_m	equivalent magnetic current density
K,K'	peak flux linkage
L,L'	stator winding inductance
L_e	end-winding inductance

L_s	total slot inductance
L_{gm}	total airgap-magnet inductance
ℓ_a	effective length of end-winding reluctance
ℓ_g	effective airgap length
ℓ_m	length of magnet
ℓ_r	rotor pole width
ℓ_s	stator pole width
M	magnetisation
N	number of stator winding turns per pole
n	turns factor
n_{min}	optimum turns factor to operate generator at minimum speed
P	total power of generator
P_L	power supplied to load
P_{Lmax}	maximum output power
P_{max}	maximum power of generator
p	pole pairs/coefficients
R,R'	stator winding resistance
R_L	resistance of tungsten bulb
R_D	dummuy resistor
R_V	variable resistor
R_g	gate resistance
r	radius of rotor/coefficient
S	reluctance
S_g	airgap reluctance
S_m	reluctance of magnet
S_e	end-winding reluctance
S_s	reluctance per slot
S_T	total reluctance
S_{DE}	airgap reluctance
S_{EF}	leakage reluctance
S_1,S_2	coefficients
[S]	stiffness matrix
T	total torque of generator/arc length of magnet pole
T_{max}	maximum torque of generator
T_L	equivalent output torque
T_i	equivalent iron-loss torque
T_o	turbine standstill torque
T_t	turbine torque
T_i	equivalent hysteresis loss torque

t	axial length of stator
V_D	voltage across dummuy resistor R_D
V_L	peak rated voltage across bulb
V_g	triac gate voltage
V_{gt}	triac gate turn-on voltage
V_s	peak voltage across stator winding
V_1	voltage from summer amplifier
V_2	voltage from a.c. filter
w	axial length of rotor

α	coefficient
α_m	angle of preferred magnetisation
η	efficiency
θ	mechanical displacement angle
$\dot{\theta}$	rotor speed
$\dot{\theta}_{max}$	rotor speed at which T_{max} occurs
μ_o	permeability of free space
μ	permeability
μ_{recoil}	recoil permeability
ρ	resistivity
δ	skin depth
ϕ	flux
ϕ_{DE}	useful flux
ϕ_{EF}	leakage flux
ϕ_g	airgap flux
ψ	flux linkage
ω	angular frequency
ω_{max}	angular frequency at which T_{max} occurs
	area of finite element

CHAPTER 1

INTRODUCTION

1.1 Origin of the Project

This project originated from a need to increase the light output of an air-turbine driven semi-portable safety lamp manufactured by the "Wolf Safety Lamp Co. Ltd.". These units are used mainly in an inflammable atmosphere such as in mines, oil-tankers, chemical works, etc. The manufacturer was interested in uprating the existing 55 watts lamp unit to a 250 watts version.

The redesign of the air-turbine was undertaken by the Mechanical Engineering Department of this University. This thesis describes the stages in the redesign of the permanent magnet generator, and its matching to both the turbine characteristics and lamp load. The investigation identifies those parameters which determine the output power and considers alternative rotor geometries and permanent magnet materials. In addition, a system for protecting the generator in the event of failure of the bulb has been developed.

1.2 Description of the Original System

The lamp unit is designed with an emphasis on safety. In explosive environments compressed air rather than electricity is used for power transmission because a mains electricity supply is not permissible. In the Wolf Safety Lamp compressed air drives a turbine which is mechanically coupled to a single-phase permanent magnet generator. The generator supplies a quartz halogen bulb which

has a tungsten filament. Fig.1.1 shows a schematic diagram of the air-flow path. Compressed air enters through the passage A, passes into the glass lamp housing and out through passage B to the turbine blades. The air cools the stator winding as it passes to the exhaust outlet C. This air-flow path is a safety feature of the system since accidental breakage of the glass housing causes escaping air to purge the heat from the bulb and prevent any inflammable gas from entering the system. At the same time air is diverted from the turbine blades so that no further electrical power is generated.

The lamp housing is nickel-plated brass which will not produce sparks on impact with a hard surface. It is designed to contain any high energy fragments in the event of mechanical failure of the rotor or the turbine.

The generator has a permanent magnet rotor for producing the magnetic field. By using permanent magnet excitation rather than d.c. excitation, the consequent dangers of sparks caused by bad brush contacts are eliminated. At the same time maintenance costs are reduced. However, control of the output voltage by field variation is not then feasible. In the safety lamp the effect of air-line pressure fluctuations and the initial variation of output voltage due to production tolerances are controlled by an adjustable air-pressure regulator at the inlet of the unit.

Fig.1.2 shows the complete safety lamp unit together with the turbine blade, the original 35% Cobalt steel permanent magnet rotor, and the stator core and winding. The stator core consists

of two 1.2mm thick end laminations and twenty nine 0.5mm laminations of Losil 800. The axial length of the core is 16.9mm. It has a stacking factor of 0.95. The stator winding has 12 turns of 17 s.w.g. wire per pole.

The existing generator runs at 9300 r.p.m. and powers a 12V 55W halogen bulb. The turbine air pressure is regulated at the inlet of the unit to give an output voltage of 11.5V from the generator, thus extending the lifetime of the bulb.

1.3 Design Requirements For The 250 Watt Generator

In designing the uprated generator the following requirements were taken into consideration :

(i) The generator should power a 250W, 24V quartz halogen bulb and, preferably, run at a reduced speed no greater than 7,500r.p.m. Lower running speeds are desirable to reduce noise emission from the system as well as bearing wear.

(ii) A significant increase in weight or volume would be commercially unattractive.

(iii) Where possible, existing components should be used in the new design so as to avoid re-tooling costs.

(iv) The new design must incorporate all the safety features outlined in section 1.2. In addition the turbine-driven generator should have a protection system to prevent the rotor from overspeeding when the bulb fails.

(v) The torque-speed characteristic of the generator must be matched to that of the turbine so as to ensure stable operation, allowance being made for possible air-pressure variations. At the same time, the saliency torque of the generator at standstill must be sufficiently low for the turbine to start the generator.

(vi) The permanent magnet rotor should be air-stabilised so that its magnetic properties will not deteriorate if the rotor is removed from the stator for servicing.

CHAPTER 2

DESIGN APPROACH

2.1 Introduction

A theoretical investigation of the performance of the permanent magnet generator was undertaken to identify the most important design parameters. The matching of the generator characteristics to those of the turbine and load was also examined to establish design guides.

In order to simplify the analysis, the following initial assumptions have been made,

(i) Hysteresis, eddy currents and skin effects can be neglected

(ii) The time variation of flux linkage K between the rotor magnet and stator winding is sinusoidal.

(iii) Stator winding inductance, L is constant. Although the generator is a salient pole machine, it can be treated as a cylindrical rotor machine because the effective permeability of permanent magnet materials is relatively low. Thus any variations in magnetic reluctance with changes in rotor position will be small.

(iv) Saturation of the magnetic circuit can be neglected.

(v) The circuit parameters (K, L and resistance R) are constant.

(vi) Bulb resistance, R_L is constant.

Although, in general, these initial assumptions are shown to be reasonable the effects of the iron-loss torque and a non-linear load R_L are included in Section 3.6.

2.2 Equivalent Circuit Analysis

Based on the above assumptions, the generator can be represented by the equivalent circuit of Fig.2.1 comprising a sinusoidal source of emf E in series with a self-inductance L, internal resistance R and a load resistance R_L.

For a p pole-pair machine, running at a constant rotor speed $\dot{\theta}$ $(= \frac{\omega}{p})$ radians sec^{-1} and having a total stator flux linkage $\psi = K'\cos(p\theta)$, the open-circuit emf is

$$E = \frac{d\psi}{dt} = \frac{d\psi}{d\theta}\frac{d\theta}{dt} = -K'\omega \sin(\omega t) \qquad (2.1)$$

where K' is the peak flux linkage

θ is the mechanical angle displacement between a stator pole and a rotor pole

ω is the electrical angular frequency

Analysis of the equivalent circuit gives

$$\bar{E} = (R' + R_L)\bar{I} + j\omega L'\bar{I}$$

and

$$I = \frac{E}{\sqrt{(R' + R_L)^2 + (\omega L')^2}} = \frac{K'\omega}{\sqrt{(R' + R_L)^2 + (\omega L')^2}} \qquad (2.2)$$

where I is the magnitude of the peak current.

The output power is then given as

$$P_L = \frac{I^2}{2} R_L = \frac{1}{2} \frac{(K'\omega)^2 R_L}{[(R' + R_L)^2 + (\omega L')^2]} \qquad (2.3)$$

and the equivalent output torque is

$$T_L = \frac{P_L}{(\frac{\omega}{p})} = \frac{1}{2} \frac{p\omega K'^2 R_L}{[(R' + R_L)^2 + (\omega L')^2]} \qquad (2.4)$$

The total power generated is

$$P = \frac{I^2}{2}(R' + R_L) = \frac{1}{2}\frac{(K'\omega)^2(R' + R_L)}{[(R' + R_L)^2 + (\omega L')^2]} \qquad (2.5)$$

while the average torque required to produce this power is given as

$$T = \frac{P}{(\frac{\omega}{p})} = \frac{1}{2}\frac{p\omega\ K'^2\ (R' + R_L)}{[(R' + R_L)^2 + (\omega L')^2]} \qquad (2.6)$$

As the rotor speed increases the $\omega L'$ term will eventually predominate and the generator will behave as a constant current source and the power will approach a maximum value, P_{max}, as shown in Fig.2.2.

The maximum power is then given as

$$P_{max} = \frac{1}{2}\frac{K'^2}{L'^2}(R' + R_L) \qquad (2.7)$$

and the maximum output power is

$$P_{L_{max}} = \frac{1}{2}\frac{K'^2}{L'^2}R_L \qquad (2.8)$$

The peak torque is obtained by differentiating torque T w.r.t. speed ω using equation (2.6),

$$T_{max} = \frac{pK'^2}{4L'} \qquad (2.9)$$

when the angular frequency

$$\omega = \omega_{max} = \frac{R' + R_L}{L'} \qquad (2.10)$$

At ω_{max} the power generated is

$$\frac{1}{4}\frac{K'^2}{L'}\omega_{max} = \frac{1}{2}P_{max} \qquad (2.11)$$

and the output power is

$$\frac{1}{4}\frac{K'^2}{L'}\left(\frac{R_L}{R'+R_L}\right)\omega_{max} = \frac{1}{2}P_{L_{max}} \qquad (2.12)$$

while the output torque is

$$\frac{pK'^2}{4L'}\left(\frac{R_L}{R'+R_L}\right) \qquad (2.13)$$

Fig.2.2 illustrates the torque-speed curve described by equation (2.6). It shows the distinct peak torque at $\dot{\theta}_{max}$ (= ω_{max}/p). It must be emphasised that for a non-linear R_L (tungsten bulb) equations (2.10)-(2.12) are no longer valid. The effect of a non-linear R_L is examined in Section 3.6.

The operating speed of the turbine-generator system will depend on the point of intersection of the turbine and generator torque-speed characteristics. Fig.2.5 shows typical characteristics of the turbine used in the lamp system. Stable operation at point A of Fig.2.2, which is approaching the power P_{max}, would require a turbine with a steeply drooping characteristic, in order to prevent excessive speed fluctuations with changes in air pressure. However, the actual turbine characteristic is not sufficiently steep, so to obtain a more stable intersection of the two torque-speed characteristics it was decided that operation should be to the left of T_{max}, such as point B in Fig.2.2. Equation (2.11) shows that this results in the generator producing less than half P_{max}.

2.3 Effect of Changing the Number of Stator Turns Per Pole

The parameters K', L' and R', introduced in the analysis of Section 2.2, are dependent on many design factors, one of which is the number of stator winding turns per pole, N.

The effect of varying N independently of the other parameters is now considered.

A p pole-pair single-phase winding having N turns per pole has a peak flux linkage

$$K' = 2p\ N\phi \qquad (2.14)$$

where ϕ is the peak flux per pole.

If the reluctance per pole is S then the total stator winding inductance can be written as

$$L' = 2p\ \frac{N^2}{S} \qquad (2.15)$$

Assuming the available winding cross-sectional area 'A', is fixed the area per turn will be A/N and the total length of winding per pole will be ℓN, where ℓ is the length per turn. Therefore the winding resistance will be

$$R' = 2p\ \frac{\rho(\ell N)}{(\frac{A}{N})} = 2p\ N^2\ \frac{\rho\ell}{A} \qquad (2.16)$$

where ρ is the conductor resistivity.

The existing 55W design has a winding of 12 turns per pole. To ease comparison a turns factor is defined as

$$n = \frac{N}{12} \qquad (2.17)$$

Substituting equation (2.17) into equations (2.14), (2.15) and (2.16), gives

$$K' = 2p(12n)\phi = nK \qquad (2.18)$$

$$L' = 2p\ \frac{(12n)^2}{S} = n^2L \qquad (2.19)$$

and

$$R' = 2p(12n)^2\ \frac{\rho\ell}{A} = n^2R \qquad (2.20)$$

where K, L and R are the parameters for a 12 turns per pole stator winding.

Substituting for K', L' and R', in the equations derived in Section 2.2 become

$$I = \frac{nK\omega}{\sqrt{(n^2R + R_L)^2 + (\omega n^2 L)^2}} \tag{2.21}$$

$$P_L = \frac{1}{2} \frac{(nK\omega)^2 R_L}{[(n^2R + R_L)^2 + (\omega n^2 L)^2]} \tag{2.22}$$

$$P = \frac{1}{2} \frac{(nK\omega)^2 (n^2R + R_L)}{[(n^2R + R_L)^2 + (\omega n^2 L)^2]} \tag{2.23}$$

and

$$P_{max} = \frac{1}{2} \left(\frac{K}{nL}\right)^2 (n^2R + R_L) \tag{2.24}$$

The average torque now becomes

$$T = \frac{1}{2} \frac{p\omega (nK)^2 (n^2R + R_L)}{[(n^2R + R_L)^2 + (\omega n^2 L)^2]} \tag{2.25}$$

and the peak torque

$$T_{max} = \frac{p(nK)^2}{4n^2L} = \frac{pK^2}{4L} \tag{2.26}$$

when

$$\omega = \omega_{max} = \frac{n^2R + R_L}{n^2L} \tag{2.27}$$

Fig.2.3 shows that the torque-speed curve for a given generator and load can be varied by changing the turns factor n since this alters the speed at which the peak torque occurs, the maximum value of torque being unchanged.

To minimise mechanical problems due to centrifugal forces, an upper speed limit $\dot{\theta}_{max}$ must be imposed on the generator.

Different generators, G_1, G_2, G_3 in Fig.2.4, can have different turns factors such that the peak torques all occur at the same speed, $\dot{\theta}_{max}$. At that speed, the power of the generators becomes

$$P_1 = T_{max_1} \dot{\theta}_{max} \tag{2.28}$$

$$P_2 = T_{max_2} \dot{\theta}_{max} \tag{2.29}$$

$$P_3 = T_{max_3} \dot{\theta}_{max} \tag{2.30}$$

where $$\dot{\theta}_{max} = \frac{\omega_{max}}{p} \tag{2.31}$$

p can be different for each generator.

The above expressions indicate that an effective criterion for comparing the generated power of each design is its peak torque capability T_{max}. Equation (2.26) shows that the design parameters for increasing T_{max} are p, K and L. A higher T_{max} can be achieved by increasing p and K and decreasing L. However, it must be emphasised that these parameters are not independent variables so that attempts to change any one parameter may affect the others. Thus the overall design aim has been to increase T_{max} by optimising the three parameters p, K and L.

2.4 Matching of Generator to Turbine and Load

The uprating of the turbine output power and the measurement of its torque-speed curves have been undertaken in the Department of Mechanical Engineering[1]. The performance curves are reproduced in Fig.2.5 which shows the effect of

For a given generator, specified lamp power, and voltage rating, the parameters K, L and R are fixed together with the load current I and bulb resistance R_L. The operating speed is then given by

$$\dot{\theta} = \frac{\omega}{p} = \frac{(n^2R + R_L)}{p\sqrt{(\frac{nK}{I})^2 - (n^2L)^2}} \qquad (2.32)$$

Fig.2.7 shows a typical plot of $\dot{\theta}$ against n. The graph demonstrates that a given output power can be generated at a minimum speed $\dot{\theta}_{min}$ by choosing the optimum turns factor n_{min}. n_{min} can be determined by differentiating equation (2.32) w.r.t. n to give

$$n_{min} = \frac{(\frac{K}{IL})}{\sqrt{2 + \frac{R}{R_L}(\frac{K}{IL})^2}} = \frac{\frac{V_L}{2P_L}(\frac{K}{L})}{\sqrt{2 + \frac{R}{2P_L}(\frac{K}{L})^2}} \qquad (2.33)$$

and

$$\dot{\theta}_{min} = \frac{\omega}{p}min = \frac{2\left[R + 2P_L(\frac{L}{K})^2\right]}{pL\sqrt{1 + (\frac{K}{L})^2\frac{R}{2P_L}}} \qquad (2.34)$$

where V_L is the peak voltage rating of the bulb and P_L is the power rating.

Since the stator is force-cooled, any increase in copper loss due to an increase in winding resistance with turns factor does not impose a design limitation.

The efficiency of the generator, excluding iron-losses, is given by

$$\eta = \frac{100R_L}{R_L + n^2R}\ \% \qquad (2.35)$$

By using the optimum turns factor n_{min}, it can be shown that the efficiency is given by

$$\eta = \left[\frac{2 + \frac{R}{2P_L}\left(\frac{K}{L}\right)^2}{2 + \frac{R}{P_L}\left(\frac{K}{L}\right)^2}\right] \times 100\% \qquad (2.36)$$

Equations (2.34) and (2.36) show that for a given output power P_L different generators having different K, L and R will have minimum operating speeds and different efficiencies.

To ensure that the matching of the generator to the bulb also guarantees stable operation of the turbine and generator, the operating speed $\dot{\theta}_B$ should be less than $\dot{\theta}_D$ of Fig.2.6 where

$$\dot{\theta}_B = \frac{\omega_B}{p} = \frac{(n_{min}^2 R + R_L)}{p\sqrt{\left(\frac{n_{min} K}{I}\right)^2 - (n_{min} L)^2}} \qquad (2.37)$$

To prevent over speeding the difference between $\dot{\theta}_B$ and $\dot{\theta}_D$ must take into account the maximum possible air pressure fluctuation. These conditions also apply even when the generator torque-speed curve is modified by the iron-loss torques and the non-linearity of the load resistance R_L, as shown in Section 3.6.

CHAPTER 3

EQUIVALENT CIRCUIT VERIFICATION

3.1 Introduction

It has been shown in Chapter 2 that the performance of the generator can be predicted from a simple equivalent circuit involving the parameters K, L and R. In order to verify the equivalent circuit experimental tests were performed to compare predicted and measured performance.

The existing design having a Cobalt rotor has been tested. The effects of changing the stator winding turns factor and increasing the axial length of the machine have also been investigated. Generators having different permanent magnet materials have been considered. The alternative materials are Alnico (Normal) and Alnico (High Br), which have superior characteristics, as shown in Fig.4.31. They are cast to an identical shape as the original cobalt rotor. During initial tests the Alnico rotors gave very little improvement in performance over the original design. Later investigations, described in Section 4.3, indicated that the Alnico rotors were not fully magnetised to saturation. This was later confirmed by the magnet manufacturer. Subsequent tests on remagnetised Alnico rotors show that their magnetisation state affects only the parameter K.

3.2 Measurement of K

By using an experimental rig, described in Appendix A, in which the generator is driven at a constant speed by a d.c. motor,

the open-circuit induced emf of the stator has been measured. From Section 2, the emf equation is

$$E = \frac{d\psi}{dt} = - nK\omega \sin(\omega t) \qquad (3.1)$$

K can be determined from direct measurement of E. However, this requires accurate measurement of ω. In practice E contains higher harmonic terms due to the non-sinusoidal variation of flux linkages ψ. By integrating the waveform of E, the harmonic distortion is reduced and the effect of speed on the amplitude is removed. The waveform then shows the variation of ψ with time. Fig.3.1 shows the waveform of ψ for a generator having a Cobalt rotor. Rotors of other magnetic materials gave similar waveforms. The harmonic content of the ψ waveform is tabulated in Fig.3.1. It shows that no harmonic is greater than 3% of the fundamental. By using a calibrated integrator, having unity gain at 15Hz, the peak output voltage of the integrator is given as

$$V_o = GnK$$

from which

$$K = \frac{V_o}{Gn} = \frac{V_o}{2\pi\ 15n} \qquad (3.2)$$

where G is the gain of the integrator which equals $2\pi 15$

Table 3.1 shows the measured K values for different rotors and working airgaps using the original stator winding of 12 turns per pole (n=1). The K values were found to be independent of frequency up to the maximum test speed of 10,000 r.p.m. This supports the initial assumption that the parameter K is virtually unaffected by iron losses in the magnetic circuit.

Measurement of K for the various rotors was repeated with a new 24 turns per pole (n=2) stator winding. The results are given in Table 3.1. The close agreement with the K values for the original stator winding confirm that K is independent of n, as was shown in Section 2.3.

Table 3.1 Measured Values of K for Various Rotors.

Rotor Material	Magnetisation State	Working Airgap (mm)	Measured K (m Wb)	
			n=1	n=2
Cobalt	complete	0.5	6.3	6.3
Alnico (N)	complete	0.5	8.5	8.4
Alnico (N)	incomplete	0.5	6.4	6.4
Alnico (H.Br)	complete	0.25	8.7	8.6
Alnico (H.Br)	incomplete	0.25	7.8	7.8

3.3 Measurement of L and R

3.3.1 Experimental technique

Initially short-circuit tests were used to determine the parameters L and R. Unfortunately this simple technique was not sufficiently accurate. However details of the method together with the results are given in Appendix B. A more accurate and direct technique was then devised which allowed measurement of L and R to be made over a wide frequency range with the rotor stationary. Fig.3.2 shows the circuit arrangement used for the measurement. The stator winding is connected in series with a non-inductive resistor R_D and they are supplied from a variable frequency power amplifier having a floating output. Although the value of R_D is not critical, it is preferable to choose R_D to have the same order of magnitude as the impedance of the stator. To prevent saturation of the magnetic circuit a low

excitation current of 1 amp peak is used.

The output voltage from the low noise summation circuit of Fig.3.2 is given as

$$V_1 = -(V_S \frac{R_2}{R_1} - V_D \frac{R_2}{R_V}) \qquad (3.3)$$

The voltage across the stator is

$$V_S = I(n^2R + j\omega n^2L) \qquad (3.4)$$

and the voltage across the non-inductive resistor is

$$V_D = I\ R_D \qquad (3.5)$$

where R_V is a calibrated 10 turns helical potentiometer of 1MΩ

R_D is a 1.004Ω resistor

R_2 is a 100K resistor

R_1 is a 10K resistor

By substituting equations (3.4) and (3.5) into equation (3.3), the magnitude of the peak output voltage of the summing amplifier is then given by

$$V_1 = I\sqrt{\left[\left(\frac{n^2R}{R_1} - \frac{R_D}{R_V}\right)R_2\right]^2 + \left[\omega n^2L\ \frac{R_2}{R_1}\right]^2} \qquad (3.6)$$

V_1 will have a minimum value of

$$V_1 = I\,\omega\,n^2L\,\frac{R_2}{R_1} \qquad (3.7)$$

when

$$\frac{n^2R}{R_1} = \frac{R_D}{R_V} \qquad (3.8)$$

Adjustment of R_V, the helical potentiometer, to give a minimum value of V_1 then allows the value of R to be calculated from

$$R = \frac{R_D}{R_V} \frac{R_1}{n^2} \qquad (3.9)$$

and the inductance to be calculated from

$$L = \frac{V_1 R_1}{I \omega n^2 R_2} \qquad (3.10)$$

Fig.3.3 shows typical variations of V_1 against the resistance ratio R_2/R_V. The values of V_1 shown are for a generator having a 12 turn/pole stator winding, for which n=1, and a Cobalt rotor. The curves show that as the reactance increases with frequency V_1 becomes less sensitive to R_2/R_V variations. Since the determination of R is directly dependent on the value of R_V, this reduction in sensitivity at high frequencies makes the measurement of R too inaccurate at frequencies higher than about 50Hz. However, the inductance measurement is unaffected at high frequency since the whole of V_1 is effectively across inductance L.

The high frequency measurement of R can be achieved by using the multiplication circuit shown in Fig.3.2. Multiplying the stator voltage V_s by the resistor voltage V_D and filtering out the a.c. component gives the d.c. output voltage V_2 as

$$V_2 = G_{xy} G_{ac} \frac{V_s V_D}{2} \cos\beta \qquad (3.11)$$

where G_{xy} is the gain of the multiplier and equals 0.1

G_{ac} is the gain of the a.c. filter and equals 10

V_s is the peak voltage across the stator

V_D is the peak voltage across the resistor R_D

and

$$\cos\beta = \frac{I n^2 R}{V_s} \qquad (3.12)$$

By substituting equation (3.12) into equation (3.11) and rearranging, the stator resistance is given as

$$R = \frac{2V_2}{G_{xy}G_{ac}\,I\,V_D n^2} \qquad (3.13)$$

Since the multiplier is a.c. coupled, this method of measuring R is not suitable at frequencies below 20Hz.

3.3.2 Results for L and R

With the existing winding, for which n=1, and the rotor poles aligned with the stator poles, the measured inductance variation with frequency for the various permanent magnet rotors is shown in Fig.3.4. The variation of resistance with frequency is shown in Fig.3.5. The two methods of resistance measurement give good agreement in the frequency range 20-40Hz when both methods are equally valid. The d.c. resistance measured by a Wheatstone Bridge which is also shown supports the validity of the resistance measurement techniques. For comparison purposes test results without a rotor are included. The graphs show that as the frequency is raised resistance increases and inductance decreases. However, when the rotor is removed the variation of both L and R with frequency is small. The results suggest that iron losses in the laminated stator are small but are significant in the solid permanent magnet rotor. Further investigation of these iron losses is described in Appendix C.

To study the effect of turns factor, n on L and R, iron loss effects must be isolated and comparisons of L and R are restricted to those values measured at 10Hz.

Table 3.2 compares the measured parameters of L and R for the cases when n=1 and n=2.

Table 3.2 Measured Parameters L and R for Various Rotors.

Rotor Material	Magnetisation State	Working Airgap (mm)	Turns Factor n			
			n=1		n=2	
			L(μH)	R(mΩ)	L(μH)	R(mΩ)
Cobalt	complete	0.5	250	88	248	89
Alnico (N)	complete	0.5	200	88	196	89
Alnico (N)	incomplete	0.5	200	88	196	89
Alnico (H.Br)	complete	0.25	218	88	220	89
Alnico (H.Br)	incomplete	0.25	218	88	220	89

The 12 turns per pole (n=1) winding uses a 1.422mm diameter wire. To maintain the same total winding area for the n=2 winding the diameter of the wire would have to be 1.006mm. Unfortunately the nearest s.w.g. of wire has a diameter of 0.965mm. The expected R value using this wire would be 95.5mΩ. However, the thinner gauge of wire is easier to wind around each pole and this tends to decrease the mean length per turn for the n=2 winding. Overall therefore the resistance of the winding is shown to be proportional to n^2. As expected, L is also almost proportional to n^2

The effect of changes in the relative position between the stator and rotor poles on the parameters L and R has also been examined. The results for the case when the rotor poles are aligned with the stator interpoles (i.e. displaced $\pi/2$ electrical radians from the previous position) are also shown in Figs.3.4 and 3.5. By comparing results for the two rotor positions it can be seen that, at low frequencies, the inductance and resistance

are insensitive to changes in rotor position. This supports the assumptions made in Section 2.1. The effect of iron losses however is dependent on rotor position, as shown by the variation in both L and R at higher frequencies.

3.4 Operating Speed

From equation (2.32) the rotor speed necessary for a generator to supply a specified load is given by

$$\dot{\theta} = \frac{\omega}{p} \cdot \frac{60}{2\pi} = \frac{60}{2\pi p} \frac{(n^2R + R_L)}{\sqrt{(\frac{nK}{I})^2 - (n^2L)^2}} \text{ r.p.m.} \qquad (3.14)$$

where I and R_L are parameters determined by the voltage and power rating of the bulb.

Using the measured parameters K, L and R (n=1) from Tables 3.1 and 3.2 for each of the generators powering 3 different lamp loads, the operating speed $\dot{\theta}$ has been predicted from equation (3.14). Table 3.3 shows the predicted and measured speeds for the various rotors, bulbs and turns factors. The close agreement between predictions and measurements suggest that the equivalent circuit model, described in Section 2, can be used to predict the generator operating speed and output power. Again, it must be stressed that this model does not include any iron-losses which will have to be supplied from the turbine. The calculation of the generator torque including iron-losses is covered in Section 3.6.

Table 3.3 Comparison of Predicted and Measured Operating Speeds for Various Generators.

Bulb Ratings			Measured and Predicted Rotor Speeds (r.p.m.)									
			Cobalt		Alnico (N)		Alnico (N)*		Alnico (H.Br)		Alnico (H.Br)*	
R.M.S. voltage	Power (watts)	Turns factor, n	Predicted	Measured	Predicted	Measured	Predicted	Measured	Predicted	Measured	Predicted	Measured
6	50	1	5443	5700	3712	3800	5094	5100	3647	3750	4116	4200
		2	9021	9000	2843	2900	4645	4900	2864	2990	3426	3500
12	55	1	9171	9300	6646	6700	8909	8400	6504	6600	7279	7200
		2	5672	5500	3785	3900	5237	5000	3723	3800	4215	4360
12	100	1	10293	10500	7019	7100	9633	9750	6896	7000	7783	7860
		2	15080	-	4752	4800	7765	8300	4788	4850	5728	5800

* not fully magnetised rotors.

3.5 Increasing Axial Length of the Generator

A further verification of the model was achieved by using generators of approximately twice the original axial length. The stator core now had an axial length of 31.4mm whilst the stator winding had 12 turns per pole (n=1) of 17 s.w.g. wire, as before. The rotors consisted of two standard axial length rotors fastened together. This construction was necessary due to the high cost of manufacturing and magnetising non-standard units. Using the measurement techniques described in Sections 3.2 and 3.3.1, parameters K, L and R were determined for two generators having Cobalt and Alnico (N) rotors. Figs.3.6 and 3.7 show the variation of their inductance and resistance with frequency, the rotor poles being aligned with the stator poles. Measurements without any rotor present are also included for comparison purposes. Table 3.4 shows the measured K values and L and R values at 10Hz.

Table 3.4 Parameters of Generators with Increased Axial Length.

Rotor material	Magnetisation state	Measured Parameters			Predicted Parameters		
		K(mWb)	L(μH)	R(mΩ)	K(mWb)	L(μH)	R(mΩ)
Cobalt	complete	11.7	426	119	11.7	430	123
Alnico (N)	incomplete	13.0	316	119	11.9	337	123

For machines having increased axial length ℓ_2, it can be shown that, the flux linkage is given as

$$K = K_1 \frac{\ell_2}{\ell_1} \qquad (3.15)$$

and the stator inductance is

$$L = (L_1 - L_e)\ \frac{\ell_2}{\ell_1} + L_e \qquad (3.16)$$

while the stator resistance is

$$R = R_1 \frac{(\ell_2 + \ell_s)}{(\ell_1 + \ell_s)} \qquad (3.17)$$

where K_1, L_1 and R_1 are parameters for machine with axial length ℓ_1

ℓ_s is the stator pole width and equals 19.7mm

L_e is the end-winding component of inductance which is estimated in Section 4.4. to be 40μH.

Using equations (3.15), (3.16) and (3.17) and the parameters of the standard length machine from Tables 3.1 and 3.2, the new parameters for the generator with increased axial length have been predicted. The calculated values are compared with the measured values in Table 3.4 and show reasonable agreement. Unfortunately a pair of fully magnetised Alnico (N) rotors were not available to allow construction of a longer fully magnetised Alnico (N) rotor. It can be expected that with fully magnetised Alnico (N) rotor, the K value would be 15.8mWb because the magnetisation state only affects K, as shown in Section 3.1.

Using measured parameters from Table 3.4 in equation (3.14) the predicted operating speeds for generators with n=1 stator winding powering different bulbs are shown in Table 3.5 together with their measured speed, again the close agreement confirms the validity of the model.

Table 3.5 Comparison between Predicted and Measured Operating Speeds for Different Generators and Bulbs.

Bulb Rating		Predicted and Measured Speeds in r.p.m.			
		Cobalt		Alnico (N)	
R.M.S. Voltage	Power (W)	Predicted	Measured	Predicted	Measured
12	55	4967	5100	4399	4500
12	100	5533	5700	4695	4800
24	250	11506	11900	9360	9500

3.6 Torque-Speed Characteristics

The previous two sections have shown that the operating speed for a given output power of the permanent magnet generator can be predicted with reasonable accuracy from its equivalent circuit parameters. Since the generator is driven by an air turbine, its torque-speed characteristics must be investigated so that the intersection point between turbine and generator characteristics can be assessed for stable operation.

It is well known that a tungsten filament bulb has a non-linear resistance relationship with current. Obviously this will affect the torque-speed curve of the generator-bulb circuit during the run-up and run-down of the system. It must be stressed that the prediction of the generator operating speed, as described in Section 3.4, is unaffected by a non-linear load since, at a steady-state operating speed, R_L and I are fixed by the rated voltage and power of the bulb.

Also, as discussed previously any iron losses are supplied by the turbine and will affect the torque-speed curve of the generator. Thus the torque-speed and power-speed characteristics discussed in Chapter 2 have to be modified to accommodate the

iron-losses and the non-linear load R_L.

3.6.1 Inclusion of a non-linear load resistance

Measurements were made on various bulbs to determine their resistance-current characteristics. Fig.3.8 shows the results for tungsten bulbs having ratings of 12V 55W, 12V 100W and 24V 250W. The characteristics can be represented by an analytic expression of the form

$$R_L = AI + Be^{-CI} \qquad (3.18)$$

where R_L is the bulb resistance at the peak current I, and

A, B and C are coefficients determined from measured data.

Fig.3.8 shows that equation (3.18) gives a close fit to the measured resistance-current characteristics. The torque-speed curve of a generator supplying a constant R_L can be predicted from equation (2.25). The torque-speed characteristics including a non-linear R_L can be predicted by treating I as an independent variable in equations (3.18), (2.32) and (2.25), and calculating R_L, $\dot{\theta}$ and T in sequence by direct substitution.

The predicted torque-speed curves with constant R_L and non-linear R_L are shown in Fig.3.9. The two predicted curves intersect at point A (Fig.3.9) because at this operating speed θ_A, the non-linear resistance has reached its rated value. The results show that the non-linear behaviour of R_L increases the speed at which the torque peaks and gives rise to a flatter torque-speed curve. These characteristics are an advantage when considering the stable matching of generator to turbine to prevent the overspeeding described in Section 2.4.

It should be noted that at speeds greater than $\dot{\theta}_A$, the rated operating speed, the bulb rating will be exceeded. Thus, whilst stable operation may theoretically be possible, it is likely that premature bulb failure will occur.

3.6.2 Comparison of measured and predicted torque-speed curves

With the rotor driven by a d.c. motor, as descibed in Appendix A, the torque-speed curve of the existing Cobalt generator powering a 12V 55W bulb has been measured. The result is shown in Fig.3.10 together with the predicted torque-speed curve of the generator driving the non-linear load described in Section 3.6.1. It should be noted that, because of demagnetisation the K value of the test generator had deteriorated to a lower value than that shown in Table 3.1. Thus in this section the measured K value of 5.6mWb is used for the prediction of its torque-speed characteristics. Fig.3.10 shows that the difference between the measured and predicted torques is significant. This is due to the neglect of the iron-loss and mechanical loss torques. Thus further tests have been carried out to establish the magnitude of these loss torques.

To establish the magnitude of the mechanical losses (i.e. windage and friction) a torque measurement was made using a demagnetised rotor. It was felt that the fan-shaped rotor construction may have lead to significant windage losses. However, the plots given in Fig.3.11 show that the total mechanical losses of the rig are small. It is possible that with a magnetised rotor any non-concentricity of the rotor could give a net radial force and increase the bearing friction.

Thus care was taken to align the stator and rotor to minimise this effect.

Tests on L and R in Section 3.2 have already shown that iron losses are significant. Torque measurements were carried out on a generator with an open-circuit stator winding to determine the magnitude of the iron loss torque. Fig.3.11 shows the torque-speed curve which can be compared to that for a demagnetised rotor. The difference between the two curves must be due to iron losses. A more detailed investigation of the nature and distribution of the iron losses is discussed in Appendix C.

Closer agreement between the measured and predicted torques is obtained when the measured loss torques (iron and mechanical loss torques of Fig.3.11) are added to the predicted torques (Fig.3.10). This comparison is shown in Fig.3.10. To eliminate the possibility that errors in modelling the non-linear load may be contributing to the difference between the measured and predicted torques, a short-circuit test was carried out. Fig.3.12 compares the measured torque-speed curve with its predicted torque-speed curve including the open-circuit loss torques (from Fig.3.11). It must be stressed that the iron loss mechanism in the generator under load or short-circuit conditions differs from that under open-circuit conditions, as described in Appendix C. The results show better agreement when loss torques are included in the predicted torques. The figure also demonstrates the distinct peak torque described in Section 2.2.

3.7 Conclusion

This experimental study has verified that for a given generator, with known parameters K, L and R, supplying a given bulb the operating speed can be predicted with reasonable accuracy using a simple equivalent circuit. In addition, the predicted torque-speed curve must include iron-losses and the non-linear bulb effects in order to select the desired turbine.

CHAPTER 4

DESIGN CALCULATIONS FOR PERMANENT MAGNET GENERATORS USING STANDARD METHODS

The two previous chapters have demonstrated that the performance of the permanent magnet generator can be predicted from its equivalent circuit parameters K, L and R. It has also been shown, in Section 2.3, that the important design parameters which determine its peak torque are p, K and L.

For many years the design method for permanent magnet generators[2-8] did not change significantly. This method, which relies on an equivalent magnet circuit to model the permanent magnet behaviour, was studied so that a calculation of K for the various generators could be attempted. However, this technique does not include the calculation of L so that this parameter has to be calculated from a different equivalent circuit.

As discussed in Section 2.4, the saliency torque has to be matched to the turbine torque for starting purposes and thus a method of calculating saliency torque has also been studied.

4.1 Standard Design Practice for Permanent Magnets

The standard design method is based on the following assumptions,

(i) Flux paths are well defined

(ii) The magnet has homogeneous properties

(iii) Reluctances are represented as lumped parameters

(iv) Hysteresis and eddy current effects are neglected

(v) Soft iron has infinite permeability

The behaviour of permanent magnets can be analysed by using either the normal B/H curve, or the intrinsic M/H curve as shown by Overshott[4]. However, following the usual practice[2,3,5-8], the B/H curve is used in this study.

4.1.1 Magnetisation of permanent magnets

A magnet made from material having the characteristic (OAB_rGH_c) shown in Fig.4.1, is initially unmagnetised, corresponding to point O on the curve. When placed in a magnetising jig (Fig.4.2), having a soft iron yoke of negligible reluctance, and excited by a sufficiently high current I_s, the material experiences a magnetising force H_s and the operating point moves to the saturation point A on the characteristic. Switching off the magnetising current will cause the operating point to move to the remanent flux density, point B_r (Fig.4.1).

4.1.2 Air-stabilisation of permanent magnet

When the magnet is removed from the magnetiser (Fig.4.3) the flux density at the face of the magnet is reduced because the external reluctance experienced by the magnet has increased. Assuming that the flux density in the magnet is uniform then the magnetic potential difference will be across the two ends of the magnet. The magnetic circuit in free space, external to the magnet, has three-dimensional reluctance paths and this gives rise to the associated three-dimensional components of flux. To simplify the analysis, the total reluctance of this external circuit is lumped into a single value S_g and the total flux is represented by ϕ_g. The equivalent circuit modelling this situation is shown in Fig.4.3(b). Applying Ampere's law to the magnetic circuit gives

$$I = \oint H.d\ell = H\,\ell_m + H_g\,\ell_g \qquad (4.1)$$

As there is no current in the magnetic circuit (I=0), the demagnetising field strength experienced by the permanent magnet is then given as

$$H = -H_g \frac{\ell_g}{\ell_m} \qquad (4.2)$$

where H_g is the magnetic field strength in the external air circuit

ℓ_g is the effective length of the reluctance S_g

ℓ_m is the length of the magnet

The flux density in the magnet is

$$B = \frac{\phi_g}{A_m} = \mu_o H_g \frac{A_g}{A_m} = -\mu_o \frac{A_g\ \ell_m}{A_m\ \ell_g} H \qquad (4.3)$$

where A_m is the cross-sectional area of the magnet

A_g is the effective area of the reluctance S_g

The linear variation of B with H in equation (4.3) is shown as line OG in Fig.4.1. This line is known as the air-stabilisation permeance line and is effectively the 'load line' of the magnet when it is in a free-space situation. The position where this permeance line intersects the demagnetisation curve of the material is known as the air-stabilisation point of the magnet. This is shown as point G in Fig.4.1, and its flux density level is the flux density of the magnet in air.

In practice the magnetic potential difference is distributed throughout the magnet length causing flux to 'leak' from the sides of the magnet. Thus there is considerable difficulty in defining the effective lengths and areas of the magnet and its

circuit, point G therefore, at best, can only represent an average air-stabilisation point.

4.1.3. Recoil operation of permanent magnet

Fig.4.4 shows the magnet fitted between two soft-iron pole pieces to concentrate the flux across a small working air-gap. The reduced external reluctance will lead to an increase in magnet working flux density. The circuit representing this situation is shown in Fig.4.4(b). Assuming that the reluctance of the airgap is lumped as S_{DE} and the leakage reluctance as S_{EF}, the flux passing through the small airgap of the soft-iron is ϕ_{DE} and the leakage flux between the poles is ϕ_{EF}. Analysis of the equivalent circuit shows that the total flux produced by the magnet is

$$\phi = \phi_{DE} + \phi_{EF} = -H \ell_m \left[\frac{1}{S_{DE}} + \frac{1}{S_{EF}}\right] \qquad (4.4)$$

Thus the flux density in the magnet is

$$B = -\frac{\ell_m}{A_m}\left[\frac{1}{S_{DE}} + \frac{1}{S_{EF}}\right] H$$

$$= -\mu_o \frac{\ell_m}{A_m}\left[\frac{A_{DE}}{\ell_{DE}} + \frac{A_{EF}}{\ell_{EF}}\right] H \qquad (4.5)$$

where A_{DE} is the area of the airgap reluctance

A_{EF} is the effective area of the leakage reluctance

ℓ_{DE} is the length of the airgap paths

ℓ_{EF} is the effective length of the leakage paths

The linear variation of B with H in equation (4.5) is described by line OP (Fig.4.1). Line OP is known as the working permeance line and is the new 'load line' of the magnet. With

the decrease in external circuit reluctance the operating point of the magnet moves from its air-stabilisation point G along a minor hysteresis loop[5-8] GD to intercept the working permeance line at point D. Point D is known as the final working point of the magnet. This minor hysteresis loop GD is narrow and is usually assumed to be a recoil line[5-8]. It has a slope of μ_o μ_{recoil} where μ_{recoil} is defined as the recoil permeability of the magnet material. Parker and Studders[5] have shown that the recoil permeability can vary at different air-stabilisation flux density levels. However for most engineering applications it is assumed that all recoil lines are parallel to the demagnetisation curve at the remanent flux density point B_r and the magnet manufacturer therefore specifies the value of μ_{recoil} for each material.

From the equation (4.5) it can be seen that the magnet flux density B could be split up into two components, a useful flux density B_{DE} and a leakage flux density B_{EF}. The useful flux density is then given as

$$B_{DE} = -\mu_o \frac{\ell_m}{A_m} \frac{A_{DE}}{\ell_{DE}} H \qquad (4.6)$$

and the flux density in the small airgap is

$$B_g = \frac{\phi_{DE}}{A_{DE}} = \frac{B_{DE}\ A_m}{A_{DE}} \qquad (4.7)$$

while the leakage flux density is

$$B_{EF} = -\mu_o \frac{\ell_m}{A_m} \frac{A_{EF}}{\ell_{EF}} H \qquad (4.8)$$

Line OE in Fig.4.1 represents the variation of the leakage flux density B_{EF} with H and this line is called the leakage permeance line. The useful flux density B_{DE} is the difference between the working flux density of the magnet (Point D in Fig.4.1) and its leakage flux density level (Point E). The airgap flux density B_g is then calculated by substituting for B_{DE} in equation (4.7).

It must be stressed that the working point D (Fig.4.1) is an average working point and the lines OD and OE correspond to the effective working and leakage permeances of the magnetic circuit. In practice, the estimation of leakage permeance lines for the various parts of the magnet is difficult due to the distributed and three-dimensional flux pattern. This in turn causes uncertainties in the separation of useful flux from leakage flux.

Equations (4.3), (4.5) and (4.8) suggest that the variations of B with H should be the same for magnets having identical shape and external magnetic circuit. In practice, the permeability of the magnet material, which forms part of the magnetic circuit, affects the magnetic field patterns[5]. This in turn causes variations in the air-stabilisation, working and leakage permeance lines.

4.1.4 Effect of external demagnetisation effect

If a winding carrying a demagnetising current I is placed in the airgap (Fig.4.5) the flux density of the magnet is decreased because the working point of the magnet moves from point D to J (Fig.4.6) along the recoil line GD. The equivalent

circuit representing this demagnetising effect is shown in Fig.4.5(b). By equating mmfs and fluxes it can be shown that

$$-H_J \ell_m = \phi_\ell S_{EF} \tag{4.9}$$

and

$$-H_J \ell_m - NI = \phi_u S_{DE} \tag{4.10}$$

while the flux produced by the magnet is

$$\phi_J = \phi_u + \phi_\ell \tag{4.11}$$

The working flux density at point J is

$$B_J = \frac{\phi_J}{A_m} = \frac{\phi_u}{A_m} + \frac{\phi_\ell}{A_m} \tag{4.12}$$

Substituting ϕ_ℓ and ϕ_u from equations (4.9) and (4.10) into equation (4.12) gives the flux density as

$$B_J = -H_J \frac{\ell_m}{A_m} \left(\frac{1}{S_{EF}} + \frac{1}{S_{DE}}\right) - \frac{NI}{S_{DE} A_m} \tag{4.13}$$

Equation (4.13) describes the same working permeance line as before (equation (4.5)) and is represented by line QL in Fig.4.6. This line intercepts the B=O axis at the point L corresponding to a demagnetising force given by

$$H = H_L = \frac{-NI}{\ell_m \left(1 + \frac{S_{DE}}{S_{EF}}\right)} \tag{4.14}$$

If the magnet experiences a demagnetising force large enough to move its operating point from J to G and G to M (Fig.4.6), the new recoil line would be MN when the external field is removed. This would cause an irreversible reduction in flux density from point D to point N.

In practice, point J is an average operating point because different parts of the magnet will be demagnetised to different points along their recoil lines and some parts of the magnet might even have new recoil lines when the external demagnetising field is removed.

4.1.5 Stable magnet operation

Obviously if the magnet is magnetised in its final operating magnetic circuit and the air-stabilisation stage is omitted, it is possible to operate at a much higher working flux density. However, if an external field is experienced, some demagnetisation of the magnet will occur but in many cases this will still lead to a higher recoil working point than that achieved after air-stabilisation.

Magnets stabilised by applying an external field rather than air-stabilised are known as load-stabilised or short-circuit stabilised[5]. However such magnets must only be removed from their operating magnetic circuit with care and the use of magnet keepers is essential unless remagnetisation is to be carried out.

Fig.4.32 shows some magnet materials which have almost linear demagnetisation curves. For those materials the problems of stabilisation discussed above are minimised since then the recoil lines are almost coincident with the demagnetisation curve. Obviously, therefore, these materials can offer great advantages in terms of magnet stability.

4.2 Application of Standard Magnet Design Technique to the Existing Cobalt Rotor

4.2.1 Determination of air-stabilisation permeance from design guide

For many shapes of magnet the exact calculation of air-stabilisation, working and leakage permeance lines is difficult. As mentioned in Section 4.1, these flux paths are affected by the magnet geometry, material and its external magnetic circuit. With such complex behaviour the design of permanent magnets is often simplified by the use of design guides[5,7]. These guides only give the air-stabilisation permeance because the working and leakage permeances are dependent on the magnetic circuit of the device being designed. These guides are often restricted to simple magnet geometries although, in some cases, where the magnet configuration is complex, empirical formulae based on collected data and experience are used.

The air-stabilisation permeance for rotor geometries similar to that used in the existing generator is given by Parker and Studders[5]. The design aid given by them is reproduced in Fig.4.7. It shows the variation of air stabilisation permeance with the ratio of diameter D to axial length W for rotors having different pole numbers. The approximations made are:-

(i) The total active pole arc of the magnet along the circumference equals half the total rotor circumference. Thus

$$2p\ T = \frac{\pi D}{2}$$

where p is the number of pole pairs

T is the arc length of the magnet pole

D is the diameter of the rotor

Thus, referring to Fig.4.7, the circumferential arc length between the magnet poles is

$$Y = T \qquad (4.15)$$

(ii) The effective magnet length L_m (Fig.4.7) is given as

$$L_m \simeq 2T \qquad (4.16)$$

(iii) The recoil permeability of the magnet material is equal to or greater than 3.

(vi) The flux density distribution in the magnet is uniform and thus the air-stabilisation point can be represented as a single point.

The physical dimensions of the existing Cobalt rotor design are given in Fig.4.8. From that figure, and using an axial length W of 16mm, the ratio of D/W is 4.3. Using Fig.4.7, this gives a permeance value of 8.5 μ_o. However, referring to the dimensions in Fig.4.8, it can be seen that the circumferential arc length of the magnet pole $T = \frac{D}{2}(\frac{\pi 42}{180}) = 25.3$mm and the circumferential arc length between the magnet poles $Y = \frac{D}{2}(\frac{\pi 18}{180}) = 10.8$mm.

Hence, the assumption that T=Y is not valid for this case. Since no details for the case of $T \neq Y$ are given, no allowance can be made for this discrepancy. Using a permeance of 8.5 μ_o, line OA has been drawn in Fig.4.9. It intersects the demagnetisation curve of Cobalt at point A and thus this method gives an air-stabilisation flux density of the magnet of 200mT.

4.2.2 Determination of working permeance

To determine the working flux density level of the magnet the working permeance must be defined as shown in Section 4.1.

As the rotor rotates within the stator the magnet will experience a changing working permeance line. For easy comparison, the working permeance line is defined as the permeance line of the magnet at the position when the stator flux linkage is a maximum. This is also the position when the centre lines of the rotor and stator poles are aligned as shown in Fig.4.10. Assuming that there is no leakage flux and that the stator is infinitely permeable, the slope of the working permeance line, from equation (4.5), is given as

$$\frac{B}{H} = -\mu_o \frac{\ell_m}{A_m} \frac{A_{DE}}{\ell_{DE}} \qquad (4.17)$$

where

$$\frac{A_{DE}}{\ell_{DE}} = \frac{(\ell_s + \ell_r)_W}{2} / \ell_{DE} \qquad (4.18)$$

ℓ_s is the stator pole arc (20mm)

ℓ_r is the circumferential rotor pole arc (25.3mm)

ℓ_{DE} is the airgap length between the stator and rotor poles (0.5mm)

W is the axial length of the magnet (16mm)

The effective ratio of ℓ_m/A_m of the magnet pole can be calculated from the magnetic circuit shown in Fig.4.11 by assuming that the flux flows radially from r_1 to r_2 with no leakage. The reluctance of the magnet pole is then

$$S_m = \frac{\ell_m}{\mu_o \mu_{recoil} A_m} = \frac{1}{\mu_o \mu_{recoil}} \int_{r_1}^{r_2} \frac{dr}{r\theta W} \qquad (4.19)$$

$$= \frac{1}{\mu_o \mu_{recoil} \theta W} \log(r_2/r_1) \qquad (4.20)$$

Therefore,

$$\frac{\ell_m}{A_m} = \frac{1}{\theta W} \log(r_2/r_1) \qquad (4.21)$$

where ℓ_m is the effective length of the magnet (r_2-r_1) (17mm)

A_m is the effective area of the magnet

θ is the subtended angle of the magnet pole (42^o)

μ_{recoil} is the recoil permeability of the magnet material (12)

r_2 is the outer radius of the magnet pole (34.5mm)

r_1 is the effective inner radius of the magnet pole (17.5mm)

By using equation (4.21), the effective area of the magnet A_m is calculated as $294 \times 10^{-6} m^2$. Substituting for A_{DE}/ℓ_{DE} and ℓ_m/A_m from equations (4.18) and (4.21) into equation (4.17), the gradient of the working permeance line is then given as

$$\frac{B}{H} = -\mu_o \frac{\log(r_2/r_1)}{\theta} \frac{(\ell_s + \ell_r)}{2\ell_{DE}} \qquad (4.22)$$

$$= 52.7 \times 10^{-6}$$

Line OB in Fig.4.9 represents the working permeance line for the existing Cobalt generator using equation (4.22).

4.2.3 Determination of K using calculated air-stabilisation results

A recoil line having the gradient $\mu_o \mu_{recoil}$ is drawn from the air-stabilisation point A and it intersects the working permeance line OB at point C. Since leakage flux has been neglected, the flux density level at point C represents the useful flux density B_c of the magnet. The peak flux linkage in the stator is then given as

$$\begin{aligned} K &= \phi\ 2Np\ Wb \\ &= B_c\ A_m\ N\ 2p \\ &= 21.2 \times 10^{-3} B_c\ Wb \end{aligned} \qquad (4.23)$$

The flux density at point C (Fig.4.9) is 370mT and thus the calculated K value, using equation (4.23), is 7.84mWb. However the measured K is only 6.4mWb, as shown in Table 3.1.

When the permanent magnet rotor rotates during the measurement of K, it experiences rapidly changing permeances. It then operates on its recoil line which produces changes in magnet flux density and in turn induces eddy currents in the rotor material. The eddy currents will tend to reduce the measured K value. However, tests undertaken in Section 3.1 have shown that the K value is effectively constant over the range of measured rotor speeds and this suggests that eddy current effects are small and cannot account for the difference between the measured and calculated K values.

The large difference between the calculated and measured K values must therefore be due to either leakage flux which has been neglected or inaccuracies in the determination of permeances. As shown earlier, there is difficulty in extending the design guide given by Parker and Studders since $T \neq Y$. Therefore a series of experiments was undertaken in an attempt to determine the air-stabilisation permeance.

4.2.4 Experimental determination of air-stabilisation permeance

Because of the uncertainty of calculating the air-stabilisation permeance, flux density measurements were made on the Cobalt rotor. The flux produced by the magnet was assumed to consist of three components ϕ_A, ϕ_B and ϕ_C as shown in Fig.4.12.

A search coil at position $X_1X_2X_3X_4$ (Fig.4.13) will link only flux ϕ_B (Fig.4.12). The removal of the search coil from

the magnet pole to a region of negligible magnetic field will therefore produce an induced emf given by

$$E = N \frac{d\phi_B}{dt} \qquad (4.24)$$

where N is the number of turns on the search coil, which equals 500

$d\phi_B$ is the change in flux

The change in flux could be determined from the measurements of E and change in time dt. However by integrating E the effect of time is removed. Using a low-drift calibrated integrator which is d.c. coupled, the change in output voltage of the integrator is then given as

$$V_o = G \int_{t_1}^{t_2} E dt = GN \int_{\phi_1}^{\phi_2} d\phi_B = GN(\phi_2 - \phi_1)$$

$$= GN\ \phi_B \qquad (4.25)$$

where G is the gain of the integrator which was set at 100 for the test.

Therefore the average flux density on the pole face B (Fig.4.12) is given by

$$B_B = \frac{\phi_B}{A_B} = \frac{V_o}{GNA_B} \qquad (4.26)$$

Using this measurement technique the flux density at surface B was measured as 38mT. Using another search coil in the $X_1Y_1X_3Y_3$ plane (Fig.4.13) the flux density at surface C was measured as 39mT. A different search coil in the $X_1X_2Y_1Y_2$ plane gave the flux density at surface A as 20mT. It must be stressed that the search coil measurement gives only the average flux density over a given surface.

Assuming that the measured flux density B_B on surface B represents the relevant air-stabilisation flux density, then the effective air-stabilisation flux density of the magnet is

$$B = \frac{B_B A_B}{A_m} \qquad (4.27)$$

where A_B is the area of surface B and equals
$(16mm \times 25.3mm) = 405 \times 10^{-6} m^2$

A_m is the effective area of magnet pole and equals
$294 \times 10^{-6} m^2$ (from equation (4.21))

Using equation (4.27), the air-stabilisation flux density of the magnet is 52mT. The air-stabilisation flux density of surface B calculated from Parker and Studders design guide was 200mT. Obviously the difference between the 'measured' and calculated air-stabilisation flux density was very large and this would help to explain the higher value of K calculated in Section 4.2.3.

Measurements using a Hall probe were undertaken to determine the flux density distribution on the surfaces A, B and C (Fig.4.12). Each surface was mapped into small rectangular meshes having the dimensions of the Hall probe. Preliminary measurements showed that, as expected, the flux density variation was large near the edges of the magnet.

Thus the meshes were drawn out to avoid edges, as shown in Fig.4.13. During the flux density measurements, the Hall probe was held in close contact with the surface of the magnet. The measured average flux density of each mesh is shown in Table 4.1 and the results show that the flux density distribution on each surface is not uniform.

Table 4.1 Results of Hall Probe Measurements Referring to Fig.4.13

Mesh number	Flux density (mT) at different surfaces				
	A		B	C	
	Air Stabilisation	Recoil Operation	Air Stabilisation	Air Stabilisation	Recoil Operation
1	36	9	40	20	1
2	28	8	33	54	4
3	28	8	33	15	1
4	36	9	40	50	3
5	22	4	35	15	1
6	16	2	33	50	3
7	16	2	33	20	1
8	22	4	35	54	4
9	13	1	35		
10	13	1	33		
11	9	0.1	33		
12	9	0.1	35		
13	2	0.1	40		
14	2	0.1	33		
15			33		
16			40		
Average flux density (mT) in each surface	18	3.5	35	35	2.3

The flux density measurements, using Hall probe and search coils, demonstrate that the magnet produces a non-uniform flux distribution in three dimensions and this causes uncertainties about the actual definition of the air-stabilisation point of the magnet. The data supplied by magnet manufacturers[16,18,19] shows the demagnetisation curves only in the direction of the magnets initial polarisation and a literature survey has failed to uncover any useful information of magnet properties in directions perpendicular to this.

Obviously in view of the experimental results, it would be unreasonable to place too much reliance on the use of the Parker and Studders guide as a means of designing new rotor magnets.

4.2.5 Determination of K from air-stabilisation results

The previous section has shown that the design guide is unreliable for the existing generator design. Using experimental data as a basis, therefore a second attempt at 'predicting' the magnet working point was made.

Assuming that the measured flux density on the surface B represents the relevant air-stabilisation flux density, then an effective value of 48mT is calculated by substituting the average Hall probe results (Table 4.1) in equation (4.27). This value can be used to fix point D on the demagnetisation curve in Fig.4.9. A recoil line is then drawn from point D to intercept the calculated working permeance line OB at point E. The working flux density level at point E is 270mT. Since this value is the useful flux density, a value of K = 5.72mWb is obtained using equation (4.23). As the measured K value of

6.3mWb is higher than this calculated value, the difference cannot be caused by leakage flux. With the magnet inserted in the stator, leakage flux densities from surface A and C were measured so that the leakage permeance line could be established. Table 4.1 shows that, with the rotor poles aligned with the stator poles, the average values of these flux densities are reduced considerably to 3.5mT and 2.3mT respectively and are negligible when compared to the higher calculated working flux density.

Further investigations were therefore undertaken to examine the possibility that individual poles could have different air-stabilisation points which could help to account for the difference between the measured and calculated K values.

Using the Hall probe measurement technique described in Section 4.2.4, the average flux density of each pole face B was measured. The corresponding effective air-stabilisation flux density was calculated using equation (4.27). The results are shown in Table 4.2. The pole designated number 1 was the rotor pole used in the test in Section 4.2.4.

Table 4.2 Variations of Flux Density in Each Rotor Pole.

Pole number	Flux density (mT)	
	Measured average	Effective value
1	35	48
2	31	43
3	36	50
4	39	54
5	36	50
6	33	45

Clearly pole 1 is fairly typical but there is a significant spread of results from pole to pole. Factors which can cause such variations are numerous[5]. The most likely causes are the effects of poor handling or storage, allowing the magnets to come into close proximity with other magnets or pieces of magnetic material or possibly differences in magnetisation. These problems highlight the difficulty in dealing with magnet materials of this type.

The lowest and highest air-stabilisation flux density in Table 4.2 are shown as points G and F respectively in Fig.4.9. Their corresponding working flux densities at points J and H were 265mT and 275mT. Using the flux density levels at points J and H, the lowest K value (point J) was calculated as 5.62mWb while the highest K value (point H) was 5.83mWb. Clearly the agreement with test results of K is not good.

4.2.6 Effects of increasing working airgaps

The design method was also applied to Cobalt generators having increased airgaps of 0.75mm and 1.0mm. This was to investigate variations of magnet working points due to increased airgaps, and to attempt to separate errors in the calculation of working permeance from those of air-stabilisation permeance. By using the same Cobalt rotor as in Section 4.2.5, the air-stabilisation point remains unchanged and is shown as point A in Fig.4.14. The working permeances for the increased airgaps were calculated from equation (4.22) and the lines OL and OM in Fig. 4.14 represent the permeance lines for generators which have 0.75mm and 1.0mm airgaps respectively.

A recoil line has been drawn from point A to intercept the working permeance lines OL and OM at points L and M. The calculated working flux density for the 0.75mm airgap generator at point L is 245mT while the flux density at point M for the 1.0mm airgap generator is 223mT.

Table 4.3 shows the calculated K values for the various generators using equation (4.23)

Table 4.3 Effects of Increasing Airgaps.

Working airgap (mm)	Flux linkage K (mWb)		Position in Fig.4.14	% error
	Measured	Calculated		
0.5	6.3	5.72	F	9.2
0.75	5.8	5.19	L	10.5
1.0	5.0	4.73	M	5.4

Corresponding measurements of K were carried out on generators having these increased airgaps and the results are compared with their calculated values in Table 4.3. For these tests the stator bore diameter was increased to achieve the desired airgaps. This was done to avoid any possible mechanical stress[5] on the magnet caused by the grinding of its outer diameter to achieve the required airgaps. There is some consistency in the results of Table 4.3 suggesting that it is the air-stabilisation rather than the working permeance that presents the most difficulty in design calculations.

4.2.7 Studies of Cobalt sample variations

It was decided to make measurements of K on a number of Cobalt rotors to check on any possible spread of experimental values. Employing the measurement technique described in

Section 3.2 for K, ten samples of standard Cobalt rotor were tested. Since the rotors were from the same batch, variations in K were not expected. However, the measured results plotted in Fig.4.15 showed that the K values were not constant. The average K was 6.3mWb with the highest and lowest value as 6.9mWb and 5.6mWb respectively. The lamp manufacturer confirmed that sample variations of rotors were not unusual and some rotors having low K values had to be remagnetised.

Using the rotors which gave the highest and lowest K values, Hall probe measurements were carried out on surface B (Fig.4.12) of their rotor poles when the rotors were air-stabilised. The measured average results are shown in Table 4.4 together with their corresponding effective air-stabilisation flux densities which were calculated using equation (4.27).

Table 4.4 Flux Density Measurements

Pole number	Flux density (mT)			
	Lowest K value		Highest K value	
	Measured average	Effective value	Measured average	Effective value
1	31	43	39	54
2	26	36*	40	55
3	33	45	43	59*
4	28	39	36	50
5	32	44	41	56
6	28	39	40	55

Using the highest and lowest effective value in Table 4.4 to fix the air-stabilisation points A and B in Fig.4.16, recoil lines were drawn from A and B to intersect the working

permeance line OE, which was reproduced from Fig.4.9, at point C and D. Using the flux density levels at points C and D and equation (4.23), the calculated K for point C was 5.94mWb while the value for point D was 5.55mWb. Again the results emphasise the difficulty in deciding which are the values of B and K to be used for analysis purposes.

4.3 Extension of Design Technique to Alnico Rotors

Despite the known difficulties it was decided to try to extend the design method to generators having different rotor materials, viz. Alnico (N) and Alnico (H.Br). The rotors were cast into the same configuration as the existing rotor geometry (Fig.1.2) so that changes in circuit permeances were minimised.

4.3.1 Studies on Alnico (N) rotor having a 0.5mm working airgap

Since the stator and the geometry of the Alnico (N) and Cobalt rotors were unchanged, the air-stabilisation and working permeance lines were assumed to be the same. They are reproduced from Fig.4.9 and shown as line OE and OD respectively in Fig.4.17. The predicted air-stabilisation flux density at point E is 105mT. A recoil line has been drawn from point E to intercept the working permeance line at point F. The working flux density at point F is 370mT, corresponding to a K value, using equation (4.23), of 7.84mWb.

Using the measurement technique for K described in Section 3.2, a value of K = 6.4mWb was measured which was effectively constant over the range of measured rotor speeds. This suggests that any eddy current effects on K were negligible

and could not account for the difference between the measured and predicted K values.

With the magnet inserted in the stator, leakage flux densities from surfaces A and C (Fig.4.12) were measured with a Hall probe. The average values of these flux densities were 4.5mT and 3.0mT respectively, small enough to be neglected. Thus leakage flux could not have contributed to the lower measured K value.

Hall probe measurements were undertaken to establish the air-stabilisation point, as was used in Section 4.2.4. Preliminary measurements with a Hall probe mounted on a jig had shown that the flux density at the centre of each rotor pole face B (Fig.4.12) varied from pole to pole. The results are presented in Table 4.5.

Table 4.5 Variations in Flux Density.

Pole number	Flux density (mT)
1	45
2	47
3	44
4	43
5	45
6	46
Average flux density (mT)	45

As seen in Table 4.5, the flux density of pole number 1 equals the average value. Thus pole number 1 was chosen to represent a typical rotor pole and its surfaces A, B and C were mapped into rectangular meshes as shown in Fig.4.13. Hall probe

measurements were carried out on each mesh. The results are shown in Table 4.6.

Table 4.6 Results of Hall Probe Measurements Referring to Fig.4.13 during Air-Stabilisation

mesh number	Flux density (mT) at different surfaces A	B	C
1	51	58	20
2	42	50	50
3	42	50	25
4	51	58	55
5	16	55	25
6	10	45	55
7	10	45	20
8	16	55	50
9	10	55	
10	10	45	
11	5	45	
12	5	55	
13	2	58	
14	2	50	
15		50	
16		58	
Average flux density (mT) in each surface	19.4	52.0	37.5

Using the average flux density of surface B in Table 4.6 and equation (4.27), the effective air-stabilisation flux density is 71.6mT which is considerably lower than the predicted value of 105mT (point E). Thus the air-stabilisation point is shown as point B in Fig.4.17. A recoil line drawn from point B intercepts the working permeance line OD at point G gives a flux density level at point G of 345mT. The calculated K is then 7.31mWb which is still higher than the measured value of 6.4mWb.

During the initial development stage, the magnet manufacturer could only guarantee that the Cobalt rotor was fully

magnetised and not necessarily the Alnico (N) rotor. As explained earlier, magnets of identical shape and similar material should have the same air-stabilisation permeance line and thus the air-stabilisation point C must lie on its permeance line OE. Assuming that the Alnico (N) rotor was not fully magnetised, a likely minor demagnetisation curve (KCJ) was sketched in to pass through point C. A recoil line drawn from point C intercepts the working permeance line OD at point H gives a flux density level at point H of 260mT. The calculated K is then 5.52mWb which is now lower than the measured value.

It must be emphasised that the minor demagnetisation curve (KCJ) is a speculative curve and points C and H correspond to effective working points. In practice, different parts of the complex shape magnet have different minor demagnetisation curves, recoil permeabilities, air-stabilisation, working and leakage permeances. Obviously with such complex behaviour, and the possibility of an incompletely magnetised magnet, good agreement between measured and calculated K cannot be expected. The possibility that the magnets needed remagnetising was suggested to the manufacturer who then agreed to check on this.

When a fully magnetised Alnico (N) rotor was made available, Hall probe measurements were repeated and the effective air-stabilisation flux density was 92mT. This 'measured' value was now closer to the earlier predicted value of 105mT. This is shown as point M in Fig.4.17. A recoil line drawn from point M to intercept the working permeance line OD at point L gives a working flux density at point L of 360mT. The corresponding calculated

K is 7.63mWb whilst the measured value was 8.5mWb. This trend which showed higher measured K values was similar to that observed for the Cobalt generators in Sections 4.2.5 and 4.2.6.

4.3.2 Studies on Alnico (H.Br) rotor having a 0.25mm working airgap

The geometry of the Alnico (H.Br) rotor was identical to the existing Cobalt rotor, thus the air-stabilisation permeance line was assumed to be unchanged. This is shown as line OB in Fig.4.18. The outer diameter of the rotor was 69.5mm and, when used with the standard stator, the working airgap of the generator was 0.25mm. Using the appropriate data in equation (4.22), the calculated working permeance line is shown as line OE in Fig.4.18.

In the initial development stage, the Alnico (H.Br) rotor was again shown to be not fully magnetised. Hall probe measurements were undertaken when the rotor was air-stabilised and the effective air-stabilisation flux density was 74mT. This is shown as point A on the air-stabilisation permeance line OB. A recoil line drawn from point A gives a working flux density at point C of 315mT and a calculated K of 6.68mWb. The measured K value was 7.8mWb.

Assuming the rotor to be fully magnetised and using the air-stabilisation permeance line OB, the predicted air-stabilisation flux density is 95mT (point B in Fig.4.18). The corresponding working flux density at point D is 395mT and the calculated K is 8.37mWb. When a fully magnetised Alnico (H.Br) rotor was made available, it had a measured air-stabilisation flux density of 85mT shown as point F in Fig.4.18. The

corresponding working flux density, at point G, is 385mT and the calculated K is 8.16mWb. The measured K value now had a higher value of 8.7mWb. This trend, showing higher measured K, was similar to that observed in the other generators investigated.

Five Alnico (H.Br) rotors were made available and their K values were measured to determine the sample variations. The results are plotted in Fig.4.19 and they shown that the K values are reasonably constant. As shown in Fig.4.20 the gradient of the Alnico (H.Br) demagnetisation curve is less than that of cobalt near its coercivity point H_c. If both magnets experience equal demagnetising force, H_{ext}, it can be seen that the cobalt material will experience a larger drop in the flux density than the Alnico (H.Br) material. This would make the Alnico (H.Br) magnet more stable than Cobalt and help to explain the more consistent K values measured on Alnico (H.Br) generators.

Clearly the previous sections have shown how difficult it is to get consistent predictions of K values even from sample rotors. Any attempt therefore to predict for new rotor designs without using test samples would be unlikely to succeed.

4.4 Inductance Calculations

The calculation of stator inductance L, when the rotor is at the position of peak stator flux linkage, was undertaken with the following assumptions,

(i) The reluctance paths seen by the stator winding are assumed to be those shown in Fig.4.21

(ii) The reluctance path between the rotor poles is neglected

(iii) The soft iron stator has infinite permeability

(iv) The permeability of the magnet is constant and equals its recoil permeability μ_{recoil}

(v) Eddy current, hysteresis and skin effects are neglected.

Based on these assumptions an estimation of the stator inductance is given by

$$L = 2p\frac{N^2}{S_T} = \left[\frac{1}{S_g + S_m} + \frac{2}{S_s} + \frac{1}{S_e}\right] 2pN^2 \qquad (4.28)$$

$$= L_{gm} + L_s + L_e$$

where p is the number of pole pairs and equals 3

N is the number of turns per pole and equals 12

S_T is the total reluctance per pole

S_g is the airgap reluctance per pole

S_m is the magnet reluctance per pole

S_s is the reluctance per slot

S_e is the end winding reluctance per pole

L_{gm} is the total magnet-airgap inductance

L_s is the total slot inductance

L_e is the total end winding inductance

The airgap reluctance is given as

$$S_g = \frac{\ell_g}{\mu_o A_g} = \frac{2\ell_g}{\mu_o(\ell_s + \ell_r)t}$$

where ℓ_g is the airgap between the rotor and stator

A_g is the effective airgap area defined by equation (4.18)

and assuming that the flux flows radially in the magnet pole, as shown in Fig.4.11, the magnet reluctance is

$$S_m = \frac{\ell_m}{\mu_o \mu_{recoil} A_m} \qquad (4.29)$$

By substituting for ℓ_m/A_m from equation (4.21), the magnet reluctance is then given as

$$S_m = \frac{\log_e(r_2/r_1)}{\mu_o \mu_{recoil}\ \theta t} \qquad (4.30)$$

For the existing generator having a Cobalt rotor and a 0.5mm airgap, the calculated airgap reluctance is $1.1 \times 10^6 H^{-1}$ while the magnet reluctance is $6.0 \times 10^6 H^{-1}$. Thus the total airgap-magnet inductance is

$$L_{gm} = \frac{2pN^2}{S_m + S_g} = 2p \times 20.3\mu H = 122\mu H \qquad (4.31)$$

With a rectangular open slot shown in Fig.4.22, the inductance due to ϕ_b is given as[43]

$$L_b = \frac{N^2}{C}\ \mu_o tb \qquad (4.32)$$

and the inductance due to ϕ_a is

$$L_a = \int_o^a (\frac{Nx}{a})^2 \mu_o \frac{t\delta x}{c} = \frac{N^2}{3c}\ \mu_o ta \qquad (4.33)$$

Therefore the inductance per slot is expressed as

$$L_{s_1} = L_a + L_b = N^2 \mu_o \frac{t}{c}(b + \frac{a}{3}) \qquad (4.34)$$

For the existing stator design, which has the dimensions given in Fig.4.22, the inductance per slot is 2.5μH while the total slot inductance is then

$$L_s = 2p(2L_{s_1}) = 30\mu H \qquad (4.35)$$

The calculation of end-winding inductance L_e is generally agreed to be difficult because the end-winding flux involves a three-dimensional field pattern with complex boundaries. It has been shown[17] that the estimation of end-winding inductance using various formulae, which were derived by a number of research workers, can give different estimations. Moreover, these formulae are given for specific machines which have soft iron rotors and are not general enough to be extended to cover permanent magnet machines which have low working permeability rotors.

Assuming that the paths of the end flux ϕ_e is as shown in Fig.4.23 and the permeability of the iron is infinite, then the end-winding inductance is given approximately by

$$L_e = 2pN^2\mu_o \frac{A_a}{\ell_a} \qquad (4.36)$$

By substituting L_{gm}, L_s and L_e from equations (4.31), (4.34) and (4.36) into equation (4.28), the stator inductance is then

$$L = 2pN^2\mu_o \left[\frac{t}{\left\{\frac{2\ell_g}{\ell_s+\ell_r} + \frac{\log(r_2/r_1)}{\theta\mu_{recoil}}\right\}} + \frac{2t}{C}\left(b+\frac{a}{3}\right) + \frac{A_a}{\ell_a} \right] \qquad (4.37)$$

Equation (4.37) shows that the stator inductance varies linearly with the axial length t and at t=0, $L=L_e$ the end-winding inductance.

Experiments were undertaken to obtain a value for the end-winding inductance of the generator. Direct accurate

measurement of L_e is not possible because this would require a machine having a very short axial length such that t→0. Using the method described by Barnes[44], the end-winding inductance can be estimated by extrapolating the measured inductances of generators having different axial lengths to the t=0 axis. These generators were constructed by stacking up identical standard axial length stators and permanent magnet rotors into single units as shown in Fig.4.24. The magnetisation state of the rotors has negligible effect on the stator inductance as demonstrated in Section 3.3.2 and thus rotors of the same magnet material can be randomly selected for the manufacture of these multiple length rotors.

The inductance of these generators was measured using the inductance measuring technique described in Section 3.3.1. A low frequency of 10Hz was used in the tests to minimise eddy current effects. Fig.4.25 shows the measured inductance variation with axial length. By extrapolation, the estimated end-winding inductance L_e is 40μH.

The tests were repeated for Alnico (N) rotors, and for the stators without rotors. In both cases, as is shown in Fig.4.25, the end-winding inductance is also estimated as 40μH.

Tests at 400Hz for each of the three cases above show that whilst eddy current effects reduce the overall stator inductance and make it non-linearly dependent on axial length, as shown in Fig.4.25, extrapolation still gives an estimated end-winding inductance of 40μH.

Thus the tests have demonstrated that, within experimental limits, the end-winding inductance of the existing generator is 40μH and it is insensitive to rotor materials and eddy current interactions.

The stator inductance of the existing Cobalt generator, which has a 0.5mm airgap, is calculated by adding its individual inductance components L_{gm}, L_s and L_e using equation (4.28). The calculated inductance is given in Table 4.7 and is compared with its measured value reproduced from Table 3.2.

Table 4.7 Comparison of Calculated and Measured Inductances of Cobalt Generator

Airgap (mm)	Stator Inductance (μH)			% Errors
	Calculated	Measured	Difference	
0.5	192	250	58	23
0.75	183	230	47	20
1.0	175	215	40	19

For comparison purposes, the inductance calculation of the standard axial length Cobalt generator has been extended to cover generators having working airgaps of 0.75mm and 1.0mm. The calculated inductances are given in Table 4.7 together with their corresponding measured values. For these generators, the stator inner diameter was increased to achieve the desired airgap.

The inductance of standard axial length generators having Alnico (N) and Alnico (H.Br) rotors have been calculated and are compared with their measured values in Table 4.8.

Table 4.8 Comparison of Calculated and Measured Inductances for Different Materials and Airgaps

Rotor material	Recoil permeability	Airgap (mm)	Stator Inductance (μH)			% Error
			Calculated	Measured	Difference	
Cobalt	12	.5	192	250	58	23
Alnico (N)	6	.5	136	200	64	32
Alnico (N.Br)	7	.25	150	218	68	31

Results given in Tables 4.7 and 4.8 show that good agreement has not been achieved from these tests and it is probable that with a low permeability rotor there is a significant component of flux which passes between adjacent rotor magnet poles. Thus by introducing an interpolar rotor reluctance S_p in parallel with the magnet reluctance S_m, a new equivalent circuit as shown in Fig.4.2.6 is obtained. From analysis, it can be shown that the stator inductance is now given as

$$L = N^2 2p\left[\frac{1}{S_g + S_{mp}} + \frac{2}{S_s} + \frac{1}{S_e}\right] \qquad (4.38)$$

and the magnet-interpolar permeance is

$$\frac{1}{S_{mp}} = \frac{1}{S_m} + \frac{1}{S_p} \qquad (4.39)$$

Substituting equation (4.39) into (4.38) and rearranging it, the interpolar rotor reluctance is

$$S_p = \frac{1}{\left[\frac{1}{\left(\frac{2pN^2}{L-L_e-L_s}\right) - S_g}\right] - \frac{1}{S_m}} \qquad (4.40)$$

Using the experimental values of L and L_e and the calculated values of L_s, S_g and S_m in equation (4.40), a value of S_p for each rotor is calculated and is shown in Table 4.9.

Table 4.9 Table of Calculated Interpolar Reluctances S_p

Rotor Material	Airgap (mm)	Reluctances $\times 10^6 H^{-1}$ S_m	S_g	S_p
Cobalt	0.5	6	1.1	9.65
Cobalt	0.75	6	1.65	10.0
Cobalt	1.0	6	2.2	10.1
Alnico (N)	0.5	12	1.1	10.3
Alnico (H.Br)	0.25	10.3	0.55	10.9

The value of S_p obtained in this way is fairly constant and has an average value of $10.2 \times 10^6 H^{-1}$.

Whilst this combination of experimental and calculated reluctances could probably be used for similar rotor geometries, any drastic change in rotor materials or geometries would make the calculation invalid.

4.5 Saliency Torque

As discussed in Section 2.4, the need for the saliency torque to be less than the turbine torque at standstill is an important design requirement for starting purposes. The saliency torque can be calculated by the use of the Maxwell stress concept[30,40]. The magnetic forces transmitted through space, or non-magnetic medium are considered by the following stress system,

(a) A tensile stress of magnitude $\frac{1}{2}BH$ Nm^{-2} (Fig.4.27)

(b) A compressive stress also of magnitude $\frac{1}{2}BH$ Nm^{-2} (Fig.4.28)

In the general case, when the flux density B acts at an angle θ normal to a surface the stress 'd' makes an angle 2θ with the normal (Fig.4.29)

The normal stress is then given as

$$d_n = \frac{B^2}{2\mu_o} \cos 2\theta = \frac{(B_n^2 + B_t^2)}{2\mu_o} (2\cos^2\theta - 1)$$

$$= \frac{1}{2\mu_o} (B_n^2 - B_t^2) \qquad (4.41)$$

while the tangential stress is

$$d_t = \frac{B^2}{2\mu_o} \sin 2\theta = \frac{(B_n^2 + B_t^2)}{2\mu_o} (2\cos\theta\sin\theta)$$

$$= \frac{B_n B_t}{\mu_o} \qquad (4.42)$$

where $\cos\theta = \dfrac{B_n}{\sqrt{B_n^2 + B_t^2}}$

$$\sin\theta = \frac{B_t}{\sqrt{B_n^2 + B_t^2}}$$

B_n is the normal component of B

B_t is the tangential component of B

By applying the stress calculation across the airgap path at radius r (Fig.4.30), the total torque developed is expressed as

$$T = rF = r2p \int_o^{\pi/p} d_t \, tr \, \delta\theta$$

$$= \frac{r^2 2pt}{\mu_o} \int_o^{\pi/p} B_n B_t \, d\theta \qquad (4.43)$$

Equation (4.43) shows that the saliency torque can be calculated if B_n and B_t at every point at radius r is known. Obviously the difficulties in predicting a sensible airgap flux density as discussed in Sections 4.1 and 4.2 would make it extremely unlikely that its components B_n and B_t could be obtained with any certainty. Hence saliency torque would be difficult to obtain without recourse to the building of test rotors.

4.6 Types of Permanent Magnet Materials and Their Considerations

The variety of permanent magnet materials available in the world market is extensive and they are generally classed as anisotropic and isotropic materials. Anisotropic magnets normally have superior properties compared to the isotropic types if they are used along the axis of initial polarisation. Fig.4.31 shows the demagnetisation curves of a limited range of metallic magnets[16] whilst Fig.4.32 illustrates the almost linear curves of the ferrite[16] and rare-earth[18,19] magnets. Table 4.10 compares the properties of various magnetic materials examined in this thesis.

Metallic magnets, which were early developments in magnet technology, have non-linear B/H curves and they are sensitive to irreversible demagnetisation, as described in Section 4.14. Ferrite magnets, which have recoil lines almost coincident with their demagnetisation curves, are more stable magnetically and are less prone to irreversible demagnetisation compared to metallic magnets. In a number of applications[6], these magnets have replaced metallic magnets because of their more stable

magnetic properties and lower relative cost. However ferrite magnets have low flux densities and tensile strength.

Recent developments in magnet technology for space research has introduced a new range of high energy rare-earth magnets. These magnets have better magnetic properties than the ferrite or metallic magnets, but they are relatively more expensive. However, with increasing manufacturing efficiency and quantity, and with the rapid rise in the cost of Cobalt which is an element used in most metallic magnets, the rare-earth magnets will soon be more competitive because less of this magnetic material is required to produce the same amount of flux.

The mechanical strength of the magnet material is also a major design consideration to prevent the rotor from disintegrating when it is operating at high speeds and experiencing high centrifugal force. In certain rotor designs[23], the rotor would have to be die cast with aluminium to give extra mechanical strength. The need for such a reinforcement structure, which would increase manufacturing difficulty and cost, cannot be determined until the rotor material and geometry has been decided, and discussed with the magnet and lamp manufacturer. Thus when selecting magnet materials, the designer must be able to view the production of the generator as a whole, for extra cost of one component may well be more than counterbalanced by consequent savings on other components.

As shown in Sections 4.2, 4.3 and 4.4 the permanent magnet material properties affect both K and L. Thus it was decided to investigate the effects of other magnet materials on K and L.

Table 4.10 Comparison of Properties of Various Magnets

Material	Type		Remanence Br(T)	Coercivity H_c (KAm^{-1})	$(BH)_{max}$ KJm^{-3}	Relative recoil permeability μ_{recoil}	Production	Machinability
35% Cobalt	metallic	isotropic	0.9	-20	2.6	12.0		
Alnico (Normal)	metallic	isotropic	0.725	-45	5.3	6.0		
Alnico (H.Br)	metallic	isotropic	0.8	-40	5.2	7.0	casting or sintering	Hard and brittle, grinding only
Alcomax IV	metallic	anisotropic	1.15	-60	11.8	4.4		
Supermagloy 20	rare-earth	anisotropic	0.92	-600	158.7	1.06		
Supermagloy 16	rare-earth	anisotropic	0.8	-560	120.0	1.06		
Supermagloy 10	rare-earth	anisotropic	0.625	-422	73.1	1.06		
HERA	rare-earth	anisotropic	0.55	-400	55.0	1.08	molding	no need of special tools

By using rotor and stator geometries which are identical to the existing design, the air-stabilisation and working permeance lines remain unchanged and are shown as lines OA and OB respectively in Fig.4.33. Three types of magnet materials, Alcomax IV, Feroba III and Supermagloy 20 are considered and their respective demagnetisation curves are drawn in Fig.4.33.

Using the calculation procedure described in Section 4.2.5, the air-stabilisation and working flux densities for the various magnets are calculated from Fig.4.33. The working flux density levels are shown in Table 4.11 together with their calculated K values. The inductances are calculated by using experimental values of S_e and S_p and calculated values of S_m, S_g and S_s in equation (4.38) and the results are also given in Table 4.11. Because any changes in rotor design affect both K and L, it is more sensible to observe their combined effect on the peak torque ($T_{max} = \frac{pK^2}{4L}$) when considering design changes. The value of T_{max} for the various rotors is calculated and compared in Table 4.11. The T_{max} of the existing Cobalt rotor, determined from calculated values of K = 5.72mWb and L = 247μH, is 0.099Nm. The comparison of T_{max} normalised to that of cobalt given in Table 4.11 suggests that a generator having a Supermagloy 20 rotor can generate 14 times more power than the existing design at the same speed. However the cost of a Supermagloy 20 rotor is about 20 times that of cobalt. So it can be seen that the design of a new rotor for the uprated generator requires a better utilization of permanent magnet materials to be cost-effective.

Table 4.11 Comparison of Calculated K and L Values.

Rotor material		Air-stabilisation		Recoil operation		Calculated K (mWb)	Calculated L (μH)	Calculated T_{max} (Nm)	T_{max} normalised to that of Cobalt
Type	Commercial name	Position in Fig.4.33	Flux density (mT)	Position in Fig.4.33	Flux density (mT)				
Metallic	Alcomax IV	C	140	E	420	8.9	208	.286	2.89
Ferrite	Feroba III	D	240	F	360	7.63	162	.270	2.73
Rare-earth	Supermagloy 20	A	520	B	820	17.38	162	1.398	14.12

4.7 Conclusion

This study has shown that the parameters K and L can only be calculated with limited accuracy using the design methods described in Sections 4.2 and 4.4. Furthermore, these methods are dependent on experimental data and cannot be used with confidence if the generator is radically redesigned. As described in Section 4.5, there is also difficulty in calculating saliency torque using the standard design method for permanent magnets. For these reasons a computer-aided design method described in Chapter 5 has been developed for the calculation of K, L and saliency torque based on a more fundamental study of the magnetic field of any proposed generator design.

CHAPTER 5

COMPUTER AIDED DESIGN

5.1 Introduction

The limitations of the standard design method can be overcome by analysing the magnetic circuit in greater detail. This is achieved by treating the circuit as a boundary value problem and solving the governing magnetic field equations. It is then possible to calculate the parameters K and L, and the saliency torque, and obtain an insight into the dependence of the performance of the generator on geometrical and material properties.

Because the geometry of the generator is rather complicated, and since it is important to account for the exact magnetisation and demagnetisation behaviour of the soft iron and permanent magnet pole pieces, it is not possible to use analytical[42] or integral[41] methods for solving the field equations. Therefore the field distribution has been computed by the numerical method of finite elements, which, like all numerical methods, reduces the problem to the inversion of a matrix of finite order. The finite element method[22-28,31-33] has been used widely for solving non-linear Poissonian problems, and is preferred to alternative methods such as the finite difference method[29,30,34,35,38] because of the ease with which irregularly shaped bounded regions can be discretized into a non-uniform mesh.

Computer programs, based on the finite element method, have been developed and used to calculate the two-dimensional

magnetic field in the active length of the machine during the initial magnetisation of the permanent magnets, subsequent air-stabilisation, and, finally, during recoil operation. The programs can calculate flux lines, magnetic induction, forces and torques for any arrangement of permanent magnet materials, iron cores and current carrying windings.

It has been assumed that the metallic magnets, viz. Cobalt, Alnico (N), Alnico (H.Br) and Alcomax IV, are magnetised with the complete rotor mounted in the stator core, the stator winding being used for excitation. The magnetisation calculation provides important information regarding the level of saturation attained throughout the rotor during magnetisation, and the direction of magnetisation, which is used in the subsequent air-stabilisation and recoil operation calculations. During air-stabilisation, when the complete rotor is removed from the stator core, the stabilised operating point varies throughout the magnet material. Thus, when the rotor is re-inserted into the stator, different regions of the magnet recoil from different stabilised points on the demagnetisation curve.

Since, in practice, the rare earth magnets would be magnetised in a separate magnetising jig, it has been assumed that they are fully magnetised in a specified direction before the rotor is assembled.

Once the magnetic field distribution has been calculated, the parameters K and L, and saliency torque, can be predicted to a much greater accuracy than could have been achieved by the methods described in chapter 4. Thus the prediction of the performance of the generator has been reduced to a mathematical

problem which takes account of field dependent material properties. Unfortunately complete information on the fundamental behaviour of permanent magnet materials is not available. For example, to the writer's knowledge, the dependence of the demagnetisation characteristic on the level of saturation attained during initial magnetisation has not been measured, nor has the variation of recoil permeability with stabilised operating point for metallic magnets, or the magnetic properties normal to the initial polarization direction. As a result the full potential of the mathematical models cannot be exploited.

To ease the calculations the following assumptions are made :

i) The magnetisation and demagnetisation curves are single valued, that is hysteresis is neglected.

ii) Eddy current effects are neglected.

iii) The permanent magnet materials are completely saturated during magnetisation, thus all parts of a magnet have the same demagnetisation curve.

iv) During recoil operation of the magnet the narrow recoil hysteresis loops, shown in Fig.4.1, are assumed to be recoil lines having a gradient of $\mu_0 \mu_{recoil}$, where μ_{recoil} is the recoil permeability of the magnet and has the value specified by the manufacturer.

v) The field problem is bounded at a boundary which is coincident with the outer surface of the stator core.

The calculations have been limited to a two-dimensional cross-section of the generator and do not account for the effect

of stray fields at the ends of the machine. However since the axial length of the generator is so short the end-winding inductance is a significant component. Therefore the end-winding inductance, which has been estimated earlier in section 4.4, is included in the calculation of total stator inductance.

The implementation of the finite element method has been eased by the availability of an automatic data generation routine which greatly reduces the amount of input data needed to specify the problem. Graphical routines have been developed to display the results of the finite element analysis and assist in the detection of input data errors, and assessment of the effects of changing machine geometry and magnetic materials.

5.2 Field Equations

In static magnetic field problems, the relationships between the vectors, H, B, J and M are given by Maxwell's equations :-

$$\text{Curl } H = J \tag{5.1}$$

$$\text{Div } B = O \tag{5.2}$$

$$B = \mu_0(H+M) \tag{5.3}$$

The magnetisation, M is given by

$$M = (\mu_r - 1)H$$

for soft magnetic materials, while that for hard magnetic materials, which are assumed to be anisotropic, is

$$M = M(B_{mag})$$

where B_{mag} is the component of the field in the preferred

direction of magnetisation. The component of magnetisation normal to the preferred direction is neglected.

The effect of the permanent magnet material can be represented by an equivalent current density distribution, J_m [36]. Assuming there are no macroscopic currents in the magnet

$$\text{Curl } H = 0 \tag{5.4}$$

$$\therefore \quad \text{Curl } \frac{B}{\mu_0} = \text{Curl}(H+M) = \text{Curl } M = J_m \tag{5.5}$$

Introducing the vector potential, A defined by

$$B = \text{Curl } A \tag{5.6}$$

and Div A = O, then the quasi-Poissonian equation is

$$\frac{\partial}{\partial x}\left(\frac{1}{\mu}\frac{\partial A}{\partial x}\right) + \frac{\partial}{\partial y}\left(\frac{1}{\mu}\frac{\partial A}{\partial y}\right) = -(J + J_m) \tag{5.7}$$

where J is the current density associated with current carrying conductors and J_m is the equivalent current density which represents $\text{Curl}(B/\mu_0)$ for the region containing the permanent magnet. In the magnet μ takes the value of μ_0 and represents $\mu_0\mu_r$ elsewhere.

Equation 5.7 can be solved, for specified boundary conditions, by the finite element method [36], which accounts for the field dependence of the source term, J_m.

5.3 Variational Formulation

The numerical solution of the finite element method to the partial differential equation (5.7) is obtained by formulating the problem in variational terms. By minimising an

integrated quantity, a functional, over the problem space, equation (5.7) together with the specified boundary conditions is satisfied. The appropriate functional[28] for a Poissonian class of problem is,

$$I = \int_R \left[\int_o^B HdB - JA \right] dR \qquad (5.8)$$

where R is the field region. Substituting for H and accounting for J_m, this becomes

$$I = \int_R \left[\int_o^B \frac{B}{\mu(B)} dB - (J+J_m)A \right] dR \qquad (5.9)$$

The first term of equation (5.9) represents the stored magnetic energy, whilst the second term represents electrical energy.

A slightly different formulation which incorporates the permanent magnetisation directly into the functional is obtained by substituting for H directly from equation (5.3) into equation (5.8) to give

$$I = \int_R \left[\int_o^B \frac{B}{\mu_0} dB - \int_o^B MdB - JA \right] dR \qquad (5.10)$$

where J is the specified current density in any current carrying conductors. For soft iron when $M = (\mu_r - 1) H$, then the functional is

$$I = \int_R \left[\int_o^B \frac{B}{\mu(B)} dB \right] dR \qquad (5.11)$$

The advantage of the formulation of equation (5.10) over equation (5.9) lies mainly in the ease with which the sources

of the field due to the magnetisation can be evaluated.

5.4 The Finite Element Method

The finite element method[52-57] develops the solution by minimising the appropriate energy functional given in section 5.3 over the problem space. It is implemented by dividing the space into a number of simple shapes, or elements, based on a distribution of nodes. These can be simple 1st order triangles within which B, $\mu(B)$ and J are assumed to be constant. Within these elements the field is related to the unknown function nodal values by simple relationships and this allows the functional to be evaluated and minimised readily.

In a translationally symmetric system, the only components of the field vectors are,

$$A = A_z, \qquad J = J_z$$

$$B = B_x \underline{i}_x + B_y \underline{i}_y = \frac{dA}{dy} \underline{i}_x - \frac{dA}{dx} \underline{i}_y \tag{5.12}$$

$$H = H_x \underline{i}_x + H_y \underline{i}_y$$

The general functional is

$$I = \int \left[\int_0^B \frac{B}{\mu} \, dB - \int_0^B M \, dB - JA \right] dx\,dy \tag{5.13}$$

R

where μ takes the value μ_0 in the permanent magnet and $\mu_0\mu_r$ elsewhere, M takes a value only in the permanent magnet, and J is a specified conduction current density.

For 2-dimensional planar problems equation (5.13) becomes

$$I = \int_R \left[\frac{1}{2\mu} \left\{ \left(\frac{\partial A}{\partial x}\right)^2 + \left(\frac{\partial A}{\partial y}\right)^2 \right\} - \int_0^B MdB - JA \right] dxdy \qquad (5.14)$$

If the angle between the preferred direction of magnetisation of the permanent magnet material and the positive Y-axis, is α_m, then the component of B in the preferred direction is,

$$B_{mag} = B_y \cos(\alpha_m) + B_x \sin(\alpha_m) \qquad (5.15)$$

and it follows that the field dependent magnetisation is $M(B_{mag})$. Within any triangular element, e, the vector potential function, A is assumed to vary linearly according to,

$$A^R = p^e + q^e x + r^e y \qquad (5.16)$$

Applying equation (5.16) to each vertex, 1, 2 and 3, of the typical element e of Fig.5.1 gives

$$\begin{aligned} A_1^e &= p^e + q^e x_1^e + r^e y_1^e \\ A_2^e &= p^e + q^e x_2^e + r^e y_2^e \\ A_3^e &= p^e + q^e x_3^e + r^e y_3^e \end{aligned} \qquad (5.17)$$

from which

$$p^e = \left\{ \frac{A_1^e \begin{vmatrix} x_2 & y_2 \\ x_3 & y_3 \end{vmatrix}^e + A_2^e \begin{vmatrix} x_3 & y_3 \\ x_1 & y_1 \end{vmatrix}^e + A_3^e \begin{vmatrix} x_1 & y_1 \\ x_2 & y_2 \end{vmatrix}^e}{2\Delta} \right\}$$

$$= \frac{1}{2\Delta} \sum_{i=1}^{3} A_i^e \, p_i^e \qquad (5.18)$$

where Δ is the area of the element,

$$q^e = \{ \frac{A_1^e(y_2-y_3)^e + A_2^e(y_3-y_1)^e + A_3^e(y_1-y_2)^e}{2\Delta} \}$$

$$= \frac{1}{2\Delta} \sum_{i=1}^{3} A_i^e \; q_i^e \qquad (5.19)$$

$$x^e = \{ \frac{A_1^e(x_3-x_2)^e + A_2^e(x_1-x_3)^e + A_3^e(x_2-x_1)^e}{2\Delta} \}$$

$$= \frac{1}{2\Delta} \sum_{i=1}^{3} A_i^e \; r_i^e \qquad (5.20)$$

From equations (5.12) and (5.15), it follows that the magnet flux density is

$$B_{mag} = - \frac{\partial A}{\partial x} \cos(\alpha_m) + \frac{\partial A}{\partial y} \sin(\alpha_m)$$

$$= \frac{1}{2\Delta} \sum_{i=1}^{3} [-q_i^e \cos(\alpha_m) + r_i^e \sin(\alpha_m)] A_i^e \qquad (5.21)$$

The condition for minimisation of the functional, I of equation (5.14) is $\frac{\partial I}{\partial A_i} = 0$ for all nodes and

$$\sum_R \frac{\partial I}{\partial A_i^e} = 0 \text{ for all elements} \qquad (5.22)$$

For a typical element, e,

$$\frac{\partial I}{\partial A_i^e} = \frac{\partial I}{\partial A_1}, \; \frac{\partial I}{\partial A_2}, \; \frac{\partial I}{\partial A_3} \qquad (5.23)$$

From equation (5.14)

$$\frac{\partial I}{\partial A_i} = \int_R [\frac{1}{\mu} \{ \frac{\partial A}{\partial x} \frac{\partial}{\partial A_i} (\frac{\partial A}{\partial x}) + \frac{\partial A}{\partial y} \frac{\partial}{\partial A_i} (\frac{\partial A}{\partial y}) \}$$

$$- \frac{\partial}{\partial A_i} M(B_{mag}) \; B - J \frac{\partial A}{\partial A_i}] \; dxdy \qquad (5.24)$$

Using equations (5.18), (5.19), (5.20) and (5.21) to calculate the components of equation (5.24) and assuming μ and J are constant over an element, gives

$$\frac{\partial A}{\partial x} \cdot \frac{\partial}{\partial A_1} \left(\frac{\partial A}{\partial x}\right) = q^e \cdot \frac{q_1}{2\Delta}$$

$$= \frac{1}{2\Delta} \begin{bmatrix} q_1, q_2, q_3 \end{bmatrix} \begin{bmatrix} A_1 \\ A_2 \\ A_3 \end{bmatrix} \cdot \frac{q_1}{2\Delta}$$

$$\frac{\partial A}{\partial y} \cdot \frac{\partial}{\partial A_1} \left(\frac{\partial A}{\partial y}\right) = r^e \cdot \frac{r_1}{2\Delta}$$

$$= \frac{1}{2\Delta} \begin{bmatrix} r_1, r_2, r_3 \end{bmatrix} \begin{bmatrix} A_1 \\ A_2 \\ A_3 \end{bmatrix} \cdot \frac{r_1}{2\Delta}$$

$$\frac{\partial}{\partial A_1} M(B_{mag})B = M(B_{mag}) \frac{1}{2\Delta}(-q_1\cos(\alpha_m)+r_1\sin(\alpha_m))$$

and

$$\frac{\partial A}{\partial A_1} = \frac{\partial (p^e+q^e x+r^e y)}{\partial A_1}$$

$$= \frac{1}{2\Delta} \frac{\partial \left[\sum_{i=1}^{3} (A_i p_i + A_i q_i x + A_i r_i y)\right]}{\partial A_1}$$

$$= \frac{1}{2\Delta} \left[p_1 + q_1 x + r_1 y \right]$$

Thus,

$$\frac{\partial I}{\partial A_1} = \frac{\begin{bmatrix} q_1, q_2, q_3 \end{bmatrix}}{4\Delta^2 \mu} \begin{bmatrix} A_1 \\ A_2 \\ A_3 \end{bmatrix} q_1 \iint dxdy$$

$$+ \frac{\begin{bmatrix} r_1, r_2, r_3 \end{bmatrix}}{4\Delta^2 \mu} \begin{bmatrix} A_1 \\ A_2 \\ A_3 \end{bmatrix} r_1 \iint dxdy$$

$$- \frac{M(B_{maq})}{2\Delta} (-q_1\cos(\alpha_m) + r_1\sin(\alpha_m)) \iint dxdy$$

$$- \frac{J}{2\Delta} \iint (p_1 + q_1 x + r_1 y) dxdy \qquad (5.25)$$

Using $\iint dxdy = \Delta$ and $\frac{1}{2\Delta}\iint(p_1+q_1x+r_1y) = \frac{\Delta}{3}$ gives

$$\frac{\partial I}{\partial A_1} = \frac{1}{4\Delta\mu}\left[(q_1q_1+r_1r_1),\ (q_1q_2+r_1r_2),\ (q_1q_3+r_1r_3)\right]\begin{bmatrix}A_1\\A_2\\A_3\end{bmatrix}$$

$$-\frac{M(B_{mag})}{2}\left[-q_1\cos(\alpha_m) + r_1\sin(\alpha_m)\right] - J\frac{\Delta}{3} \qquad (5.26)$$

In equation (5.26), the value of an equivalent magnetic current at each node of a magnetised element is written explicitly in terms of the nodal coordinates and the state of magnetisation of the permanent magnet material.

Thus by deriving similar expressions for $\frac{\partial I}{\partial A_2}$ and $\frac{\partial I}{\partial A_3}$,

$$\frac{\partial I}{\partial A_1^e} = \frac{1}{4\Delta\mu}\begin{bmatrix}S_{11} & S_{12} & S_{13}\\ S_{12} & S_{22} & S_{23}\\ S_{13} & S_{23} & S_{33}\end{bmatrix}\begin{bmatrix}A_1\\A_2\\A_3\end{bmatrix}$$

$$-\begin{bmatrix} J\frac{\Delta}{3} + \frac{M(B_{mag})}{2}\left(-q_1{}^e\cos(\alpha_m) + r_1{}^e\sin(\alpha_m)\right)\\ J\frac{\Delta}{3} + \frac{M(B_{mag})}{2}\left(-q_2{}^e\cos(\alpha_m) + r_2{}^e\sin(\alpha_m)\right)\\ J\frac{\Delta}{3} + \frac{M(B_{mag})}{2}\left(-q_3{}^e\cos(\alpha_m) + r_3{}^e\sin(\alpha_m)\right)\end{bmatrix} \qquad (5.27)$$

where a typical coefficient of the square symmetric matrix is described in terms of the vertex coordinates according to,

$$S_{12} = (y_2-y_3)(y_3-y_1) + (x_3-x_2)(x_1-x_3) \qquad (5.28)$$

Assembling similar matrices for every element leads to a set of algebraic equations in which the vector potential at the

nodal points are the unknowns. The resulting equations are non-linear because of the dependence of $M(B_{mag})$ on the nodal potentials and the non-linear magnetisation characteristic of the soft iron elements. Thus the matrix representation of the whole system is

$$\begin{bmatrix} & & \\ & S & \\ & & \end{bmatrix} \begin{bmatrix} A_1 \\ A_2 \\ \vdots \\ A_n \end{bmatrix} = \begin{bmatrix} \mu_1 J \frac{\Delta_1}{3} + \mu_1 \frac{M}{2} a_1 \\ \\ \vdots \\ \mu_n J_n \frac{\Delta_n}{3} + \mu_n \frac{M_n}{2} a_n \end{bmatrix} \quad (5.29)$$

The assembled matrix $[S]$, where coefficients are a function of the x and y coordinates, is symmetrical about the leading diagonal and is banded, since nodal equations only involve contributions from elements connected to that node.

5.5 Boundary Conditions

In order to solve for the magnetic field distribution, the problem has to be bounded. Theoretically all the boundaries should be at infinity. But when the stator core has high permeability, it is acceptable to assume that the outer surface of the core is a flux line, i.e. there is no leakage flux from the back of the stator core. The same boundary has been assumed to apply during air-stabilisation and obviously this introduces some error. A technique[39] known as 'ballooning' would be appropriate to extend the boundary to infinity, however with limited time available this technique was not used in the computer programs.

5.5.1 The location of boundary surfaces

Because of symmetry, calculations of the magnetic field under 'open-circuit' conditions can be restricted to a half pole-pitch of the machine, the pole axis being a flux line and the interpole-axis an equipotential line. These boundary conditions are summarized in Fig.5.2. The symmetry of Fig.5.2 would also hold under load conditions if the armature reaction were entirely demagnetising, which would correspond to a short-circuit case at zero power factor, or entirely magnetising. If the rotor poles are displaced from the stator poles the calculation needs to embrace a complete pole-pitch of the machine.

5.5.2 Dirichlet boundary conditions

For a Dirichlet boundary condition[57], i.e. when the vector potential A is specified at the boundary, the finite element equations have to be modified so that the boundary condition is accounted for in the assembled matrix representation of the problem. In two-dimensional cartesian coordinates the Dirichlet boundary condition corresponds to a flux line.

5.5.3 Neumann boundary conditions

For a Neumann boundary condition[57], i.e. when the normal gradient of the vector potential $\frac{\partial A}{\partial n}$ is specified at the boundary, an additional term has to be included in the functional of equation (5.13). For $\frac{\partial A}{\partial n} = 0$, this term is zero, since the condition of zero tangential H is a natural boundary condition of the finite element method. In two-dimensional cartesian coordinates the Neumann boundary condition corresponds to a specified tangential flux density at the boundary surface.

5.5.4 Periodic boundary condition

A further type of boundary condition which has to be imposed when the symmetry of Fig.5.2 no longer holds is that of periodicity. During the saliency torque calculation, for example, when the rotor poles are mis-aligned with either the stator poles or interpoles, the calculations have to be extended to embrace a full pole pitch. At the radial boundaries 1 and 2 in Fig.5.3, the tangential components of the field will then be identical. It is then necessary to set $A_1 = -A_2$ at the corresponding boundary nodes.

5.6 Solution Of Finite Element Equations

The two principal methods of solving the set of non-linear algebraic equations resulting from the finite element method are the Direct method and the Iterative method.

5.6.1 Direct methods

By representing equation (5.29) as,

$$[S][A] = [b] \tag{5.30}$$

a solution is required for

$$[A] = [S]^{-1}[b] \tag{5.31}$$

The matrix equations can be solved from an initial estimate of the permeability distribution throughout the bounded region. Once the vector potential values have been calculated the flux density and hence the new permeability in each triangular mesh can be calculated. By using updated permeabilities the vector potentials can then be recalculated. The calculation of the vector of vector potentials, A, on each

iteration is by direct inversion of the stiffness matrix $[S]$. This iterative sequence can be continued until the solution for the vector potentials has converged to a specified and acceptable accuracy.

The disadvantage of a matrix inversion solution is that it requires a relatively large computer memory storage since the complete matrix $[S]$ has to be stored. If the problem is very large the time taken to solve the equations becomes excessive since the computing time is approximately proportional to the cubic power[58] of the number of equations.

To reduce both the computer memory storage and the solution time, various direct methods of solution which exploit the sparsity and banded form of the stiffness matrix $[S]$, such as Gaussian Elimination, Symmetric Choleski Factorisation, Pivotal Elimination and Chord Method, can be used. A standard ICL Scientific Subroutine, MCHB[66], which uses Gaussian Elimination to invert a banded symmetric matrix, is incorporated into the computer programs for solving the finite-element equations.

5.6.2 Iterative method

An alternative to the direct method of equation (5.30) is to employ an iterative method. From the matrix equation (5.29), the equation representing a particular node i takes the form

$$\sum_{j=1}^{n} S_{ij}A_j = b_i \qquad (5.32)$$

Therefore

$$A_i = \frac{b_i}{S_{ii}} - \sum_{\substack{j=1 \\ j\neq i}}^{n} \frac{S_{ij}}{S_{ii}} A_j \qquad (5.33)$$

where S_{ii} is the leading diagonal term in the matrix $[\overline{S}]$.

To initiate an iterative solution, the vector potentials are estimated so that the flux densities and hence permeabilities can be calculated. By using equation (5.33) a better estimate of the vector potential A_i for node i can be obtained. Equation (5.33) is applied to each node in turn, thus improving the estimates of the vector potential and permeability.

The vector potentials are calculated by an iterative process which can be summarized by

$$A_i^{m+1} = \frac{b_i^m}{S_{ii}} - \sum_{\substack{j=1 \\ j\neq i}}^{n} \frac{S_{ij}}{S_{ii}} A_j^m \qquad (5.34)$$

where m is the iteration number.

In order to improve the convergence of the iterative procedure, it is possible to accelerate the change in vector potential in successive iterations by using an acceleration factor γ. The accelerated vector potential is given by

$$A_i^n = A_i^m + \gamma (A_i^{m+1} - A_i^m) \qquad (5.35)$$

where A_i^{m+1} and A_i^m is given in equation (5.34).

If $\gamma < 1$, the method is termed under-relaxation, and over-relaxation if $\gamma > 1$. This procedure is called Successive Over-relaxation[60-62] or SOR.

5.6.3 Calculation of flux densities from vector potentials

The flux density, which is assumed to be constant in each element, can be calculated from the nodal vector potentials.

From equations (5.12), (5.16), (5.19) and (5.20), the flux density components are

$$B_x = \frac{\partial A^e}{\partial y} = r^e = \frac{1}{2\Delta} \sum_{i=1}^{3} A_i^e \; r_i^e \qquad (5.36)$$

and

$$B_y = - \frac{\partial A^e}{\partial x} = -q^e = - \frac{1}{2\Delta} \sum_{i=1}^{3} A_i^e \; q_i^e \qquad (5.37)$$

The flux density in an air or soft iron element is then

$$B = \sqrt{B_x^2 + B_y^2} \qquad (5.38)$$

whilst the flux density in a permanent magnet element is

$$B_{mag} = B_y \cos(\alpha_m) + B_x \sin(\alpha_m) \qquad (5.39)$$

5.7 Representation Of The B/H Curves

In field calculations, it is essential to represent the magnetic behaviour of all materials by suitable functions relating B and H. The B/H characteristics can be modelled by analytic functions[46-50] or by discrete points, with interpolation techniques[45]. Analytic functions are preferred since they do not introduce any discontinuity in the gradient of the characteristic.

The original stator laminations were stamped from Losil 800, an unorientated 1.6% silicon steel having a thickness of 0.5mm. The magnetisation curve for Losil 800 is shown in Fig.5.4. Transil 335, an unorientated 2.6% silicon steel with a thickness of 0.35mm was considered as an alternative material for reducing eddy current losses in the stator. Transil 335 has a higher

resistivity and available laminations were thinner than those of Losil 800. An investigation of alternative stator laminations is described in Appendix C. The magnetisation curve of Transil 335 is also shown in Fig.5.4 together with that of mild steel which was used on some of the rotors to be considered.

During the magnetisation calculation, described in section 5.11.1, the magnetisation curve of the permanent magnet material must also be defined. Fig.5.5 shows the magnetisation curves for 35% Cobalt and Alnico(N). The magnetisation calculations of rare earth magnets are not considered as they are assumed to be fully magnetised in a specified direction.

Of the various mathematical functions[46-50] which can be used to represent the magnetisation curves shown in Figs.5.4 and 5.5, it has been found that the most suitable function is

$$B = \mu_0 H + s_1 \tan^{-1} a_1 H + s_2 \tan^{-1} a_2 H \qquad (5.40)$$

where the coefficients s_1, s_2, a_1 and a_2 depend on the particular material. The ccefficients have been determined by a least squares fit technique[37] using a routine which is available in the University of Sheffield ICL 1906S computer. Figs.5.4 and 5.5 show that whilst equation (5.40) is an excellent fit to the magnetisation curve of the soft iron materials, it is only accurate for highly saturated permanent magnet materials. It will be seen from Fig.5.5 that by including an extra term[47], $S_3 He^{-a_3 H}$, into equation (5.40), improved accuracy at low flux densities can be achieved. However, such a refinement is unnecessary in the study since the magnets are to be magnetised to saturation.

After magnetisation the magnet has to be air-stabilised. The magnet then operates on its demagnetisation curve. Fig.5.6 shows the demagnetisation curves for the metallic magnets, while Fig.5.7 shows the demagnetisation curves for the rare-earth magnets. A suitable function to represent these curves is[2]

$$H = \frac{H_c(B_r - B)}{B_r(1+\alpha B+\beta B^2)} \qquad (5.41)$$

where

$$\alpha = \frac{H_c - 2H_m}{B_m H_m}$$

$$\beta = \frac{H_m B_r - B_m H_c}{B_m^2 H_m B_r}$$

B_m is the flux density at $(BH)_{max}$

H_m is the magnetic field strength at $(BH)_{max}$

B_r is the remanence flux density

H_c is the coercivity magnetic field strength

$(BH)_{max}$ is the maximum energy product of the material

Figs.5.6 and 5.7 show that the accuracy of the curve fit is high for both metallic and rare-earth magnets.

After air-stabilisation, the rotor is inserted into the stator and the magnet then operates on a recoil line as shown in Fig.4.1. The equation of a recoil line takes the form,

$$H = \frac{B - B_{stab}}{\mu_0 \mu_{recoil}} + H_{stab} \qquad (5.42)$$

where B_{stab} and H_{stab} identify the air-stabilisation point on the demagnetisation curve, and B and H represent the working point of the magnet.

5.8 Implementation Of The Finite Element Method

The major advantages of the finite element method over the standard design method described in section 4.1 lie mainly in the ability to account for leakage flux in complex configurations of magnetic circuit and to allow different parts of the magnet to operate at different flux density levels. The results of the finite element calculation are used to calculate the parameters K and L, and the saliency torque.

Computer programs have been developed to implement the variational formulation of equation (5.13). The set of non-linear equations developed in section 5.4 have been solved iteratively by Gaussian Elimination, a direct method of solving a banded matrix as described in section 5.6.1. From initial estimates of the flux density B and permeability μ, the finite element equations are solved to determine the nodal vector potentials. With known vector potentials the iterative calculation is repeated for updated values of B and μ and the process continued until the variations in all the nodal vector potentials between successive iterative cycles, δA, is less than 0.05%. Using equation (5.38), the maximum error in calculating the flux density in any element is

$$\varepsilon = \frac{2.\delta A.3 + 2.\delta A.3}{2} = 6.\delta A = 0.3\%$$

However the overall accuracy of the solution depends very much on the size of the mesh.

To reduce the possibility of instability in the iterative calculation, when the solution would begin to oscillate, and to guarantee convergence to a solution, the permeabilities are

under-relaxed by a factor ω. The under-relaxed permeability is given by

$$\mu_i^n = \mu_i^m + \omega (\mu_i^{m+1} - \mu_i^m) \qquad (5.43)$$

where μ_i^m is the permeability after m iterations

μ_i^{m+1} is the updated permeability

An under-relaxation factor is also applied to the change in B, hence M, between successive iterations. As ω decreases, the number of iterations rises, but if ω is too large the calculation becomes oscillatory. The rate of convergence depends on the factor ω, initial estimates of the magnetic flux density and the problem configuration. Due to lack of time, no attempt has been made to optimise the under-relaxation factor.

Calculations confirm that 'safe' under-relaxation factors lie within the range 0.1 to 0.25, as suggested by Binns[36]. The rate of convergence of the calculation also depends on the initial estimate of the flux density in the permanent magnet. For the air-stabilisation calculation, when the final flux density is expected to be low the initial flux density has been varied between $0.1B_m$ and $0.7B_m$. For recoil operation calculation, when the flux density is expected to be higher because of the presence of stator iron, a first estimate between B_m and $0.9B_m$ has been used.

During the air-stabilisation and recoil operations, all parts of the magnet are initially assumed to operate at the same estimated working flux density so that the equivalent current distribution (J_m) becomes merely a current sheet at the surface

of the magnet. As the iterative calculation proceeds, the equivalent current density of each magnet element is redistributed over the magnet depending upon the non-uniformity of the flux density distribution within the magnet.

Field calculations under load conditions have not been considered because section 3.6 has shown that with known K, L, R, I and R_L the electrical torque developed can be predicted.

5.9 Data Preparation For The Finite Element Method

The application of the finite element technique requires a large amount of data preparation. The input data required to execute the calculation includes nodal coordinates, element nodes, material properties and boundary conditions. A large proportion of this data can be generated automatically, reducing both labour and the likelihood of data errors.

5.9.1 Mesh generation

A commercially available discretisation program has been used to generate all the mesh data automatically from a much smaller amount of data needed to define the problem. The program is available on the University of Sheffield ICL 1906S computer, and is known as 'Program for Automatic Finite Element Calculations' or PAFEC[61]. In order to use this mesh generation facility each problem has to be subdivided into trapezoidal or triangular blocks, as shown in Fig.5.8. The vertex coordinates of each block are specified together with an integer number which represents the material of that block. The mesh density in each block can be varied. Fine meshes are used in regions in which the gradient of the field is expected to vary rapidly

in space. Coarser meshes are used if field variations are expected to be fairly uniform. Obviously if the mesh is too coarse, it will affect the accuracy of the calculation since the finite element calculation assumes a linear variation of A between nodes, and a constant flux density within each element.

Fig.5.9 shows two finite element meshes generated using PAFEC. The node numbering sequence in each mesh is not optimised with respect to matrix bandwidth and thus produces an unacceptably high bandwidth. As it stands such data would be very inefficient if used with the direct methods of solution described in section 5.6.1 even if sparsity of the matrix was exploited.

5.9.2 Bandwidth minimisation

The bandwidth of a matrix equation is defined as the difference between the highest and lowest equation numbers to which that equation is coupled. Since a direct method is used to solve the finite element equations, the bandwidth is critical in determining the computer storage requirement because only the banded coefficients (both zero and non-zero) about the leading diagonal are stored. Therefore the bandwidth of the matrix [S] must be minimised for high computing efficiency.

In the discretized field region, the maximum bandwidth of the finite element equations is determined by the maximum difference between connected nodes. Thus the node numbering is a very important consideration in solving the field problem. The node numbering in the mesh generated by PAFEC, although systematic, does not minimise the bandwidth of the coefficient

matrix [S]. To optimise the nodal numbering, a method developed by Cuthill-McKee[62-63] has been used to renumber the nodes. For example, the initial bandwidth of the mesh, shown in Fig. 5.9a, generated by PAFEC is 190, but after using the Cuthill-McKee algorithm the bandwidth is reduced to 25.

When periodic boundary conditions are to be imposed, additional elements are added temporarily to the mesh system generated by PAFEC. These elements link the nodes at the periodic boundaries so that the bandwidth minimisation scheme can account for the subsequent coupling of those nodes when the periodic boundary conditions are incorporated into the finite element equations. Fig.5.10 shows a typical finite element mesh system and the additional elements which link the periodic nodes. Once the bandwidth has been minimised the added elements are removed. The bandwidth of Fig.5.10 mesh after PAFEC is 310, but after being optimised it reduces to 34.

5.9.3 General sequence of using finite element programs

After optimising the node numbering of the mesh so as to minimise the bandwidth of the matrix [S], additional data is required to completely specify the problem. The finite element programs require the following additional data :-

i) The node numbers at which Dirichlet boundary conditions are specified, i.e. A is specified.

ii) The node numbers at which Neumann boundary conditions are specified, i.e. $\frac{\partial A}{\partial n}$ is specified.

iii) The coefficients of equations (5.40) and (5.41) which define the B/H characteristics of the soft iron and permanent magnet materials.

iv) The element numbers in which a specified conduction current of density J is to be imposed.

v) The maximum number of iterations to be performed.

Fig.5.11 summarises the sequence by which the final data file is obtained.

As described in section 5.4, each finite element mesh within the permanent magnet material is characterised by a preferred direction of magnetisation α_m, a known demagnetisation curve, an air-stabilisation flux density B_{stab}, a recoil characteristic and a working flux density B. The characteristics α_m, B_{stab} and B have to be calculated in three stages, which correspond to the magnetisation, air-stabilisation and recoil operation calculations.

Fig.5.12 shows the flow chart for the magnetisation calculation which is used to generate α_m in each magnet element for the metallic magnets. The air-stabilisation calculation, summarised in Fig.5.13, is used to establish B_{stab} whilst the recoil operation calculation summarised in Fig.5.14 calculates the working flux density B. The calculation of L, and saliency torque, uses data generated in the recoil calculation, as shown in Fig.5.14.

All the computer programs and data are stored in disc files and the programs are run on the University of Sheffield ICL 1906S computer. The general organization of the programming sequence is shown in Fig.5.15.

5.10 Calculation Of Peak Flux Linkage K

The determination of the parameter K requires three stages

in the field calculation. These correspond to initial magnetisation, air-stabilisation and recoil operation. The parameter K is obtained directly from the recoil operation calculation.

5.10.1 Initial magnetisation of metallic permanent magnet rotors

Since the information about the actual design of the magnetiser is not available, the following assumptions have been made :-

i) The material and geometry of the magnetiser are identical to those of the original stator, as shown in Fig.1.2.

ii) The magnetising winding is identical to the existing stator winding.

iii) The rotor and stator poles are aligned in the position of maximum stator flux linkage, as shown in Fig.4.10.

The magnetisation process is simulated by assuming a very high current passes through the stator winding to establish, if possible, an average magnetic field strength in the permanent magnet material of about five times that of coercive force of the magnet.[5,7,51] At the end of the magnetisation calculation, every finite element within the permanent magnet is scanned to ensure that it is completely magnetised to saturation. If the magnet has not been completely magnetised to saturation the calculation can be repeated with a higher magnetising current. Thus it can be seen that the magnetisation finite element program is a very useful aid to magnet manufacturers because it can be used for assessing the design of new magnetisers. However, such assessments are beyond the scope of this thesis.

Incomplete magnetisation of the magnet, which has been discussed in section 4.3, could have been taken into account in subsequent calculations if more data on minor B/H curves were available from the magnet manufacturer.

The magnetisation calculation gives the flux density components B_x and B_y in each element in the magnet, as shown in Fig.5.16. For isotropic magnetic materials, this information is used to calculate the direction of magnetisation α_m in each finite element within the magnet. The direction is calculated from

$$\alpha_m = \tan^{-1}(B_x/B_y) \qquad (5.44)$$

In complex rotor geometries α_m will vary from element to element. For anisotropic metallic magnets, like Alcomax IV, the direction of magnetisation α_m is assumed to be that specified by the manufacturer.

5.10.2 Air-stabilisation calculation

After the magnetisation stage the permanent magnet rotor has to be air-stabilised as discussed in section 4.1. This is done by removing the rotor from the magnetiser. The magnet now operates on the demagnetisation curve. Each magnet element is then assumed to have its demagnetisation curve acting only in the direction of magnetisation α_m. The component of magnetisation normal to α_m is neglected and its B/H value is assumed to be μ_0.

The air-stabilisation calculation gives the air-stabilisation flux density B_{stab} for every magnet element. This value of B_{stab} is then used in the recoil operation calculation so as to determine the working flux density of the element.

The importance of the air-stabilisation calculation is that in a complex rotor geometry the flux density varies throughout the magnet. Because of their non-linear demagnetisation curves, this variation in B_{stab} greatly affects the subsequent recoil operation of metallic magnets.

5.10.3 Recoil operation calculation

The rotor is reinserted into the stator for the recoil operation calculation. For the calculation of K, the stator winding is open-circuited and the rotor poles are aligned to the stator poles at the position of maximum stator flux linkage as shown in Fig.4.10.

During the recoil operation different elements of the magnet operate on recoil lines which depend on the air-stabilisation points, as described in section 4.1. These recoil lines have gradients of $\mu_0\mu_{recoil}$ where μ_{recoil} is the recoil permeability of the material. Parker and Studders[5] have shown that the recoil permeability can vary with the air-stabilisation point on the demagnetisation curve. This variation of μ_{recoil} can be incorporated into the field calculation by making μ_{recoil} a function of the air-stabilisation flux density B_{stab}. However, since the variation of μ_{recoil} has not been explored by the magnet manufacturers, the recoil permeability is assumed to be constant.

As in the preceeding calculations, the recoil operation calculation gives the vector potential A at every node in the finite element mesh. In a two-dimensional planar problem, the vector potential function has the property of a flux function.

Thus the average flux in the stator pole shown in Fig.5.17 is simply given by

$$\phi = t \frac{\sum_{j=1}^{k} 2A_j}{k} \qquad (5.45)$$

where t is the axial length of the stator

A_j is the vector potential at node j

k is the number of nodes on the parallel sides of the main stator pole, as shown in Fig.5.17

Thus the stator flux linkage is obtained from

$$K = N2p\phi \qquad (5.46)$$

5.11 Calculation Of Stator Winding Inductance L

For any salient pole generator, the stator inductance varies with rotor position because of changes in the permeability distribution. However, since the effective permeability of permanent magnet materials is relatively low, the stator winding inductance can be assumed to be constant. Tests described in chapter 3 have confirmed that this assumption is justified when predicting the electrical performance of the generator.

The stator inductance is defined as

$$L = 2p\ N \frac{\Phi}{I} \qquad (5.47)$$

As shown in section 4.4, equation (5.47) is difficult to apply if the flux paths are not well defined.

Erdelyi[38] has shown that the winding inductance of large alternators can be calculated at any load condition by using the permeability distribution, which is calculated for

that load condition and by assuming linearised behaviour for the inductance calculation. In the present work this linearisation is equivalent to assuming that the permeability in each finite element mesh is constant at the value calculated in the recoil operation. Thus by passing a current I though the stator winding, a further field calculation enables the inductance of the stator winding to be calculated. In discretized form, the inductance can be expressed as

$$L = 2p \frac{N}{I} \left[\frac{\sum_{j=1}^{k} \phi_j}{k} \right] = 2p \frac{Nt}{I} \left[\frac{\sum_{j=1}^{k} 2A_j}{k} \right] \qquad (5.48)$$

where A_j is the average vector potential in element j

k is the number of elements covered by the stator winding as shown in Fig.5.18.

The inductance calculated by equation (5.48) is the component contributed by the winding in the active length of the machine. A further inductance component due to the end-windings must be added. The calculation of end-winding inductance would require a three-dimensional field analysis as the end flux, shown in Fig.4.23, involves a three-dimensional flux pattern with complex boundaries. Tests described in section 4.4 have shown that the end-winding inductance can be assumed to be a constant of 40μH. Thus it is added into equation (5.48) for the calculation of the total stator inductance.

5.12 Saliency Torque Calculation

At starting, the torque of the selected air-turbine has to overcome the saliency torque of the generator. The saliency torque is determined from Maxwell's stress tensors[65], as discussed

in section 4.5. An alternative to Maxwell's stress is to employ a technique which calculates the change in stored energy with rotor position[64]. However with the limited time available this technique was not examined.

The total force on the rotor is obtained by integrating the magnetic stresses on a surface which completely encloses the rotor. By applying a tangential stress calculation across the airgap path at radius r in Fig.5.19, the total torque derived in equation (4.43) is expressed as

$$T = r^2 \frac{2pt}{\mu_0} \int_0^{\pi/p} B_n B_t \, d\theta \qquad (5.49)$$

In discretized form, the torque is given as,

$$T = r^2 \frac{2pt}{\mu_0} \sum_{j=1}^{i} B_{rj} B_{\theta j} \delta\theta_j \qquad (5.50)$$

where p is the number of pole pairs

t is the axial length of the generator

$B_{\theta j}$ is the radial flux density at element j

B_{rj} is the tangential flux density at element j

$\delta\theta_j$ is the subtended angle of element j from the centre of the generator

i is the number of elements in the integration path shown in Fig.5.19.

The results from the recoil operation calculation give the flux density components B_x and B_y in every element. By transforming B_{xj} and B_{yj} of element j into their cylindrical components, the tangential flux density is given as

$$B_{\theta j} = B_{xj}\cos\theta + B_{yi}\sin\theta \qquad (5.51)$$

and the radial flux density is

$$B_{rj} = -B_{xj}\sin\theta + B_{yi}\cos\theta \qquad (5.52)$$

Using equation (5.50), the total torque is calculated by summing the torque contribution of each element in the integration path in the airgap path (Fig.5.19).

To determine the maximum saliency torque, the torque has to be calculated at various degrees of misalignment between the stator and rotor poles. To ease the computation, calculations are performed by moving the stator core relative to the rotor. Thus the rotor mesh, and hence all the B_{stab} and α_m data, remains unchanged. Changing the rotor mesh would have necessitated fresh magnetisation and air-stabilisation calculations to provide data for the recoil operation calculation.

CHAPTER 6

INVESTIGATIONS OF VARIOUS GENERATOR DESIGNS

6.1 Introduction

Using the standard design methods described in chapter 4, the parameters K and L can be calculated only with limited accuracy, and there is difficulty in calculating saliency torque which is an important parameter for starting purposes, as discussed in section 2.4. Thus the finite element method described in chapter 5 is used as an alternative to the standard design methods for the calculation of K, L and saliency torque. This method offers great advantages because it can account for leakage flux, complex configurations of the magnetic circuit, directional properties of the magnet and difficulties due to different parts of the magnet operating at different flux density levels.

Initially the finite element method was used to model the test generators described in chapters 3 and 4 so that the accuracy of the method could be established. The next stage was then to consider the design of a 250W generator. Obviously the number of possible design changes is very large. Bearing in mind the design specifications outlined in section 1.3, design changes are restricted to those which have the same frame size as the present generator. The possibility of using a three-phase winding instead of a single-phase winding is discussed in Appendix D. However, after consultation with the lamp manufacturer this design was rejected because of higher production costs. Bearing in mind these economic considerations the

following design changes were investigated,

i) The effects of changing rotor designs and magnetic materials.

ii) The effects of using tangentially magnetised magnets.

iii) The effects of changing the number of poles.

Since changes in rotor designs affect both K and L it is more useful to judge their combined effect on the peak torque ($T_{max} = pK^2/4L$) when considering new designs. Using the measured K and L values from Tables 3.1 and 3.2, the T_{max} of the existing 55W Cobalt generator is 0.119Nm. Referring to the design strategy discussed in chapter 2, the T_{max} of the 250W generator should be at least 0.119 x 250/55 = 0.54Nm.

After selecting a rotor design which gives the required T_{max}, the maximum saliency torque produced by the generator must be determined. Since the rotor and stator are complex in geometry, the variation in saliency torque has to be calculated at intervals over one pole pitch in order to establish its maximum value.

The overall design approach for the 250W generator is summarized in the flow chart given in Fig.6.1. Fig.6.2 shows some of the rotor geometries which are examined in this chapter.

6.2 Verification Of Measured Parameters K and L

Initial studies were carried out on generators having

(a) Cobalt rotors with 0.5mm, 0.75mm and 1.0mm working airgaps

(b) an Alnico (N) rotor with a 0.5mm working airgap and

(c) on an Alnico (H.Br) rotor with a 0.25mm working airgap.

6.2.1 Existing 55W Cobalt design

A finite element mesh was generated so as to allow the existing Cobalt generator having a 0.5mm working airgap to be modelled. The generated mesh shown in Fig.6.3 has 251 nodes and 439 elements. The magnetic property of each element was defined as that of air, soft iron, or permanent magnet by assigning the appropriate material number to that element. The same mesh was used for the magnetisation, air-stabilisation, recoil operation and inductance calculations so that the magnetic characteristics and intermediate calculated results of each element could be maintained and be transferred between disc files.

As discussed in section 5.10.1, the magnetisation calculation of the Cobalt rotor is used to determine the preferred direction of magnetisation α_m in each magnet element. Fig.6.4(a) shows the calculated flux pattern during magnetisation and Fig. 6.4(b) shows the relative magnitude and direction of the flux density in each finite element mesh. The direction of flux density in the magnet element represents the α_m of that element. Fig.6.4(b) shows that α_m varies throughout the magnet.

After magnetisation the rotor was removed from the stator and air-stabilised, as shown in Fig.6.5. This was achieved by altering the material number of the soft iron stator to that of air. With the rotor air-stabilised, various parts of the magnet operate at different flux density levels on the demagnetisation curve. Fig.6.5(a) shows the calculated flux pattern during air-stabilisation while Fig.6.5(b) shows the corresponding flux density distribution. A contour line ABC is drawn in Fig.6.5(b) and the flux density distribution along the contour during air-

TABLE 6.1

Comparison of Calculated and Measured K and L

Rotor geometry referring to Figure	Magnet material in rotor	Working airgap (mm)	Flux linkage K(mWb)		Inductance L(μH)		T_{max}(Nm) using		Inductance L(μH) when rotor poles are aligned to stator interpoles	
			Calculated	Measured	Calculated	Measured	Calculated K & L	Measured K & L	Calculated	Measured
6.4	Cobalt	0.5	6.21	6.3	253	250	0.114	0.119	260	265
6.11	Alnico (N)	0.5	8.0	8.5	196	200	0.245	0.271	206	210
6.13	Alnico (H.Br)	0.25	8.5	8.7	222	218	0.244	0.260	225	230
6.15	Alcomax IV	0.5	8.9	9.0	310	297	0.192	205	340	328
6.17	Alcomax IV	0.5	10.45	-	214	-	0.383	-	230	-
6.20	Supermagloy 16	non-uniform	2.4	3.1	120	127	0.036	0.057	120	127
6.24	Supermagloy 10	1.0	8.65	11.2	120	128	0.468	0.735	120	128
6.30	Supermagloy 10	1.0	13.02	14.38	134	135	0.949	1.149	134	135

stabilisation is plotted in Fig.6.6. Assuming that the contour ABC represents the mid-axial length of the rotor, Hall probe measurements from Table 4.1 are included in Fig.6.6 for comparison purposes and show reasonable agreement with the calculated values.

By re-inserting the rotor into the stator core, for the recoil operation calculation, different parts of the magnet recoiled to a range of working points. The stator was not saturated and there was a high, though variable, permeability distribution throughout the stator. The calculated flux pattern and flux density distribution during the recoil operation are shown in Fig.6.7. The calculated K given in Table 6.1 shows good agreement with the measured value obtained from Table 3.1. The flux density distribution along the contour line ABC in Fig.6.7(b) for the recoil operation is compared with its Hall probe measurements, from Table 4.1, in Fig.6.6 and again shows reasonable agreement.

As discussed in section 5.11, the calculation of inductance assumes the same permeability distribution as that calculated for the recoil operation. The flux lines and flux density distribution during the inductance calculation are shown in Fig.6.8. It can be seen that the flux lines in Fig.6.8 differ from those during magnetisation (Fig.6.4) because stator and rotor materials are no longer saturated, and obviously the permeability distribution is different. As shown in Table 6.1 the calculated inductance compares well with its measured value reproduced from Table 3.2.

To confirm that the inductance was almost constant and independent of rotor position a calculation was made with the rotor pole aligned with the stator interpole. In this position, the expected stator flux linkage was almost zero (40μWb as compared to 6.21mWb previously). The new permeability distribution for this position gave a calculated inductance of 260μH which, as shown in Table 6.1, is close to its measured value and differs by only 5μH from the inductance when the stator and rotor poles are aligned. The corresponding flux density distributions and modified boundary conditions for these calculations are shown in Fig.6.9.

The comparisons of the calculated and measured K and L in Table 6.1 show that the finite element method can predict these two important parameters of the existing Cobalt design with much greater accuracy than the standard design methods, bearing in mind the three-dimensional effects, rotor sample variations, pole sample variations and the uncertain behaviour of magnets in directions normal to the initial direction of magnetisation α_m.

6.2.2 Effects of changing working airgaps in the Cobalt generators

The finite element method was next used to model Cobalt generators having different working airgaps of 0.25mm, 0.75mm and 1.0mm. The magnetisation and air-stabilisation calculation stages were omitted because the values of α_m and $B_{stab.}$ in each magnet element were those values calculated previously. The changes in airgap on the mesh were achieved by shifting those nodes at the inner bore of the stator.

The recoil operation and inductance calculations were undertaken for the different airgap values. The variation of K and L with airgap length is plotted in Fig.6.10. Measured K and L from Tables 4.3 and 4.8 are also included in the figure for comparison purposes. Again the results show very close agreement. Tests on a 0.25mm airgap Cobalt generator could not be undertaken as this would require a new lamination stamping tool for the manufacture of a smaller airgap stator. However with such good agreement for the other three cases, close agreement was also expected for the 0.25mm airgap generator. The corresponding T_{max} values are shown in Fig.6.10(c). Clearly an improvement of 17% in T_{max} is possible if the airgap of the existing generator is reduced to 0.25mm but this will be at the expense of closer manufacturing tolerances. It must be emphasised that decreasing the airgap may not always result in a higher T_{max} since an increased K may be offset by a more rapid increase in L.

6.2.3 Alnico (N) rotor

The Alnico (N) rotor had the same dimensions as the existing Cobalt rotor and hence the same mesh was used in the model. The magnetisation, air-stabilisation, recoil operation and inductance calculations were undertaken using the appropriate magnetising and demagnetisation characteristics of Alnico (N). The flux density distributions during the air-stabilisation and recoil operation are shown in Fig.6.11. A contour line ABC is drawn in Fig.6.11, and the flux density distributions along the contour for the two cases are shown in Fig.6.12. Hall probe measurements on the selected typical rotor pole are also included

in Fig.6.12. In Table 6.1, the calculated K and L values show good agreement with the corresponding measured values.

6.2.4 Alnico (H.Br) rotor

The Alnico (H.Br) rotor had a slightly larger outer diameter to achieve a working airgap of 0.25mm. To model this rotor the mesh shown in Fig.6.3 was slightly modified by shifting those nodes at the outer diameter of the rotor to obtain the smaller working airgap. The magnetisation, air-stabilisation, recoil operation and inductance calculations were undertaken using the appropriate characteristics of Alnico (H.Br). Fig. 6.13 shows the flux density distributions during the air-stabilisation and recoil operation calculations. Fig.6.14 compares the calculated and measured flux density distributions along the contour line ABC drawn in Fig.6.13.

Again good agreement between predicted and measured K and L values has been achieved as shown in Table 6.1.

6.3 Designing The 250W Generator

Section 6.2 has shown that the finite element method is capable of calculating the important design parameters K and L with sufficient accuracy. This design method was therefore used to examine various new rotor designs having different magnet materials and geometries, as well as rotors with different pole numbers.

With slight modifications, the mesh shown in Fig.6.3 was used for many of the new designs. The mesh was adapted for a particular design by moving the coordinates of the appropriate nodes to fit the boundaries of the stator and rotor, and by

altering the material number assigned to the elements to represent air, soft iron or permanent magnet. The same mesh was used for the magnetisation, air-stabilisation, recoil operation and inductance calculations so that the characteristics of each element could be maintained and be transferred between computer programs. However in some designs, a new mesh had to be used to minimise mesh errors due to badly formed triangular elements.

6.3.1 Alcomax IV rotor

A rotor construction shown in Fig.6.2'B' with blocks of anisotropic Alcomax IV[16] magnets was suggested and manufactured in the early development stages of the 250W design. The magnets were mounted on a mild steel hub and had 'U' shaped pole shoes as shown in Fig.6.15. Initially it was thought that the use of mild steel pole shoes would be an advantage because they would cause the magnets to air-stabilise at higher working flux densities and also minimise the demagnetisation effect of the external stator field. However, as shown later in this section, the use of such pole shoes leads to difficulties.

The magnetisation, air-stabilisation, recoil operation and inductance calculations were carried out using the B/H curve of mild steel for the pole shoes and centre hub, Losil 800 for the stator and Alcomax IV for the magnet. Flux density plots for the various calculation stages are shown in Fig.6.15. During the magnetisation process, it can be seen in Fig.6.15(a) that this rotor design has the disadvantage of diverting flux away from the magnet through the pole shoes. The calculated K and L values are compared with the measured values in Table 6.1 and

the results show good agreement considering the complexity of this design. The flux density distributions along the contour line ABC in Figs.6.15(b) and 6.15(c) are plotted in Fig.6.16. and Hall probe measurements included in the same figure show reasonable agreement. Fig.6.16 shows that the flux density along contour BC is lower during recoil operation than during air-stabilisation because during recoil operation, the reluctance of the stator is low and it affects the 'leakage' flux density along the contour BC.

Table 6.1 shows that the calculated T_{max} of this rotor is only 0.205Nm. Thus it can be seen that the use of the soft iron pole shoes is a disadvantage because they give rise to a high inductance which offsets the advantage of the higher K value achieved.

Calculations suggest that by reducing the size of the pole shoes as shown in Fig.6.17, the K and L values can be modified giving an increase of T_{max} to 0.383Nm. Clearly this construction could therefore be improved but the high cost of production makes it an impractical alternative.

6.3.2 Tangentially magnetised Alcomax IV rotor

The finite element method was used to study rotors with tangentially magnetised magnets. The magnet blocks are mounted on a soft iron hub in a tangential position, as shown in Fig. 6.18. To achieve the highest possible air-stabilised operation the magnets should be magnetised within the rotor iron structure. The corresponding flux density plots are shown in Fig.6.18. From these figures, it can be seen that the soft iron core shunts

the magnets during magnetisation and effectively short circuits the magnet during recoil operation, thus giving little flux across the airgap.

To overcome this flux diversion problem the central core of the rotor can be made non-magnetic as shown in Fig.6.19, leaving just small soft iron pole pieces between the magnets. The flux density plots for this design are shown in Fig.6.19. By comparing Figs.6.18 and 6.19 it can be seen that the modified rotor design (Fig.6.19) is an improvement because, during recoil operation, the majority of the magnet flux nodes flow across the airgap to the stator pole. This design was not pursued due to the complex structure now required for a non-magnetic hub.

6.3.3 Supermagloy 16 rotor

As discussed in section 4.15, magnets with almost linear demagnetisation curves, such as Supermagloy 16[19], have very stable magnetic properties and they are less likely to be demagnetised compared to metallic magnets if they are mishandled. Obviously this stable characteristic has a significant commercial advantage because the permanent magnet rotor can be removed from the lamp unit without any extra precaution during normal servicing. Recognising the need to keep down the inductance L, and on the advice of the magnet manufacturer, a rotor having a non-magnetic centre hub was constructed. Due to the high cost of Supermagloy 16 and the difficulty of machining curved faces on the material an initial trial rotor was constructed as shown in Fig.6.2'C'.

Since the magnets were magnetised before mounting on the hub, the magnetisation calculation was omitted and α_m of every

magnet element was assumed to be parallel to the X axis in Fig. 6.20. .Fig.6.20 shows the flux plots during the air-stabilisation and recoil operation calculations. Normally each magnet piece would be air-stabilised in isolation. However, as stated in section 4.1.5, the air-stabilisation point would not affect the recoil working point significantly because the demagnetisation curve of the magnet is almost linear. The calculated K and L values are compared with the measured values in Table 6.1. The results of L show good agreement, however the measured K is 30% higher than the calculated value. Thus further studies were undertaken in an attempt to understand the likely mechanism which caused the differences in the K values.

During air-stabilisation, the flux density at the centre of each magnet pole face, shown as location A in Fig.6.21, was measured with a Hall probe. The results showed that the flux density varied between 70mT and 50mT from pole to pole and the average value was 58mT. Such large variations in flux density were not expected because the air-stabilisation permeance line for each magnet was the same. This variation could be caused by variation in the Supermagloy 16 material due to manufacturing tolerances. The calculated flux density at location A was 41mT which was 70% lower than the measured average value. To correct for this higher measured value, the calculation of K was repeated for the case when B_{stab} of each magnet element was modified to 1.4 B_{stab} and the result showed that the increase in K was only 1.6%. This small increase in K was expected because the recoil line of Supermagloy 16 is almost coincident to the demagnetisation curve.

With the rotor inserted into the stator, the flux produced by the magnet was assumed to consist of five components, ϕ_A, ϕ_B, ϕ_C, ϕ_D and ϕ_E as shown in Fig.6.22. Hall probe measurements showed that the flux densities at locations D and E (Fig.6.22) were 20mT and 40mT respectively. Using the measured K value, the 'measured' flux density in the stator pole was calculated as 130mT. By comparing this 'measured' value with the leakage values at locations D and E, it would seem that, with such short magnet lengths, there was significant leakage fluxes ϕ_D and ϕ_E. But this could not have accounted for the difference between the measured and calculated K as the measured K was higher than the calculated value.

Hall probe measurement at location B in Fig.6.21 showed that the flux density during air-stabilisation was 15mT while during recoil operation, it was 20mT. This result confirmed that end-flux ϕ_B (Fig.6.22) at the end of the machine was significant for such a rotor design. With fringing fields, the reluctance path seen by the magnet will be lower than that calculated with the two-dimensional model. Thus, assuming that the two-dimensional air-stabilisation and working permeance lines are shown as lines OA and OC respectively in Fig.6.23, then for the three-dimensional case they would be shifted to lines OB and OD say, so it can be seen from Fig.6.23 that the fringing field at the ends of the machine would cause the magnet to actually operate at a higher working flux density than that calculated in the two-dimensional finite element program. This higher working flux density could explain why the measured air-stabilisation flux density and K value were higher than the

corresponding calculated values. The only way to confirm this difference between the measured and calculated values would be to develop a three-dimensional finite element program to model this rotor. However, as stated in chapter 5, the development of a three-dimensional finite element program is beyond the scope of this project.

Using the measured results of K and L in Table 6.1, the T_{max} was calculated as 0.057Nm. Obviously this rotor design was very poor in performance as there was high leakage flux and insufficient magnet mmf with such a thin slab of Supermagloy 16. Thus further study with more rare-earth magnet material was necessary, so that a rotor with such materials could be properly assessed.

6.3.4 Rotors with rare earth magnets mounted on a non-magnetic hub

Due to the high cost of the Supermagloy 16 material and the need to use larger quantities to achieve the required K value, larger magnets of cheaper, lower grade Supermagloy 10[19] material were used. Because of the uncertainties discussed in the previous section the precise amount of material required could not be determined. The design shown in Fig.6.24 was tried as a first estimate. The magnets were bonded onto mild steel backing plates which were bolted with brass screws onto a non-magnetic centre hub. If this rotor design was successful, then for the production version, an annular non-magnetic band would be used at the outer diameter of the rotor to restrain the magnets from flying out from the hub at high operating speeds.

TABLE 6.2

Increasing T_{max} using different grades of Supermagloy in a 1.0mm working airgap rotor

Supermagloy Grade	Calculated K(mWb)	Calculated L(μH)	Calculated T_{max} (Nm)
Supermagloy 10	8.65	120	.468
Supermagloy 16	10.45	120	.683
Supermagloy 20	11.99	120	.899

TABLE 6.3

Increasing T_{max} using increased radial depth of Supermagloy 10 material with a 1.0mm working airgap rotor

Maximum radial depth of magnet (mm)	Calculated K (mWb)	Calculated L (μH)	Calculated T_{max} (Nm)
8	8.65	120	.468
10	10.28	120	.660
12	11.43	120	.817
14	12.58	120	.989

Since the magnets were magnetised before mounting onto the hub, the magnetisation calculation was omitted and α_m of every magnet element was assumed to be parallel to the X-axis in Fig.6.24. The air-stabilisation, recoil operation and inductance calculations were undertaken using the B/H

characteristics of Losil 800 for the stator, mild steel for the backing plate and Supermagloy 10 for the magnet. The flux plots during the various calculation stages are shown in Fig.6.24. The calculated K and L values are shown in Table 6.1 together with the corresponding test results. While the L value shows good agreement, the calculated K is lower than the measured value. This observation is similar to that found for the Supermagloy 16 rotor discussed in the previous section. Thus flux density measurements with a Hall probe were carried out to examine the end-fringing fields and 'leakage' fields.

During air-stabilisation the flux density at the centre of each magnet pole, shown as location A in Fig.6.25, was measured and the results showed that the flux density varied between 180mT and 230mT. The large variation in flux density from pole to pole was similar to that observed in the previous case. This again suggests that there are wide manufacturing tolerances in the Supermagloy materials.

When the rotor was inserted into the stator, the flux produced by the magnet was again assumed to consist of five components ϕ_A, ϕ_B, ϕ_C, ϕ_D and ϕ_E as shown in Fig.6.26. Hall probe measurement at location E in Fig.6.26 showed that the flux density was 50mT, while the flux density at location B in Fig. 6.25 was 120mT. This measurement showed the presence of 'self-leakage' flux and end-fringing fields at the end of the machine. As explained in section 6.3.3, the end effects of the machine would cause the magnet to operate at a higher flux density level than that calculated with a two-dimensional finite element program. The higher operating flux density could help to explain

why the measured K was higher than the calculated value.

Using the measured K and L values, the T_{max} was calculated as 0.735 Nm and obviously the rotor design could be considered for the 250W generator. Saliency torque calculations were not attempted for this rotor as the two-dimensional finite element program could not account for the end-effects of the machine. Using the measurement technique described in Appendix A the maximum saliency torque for this rotor design was measured as 0.28Nm. This value is less than the standstill torque of any of the 3 nozzle turbines shown in Fig.2.5 and would therefore be acceptable.

Using the measured parameters, K, L and R and the 250W bulb ratings, I and R_L, in equation 3.14, the predicted variations of operating speed with turns factor are plotted in Fig.6.27. The graph shows that with an optimum turns factor of n = 3.37, the minimum operating speed would be 4,840 r.p.m. With a n=2 stator winding, the operating speed of the Supermagloy 10 generator was measured. The result shows good agreement with the predicted speed in Fig.6.27.

With the generator mounted on the experimental rig described in Appendix A and the n = 2 stator winding open circuit, the loss-torque speed curve was measured. The result is shown in Fig.6.28. Fig. 6.29 compares the measured torque speed curve of the generator powering a 24V 250W bulb and the corresponding predicted torque speed curve plus the loss torques of Fig.6.28. The results show good agreement and again verifying the analysis in section 3.6.1.

To examine the effect of using higher grade, but more expensive magnets in the Supermagloy[19] range, i.e. Supermagloy 16 and 20, the calculations of K and L were repeated for these two materials as direct replacements for the Supermagloy 10 material. The results are compared in Table 6.2. The increase in K with Supermagloy grades was as expected because of higher working flux densities in the magnet. The inductance L was constant for the different Supermagloys because the recoil permeability of the magnets is identical and the small permeability variations in the stator iron have negligible effect on L. The improvement in T_{max} for the 16 and 20 grade materials is also given in Table 6.2. Since an adequate design was possible with the Supermagloy 10 material and due to its much lower cost, future designs considered only this grade of material

From equation 4.5, it would seem that the K value could be increased by increasing the magnet radial depth. The maximum radial depth of the magnet shown in Fig.6.24 was 8mm and the working airgap was 1.0mm. By maintaining a constant working airgap of 1.0mm and increasing the maximum radial depth of the magnet from 8mm to 14mm in steps of 2mm, calculations of K, L and T_{max} were undertaken and the results are shown in Table 6.3. Clearly with larger amounts of rare earth magnets in the rotor, it is possible to design generators capable of producing powers in excess of 250W.

6.3.5 Supermagloy 10 magnets on a soft iron hub

By remounting the Supermagloy 10 magnets used in section 6.3.4 on a hexagonal mild steel hub, as shown in Fig.6.2'D', the

reluctance path of each magnet is lowered and this increases the working flux density and hence K. However, the final assessment depends on how the inductance L is affected by this modification. At the same time, the centre magnetic hub would reduce the fringing fields at the ends of the machine and reduce the field calculation to a more nearly two-dimensional problem.

The air-stabilisation, recoil operation and inductance calculations were undertaken using the magnetic characteristics of mild steel for the centre hub, Losil 800 for the stator and Supermagloy 10 for the magnet. The flux plots for the three calculation sequence are shown in Fig.6.30.

The calculated K and L values are compared with the measured values in Table 6.1. They show good agreement, suggesting that the mild steel centre hub has reduced the field calculation to a more two-dimensional problem. This was confirmed by the measurement of flux density at locations B and E in Fig.6.31 when the rotor was inserted into the stator. The measured values of 0.2mT and 20mT respectively are much lower than those obtained with a non-magnetic hub.

During air-stabilisation, the flux density at the centre of each magnet pole, shown as location A in Fig.6.31, was measured. The results show that the flux density varies between 310mT and 370mT from pole to pole. This variation in flux density was expected because the magnets used in this rotor were those from section 6.3.4.

As expected the measured K value has improved significantly

(28%) with the use of a magnetic hub but surprisingly, perhaps, the inductance has increased only by 12%.

Using the measured values of K and L, T_{max} is calculated as 1.15Nm which is 56% higher than that produced by the Supermagloy 10 rotor with a non-magnetic centre hub. When compared to the Cobalt rotor the improvement is dramatic giving a T_{max} improvement of 866%! Clearly, this type of rotor is technically superior to all those proposed previously and it was considered that this design should present no major manufacturing difficulty. The possibility of using arc-shaped magnets on a cylindrical hub, as shown in Fig.6.32, was briefly considered but the extra cost of the magnets far outweighed the cost of simpler hub construction.

The saliency torque of the Supermagloy 10 rotor with a mild steel hub was calculated using the finite element method described in section 5.12. The results are shown in Fig.6.33. Zero mechanical degrees in the figure refers to the position when the centre of the rotor pole is aligned to the centre of the stator pole while thirty mechanical degrees is the position when the rotor pole axis is aligned with the stator interpole axis. Fig.6.34 shows flux plots at various rotor positions. Using the measurement technique described in Appendix A, the saliency torque was measured and comparison with predictions is made in Fig.6.33. The double peak is due to the interpoles which effectively produce twelve salient poles on the stator.

The results show reasonable agreement with tests bearing in mind that there would be errors in the torque calculation introduced by regions where the flux density varies rapidly,

such as the corners of the rotor poles and stator poles. Improved torque calculation accuracy could be achieved, if the mesh density was increased. But this would require the calculations to be repeated with a new mesh. With limited time available the calculations were not attempted since the maximum saliency torque had already been determined.

To examine the effect of the stator interpoles, they were removed from the stator core, as shown in Fig.6.35. Measured saliency torques with the modified stator are plotted in Fig.6.33 and it can be seen that the maximum saliency torque has increased by 180%. This demonstrates the effectiveness of the stator interpoles in reducing the maximum saliency torque. Calculations of saliency torque for the case are also given in Fig.6.33 and again they show that the calculations are adequate for predictions of new designs. In the figure the saliency torque does not reach a maximum at 15^{o} mechanical (or $\pi/4$ electrical) because the width of the slots and stator poles are not equal. Fig.6.36 shows the flux plots at various rotor positions.

Using the measured parameters K, L and R, and the I and R_L for the 250W bulb, in equation 3.14, the variation of operating speed with turns factor is plotted in Fig.6.37. The graph shows that with optimum turns factor of n = 3.62 the minimum operating speed would be 3,600 r.p.m. The operating speed of the generator with a n = 2 stator winding was measured as 4,700 r.p.m. and is marked on Fig.6.37. Clearly the agreement is quite good.

With the stator winding open-circuited, the loss torques of the generator were measured and shown in Fig.6.38. The torque-speed curve of the generator, with a n = 2 stator winding, powering a 24V 250W bulb was measured. The result is shown in Fig.6.39 together with the predicted torque-speed curve of the generator driving the non-linear bulb plus the loss torques of Fig.6.38. Again the results show close agreement.

6.3.6 Effects of changing pole numbers

From equation 2.26, the maximum torque is given as

$$T_{max} = \frac{pK^2}{4L} \qquad (6.1)$$

From this expression an increase in pole pairs p looks attractive but the final outcome depends on how K and L are affected by changes in p. The purpose of this investigation is to establish a reasonable limit to the T_{max} of a single-phase generator having a Cobalt rotor or a Supermagloy 10 rotor, within the same frame size as the existing design. The geometry of the Cobalt rotor is similar to that shown in Fig.6.4, whilst the Supermagloy 10 rotor is similar to that shown in Fig.6.30. The radial dimensions of the generator are kept constant, so the inner and outer diameters of the stator and rotor were unchanged, and the airgap for the Cobalt rotor was maintained at 0.5mm while the airgap for the Supermagloy 10 rotor was 1.0mm.

The mesh shown in Fig.6.3 was modified for modelling generators having pole pairs between 2 and 6. This was achieved by altering the X and Y coordinates of the mesh to obtain the required pole arc. Using the coordinate system in Fig.6.40, the

modified coordinates of a node for a p pole machine is given as,

$$X_p = X_3 \frac{\cos(\theta_p)}{\cos(\theta_3)} \qquad (6.2)$$

and

$$Y_p = Y_3 \frac{\sin(\theta_p)}{\sin(\theta_3)} \qquad (6.3)$$

where

$$\theta_p = \frac{3\theta_3}{p}$$

$$\theta_3 = \tan^{-1}(Y_3/X_3)$$

X_3, Y_3 are the coordinates of a node in the p = 3 mesh, shown in Fig.6.3.

A different mesh shown in Fig.6.41, had to be used to model generators having pole pairs between 6 and 12. This was to minimise errors due to badly formed triangular meshes.

From equation 4.36, the end-winding inductance is given as

$$L_e = 2pN^2 A_a/\ell_a \qquad (6.4)$$

Since the effective area A_a is inversely proportional to p, the end-winding inductance is assumed to be 40μH for the generators, having different pole numbers, and this component must be added to the total stator inductance L.

For machines having different pole pairs p, it can be shown that the stator resistance is given as,

$$R = \frac{\rho(\frac{3\ell_s}{p} + t)p}{(\frac{3A}{p})} \times R_3 \frac{A}{\rho(\ell_s+t)3} = R_3 \frac{(\frac{3\ell_s}{p} + t)}{(\ell_s+t)} (\frac{p}{3})^2 \qquad (6.5)$$

where ℓ_s is the pole width of the existing stator design and equals 19.7mm

t is the axial length of the stator and equals 16.9mm

R_3 is the stator resistance for the p = 3 generator and equals 88mΩ

ρ is resistivity of conductor.

Fig.6.42 shows the predicted resistance variation with pole pairs using equation 6.5.

Fig.6.43 summarizes the organisation of the computer programs for the calculation of K, L and T_{max} for changes in pole pairs p.

It must be borne in mind that changing the pole numbers requires other considerations such as the cost of :

i) producing a new casting mould if the rotor is cast

ii) designing a new magnetiser if the rotor has to be magnetised after assembly

iii) producing new stator laminations.

In addition the lack of mechanical strength of the rotor poles may introduce difficulties as their width decreases.

(a) Cobalt rotors

The magnetisation, air-stabilisation, recoil operation and inductance calculations for Cobalt generators having different pole numbers were undertaken in sequence. Fig.6.44 shows the predicted variations of K, L and T_{max} with pole pairs p. For the two different meshes, the computations were duplicated to overlap at p = 6. This was to ensure that the changes in mesh systems had negligible effect on K and L predictions. Fig.6.44(a)

shows that the K value reaches a maximum at p = 8. At higher pole numbers (p > 8) the K value decreases because of higher leakage flux between the rotor poles as shown by an increase in the flux density along the contour line BC (Fig.6.7).

Fig.6.45 shows the flux plots during the various calculation stages for generators having different pole pairs.

In Fig.6.44(c) T_{max} reaches an upper limit of 0.18Nm at p = 6 at which it is 60% higher than the existing p = 3 design. Using the predicted K, L and R values from Figs.44 and 42 in equation 2.34, the minimum operating speed of the different pole generators powering a 24V 250W bulb was predicted and plotted in Fig.6.46. The results show that the lowest speed would be 14,000 r.p.m. for a p = 6 generator. Clearly therefore no Cobalt rotor could meet the desired specifications of running speed less than 7,000 r.p.m. Even if this limit was relaxed the extra cost of increased pole number designs would have to be considered. Set against this is the apparent ease with which the Supermagloy 10 rotor, tested in section 6.3.5, can be used to produce 250W in the existing stator core.

(b) <u>Supermagloy 10 rotors</u>

The air-stabilisation, recoil operation and inductance calculations for the Supermagloy 10 rotors having different pole numbers were undertaken. Fig.6.47 shows the predicted variations of K, L and T_{max} with p. In Fig.6.47(c) T_{max} is a maximum at p = 4, but this is only 4% above that for the p = 3 design. From economic considerations, obviously a 4% improvement is outweighed by the cost of producing a p = 4 stator. Fig. 6.48 shows

the flux plots during the various calculation stages for generators having different pole numbers. Using the predicted K, L and R values from Figs.6.47 and 6.42 in equation 2.34, the minimum operating speed of generators having different pole numbers powering a 24V 250W bulb was predicted and plotted in Fig.6.49. The results show that the speed for a p = 4 generator is 4,000 r.p.m. while the speed for a p = 3 generator is only 4,120 r.p.m.

6.4 Conclusion

This investigation has shown that the parameters K and L, and saliency torque, can be calculated with reasonable accuracy using the finite element method, provided the rotor does not have significant fringing fields at the ends of the machine. Using the Supermagloy 10 rotor tested in section 6.3.5, it is possible to design a 250W generator, which meets the design specificiations outlined in section 1.3. The use of the existing p = 3 stator design would minimise the overall cost of the new generator.

CHAPTER 7

OPTIMUM DESIGN OF GENERATORS

7.1 Introduction

Chapter 6 has considered the effect of various changes in rotor design on the T_{max} of the generator. A number of alternative designs based on rotors with metallic magnets and machines having increased pole numbers have already been eliminated. At this stage of the development work the lamp manufacturer was able to outline more definite design specifications. It was decided to select a new turbine nozzle angle giving an improved turbine output power and to try and ascertain the best design compromise for both the 250W and 55W generators using, where possible, the same generator components in order to reduce costs. Table 7.1 summarises the specifications for a 250W generator and a 55W generator.

The quantities marked * in Table 7.1 have not yet been finalised and can all be traded against each other to some extent. They will all incur different initial cost and/or operational penalties. The investigations in this Chapter attempt to demonstrate how these variables are interrelated and establish a possible design strategy.

Possible rotor designs for the 250W generator are examined in Section 7.5. Finally, for system protection, an electronic circuit has been designed to load the generator and prevent the rotor from overspeeding in the event of bulb failure.

Table 7.1

Design variables	250W generator	55W generator
Stator core	As existing stator design	
* Number of turns in stator winding	To be decided but preferably to be the same for both generators so that the stator winding can be standardised	
* Rotor magnet material	Rare-earth; actual material to be selected	35% Cobalt
* Rotor magnet geometry	To be determined but based on a soft iron centre hub	As the existing design
Airgap length	1.5mm, to give clearance for the use of an annular ring restrainer around the outer diameter of the rotor	0.5mm
Turbine nozzles	3 type 1 at 20°	1 type 1 at 20°
* Turbine pressure	To be decided but approximately 70 p.s.i. or less	To be decided but approximately 55 p.s.i. or less
* Operating speed	Preferably less than 7,500 r.p.m.	Preferably less than 9,000 r.p.m.
Bulb ratings	24V 250W	12V 55W
Type of lamp	Quartz halogen	Quartz halogen

7.2 Matching of Generator to Operate at Minimum Operating Speed

Section 2.4 has shown that by matching the generator and load, the operating speed of the generator can be minimised by using the optimum turns factor n_{min} which is given as

$$n_{min} = \frac{\frac{K}{IL}}{\sqrt{2 + \frac{R}{R_L}(\frac{K}{IL})^2}} \qquad (7.1)$$

If the Supermagloy 10 rotor tested in Section 6.3.5 is used in the 250W generator, and the generator and bulb are matched for $n_{min} = 3.6$, then the minimum operating speed is 3,600 r.p.m. Fig.7.1 shows the predicted torque-speed curve for this design and the desired operating point A. The turbine curves, reproduced from Fig.2.5, are also included in Fig.7.1 from which it is obvious that at the air-pressure of 70 p.s.i., the turbine and generator are not matched. For this generator design an operating pressure of approximately 120 p.s.i. would be required. The strategy of using optimum turns factor does not consider the limitations imposed by the turbine. Consequently a different approach has to be adopted to guarantee a suitable matching of turbine and generator within the specified turbine pressures and operating speeds.

7.3 Matching of Generator to Turbine

The turbine torque-speed curves for 3 type 1 20^{o} nozzles, shown in Fig.7.2, can be considered as a straight line of the form,

$$T_t = T_o - C\dot{\theta} = DP_{si} - C\dot{\theta} \qquad (7.2)$$

where T_o is the torque at standstill, which must be greater than the maximum saliency torque of the selected generator for starting purposes

C is the gradient of the torque-speed curves and equals 12.5×10^{-6}

$\dot{\theta}$ is the speed in r.p.m. and equals $\frac{\omega}{p} \frac{60}{2\pi}$

D is the pressure constant and equals 8.783×10^{-3}

P_{si} is the air pressure in p.s.i.

The power produced by the turbine is given as

$$P_T = T_t \frac{\omega}{p} = (T_o - C \frac{\omega}{p} \frac{60}{2\pi}) \frac{\omega}{p}$$

$$= -(\frac{1}{p}\sqrt{\frac{30C}{\pi}}\omega - \frac{T_o}{2}\sqrt{\frac{\pi}{30C}})^2 + \frac{T_o^2}{4} \frac{\pi}{30C} \qquad (7.3)$$

Fig.7.3 shows the parabolic power-speed curves of the turbine for different air-pressures. A datum line representing 250W is drawn in Fig.7.3 and obviously the turbine must be operating above the 250W line. This immediately restricts the operating speed range of turbine, and any power in excess of the output power and iron losses must be dissipated in the copper windings of the generator ($I^2n^2R/2$), assuming at this stage that mechanical losses can be neglected compared to the generated power.

The power demanded from the turbine by the generator, bulb and iron losses is given as

$$P_T = T_t \frac{\omega}{p} = \frac{I^2}{2}(n^2R + R_L) + T_i \frac{\omega}{p} \qquad (7.4)$$

where the iron loss torque, from Fig.6.38, is represented as

$$T_i = T_1 + C_1\dot{\theta} \qquad (7.5)$$

7.3.1 Design strategy for a specified generator, bulb rating and turbine-nozzle design

For a given generator design, the parameters p, K, L and R are fixed, and for a known bulb rating, I and R_L are specified. From equation (3.14), the operating rotor speed is related to the turns factor by

$$\dot{\theta} = \frac{\omega}{p}\frac{60}{2\pi} = \frac{60}{2\pi p}\frac{(n^2R + R_L)}{\sqrt{(\frac{nK}{I})^2 - (n^2L)^2}} \text{ r.p.m.} \qquad (7.6)$$

Substituting equations (7.2) and (7.5) into equation (7.4), the power supplied by the turbine is given as

$$P_T = (DP_{si} - C\dot{\theta})\frac{2\pi}{60}\dot{\theta}$$

$$= \frac{I^2}{2}(n^2R + R_L) + (T_1 + C_1\dot{\theta})\frac{2\pi}{60}\dot{\theta} \qquad (7.7)$$

Therefore, the air pressure required for a given bulb rating, generator and turbine-nozzle design is expressed as,

$$P_{si} = \frac{\frac{60}{2\pi\dot{\theta}}\frac{I^2}{2}(n^2R + R_L) + (C + C_1)\dot{\theta} + T_1}{D} \qquad (7.8)$$

Thus for any selected value of turns factor n, the required operating speed $\dot{\theta}$ is determined from equation (7.6) and the air pressure from equation (7.8).

Case Study:

For example, if the Supermagloy 10 rotor described in Section 6.3.5 is used in the 250W generator, Fig.7.4 shows the variations of operating speed $\dot{\theta}$ and air pressure P_{si} with turns factor n. The plots show that if the operating speed is 5,600 r.p.m., the turns factor is fixed at n=1.5 and the air pressure at 63 p.s.i.

The curves can be used in the opposite order, selecting first an air pressure and then finding the corresponding turns factor and speed. Obviously for higher electrical efficiency the turns factor should be kept as small as possible thus keeping the winding resistance to a minimum. Ultimately a compromise must be made between operating speed and air pressure, the former influencing such factors as audible noise and bearing wear, and the latter the air consumption of the lamp system.

7.3.2 Design strategy for a specified bulb rating and turbine characteristic

The previous approach described in Section 7.3.1 has assumed that the rotor design has previously been specified, thus fixing p, K, L and R. Alternative rotor designs using different types or amounts of magnet material, in order to reduce the rotor cost, will lead to different solutions for P_{si}, n and $\dot{\theta}$. For rotors with rare-earth magnets mounted on a soft iron centre hub and the pole number remaining unchanged, it has been found in section 7.4 that the inductance L is fairly constant. Thus for a selected operating air pressure P_{si}, the three variables n, ω and K are interrelated by

$$n = \sqrt{\left[\frac{2(DP_{si}-C\dot{\theta}-T_1-C_1\dot{\theta})\frac{2\pi}{60}\dot{\theta}}{I^2R} - \frac{R_L}{R}\right]} \qquad (7.9)$$

$$\omega = \dot{\theta}\,\frac{2\pi p}{60}$$

$$K = \frac{I}{n\omega}\sqrt{(n^2R+R_L)^2 + (n^2\omega L)^2} \qquad (7.10)$$

where K essentially fixes the rotor magnet dimensions for a specified material as shown in Fig.7.8.

Thus for any selected operating speed $\dot{\theta}$ the required turns factor is calculated from equation (7.9) and the K value from equation (7.10).

Assuming that the stator inductance is 140μH and the winding resistance is 88mΩ for a 12 turn stator, Fig.7.5 shows the plots of equations (7.9) and (7.10) for air pressures of 60,65 and 70 p.s.i. and a 24V 250W bulb. From the curves a desired air pressure and speed gives the necessary turns factor n and corresponding flux linkage K.

Case Study

Assume an air pressure of 60 p.s.i. is selected. In the interests of low operating speed, say 5,800 r.p.m., the required turns factor is n = 1.17 and flux linkage is 17.0mWb from Fig.7.5. Fig.7.8 shows that this value of K will require Supermagloy 10 magnets having a radial depth >8mm with a corresponding cost penalty.

If electrical efficiency is sacrificed and the turns factor of n = 1.85 is selected, then this corresponds to a higher operating speed of 6,360 r.p.m. But a lower K value of 11mWb is required, needing approximately 5.3mm radial depth and 20mm pole width Supermagloy 10 material, with a cost advantage.

A typical plot of K variations with $\dot{\theta}$ for a given air pressure is shown in Fig.7.6. Obviously, for minimum magnet material, the rotor is designed to produce a value of $K = K_{min}$. However the graph shows that if K is increased from K_{min} to K_1, the operating speed drops significantly from $\dot{\theta}_{min}$ to $\dot{\theta}_1$. For optimum performance, it is preferable to have a K value between

K_1 and K_2 because at K values above K_2, a small reduction in speed from say $\dot{\theta}_2$ to $\dot{\theta}_3$ would demand a large increase in K from K_2 to K_3 which is not cost effective. In Fig.7.5, for operating air pressures of 60 and 65 p.s.i., the optimum K values would be between 10mWb to 12mWb.

7.4 Rotor Design Choice

The design strategy described in Section 7.3.2 has shown that the optimum K value for the 250W generator, which is driven by a turbine having air pressures of 60 to 65 p.s.i., lies between 10 and 12mWb. The finite element method is used to calculate the stator flux linkage K and inductance L of various rotor designs which have geometries similar to that shown in Fig.7.7. The outer diameter of all the rotors is 67mm to give a 1.5mm airgap clearance for the use of annular non-magnetic restrainer around the outer diameter of the rotor. The centre hexagonal hub is manufactured from mild steel. The pole width and radial depth of the magnet is shown as pw and rd in Fig.7.7. For the production rotor design, the regions between the magnet poles will be filled with epoxy to minimise windage losses.

Two different rare-earth magnet materials, Supermagloy 10 and HERA, are used in the rotor designs. Their typical demagnetisation curves are shown in Fig.4.32. The Supermagloy 10 is a sintered material, while the HERA is a polymer based rare-earth magnet having improved machining and handling properties and is capable of being made into complex geometries. However, the B/H properties of HERA are slightly inferior to that of Supermagloy 10, and hence requiring larger amount of HERA

material to produce the same K value as Supermagloy 10. There may, however, still be a cost advantage because the HERA material is significantly cheaper than the Supermagloy 10.

Figs.7.8 and 7.9 show the variations of computed K and L with magnet radial depth for different pole widths and magnet materials. The graphs in Fig.7.8 show that, as expected, increase in magnet volume and/or better magnet material results in higher K values. In Fig.7.9 it can be seen that for this type of rotor design the stator inductance L is only sensitive to changes in magnet radial depth rd because the recoil permeability of the two rare-earth magnets is identical and near unity.

It was decided that the K value for the 250W generator should be 11.2mWb. In Fig.7.8 three rotor designs give this value of K and they are labelled as designs A, B and C. The specifications of the three rotors are summarized in Table 7.2.

7.5 Final Rotor Designs

The rotor designs, selected in Section 7.4 and summarized in Table 7.2, were manufactured and tested to evaluate their performances. Results show that while the Supermagloy 10 rotors meet the design specifications, the HERA rotor produces a K value which is lower than the predicted value. Hence the HERA rotor was redesigned to give the required K value and this rotor is labelled as design D. Fig.7.10 shows rotor designs A, B and D.

Table 7.2 Possible Rotor Designs for 250W Generator

	Rotor Design			
	A	B	C	D
Magnet material	Supermagloy 10		HERA	
Centre hub	Hexagonal mild steel hub			
Working airgap	1.5mm			
Magnet radial depth	4.5mm	6.0mm	7.0mm	9.0mm
Magnet pole width	22mm	20mm	22mm	24mm
Predicted K (mWb)	11.2	11.2	11.2	10.5
Predicted L (μH)	162	147	139	132
Calculated T_{max}(Nm)	0.581	0.64	0.677	0.626

Table 7.3 Comparison of Various Rotor Designs

Rotor design	Flux linkage K(mWb)		Inductance L(μH)		R(mΩ)
	Predicted	Measured	Predicted	Measured	Measured
A	11.2	12.2	162	160	88
B	11.2	11.6	147	150	88
C	11.2	9.5	139	135	88
D	10.5	10.1	132	-	88

7.5.1 Design A

Using the measurement techniques described in Chapter 3, the K, L and R values of the Supermagloy 10 rotor were measured and are shown in Table 7.3. For comparison purposes predicted K and L values are included in the Table and they show good agreement with measured values. Hall probe measurements were carried out at location A (Fig.6.31) of each rotor pole during air-stabilisation flux density. The results show that the flux density varies between 220mT and 275mT. This variation in flux density from pole to pole is similar to that observed for the Supermagloy rotors tested in Sections 6.3.3 and 6.3.5. With rare-earth magnets such large fluctuations in air-stabilisation flux density are not expected because the the recoil line is almost coincident to the demagnetisation curve. The possible cause for this flux density fluctuation is likely, therefore, to be caused by variations in demagnetisation curve due to manufacturing tolerances. Studies undertaken by Adler[68] have shown that the demagnetisation curve of sintered rare-earth magnets can distort after grinding, which is the process used in the manufacture of the Supermagloy 10 rotors. This could contribute to the variation in air-stabilisation flux density from pole to pole. However, evidence from other users of Supermagloy 10 material suggests that difficulties in holding the material to its specifications, at the production stage, are likely to be the major cause of this variation.

With the stator open-circuit the loss torque speed curve was measured and is shown in Fig.7.11. The results give the parameters T_1 and C_1 of equation (7.5). Using the measured

generator parameters K, L and R, the loss torque parameters T_1 and C_1, and the turbine parameters D and C, the variations of operating speed $\dot{\theta}$ and air-pressure P_{si} with turns factor n, for a 24V 250W bulb, are plotted in Fig.7.12. The measured speed and required air pressure for the 250W generator with an n=2 stator winding is marked on the figure and shows close agreement with the predicted results.

The measured torque speed curve of the generator (n=2) with a 24V 250W bulb is shown in Fig.7.13. The predicted torque-speed curve, which includes the loss torques of Fig.7.11, is also plotted on the same figure and it shows close agreement with the measured result. The figure also shows the desired turbine characteristics for driving the 250W generator. The torque speed curve of the generator with a short-circuited stator winding was measured. The result is plotted in Fig.7.13 and it shows the distinct peak torque described in Section 2.2. The predicted troque-speed curve is included in the figure, and again it shows good agreement with the measured curve.

For this rotor design, the saliency torque at various rotor positions was measured and is plotted in Fig.7.14. In the figure the maximum saliency torque is 0.28Nm and from equation (7.2) at $\dot{\theta}$=0, the required air pressure for the turbine to start the generator has to be greater than 32 p.s.i. The saliency torque measurements were repeated with a stator which had the interpoles removed. The results, plotted in Fig.7.14, show that the maximum saliency torque has increased to 0.84Nm, hence to start such a generator design, an air pressure greater than 95.6 p.s.i. would be required. Obviously this shows that

the interpoles help to reduce the maximum saliency torque and, in turn, the required starting air pressure. For comparison purposes, computed saliency torques are included in Fig.7.14 and they show reasonable agreement.

From Fig.7.12, a generator with an n=2 winding seems a suitable compromise between speed and air pressure. The required operating air pressure is 67 p.s.i., which can overcome the maximum saliency torque at standstill, and the operating speed is 5,700 r.p.m.

7.5.2 Design B

The K, L and R values of the Supermagloy 10 rotor, design B, were measured and the results show good agreement with the predicted values of K and L in Table 7.3. Hall probe measurements undertaken on the rotor poles during air-stabilisation again show that the air-stabilisation flux density varies. In this case the variation is from 220mT to 290mT, hence again demonstrating the wide manufacturing tolerances in the Supermagloy 10 magnets.

The loss torque-speed curve was measured and the result is shown in Fig.7.11. The graphs in Fig.7.11 show that the loss torques for rotor designs A and B are similar. This is expected because the magnetic properties and geometry of the two generators do not differ significantly.

Fig.7.15 shows the predicted variations of $\dot{\theta}$ and P_{si} with n for a 24V 250W bulb. The measured speed at 67 p.s.i. for an n=2 generator, plotted in the same figure, shows close agreement with the predicted results.

Fig.7.16 compares the predicted and measured torque speed curves for the n=2 generator with a short-circuited stator winding and a 24V 250W bulb. The results again show good agreement. The figure includes the selected turbine characteristic which intersects the 250W generator at the operating speed of 5,800 r.p.m.

The measured saliency torques with the existing stator design and that without the interpoles are plotted in Fig.7.17. Computed values included in the same figure show good agreement. The results again demonstrate that the stator interpoles help to reduce the maximum saliency torque from 0.84 to 0.28Nm, which corresponds to a starting air pressure of at least 32 p.s.i.

Fig.7.15 shows that a suitable turns factor for the 250W generator is n=2 and the corresponding operating speed and air pressure are 5,800 r.p.m. and 65 p.s.i. respectively.

7.5.3 Design C

With the HERA rotor, design C, in the generator, the parameters K, L and R were measured. The results are compared with the predicted K and L values in Table 7.3. While the inductances show good agreement the measured K value is 15% lower than the predicted value. For all the previous test rotors it was thought that the three-dimensional effect caused the measured K to be higher than the predicted value, and hence the result of this HERA rotor was in complete contradiction to this explanation. Thus investigations were carried out to establish the likely cause for this large and positive difference in K value. Hall probe measurements undertaken on the

rotor poles during air-stabilisation show that the air-stabilisation flux density varies between 190mT and 205mT. The variation in flux density is less than that observed for the Supermagloy rotors tested in Sections 6.3.3, 6.3.5, 7.5.1 and 7.5.2. This suggests that the HERA magnet material has a closer manufacturing tolerance than the Supermagloy 10 materials.

Measurements showed that the axial length was only 15.5mm instead of the specified 16.0mm. Assuming a linear increase in K with length, a 16mm long rotor would have a K value of 9.8mWb which is still 12.5% less than the computed value of 11.2mWb.

From the data supplied by the HERA manufacturer, it can be seen that there are possible manufacturing tolerances in the demagnetisation curve such that the remanent flux density B_r (=550mT) has a possible variation of ±5% and the coercivity H_c (=400kAm^{-1}) has a tolerance of +8% and -2%. Using the finite element method, the calculation of K was repeated for the design C rotor with the 'worst case' demagnetisation characteristics i.e. B_r down by 5% and H_c by 2%. The recomputed K value is 10.5mWb which is still 6.6% higher than the 'measured' K value of 9.81mWb. Obviously the specified manufacturing tolerance cannot account for the 12.5% difference between the 'measured' and computed K values.

Error analysis on the calibrated measurement equipment, which consists of an integrator, frequency meter and a digital voltmeter, used for measuring K has shown that the maximum instrumentation error is 3%. It is considered that the unaccounted 3.6% difference between the 'measured' and the

worst case recomputed K value could have been caused by changes[68] in the magnetic property of the HERA material during the grinding process of the rotor. However, the magnet blocks were removed from the rotor and their B/H curve was checked by the magnet manufacturer and found to be unchanged. Errors in the field analysis, using the finite element method, due to the assumptions made in the model and the uncertain behaviour of permanent magnets at directions normal to the preferred direction of magnetisation together with the three-dimensional effects must therefore still be significant. To investigate which of these contribute the 3.6% error would require a large amount of labour to study and model the fundamental behaviour of permanent magnets. With limited time available, the investigation was not undertaken because this would mean a major diversion from the main aim of the project which was to design a 250W generator.

It was decided to repeat the calculation of K with a suitably lower demagnetisation curve to correct for the 12.5% error. Finite element calculations have shown that with a demagnetisation curve having B_r=479mT, B_m=239mT, H_c=-348KAm^{-1} and H_m=-170KAm^{-1} gives the correct K value of 9.8mWb. The L value was 139μH, and hence this modified B/H curve was used to represent the HERA characteristics for future design calculations. It should be noted however that this is an empirical change which gives the desired correction between measurement and prediction, and it should not be assumed that this new modified B/H curve represents the true characteristic of HERA material.

The measured saliency torques at the various mechanical angles are plotted in Fig.7.18. The results show that the stator interpoles helped to reduce the maximum saliency torque from 0.46 to 0.15Nm, which is lower than that for designs A and B due to the lower airgap flux density of design C.

Using the measured parameters K, L and R from Table 7.3, the variations of $\dot{\theta}$ and P_{si} with n are plotted in Fig.7.19. Measurements with an n=2 generator are included in the figure and they show close agreement.

Fig.7.20 gives the predicted torque speed curve of the n=2 generator with a 24V 250W bulb. The torque-speed curve of the generator could not be measured because, during the test, one of the magnet blocks cracked at about 4,00 r.p.m. However good agreement between predicted and measured torque-speed curves can be expected because studies, for rotor designs A and B, have shown that the equivalent circuit can be used to predict the generator torques to a good accuracy.

The graphs in Fig.7.19 show that rotor design C can be used in the 250W generator even though the K value is only 9.5mWb. A suitable turns factor is n=2.8 and the corresponding operating speed and air pressure are 6,500 r.p.m. and 66 p.s.i. respectively.

7.5.4 Design D

Using the modified B/H curve of the HERA estimated in Section 7.5.3, the finite element method was used to calculate the K and L values of rotors having different magnet radial depths and pole widths as shown in Figs.7.21 and 7.22.

Fig.7.21 shows that for a K value of 11.2mWb the magnet radial depth must be greater than 10mm. It was decided that a good compromise between magnet volume and K value would be to choose a rotor design which gave K=10.5mWb. This rotor design is represented as point D in Fig.7.21 and the specifications are summarised in Table 7.2.

Full tests on the rotor design D have not been carried out since this rotor was manufactured at a late stage of the investigation. A test has shown that the K value is 10.1mWb but the axial length of the rotor is only 15.5mm instead of the specified 16mm. Hence the extrapolated K value, for a 16mm axial length rotor, is $10.1 \times 16/15.5 = 10.43$mWb which is only 0.67% lower than the predicted value.

Using the measured K and R, and predicted L values given in Table 7.3, the variations of operating speed $\dot{\theta}$ and air pressure P_{si} against turns factor n are plotted in Fig.7.23. The 12 turn and 24 turn stator (n=1, n=2 respectively) were used to test the design. The corresponding air pressure and operating speed for these two units are marked on Fig.7.23 to show the good agreement achieved.

Fig.7.24 shows the predicted torque speed curves for an n=1 and n=2 generator with a 24V 250W bulb. The desired turbine characteristics are also included in the same figure. The results show that if low operating speed is a major consideration then a generator with n=2 is a suitable choice. Alternatively if low air pressure is preferred, then an n=1 generator with high operating speed can be used, or, of course, any other intermediate n value.

7.5.5 Summary of designs

The study has shown that any of the rotor designs summarized in Table 7.2 can be used in the 250W generator with different operating speeds and air pressures. Assuming that the rotor design D is selected for the 250W generator with a turns factor of n=2 and allowing for manufacturing tolerances in magnetic properties such that the flux linkage K is 10.5mWb ± 5%, the variations of torque and output power with speed are shown in Fig.7.25. The results show that variations in K require different air pressures to match the turbine with the generator but that these pressure changes are small. Thus final 'trimming' for each generator could be carried out on the pressure regulator fitted to each production unit if such variations in K were found in practice.

The final choice of rotor design ultimately depends on the lamp manufacturer who has to consider magnet material cost, guaranteed tolerances in magnetic properties, and rotor assembly costs together with operating costs and other user orientated selling features.

7.6 System Protection

Fig.7.26 shows the torque speed curve of the turbine intersecting that of the 250W generator at point A. In the event of bulb failure due to either an accident or normal deterioration of the filament, the generator has no load and the turbine accelerates until it intersects the loss torque T_i at point B. Assuming that the turbine and iron loss torque speed characteristics are represented by equations (7.2) and

(7.5), the speed at point B is then given as

$$\dot{\theta}_B = \frac{DP_{si} - T_1}{C + C_1} \text{ r.p.m.} \qquad (7.11)$$

For example if the operating air pressure at point A is 70 p.s.i., then $\dot{\theta}_B$ is 40,650 r.p.m. However in practice $\dot{\theta}_B$ is less than that given by equation (7.11) because in the actual lamp system there will be windage losses which help to reduce the speed from $\dot{\theta}_B$ to $\dot{\theta}_C$, as shown in Fig.7.26. Since data on windage losses are not available, $\dot{\theta}_C$ cannot be determined.

If the rotor is allowed to overspeed to $\dot{\theta}_B$, when the bulb fails, a very rigid restrainer, which can be expensive to produce, is required to prevent the rotor from disintegrating. Besides that, there are other considerations to bear in mind such as excessive wear on the bearings, excessive noise levels, and the mechanical stresses acting on the turbine blades at the high no-load speed.

Alternative protection systems can be devised to prevent the turbine-rotor from overspeeding when the bulb fails. For commercial reasons, the protection system has to be reliable, simple to manufacture, low in cost, compact enough to be housed in the existing brass casing and must be triggered automatically when the lamp fails and reset after the fault has been rectified.

One method of preventing overspeeding is to reduce or cut-off the air supply to the turbine, when the lamp fails, by means of a solenoid-controlled air valve which is triggered electronically via detector circuits. However, reliable and compact solenoid-controlled valves are expensive, and to

incorporate them into the lamp would necessitate major modifications to the air ducts of the brass casing. Thus the manufacturer decided that, if possible, the protection system should be completely solid-state with no moving parts. The simplest method is to use the generator to load the turbine, hence preventing overspeeding. Point A in Fig.7.27 represents the operating point of the generator with a 24V 250W bulb. When the bulb fails, an electronic circuit switches in a load R_D ($<R_L$) across the stator terminals and the torque-speed curve of the generator is modified from OA to OED. The torque of the generator at point D is greater than that produced by the turbine at point A so the turbine will decelerate from point A to the intersection point E.

A number of alternative electronic circuits are examined in Appendix E. The simplest circuit is chosen for more detailed analysis. Fig.7.28 shows the circuit which consists of a triac T1, a load resistor R_D, and a capacitor C.

At this stage of the investigation is has been assumed that rotor design B is used in the 250W generator which has a turns factor of n=2.

7.6.1 Ratings of triac T1 and resistor R_D

It is assumed that after the bulb has failed a resistor R_E, which represents the combined resistance of R_D and T1, is connected across the stator terminals. A number of torque speed curves for the generator, for various R_E values, are plotted in Fig.7.29. Point A is the rated operating point of the 250W generator and the torque speed curve of the selected turbine is

line AE. Allowing for the maximum air pressure fluctuation of +3 p.s.i., the curves show that a suitable value of R_E, to prevent overspeeding, is 0.4Ω. Using equation (2.21), the maximum theoretical current as $\omega \to \infty$ is given as

$$I_{max} = \frac{K}{\sqrt{2}nL} = 27.5A$$

At point D ($\dot{\theta} = 5,800$ r.p.m.) then the expected current is only 22.6A. However, taking into account the possibility that if K has +5% tolerance, then a suitable current rating for the Triac is 30A. Triacs are available with an isolated mounting stud or with the one terminal connected to the stud. In order to use the lamp housing as a heat sink an isolated stud device was selected for safety reasons. Triac 2N6165 was selected having the specification shown in Table 7.4.

Tests have shown that with forced cooling a resistance wire rated at 10A can readily carry currents up to 30A without glowing, and with such a high volume of air flow inside the lamp unit, the resistor R_D (=0.4Ω) can be wound from resistance wires which have 10A ratings.

Table 7.4 Specifications of Triac 2N6165 at $T_c < 70^oC$

V_{DRM}	600V
I_T(r.m.s.)	30A
I_{TSM}	250A
V_{GT}	2V
I_{GT}	100mA
I_{GTM}	10A
P_{GM}	40W
$P_{G(AV)}$	1W

7.6.2 Circuit design to ensure that the triac will not fire under normal operating condition

The capacitor C must be chosen such that during run-up to operating speed the triac must not fire. Tests on the triac have shown that the gate resistance R_g, prior to the triac being turned on, is 90Ω and the gate turn-on voltage v_{gt} is 0.65V.

Assuming that the impedance of the protection circuit is high compared to the bulb resistance R_L, the gate voltage in Fig.7.28 is given as

$$v_g = v_L \frac{R_g}{(R_g+R_D) + \frac{1}{j\omega_A C}} \qquad (7.12)$$

To prevent the triac from firing at rated voltage v_L, the gate voltage must be less than v_{gt} such that,

$$v_{gt} > v_L \frac{R_g}{(R_g+R_D) + \frac{1}{j\omega_A C}} \qquad (7.13)$$

Rearranging equation (7.13), the capacitor C is expressed as,

$$C < \frac{1}{\omega_A \sqrt{(\frac{v_L R_g}{v_{gt}})^2 - (R_g+R_D)^2}} \qquad (7.14)$$

$\therefore$ C < 117nF.

Thus a suitable value of C is 100nF.

7.6.3 Transient analysis of gate voltage

A circuit analysis has been undertaken to show that the transient gate voltage occurring at bulb failure, prior to the triac being turned-on, is sufficient to trigger the triac. Since the triac will attempt to switch off at each current zero,

analysis is also necessary to ensure a design capable of retriggering the triac at such points.

(a) <u>When the lamp fails at current i=0</u>

Under normal operating conditions, with the switch S (Fig.7.30) in position 1, the emf of the generator is given as

$$v = nK\omega \sin(\omega t+\theta) \qquad (7.15)$$

and the current is

$$i = I \sin(\omega t) \qquad (7.16)$$

where
$$\theta = \tan^{-1}\left(\frac{\omega L n^2}{R_L+n^2R}\right) \qquad (7.17)$$

At the instant when the lamp fails, with the switch S in position 2, the voltage equation is

$$nK\omega \sin(\omega t+\theta) = n^2L\frac{di}{dt} + i(n^2R+R_D+R_g) + \frac{1}{C}\int idt \qquad (7.18)$$

Differentiating equation (7.18) gives

$$nK\omega^2 \cos(\omega t+\theta) = n^2L\frac{d^2i}{dt^2} + (n^2R+R_D+R_g)\frac{di}{dt} + \frac{i}{C} \qquad (7.19)$$

It can be shown[69] that the solution of equation (7.19) takes the form,

$$i = i_t+i_{ss}$$

$$= Be^{-\alpha t}\sin(\beta t+\psi) + \frac{nK\omega}{Z}\sin(\omega t+\theta-\phi) \qquad (7.20)$$

where i_t is the transient current component

i_{ss} is the steady state current component

B and ψ are arbitrary constants

$$\alpha = \frac{R''}{2n^2L}$$

$$\beta = \sqrt{\frac{1}{n^2LC} - \left(\frac{R''}{2^2nL}\right)^2}$$

$$Z = \sqrt{R''^2 + \left(\omega n^2L - \frac{1}{\omega C}\right)^2}$$

$$\phi = \tan^{-1}\left(\frac{\omega n^2L - \frac{1}{\omega C}}{R''}\right)$$

$$R'' = n^2R + R_D + R_g$$

Applying the initial conditions at t=0,

$$i = 0 \qquad (7.21)$$

and

$$n^2L \frac{di}{dt} = nK\omega \sin\theta \qquad (7.22)$$

and equating equations (7.20) and (7.21) gives

$$B \sin\psi = -\frac{nK\omega}{Z} \sin(\theta-\phi) \qquad (7.23)$$

By using equations (7.20) and (7.23) in equation (7.22), it can be shown that

$$B \cos\psi = \frac{nK\omega}{\beta}\left[\frac{\sin\theta}{n^2L} - \frac{\alpha}{Z}\sin(\theta-\phi) - \frac{\omega}{Z}\cos(\theta-\phi)\right] \qquad (7.24)$$

For a given bulb rating, I and R_L are fixed. For a generator design, the parameters K, L and R are specified and with a selected turns factor n, the operating speed is fixed. With $R_D = 0.4\Omega$ and $C = 100nF$, the constants B and ψ can be determined from equations (7.23) and (7.24).

The gate voltage is given as

$$v_g = iR_g \qquad (7.25)$$

By substituting equation (7.20) into (7.25), the variation of gate voltage with time is plotted in Fig.7.31. The results show that the triac will trigger in less than 50nS when the operating frequency is 290Hz.

(b) <u>When the lamp fails at peak current such that i=I</u>

To simplify analysis, the emf of the generator is expressed as

$$v = nK\omega \cos(\omega t+\theta) \qquad (7.26)$$

and the current is

$$i = I \cos(\omega t) \qquad (7.27)$$

At the instant when the bulb fails the voltage equation is given as

$$nK\omega \cos(\omega t+\theta) = n^2L \frac{di}{dt} + iR'' + \frac{1}{C}\int idt \qquad (7.28)$$

The solution of equation (7.28) takes the form

$$i = Ae^{-\alpha t}\sin(\beta t+\gamma) + \frac{nK\omega}{Z} \cos(\omega t+\theta-\phi) \qquad (7.29)$$

where A and γ are arbitrary constants.

Subjecting initial conditions to the circuit in Fig.7.30 such that at t=0

$$i = I \qquad (7.30)$$

and

$$\frac{1}{C}\int idt = v_L \qquad (7.31)$$

Therefore, the current equation is

$$I = A \sin\gamma + \frac{nK\omega}{Z} \cos(\theta-\phi) \qquad (7.32)$$

and voltage equation gives

$$nK\omega \cos\theta = n^2L \frac{di}{dt} + I\ R'' + v_L \qquad (7.33)$$

Using equations (7.32) and (7.33), it can be shown that

$$A \sin\gamma = I - \frac{nK\omega}{Z} \cos(\theta-\phi) \qquad (7.34)$$

and

$$A \cos\gamma = \frac{1}{\beta} \{\frac{nK\omega \cos\theta - V_L - I_m R''}{n^2 L} - \frac{nK\omega^2}{Z} \sin(\theta-\phi)$$

$$+ \alpha\left[I - \frac{nK\omega}{Z} \cos(\theta-\phi)\right]\} \qquad (7.35)$$

From equations (7.34) and (7.35), the arbitrary constants A and γ are solved. By using equations (7.29) and (7.25), the instantaneous gate voltage v_g is plotted in Fig.7.32. The curve shows that the gate voltage will immediately trigger the triac, assuming that there is no turn-on time delay in the triac. However the voltage is over 1KV and might damage the triac, so a transient suppressor is connected across the terminals, mt_1 and mt_2, of the triac to absorb this voltage surge. A suitable suppressor is a semiconductor device known as voltage dependent resistor (VDR). Assuming that the operating voltage of the VDR is 75V, the sustained surge current I is 14.73A and the pulse width, from Fig.7.32, is 26μs the energy in the pulse is

$$E = 75 \times 14.73 \times 26 \times 10^{-6} = 29\ mJ$$

The VDR, R.S. No. 238-485, is chosen as its operating voltage is 75V and pulse dissipating energy is 10J.

(c) <u>When the triac turns off at current i=0</u>

At each half cycle of current, the triac switches off when the current through it is zero. Using the analysis derived in Section 7.6.3(a), with R_L=0, the gate voltage at various frequencies is plotted in Fig.7.33. The results show that the

gate voltage is sufficient to retrigger the triac at operating frequencies between 29OHz to 4OHz. Since the lower frequency limit, when the generator slows down to point E in Fig.7.29, is lOOHz the analysis has shown that the protection system will work within the designed speed range, i.e. 5,8OO r.p.m. to 2,OOO r.p.m.

7.6.4 Circuit analysis to determine the upper speed limit when there is no bulb connected to the generator

Assuming that there is no bulb across in the generator when the air supply is switched on, the generator will accelerate from point O towards point B (Fig.7.34). But when the generator reaches point J, the protection circuit switches on and alters the torque-speed curve from OB to OEK. The generator operating point moves from J to K and slows down to point E. Using the equivalent circuit in Fig.7.28 and assuming that the impedance of the protection circuit is larger than that of the generator, the gate voltage is expressed as

$$v_g = Kn\omega \frac{R_g}{(R_g+R_D) + \frac{1}{j\omega C}} \approx Kn\omega^2 R_g C \qquad (7.36)$$

Using equation (7.36) the angular frequency when v_g reaches v_{gt} is given as

$$\omega = \omega_k = \sqrt{\frac{v_{gt}}{nK R_g C}} \qquad (7.37)$$

and the upper speed limit of the generator is then

$$\dot{\theta}_K = \frac{10}{\pi} \sqrt{\frac{v_{gt}}{nK R_g C}} \text{ r.p.m.} \qquad (7.38)$$

$$= 5,610 \text{ r.p.m.}$$

7.6.5 Prevention of over voltage across the 250W 24V bulb

Fig.7.35 shows the variations of torque, bulb voltage and power with speed for the n=2 generator, which has a design B rotor, supplying a 24V 250W bulb. Point A is the operating point and line FA is the selected turbine characteristic. Allowing for possible air pressure fluctuations of ± 3 p.s.i., the variations in bulb voltage is 24 ± 2V and for bulb power it is 250 ± 30W. Obviously the bulb will be overloaded if the air pressure increases by 3 p.s.i. A protection system has been devised to prevent excessive over voltage being applied across the bulb.

By connecting a diac, IN5762A which has a voltage rating of $v_D = 34V$, in parallel with the capacitor C the protection circuit, shown in Fig.7.36, is adapted to include an over voltage facility such that the triac will trigger when the lamp voltage is given as

$$v_L = \frac{(v_D + v_{gt})}{\sqrt{2}} = 24.5V$$

7.6.6 Implementation of protection circuit

Tests were undertaken on the 250W generator with the protection circuit, shown in Fig.7.36, connected across the stator terminals. With the bulb in circuit, the results showed that the protection circuit was only activated when the voltage across the bulb exceeded 25V, hence verifying the over voltage calculation in Section 7.6.5.

At the rated operating speed of the generator the bulb was switched off to simulate bulb failure and this triggered the protection circuit. By slowing down the generator, which was

driven by a d.c. motor, the protection circuit ceased to function when the speed was less than 1,000 r.p.m. Since the results in Fig.7.29 show that the lower speed limit is 2,000 r.p.m., the protection circuit meets the 'latching on' requirement when the generator slows down.

A typical waveform of the gate voltage, after the triac has fired, is shown in Fig.7.37. In the figure t_1 is the time taken for the transient gate voltage v_g to reach v_{gt} and v_4 is the saturation voltage of the triac.

The effective resistance of the triac at 100Hz was measured as 60mΩ. Hence the total resistance of the protection circuit is 0.46Ω. This modifies the torque speed curve of the generator and the lower speed limit is now 2,300 r.p.m., as shown in Fig.7.29.

Tests showed that, with the bulb out of circuit and the generator started from standstill, the protection circuit activates at 5,300 r.p.m., hence verifying the calculations undertaken in Section 7.6.4.

Finally, the protection circuit was tested in the actual lamp system with the generator driven by the air turbine. The results confirm the capability of the protection circuit to prevent over speeding and over voltage, as tested above. After the bulb was switched off, the generator slowed down to a stable speed of 2,900 r.p.m.

7.7 Matching the 55W Cobalt Generator with Turbine Characteristics

The torque speed curves of the turbine with a single type 1, 20° nozzle are shown in Fig.7.38 together with the curves for the existing turbine with a single type 1, 32° nozzle. The plots in

the figure give the turbine constants C and D of equation (7.2) and the curve in Fig.3.11 determines the loss torque constants T1 and C1 of equation (7.5). For a given bulb, I and R_L are fixed. Using the measured parameters of a Cobalt generator K, L and R from Tables 3.1 and 3.2, the variations of operating speed $\dot{\theta}$ and air pressure P_{si} with turns factor n, for the two nozzle designs, are plotted in Fig.7.39. The results in the figure show that for the existing generator with n=1, the operating speed is 9,200 r.p.m. and the air pressure, for a single type 1 32^{o} nozzle, is 53 p.s.i. If the new 20^{o} nozzle is used and the turns factor is n=2, the operating speed reduces to 5,700 r.p.m. and required air pressure is 57 p.s.i. The measured maximum saliency torque is 0.046Nm and the minimum air pressure required to start the generator is 16.4 p.s.i. which is obviously less than the operating air pressure of 57 p.s.i.

7.8 Conclusion

After consultation with the lamp manufacturer, the rotor design D seems a likely design to be used in the 250W generator because the HERA material is substantially cheaper than the Supermagloy 10 material. Hence the design variables, which are not fixed in Table 7.1, can now be finalised and they are summarised in Table 7.4. Tests have shown that the protection circuit, shown in Fig.7.36, can also be used for the 250W generator having a rotor design D and a turns factor of n=2.

Table 7.4

Design variables	250W generator	55W generator
Number of turns in stator winding	24 turns per pole winding using 0.965mm diameter copper wires	
Rotor magnet material	HERA	35% Cobalt
Rotor magnet geometry	magnets having 24mm pole width and 9mm radial depth mounted on a mild steel centre hub	As the existing design
Turbine air pressure	63 p.s.i.	57 p.s.i.
Operating speed	7,000 r.p.m.	5,700 r.p.m.
Protection circuit	Yes	No

CHAPTER 8

CONCLUSIONS

With the market for semi-portable safety lamp units growing, there is a need to uprate the existing 55W design to 250W. It is hoped that the 250W lamp units will capture a large share of the safety lamp market because other manufacturers have produced only 100W units. This need to uprate the lamp requires a re-examination of the overall design. A design engineer must view the design of the lamp as a whole, for extra cost of one component may well be more than offset by consequent savings on other components. The 250W generator design must also consider the constraints imposed by the specifications outlined in section 1.3, and the turbine design.

The early part of the investigation has been concerned with the modelling of the permanent magnet generator which powers the lamp. An equivalent circuit shown in Fig.2.1 has been developed. Tests have shown that, with known generator parameters (p, K, L, R and n) and a given lamp rating (I and R_L), the operating speed of the generator can be predicted with an accuracy of 7%. Analysis has identified that the most important design parameters for uprating the peak torque T_{max}, are pole-pairs, p, stator flux-linkage K, and inductance L.

Studies have shown that the predicted torque-speed characteristic of the generator must account for the loss torques and the non-linearity of the bulb load when selecting the desired turbine. To ensure stable system operation, a

suitable turns factor n is used to modify the torque-speed characteristic of the generator to intersect that of the turbine at a region to the left of T_{max} where the gradient of the generators torque-speed curve is positive.

The next stage was then to consider the factors influencing the parameters K and L. It has been found that these two parameters are affected by the permanent magnet materials and the generator geometry. Using the standard magnet design methods described in chapter 4 the parameters K and L can only be calculated with limited accuracy. These methods rely on empirical data and this creates uncertainties in the design calculations if the generator is radically re-designed with different magnetic materials and geometries.

For a more fundamental study of a generator design the finite element method is used to calculate the parameters K and L, and the saliency torque. The latter is an important parameter for matching the turbine to the generator at standstill. The finite element method has significant advantages over standard design methods, because it can account accurately for leakage flux, it can handle complex configurations of magnetic circuit, it allows different parts of the magnetic materials to have different flux densities and permeabilities and it enables the directional properties to vary throughout the permanent magnet materials. A suite of two-dimensional finite element programmes has been written which allows the magnetic field distribution within the active length of the machine to be calculated during initial magnetisation of the magnets, during stabilisation, when

the magnets are removed from the magnetising jig, and finally, during recoil operation, when the magnets are replaced in the generator. It has been shown that, provided the fringing fields at the ends of the machine are a small proportion of the total field, the stator flux linkage K can be calculated with an accuracy between +10% and -12.5%. The accuracy of the predicted stator inductance, which includes an estimated end-winding component, is between +2% and -6.7% while that for the maximum saliency torque is between ±10%. Errors in the finite element calculations might have arisen because of assumptions made in the model regarding the behaviour of permanent magnets in directions normal to the preferred direction of magnetisation. In addition three-dimensional effects were not taken into account. Measurements have shown that magnet manufacturing tolerances, particularly on the rare-earth materials, are significant as evidenced by variations in the magnetic properties of complete rotor assemblies and of individual poles.

Recognising the possible sources of errors, the finite element method can be used for designing permanent magnet generators with an accuracy acceptable for many engineering applications. The method was used to study the effects of changing the pole number on generators having Cobalt and Supermagloy 10 rotors. The results have shown that the optimum number of pole-pairs for the Cobalt generator is 6, which increases the T_{max} by 60% over the existing 3 pole-pair design. However, the minimum operating speed of such a generator to supply a 250W lamp would be 14,000 r.p.m. which does not meet the design specifications. The optimum number of pole-pairs

for the Supermagloy 10 generator is 4, but its T_{max} is only 4% greater than that of a 3 pole-pair design. For economic considerations such a small improvement in performance is off-set by the cost of producing a new 8-pole stator lamination. The minimum speed of a 6-pole, 250W generator having a Supermagloy 10 rotor and an optimum turns factor of n_{min} = 3.6 would be 3,600 r.p.m. This meets the design specifications.

Ideally, the generator should be designed with the optimum turns factor n_{min} so as to minimise the full-load operating speed. However the calculation of n_{min} does not consider the limitations imposed by the air-turbine or the efficiency of the overall system. Hence a different design strategy has been developed to match the generator to a given turbine. Various rare-earth rotors have been designed for the 250W generator. Tests on these prototypes have shown that with an n = 2 stator winding the generators can produce 250W at operating speeds below 7,500 r.p.m. and air-pressures less than 70 p.s.i. Design calculations and tests have shown that the operating speed of the 55W Cobalt generator is reduced from 9,200 r.p.m. to 5,700 r.p.m. if the turns factor is increased to 2. This has a cost advantage in standardizing the stator winding for both the 55W and 250W generators but does incur the disadvantage of a higher operating air-pressure and air consumption over the existing design.

For system protection an electronic circuit has been designed to switch a load onto the generator and prevent the rotor from overspeeding in the event of bulb failure. An extra facility has also been devised to prevent excessive overvoltage

being applied across the bulb. The complete electronic circuit is easy to incorporate into the lamp unit, is low in cost, simple to manufacture and has been overdesigned for high reliability. This makes it an attractive commercial proposition as an extra safety feature for the 250W safety lamp unit.

This project has demonstrated that by using various mathematical models, rather than standard design methods which rely too much on experience and empirical data, it is possible to design an air-driven turbo-generator for optimum cost and performance and greatly reduce the development time. Both of these are important for commercial success.

REFERENCES

1. HOSKINS, D.G. :'Performance of a small air turbine', Investigation conducted in the Department of Mechanical Engineering, University of Sheffield, 1976.

2. HANRAHAN, D.J. and TOFFOLO, D.S. :'Permanent magnet generators', Part 1, IEEE Trans., 1957, p.1098
Part 2, IEEE Trans., 1963, p.68

3. GINSBERG, D., and MISENHEIMER, L.J. :'Design calculations for permanent magnet generators', IEEE Trans., 1953, p.96.

4. OVERSHOTT, K.J. and BURNETT, J. :'Analysis of the dynamic operation of permanent magnets', Proc IEE conference on Advances in Mag. and Appl., Sept. 1976

5. PARKER, R.J. and STUDDERS, R.J. :'Permanent magnets and their applications', J. Wiley & Sons., 1962

6. POLGREEN, G.R. :'New applications of modern magnets', McDonald., 1969

7. HADFIELD, D. :'Permanent magnets and Magnetism', Iliffe Books Ltd., 1962

8. MAINER, O.E. :'Theoretical treatment of permanent magnet alternator', J. Elect. Engng. Educ., Vol.6, p.417., 1977

9. ROSS, I.N. :'Rare earth magnets', Electrical Review, 21 May 1976.

10. Design Idea of the Month. :'Plastic magnets combine low cost with ease of moulding', Design Engineering, March 1975.

11. GALE, K. :'Combining the best properties of three magnets all in one', The Engineer, 17 July 1975.

12. BENZ, M.G. and MARTIN, D.L. :'Cobalt-Mischmetal-Samarium Permanent Magnet Alloys : Process and properties', J. Applied Physics, Vol.42, No.7, June 1971.

13. NOODLEMAN, S. :'Factors in applying rare-earth Cobalt magnets to D.C. motors', Cobalt, 1974-4.

14. MARTIN, D.L. and BENZ, M.G. :'Cobalt-rare earch permanent magnet alloys', Cobalt, No.50, March 1971.

15. A Review Article. :'Rare-earth magnets', Engineering Materials and Designs, July 1977.

16. Technical Bulletin, No.1, 3.1972. :'Magnetic properties and design data for standard P.M.A. materials', Former Permanent Magnet Association, Sheffield.

17. EREN, H. :'Endwinding leakage reactance evaluation', M.Eng. 1975, Electronic & Electrical Engineering Department, University of Sheffield.

18. Technical leaflets. :'Magnetic properties of Hera', Magnetic Polymer Ltd., Swindon.,1977

19. Technical leaflets. :'Magnetic properties of Supermagloys', Performations Ltd., Swindon.,1977

20. BRAINARD, M.W. :'Synchronous machines with rotating permanent magnet field', Trans. AIEE, 1952, 71, p.670.

21. MARX, M.F. and LEWIS, T.D. :'Electromagnetic force motor design using rare earth-cobalt permanent magnets', NAECON '77, RECORD-1119.

22. BINNS, K.J., BARNARD, W.R. and JABBAR, M.A. :'Hybrid permanent-magnet synchronous motors', Proc. IEE, Vol.125, No.3, March 1978.

23. BINNS, K.J. and KURDALI, A. :'Permanent magnet a.c. generators', Proc. IEE, Vol.126, No.7, July 1979.

24. TAN, G.H., BIRCH, T.S., HOWE, D. and BROWN, R. :'Design calculations for a small permanent magnet generator', Proc. U.P.E.C., April 1979.

25. WOTARABE, T., ASAKAWA, K. and NISHIMOTO, K. :'Small-sized D.C. servo-motor', Fujitsu Sc. and Tech. J., Dec. 1977.

26. NAKATA, T., TAKAHASHI, N. and YONEDA, K. :'Application of rare-earth Cobalt magnets - application to analogue electronic watches', IEE, Japan, Mag-77-23.

27. REICHERT, K. and FREUNDL, H. :'Computer-aided design of permanent magnet systems', Brown Boveri Review, No.9, 1972.

28. KAMMINGA, W. :'Finite-element solutions for devices with permanent magnets'. J. Phys.D : Appl. Phys., Vol.8, 1975.

29. HARROLD, W.J. :'Calculation of equipotentials and flux lines in axially symmetrical permanent magnet assemblies by computer', Trans. IEEE Mag., Vol. Mag.-8, No.1, March 1972.

30. MOZENC, M.L., CARLSON, R., HECTOR, J. and PESQUE, J.J. :'Characterisation of a new machine with ferrite magnets by resolving the partial differential equation for the magnetic field', Proc. IEE, Vol.124, August 1977.

31. REICHERT, K. :'The calculation of magnetic circuits with permanent magnets by digital computers', Trans. IEEE Mag., Vol. Mag-6, No.2, June 1970.

32. SILVESTER, P., CABAYAN, H.S. and BROWNE, B.T. :'Efficient techniques for finite element analysis of electrical machines', Trans. IEEE, Vol. PAS-92, July 1973.

33. CHAN, M.V.K. and SILVESTER, P. :'Finite element analysis of magnetically saturated d.c. machines', Trans. IEEE, Vol. PAS-90, Sept. 1971.

34. SLOMCZYNSKA, J. :'Nonlinear analysis of the magnetic flux distribution in the magnetised magnet stabilised in air', Trans. IEEE, Mag., Vol. Mag-10, No.4, Dec. 1974.

35. SLOMCZYNSKA, J. :'No-load magnetic-field distribution in permanent magnet electrical machines', Trans. IEEE Mag., Vol. Mag-11, No.6, Nov. 1975.

36. BINNS, K.J., JABBAR, M.A. and BARNARD, W.R. :'Computation of the magnetic field of permanent magnets in iron cores', Proc. IEE, Vol.122, No.12, Dec. 1975.

37. DORN, W.S. and McCRACKEN, D.D. :'Numerical methods with Fortran IV case studies', J. Wiley & Sons, p.313.

38. FUCHS, E.F. and ERDELYI, E.A. :'Determination of waterwheel alternator steady-state reactance from flux plots', Trans. IEEE, PAS-91, 1972, p.2510.

39. SILVESTER, P.P., LOWTHER, D.A., CARPENTER, C.J. and WYATT, E.A. :'Exterior finite elements for 2-dimensional field problems with open boundaries', Proc. IEE, No.124, 1977, p.1267.

40. CARTER, G.W. :'The electromagnetic field in its engineering aspects', Longmans, London.

41. BEWLEY, L.V. :'Two-dimensional fields in Electrical Engineering', Macmillan Co., 1948.

42. BINNS, K.J. and LAWRENSON, P.J. :'Analysis and computation of electric and magnetic field problems', Pergamon Press, 1973.

43. SAY, M.G. :'Alternating Current Machines', Pitman, 1978.

44. BARNS, E.C. :'An experimental study of induction machine end-turn leakage reactance', Trans. AIEE, Vol.70, 1951, pp.671-679.

45. TRUTT, F.C., ERDELYI, E.A. and HOPKINS, R.E. :'Representation of the magnetisation characteristic of D.C. machines for computer use', Trans. IEEE, Vol.PAS-87, pp.665-669, 1968.

46. WIDGER, G.F.T. :'Representation of magnetisation curves over extensive range by rational-fraction approximations', Proc. IEE, 1969, 116(1), pp.156-160.

47. MACFADYEN, W.K., SIMPSON, R.R.S., SLATER, R.D. and WOOD, W.S. :'Representation of magnetisation curves by exponential series', Proc. IEE, Vol.125, No.8, Aug. 1973, pp.902-904.

48. FISCHER, J. and MOSER, J. :'The reproduction of magnetisation curves by simple algebraic and transcendental functions', (in German), Archiv. f. Electrotechnik, Vol.24, pp.286-299, 1956.

49. LEHMAN, S. :'Analytic representation of magnetisation characteristics for digital computer', Elektronische Datenverarkertung, Vol.6, pp.165-172, 1964.

50. REPPE, K. :'The representation of magnetisation curves for various types of iron on a computer', Siemens Review, Vol. 37, pp.507-508, 1970.

51. Technical Bulletin No.7, 11.1966. :'Magnetising of permanent magnets', Former Permanent Magnet Association, Sheffield.

52. ZIENKIEWICZ, O.C. and CHEUNG, Y.K. :'Finite elements in the solutions of field problems', The Engineer, Vol.220, pp.507-510, 1965.

53. WALSH, J. :'Finite-difference and finite-element methods of approximations', The Royal Society of London, Vol. 323, pp.155-165, 1971.

54. GALLAGHER, R.H. :'Finite element analysis fundamentals', Prentice-Hall, 1975.

55. SILVESTER, P. and CHARI, M.V.K. :'Finite element solution of saturable magnetic field problems', Trans. IEEE, Vol. PAS-89, No.7, 1970.

56. SILVESTER, P. and CHARI, M.V.K. :'Analysis of Turbo-alternator magnetic fields by finite elements', Trans. IEEE, Vol. PAS-90, No.2, 1971.

57. ZIENKIEWICZ, O.C. :'The finite element method in Engineering Science', McGraw-Hill.

58. ISAACSON, E. and KELLER, H.B. :'Analysis of numerical methods', John Wiley, 1966, p.34.

59. WEXLER, A. :'Finite element for technologist', Polytechnic of Central London, Lecture Notes, May 1974.

60. AHMED, S.V. :'Accelerated convergence of Numerical solution of linear and non-linear vector field problems', Computer Journal, Vol.8, p.73, 1965.

61. AHMED, S.V. and ERDELYI, E.A. :'Non-linear theory of salient pole machines', Trans. IEEE, Vol. PAS-85, pp.61-70, 1966.

62. ANDERSON, O.W. :'Transformer leakage flux program based on the finite-element method', Trans. IEEE, Vol. PAS-92, pp.682-689, 1973.

63. HENSHELL, R.C. :'PAFEC 75' scheme, PAFEC Ltd., PAFEC House, 40 Broadgate, Beeston, Nottingham.

64. CUTHILL, E.H. and McKEE, J.M. :'Reducing the Bandwidth of Sparse Symmetric Matrices', Proc. 24th Nat. Conf. Assoc. Comput. Mach. ACM Publication, p.69, New York, 1969.

65. CUTHILL, E.H. :'Reducing the boundwidth of sparse symmetric Matrices', Naval Research, Washington, 1969.

66. KAMBERBEEK, E.M.H. :'On the theoretical and experimental determination of the electromagnetic torque in electrical machines', Philips Research Reports Supplements, 1970, No.4.

67. CARPENTER, C.J. :'Surface-integral methods of calculating forces on magnetised iron parts', Proc. IEE, Vol.107C, p.19-28, 1960.

68. I.B.M. Scientific subroutines. :'Mathematics - Linear equations', Subroutine MCHB and DMCHB, pp.148-151.

69. BINNS, K.J. and BARNARD, W.R. :'Novel Designing of self-starting synchronous motor', Proc. IEE, Vol.118, No.2, pp.369-372, 1971.

70. ADLER, E. and HILZINGER, H.R. :'The influence of surface conditions on magnetic properties of sintered Co_5Sm magnets', Vol.9, 1978, J. Mag. of Mag. Mat., pp.188-190.

71. BENSON, F.A. and HARRISON, D. :'Electric Circuit Theory', Edward Arnold Ltd., 1966.

72. EDWARDS, J.D. :'Electrical Machines', Int. Textbook Co. Ltd., 1973, pp.24-27.

73. HINDMARSH, J. :'Electrical Machines and their applications', Pergamon Press, 1970, pp.28-31.

74. BROWN, R. :'Electromagnetic Theory', Final year notes, University of Sheffield.

75. BRAILSFORD, F. :'Investigation of eddy current anomaly in electrical sheet steels', J. I.E.E., Vol.95, 1948, p.38.

76. BRAILSFORD, F. and BURGESS, J.M. :'Internal wave form distortion in silicon iron laminations for magnetisation at 5QHz', Proc. I.E.E., Vol.108C, 1961, p.458.

77. BUTLER, O.I. and MANG, C.Y. :'The predetermination of magnetic properties of ferromagnetic laminae at power and audio frequencies', J.I.E.E., Vol.95, p.25.

78. BULLINGHAM, J.M. and BERNAL, M.J.M. :'Investigation of the effect of non-linear B/H loops on the calculation of eddy current losses', Proc. IEE, Vol.114, No.8, p.1174.

79. ASPDEN, H. :'The eddy current anomaly in electrical sheet steel', Proc. IEE, Vol.103, 1956, p.272.

80. BARTH, J.B. :'Alternating electromagnetic fields, eddy currents and power loss in solid iron', Proc. IEE, Vol.128, No.11, p.1454.

81. SABIR, S.A.Y. and SHEPHERD, W. :'Magnetic properties of Alcomax III with dynamic excitation',Proc. I.E.E.,Vol. 121,No.8,1974

APPENDIX A

EXPERIMENTAL EQUIPMENT

The rig used for testing the permanent magnet generator is shown in Fig.A.1 and a schematic diagram of the various components is shown in Fig.A.2. The permanent magnet rotor is mounted on a shaft which is supported by two high-speed bearings and linked to a d.c. drive motor via a brass coupling. This brass coupling has a torque-limiting pin, a safety device, designed to shear in the event of accidental locking of the rotor.

The stator of the generator is mounted in a Bakelite housing which has a concentric support shaft. This shaft, mounted on low friction bearings, is restrained by the cantilever arm of the torque measuring system. It is designed to permit axial movement of the stator which is a useful facility for allowing the rotor to be changed without having to dismantle the test rig. Fig.A.3 shows the stator when it is retracted away from the rotor.

(a) Speed Measurement

The speed of the rotor can be determined from the frequency of the stator output voltage. The relationship between speed $\dot{\theta}$ and frequency f is given by

$$\dot{\theta} = \frac{\omega}{p} \text{ radians sec}^{-1} = \frac{\omega}{p} \frac{60}{2\pi} \text{ r.p.m.}$$

$$= 60 \frac{f}{p} \text{ r.p.m.} \qquad \text{(A.1)}$$

where f is measured with a calibrated frequency meter which has a 0.1Hz resolution.

Alternatively the output voltage E from a d.c. tacho-generator, which is coupled to the d.c. drive motor, can be used for measuring speed. The speed is expressed as

$$\dot{\theta} = \frac{E}{K_1} \qquad (A.2)$$

where K_1 is the open-circuit speed-emf constant of the tacho-generator. The voltage E is used as a speed signal for an X-Y plotter for plotting the torque-speed curve of the generator.

(b) Torque Measurement

The torque produced by the generator and transmitted to the stator is determined by measuring the required restraining force on the cantilever arm fixed on the stator support shaft, as shown in Fig.A.4. This restraining force F is measured with a load cell. The torque is expressed as

$$T = Fr \text{ Nm} \qquad (A.3)$$

where r is the length of the cantilever arm.

Fig.A.5 shows the load cell, labelled A, and the signal processor unit labelled as B. The load cell, which has a maximum force rating of 1kg, is a strain gauge unit. The signal processor unit consists of a d.c. amplifier, D.V.M. and power supply for the strain gauge. These two units are manufactured by Shape Instruments Ltd., and are known as 'ML series with 1kg load'. The torque measuring equipment was tested and found to be within the manufacturers specifications, i.e. the linearity and hysteresis is less than 0.05% of f.s.d.

The output voltage from the signal processor unit has a +2V offset. The X-Y plotter used (Hewlett Packard No.7035B) could not be zeroed with such a large offset voltage and the circuit shown in Fig.A.6 was used to back-off the 2V offset.

(c) Saliency Torque Measurement

With the generator mounted in the experimental rig the saliency torque, at standstill, is determined by measuring the torque experienced by the stator. This torque is measured with the equipment described in Section (b). With mechanical degrees marked on the yoke of the stator core and a pointer mounted on the rotor, as shown in Fig.A.7, the saliency torque can be measured at various rotor displacement angles.

(d) Generator Test Circuit Arrangement

With the circuit arrangement shown in Fig.A.8, short-circuit, open-circuit and load tests can be carried out with SW switched to positions 1, 2 and 3 respectively. To avoid external wiring resistance the stator winding terminals are connected directly together during the short-circuit test.

For the measurement of K, SW is switched to position 2 and the integrator circuit shown in Fig.A.9 is used. The output voltage of the integrator is given as

$$V_o = GnK \qquad (A.4)$$

where $G = \frac{1}{CR_1} = 2\pi 15$

and assuming $\omega CR_2 >> 1$.

(e) Power Supply for D.C. Drive Motor

The Ward-Leonard system, which is a facility available in the Department, is used for varying the speed of the d.c. drive motor on the experimental rig. Fig.A.10 shows the circuit arrangement. In this system the separately excited drive motor is supplied with a constant field current I_m. The armature supply is obtained from a separately excited d.c. generator driven at a constant speed $\dot{\theta}_g$ by an induction motor. The armature voltage of the d.c. generator is given as

$$E_g \simeq K_g \dot{\theta}_g I_g \qquad (A.5)$$

The speed of the d.c. drive motor is expressed as,

$$\dot{\theta} \simeq \frac{E_g}{K_m I_m} = \frac{K_g \dot{\theta}}{K_m I_m} I_g \qquad (A.6)$$

By varying V_g, and hence I_g, on the control console, the speed $\dot{\theta}$ can be changed. In the control console, dV_g/dt can be selected for different accelerations $\ddot{\theta}$ of the drive motor. This facility is used for plotting the torque speed curve of the permanent magnet generator automatically on an X-Y plotter. The smooth and slow acceleration avoids inertia torque fluctuations at the measurement point.

APPENDIX B

SHORT-CIRCUIT MEASUREMENTS TO EVALUATE L AND R

Using the experimental rig described in Appendix A and driving the generator at constant speed, the short-circuit current of the permanent magnet generator is given by

$$I = \frac{K\omega n}{\sqrt{(n^2R+R_a)^2+(\omega n^2L+\omega L_a)^2}} \qquad (B.1)$$

where K, L and R are parameters of the generator

R_a is the resistance of the ammeter and wires

L_a is the inductance of the ammeter and wires

n is the stator winding turns factor

$\omega = 2\pi f$

Rearranging equation (B.1) gives the r.m.s. short-circuit current as

$$I_{rms} = \frac{nK}{\sqrt{2}L_T} \frac{\alpha}{\sqrt{1+\alpha^2}} \qquad (B.2)$$

where

$$\alpha = \frac{2\pi f L_T}{R_T} \qquad (B.3)$$

$$L_T = n^2L + L_a \qquad (B.4)$$

$$R_T = n^2R + R_a \qquad (B.5)$$

The shape factor $(\alpha/\sqrt{1+\alpha^2})$ is isolated from its amplitude by, converting equation (B.2) to

$$\log I_{rms} = \log \left[\frac{nK}{\sqrt{2}L_T}\right] + \log\left[\frac{\alpha}{\sqrt{1+\alpha^2}}\right] \qquad (B.6)$$

Fig.B.1 shows the variation of $\frac{\alpha}{\sqrt{1+\alpha^2}}$ with α plotted on log-log axes. With the n=1 stator winding, the measured I_{rms} variation with frequency for the various rotors is shown in Fig. B.2. It can be seen that the measured curves in Fig.B.2 are similar in shape to that shown in Fig.B.1. By overlaying Fig. B.1 on Fig.B.2 and sliding Fig.B.1 about parallel to the X and Y axes, a position can be found at which the two curves are best matched. At this position the frequency on Fig.B.2 corresponding to $\alpha = 1$ on Fig.B.1 is read off the curve. At this point (α=1)

$$I_{rms_1} = \frac{nK}{2L_T} \qquad (B.7)$$

from equation B.2 where K is the measured flux linkage from Table 3.1

and, from equation B.3,

$$1.0 = \frac{2\pi f_1 L_T}{R_T} \qquad (B.8)$$

Rearranging equations (B.7) and (B.8), the inductance is given as

$$L_T = \frac{nK}{2I_{rms_1}} \qquad (B.9)$$

and the resistance is

$$R_T = 2\pi f_1 L_T \qquad (B.10)$$

Using this curve-fitting technique, L_T and R_T are determined

for the various generators.

With a Wheatstone Bridge, R_a and L_a were measured as 20mΩ and 10μH respectively. Table B.1 shows the parameters, R and L, obtained after subtracting the values of R_a and L_a from R_T and L_T.

TABLE B.1

Parameters L and R from short-circuit tests

Rotor Material	Magnetisation state	Working airgap (mm)	L(μH)	R(mΩ)
Cobalt	complete	0.5	260	110
Alnico (N)	complete	0.5	190	110
Alnico (H.Br)	complete	0.25	250	110
Alnico (N)	incomplete	0.5	200	110
Alnico (H.Br)	incomplete	0.25	240	110

The tests were repeated after those rotors which were not fully magnetised initially had been remagnetised. The results are included in Table B.1.

This measurement technique for L and R does not give accurate results because, over the wide current range of the test, different calibrated ammeters have to be used to minimise meter-reading errors. Since this requires stopping and restarting the test in order to change ammeters it causes R to change since the winding temperature changes. Even without having to change

ammeters, R would increase as the short-circuit current increases due to higher winding temperatures.

Due to the rig design, forced cooling is not effective. Therefore, to minimise temperature effects, measurements were taken in less than a minute run-up time. Results during run-down have shown that the rise in winding temperature reduces the current due to increase in effective resistance. Obviously this introduces errors into the technique. However, the study shows that the short-circuit current varies with frequency in a similar manner to that predicted from the model described in section 2.2

APPENDIX C

IRON LOSSES IN THE ROTOR AND STATOR

(a) Introduction

Investigations have been undertaken to examine the iron losses which are neglected in the equivalent circuit described in chapter 2. The air-turbine has to supply the electrical power output, the winding copper losses and the iron losses. The winding loss is readily calculated from the known current and stator resistance, but the iron losses, due to hysteresis and eddy currents, are much more difficult to assess.

The production stator consists of 0.5mm laminations which are stamped from Losil 800 material. For machines operating at above 50Hz, thinner laminations are usually selected to reduce eddy currents. Therefore as an initial trial study a stator core of identical geometry was manufactured from 0.35mm laminations. Unfortunately material have the same properties as the Losil 800 was not available in thinner laminations and the new stator was made from Transil 335 material. The specifications of the two different stator cores are given in Table C.1. These two stator cores were used in the iron loss studies. Individual laminations of these stator cores had their burrs removed and were insulated with varnish to minimise any experimental error caused by short-circuited laminations.

TABLE C.1

Specifications of stator cores

	Stator material	
	Losil 800	Transil 335
Number of laminations	29 0.5mm pieces 2 1.2mm pieces	41 0.35mm pieces 2 1.2mm pieces
Resistivity (Ωm)	37×10^{-8}	47×10^{-8}
Percentage of silicon doping	1.6%	2.8%
B/H curve	See Fig.5.4	

(b) Iron Loss Mechanisms

(i) Stator winding open-circuit

With the stator winding open-circuit and the rotor driven, the alternating flux linkage causes eddy current and hysteresis losses in the stator core. Since the stator has a complex geometry, the iron loss density in the stator is not uniform. As the rotor rotates the magnet experiences changing working permeance lines as shown in Fig.C.1. This sets up a pulsating flux density B_E in the solid rotor and causes rotor eddy current losses, as well as hysteresis losses due to the minor recoil loop. In practice different parts of the magnet experience different magnitudes of flux density pulsations and this makes iron loss analysis difficult.

(ii) Stator winding on-load

When the stator winding carries a current, there is a further component of flux pulsation B_F in the magnet which is caused by the demagnetisation mmf H_D. Consider the worst case when the generator has a highly inductive load shown in Fig.C.2, the magnet then experiences a demagnetising mmf which is a maximum when the rotor is at position 1 and zero at position 2. The magnet working points under such conditions are summarized in Fig.C.3. The calculation of iron losses under load conditions was not pursued because of the time limitations.

(c) Total Loss Measurement

The terms total loss and loss-torques refer to the tests which have been carried out with an open-circuit stator. These loss measurements include the iron losses due to eddy currents and hysteresis and any friction and windage losses.

Loss torque experiments were performed to determine the magnitude of the hysteresis and eddy current loss in the generator. With the Cobalt generator mounted in the test rig and the rotor driven at constant speed, the torque-frequency (speed) curve of the generator was measured with each stator core. The results, which represent the loss torques, are plotted in Fig.C.4. Surprisingly they show negligible difference for the two stators despite the different lamination thicknesses. The torque-frequency curve obtained by using a demagnetised rotor is also included in the same figure as a measure of the friction and windage losses of the test rig. It must be emphasised that these mechanical loss torques are not

representative of those in the production lamp system since a different bearing system has been used and no air supply or turbine was present.

Since the hysteresis power loss is caused by the cycling of the material through its hysteresis loop and eddy current power loss results from the induction of circulating currents within the magnetic material, the total iron loss can be represented[70,71] as

$$P_i = a_1 f + b_1 f^2 \qquad (C.1)$$

and the iron-loss torque is

$$T_i = a_2 + b_2 f \qquad (C.2)$$

where a is a function of volume of material and peak flux density

and b is a function of volume of material, r.m.s. flux density squared, lamination thickness squared and resistivity of the material.

The difference between the total loss torques and mechanical loss torques in Fig.C.4 represents the iron loss torques which fit the typical iron-loss torque frequency variation given by equation (C.2).

The oscillograms shown in Fig.C.5 are the integrated emfs obtained from search coils wound on the main pole, yoke and interpole of the stator core. The average flux densities at those parts were calculated and are used in the stator loss calculations of the following section (d).

(d) Stator Loss

With the previous measurements of the total iron losses showing little difference for the two stator cores, further investigation of the subdivision of the losses was necessary. Measurements of losses in the stator yoke were carried out by using a distributed toroidal winding around the yoke, as shown in Fig.C.6. This arrangement, without the rotor, ensures that the majority of the flux linkages are confined to the yoke. A power measurement technique shown in Fig.C.7 is used for the stator iron loss experiment. The output voltage of the A.C. filter is given as

$$V_2 = G_{XY}\, G_{AC}\, \frac{N_1 \frac{d\phi}{dt} I_c R_c}{2} \cos\alpha \qquad (C.3)$$

The iron loss is expressed as

$$P_i = \frac{N_2 I_c}{2} \frac{1}{N_1} \frac{d\phi}{dt} \cos\alpha$$

$$= \frac{N_2 V_2}{N_1^2 G_{XY} G_{AC} R_c} \qquad (C.4)$$

where N_1 is the number of turns on the search coils

N_2 is the number of turns on the excitation coils

G_{XY} is the gain of the analog multiplier, and equals 0.1

G_{AC} is the gain of the A.C. filter, and equals 10

R_c is a dummy resistor, and equals 0.1Ω

$\cos\alpha$ is the power factor.

The solid lines in Fig.C.8 show the measured loss per cycle for the Losil 800 stator. Measurements were made at flux densities corresponding to those measured in the different parts

of the stator under open-circuit conditions when the rotor was driven. The losses for the appropriate material, yoke volume and flux densities have been extracted from the manufacturer's data and are shown as points in the figure. The measured losses and the losses obtained from the manufacturer's data for the Transil 335 stator are also shown in Fig.C.8. The results show that the measured losses are less than those obtained from the manufacturer's data. Possible reasons for this difference in the losses are variations in material properties due to the effects of stamping on material properties, and the non-uniform cross-section of the yoke causing the flux density to be lower than that stated.

It can be shown[72] that the eddy current loss per unit volume in a stack of infinitely long and wide laminations is given as,

$$P_e = \frac{\omega^{3/2} a B^2}{4\sqrt{2\mu\mu_0\rho}} \left[\frac{\sinh(\frac{a}{\delta}) - \sin(\frac{a}{\delta})}{\cosh(\frac{a}{\delta}) - \cos(\frac{a}{\delta})} \right] \text{ Wm}^{-3} \qquad (C.5)$$

where ω is the angular frequency

B is the peak average flux density per lamination

a is the lamination thickness

ρ is the resistivity

μ is the relative permeability at flux density B

δ is the skin depth, and equals $\sqrt{\frac{2\rho}{\mu\mu_0\omega}}$

Using equation (C.5), the eddy current loss per cycle is predicted for the two stator cores at the various flux densities and frequencies. The results which exclude hysteresis loss are plotted as broken curves in Fig.C.8. The gradients of the

measured and predicted curves in Fig.C.8 are different, suggesting poor agreement in the eddy current loss. However they show the same order of magnitudes.

Using the measured stator yoke loss in Fig.C.8 and allowing for suitable changes in flux density at different sections of the stator, the total stator iron losses have been estimated and shown in Fig.C.9.

(e) Rotor Loss

With a search coil wound around a rotor pole and the open-circuit stator rotating, the waveform of the flux pulsations in the rotor due to the changing working permeance, as discussed in section (b)(i), is shown in Fig.C.10. The measured waveform has been synthesized to determine the relative magnitudes and phases of the harmonics and the result is given in Fig.C.10.

With such a complex rotor geometry it would be extremely difficult to predict the hysteresis and eddy current losses due to the flux pulsations. However an approximate estimate of the eddy current loss can be predicted by making the following assumptions;

(i) The flux variation of Fig.C.10 is uniform in the rotor shown in Fig.C.11.

(ii) The single valued working permeability is the recoil permeability of Cobalt, μ_{recoil}.

(iii) The total power loss includes the harmonic power losses.

(iv) The eddy currents at the fundamental frequency and higher harmonics do not interact with each other.

(v) The rotor is infinitely long and wide.

By modifying equation (C.5), the eddy current loss is given as

$$P_r = \sum_{n=1}^{9} \frac{\omega_n^{3/2}\ \phi_n^{2}}{4\sqrt{2\rho\mu_o\mu_{recoil}}} \left[\frac{\sinh(\frac{a}{\delta_n})-\sin(\frac{a}{\delta_n})}{\cosh(\frac{a}{\delta_n})-\cos(\frac{a}{\delta_n})}\right] \frac{\log_e(r_1/r_2)}{\theta} \qquad (C.6)$$

where n is the harmonic number

ϕ_n is the flux linkage of harmonic n

ω_n is twice the stator winding frequency

Only harmonics up to the ninth were considered because higher order harmonics could not be determined accurately using the synthesizing technique. The measurement of harmonics can be improved by modifying the test rig, such that the stator can be driven at constant speeds, and using a spectrum analyser.

The predicted eddy current loss in the rotor is compared with the stator loss in Fig.C.9. The results show that the rotor loss is significant, although the theory used in the calculations is not refined and will not give accurate results.

(f) Discussion Of Results

By subtracting measured mechanical loss from the measured total loss in Fig.C.4, the measured iron losses for the Cobalt rotor with the two different stators are compared with the predicted iron losses (stator plus rotor) in Fig.C.9. The spread of predictions is very small and compares favourably with the spread of measured losses.

The study has shown that the rotor iron losses are much higher than those of the stator. Hence the reduction in total

iron losses is small when the existing stator material is replaced with Transil 335. Obviously the use of a Transil 335 stator core is not cost-effective because of the higher material cost.

Since the generator is complex in geometry and the rotor has complicated flux pulsations, eddy current loss predictions based on a one-dimensional model and a sinusoidal flux density cannot be very accurate. Other possible reasons for the difference between measured and predicted iron losses are :

(i) variations in lamination properties after stamping

(ii) changing permeabilities with instantaneous alternating flux densities due to hysteresis

(iii) the interaction of harmonic eddy currents which tends to reduce the effective skin depth and cause an increase in eddy current loss

(iv) the neglect of hysteresis loss in the rotor material.

Other causes of such discrepancies have been proposed by past workers[73-78] researching into iron loss mechanisms. Possible explanations suggested by them are :

(i) flux distortion in each lamination even though the total average flux density is sinusoidal

(ii) distortion in hysteresis loops at high frequency giving an increase in hysteresis loss.

Finally a literature survey has failed* to uncover any iron loss investigation for permanent magnets. This has hindered the complete understanding of iron loss mechanisms in the generator.

* reference since located [81]

APPENDIX D

COMPARISON OF GENERATORS HAVING SINGLE-PHASE AND THREE-PHASE WINDINGS

(a) Single-Phase Winding

The geometry of the single-phase generator is assumed to be that shown in Fig.D.1 in which the stator has a 3 coil concentrated winding. With the coils connected in series, the peak flux linkage is given as,

$$K_1 = NK_{AA} = 3K_{AA} \qquad (D.1)$$

where K_{AA} is the flux linkages per coil.

As the coils are identical and the self-inductance per coil is L_{AA}, then the total stator inductance is

$$L_1 = N^2 L_{AA} = 9L_{AA} \qquad (D.2)$$

(b) Three-Phase Windings

Fig.D.2 shows the geometry of the generator modified to accommodate a three-phase winding. The total induced voltage in stator phase A, with all three phases excited, is

$$L_{AA}\frac{di_A}{dt} + L_{AB}\frac{di_B}{dt} + L_{AC}\frac{di_C}{dt} \qquad (D.3)$$

where L_{AB} and L_{AC} are mutual inductances.

Since there is a 120° electrical spatial displacement between the phases, the mutual flux due to currents in phases B and C will be demagnetising on phase A when positive currents flow in phases B and C. For a sinusoidal flux distribution, neglecting leakage, the mutual inductance is expressed as

$$M = L_{AB} = L_{AC} = L_{AA} \cos 120^{o} = - \frac{L_{AA}}{2} \qquad (D.4)$$

since all the phases are identical.

For a balanced load,

$$i_A + i_B + i_C = 0 \qquad (D.5)$$

By substituting equations (D.4) and (D.5) into equation (D.3), the total induced voltage in phase A is

$$L_{AA} \frac{di_A}{dt} - \frac{L_{AA}}{2} \frac{d(-i_A)}{dt} = \frac{3}{2} L_{AA} \frac{di_A}{dt} \qquad (D.6)$$

From equation (D.6), the apparent inductance detected at the phase terminals is 3/2 times the value measured with only that particular phase A excited. Therefore the effective inductance per phase is

$$L_3 = \frac{3}{2} L_{AA} \qquad (D.7)$$

The peak flux linkage per phase is given by

$$K_3 = K_{AA} \qquad (D.8)$$

(c) Comparison of T_{max}

The peak torque of the single-phase generator is

$$T_{max_1} = \frac{K_1^{\,2}}{L_1} = \frac{K_{AA}^2}{L_{AA}} \qquad (D.9)$$

whilst that for the three-phase generator is given as

$$T_{max_3} = 3 \times \frac{K_3^{\,2}}{L_3} = \frac{2K_{AA}^2}{L_{AA}} \qquad (D.10)$$

Hence,

$$T_{max_3} = 2T_{max_1} \qquad (D.11)$$

(d) Conclusion

With three-phase windings, it has been shown that a doubling of T_{max} is possible compared to that for a generator with a single-phase winding. An identical result would be obtained for pole numbers other than two.

A three-phase generator with a single-phase load will require a three-phase, full-wave rectifier, as shown in Fig.D.3. The additional rectification circuitry will increase both the cost and the ohmic losses, and reduce the reliability of the system. A three-phase distributed winding will require a completely new design of stator lamination. Because of the high tooling cost which would be involved, and the lower reliability of the three-phase generator, it was decided to retain a single-phase design for the 250W generator.

APPENDIX E

PROTECTION CIRCUITS

Various electronic circuits were considered for switching a load resistor R_D across the stator terminals in the event of bulb failure, hence preventing the generator from over speeding.

A protection circuit has been developed which is simple in design, uses very few components and, most important, is low in cost. All the circuits which were considered used a Triac as the main switching element.

(a) Design 1

By analysing the circuit given in Fig.E.1, the triac gate voltage is given by

$$V_g = V_2 \left(\frac{R_3}{R_2+R_3}\right) \left(\frac{R_4+R_5}{R_4}\right) - V_6 \frac{R_5}{R_4} \qquad (E.1)$$

If $R_2+R_3 = R_4+R_5$, then

$$V_g = V_2 \frac{R_2}{R_3} - V_6 \frac{R_5}{R_4} \qquad (E.2)$$

During normal operating conditions, the differential circuit ensures that $V_g < V_{gt}$, the voltage required to fire the triac. When the bulb fails, $V_6 = 0$. From equation (E.2), V_g will increase and trigger the triac when $V_g > V_{gt}$, hence loading the generator with R_D.

Disadvantages:

(i) R_D has to be about 1Ω to ensure that there is sufficient voltage supply to the op-amp

(ii) High component count, hence expensive to manufacture

(iii) High values of electrolytic capacitors, which have low MTBF, are required. In the event of a capacitor becoming short-circuited they could cause dangerous sparks because of their high stored energy.

Advantages:

(i) Positive detection circuit

(ii) Circuit design is not critical to component tolerance

(b) Design 2

Fig.E.2 shows a design which uses a latching circuit to trigger the triac. Under normal operating conditions, $V_g = 0$. If the bulb fails, voltages V_1 and V_2 rise. This in turn increases V_3 to change the flip-flop circuit from state '0' to '1' and so triggers the triac.

The disadvantages and advantages of this design are the same as those given for design 1.

(c) Design 3

With the bulb in circuit the secondary output voltage of transformer T_r in Fig.E.3 keeps triac T_2 on and triac T1 off. In the event of bulb failure, T_2 switches off and T1 is triggered.

Disadvantage:

(i) Needs a transformer as a sensor, which could be bulky and costly

Advantages:

(i) Low in component count

(ii) Positive detection circuit

(iii) Simple in design

(d) Design 4

Fig.E.4 shows a circuit which uses a thermal sensor R_T as a detector. Typically, R_T could be 100Ω at temperatures above 70°C and 10KΩ at temperatures lower than 40°C. R_T is attached to the bulb envelope for better thermal contact. With a working bulb, the heat from the bulb will reduce R_T and the gate voltage, which is less than v_{gt}, is

$$v_g = v_L \frac{R_T}{R_T+R_1} \simeq v_L \frac{R_T}{R_1} \qquad (E.3)$$

When the bulb fails, the compressed air will cool the thermal sensor R_T. This will cause the gate voltage to rise to

$$v_g \simeq v_L \qquad (E.4)$$

which in turn triggers the triac.

Disadvantages:

(i) Thermal delay time might be excessive

(ii) Mounting difficulties of R_T to bulb if bulb needs to be changed

Advantage:

(i) Simple in design

(ii) Low in component count

(e) Design 5

By replacing the thermal sensor R_T of design 4 with a light dependent resistor LDR, the circuit is modified to that shown in Fig.E.5. With an operating bulb, the light will keep the resistance of LDR low. This in turn causes the gate voltage V_g to be less than v_{gt} and triac T1 off. When the

bulb fails, the resistance of LDR increases and causes the voltage v_g to rise which triggers the triac. Tests have shown that this circuit works.

Disadvantages:

(i) LDR has to be mounted in a suitable position to prevent high ambient light from de-activating the circuit

(ii) Inspite of the bulb being force cooled, the thermal time constant of the bulb will cause the light output to decay gradually so that there will be a delay between bulb failure and the triac being triggered.

Advantages:

(i) Simple in design

(ii) Sensor needs no direct contact with the bulb

(f) Design 6

Fig.E.6 shows a protection circuit which uses transient voltages to switch on the triac. During normal bulb operation, the impedance of C is sufficiently high to prevent the triac from triggering. When the bulb fails, there will be a transient voltage at the triac gate terminal sufficient to trigger the triac.

Advantages:

(i) Simple in design

(ii) Almost instantaneous triggering of triac

(iii) No sensors required

This circuit was finally selected for the protection of the generator. The design is considered in detail in Section 7.5.

Fig 1.1

Schematic Diagram Of The Air Flow

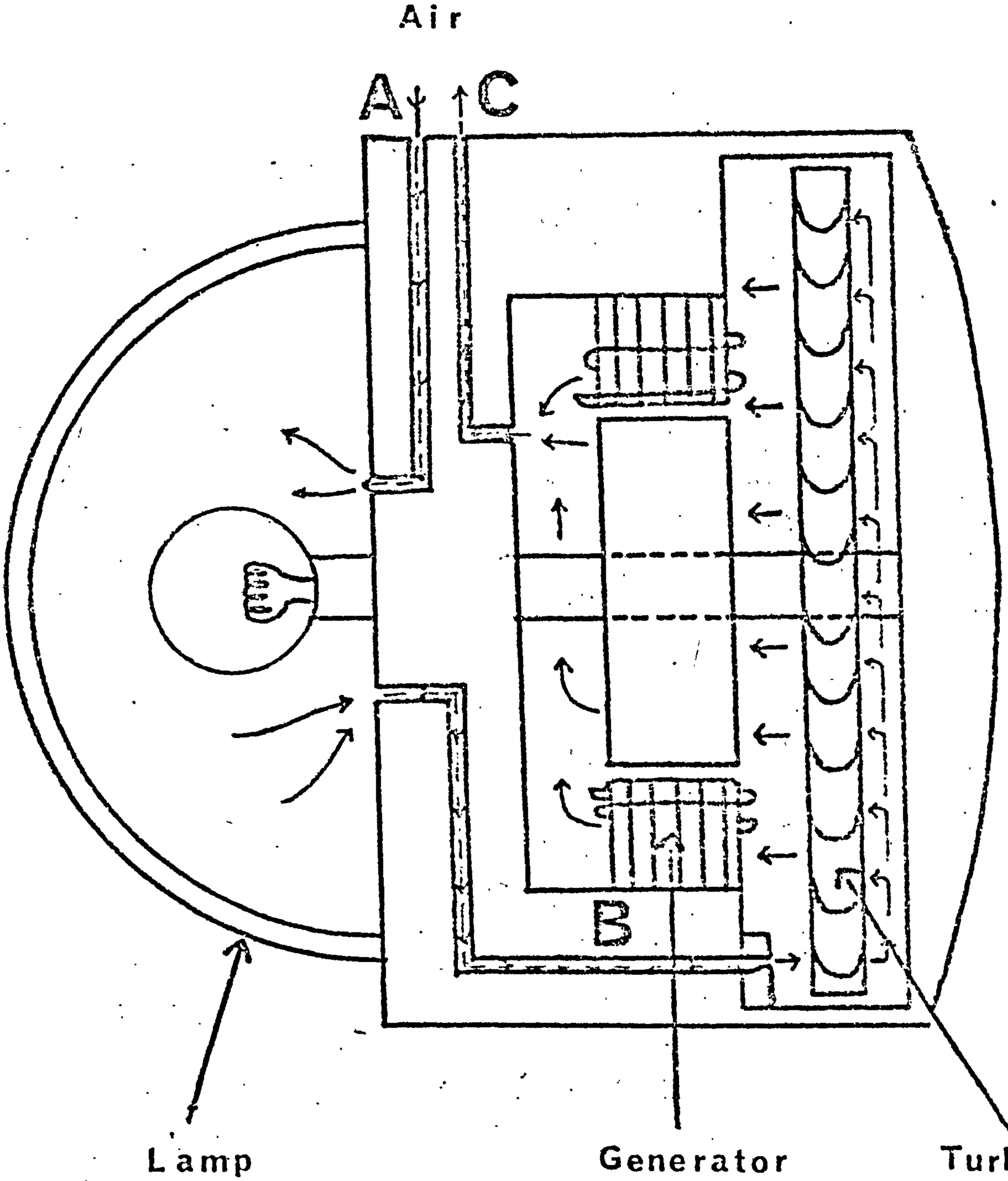

Fig 1·2

The Safety Lamp Unit And The Turbine – Generator

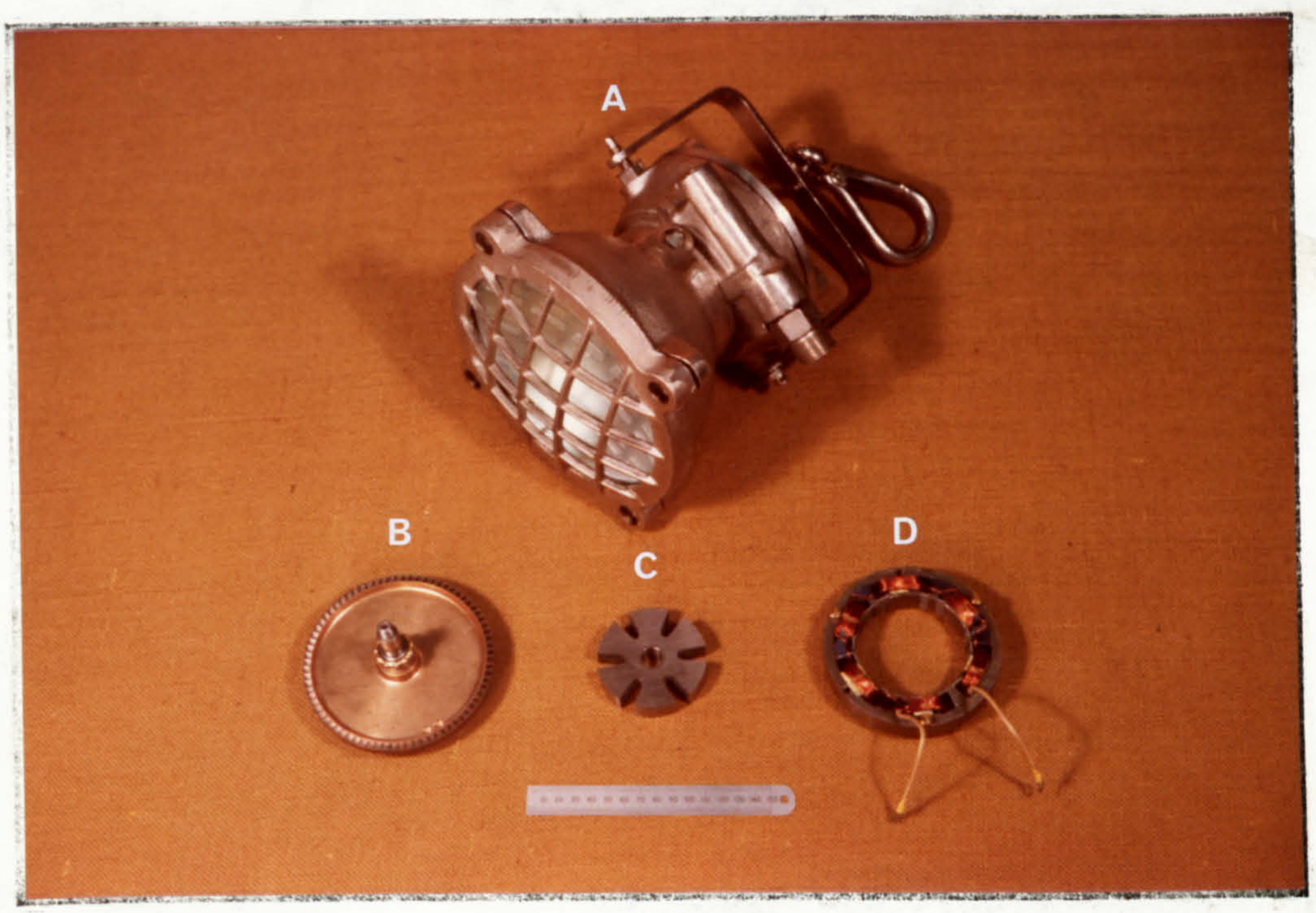

Key:

A : Lamp unit

B : Turbine

C : Rotor

D . Stator

2·1 Equivalent Circuit Of Generator

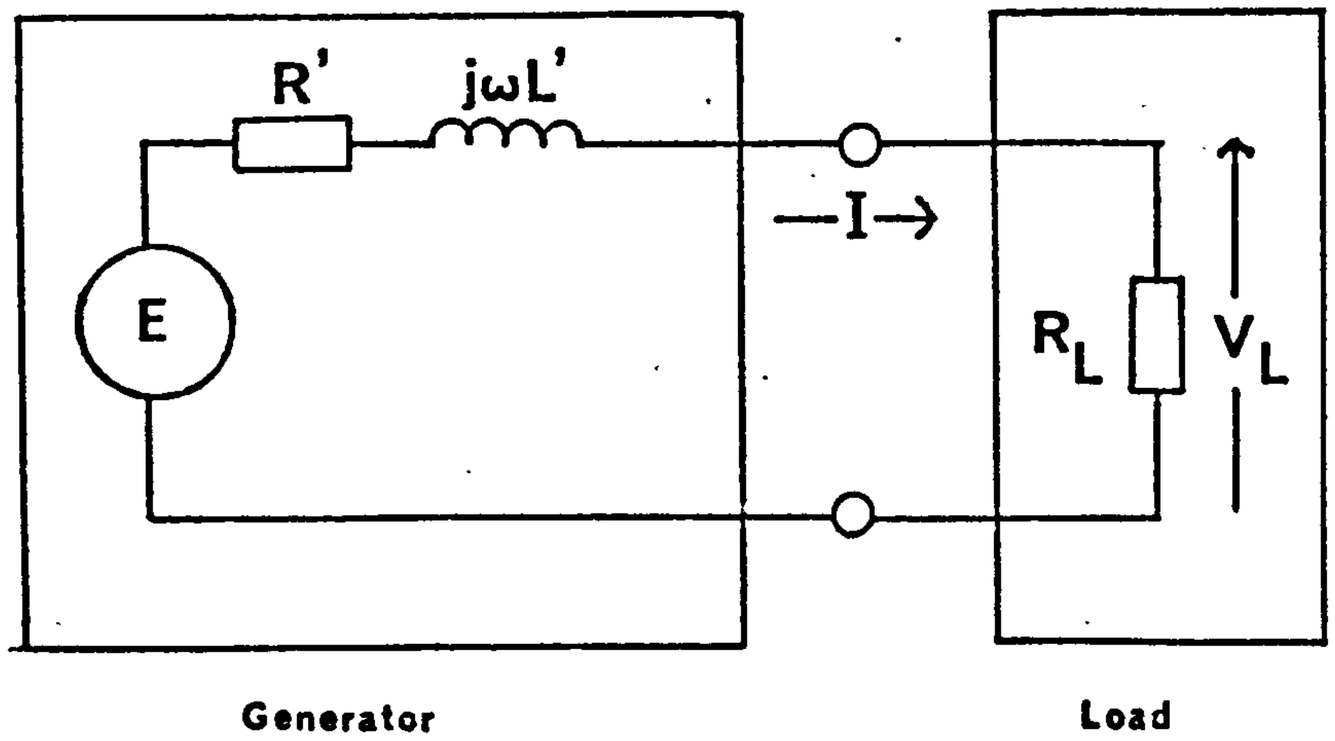

2·2 Performance Of Generator

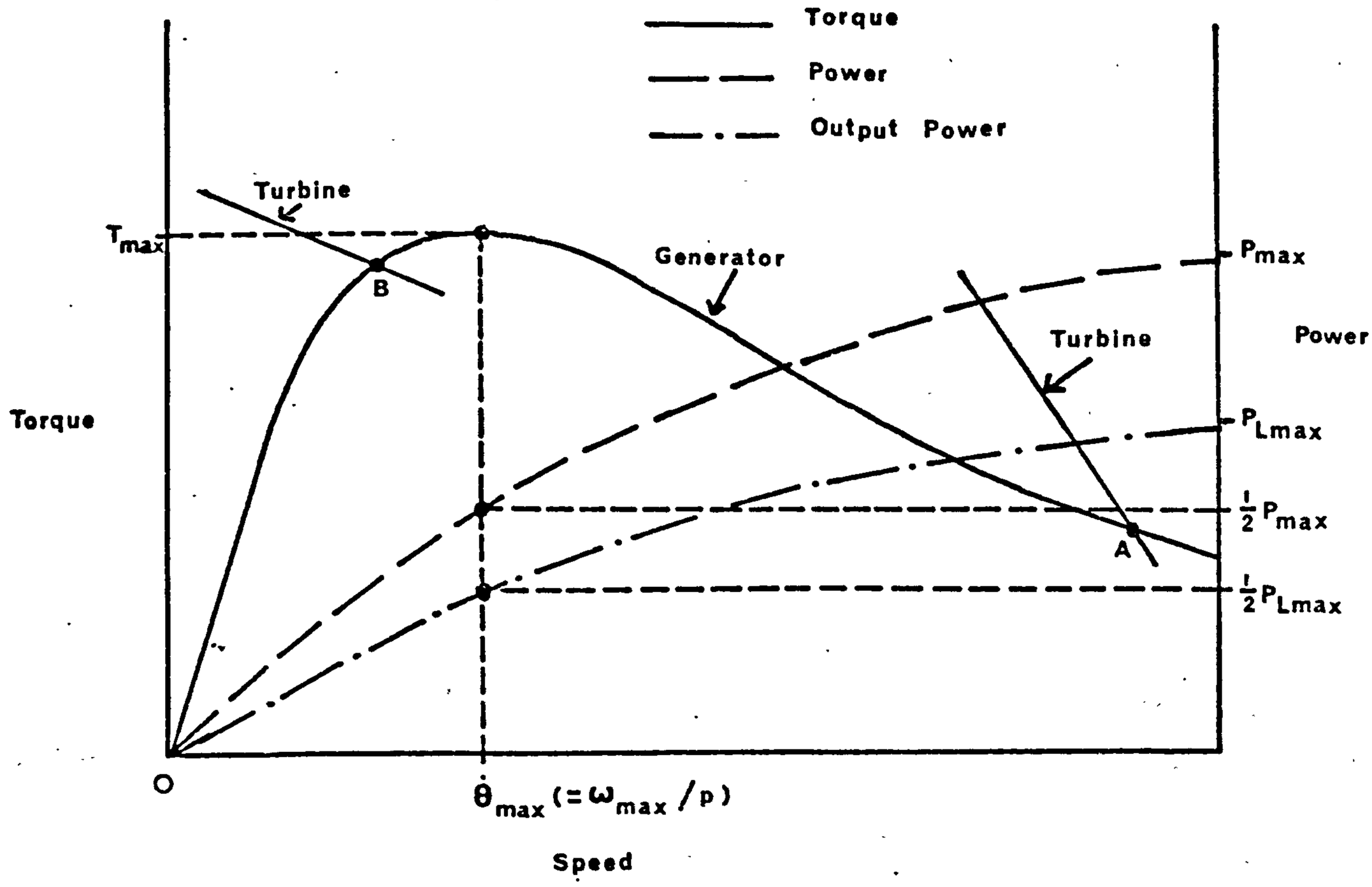

Fig 2·3
Fig 2·4

2·3 Effect Of n On Torque – Speed Curves

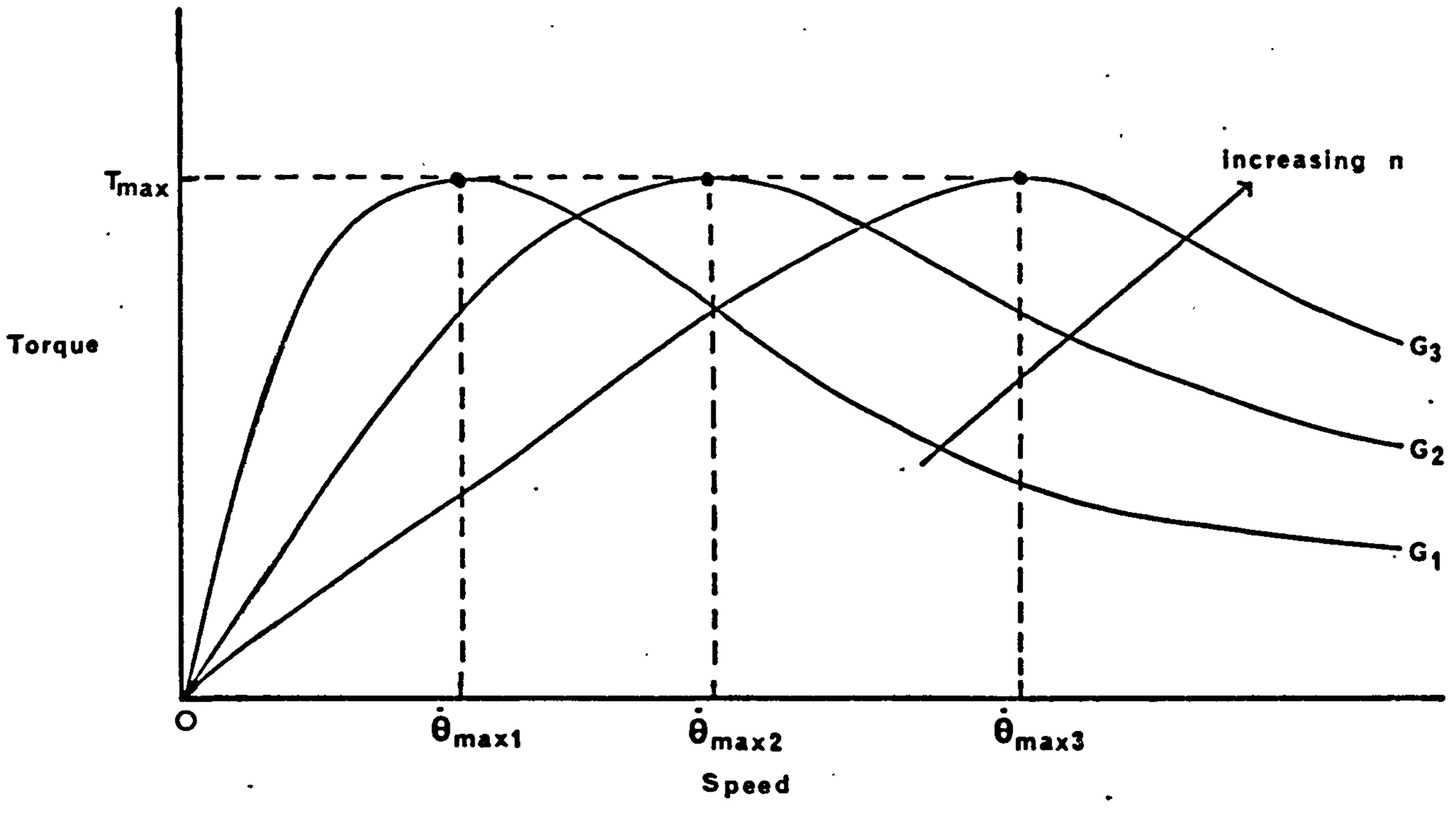

2·4 Comparison Of Torque-Speed Curves

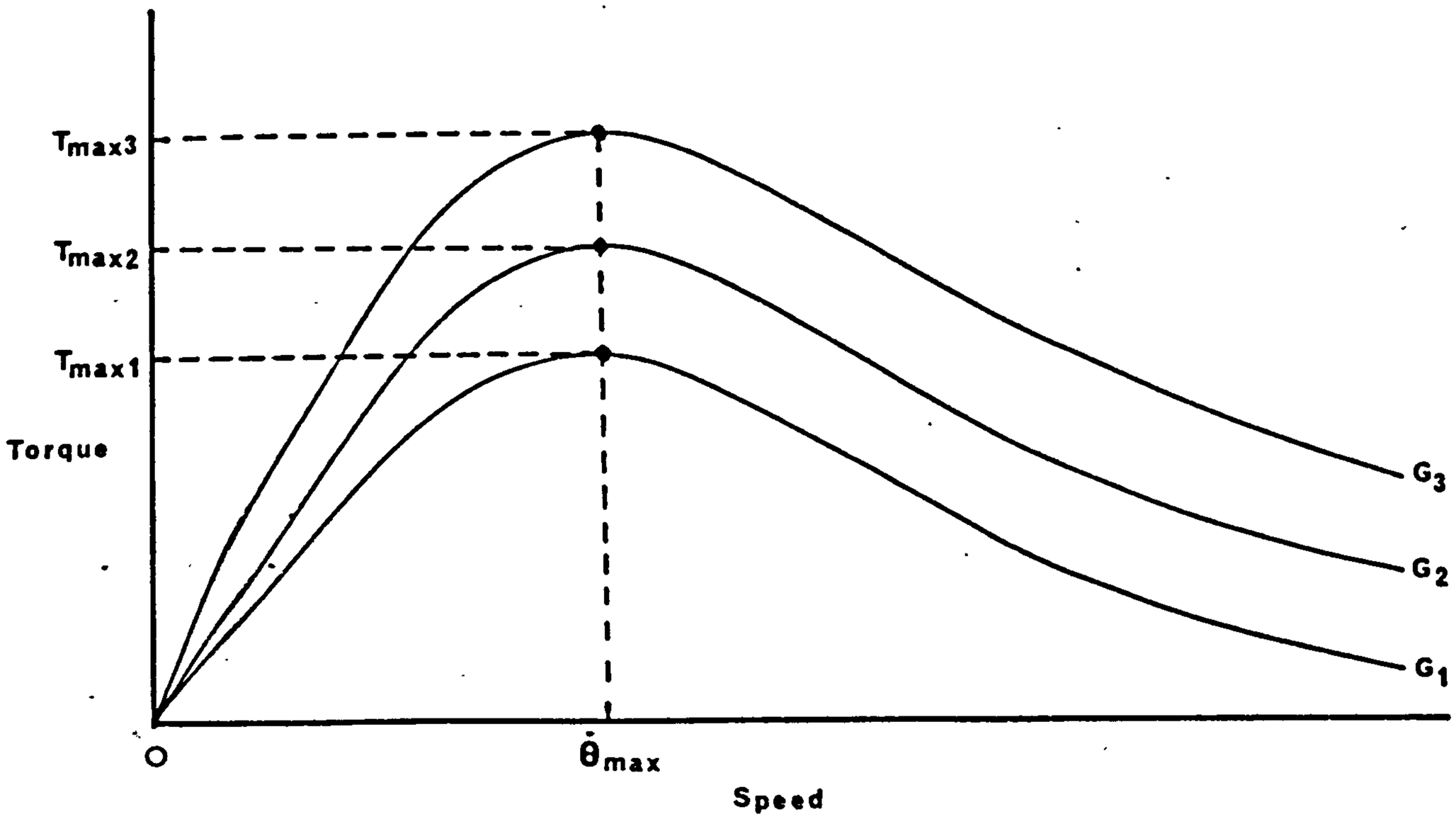

Fig 2·5

Measured Turbine Torque-speed Characteristics

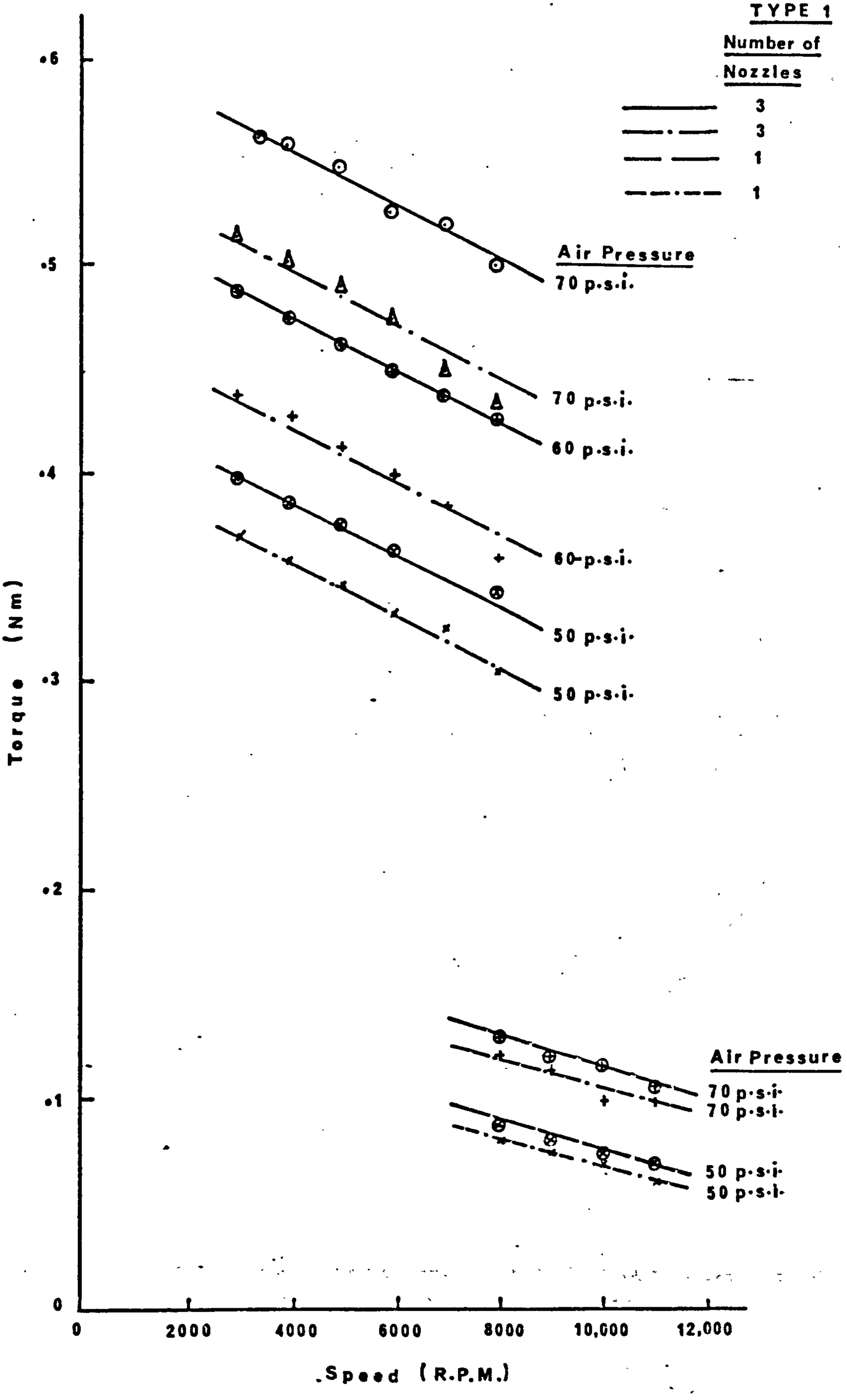

Fig 2·6

Fig 2·7

2·6 Matching The Turbine With The Generator

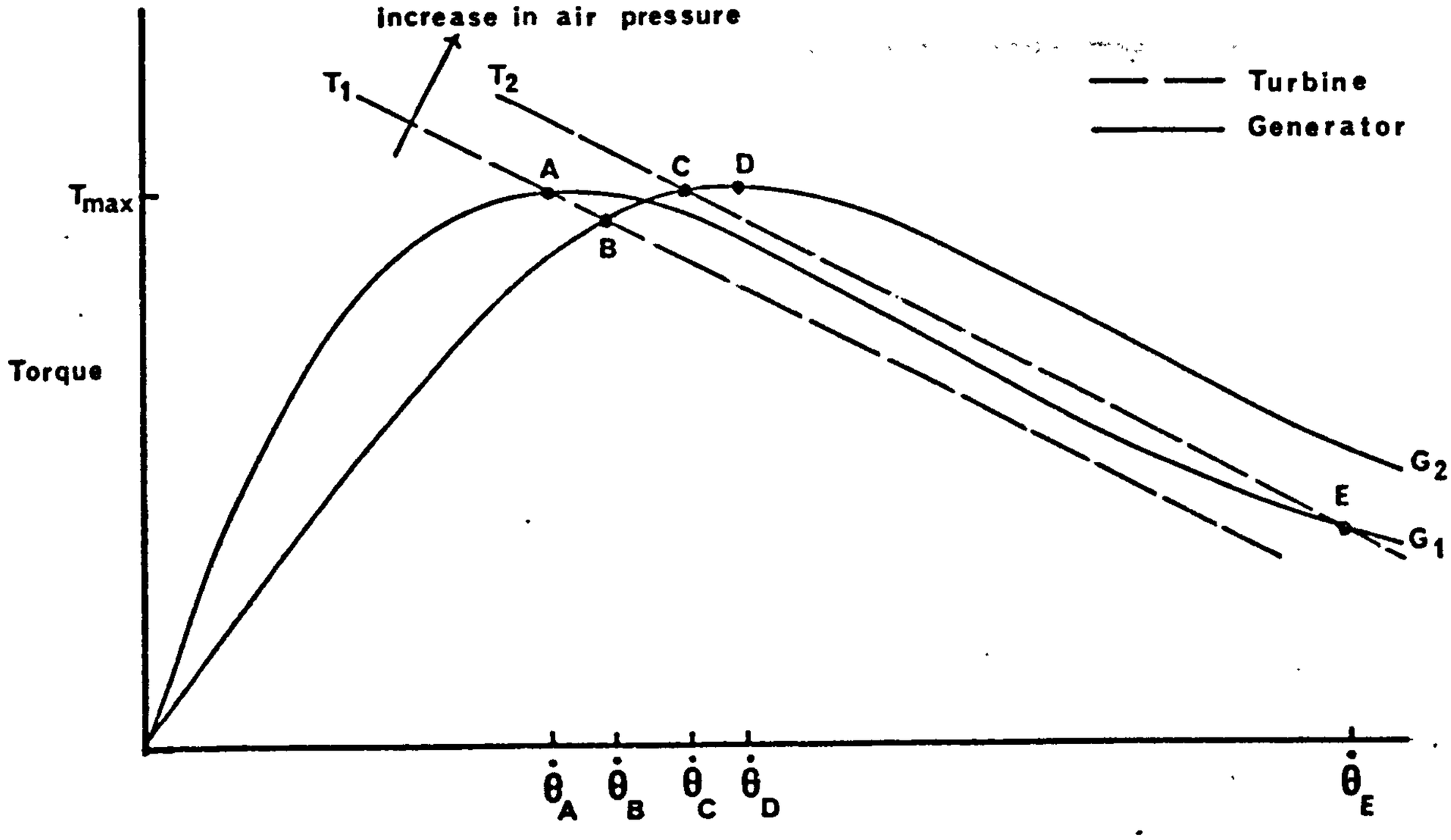

2·7 Variation Of Speed Against Turns Factor For A Specified Bulb Rating

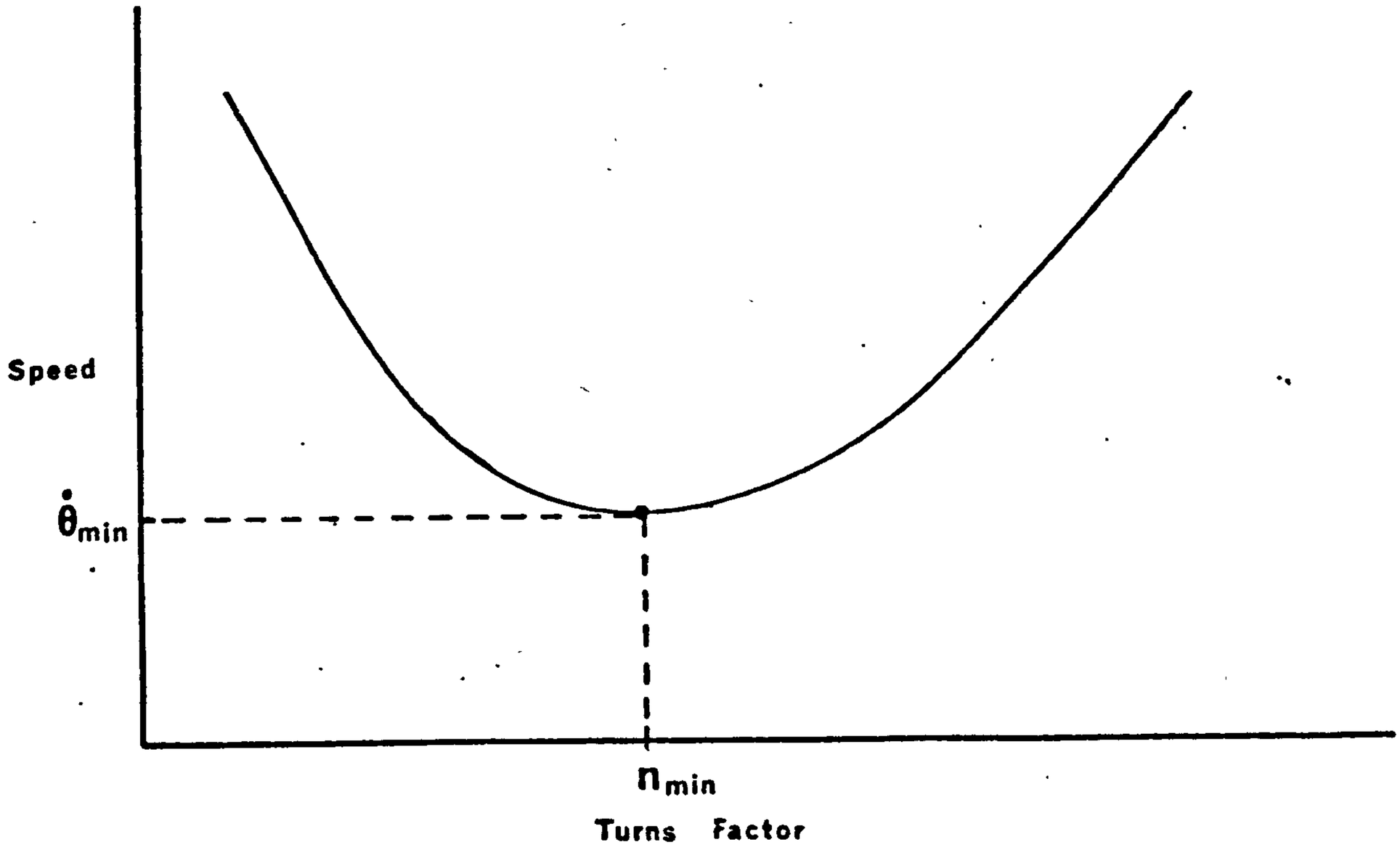

Fig 3·1

Waveform Of Flux Linkage Ψ

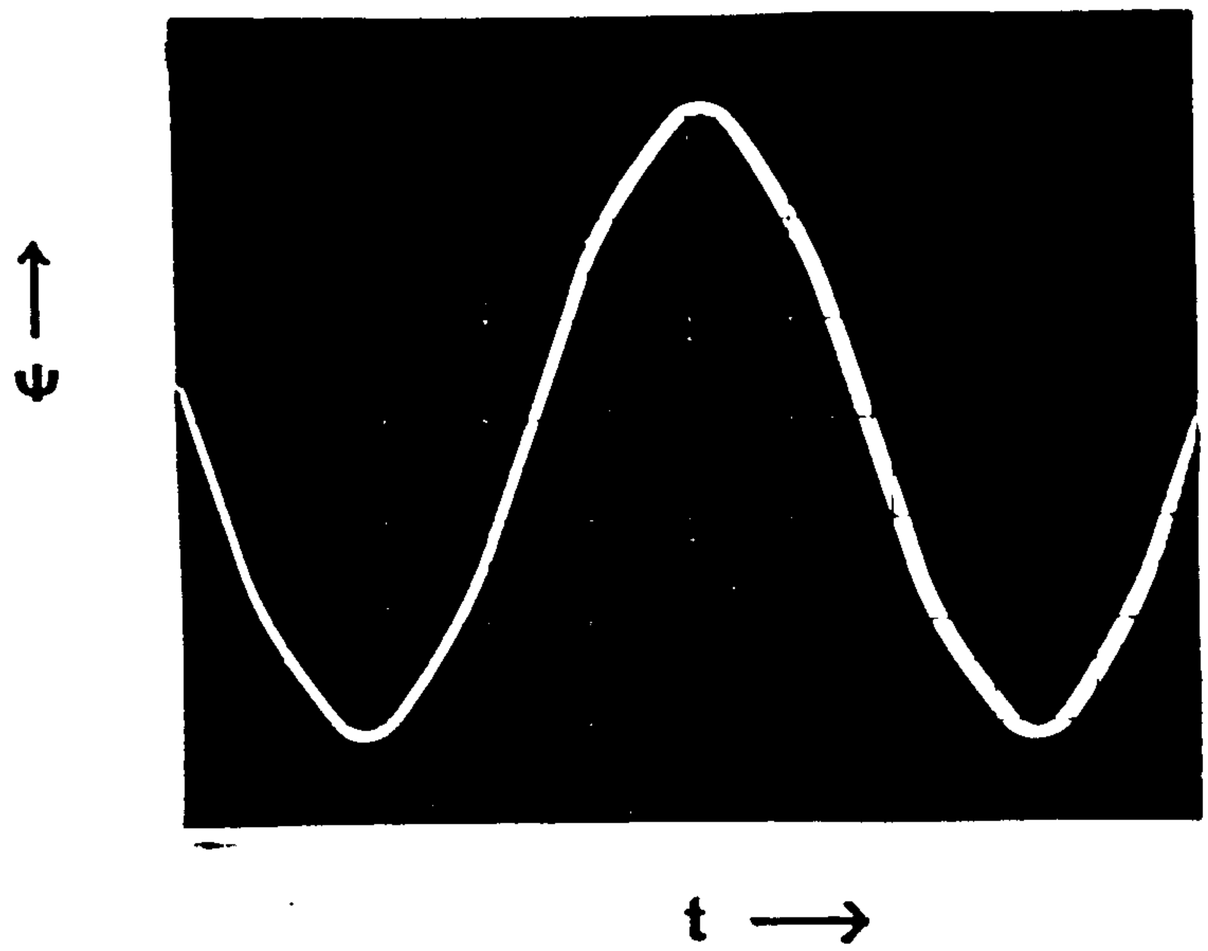

Spectrum Analysis Of ψ

Frequency	Distortion (%)
Fundamental f = 300 Hz	100
Harmonic	Normalised To f
3rd 5 th 7 th 9 th n th >9	1·5 2·6 1·0 0·3 <0·1

Fig 3·2

Circuit Arrangement For Measurement Of L

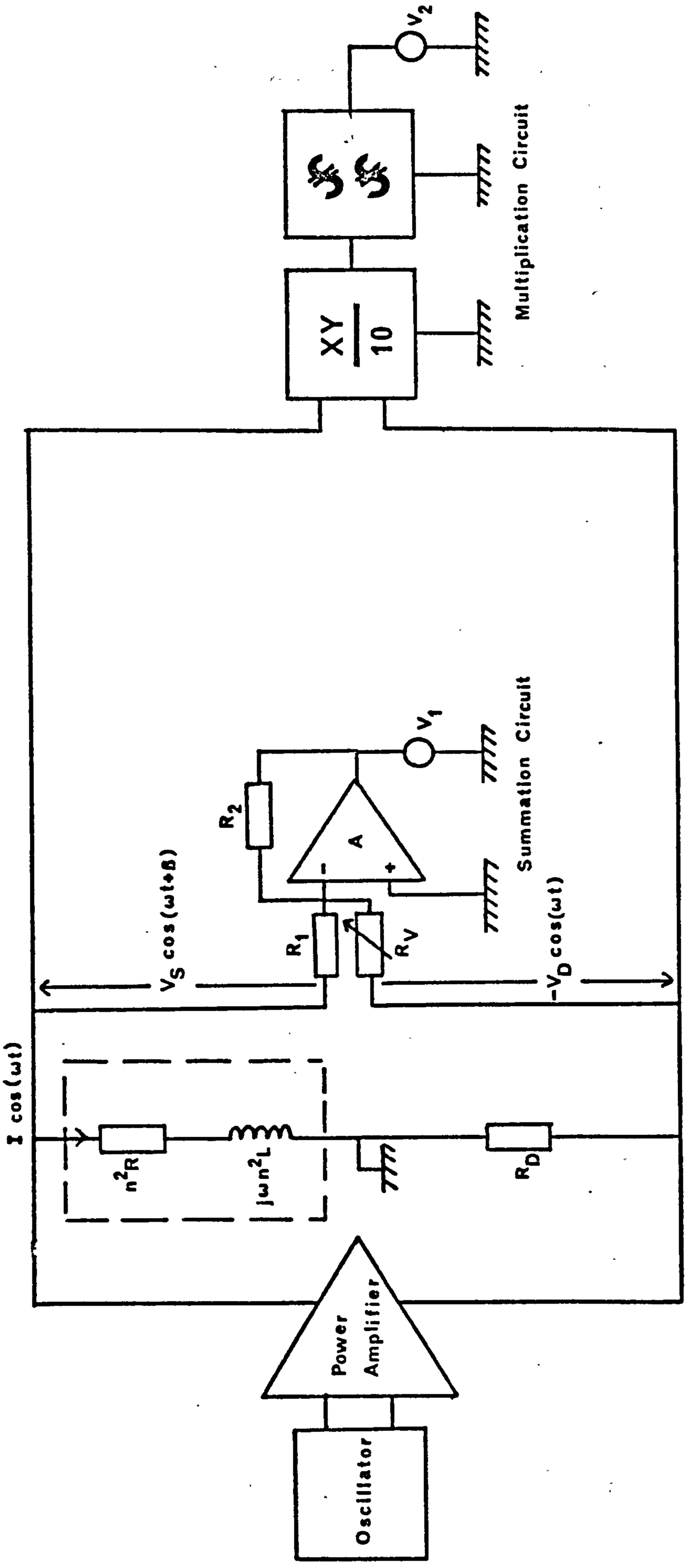

Fig 3·3

Variation Of V_1 With R_2/R_V

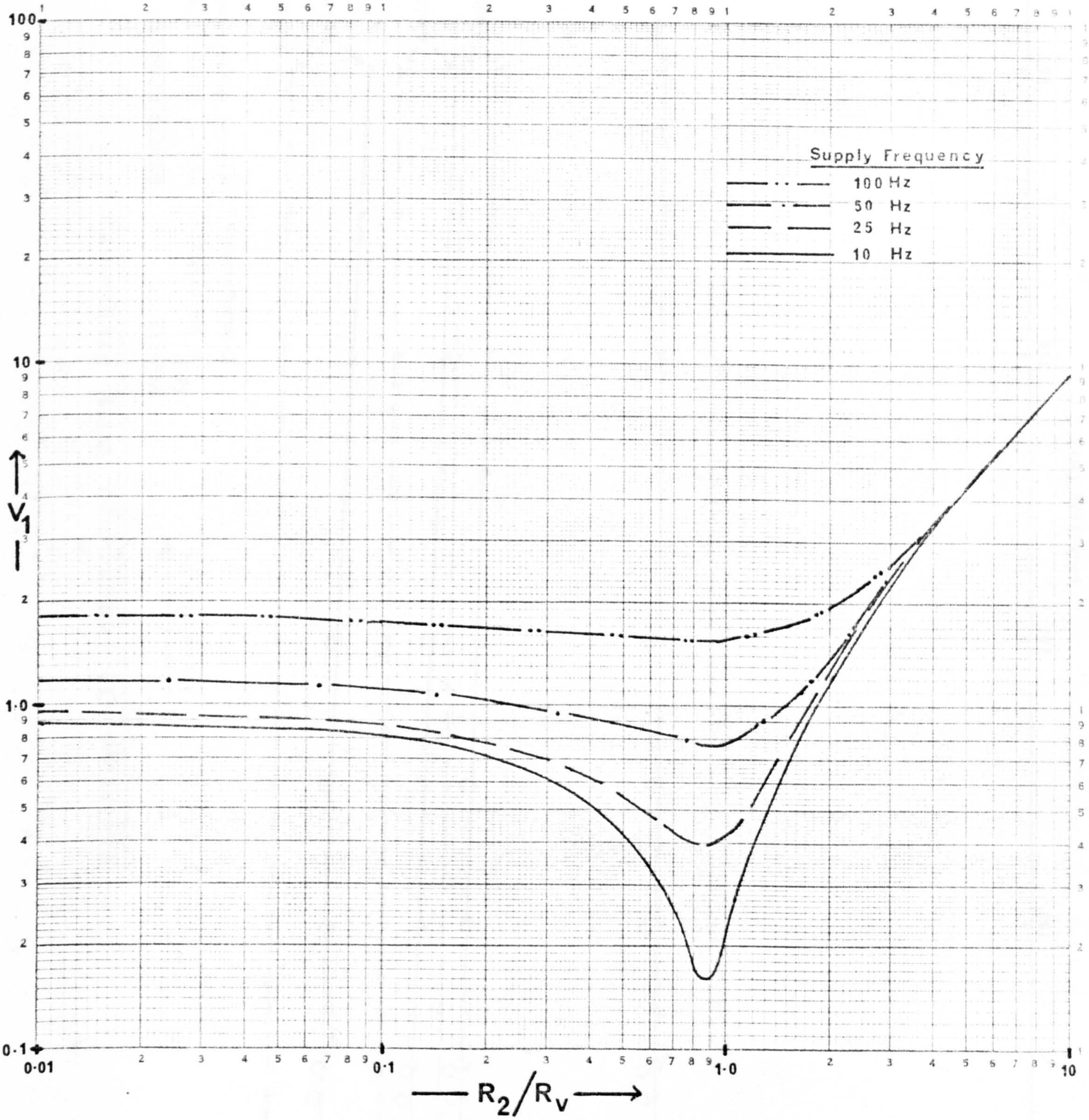

Variation Of Inductance With Frequency

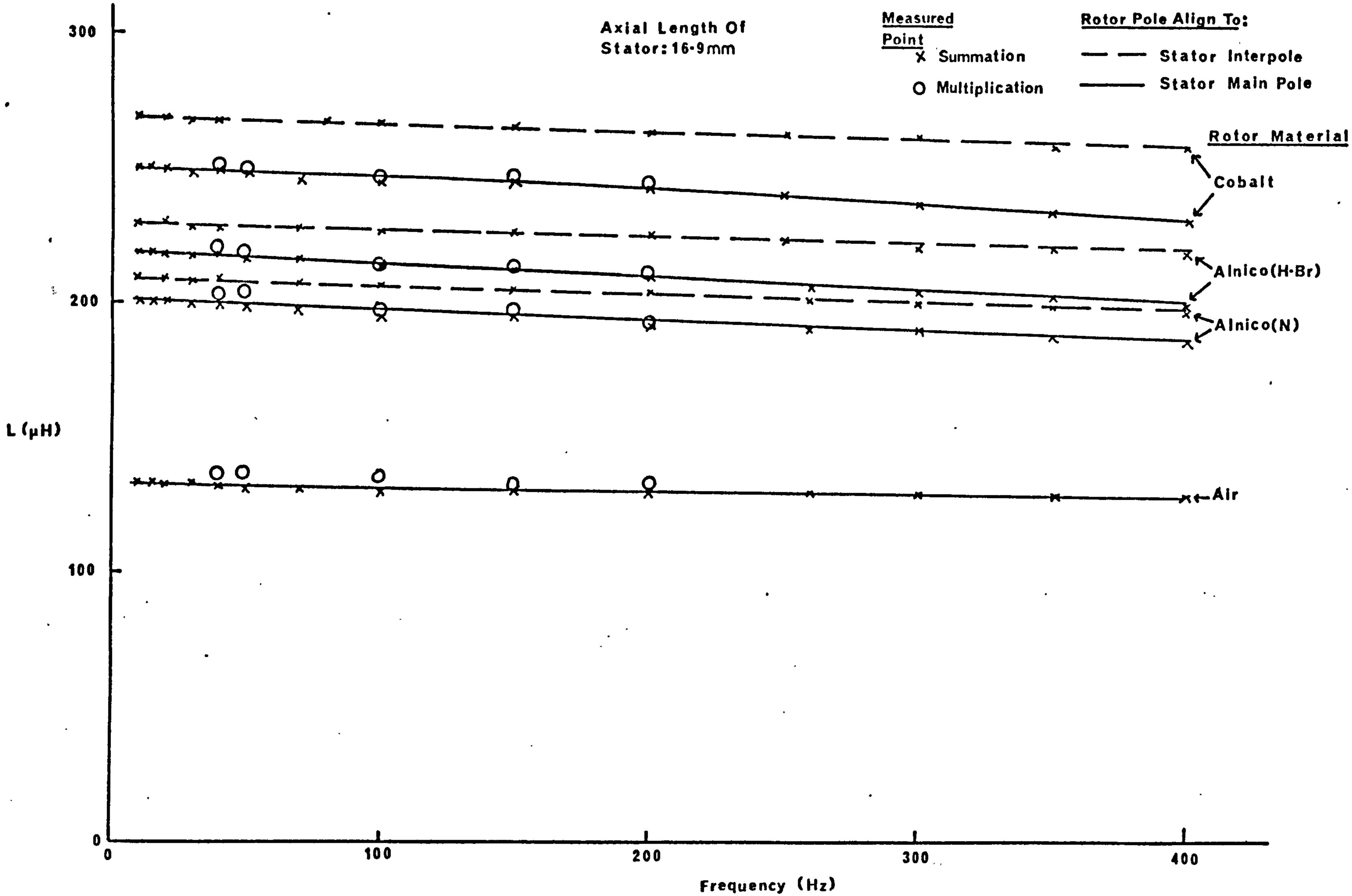

Fig 3.4

Variation Of Resistance With Frequency

Axial Length Of Stator = 16·9 mm

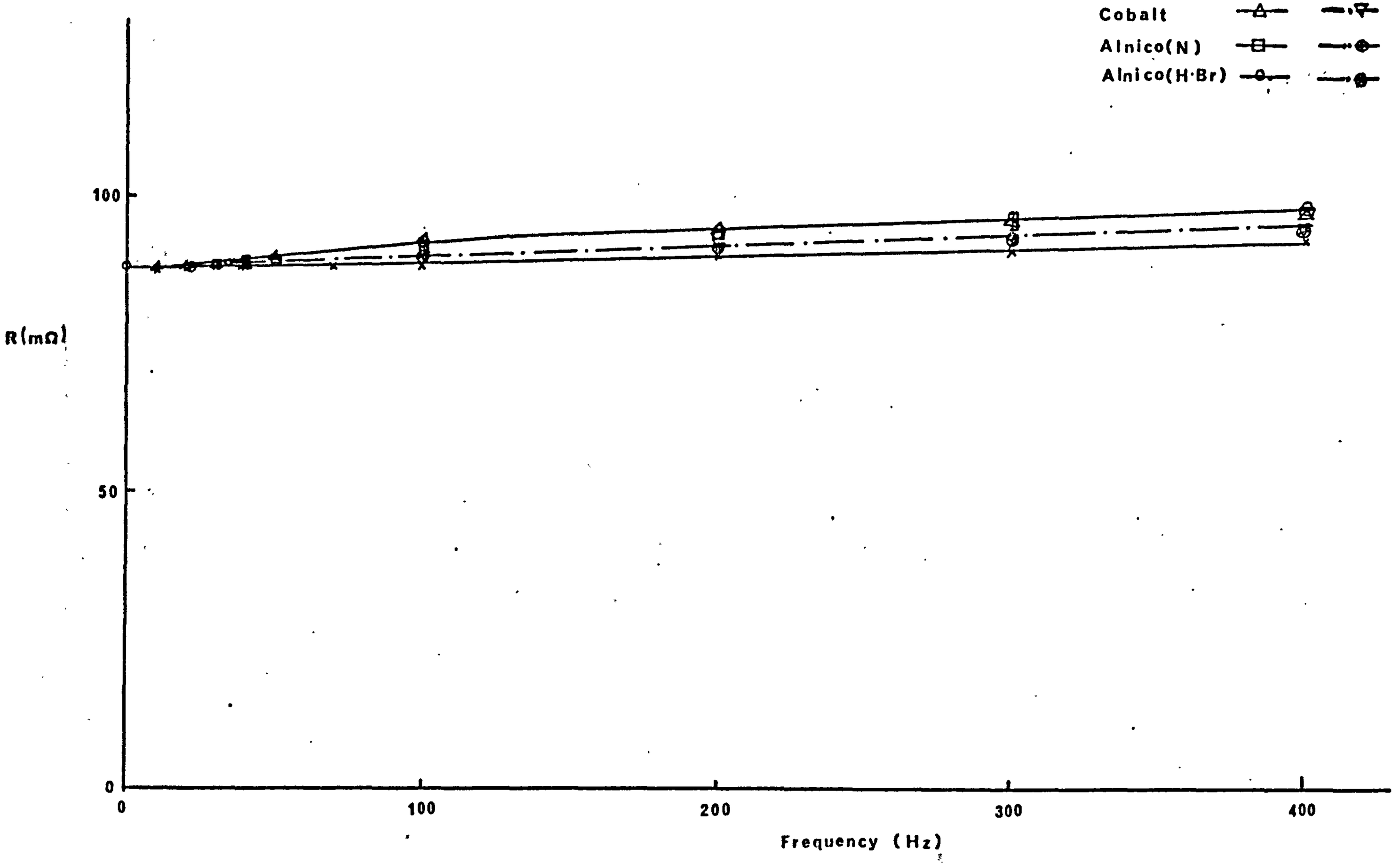

Fig 3.5

Variation Of Inductance With Frequency

Axial Length Of Stator = 32·4 mm

Measured Point

X Summation

O Multiplication

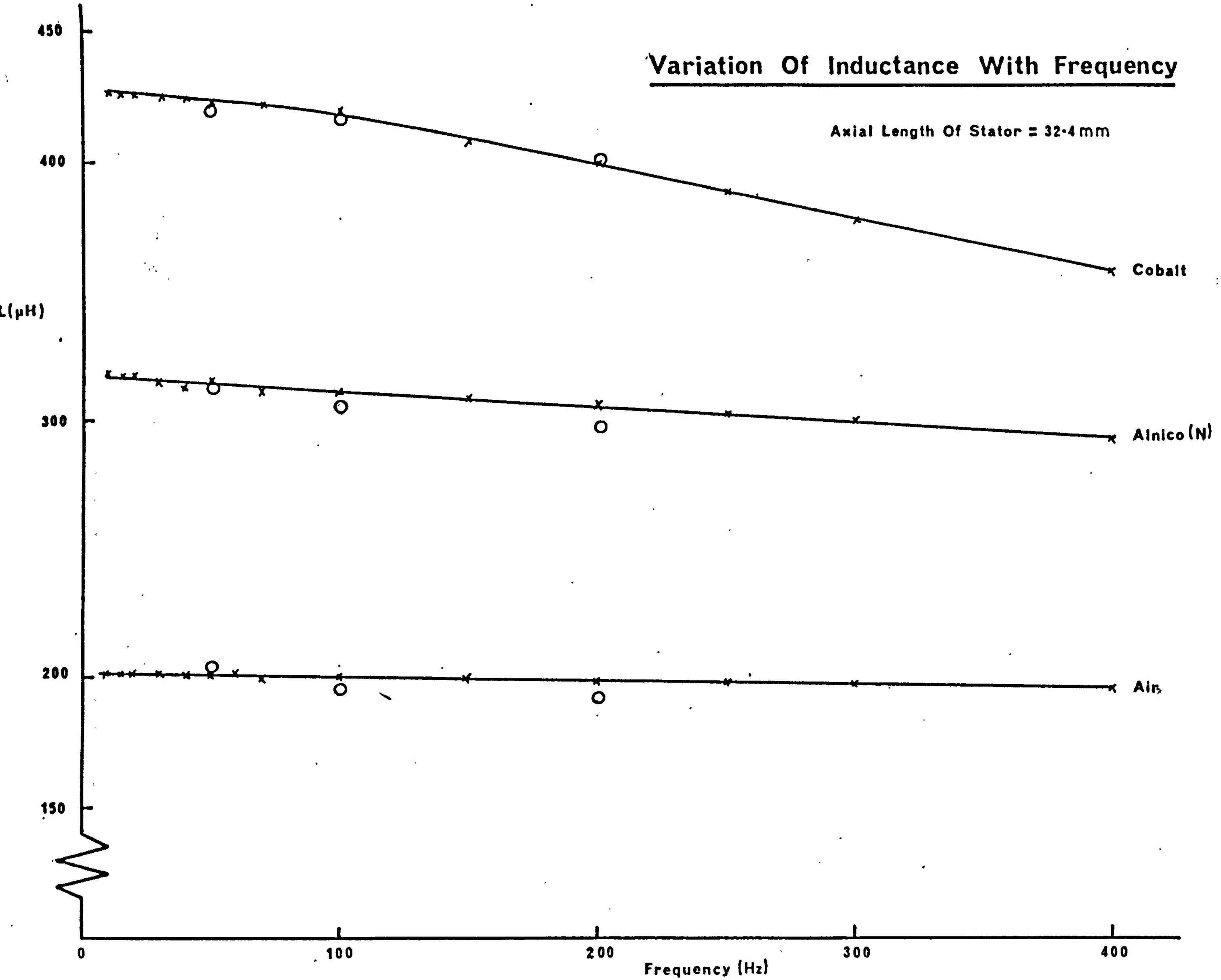

Fig 3·6

Fig 3·7

Variation Of Resistance With Frequency

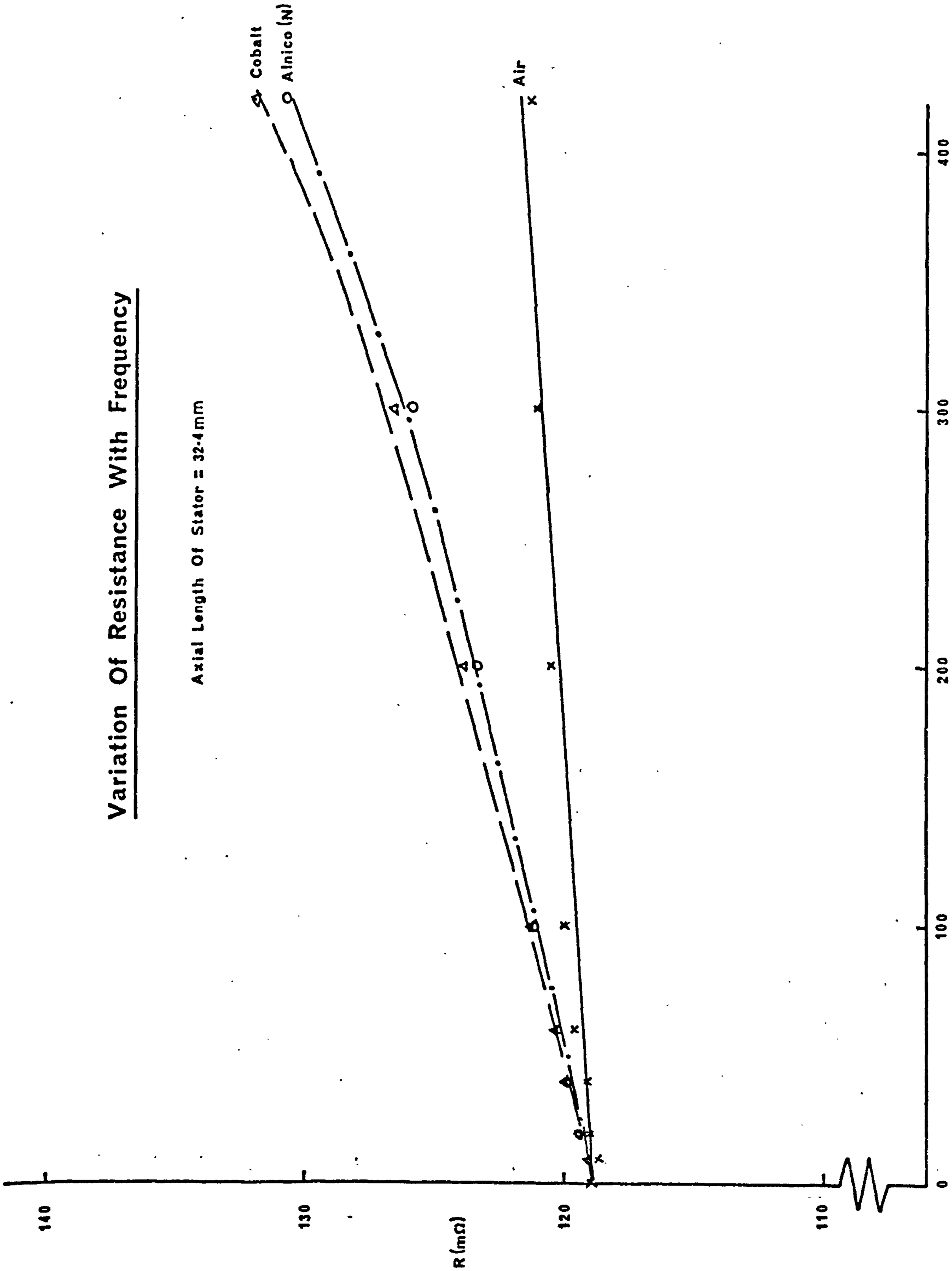

Fig 3·8

Characteristics Of Non-Linear Bulb R_L

$$R_L = AI + Be^{-CI}$$

Bulb Ratings	Measured Point	Predicted Characteristics	Bulb Constants A	B	C
12V 55W	o	—— ——	·401	·6	·5
24V 250W	x	———	·156	·6	·5
12V 100W	Δ	—·—	·122	·4	·5

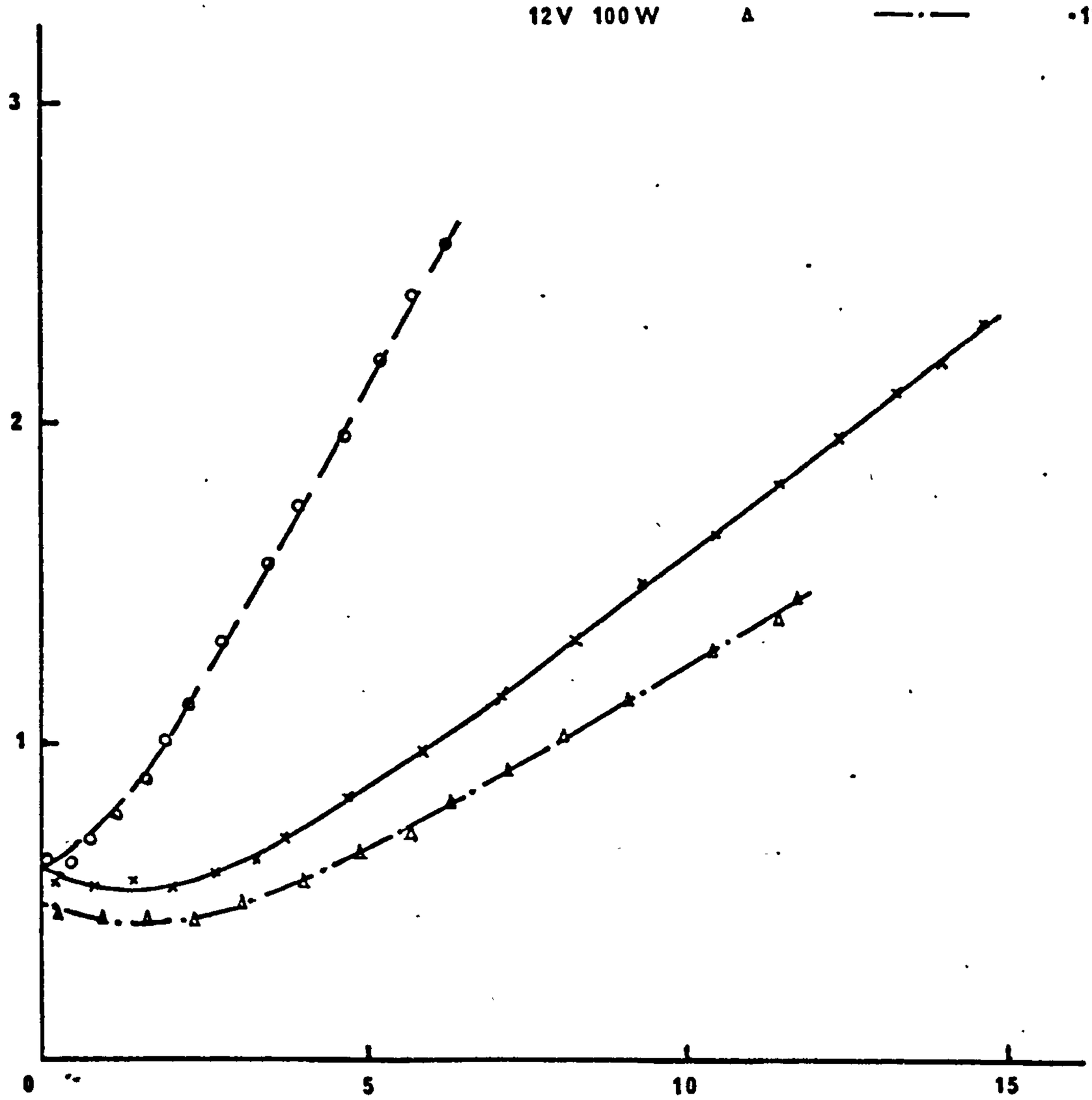

Torque – Speed Curve For Linear And Non – Linear R_L

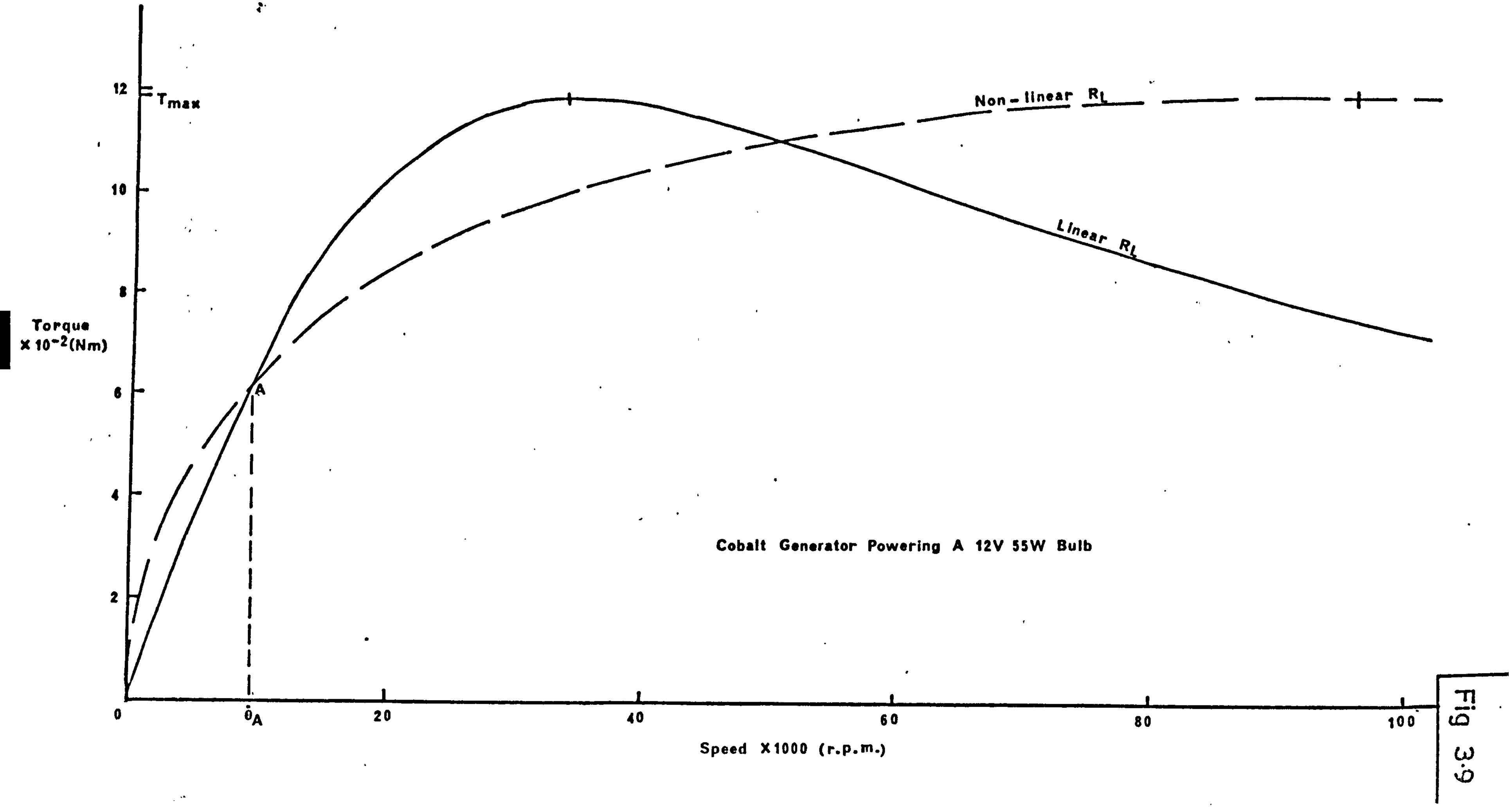

Cobalt Generator Powering A 12V 55W Bulb

Fig 3.9

Fig 3·10

Torque–Speed Curve Of The 55W Cobalt Generator

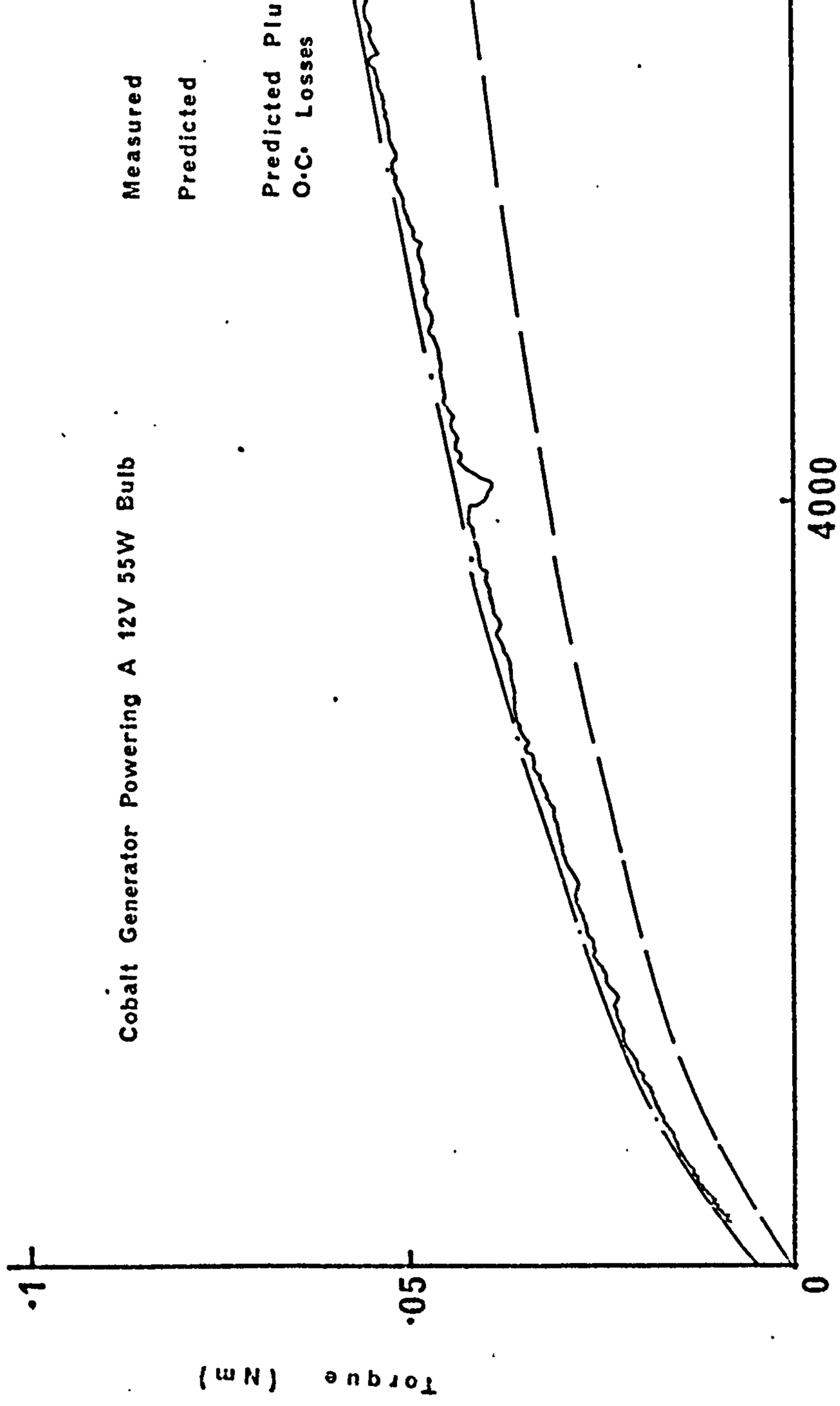

Measured Loss Torque

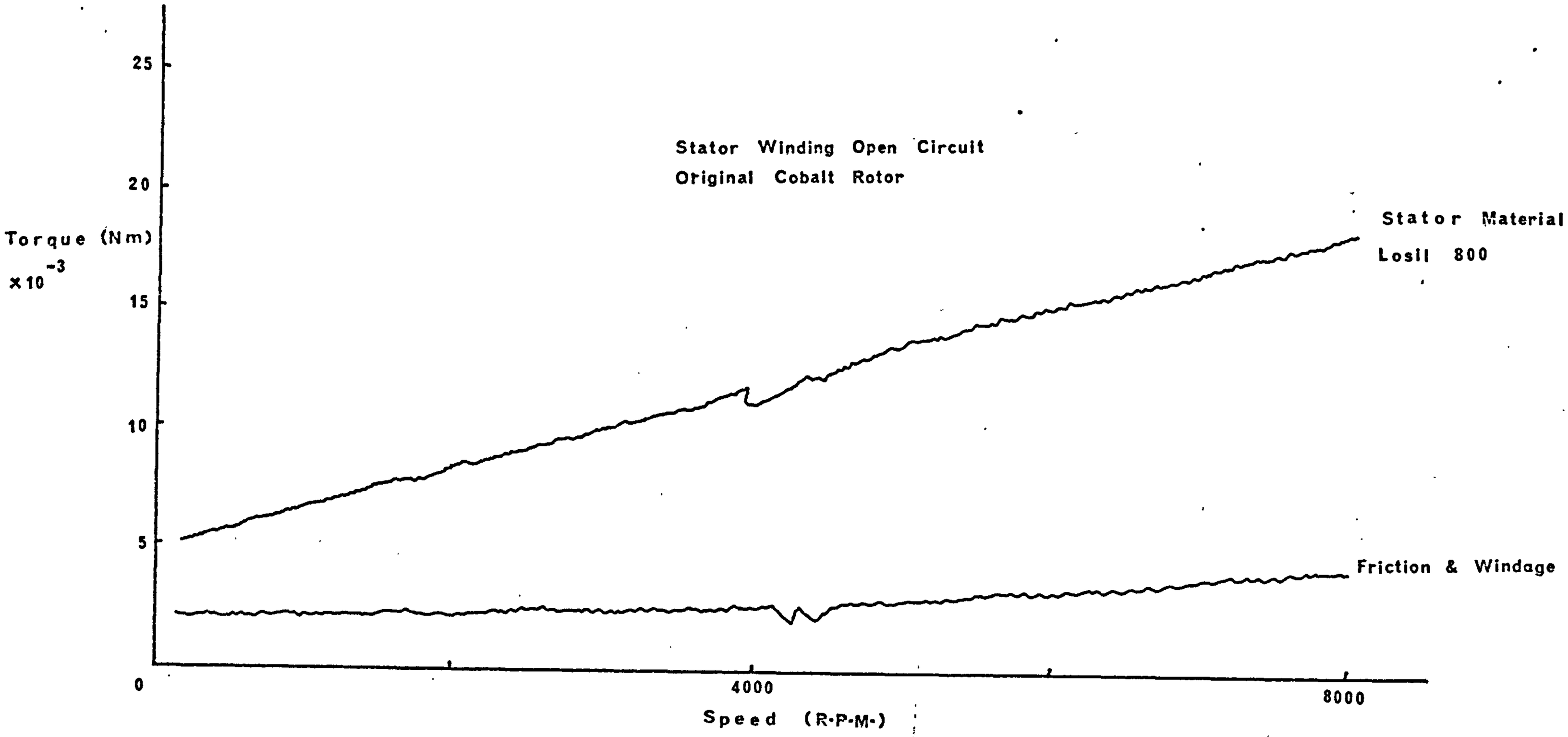

Fig 3.11

Fig 3·12

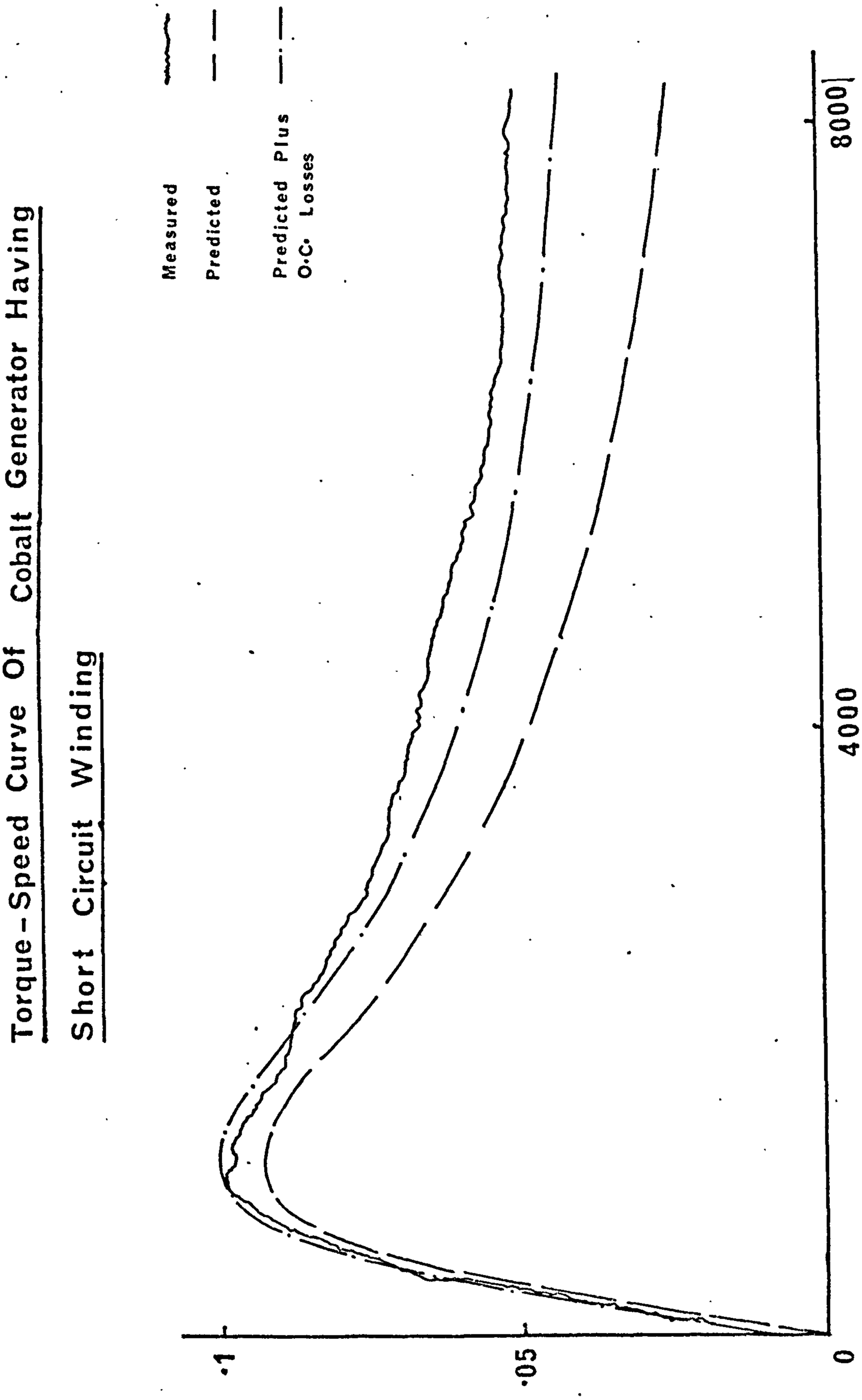
Torque-Speed Curve Of Cobalt Generator Having
Short Circuit Winding
Measured
Predicted
Predicted Plus O.C. Losses
8000
4000
0
Speed (r.p.m.)
.1
.05
0
Torque (Nm)

Fig 4·1

Fig 4·2

4·1 Magnet Working Point

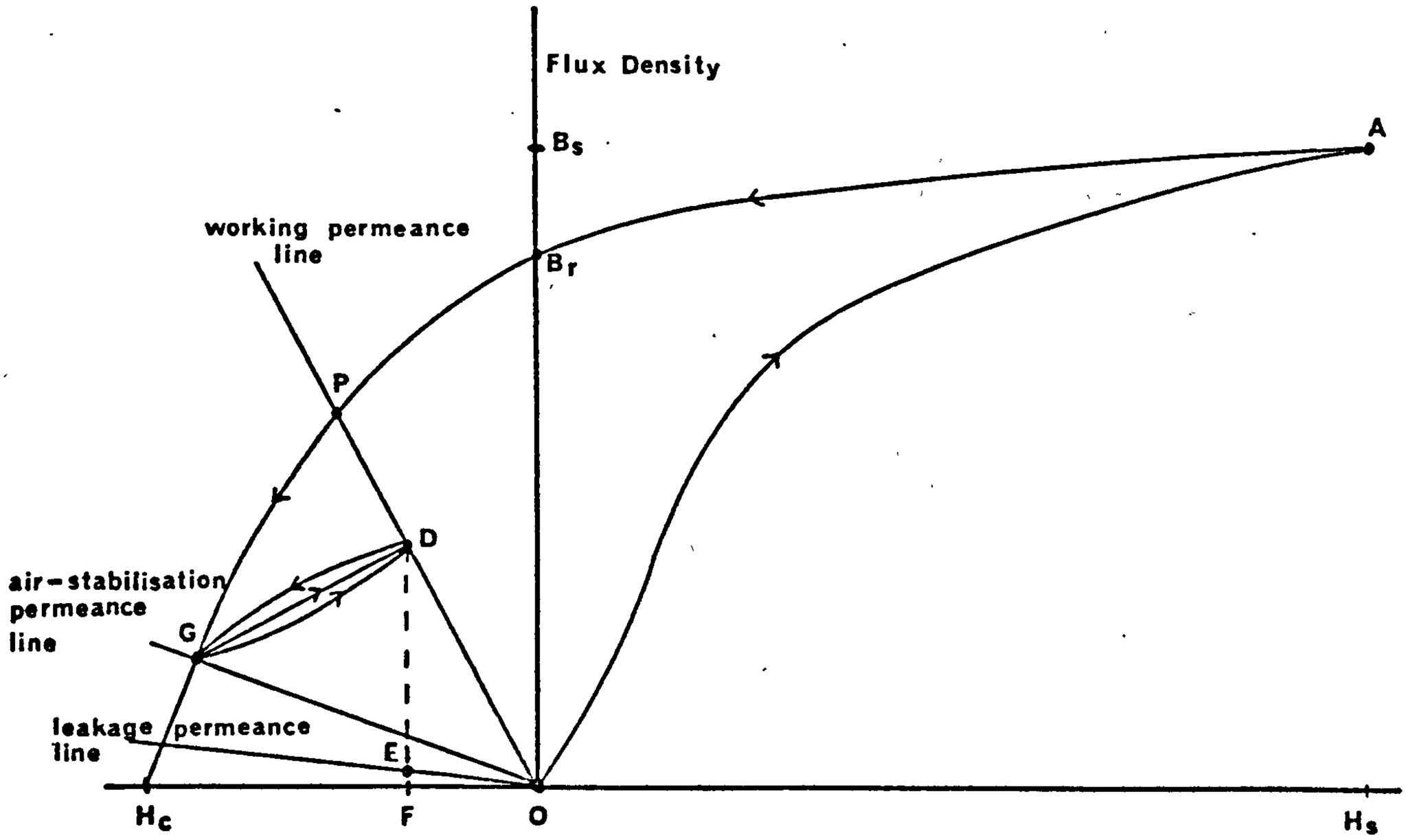

4·2 Magnet In Magnetising Jig

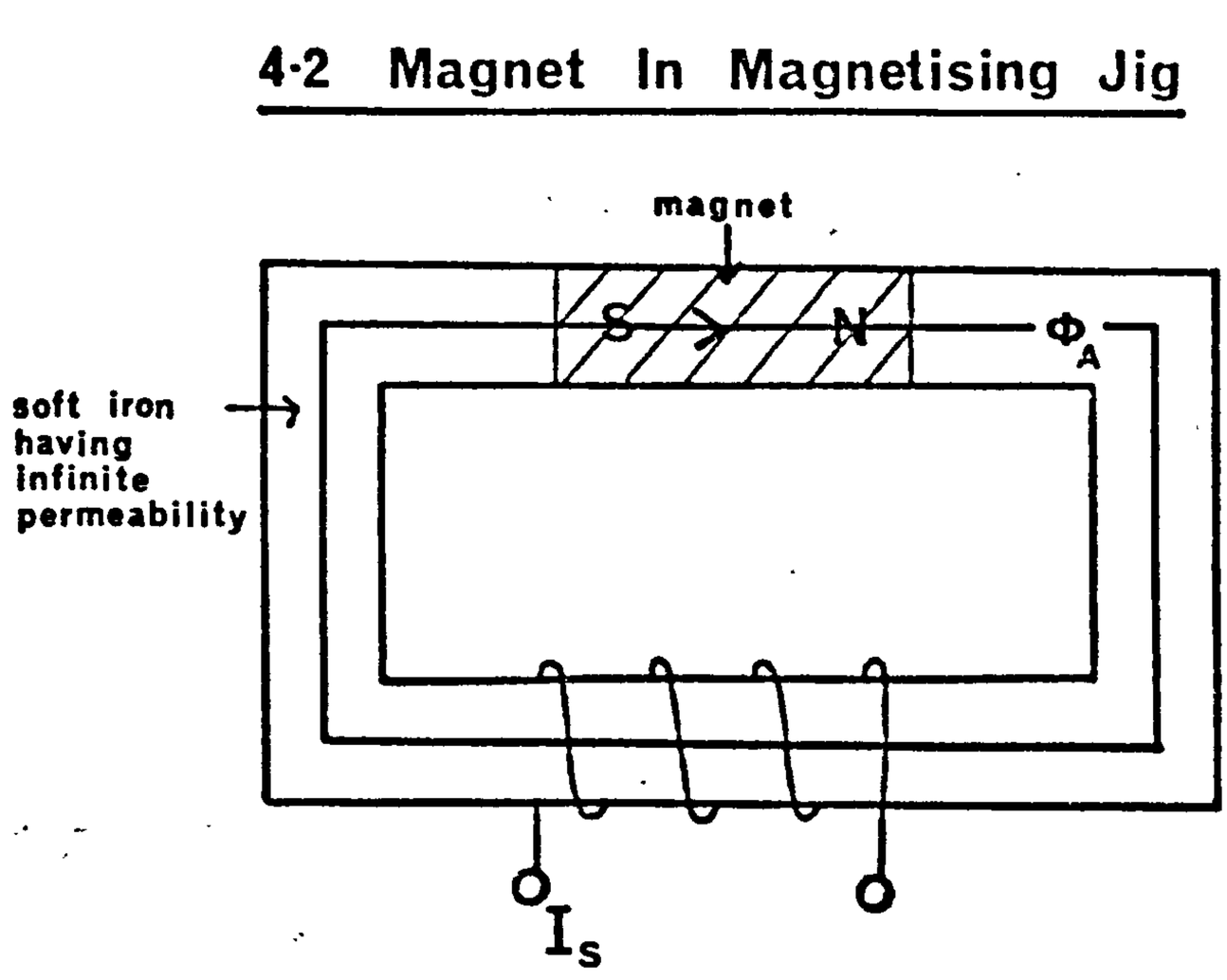

Fig 4·3
Fig 4·4

4·3

(a) Magnet Stabilised In Air

(b) Corresponding Equivalent Circuit

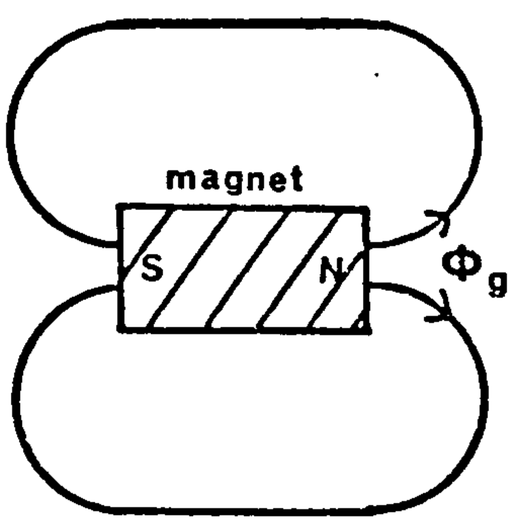

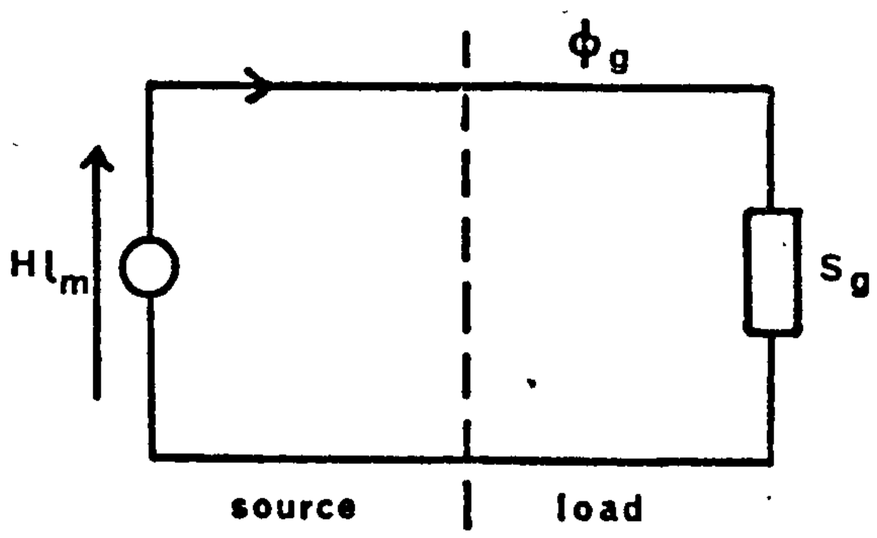

4·4

(a) Magnet During Recoil Operation

(b) Corresponding Equivalent Circuit

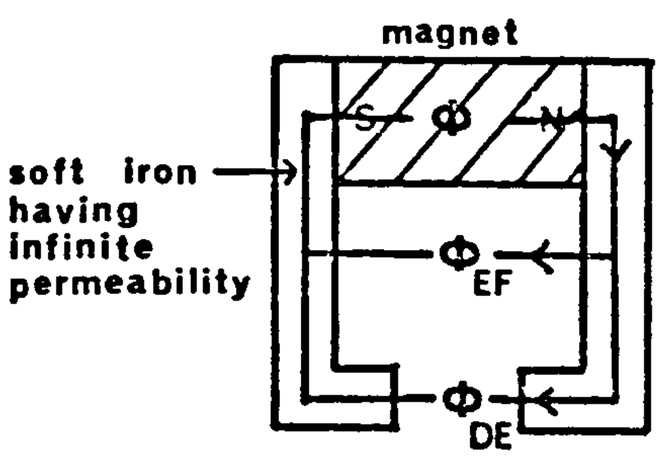

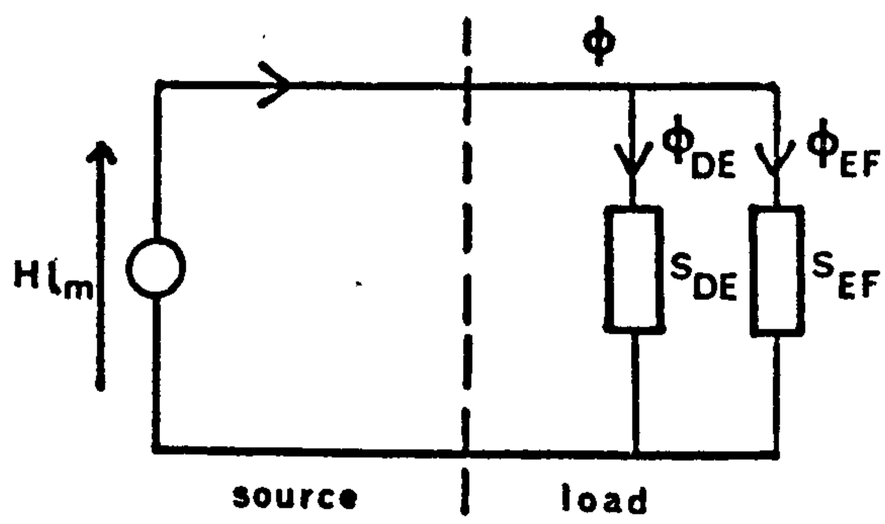

Fig 4·5

Fig 4·6

4·5

(a) Magnet With Demagnetisation Field

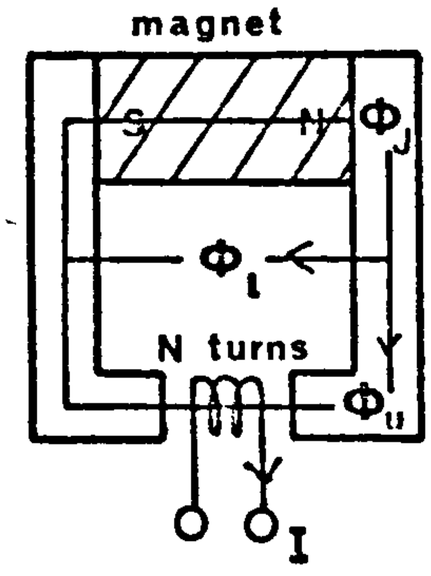

(b) Corresponding Equivalent Circuit

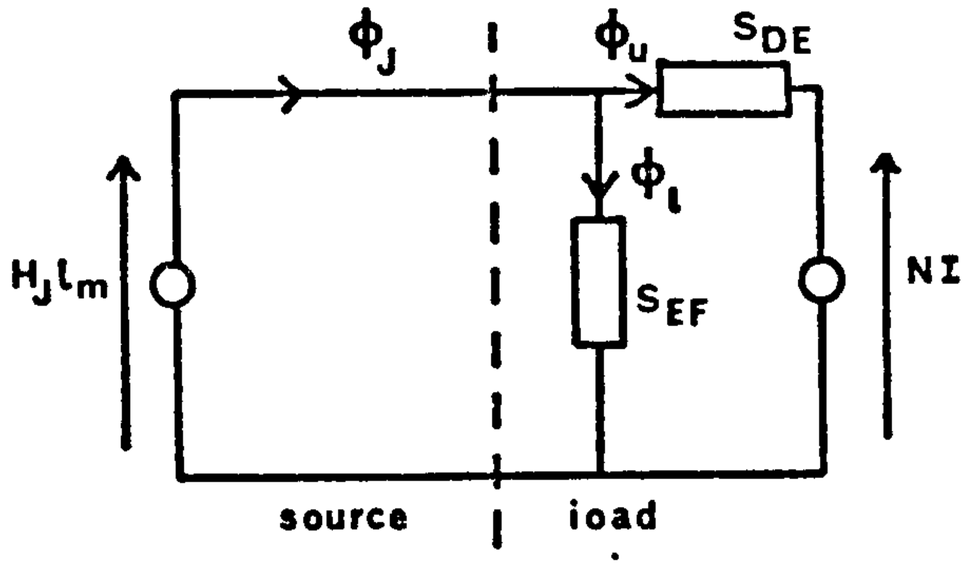

4·6 Magnet Operating Points

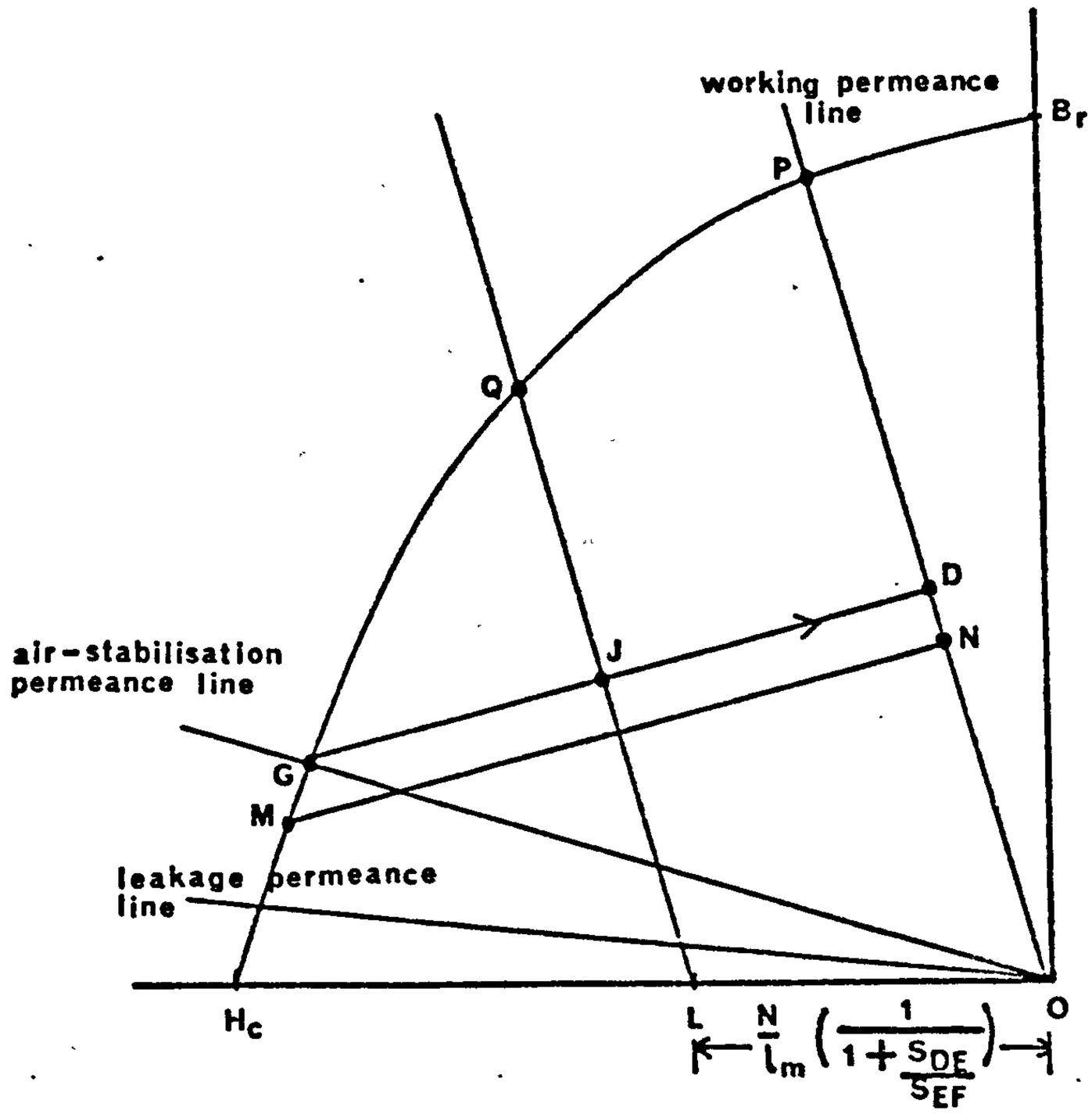

Fig 4·7
Fig 4·8

4·7 Air Stabilisation Permeance Coefficient For Multipole Rotors

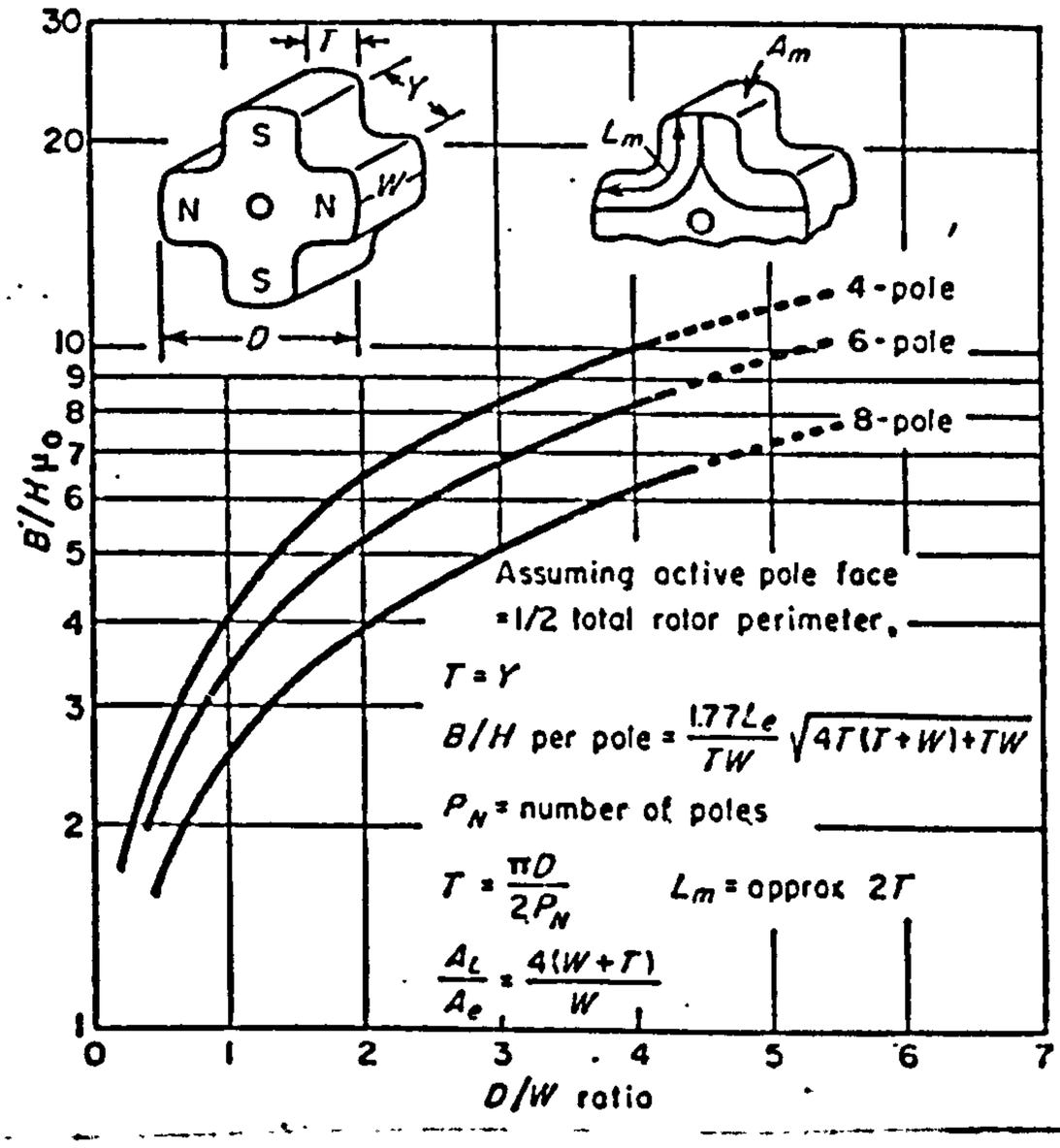

Reproduced From Parker & Studders[5]

4·8 Physical Dimension Of The Existing Cobalt Rotor

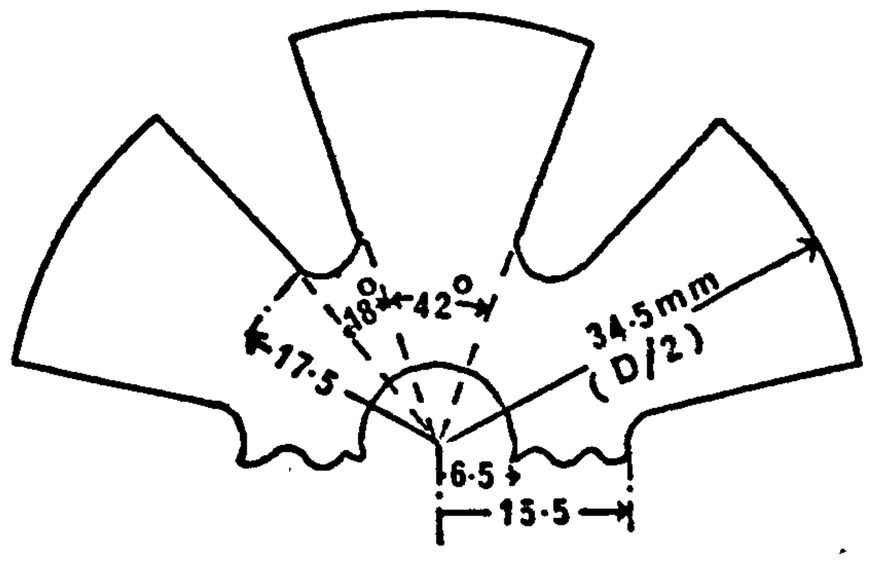

Axial Length w = 16mm

Fig 4·9

Working Points Of Cobalt Magnets

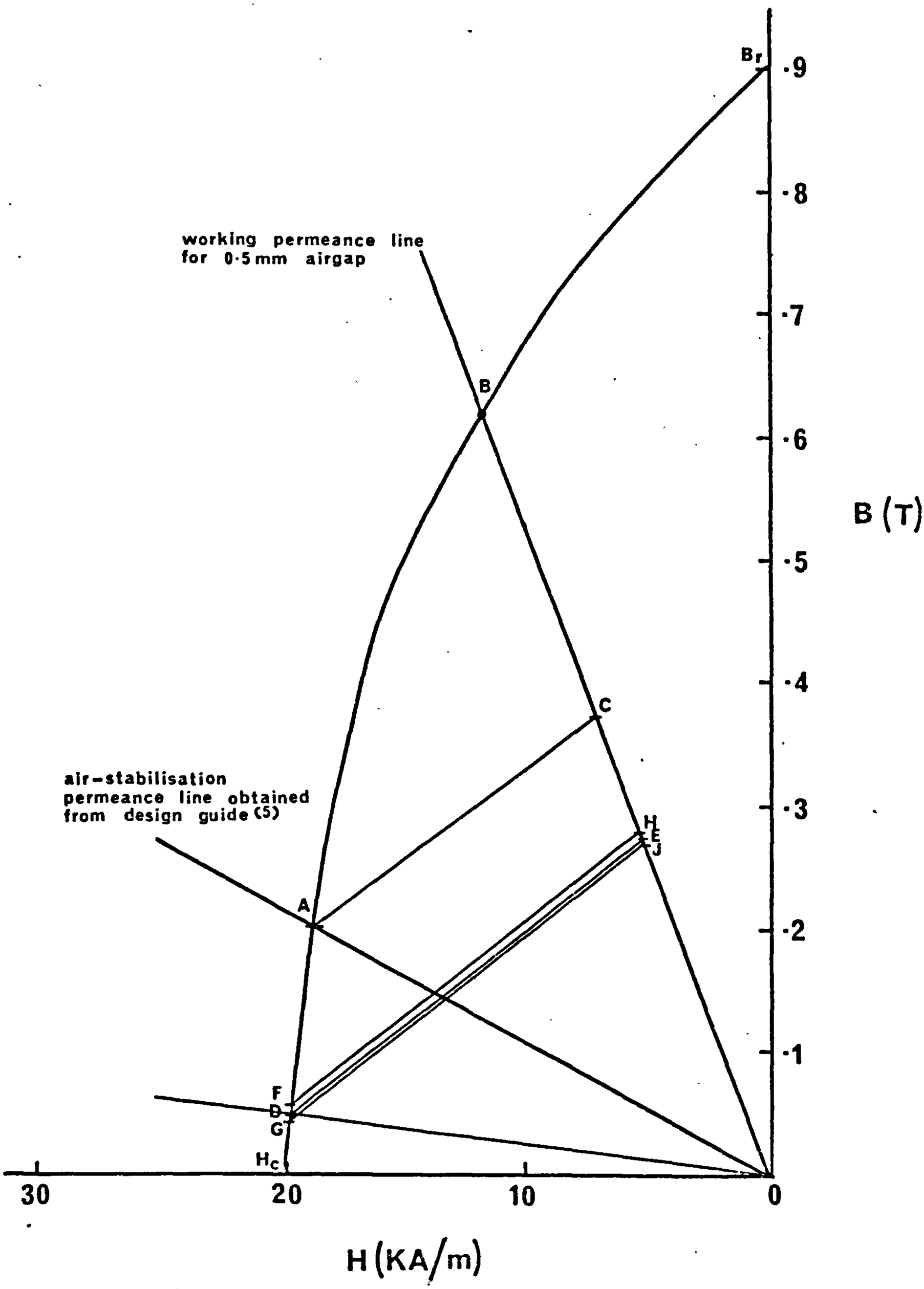

Fig 4·10
Fig 4·11

4·10 Airgap Flux Path

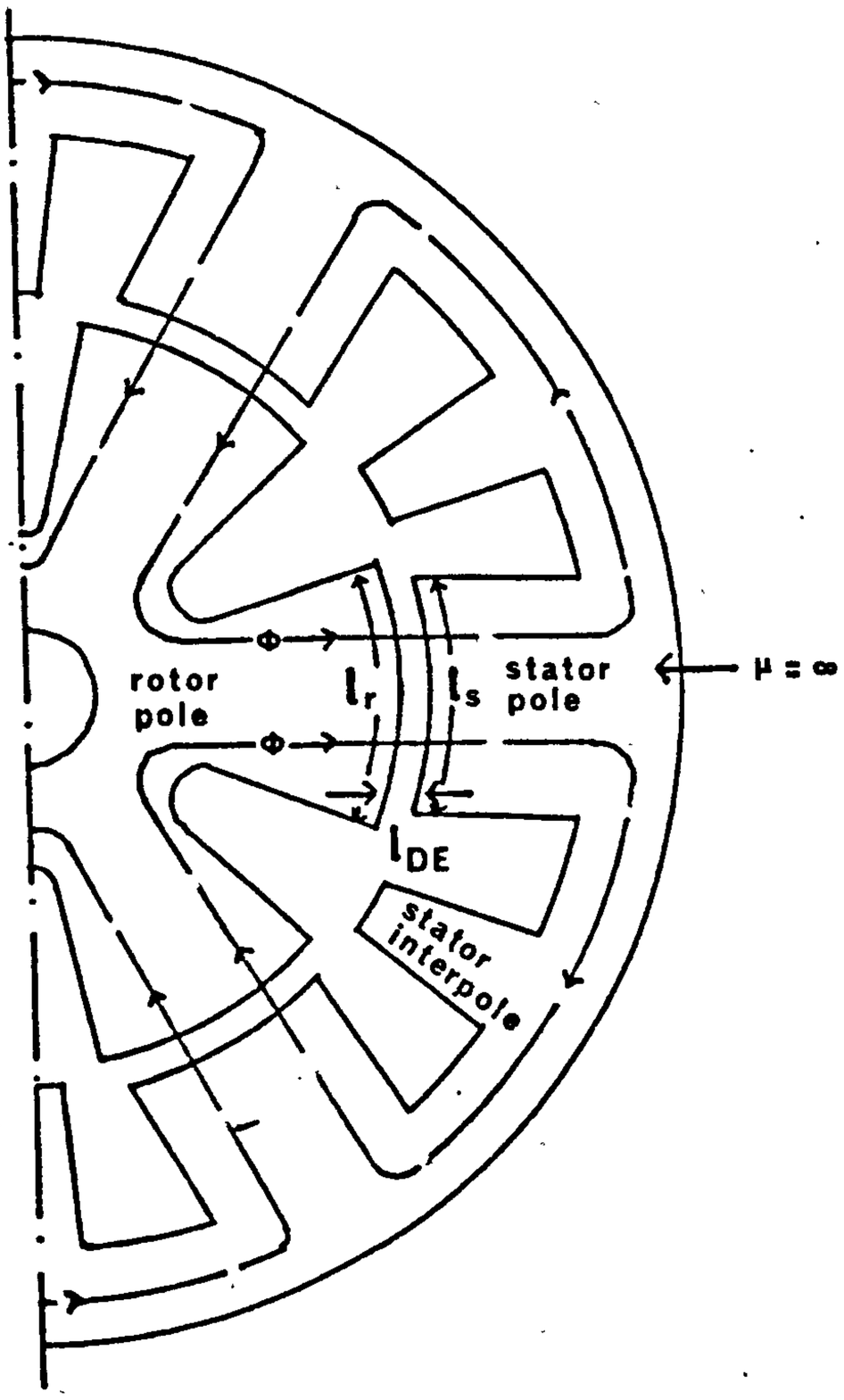

4·11 Calculation Of l_m/A_m For Rotor Pole

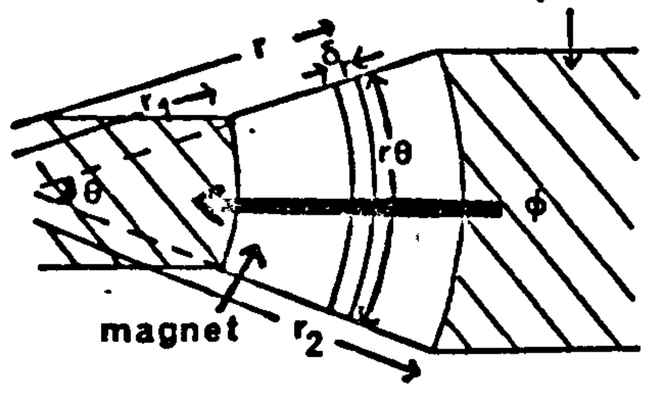

Fig 4·12

Fig 4·13

4·12 Flux Paths Of Rotor Poles

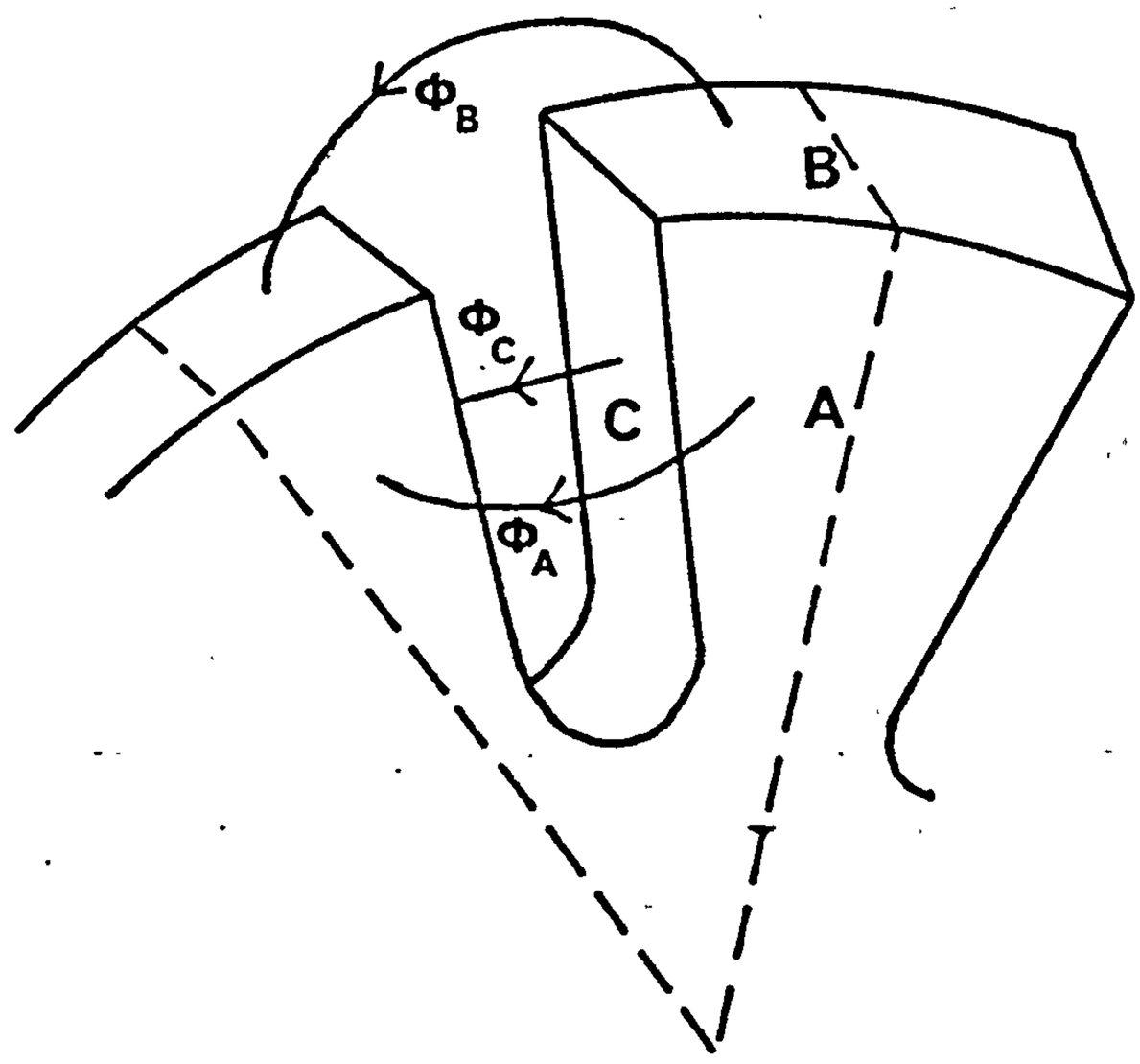

4·13 Location Of Hall Probes On Rotor Pole Surfaces

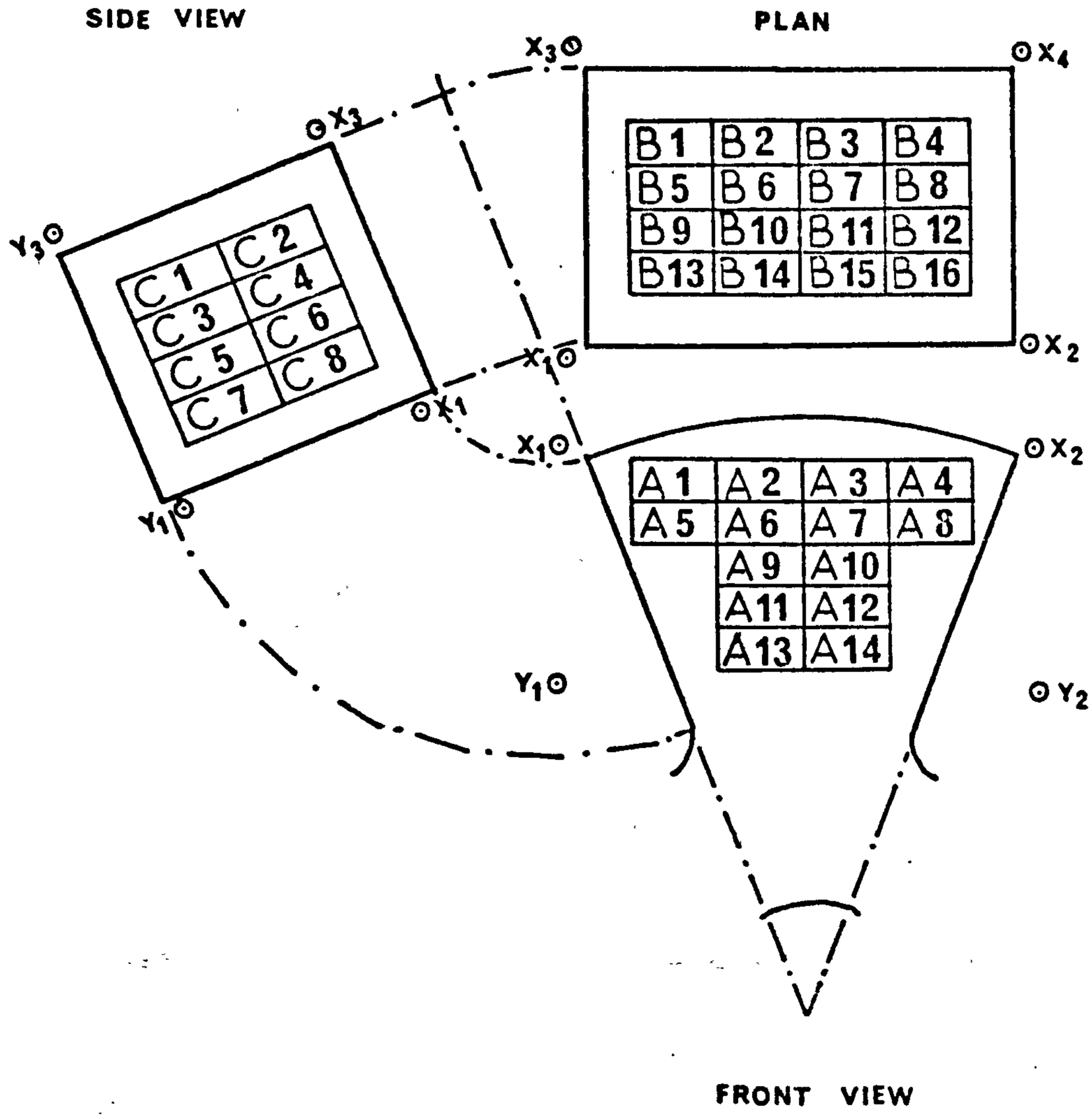

Fig 4·14

Effects Of Increasing Working Airgaps

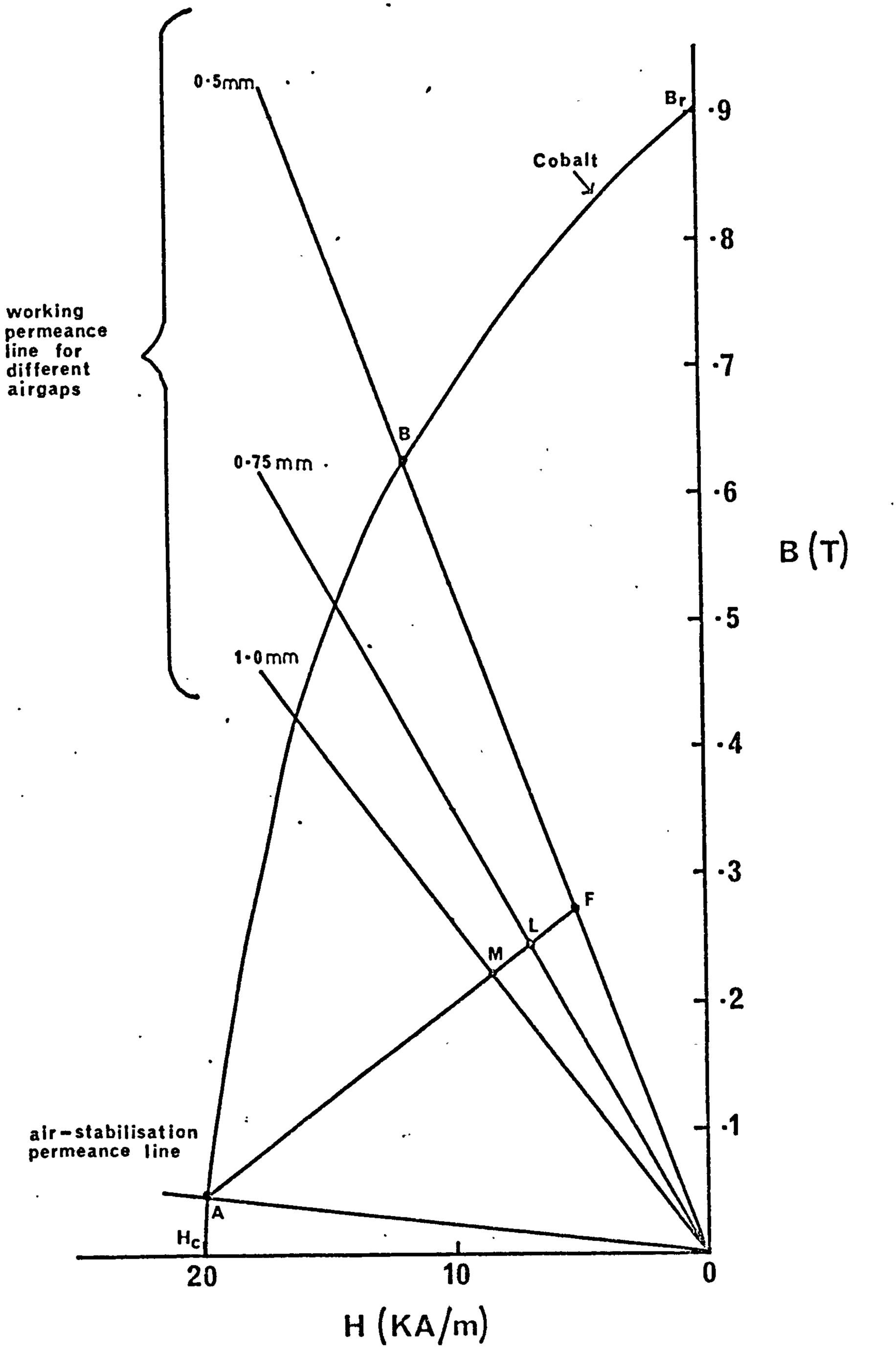

Fig 4·15

Sample Variation Of Cobalt Rotors

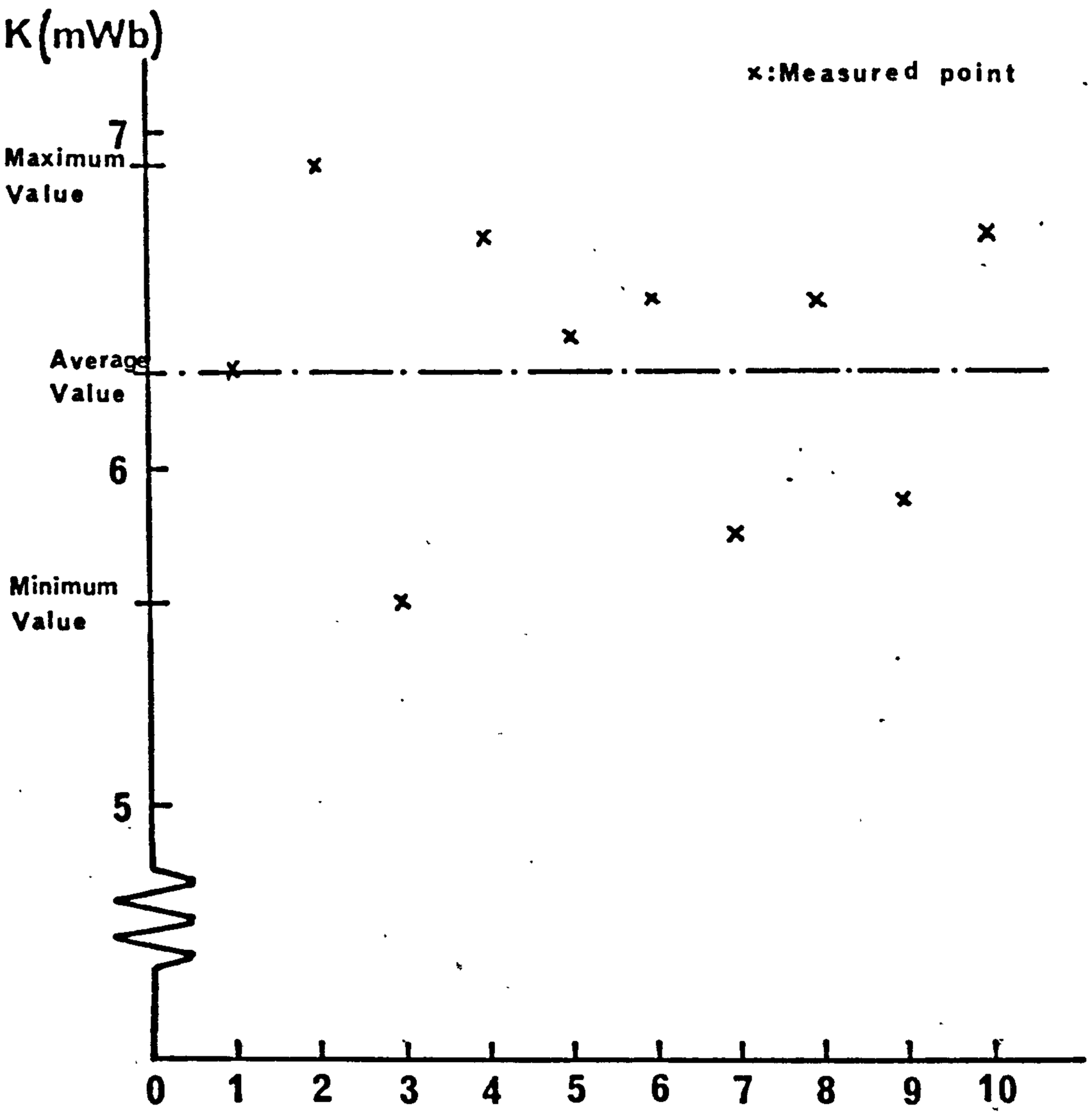

Fig 4·16

Variation Of Working Points

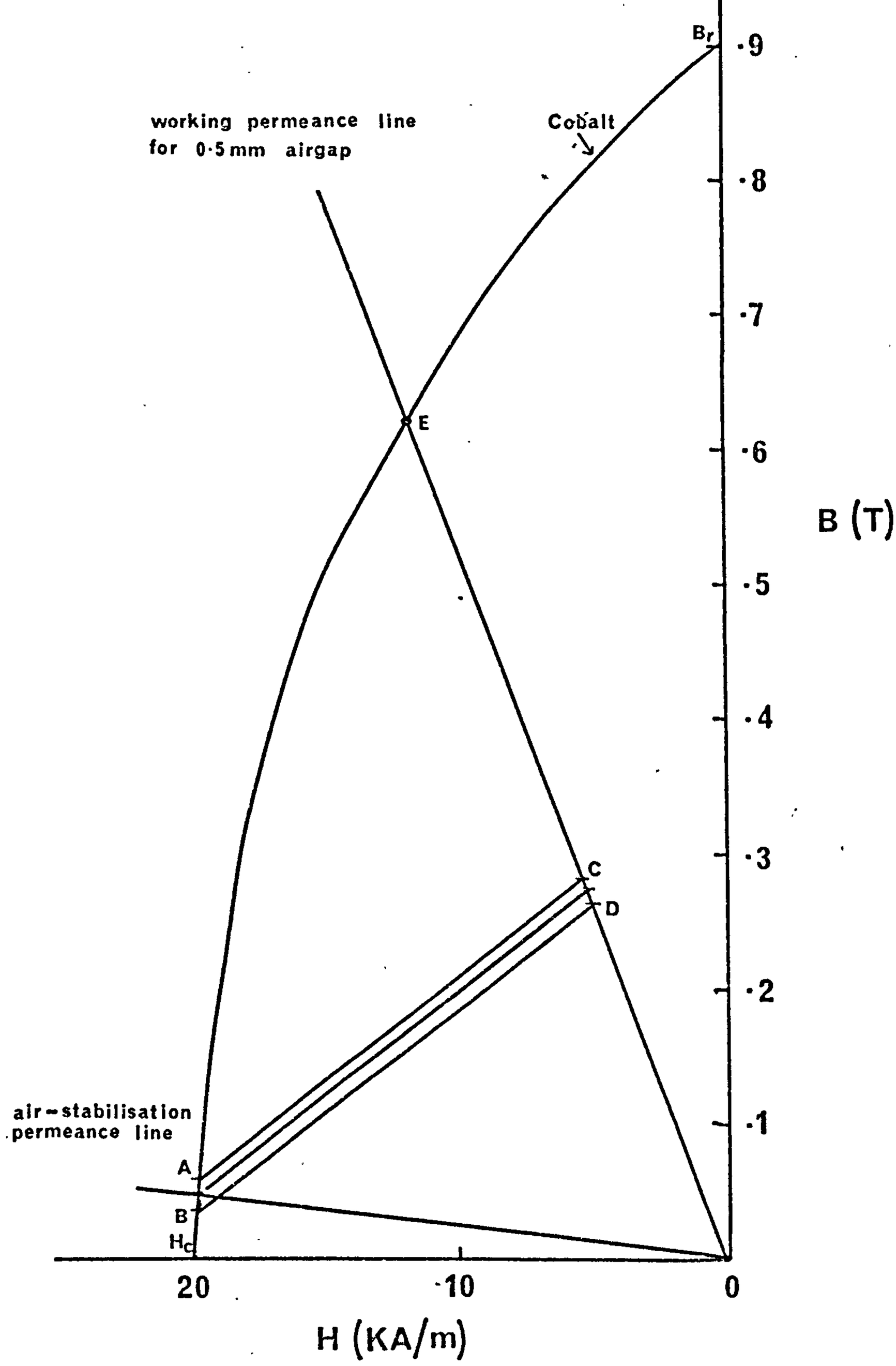

Fig 4·17

Working Points Of Alnico Magnets

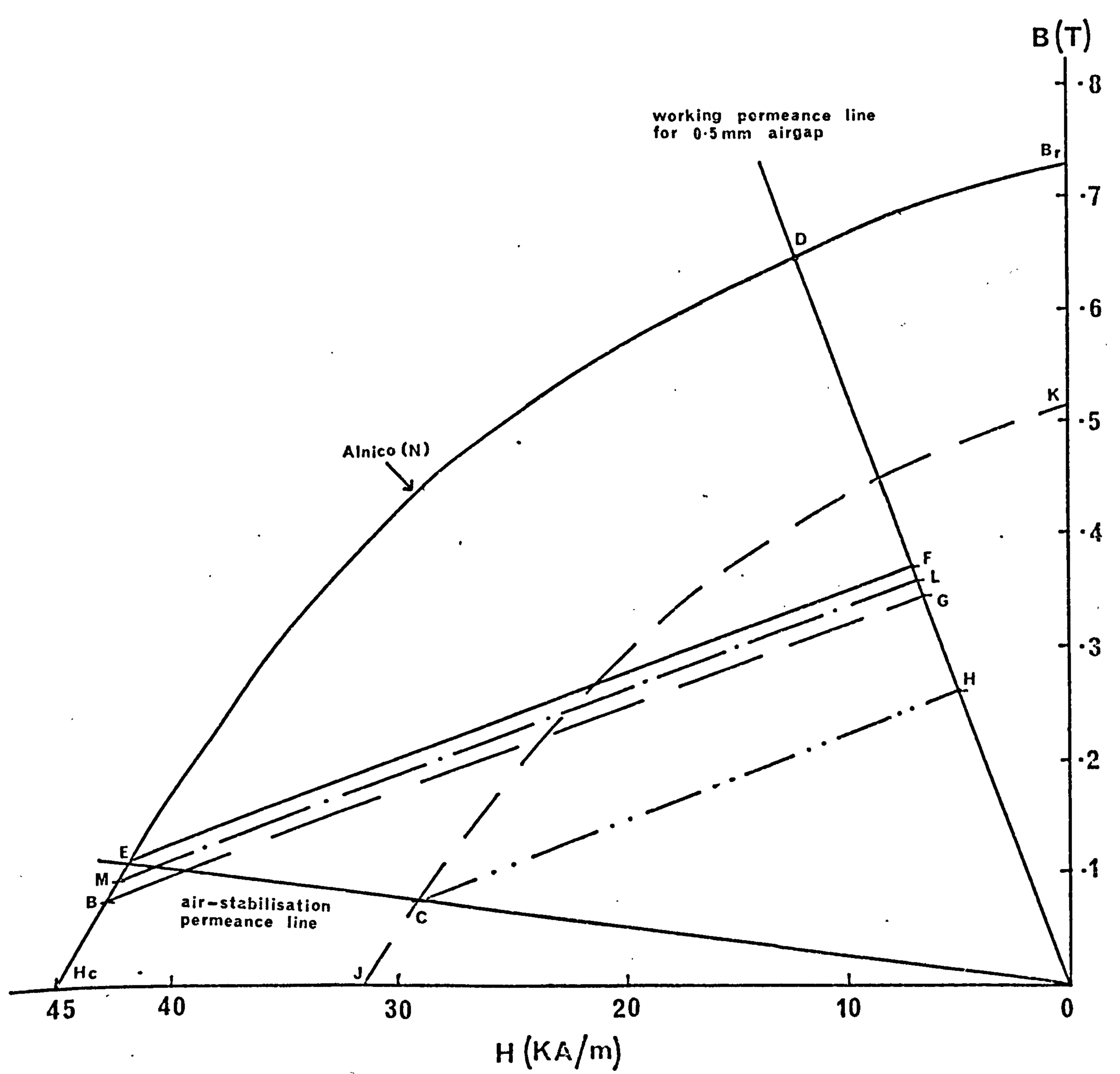

Fig 4·18

Working Points Of Alnico Magnets

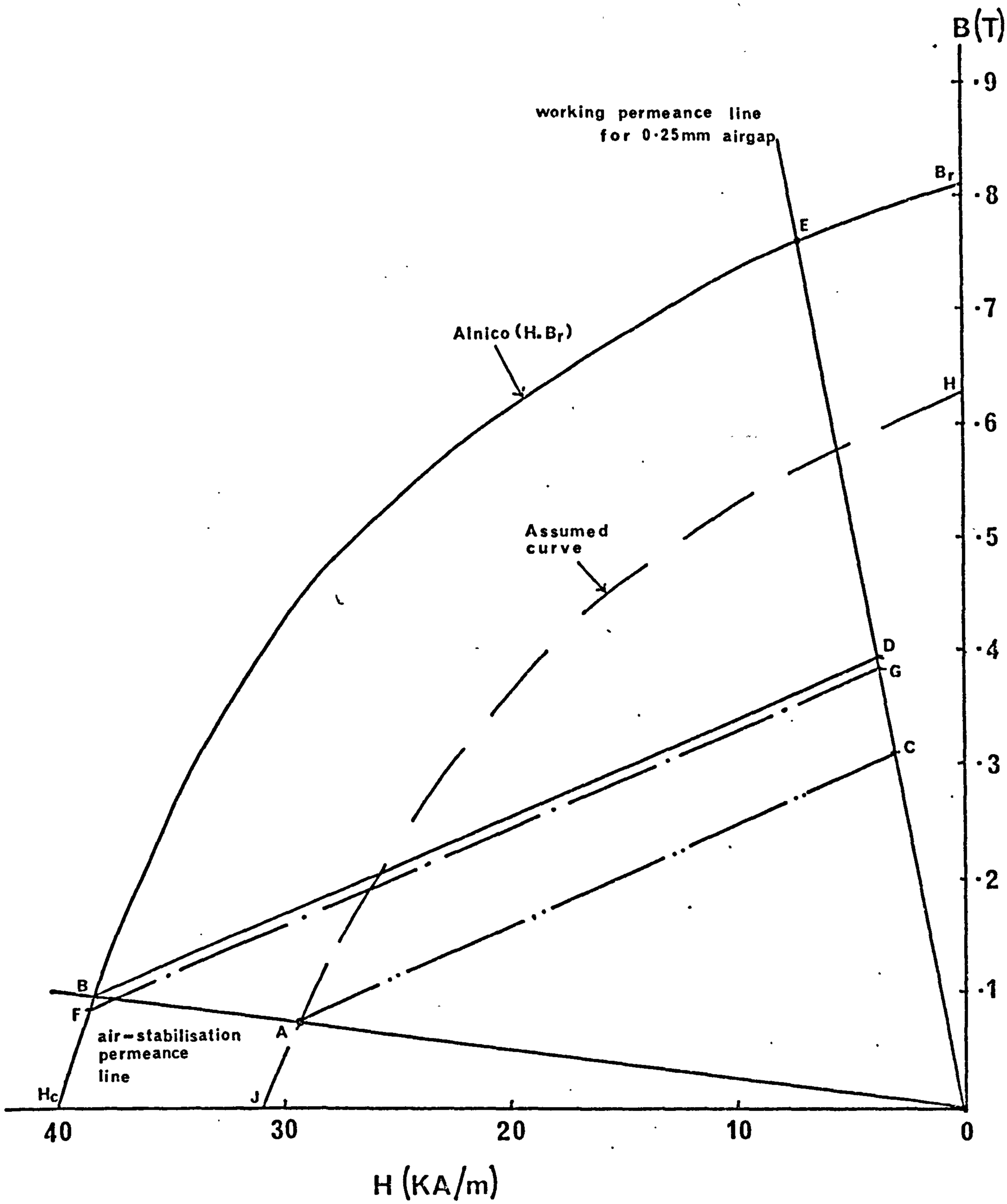

Fig 4·19

Fig 4·20

4·19 Sample Variation Of Alnico (H.Br) Rotors

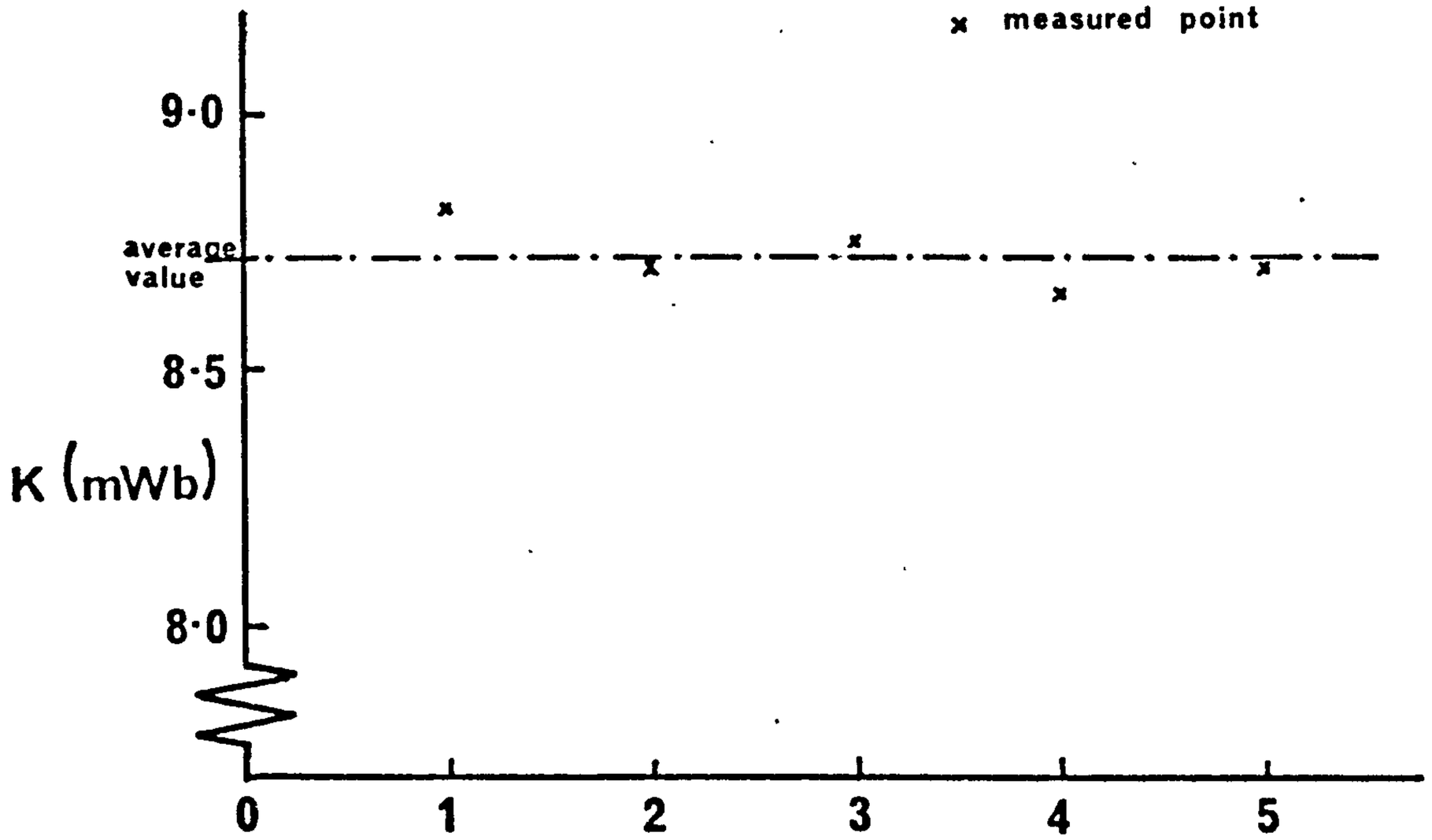

4·20 Effect Of External Demagnetising Field

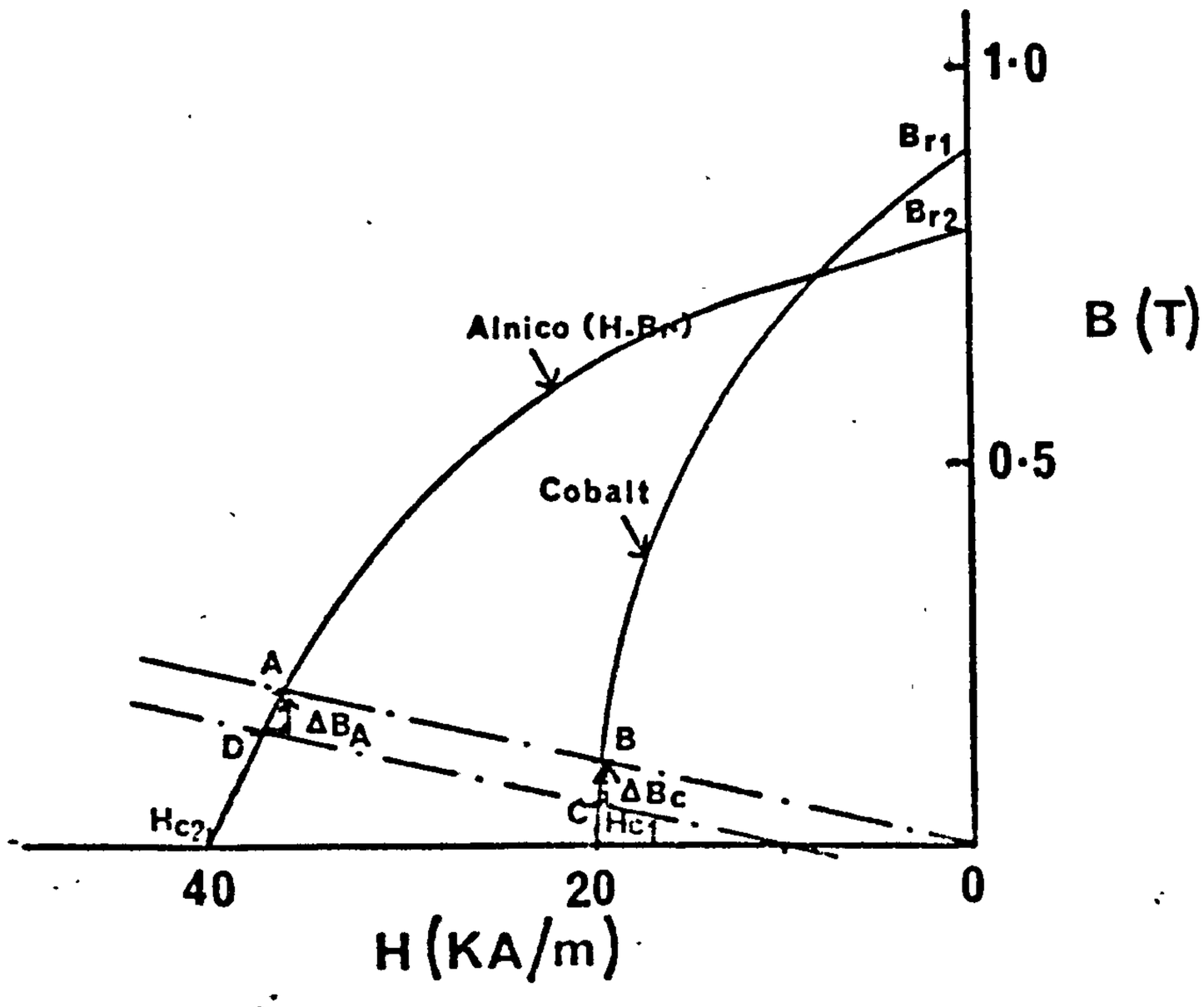

Fig 4·21

Fig 4·22

4·21 Reluctance Paths Per Pole

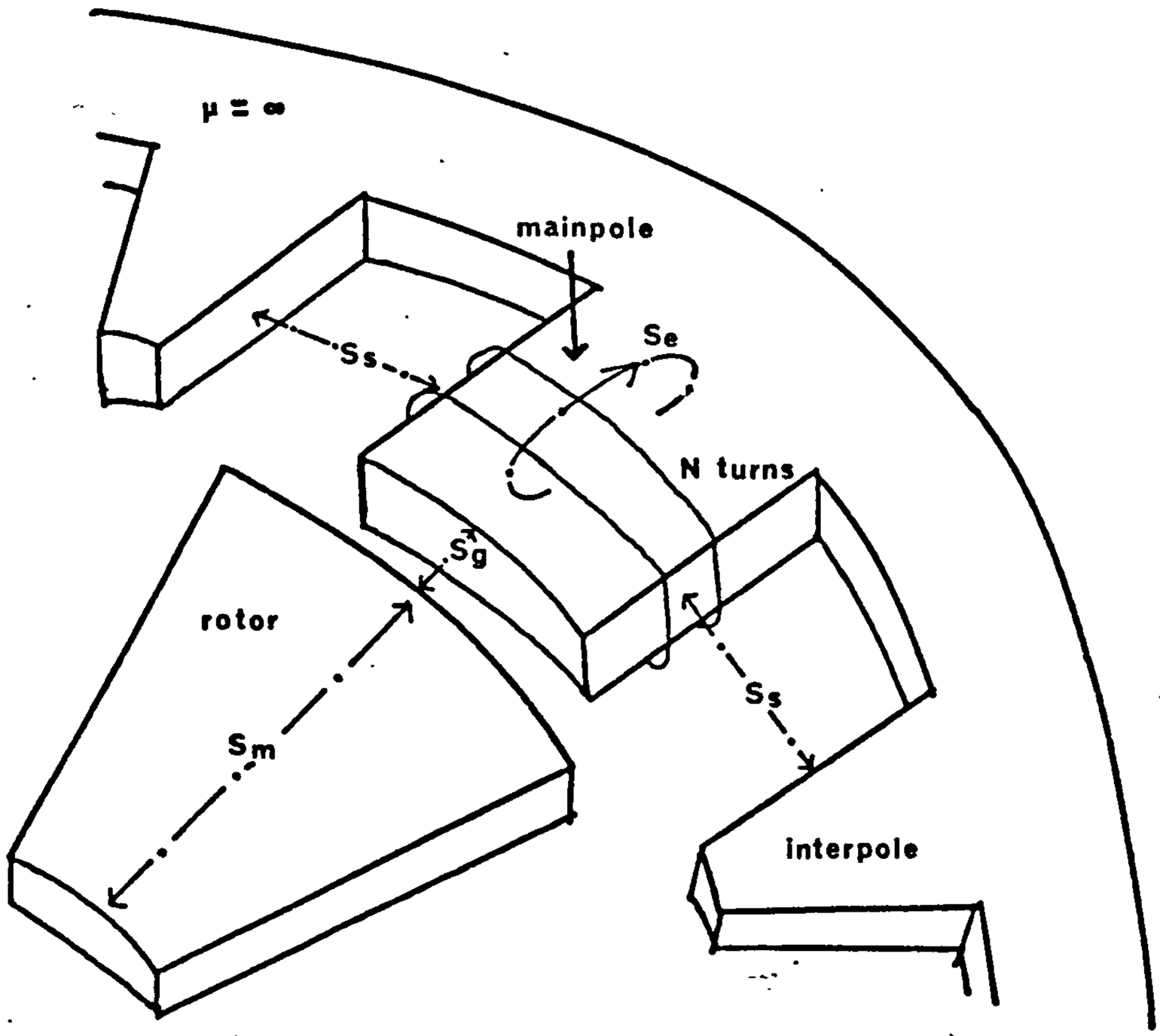

4·22 Slot Reluctance Path

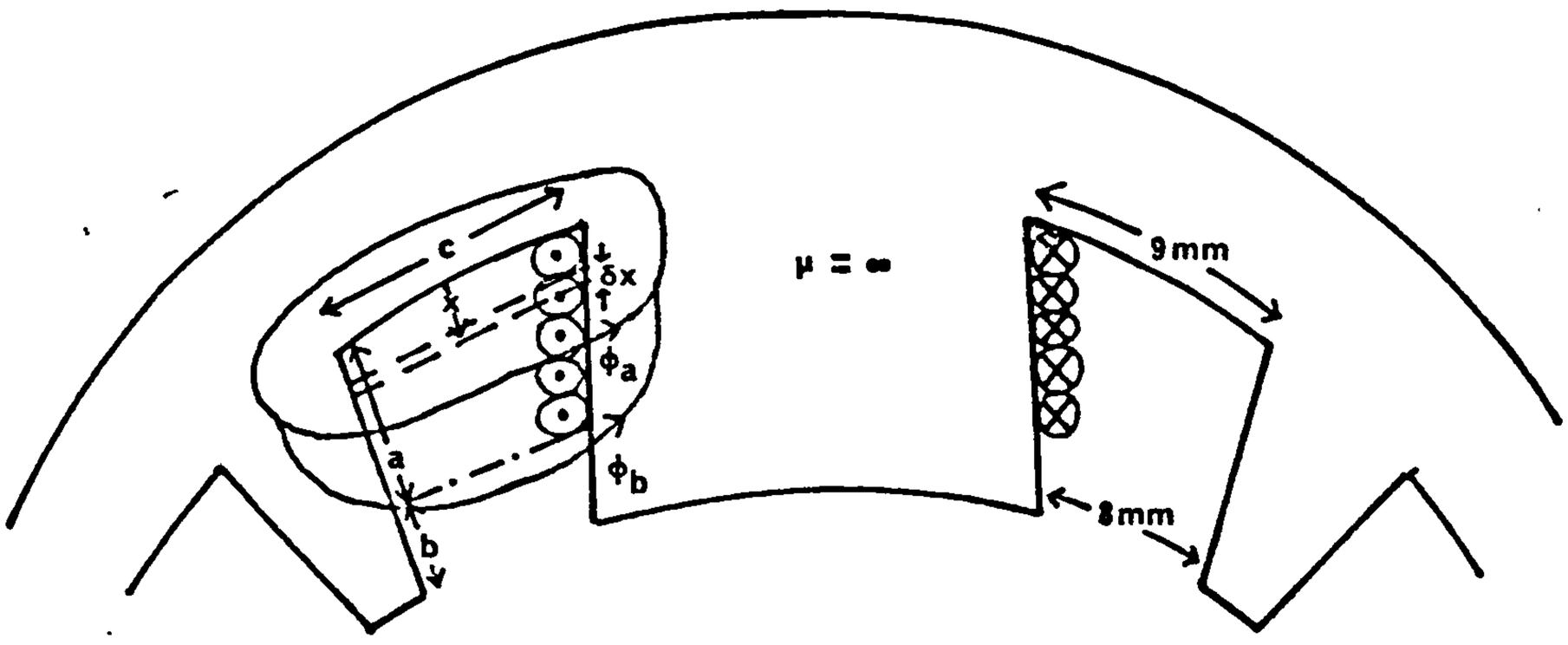

a = 9 mm
b = 4 mm
c = 8·5 mm
t = 16·9 mm

Fig 4·23

Fig 4·24

4·23 End-Flux Path

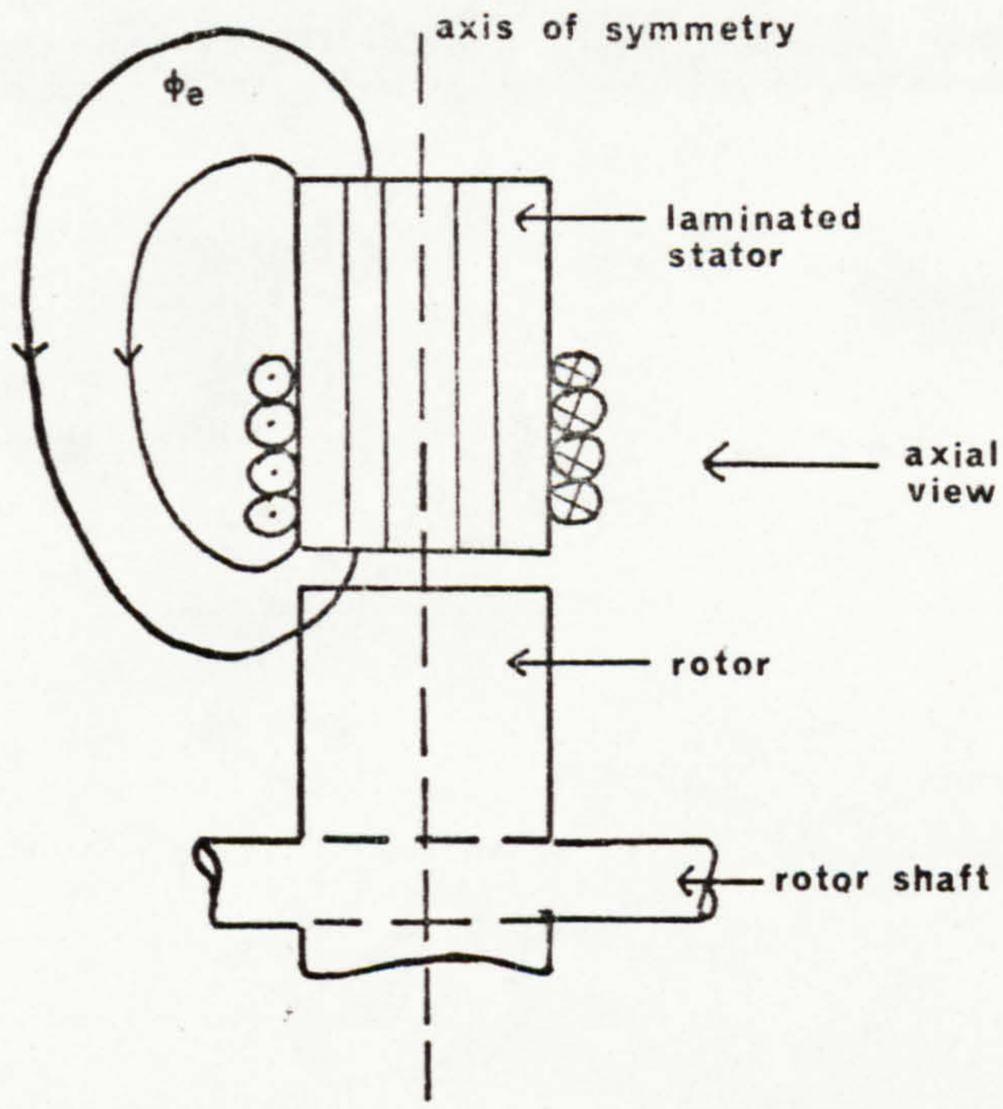

4·24 Components Of Increased Axial Length Generators

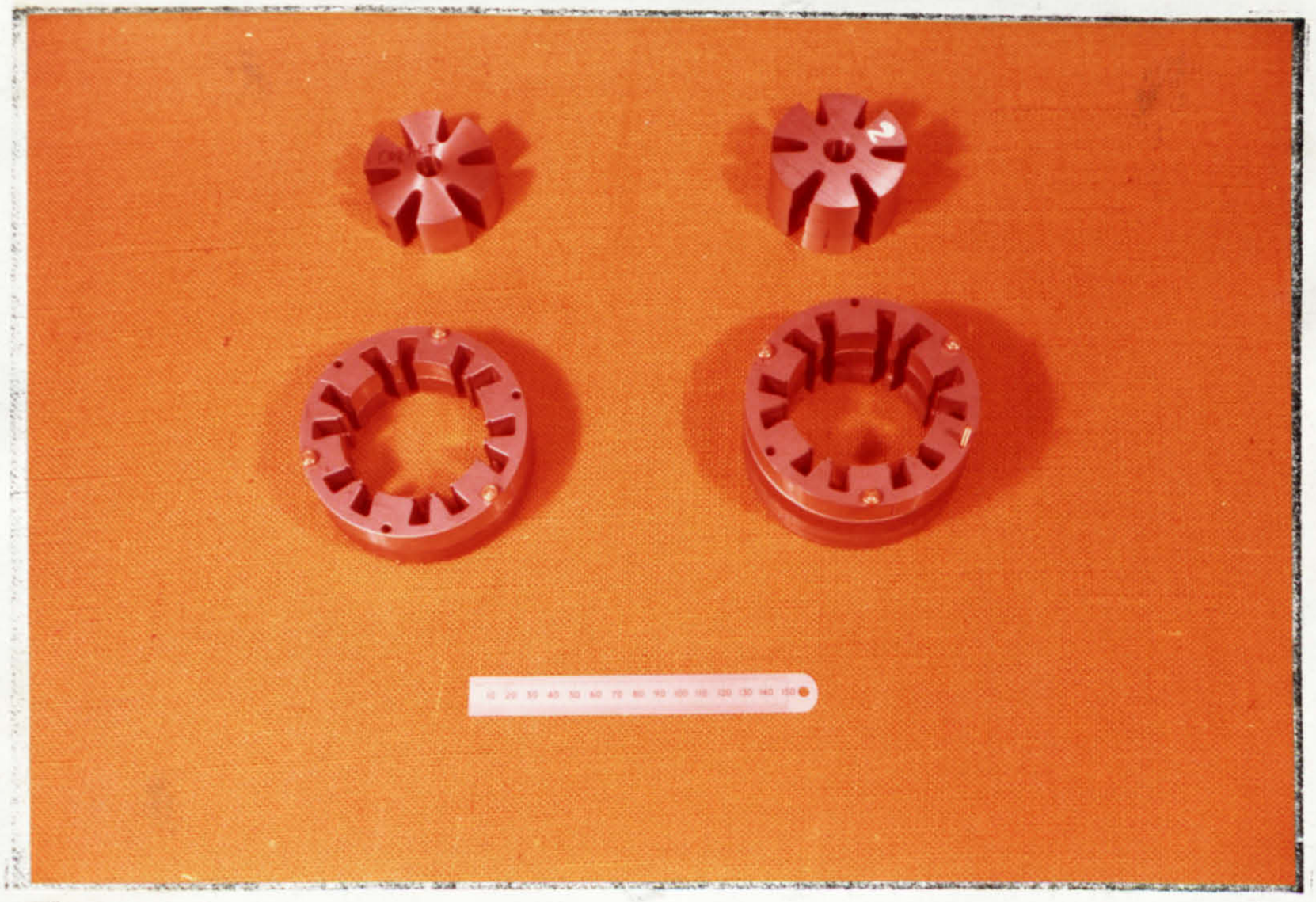

Fig 4·25

Variation Of Inductance With Axial Length

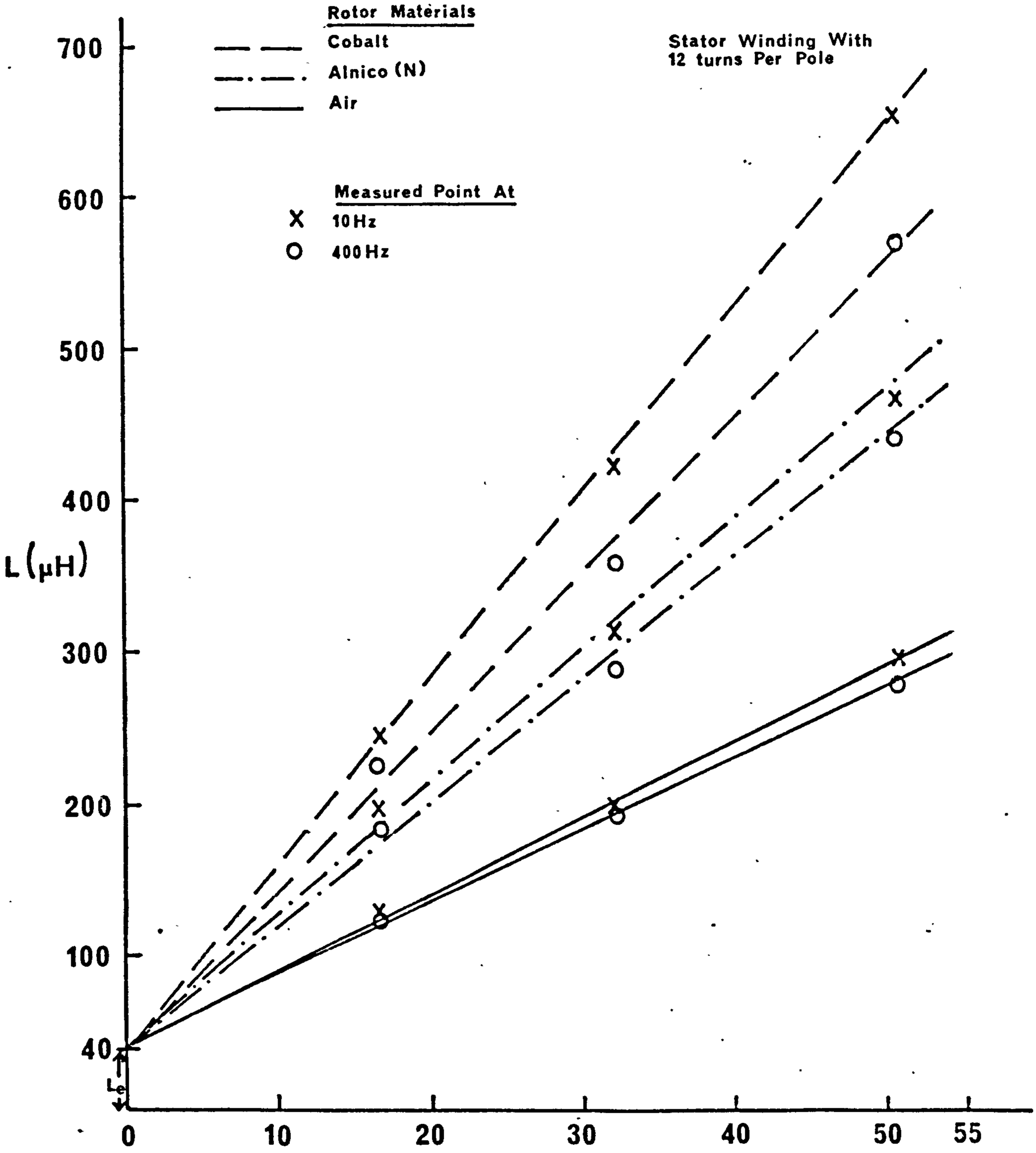

Fig 4·26
Fig 4·27
Fig 4·28
Fig 4·29

4·26 Equivalent Circuit With The Interpolar Reluctance

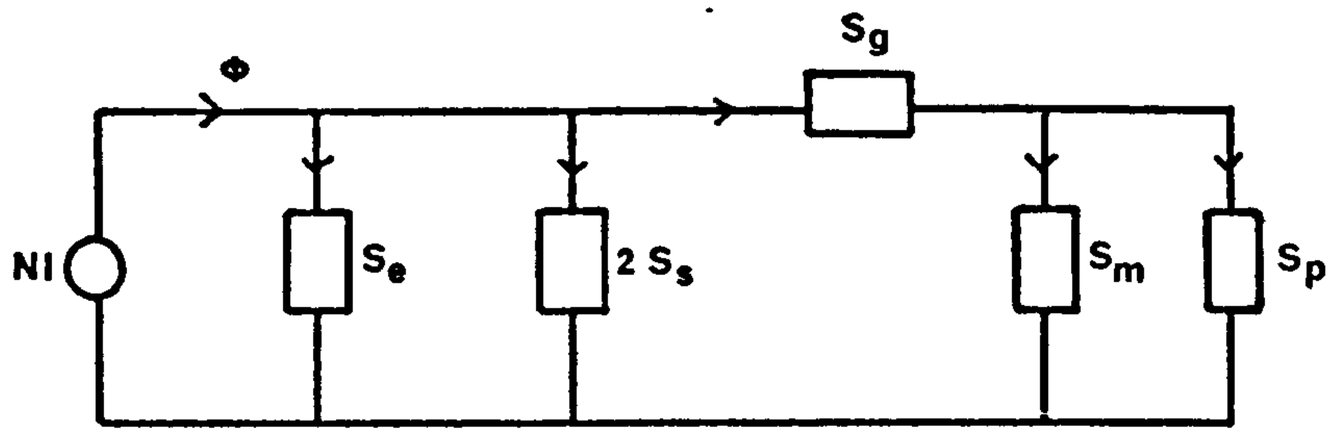

4·27 Tensile Stress

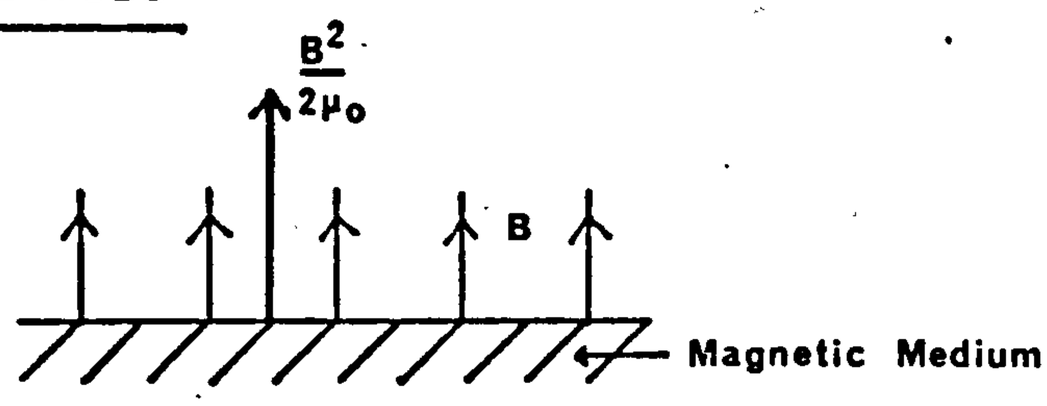

4·28 Compressive Stress

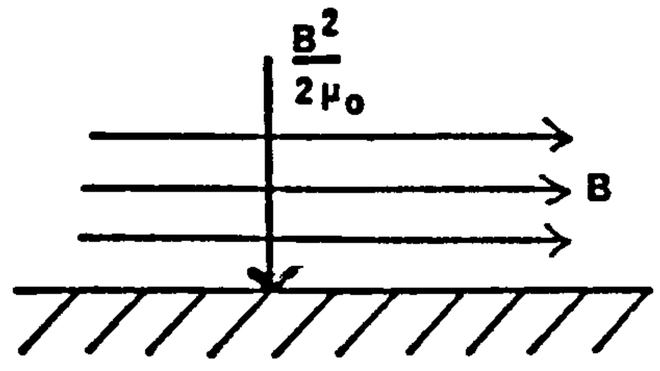

4·29 Stress System

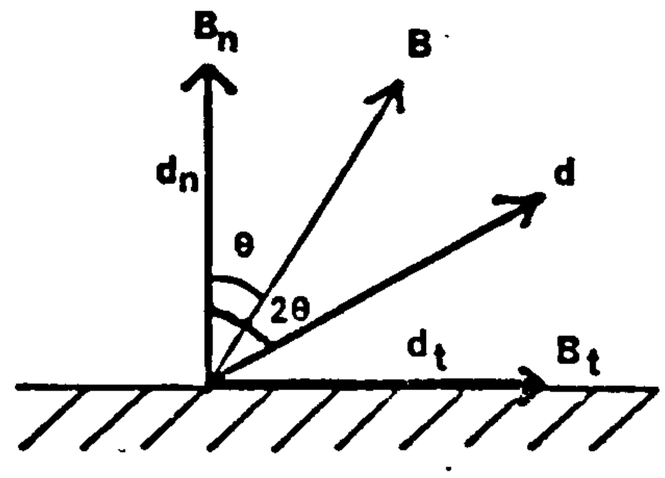

Fig 4·3C

Torque Calculation Using Maxwell Stress

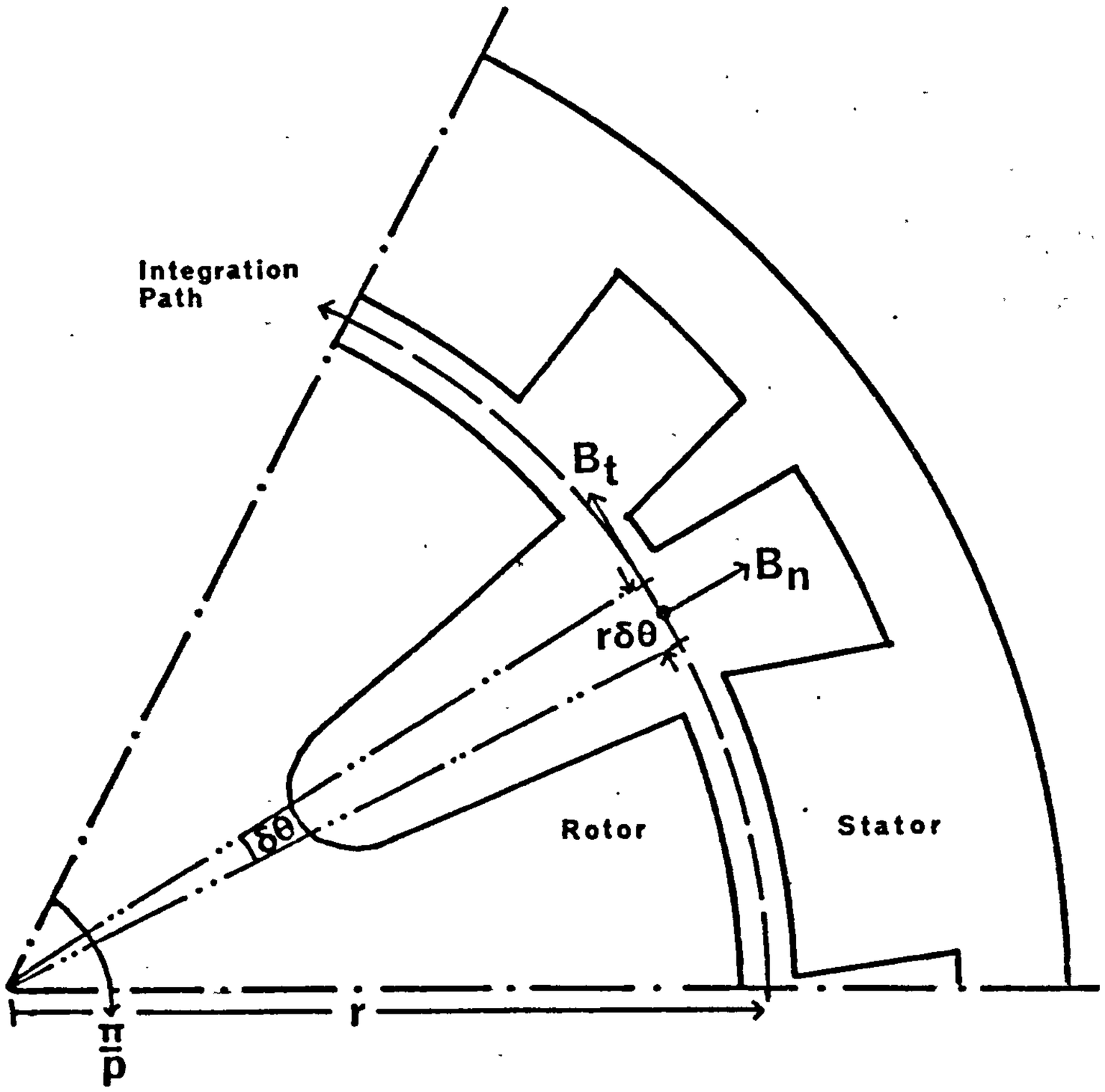

Fig 4·31
Fig 4·32

4·31 Demagnetisation Curves Of Metallic Magnet

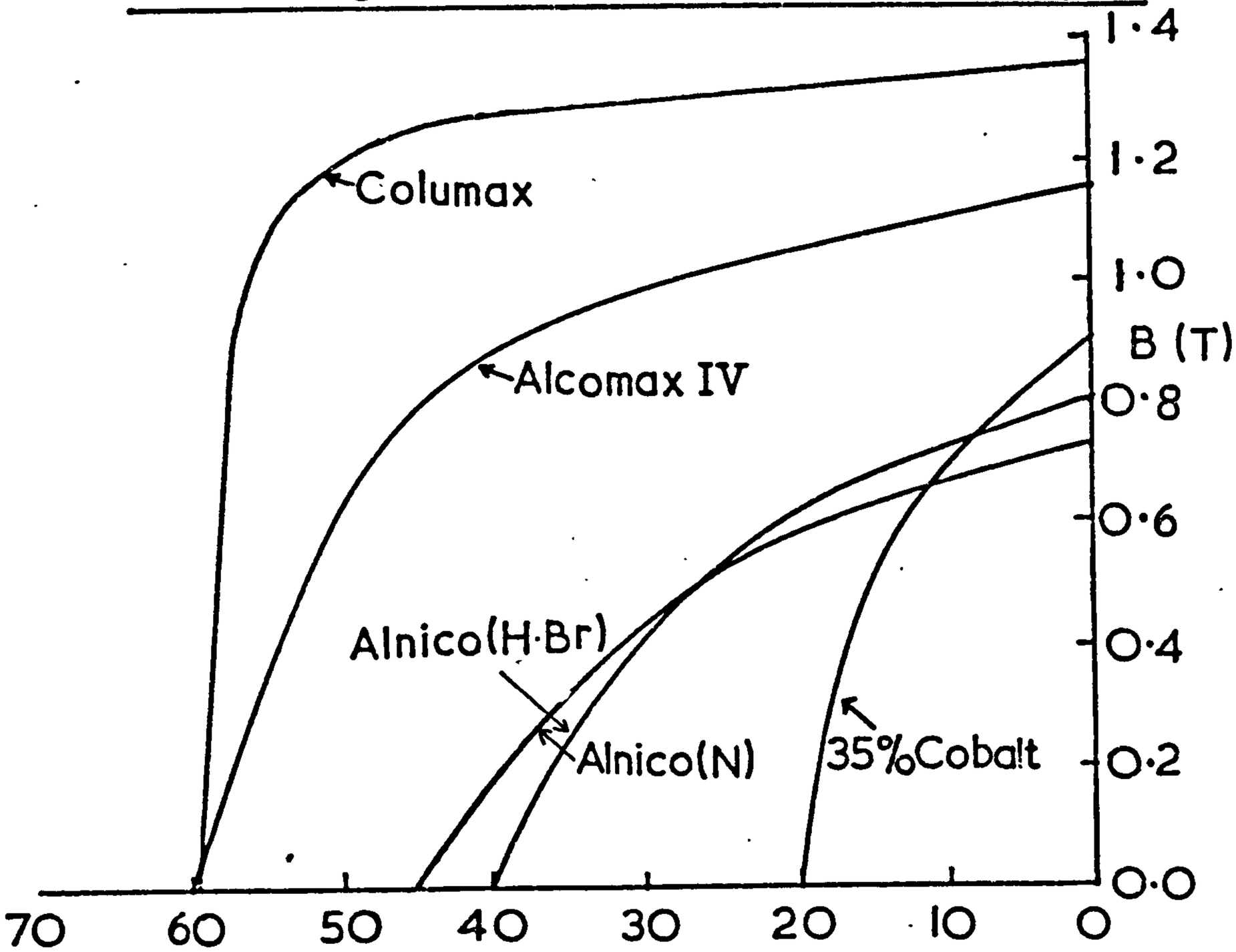

4·32 Demagnetisation Curves Of Rare Earth And Ferrite Magnets

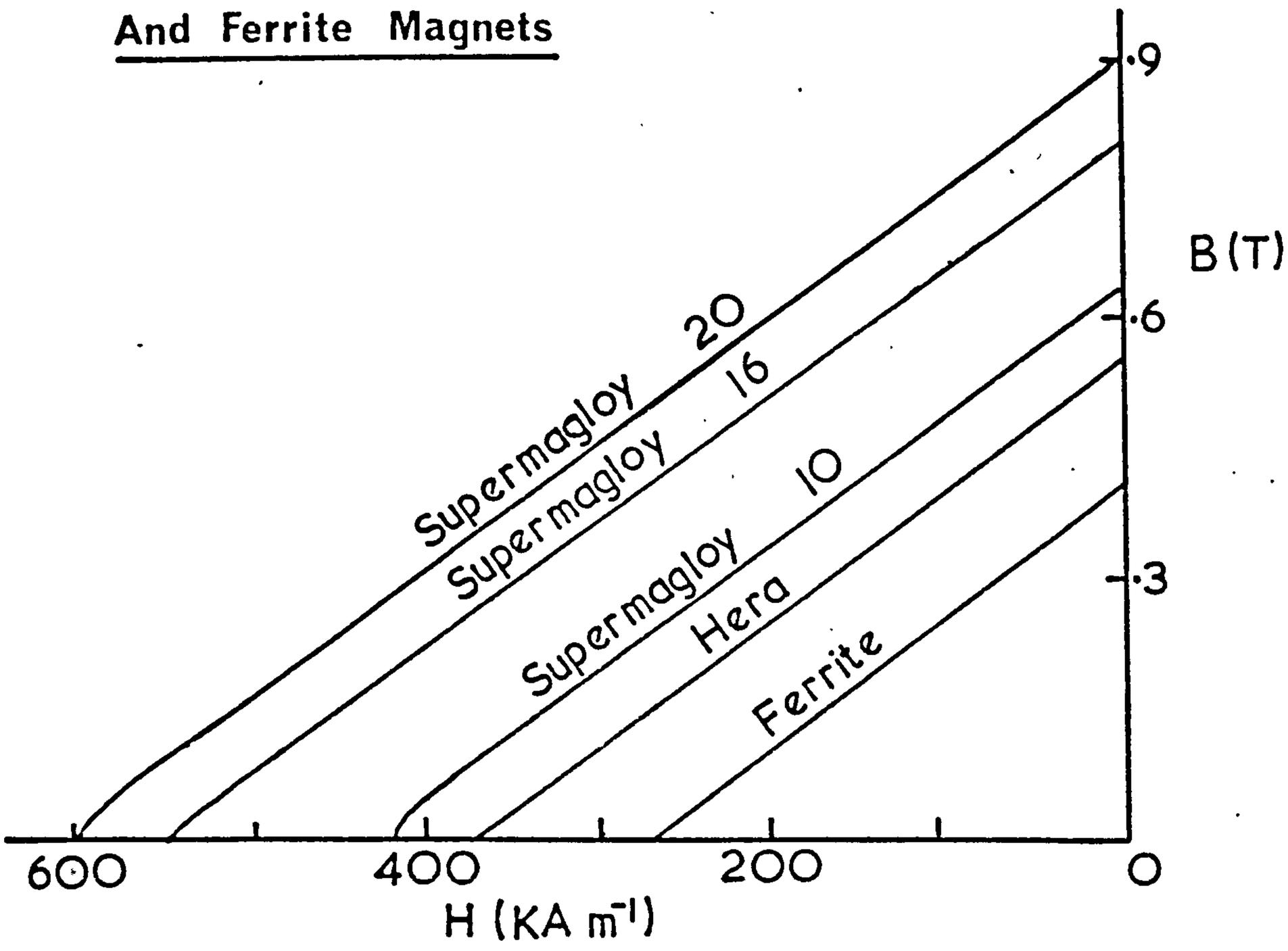

Fig 4·33

Design Calculation

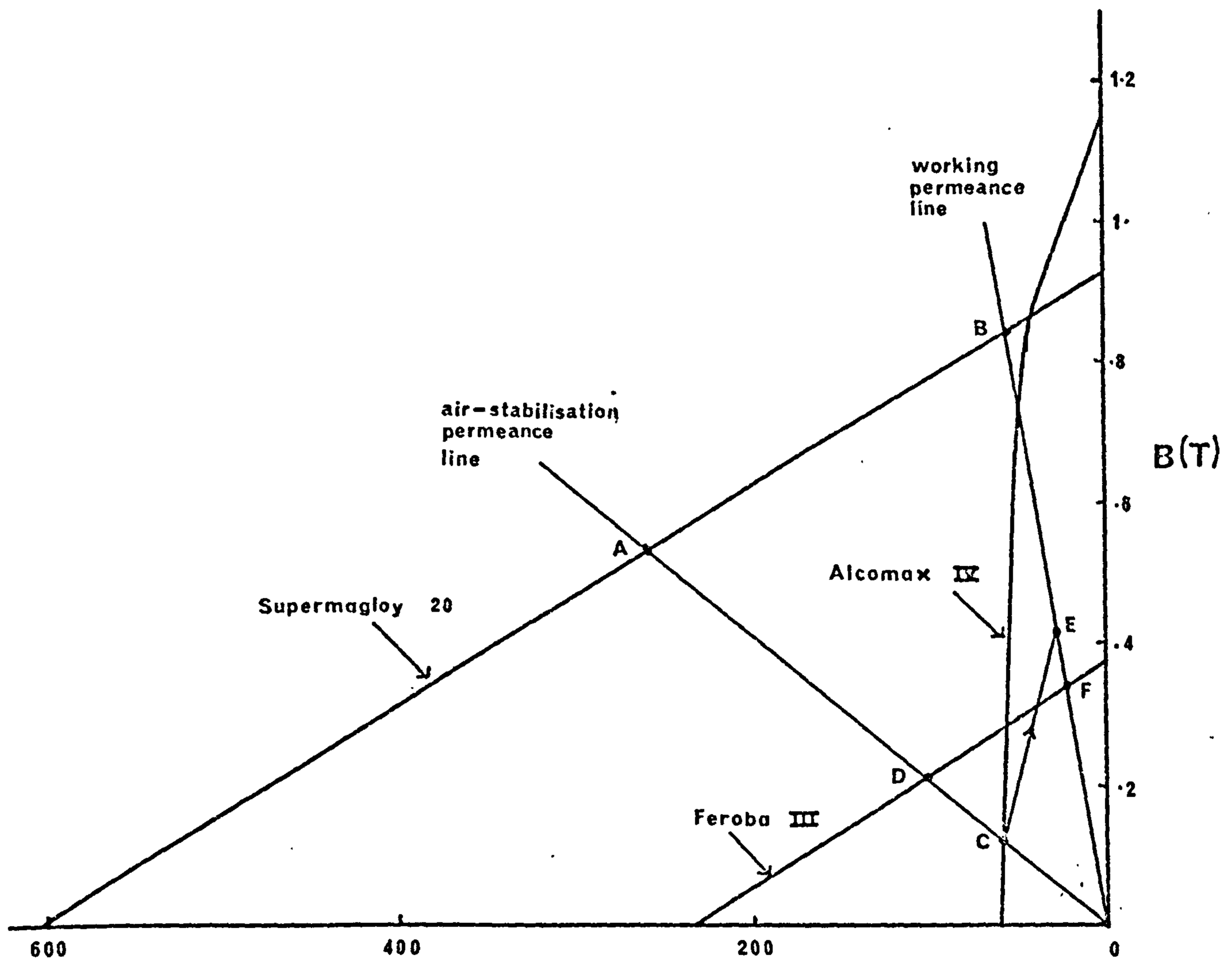

H (KA/m)

Fig 5·1

Coordinates Of A Finite Element Mesh

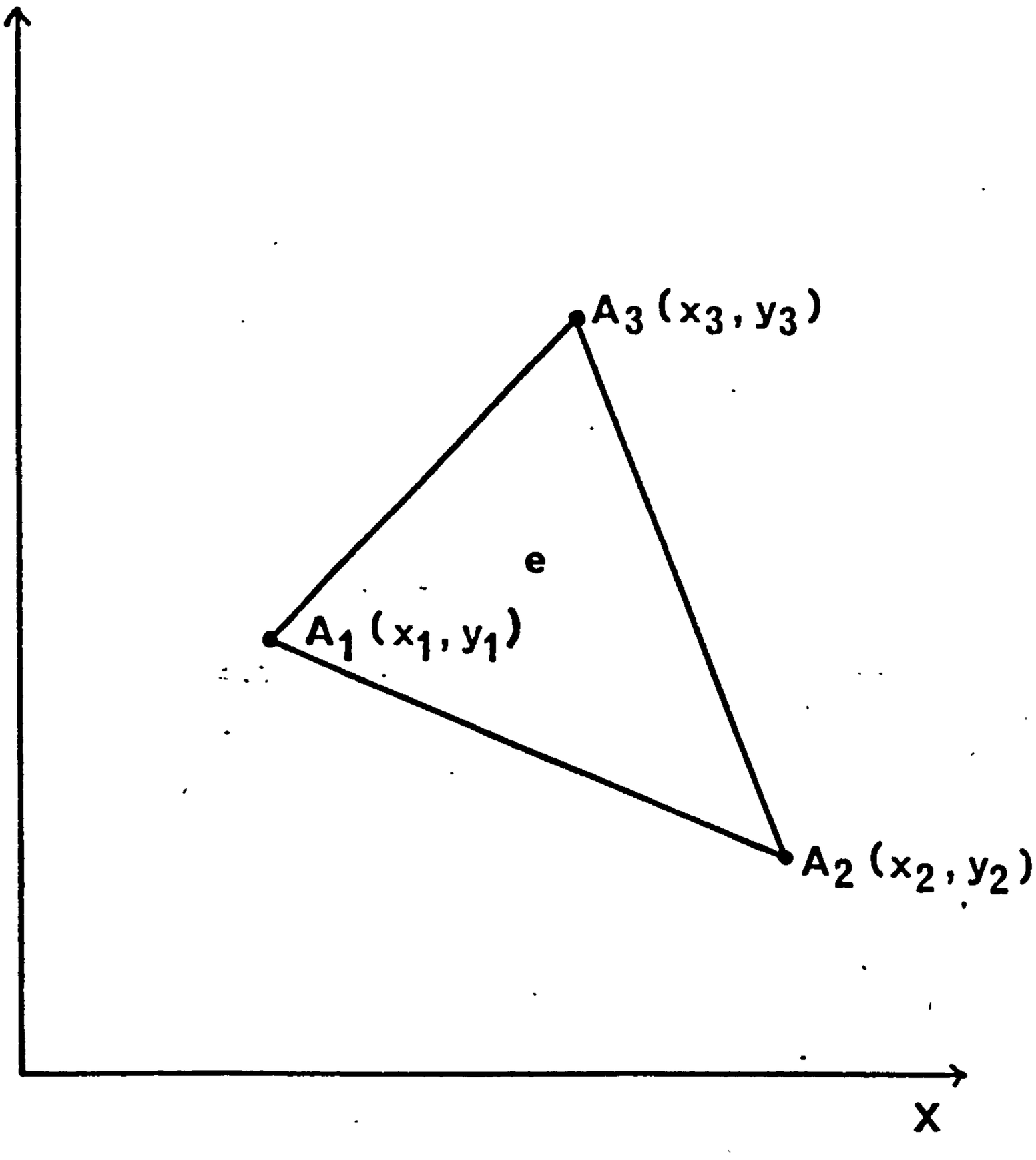

Fig 5·2
Fig 5·3

5·2 Boundaries Of A Field Problem

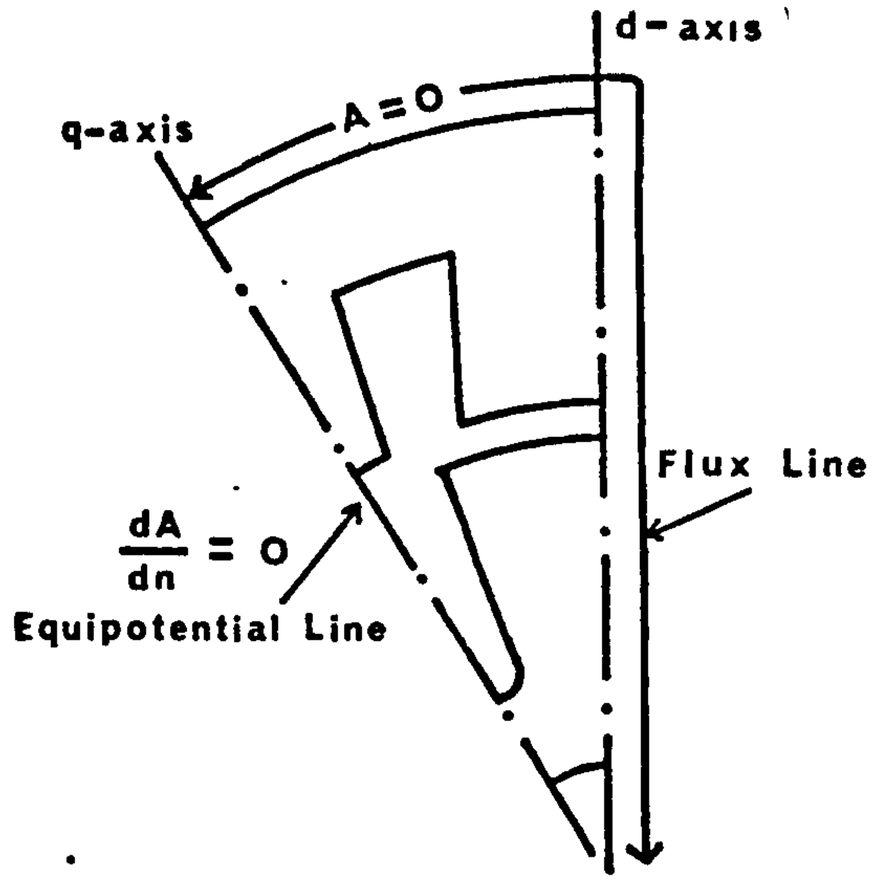

5·3 Periodic Boundaries

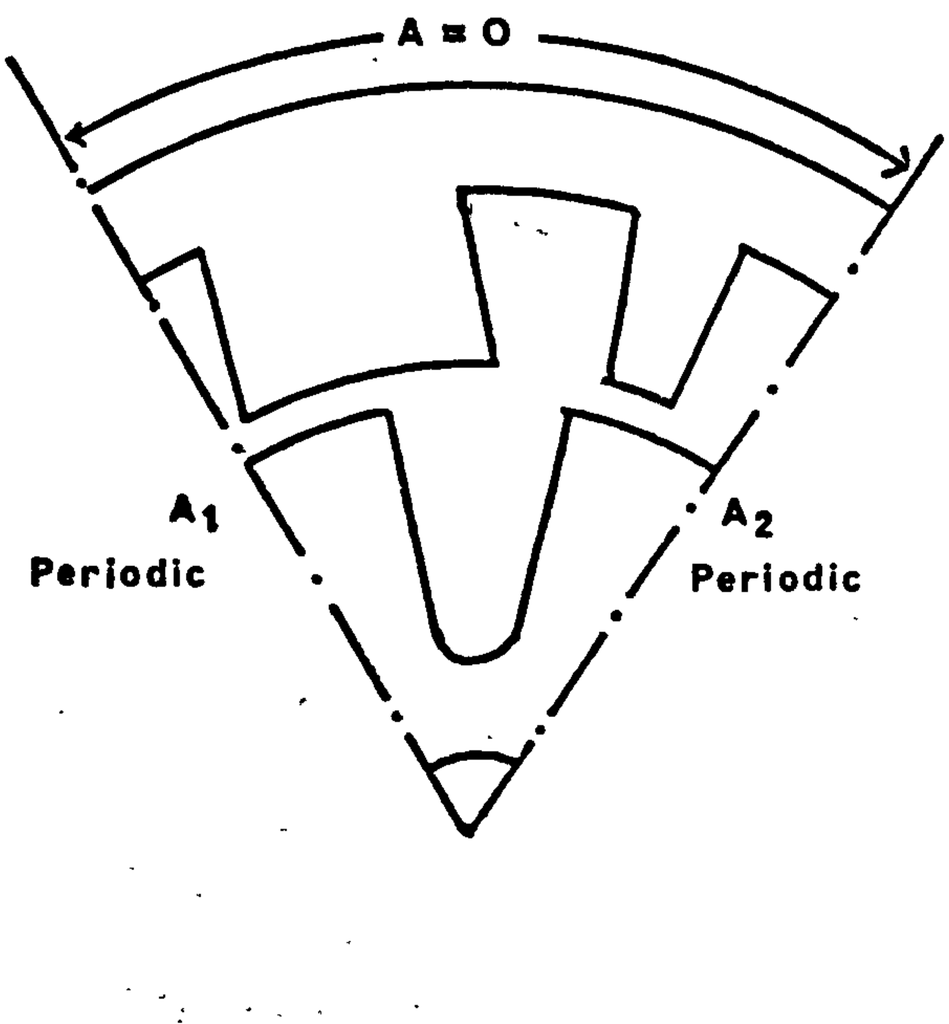

B-H Curves Of Soft Iron Materials

Analytical Expression Of B-H Curve

$$B = \mu_o H + S_1 \tan^{-1}(A_1 H) + S_2 \tan^{-1}(A_2 H)$$

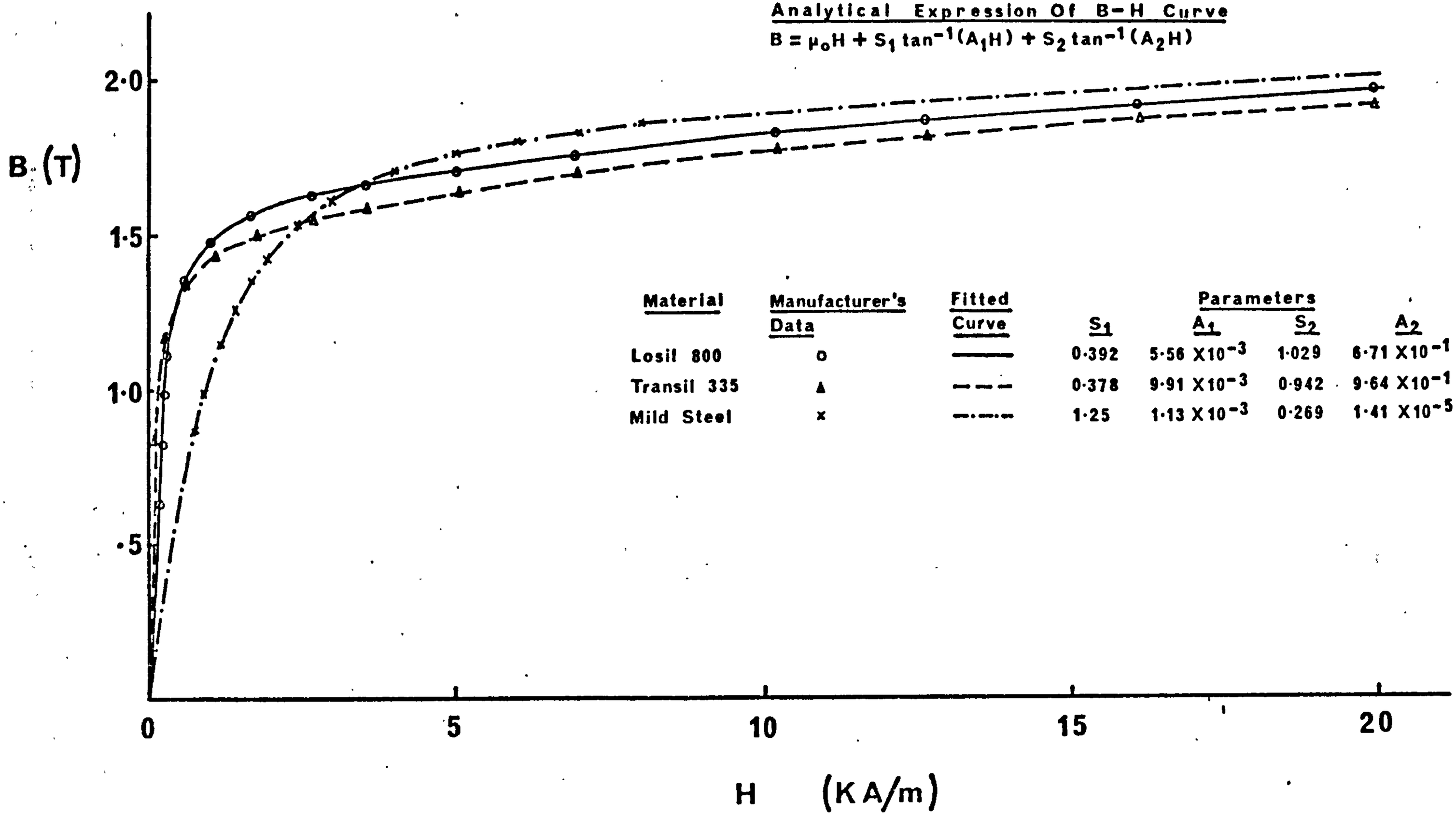

Material	Manufacturer's Data	Fitted Curve	Parameters S_1	A_1	S_2	A_2
Losil 800	o	———	0·392	$5{\cdot}56 \times 10^{-3}$	1·029	$6{\cdot}71 \times 10^{-1}$
Transil 335	▲	– – –	0·378	$9{\cdot}91 \times 10^{-3}$	0·942	$9{\cdot}64 \times 10^{-1}$
Mild Steel	×	—·—·—	1·25	$1{\cdot}13 \times 10^{-3}$	0·269	$1{\cdot}41 \times 10^{-5}$

Fig 5.4

Magnetisation Curves Of Metallic Magnets

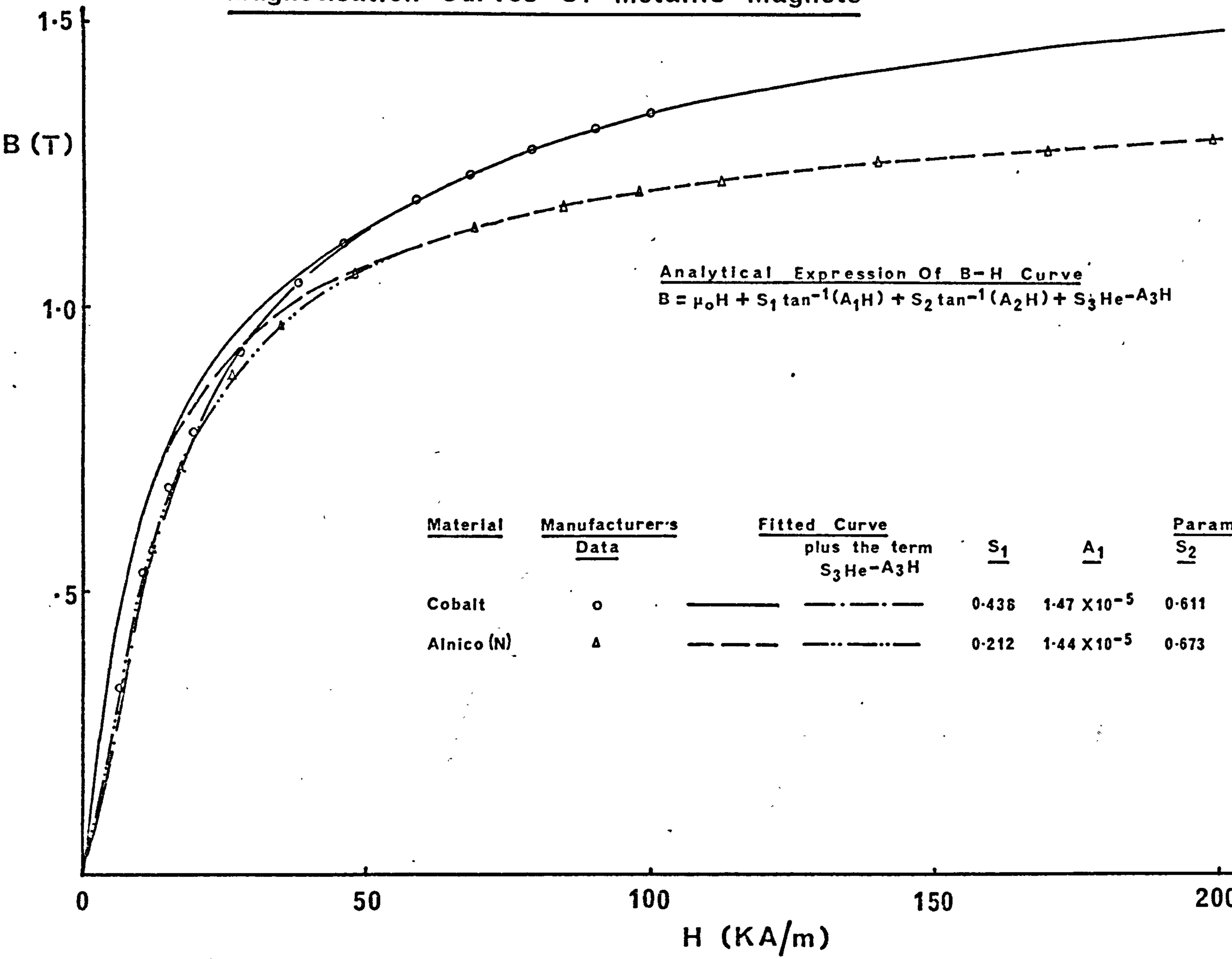

Analytical Expression Of B–H Curve

$$B = \mu_o H + S_1 \tan^{-1}(A_1 H) + S_2 \tan^{-1}(A_2 H) + S_3 He^{-A_3 H}$$

Material	Manufacturer's Data	Fitted Curve plus the term $S_3 He^{-A_3 H}$	S_1	A_1	S_2	A_2	S_3	A_3
			Parameters					
Cobalt	o	———	0·436	$1·47 \times 10^{-5}$	0·611	$1·21 \times 10^{-4}$	$-7·77 \times 10^{-5}$	$1·67 \times 10^{-4}$
Alnico (N)	Δ	— — —	0·212	$1·44 \times 10^{-5}$	0·673	$1·16 \times 10^{-4}$	-6×10^{-5}	$1·43 \times 10^{-4}$

Fig 5.5

Demagnetisation Curves Of Metallic Magnets

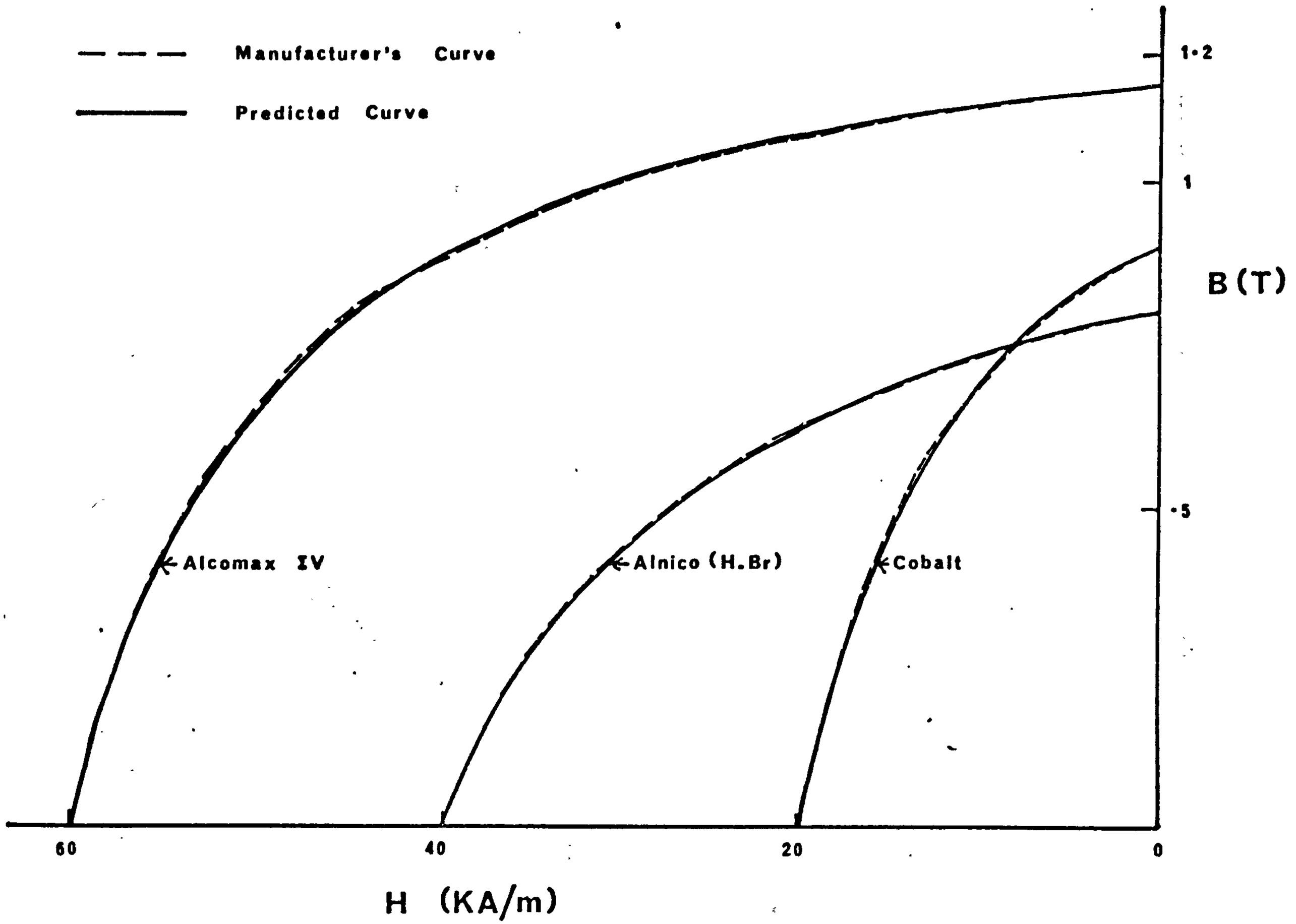

Fig 5.6

Demagnetisation Curves Of Rare Earth Magnets

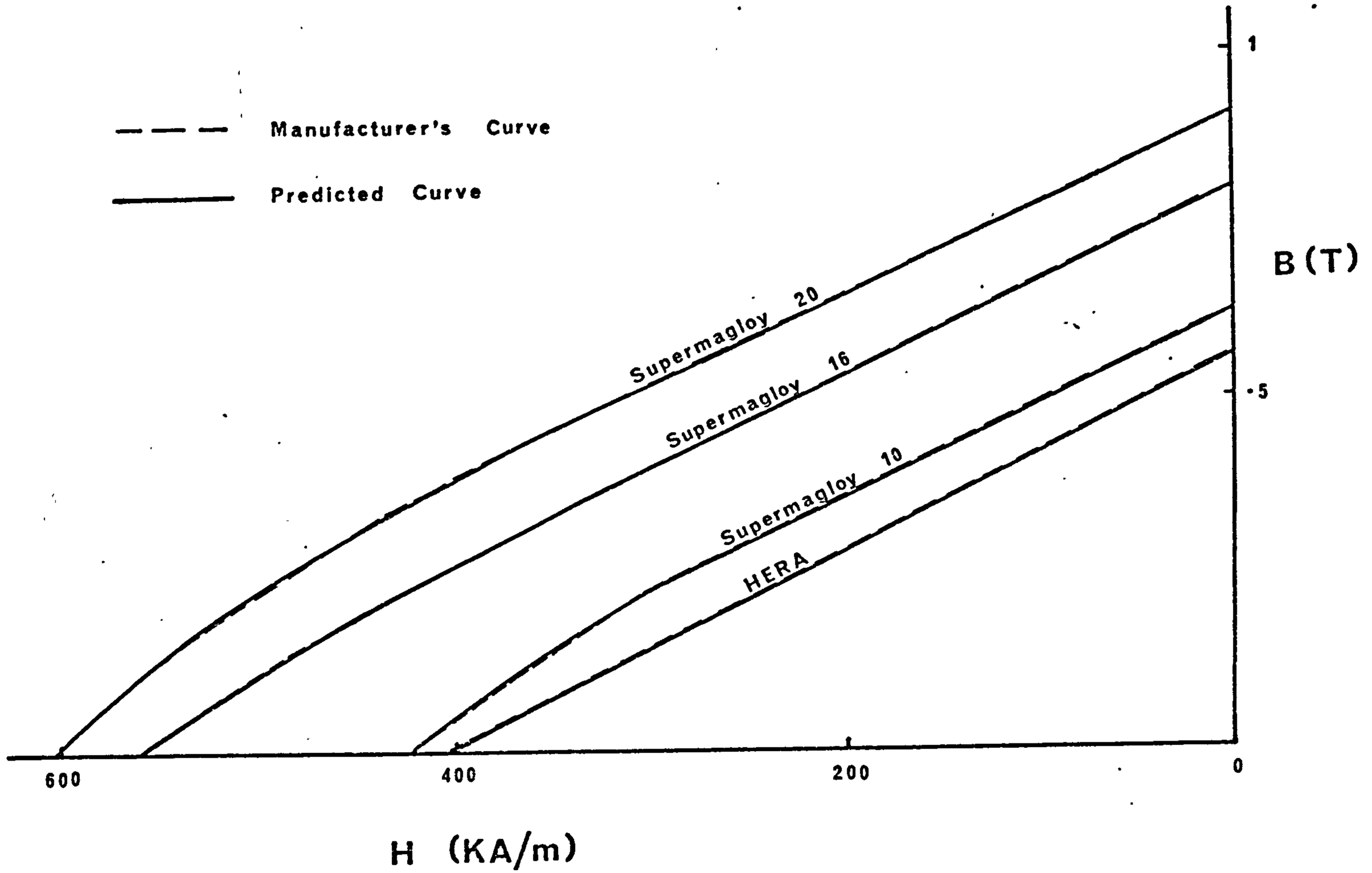

Fig 5.7

Fig 5·8

Discretization Of Field Problem Using PAFEC

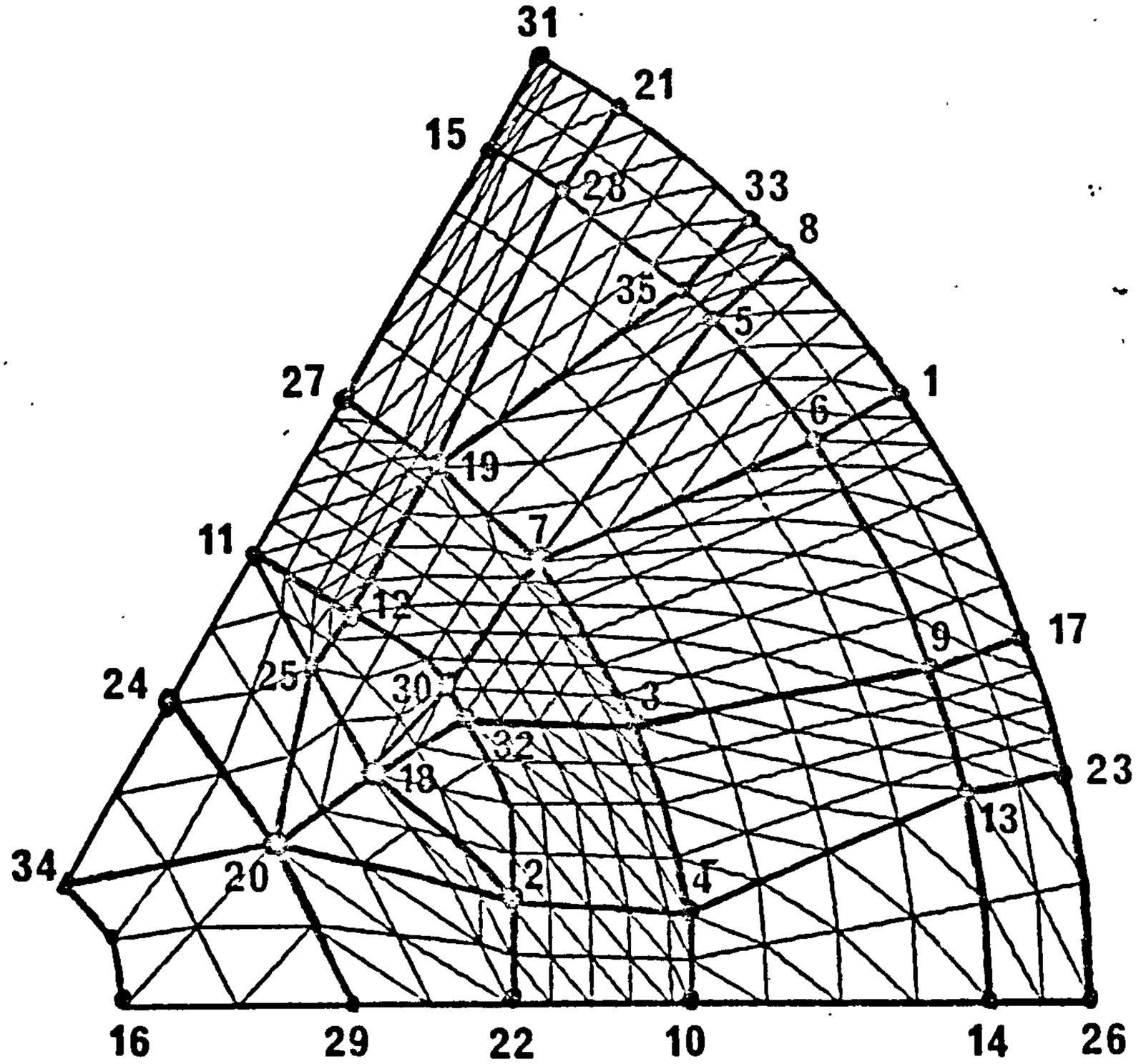

Fig 5·9(a)
Fig 5·9(b)

Typical Finite Element Meshes

(a) Half Pole Pitch

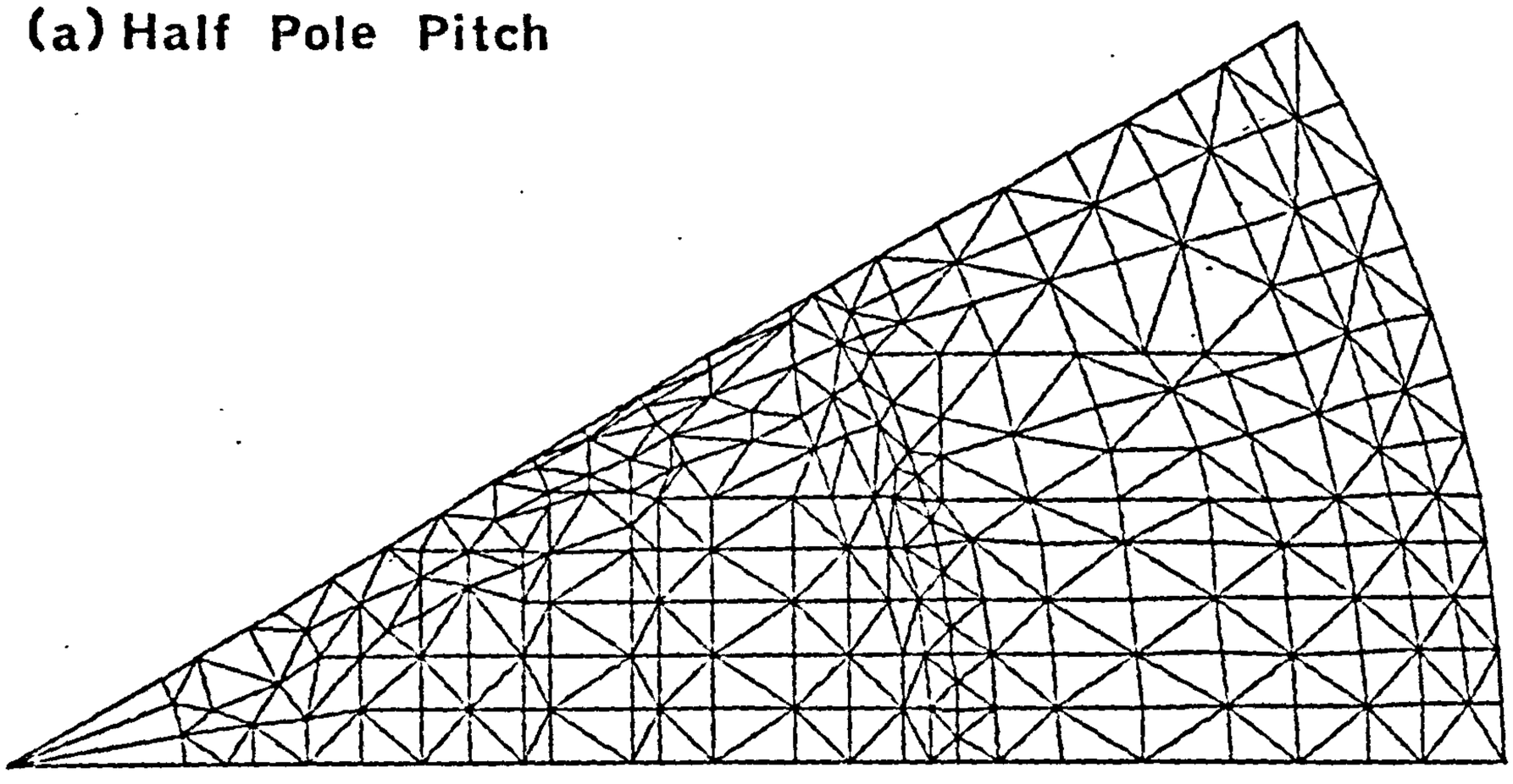

(b) Full Pole Pitch

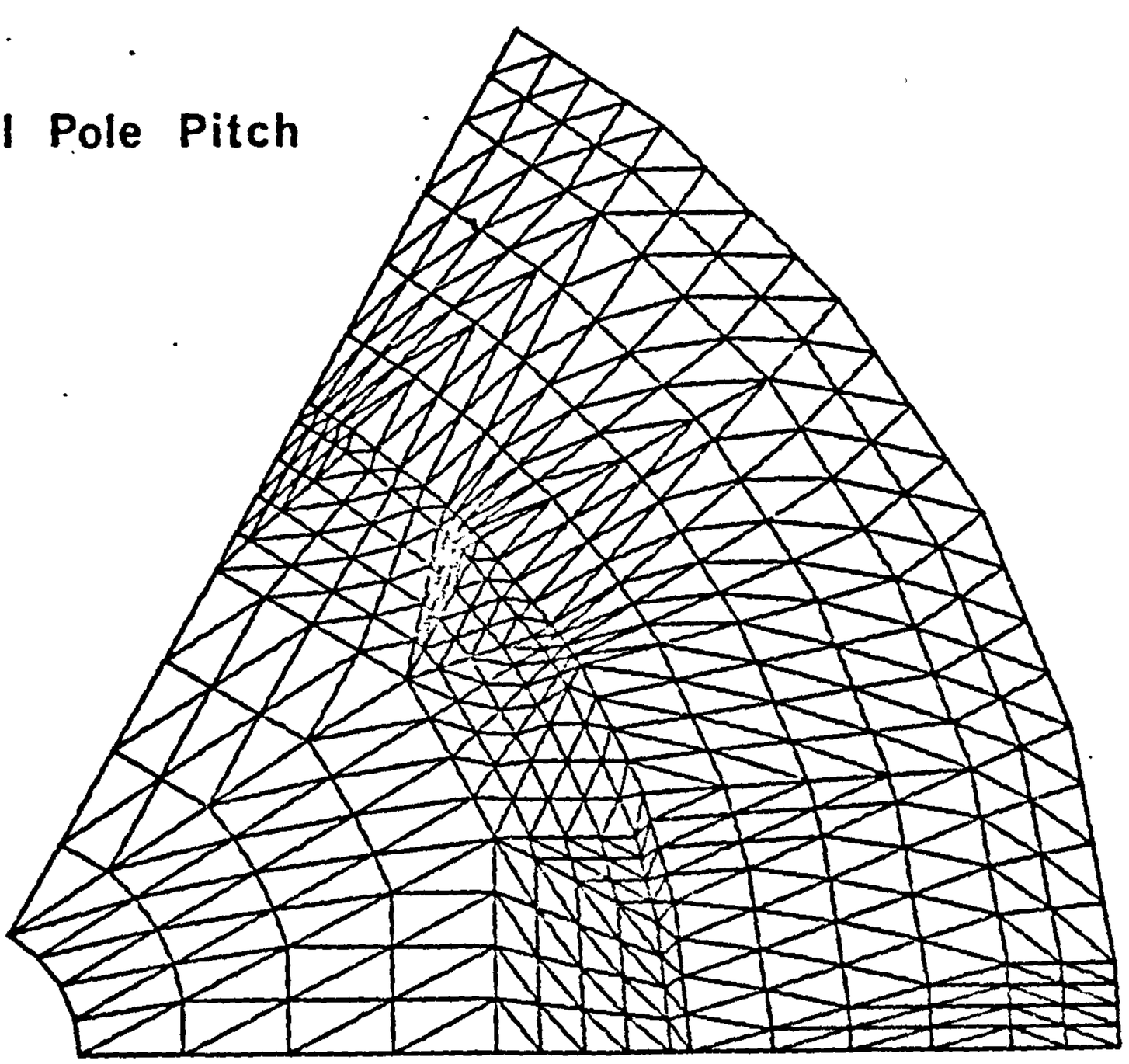

Fig 5·IC

Finite Element Mesh With Added Elements For Periodic Boundaries

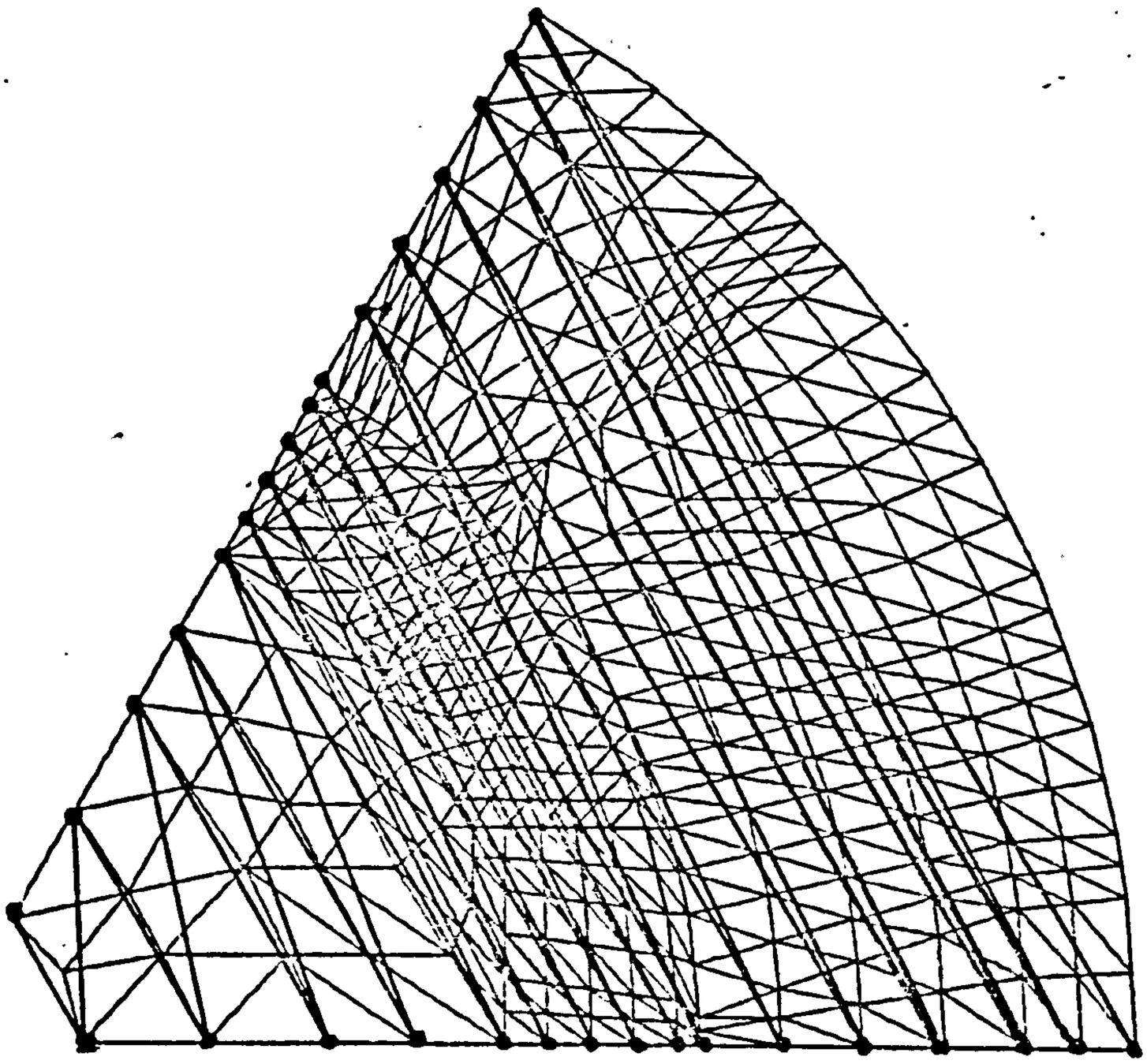

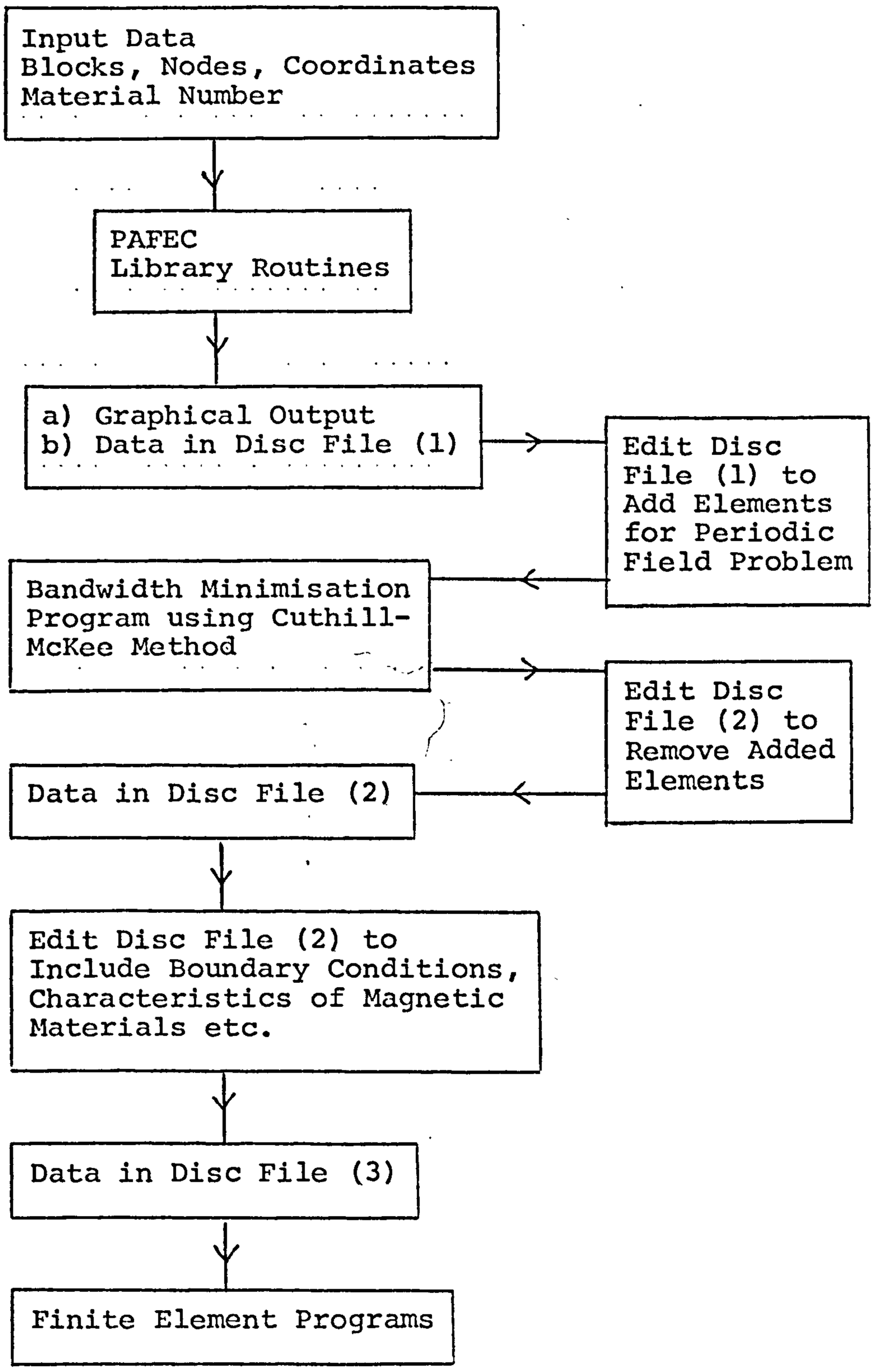

Flow chart for data preparation.

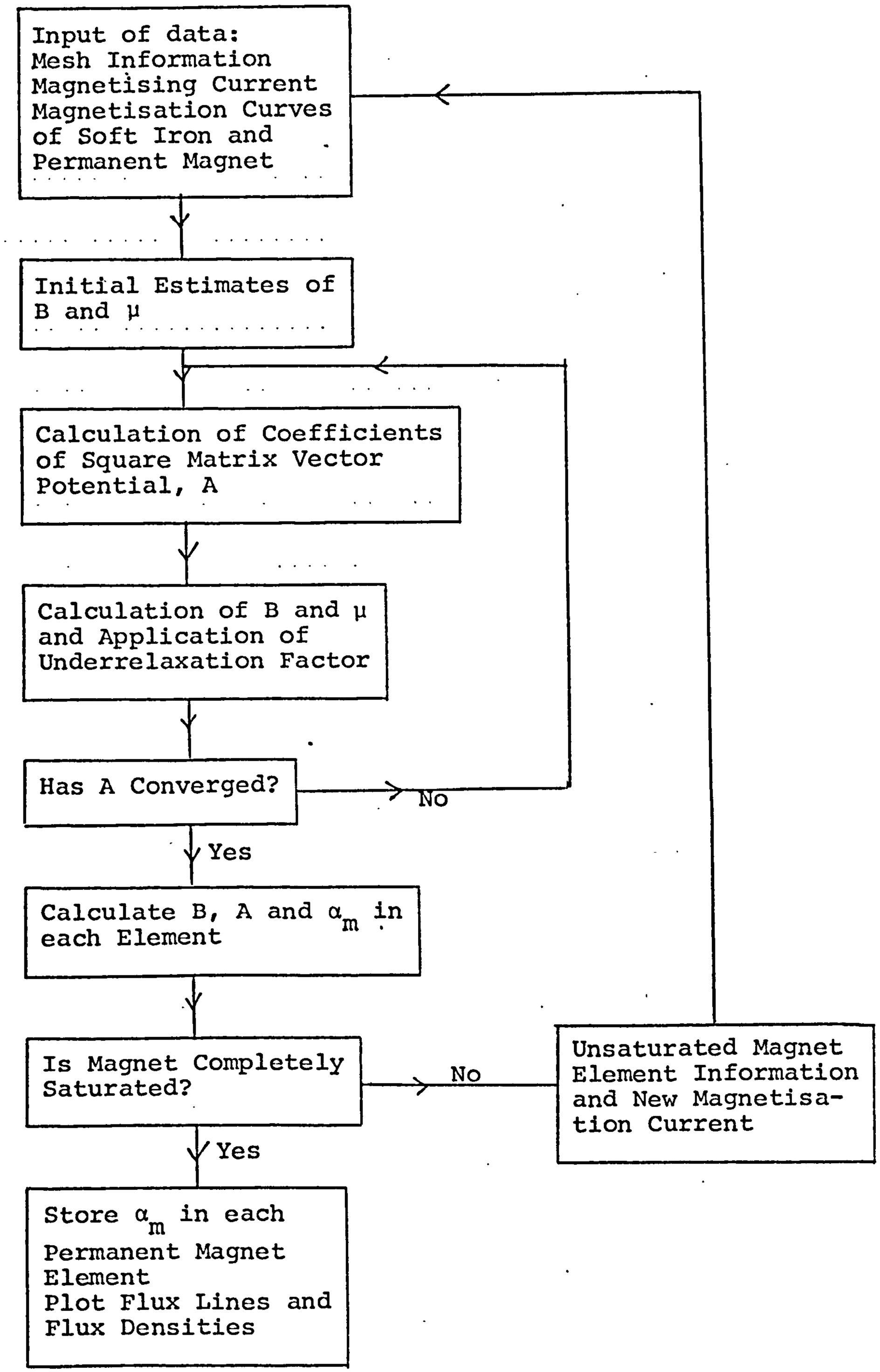

Flow chart to magnetisation calculation.

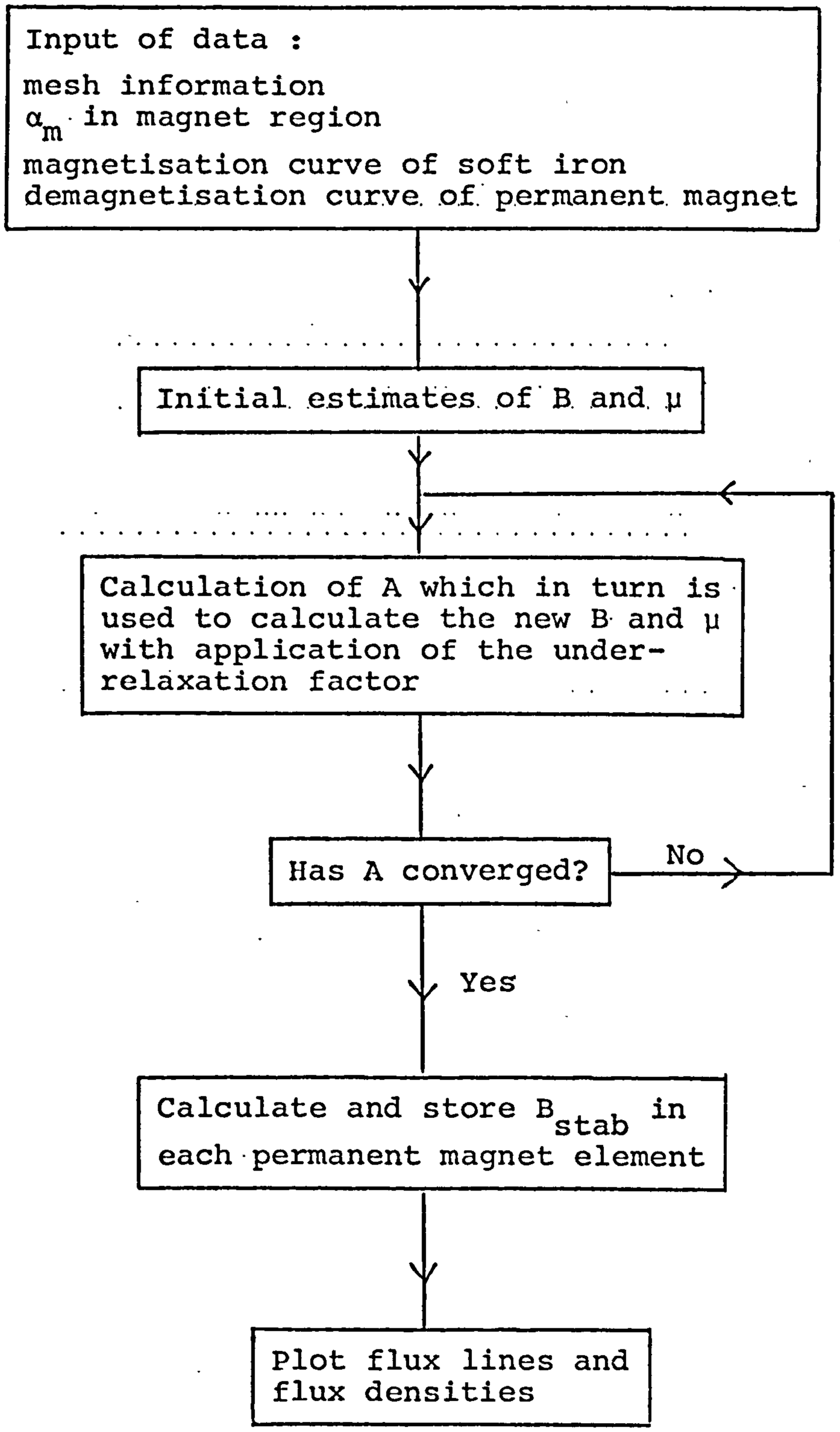

Flow chart for air-stabilisation calculation

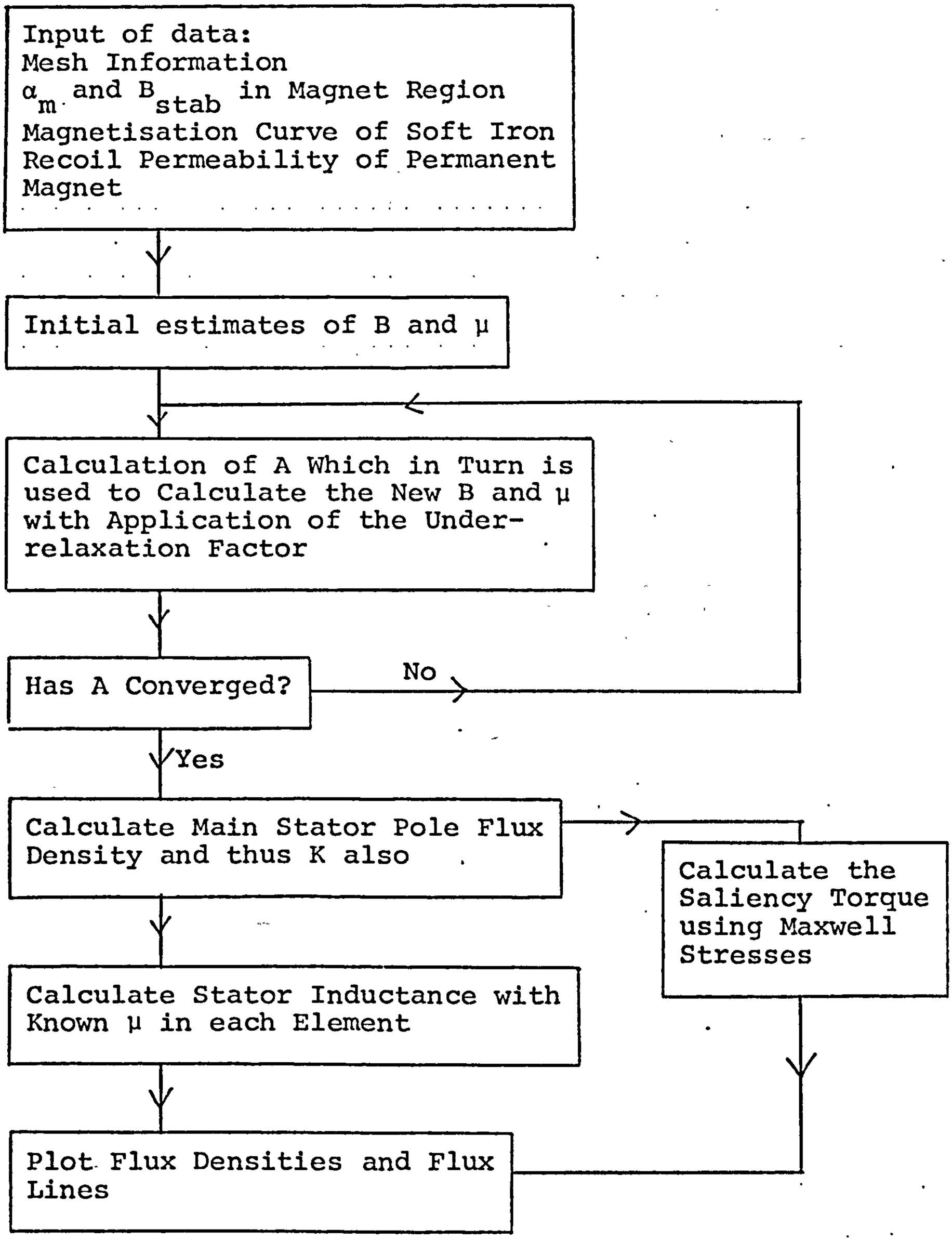

Flow chart for recoil operation calculation including inductance and saliency torque calculation.

Fig 5·15

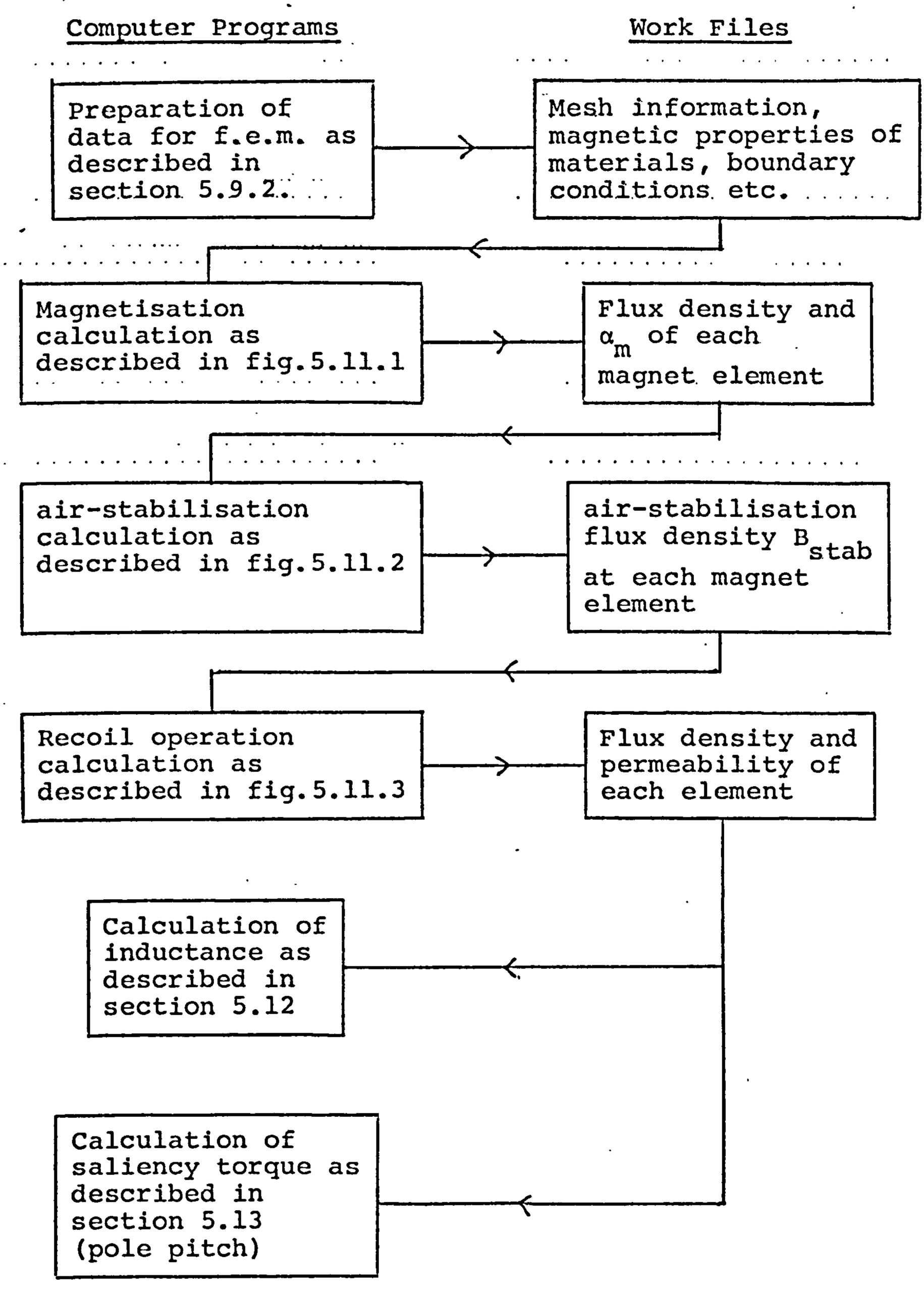

Organization of computer programs

Fig 5·16

Fig 5·17

5·16 Flux Density In An Element

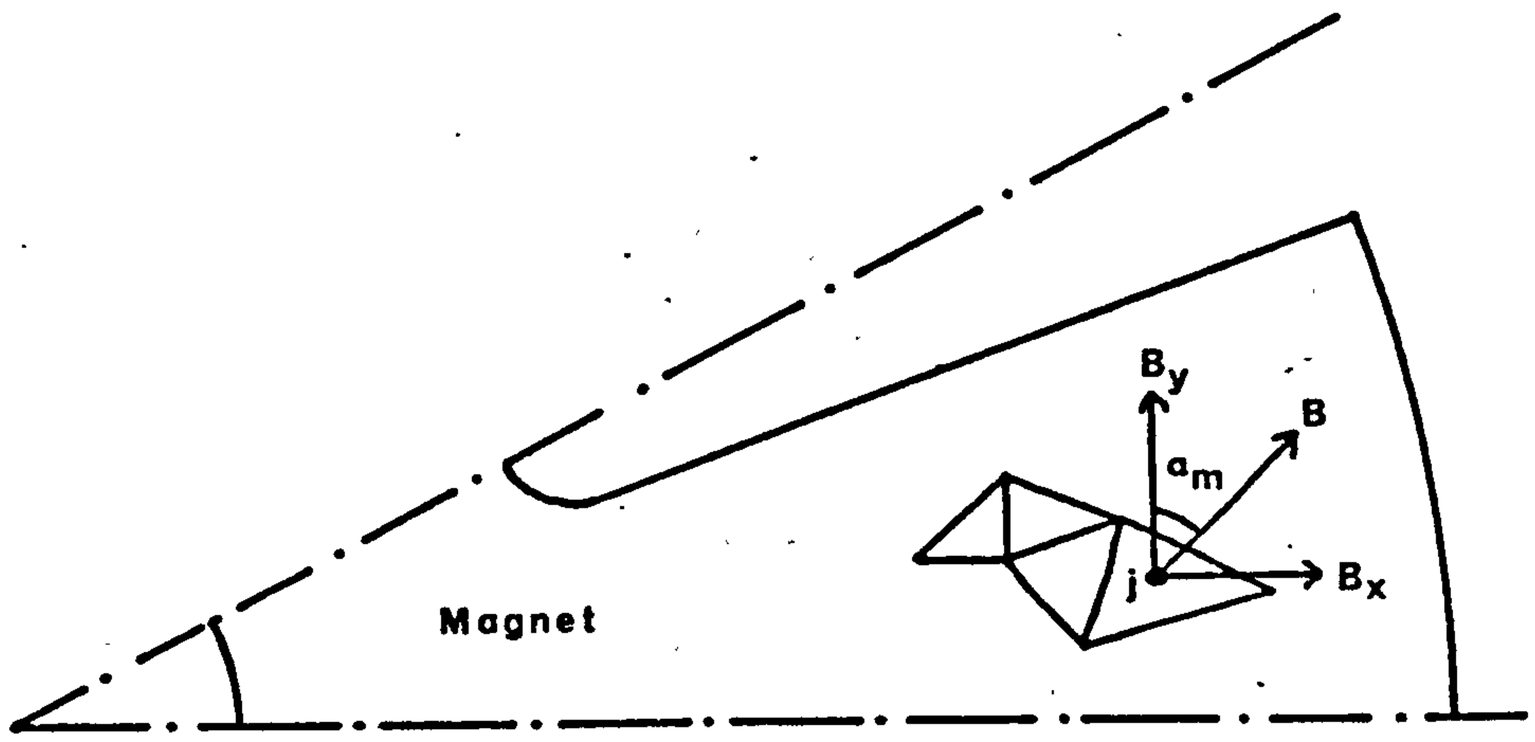

5·17 Field Problem For The Calculation Of Peak Flux Linkage K

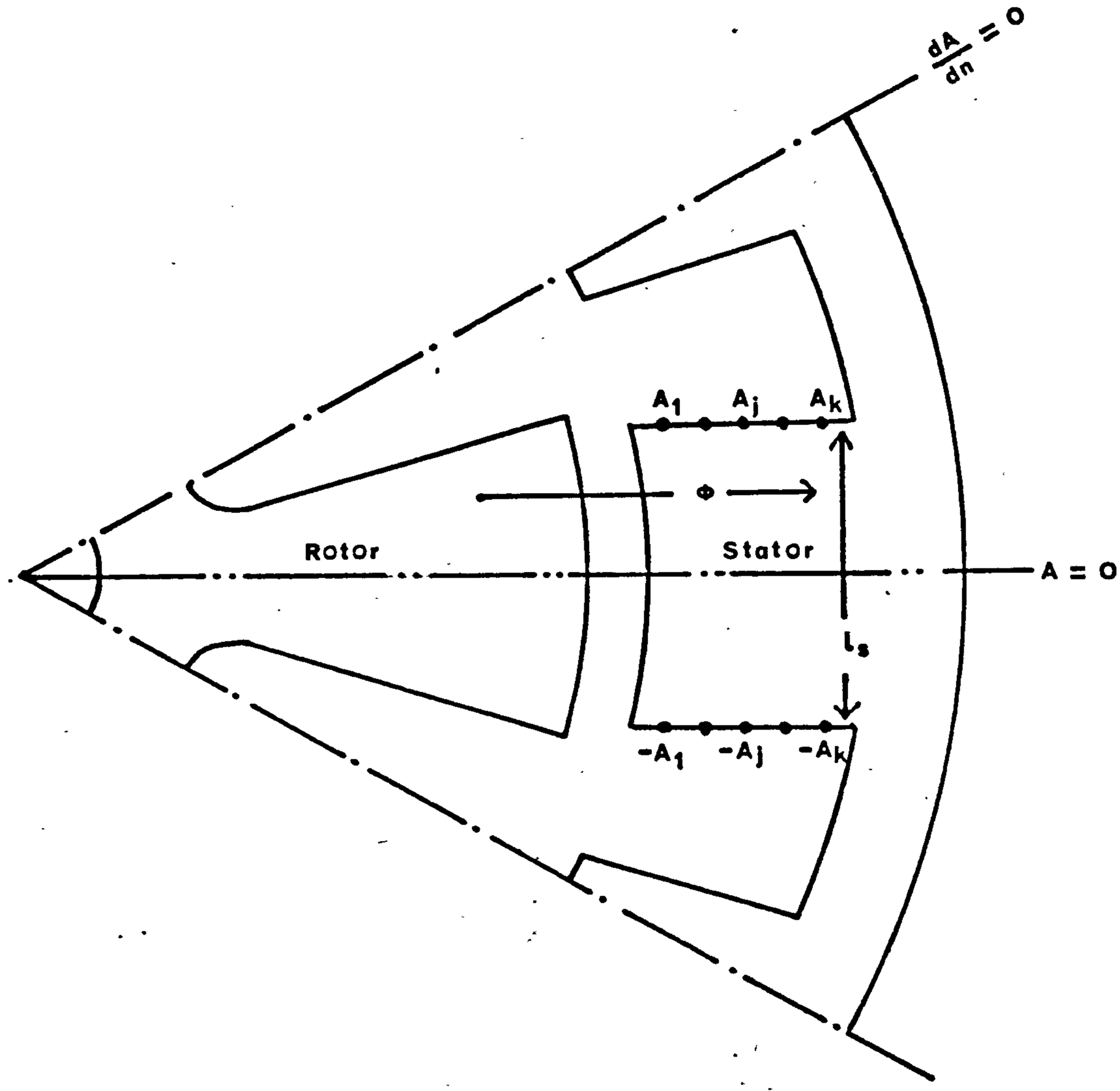

Fig 5·18

Fig 5·19

5·18 Field Problem For The Calculation Of Stator Inductance

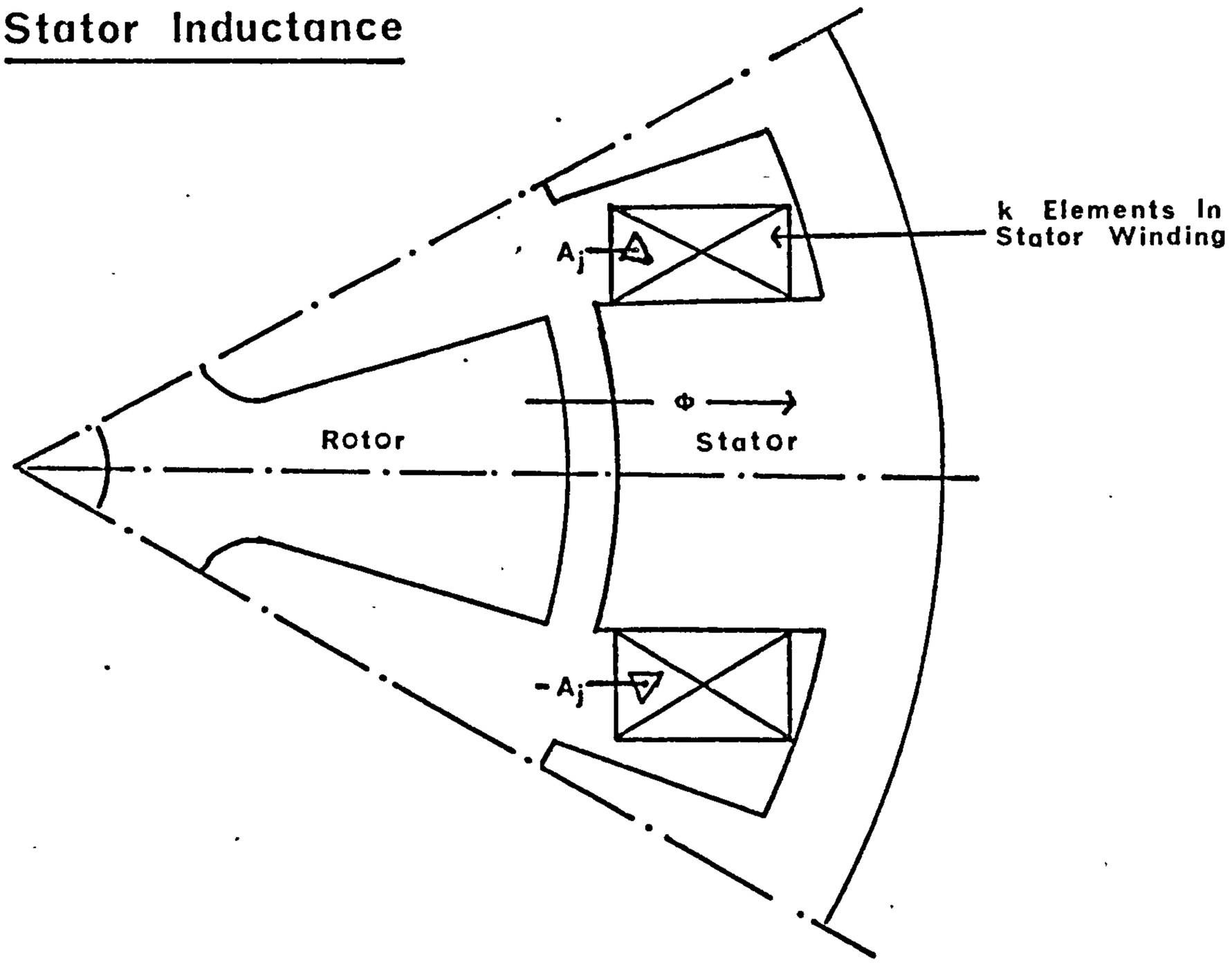

5·19 Field Problem For The Calculation Of Saliency Torque

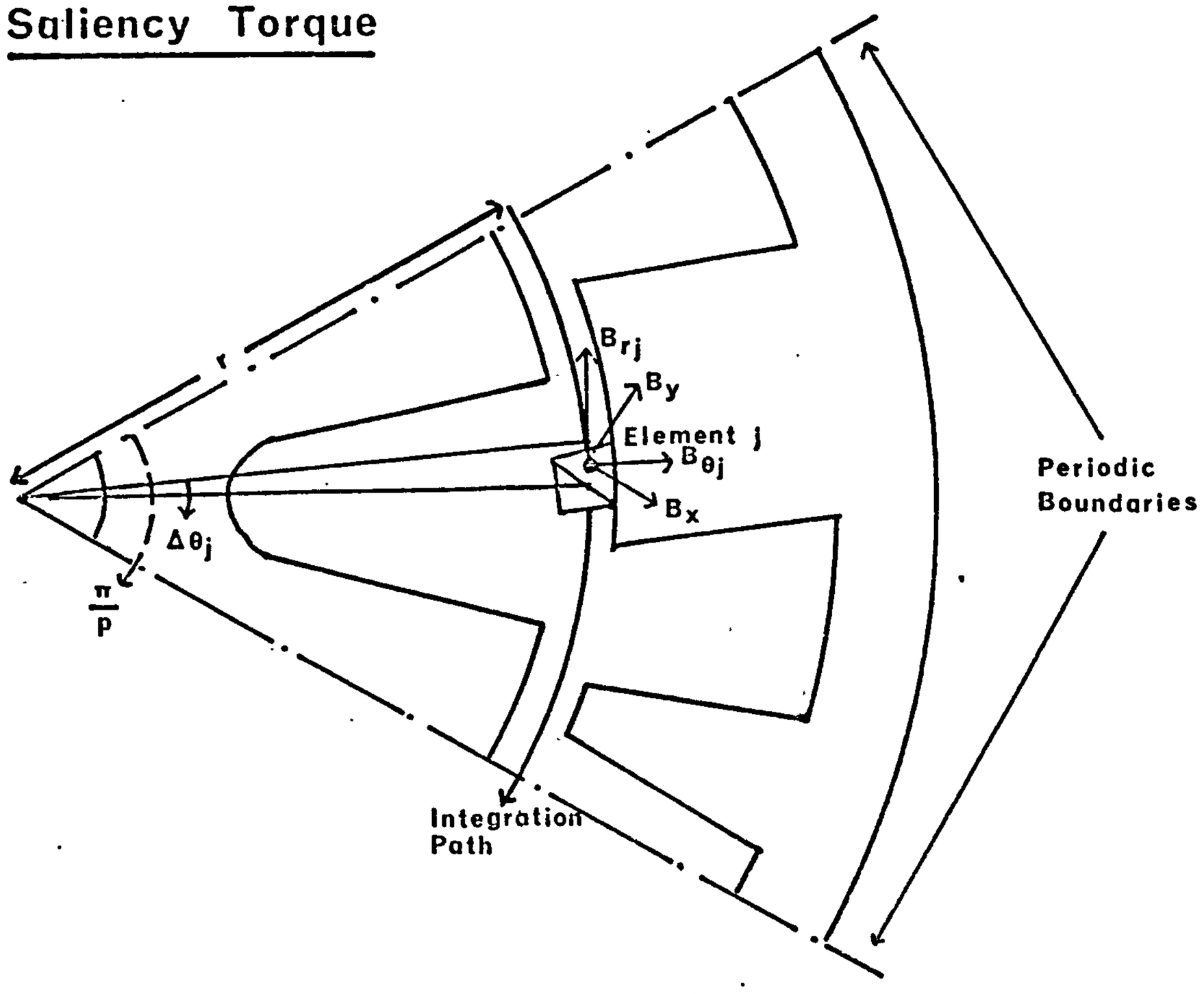

Fig 6-1

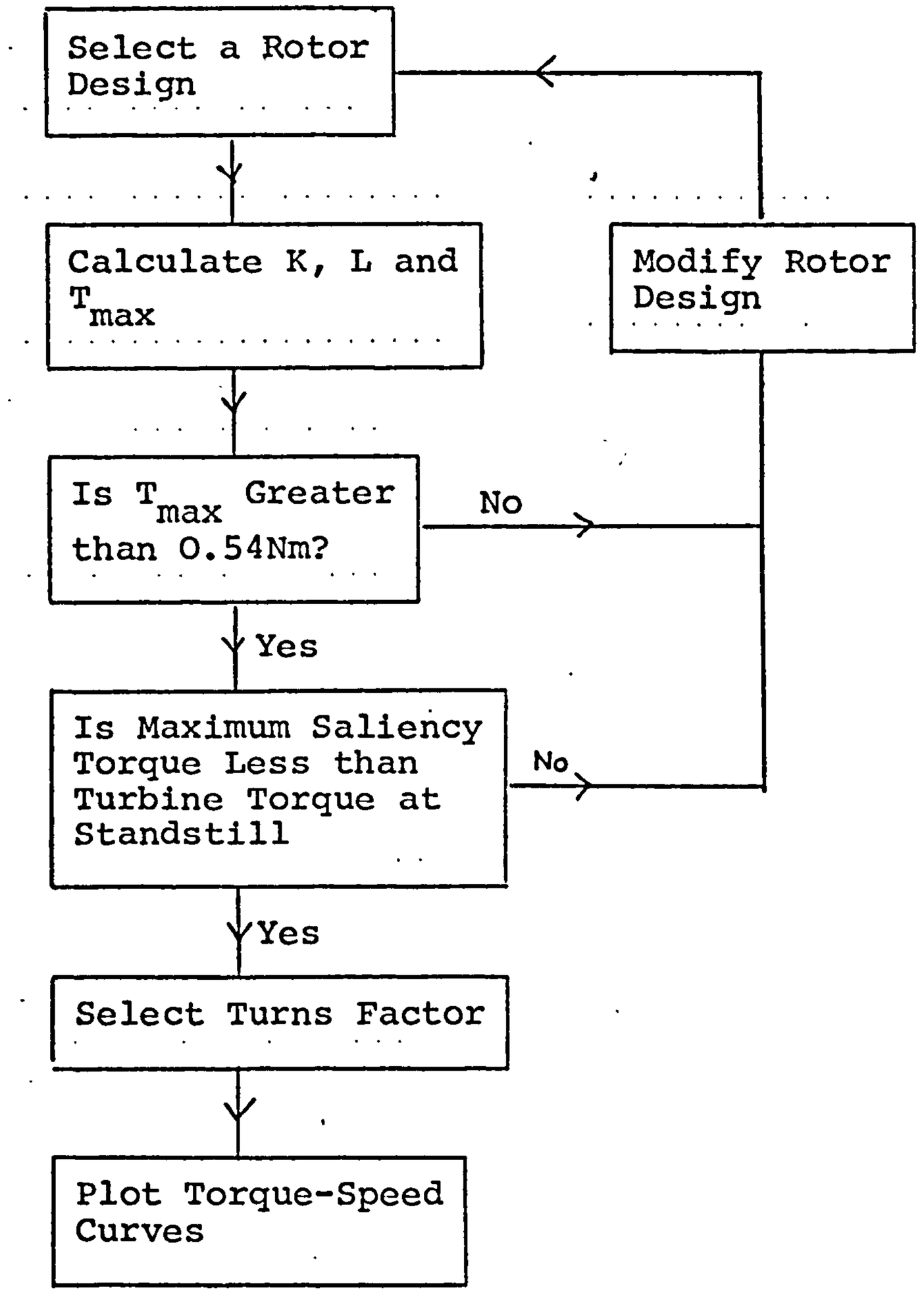

Design approach for the 250W generator.

Fig 6·2

Various Test Rotors

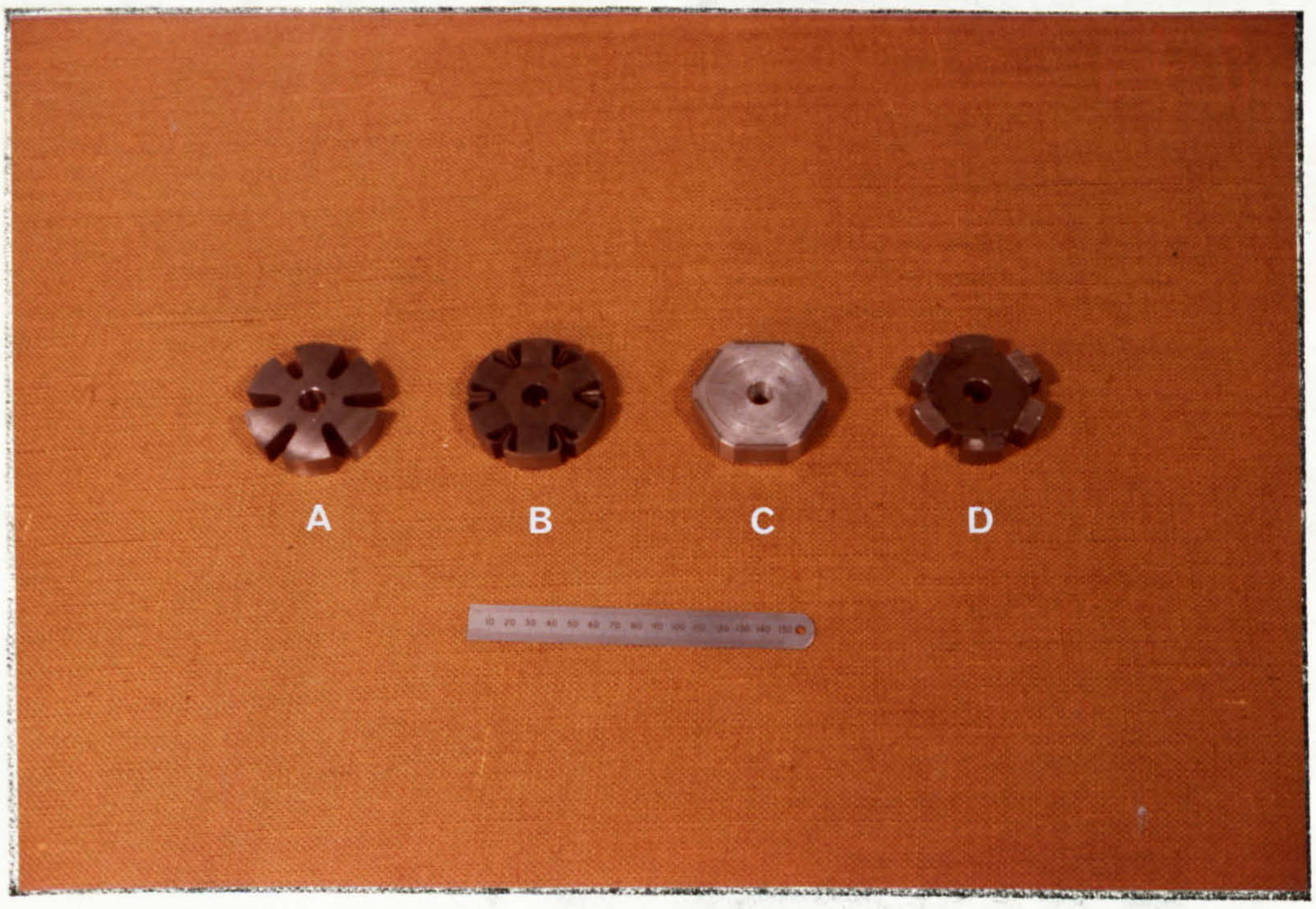

A Finite Element Mesh

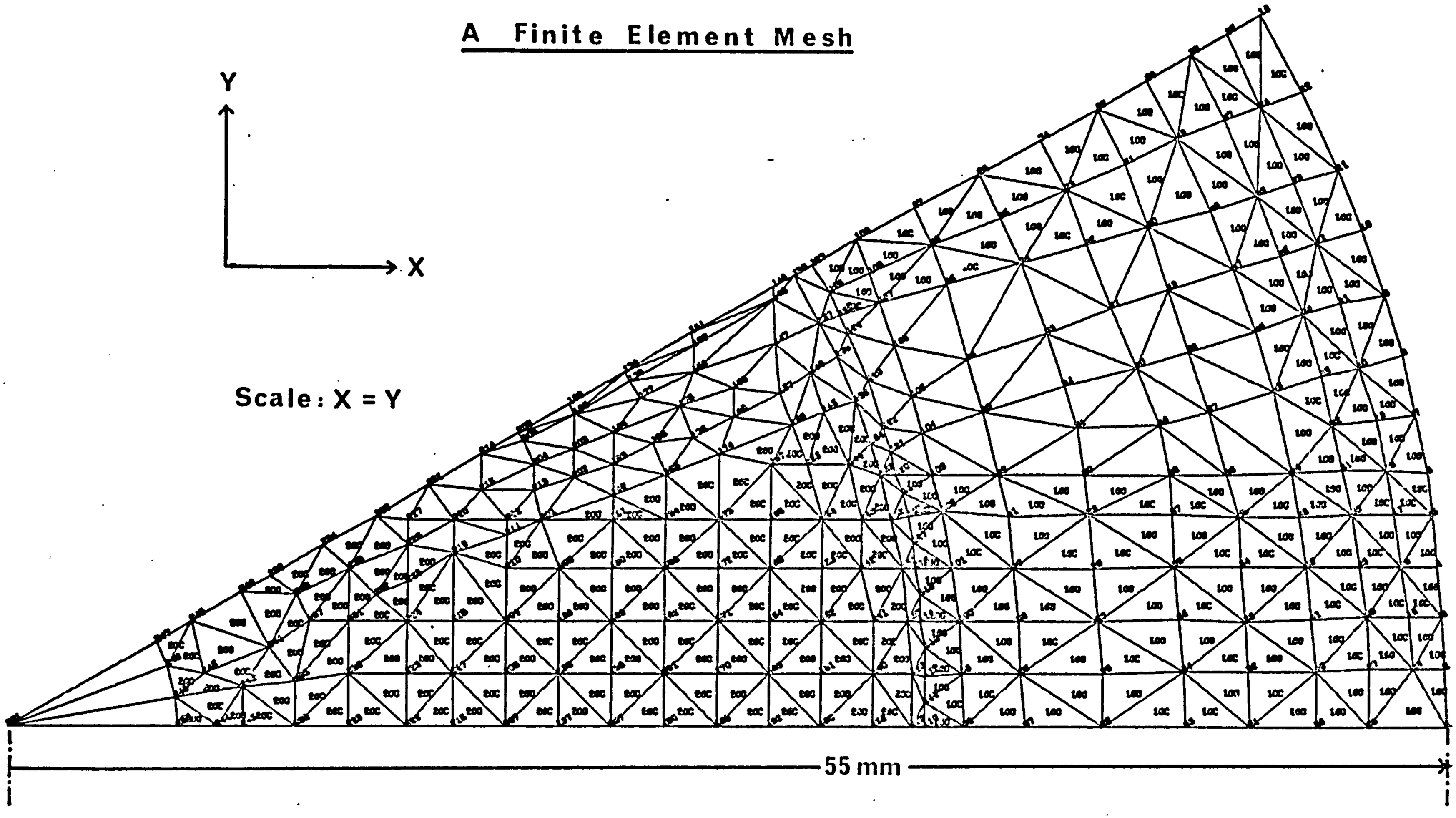

Fig 6.3

Fig 6·4

Magnetisation Of Cobalt Rotor

(a) Flux Lines

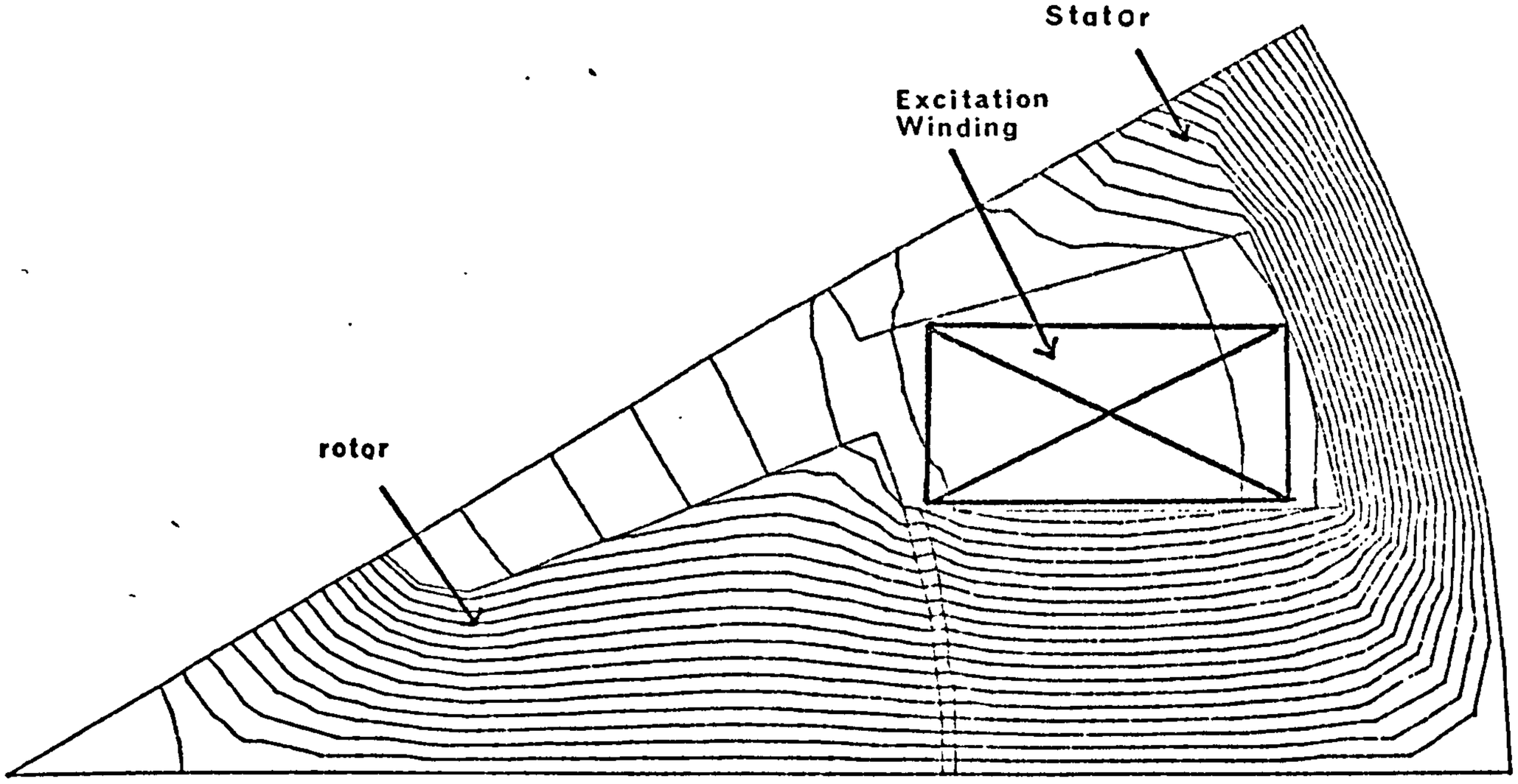

(b) Flux Density Distribution

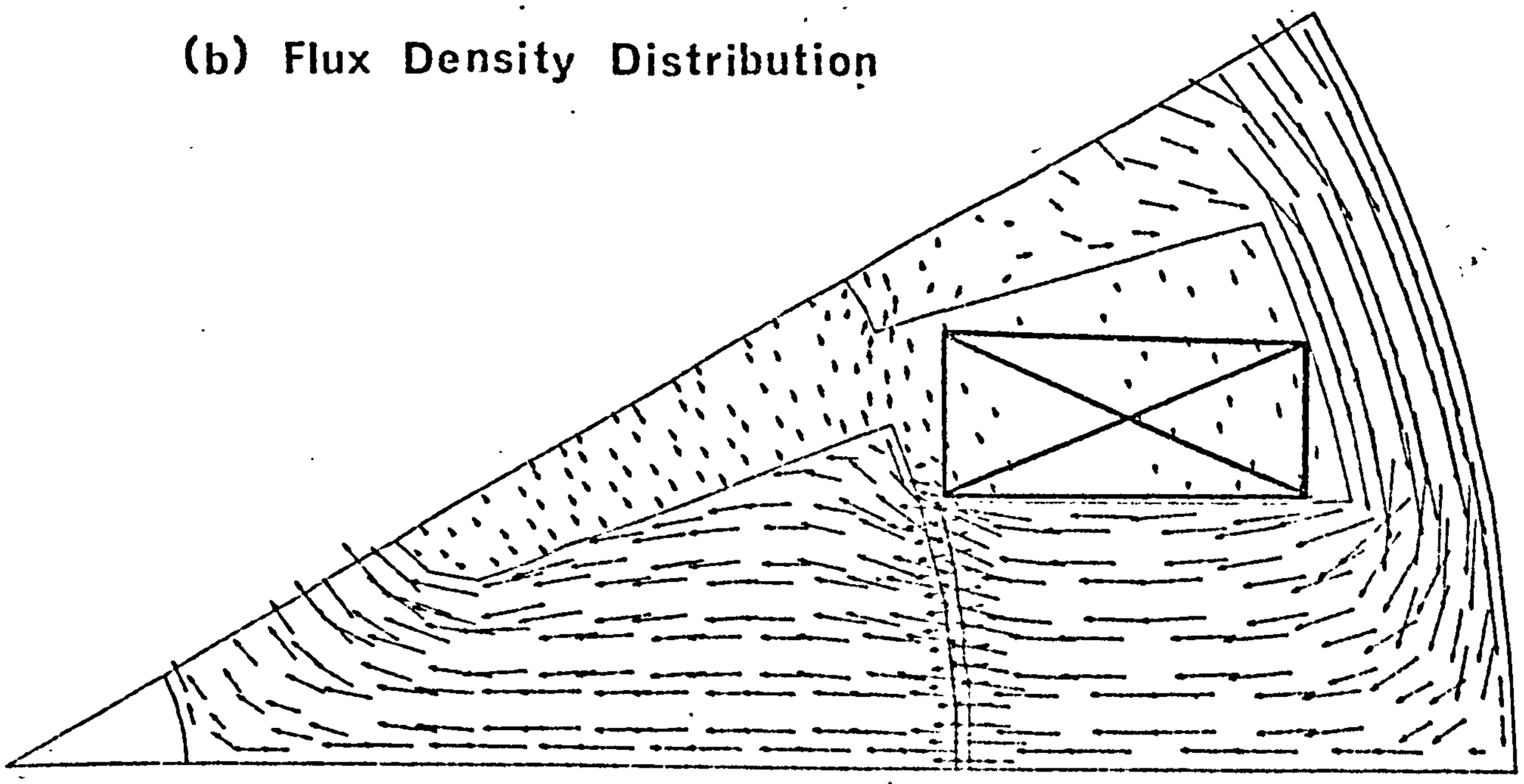

Fig 6·5

Air-Stabilisation Of Cobalt Rotor

(a) Flux Lines

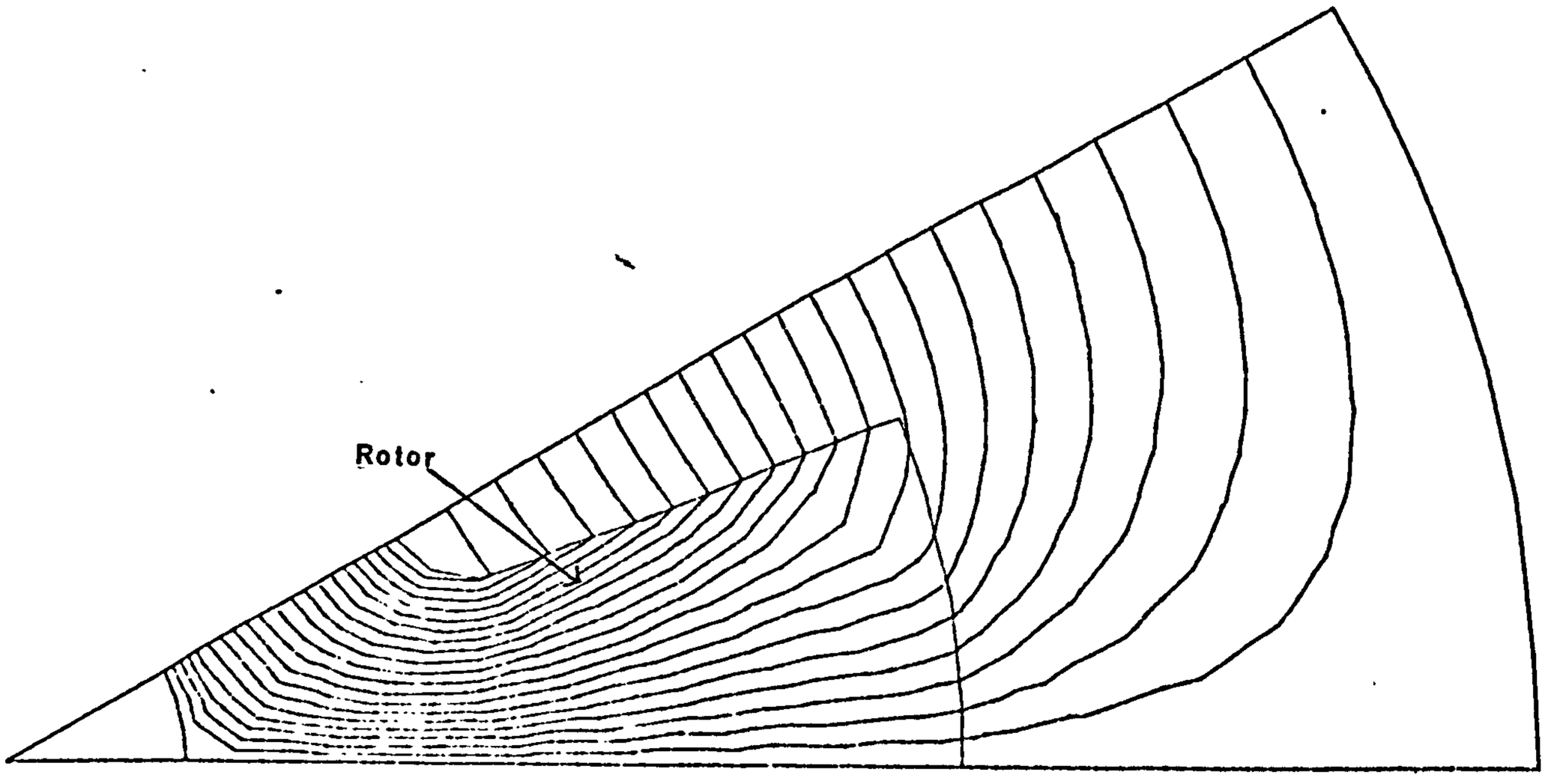

(b) Flux Density Distribution

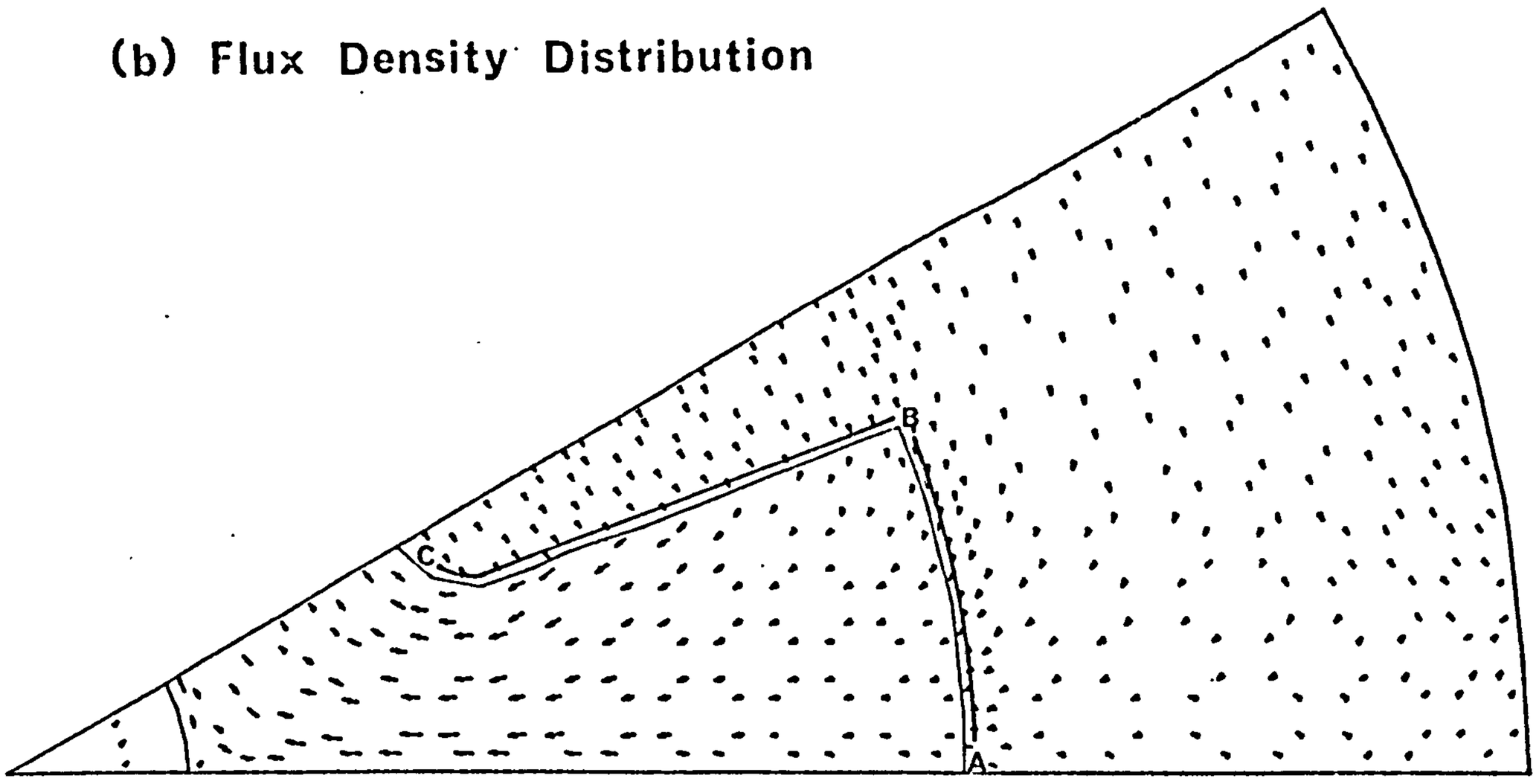

Fig 6·6

Fig 6·7

6·6 Flux Density Distribution On Rotor Surface

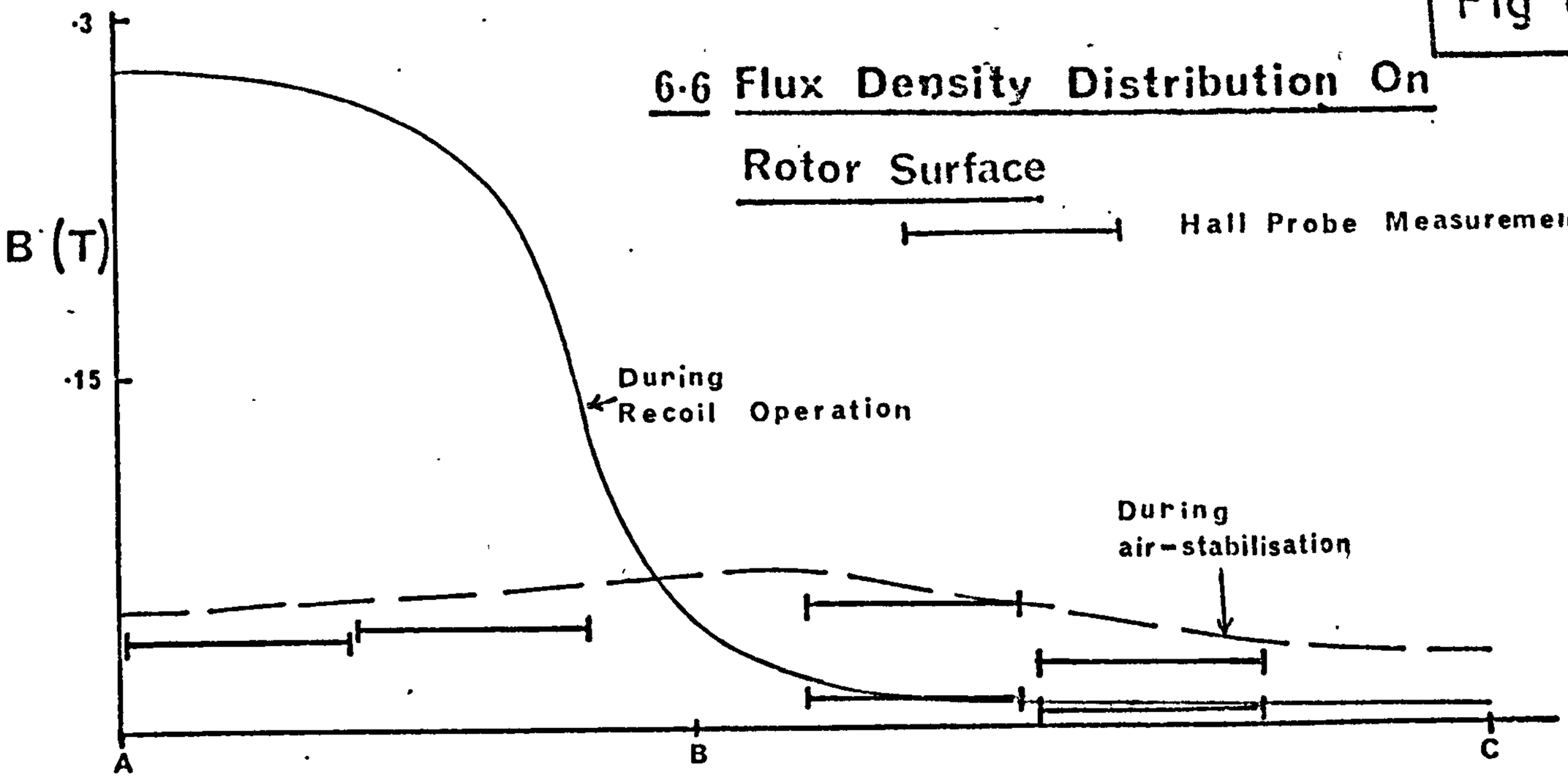

6·7 Recoil Operation Of Cobalt Rotor

(a) Flux Lines

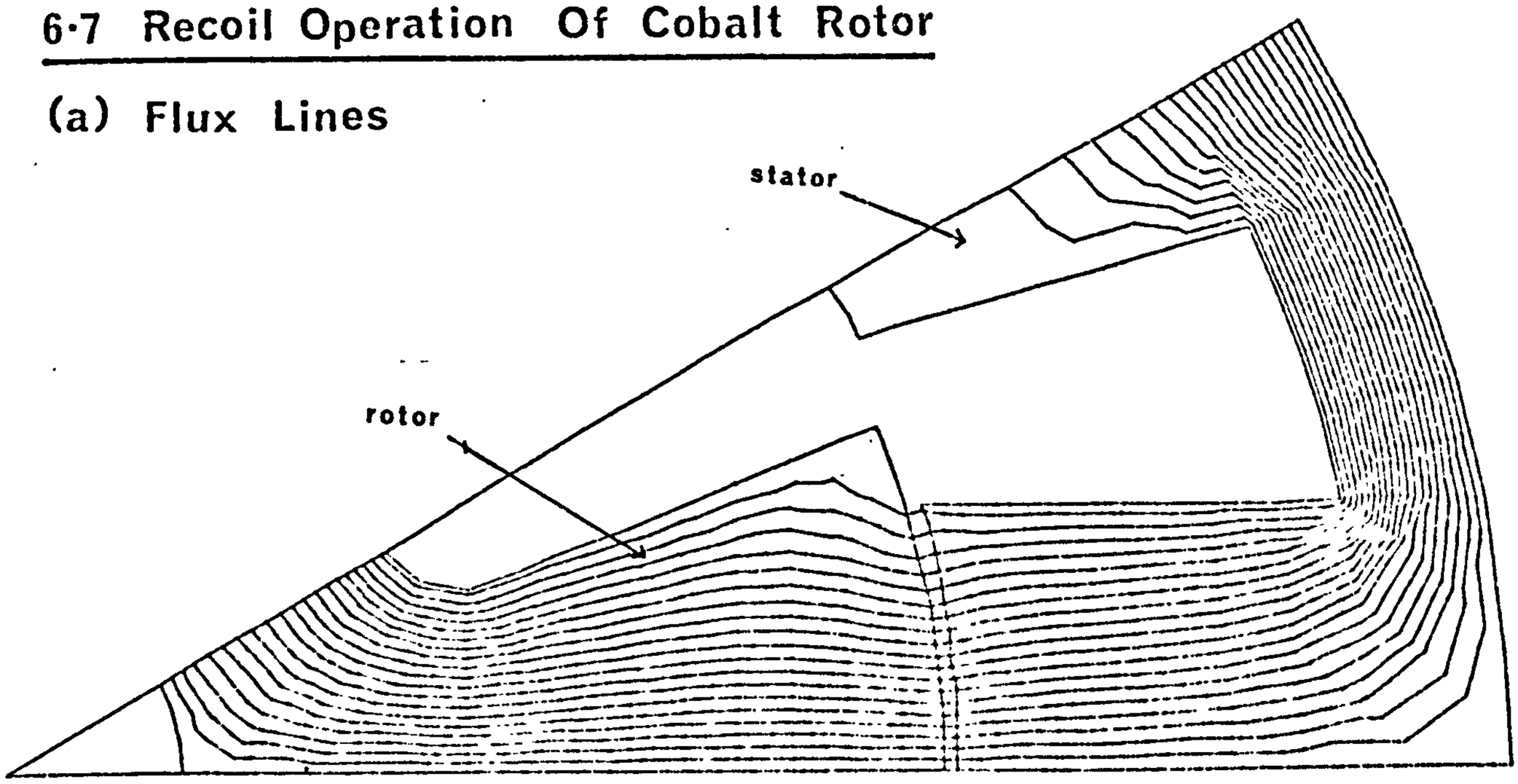

(b) Flux Density Distribution

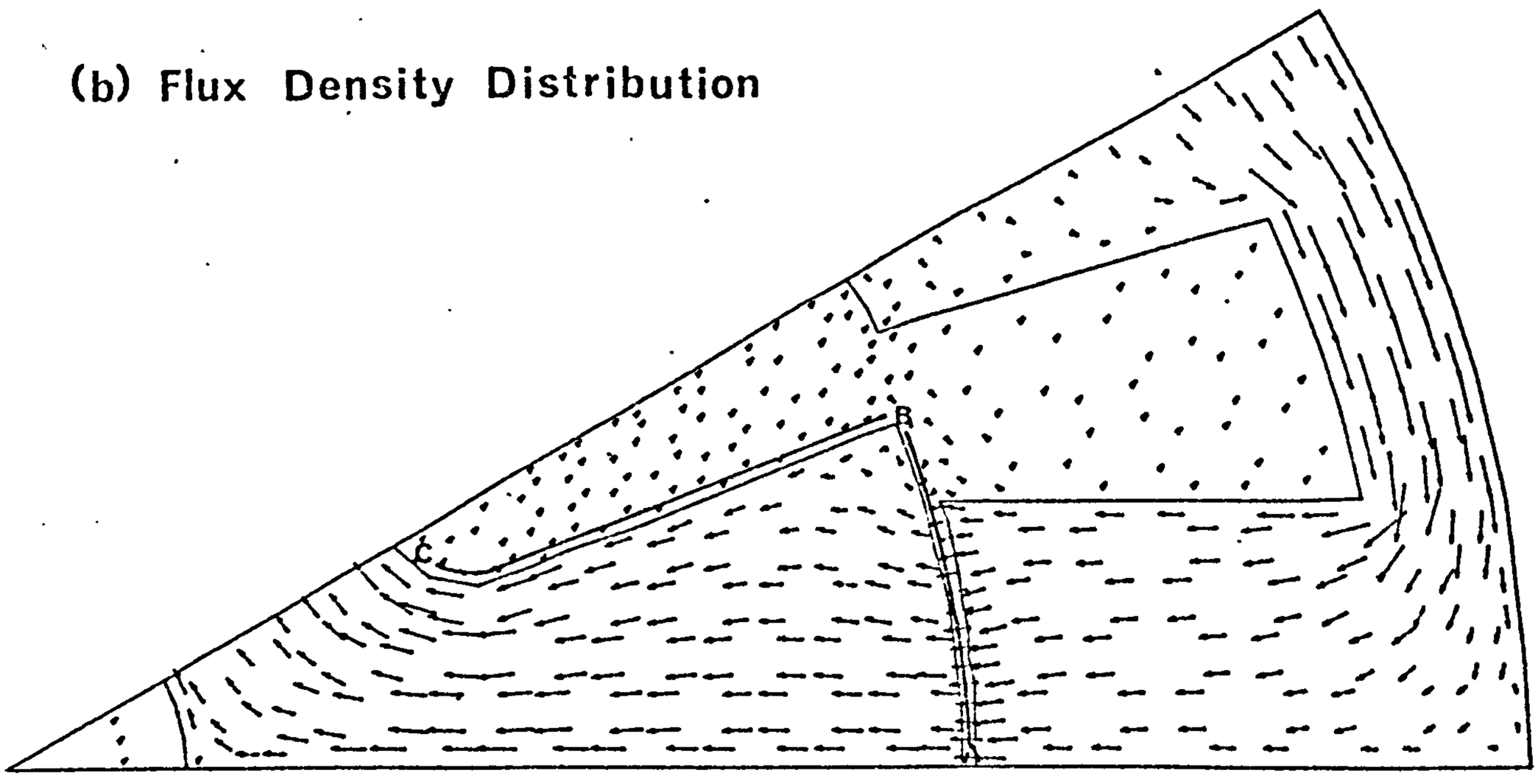

Fig 6·8 .

Inductance Calculation Of Cobalt Rotor

(a) Flux Lines

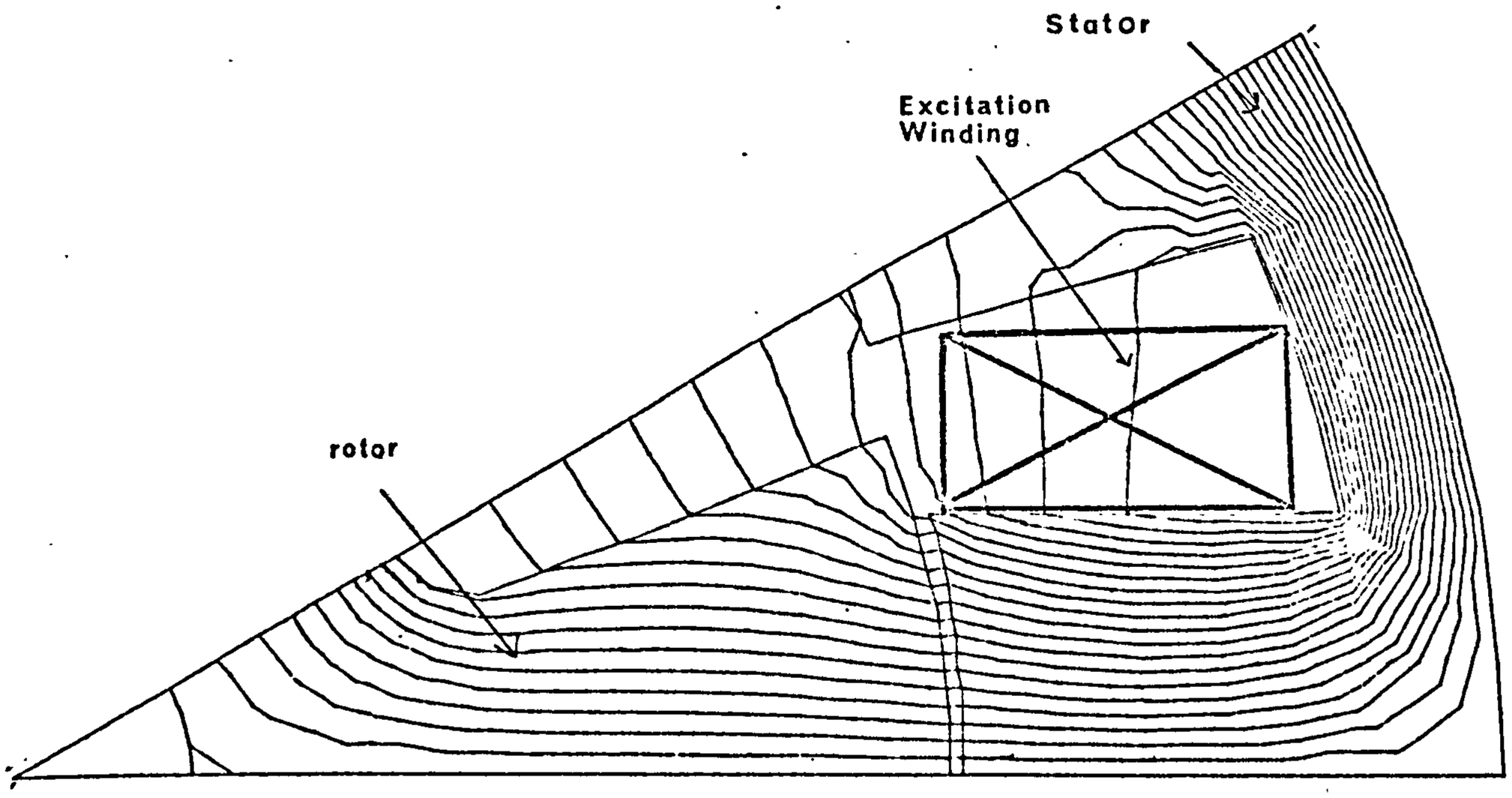

(b) Flux Density Distribution

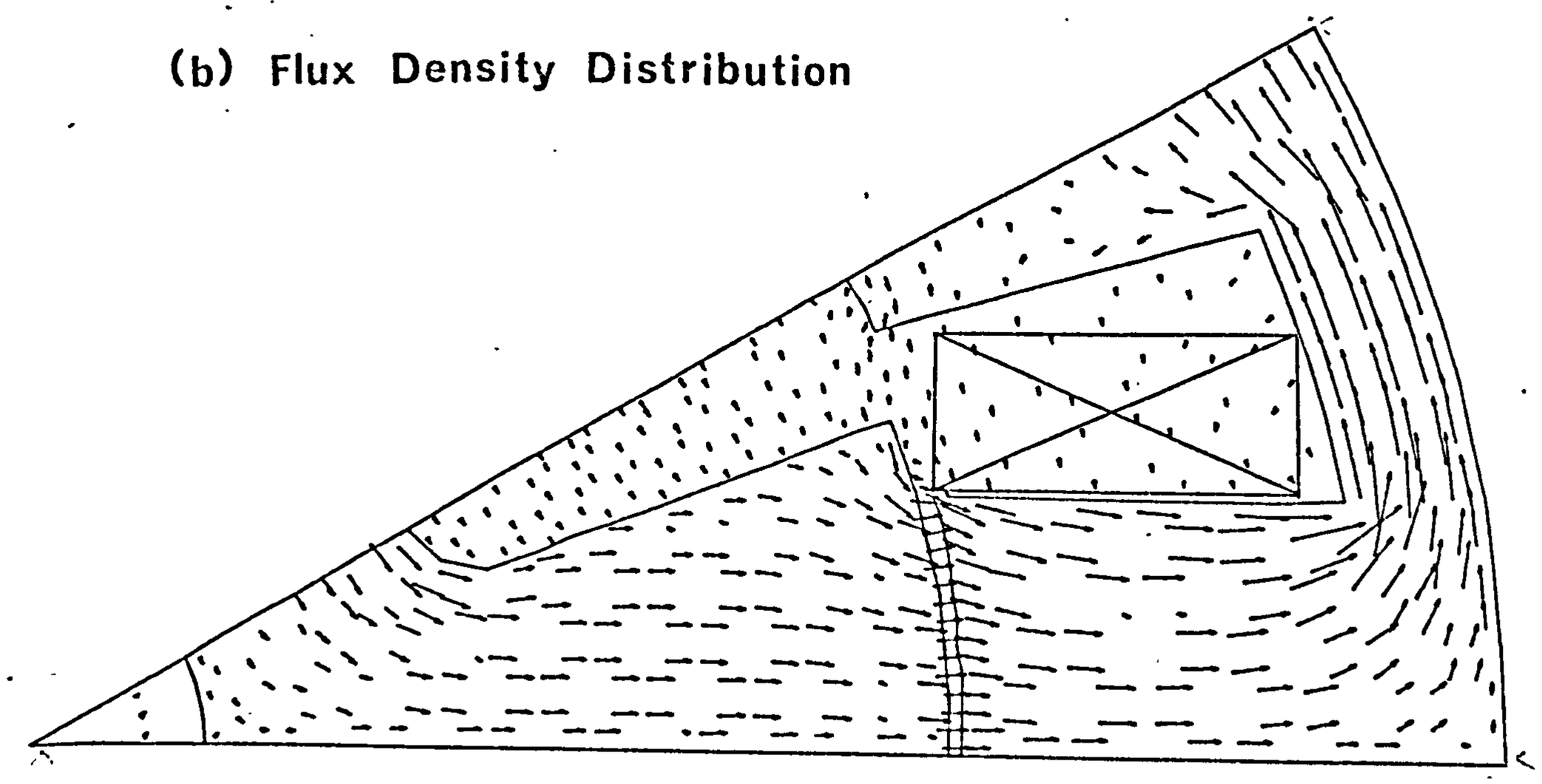

Fig 6·9

Flux Density Distribution When Rotor Poles Are Aligned To Stator Interpoles

(a) Recoil Operation

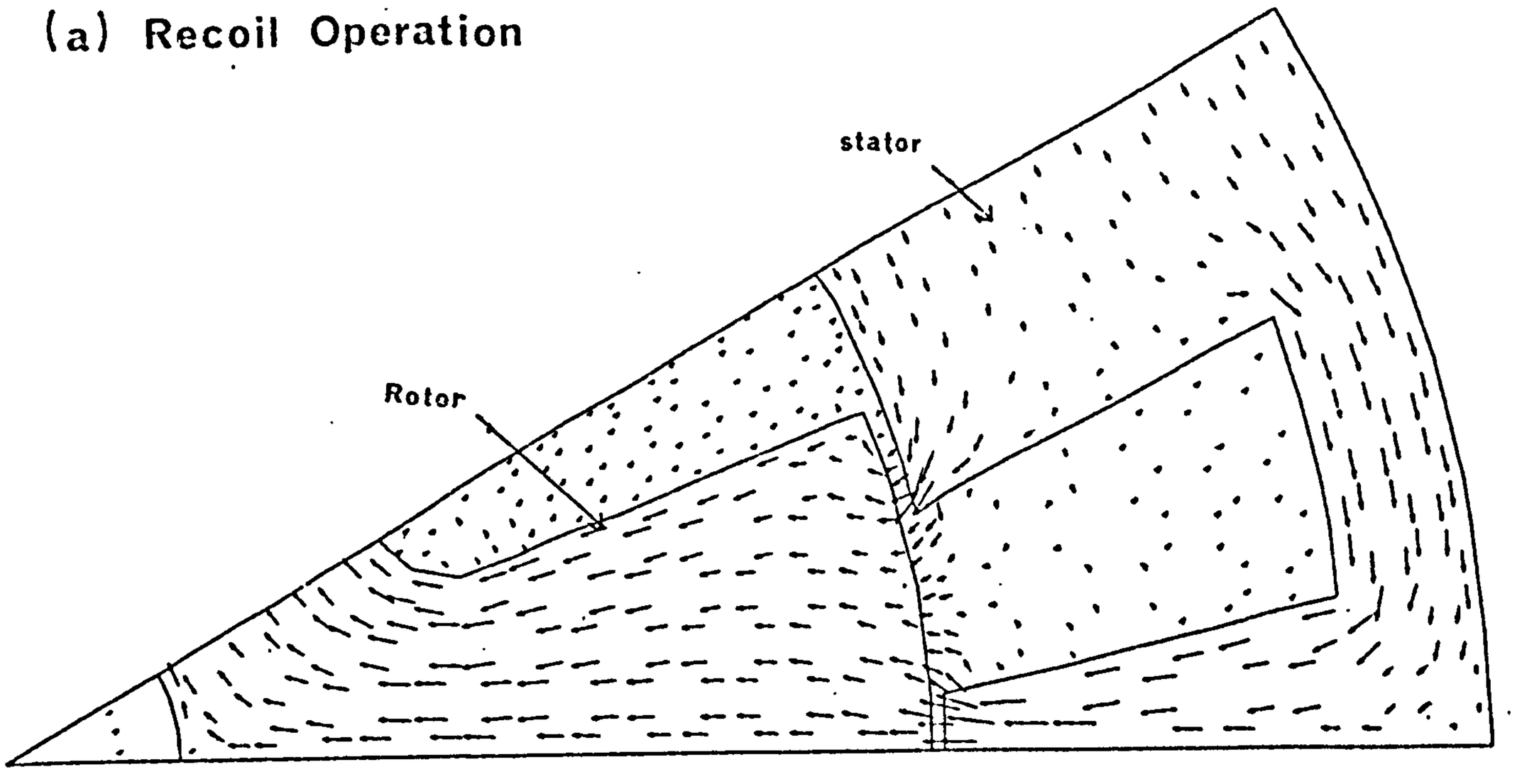

(b) Inductance Calculation

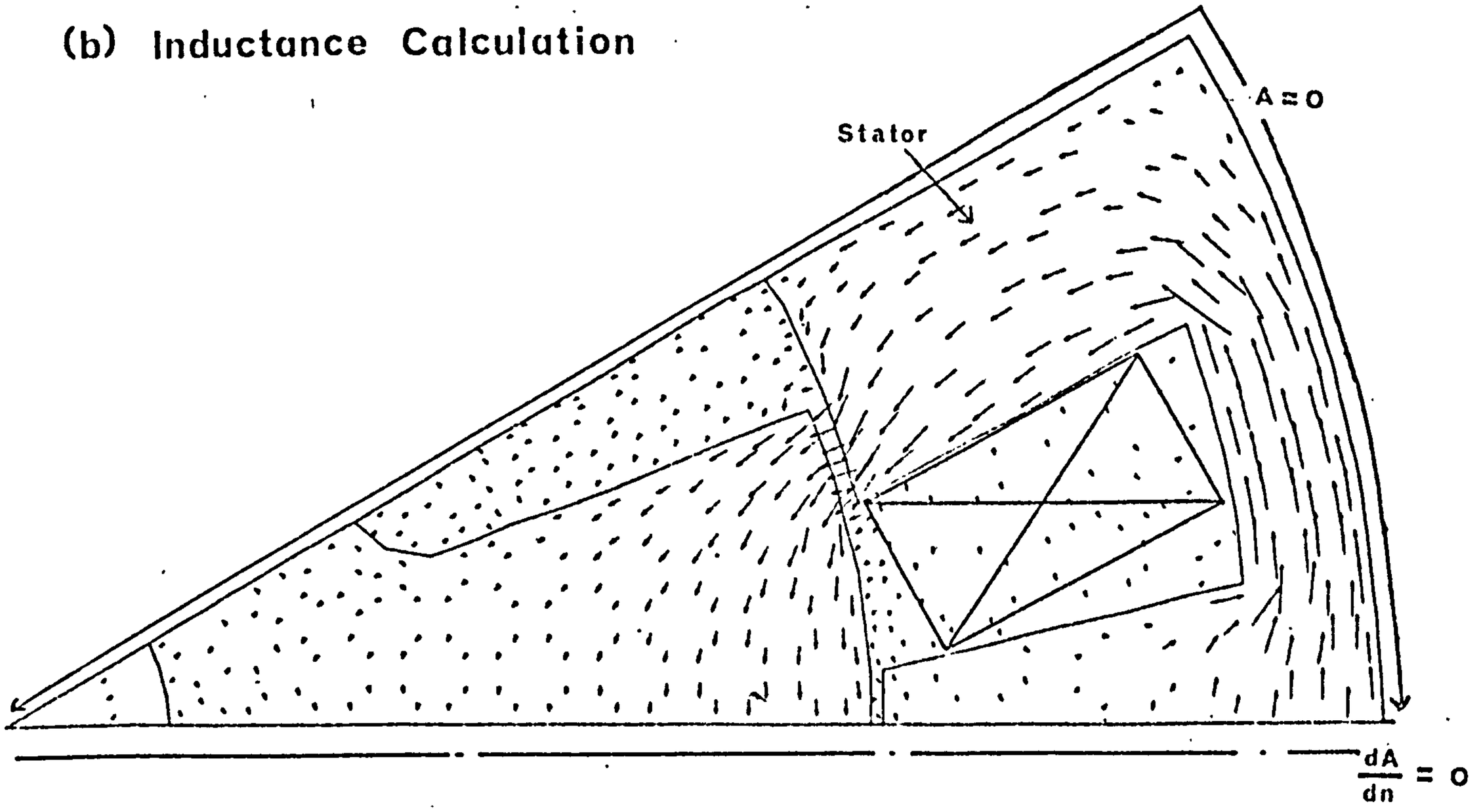

6·10 Parameters Of Cobalt Generator Having Different Airgaps

(a)

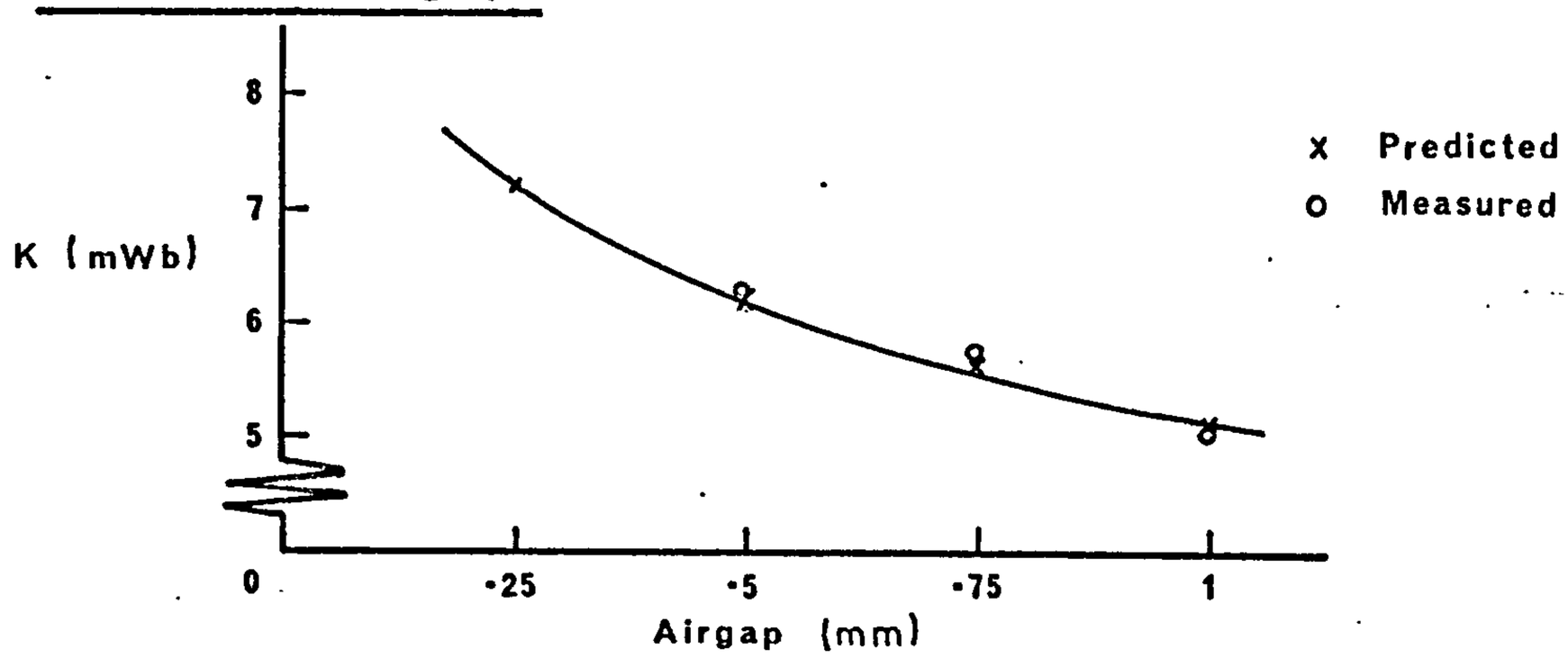

(b)

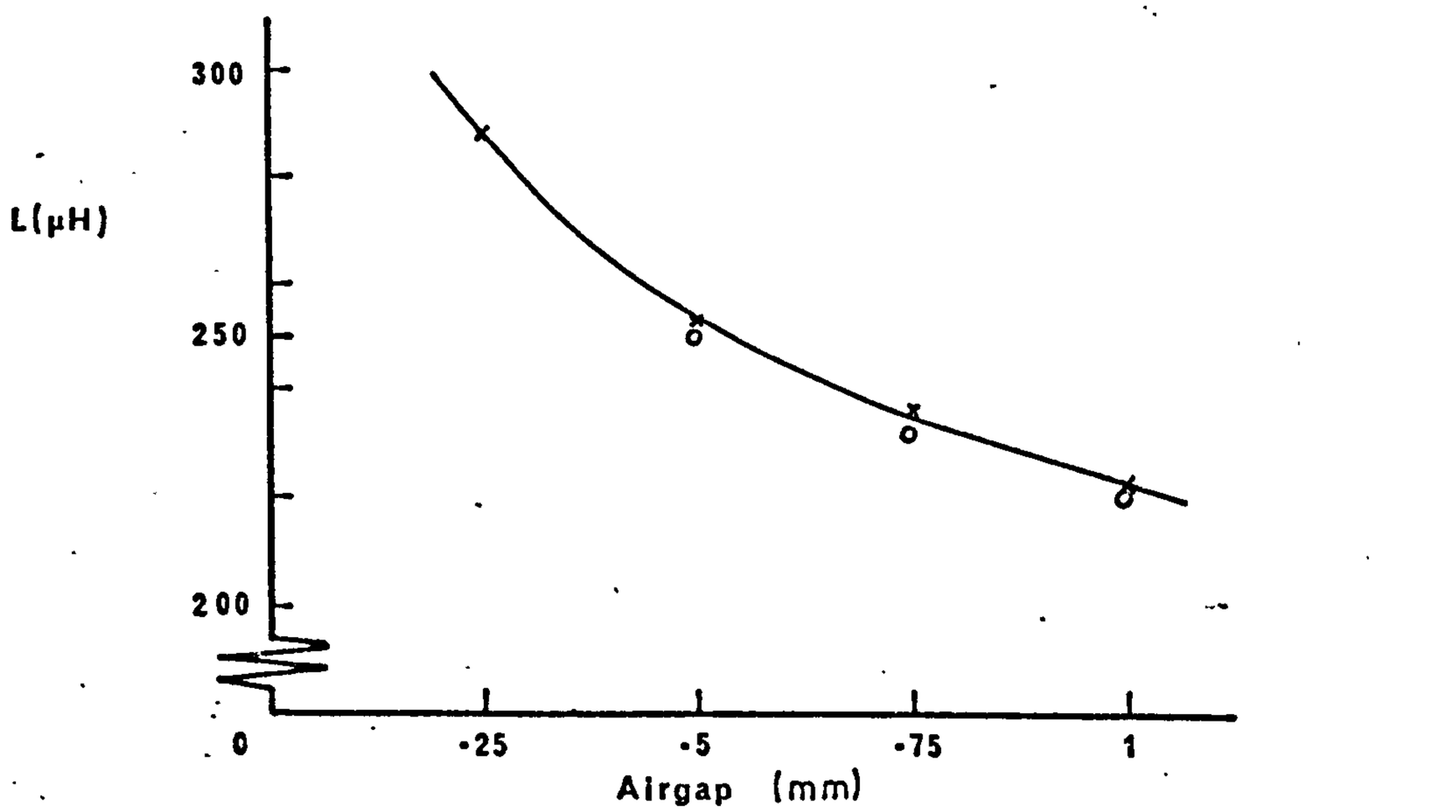

(c)

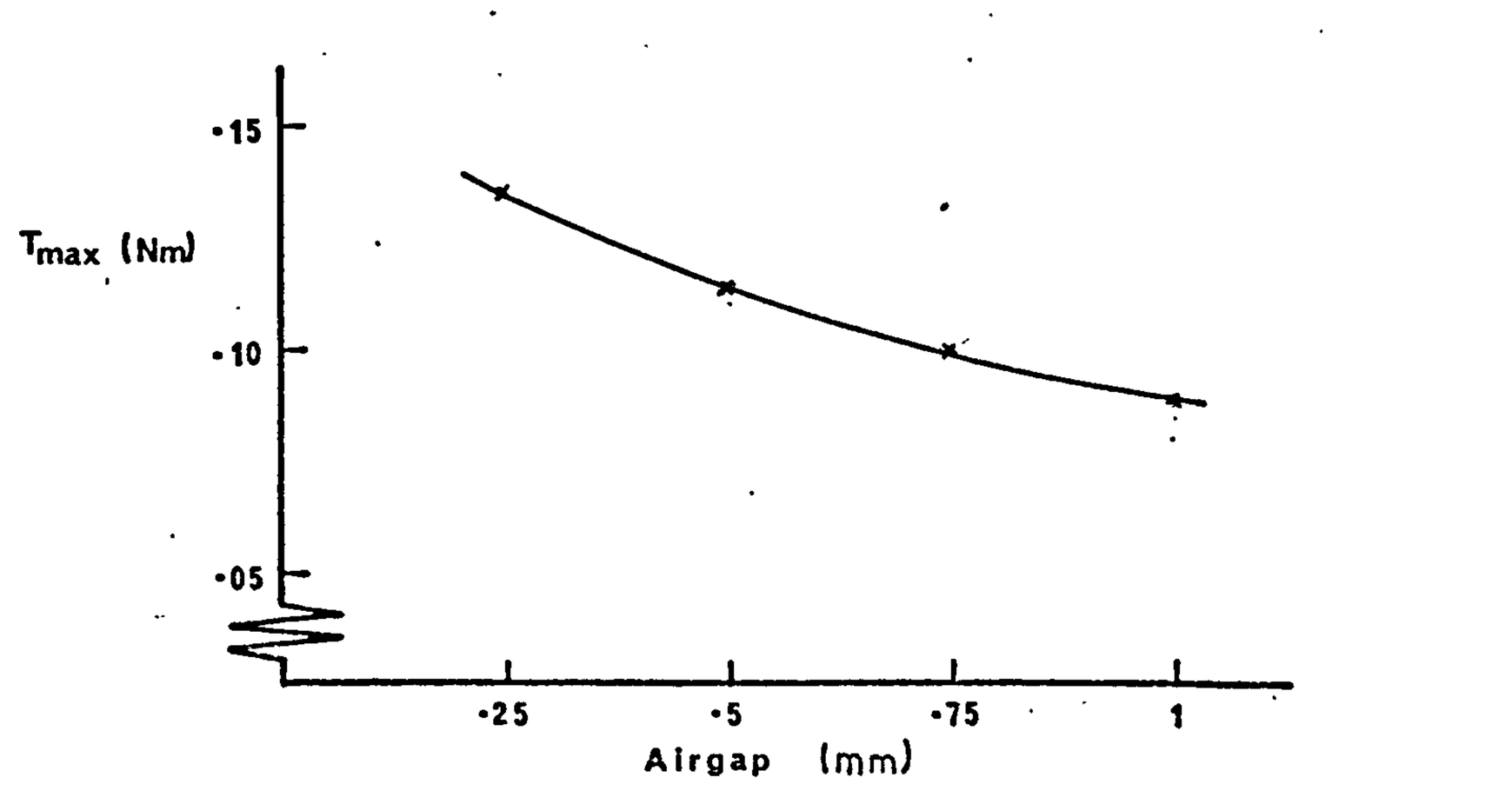

Fig 6·11

Flux Density Distribution Of Alnico (N) Rotor

(a) Air-Stabilisation

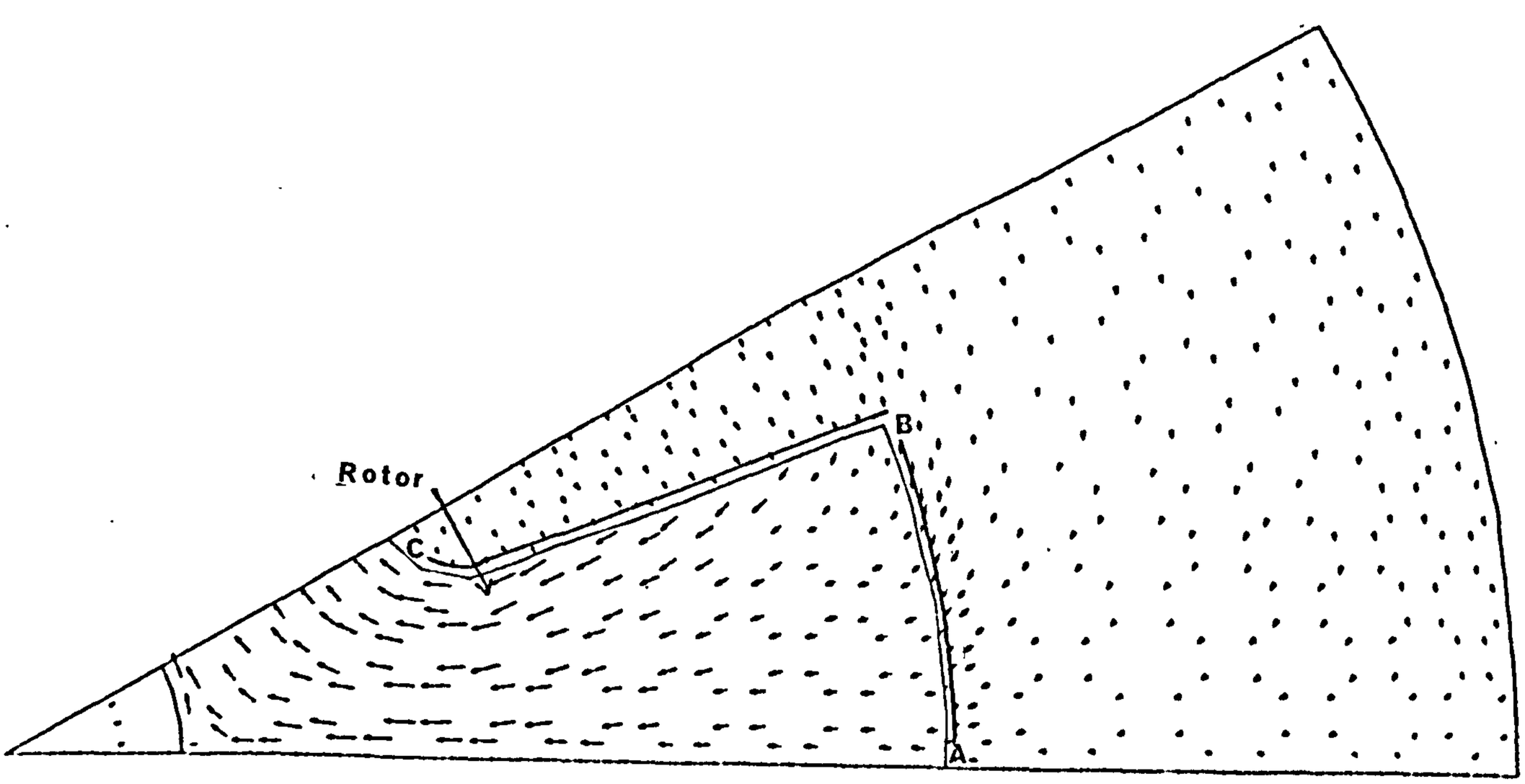

(b) Recoil Operation

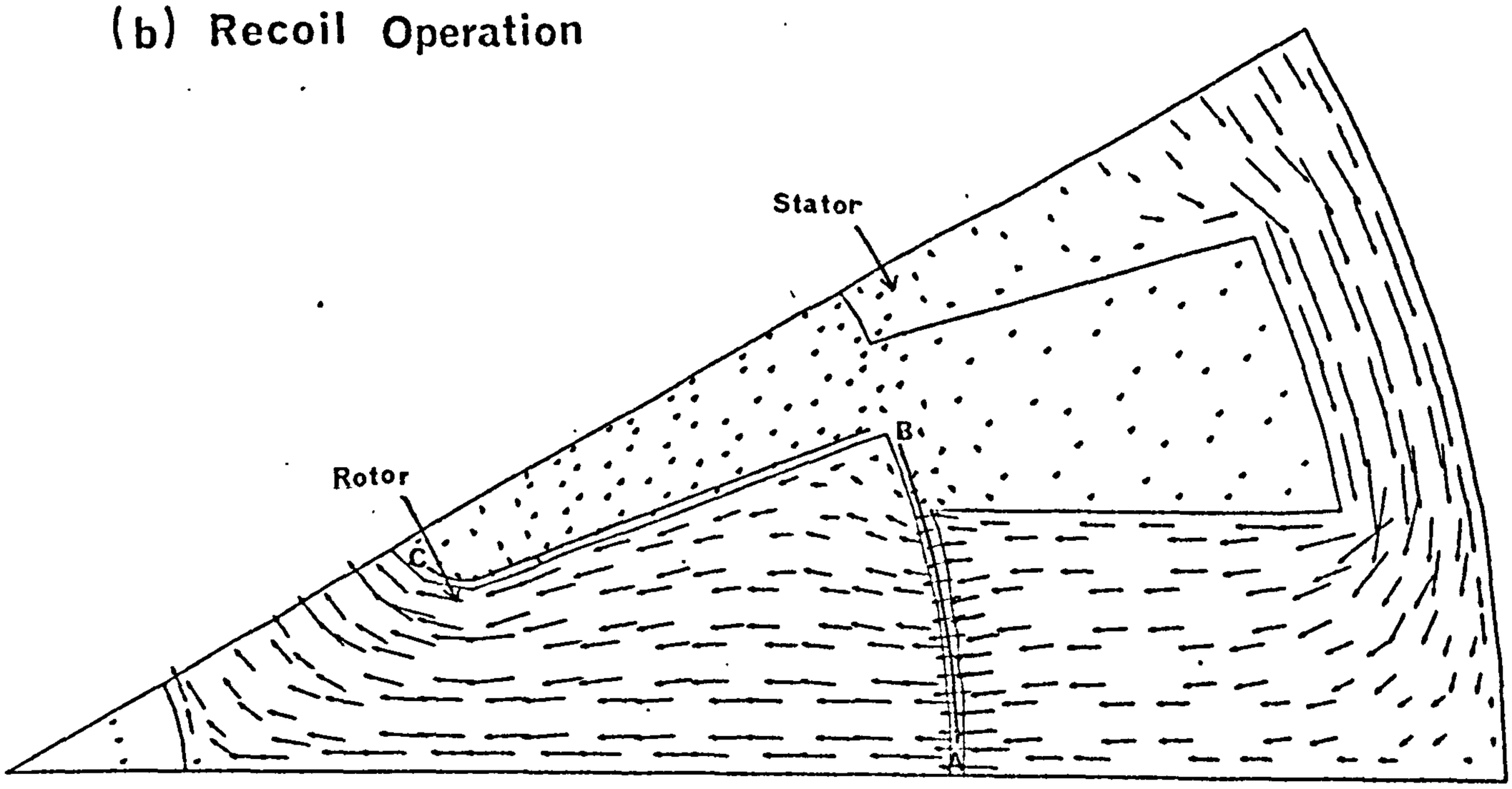

Fig 6·12

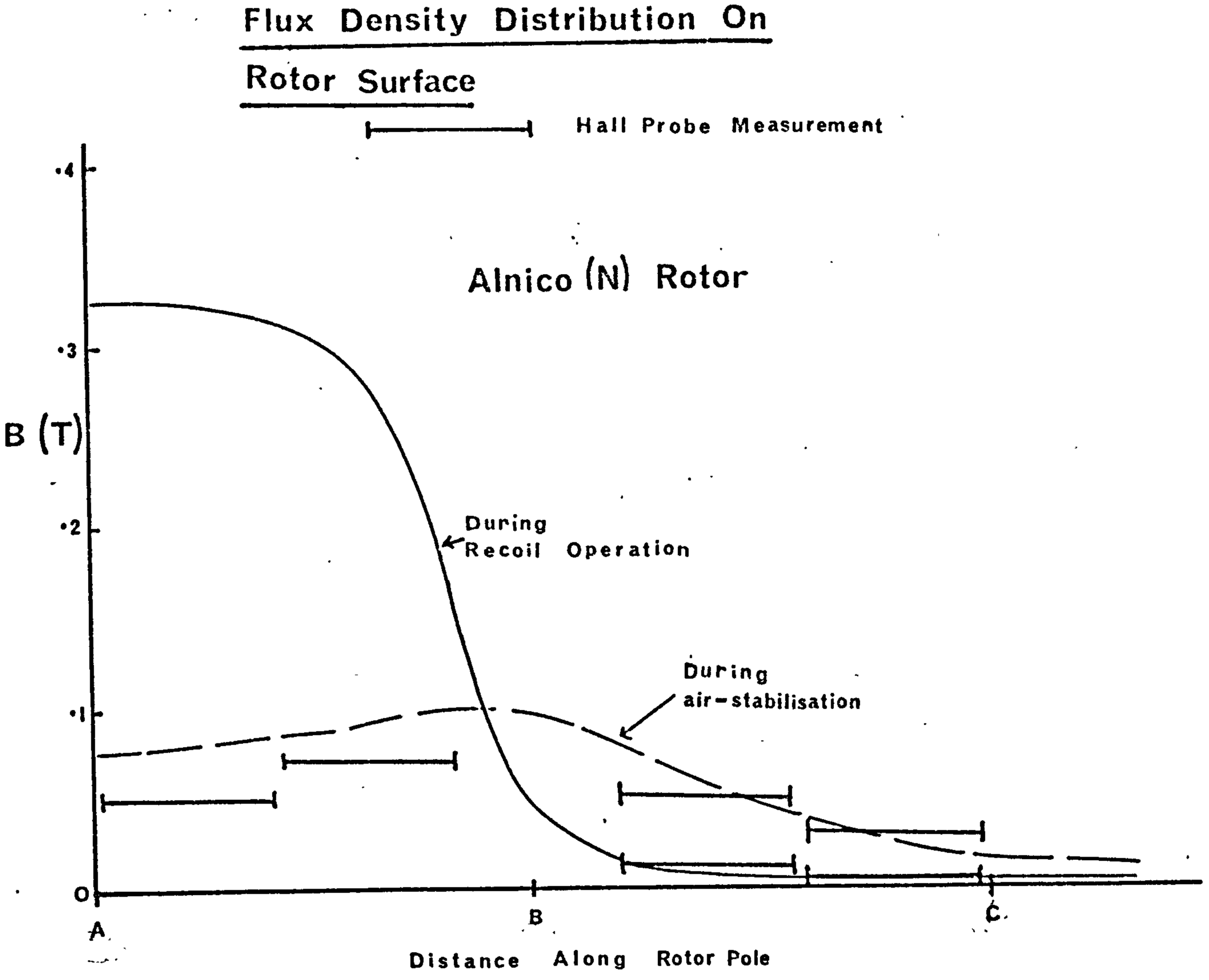
Flux Density Distribution On
Rotor Surface
Hall Probe Measurement
Alnico (N) Rotor
B (T)
·4
·3
·2
·1
0
During
Recoil Operation
During
air-stabilisation
A
B
C
Distance Along Rotor Pole

Fig 6·13

Flux Density Distribution Of Alnico (H.Br) Rotor

(a) Air - Stabilisation

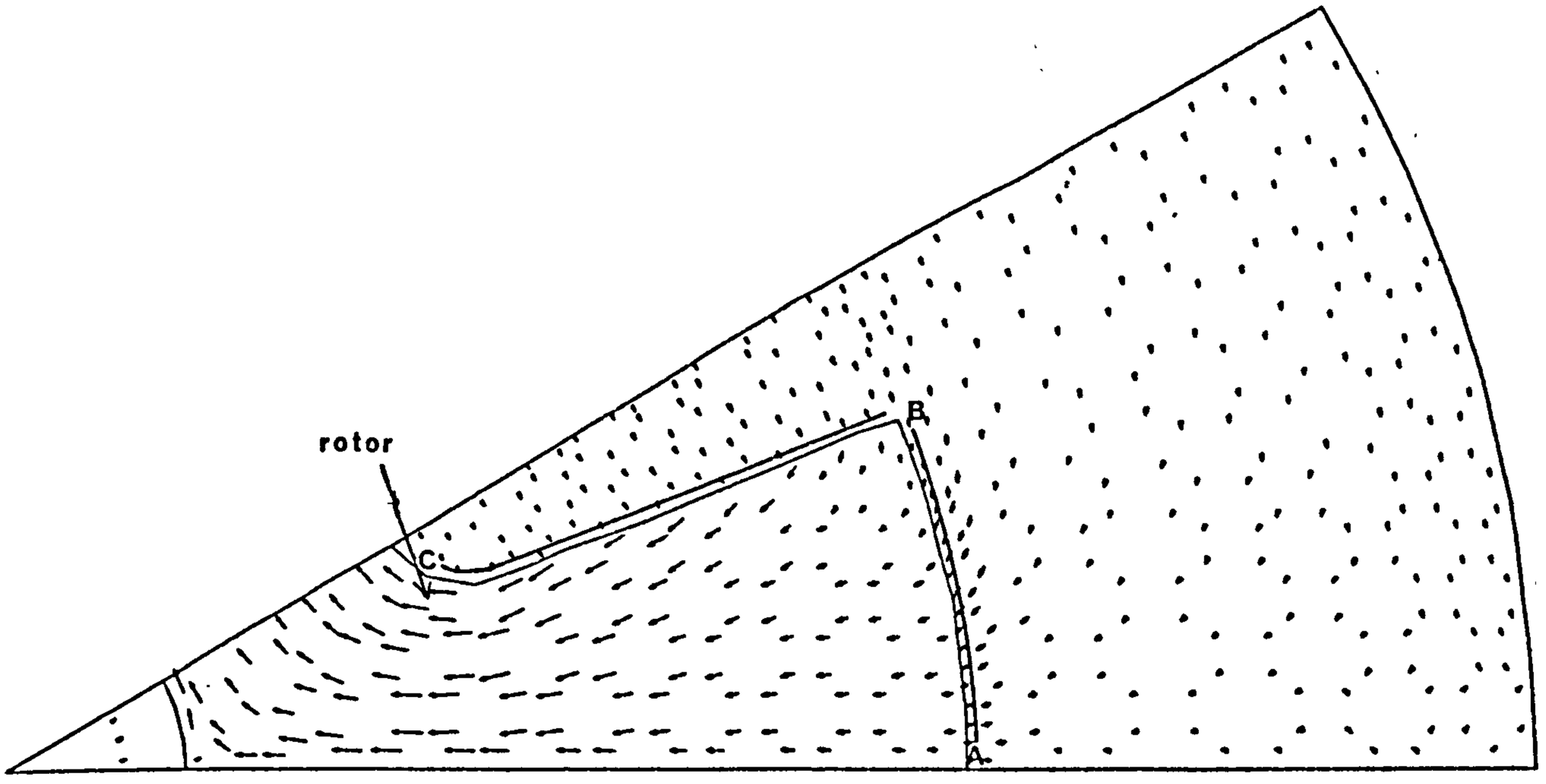

(b) Recoil Operation

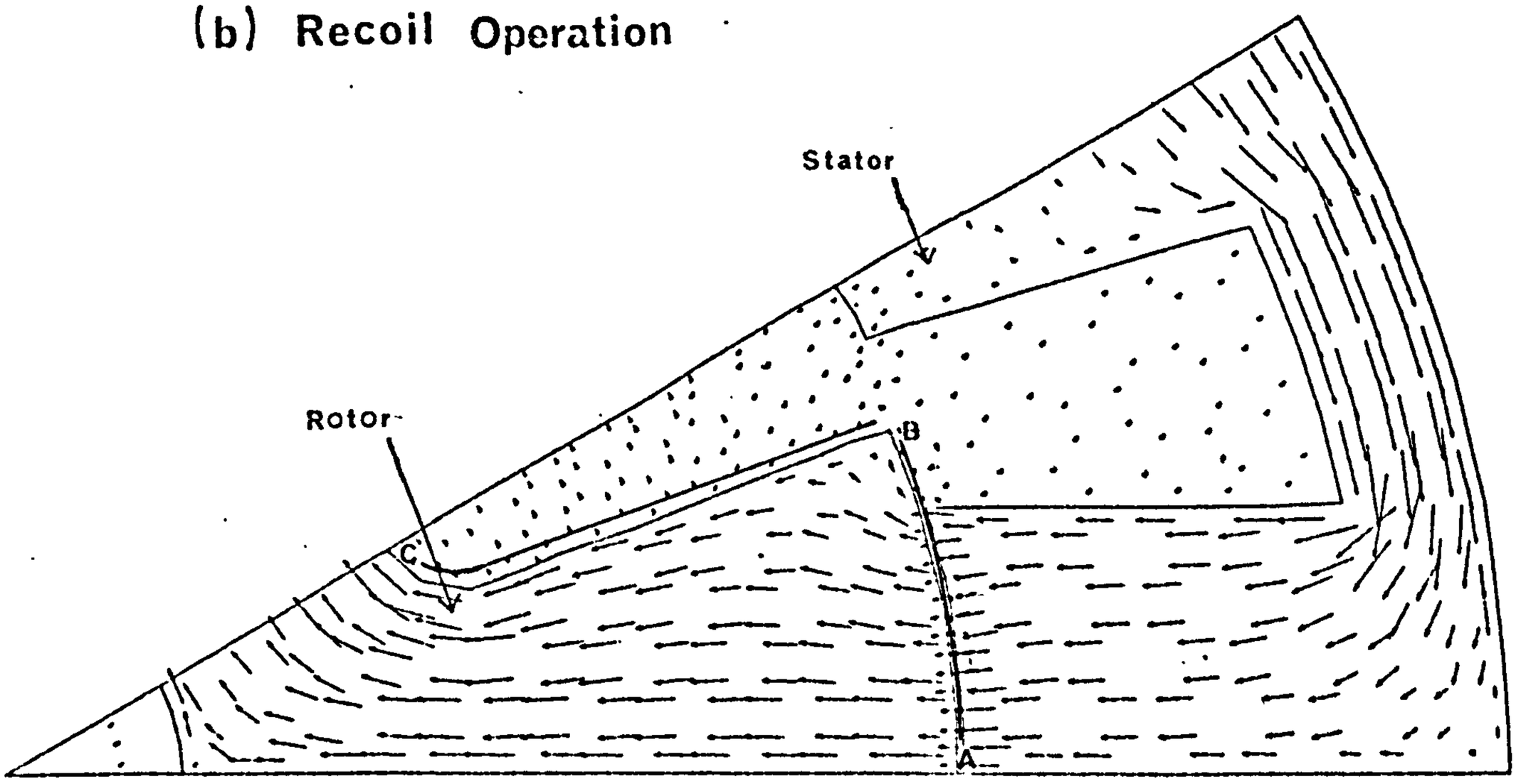

Fig 6·14

Flux Density Distribution On Rotor Surface

Hall Probe Measurement

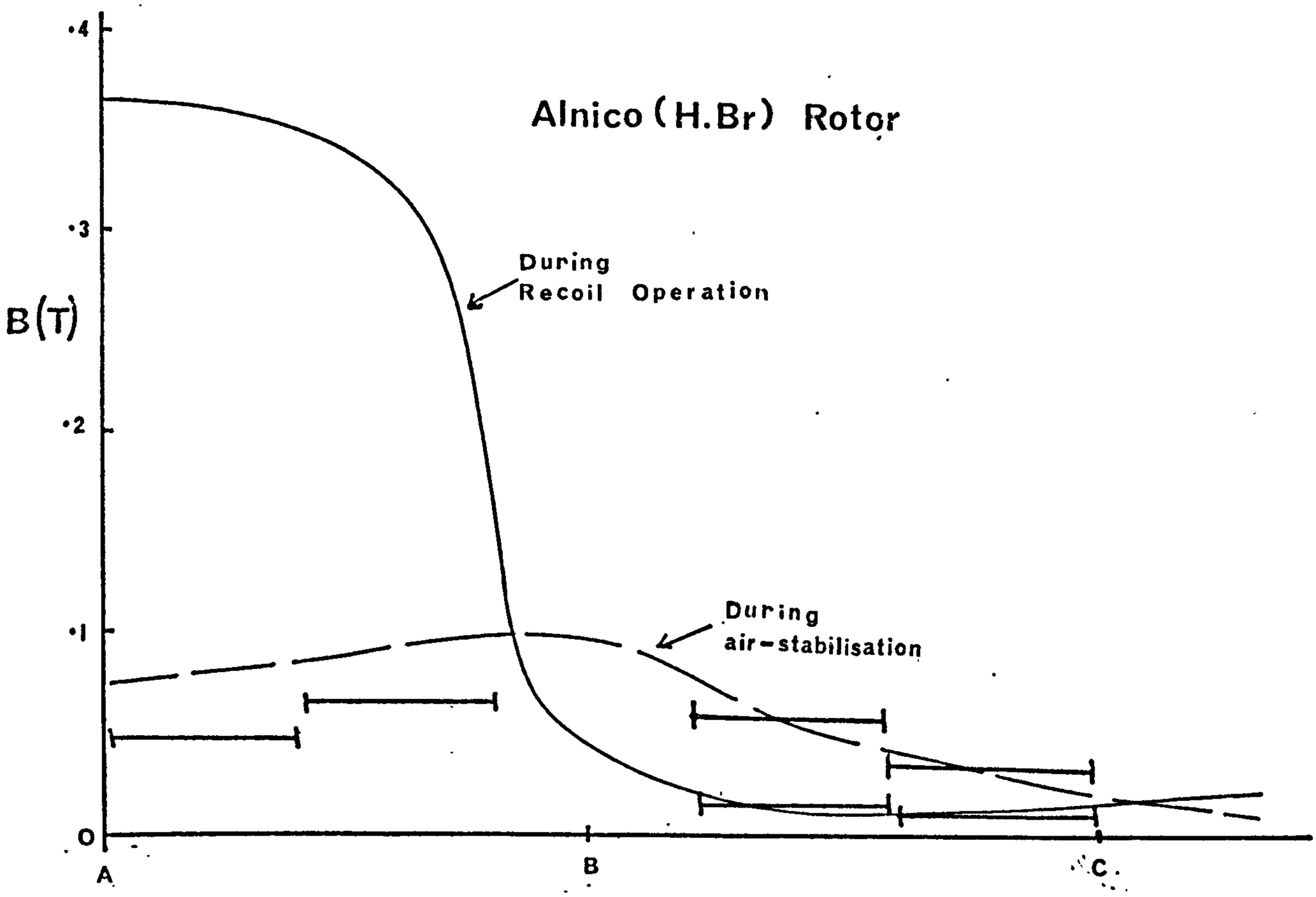

Fig 6·15(a)
Fig 6 15(b)

Flux Density Distribution Of Alcomax IV Rotor

(a) Magnetisation

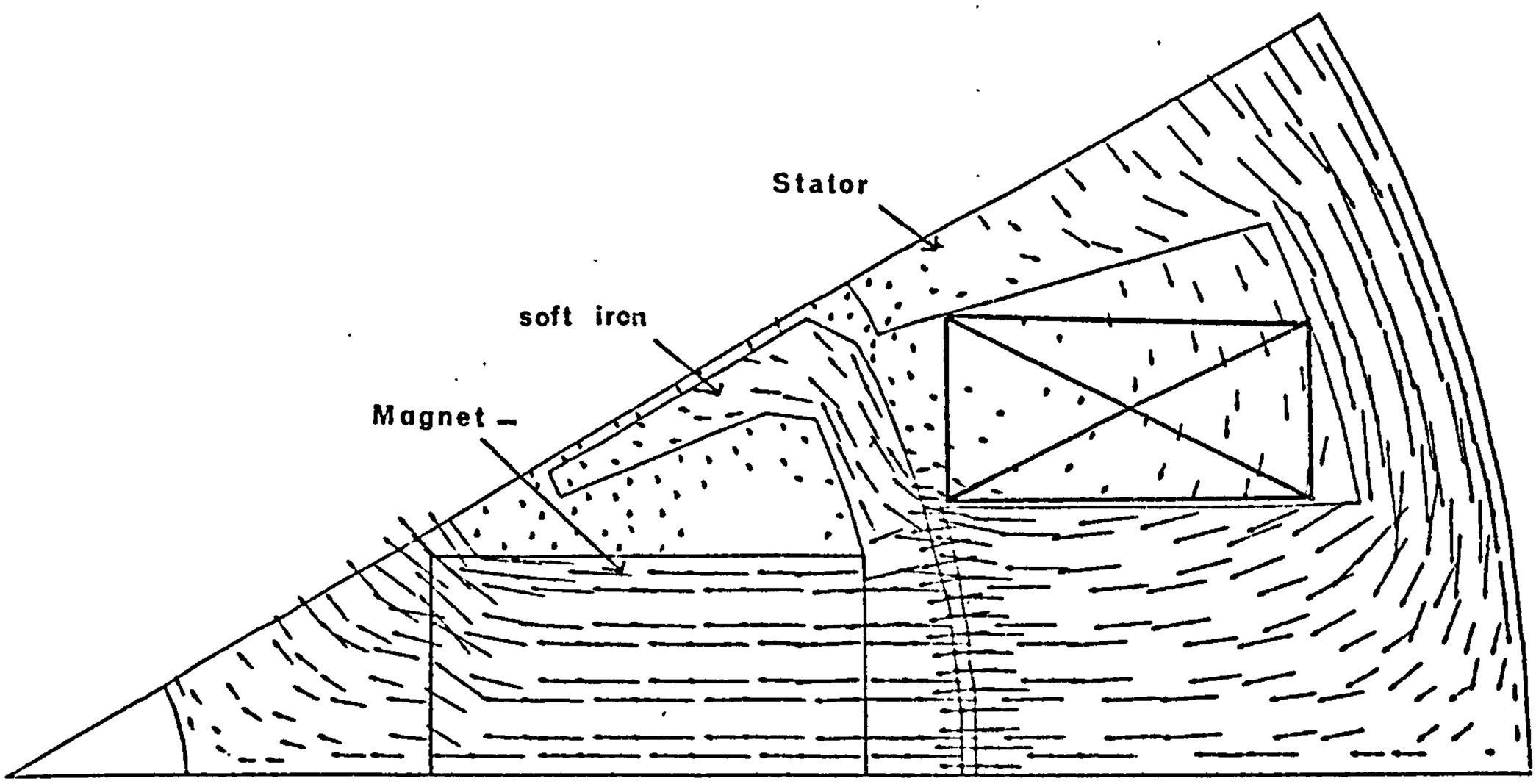

(b) Air-Stabilisation

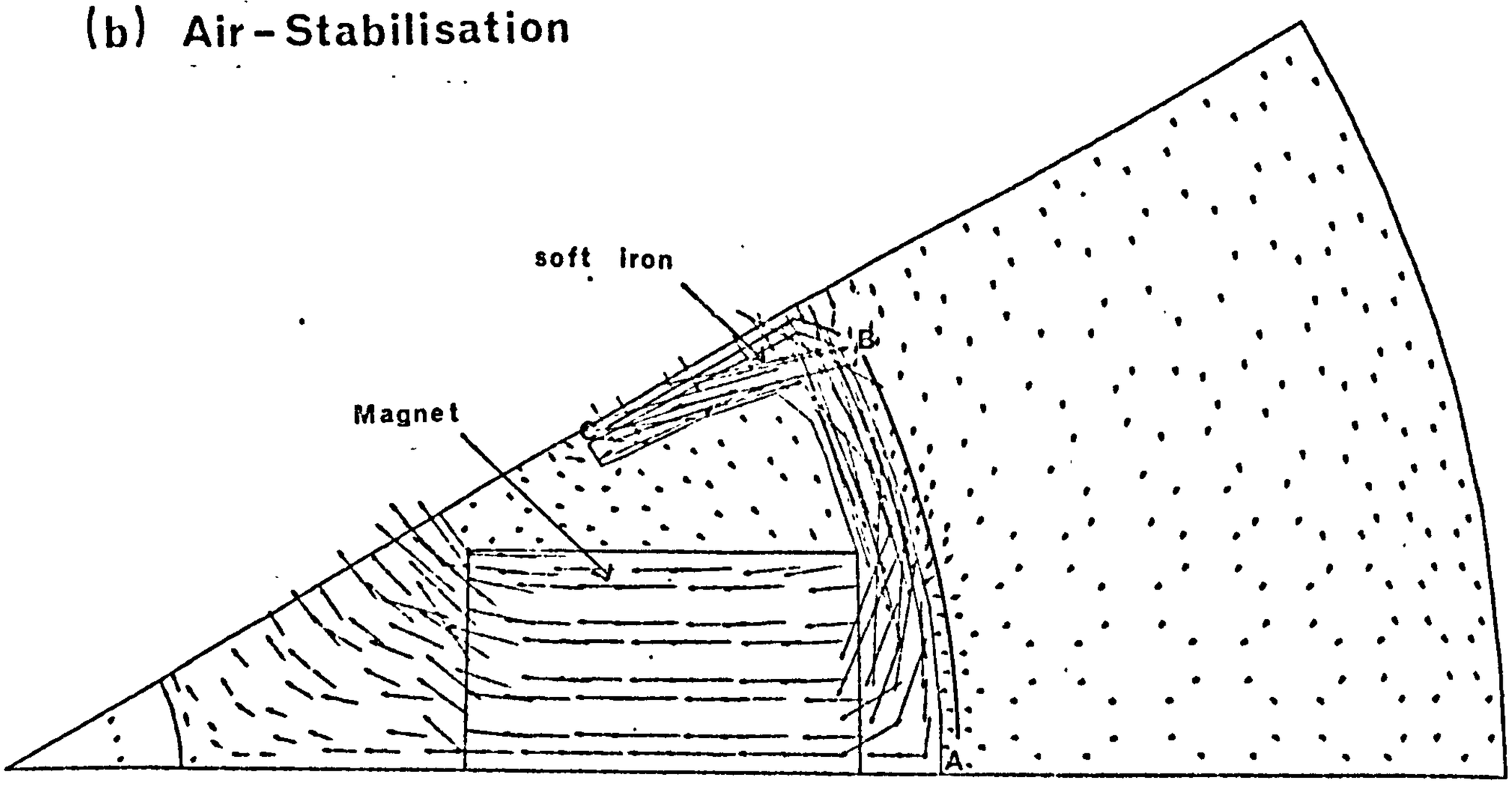

Fig 6·15(c)
Fig 6·15(d

Flux Density Distribution Of Alcomax IV Rotor

(c) Recoil Operation

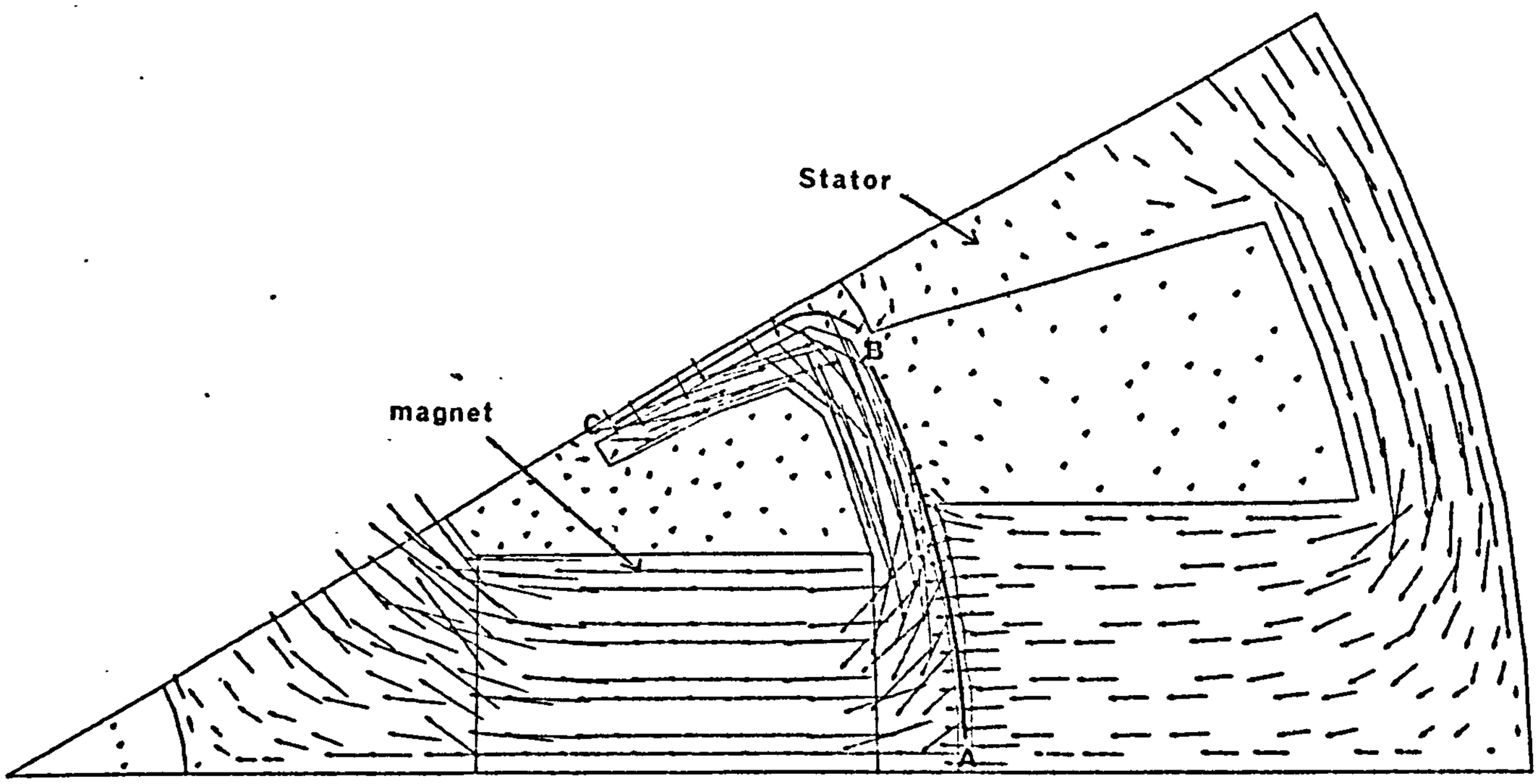

(d) Inductance Calculation

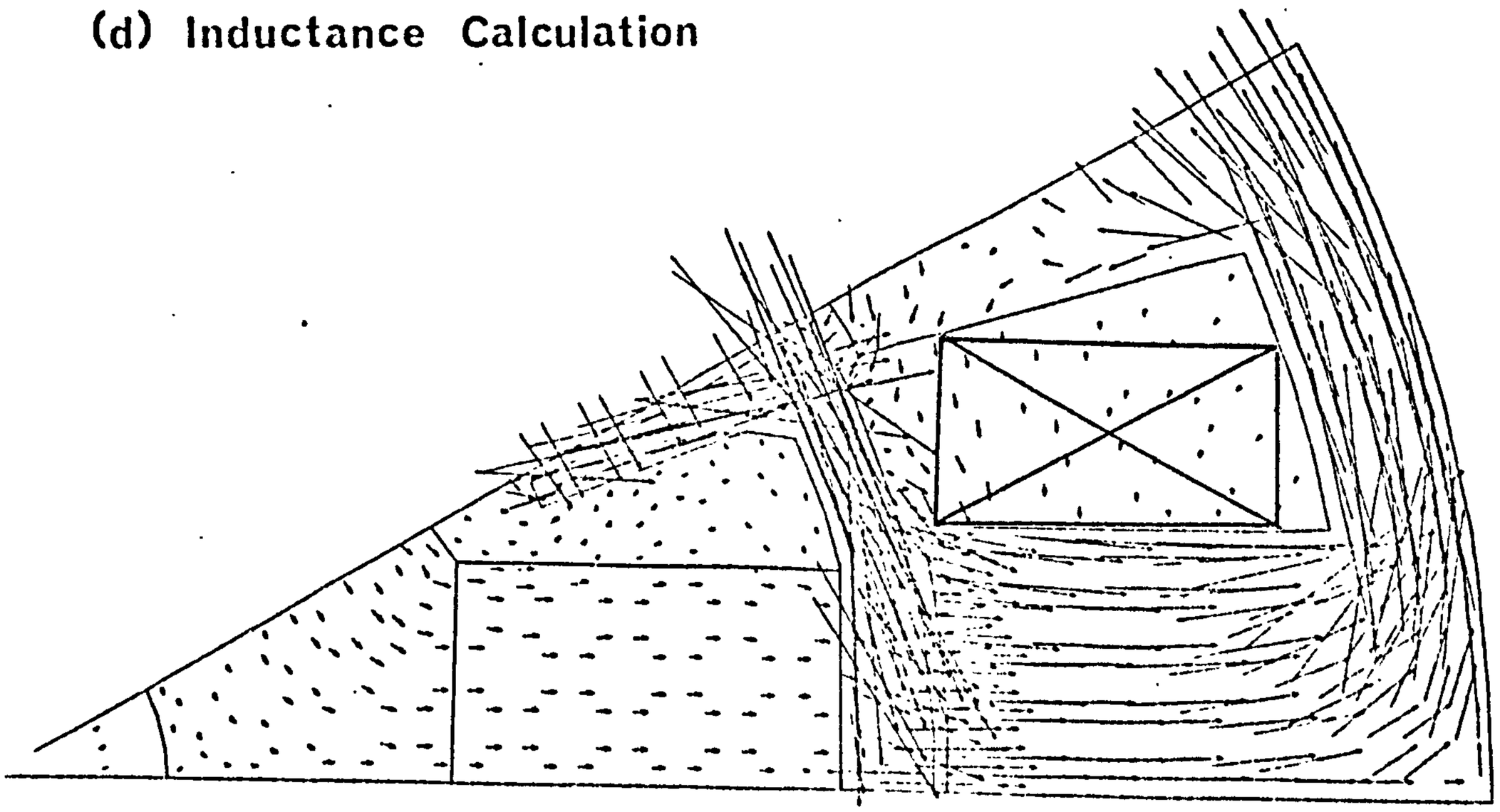

Fig 6·16

Flux Density Distribution On Rotor Surface

Hall Probe Measurement

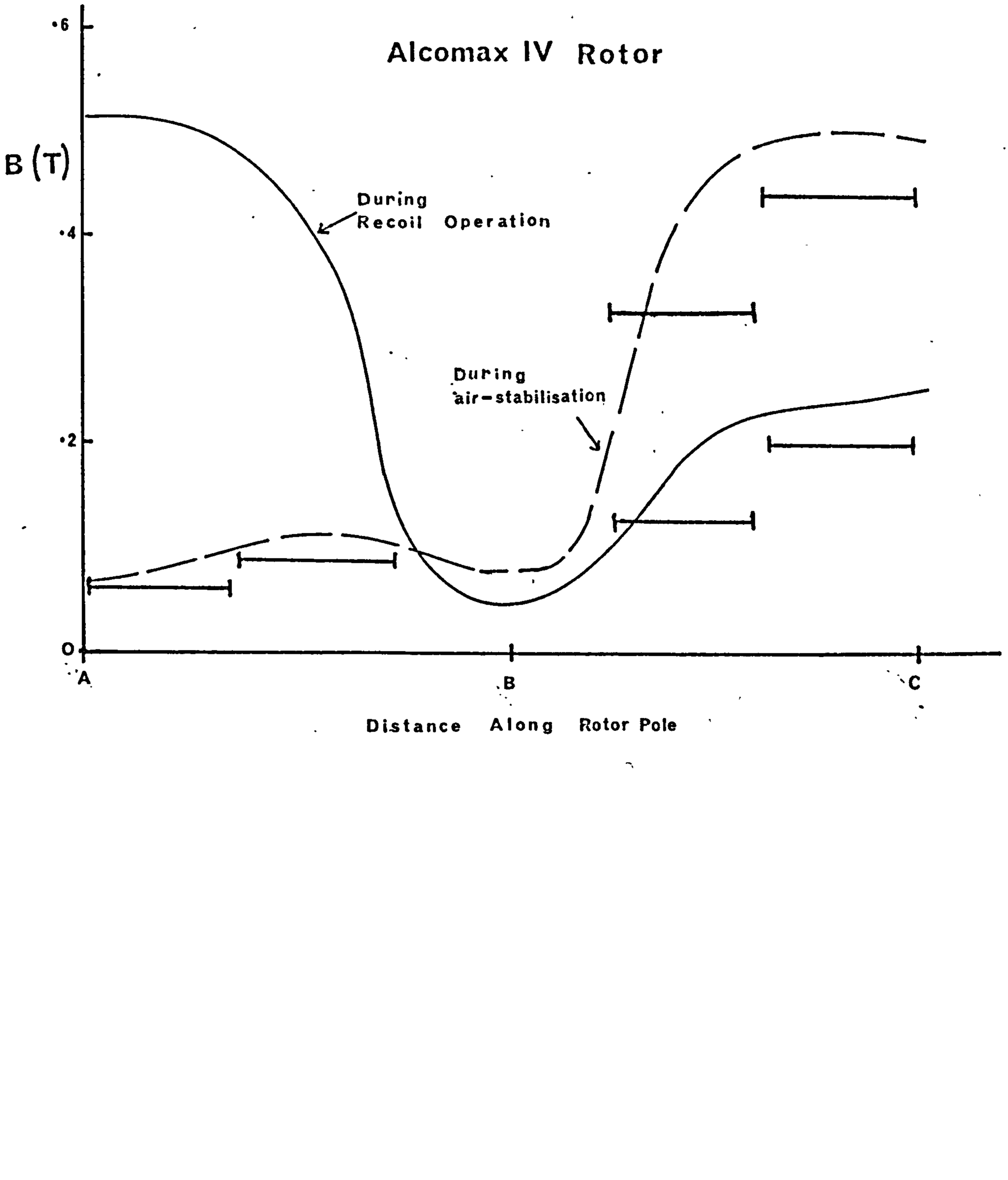

Flux Density Distribution Of Alcomax IV

Rotor Having Modified Pole Shoe

(a) Air - Stabilisation

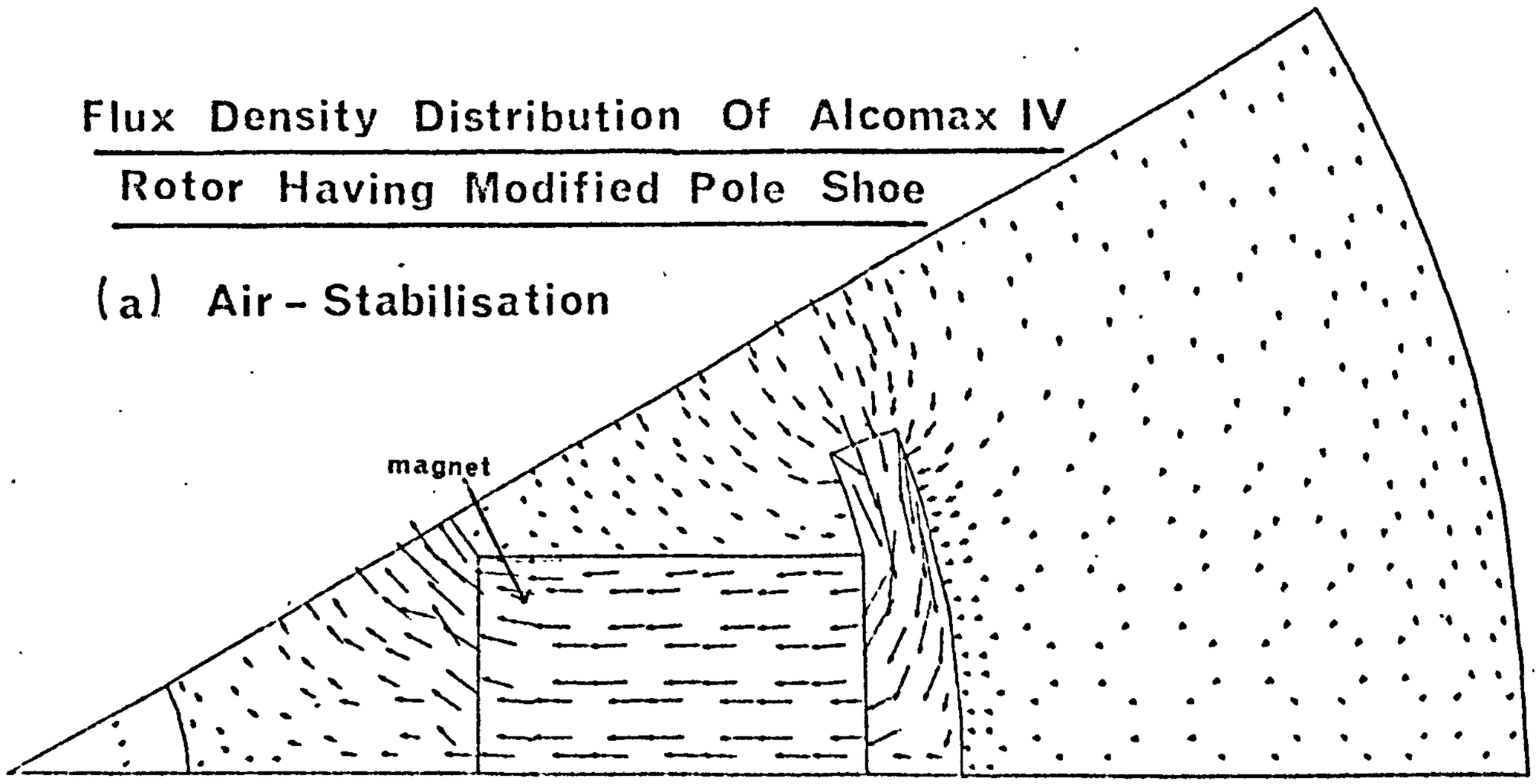

(b) Recoil Operation

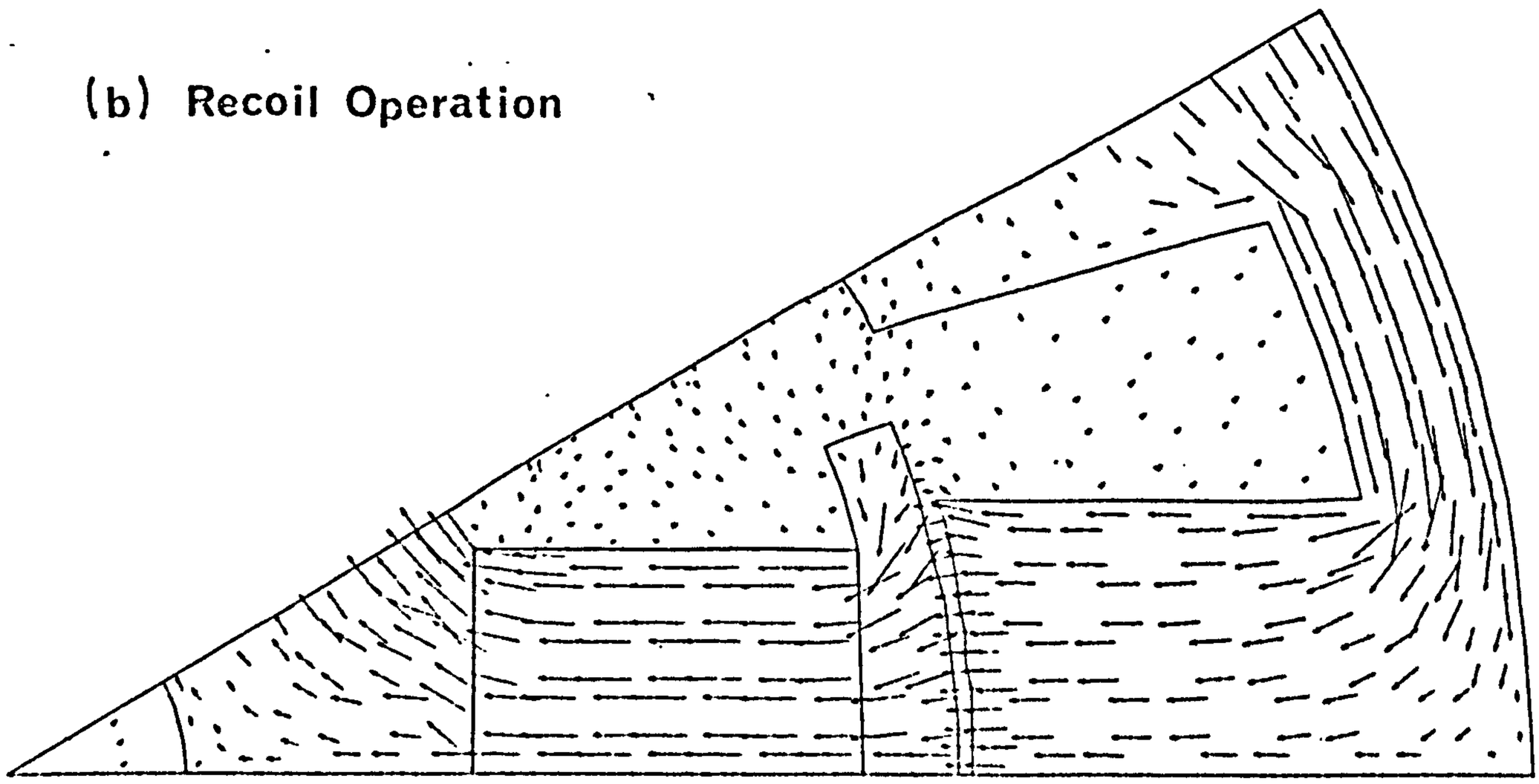

(c) Inductance Calculation

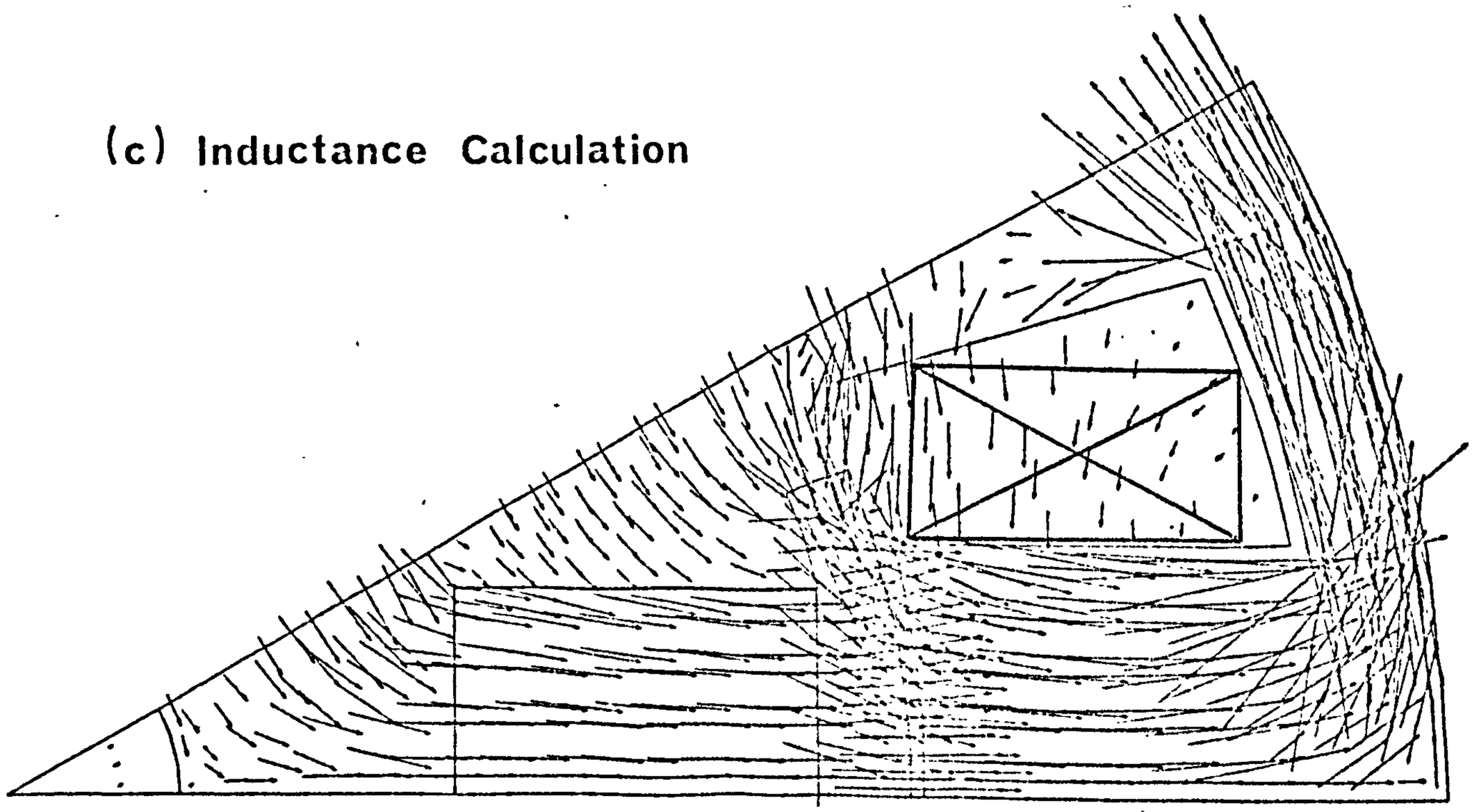

Fig 6·18

Flux Density Distribution Of Alcomax IV Rotor Having Tangentially Magnetised Magnets

(a) Magnetisation

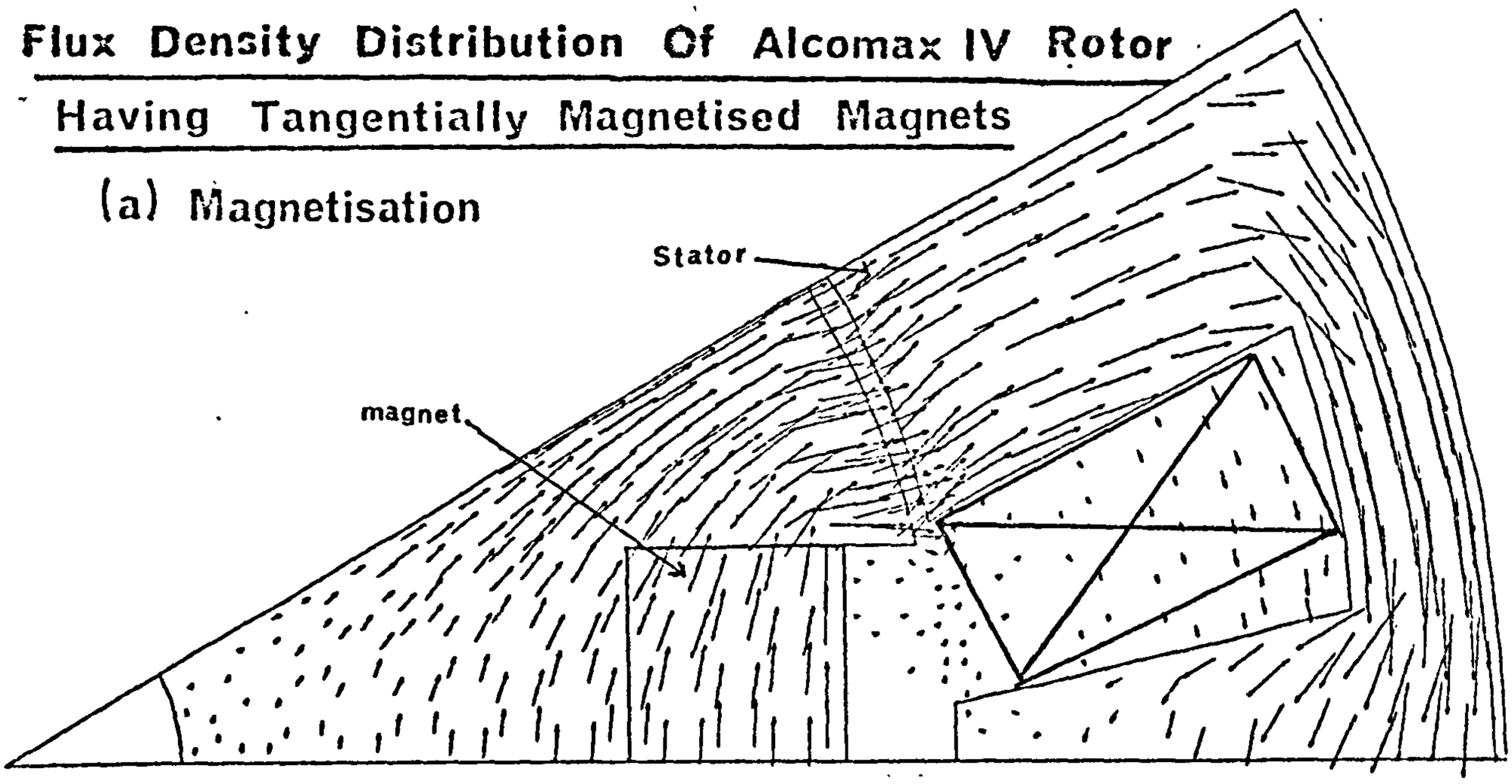

(b) Air-Stabilisation

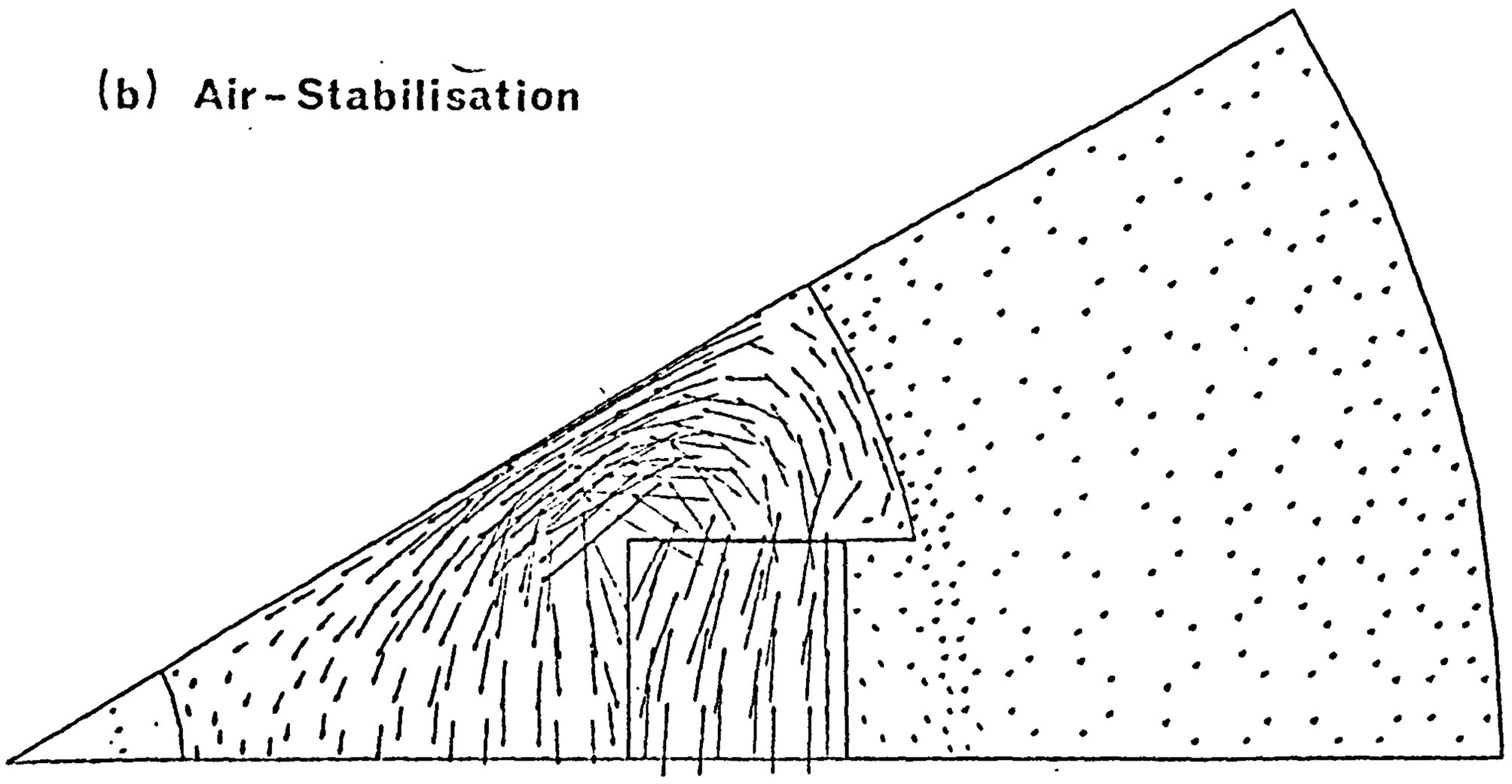

(c) Recoil Operation

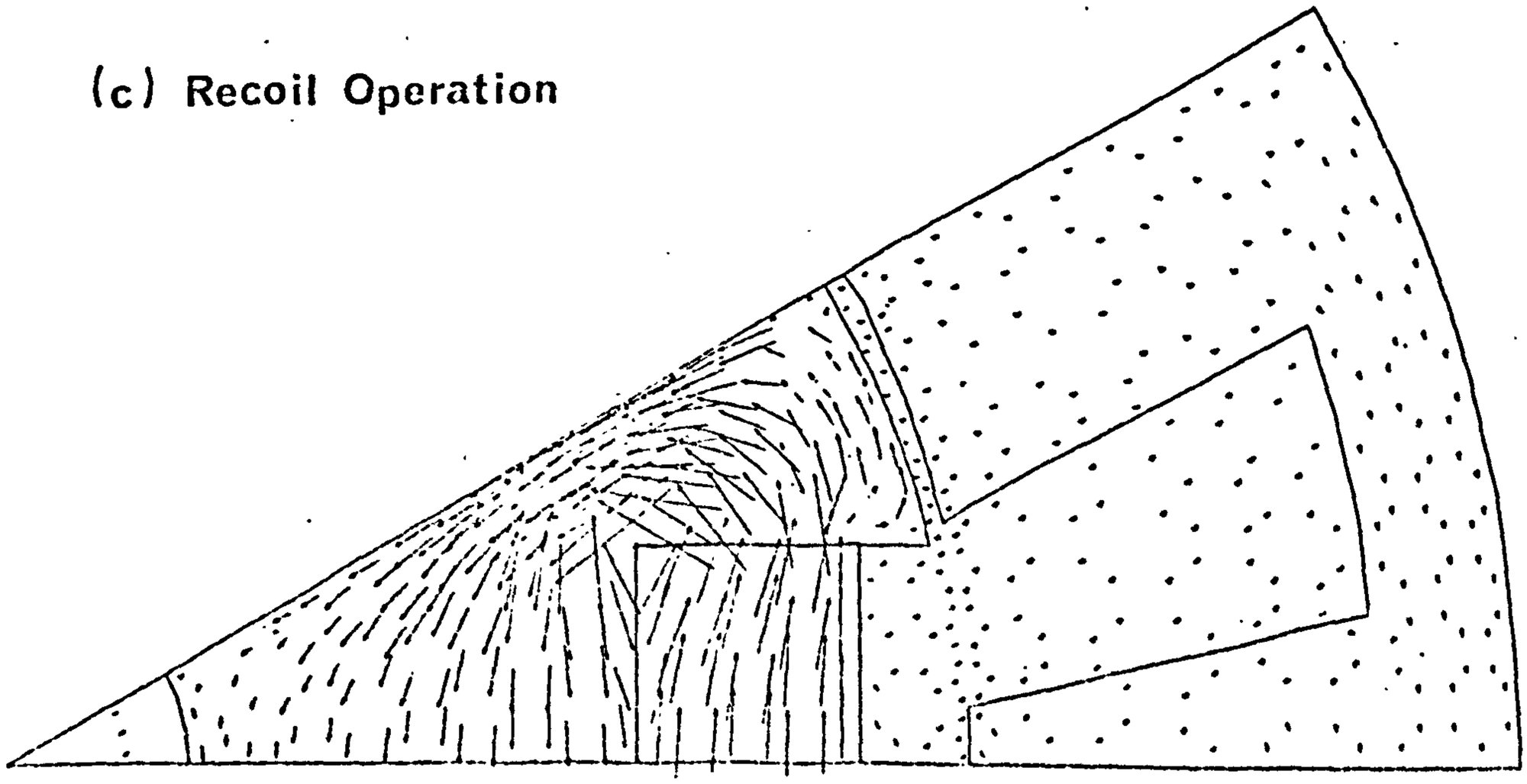

Fig 6·19

Flux Density Distribution Of Alcomax IV Rotor Having A Non- Magnetic Hub

(a) Magnetisation

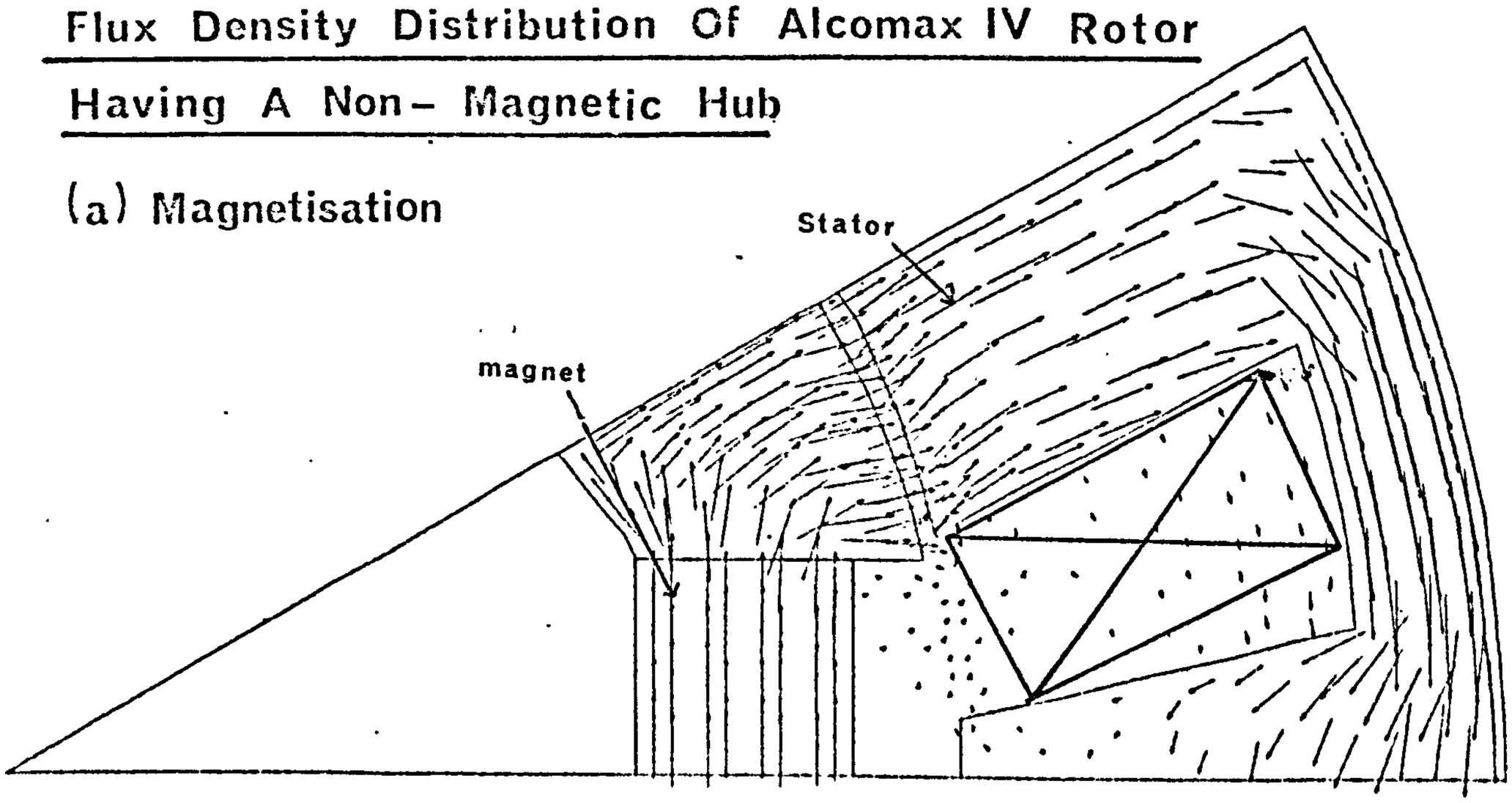

(b) Air- Stabilisation

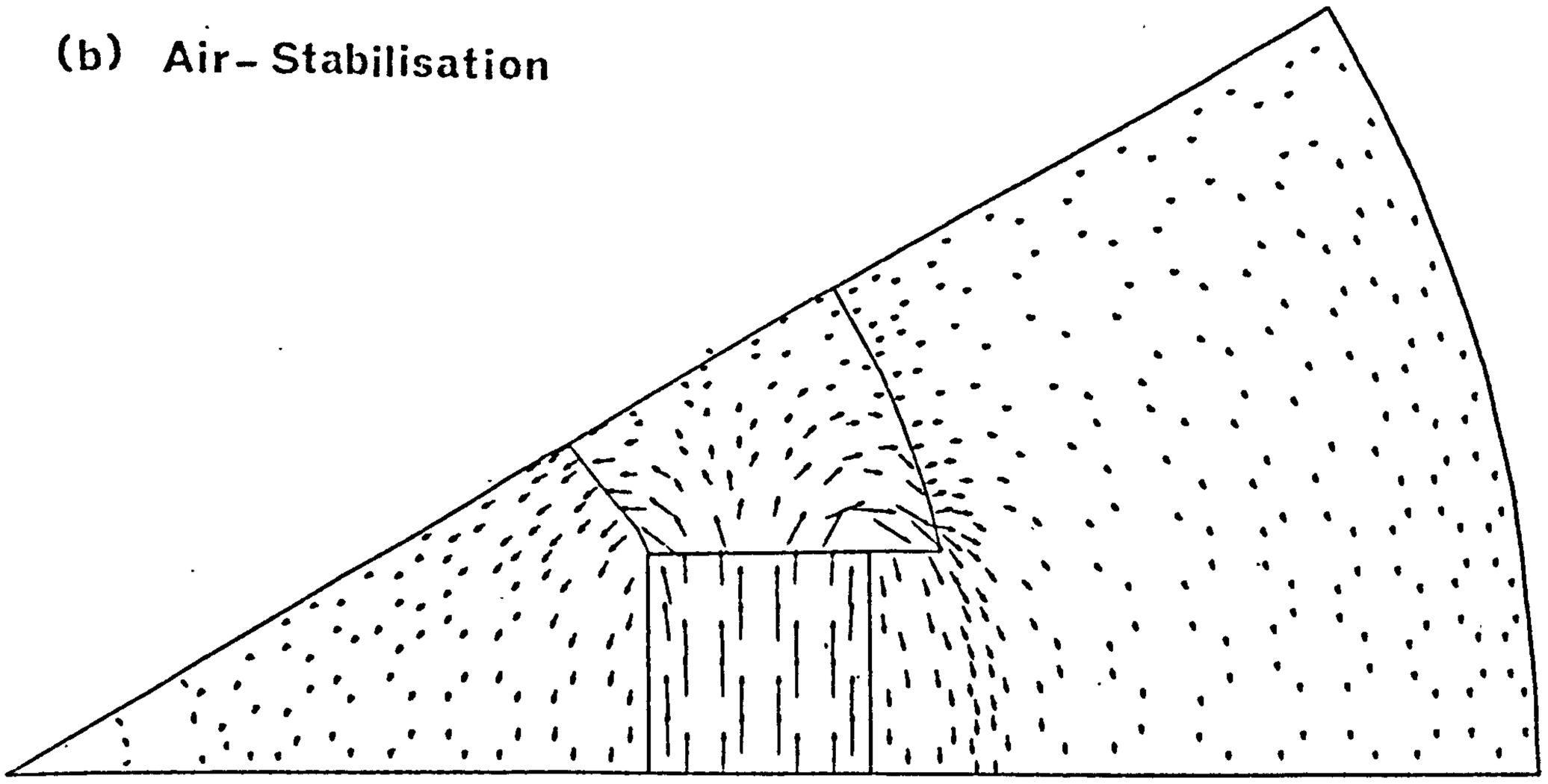

(c) Recoil Operation

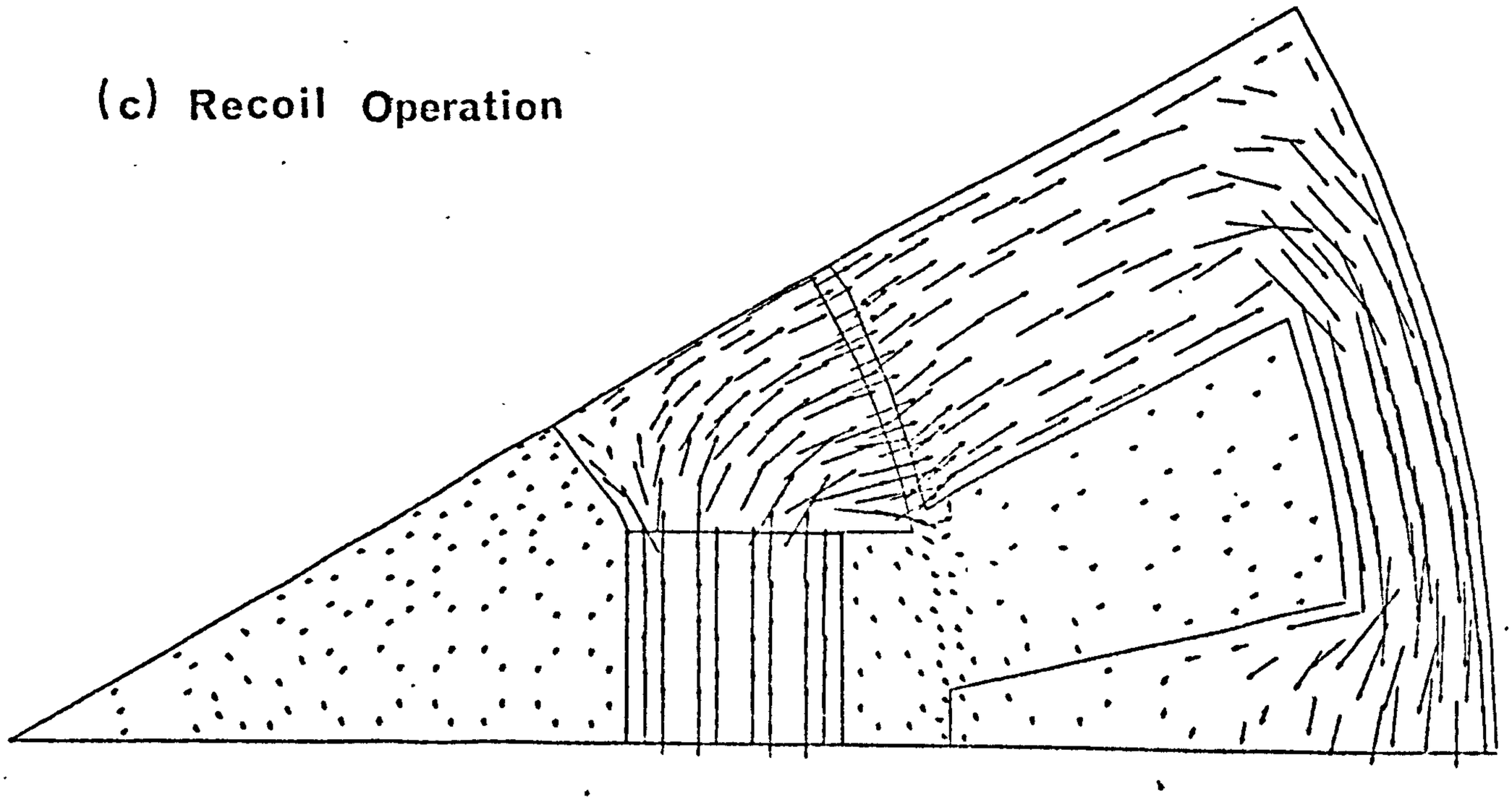

Fig 6·2C

Flux Plots Of Supermagloy 16 Rotor

(a) Air – Stabilisation

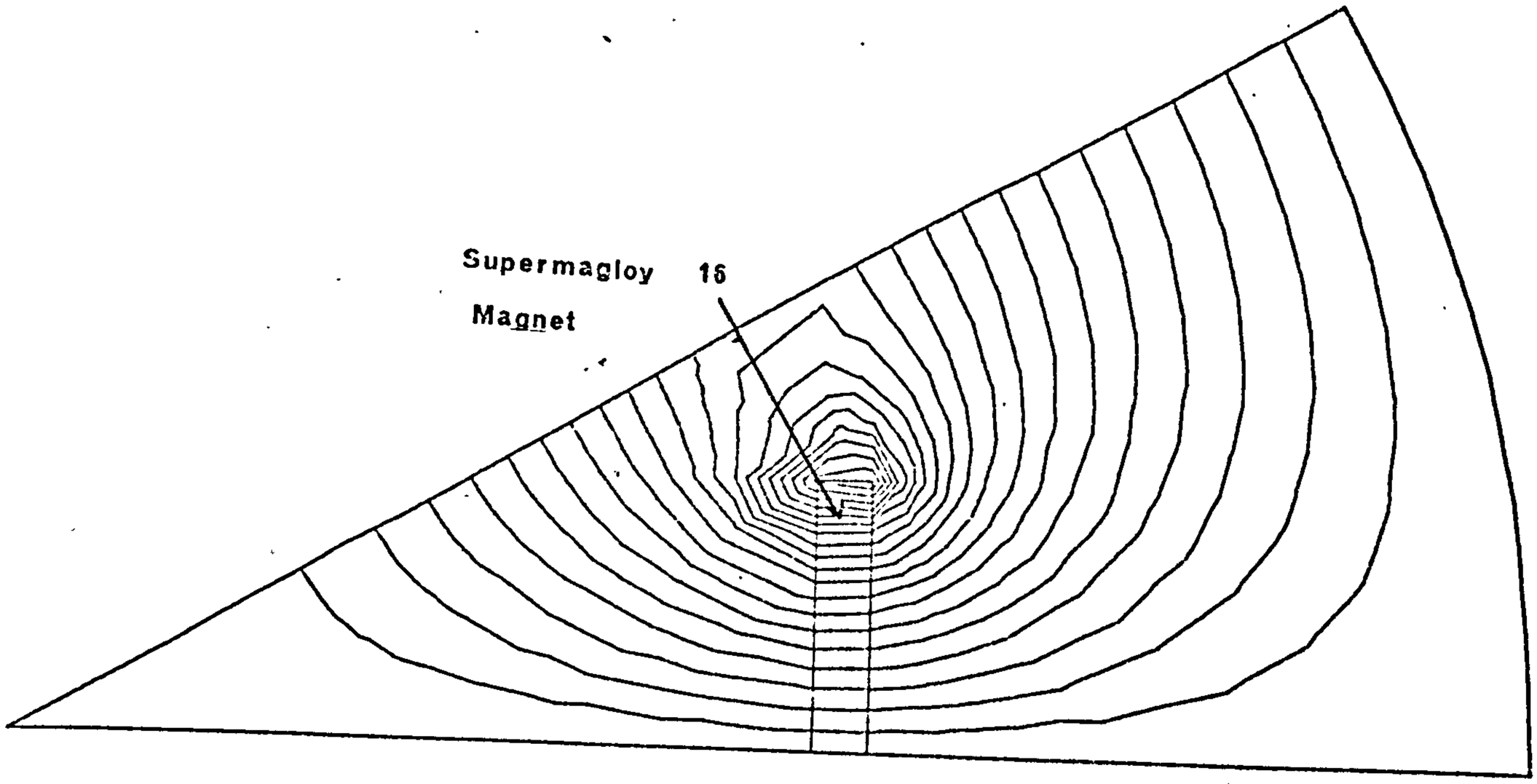

(b) Recoil Operation

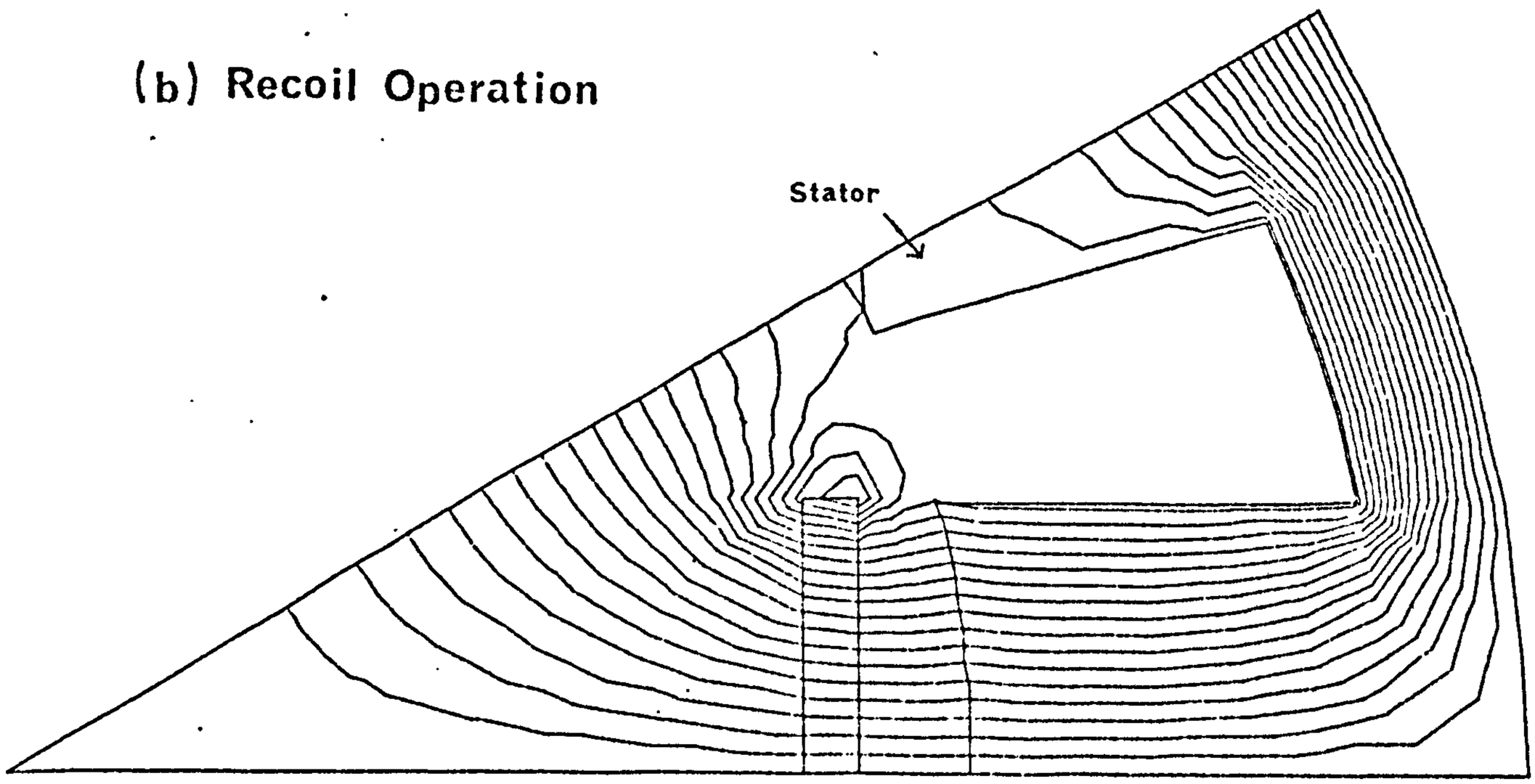

Fig 6·21
Fig 6·22
Fig 6·23

6·21 Location Of Hall Probes During Air Stabilisation

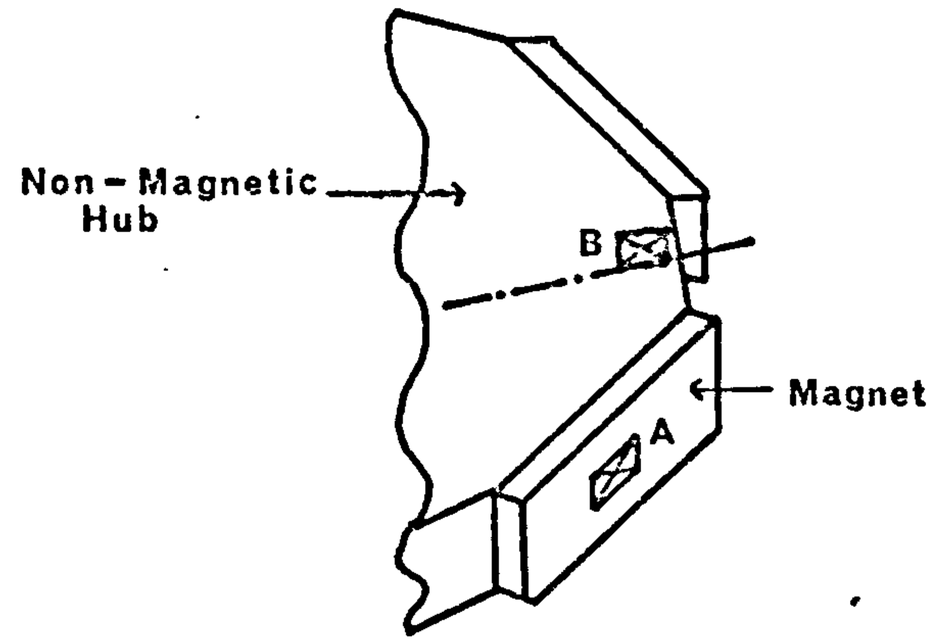

6·22 Flux Paths Of Magnet

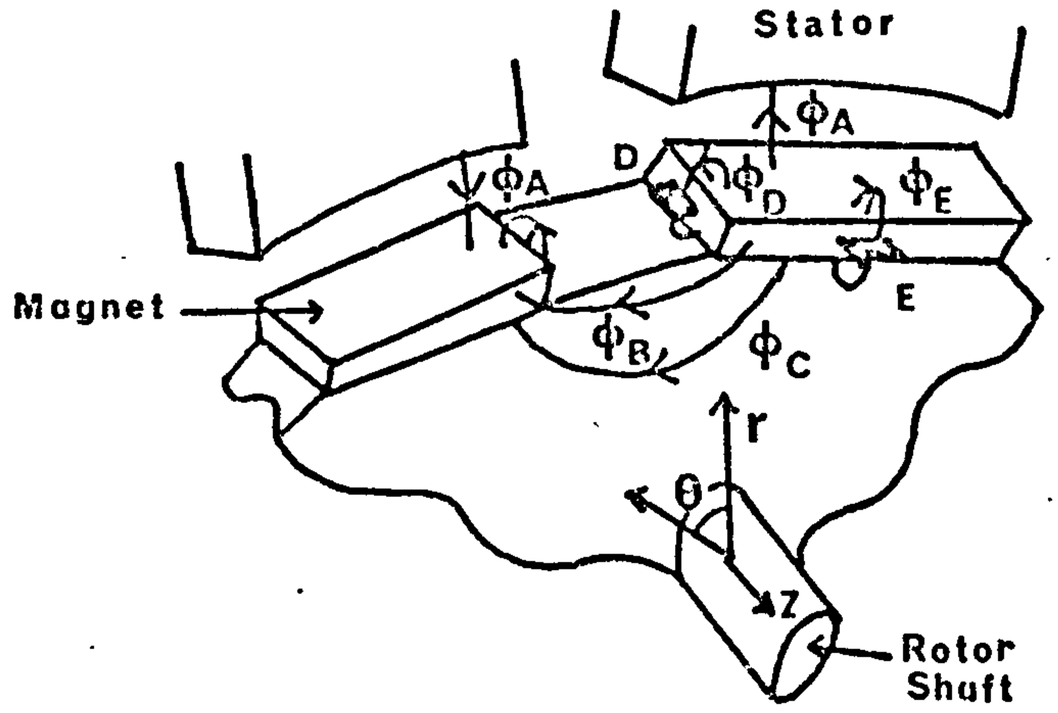

6·23 Effect Of 3-D Fields On Magnet Working Points

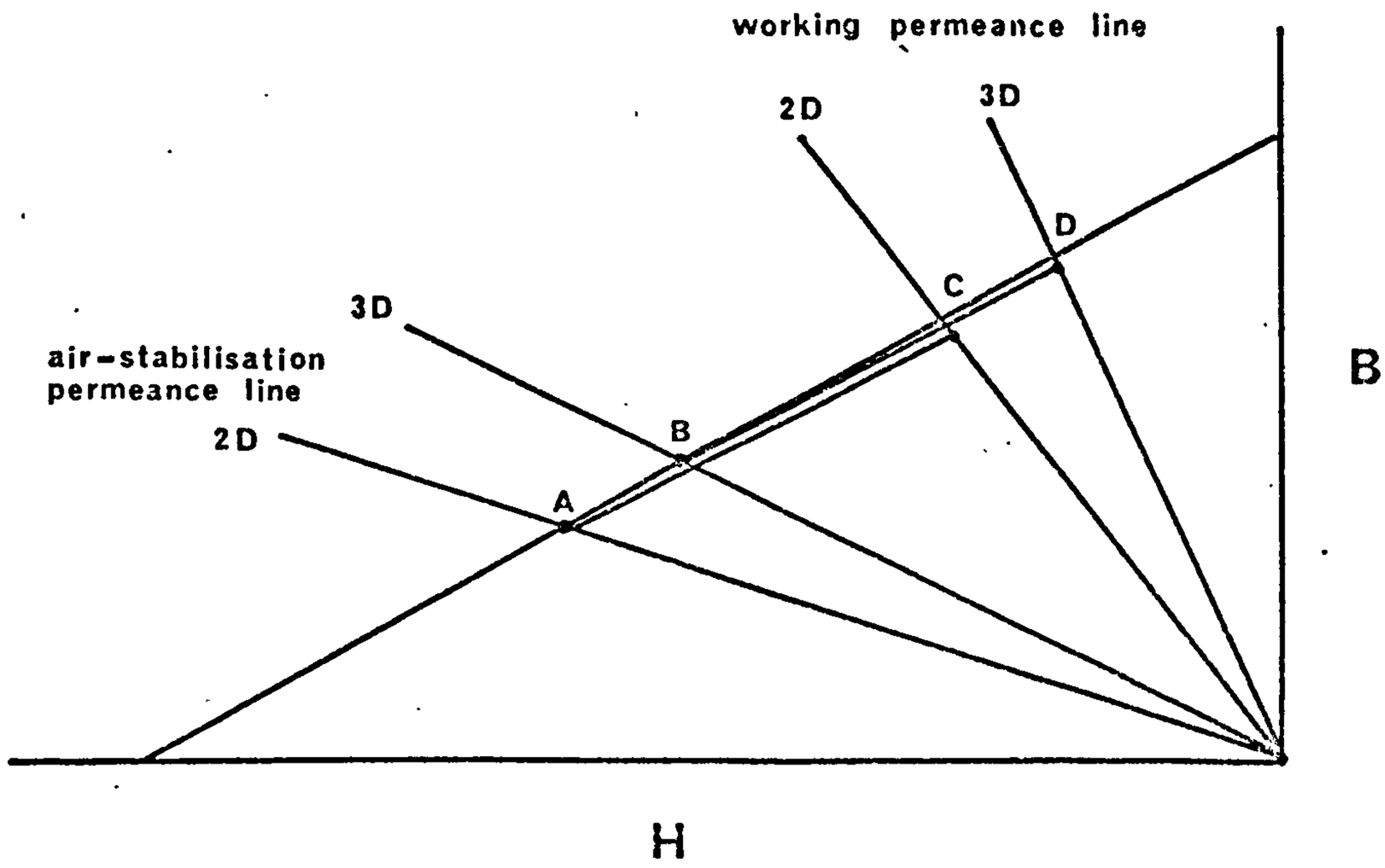

Fig 6·24

Flux Plots Of Supermagloy 10 Rotor With A Non- Magnetic Hub

(a) Air - Stabilisation

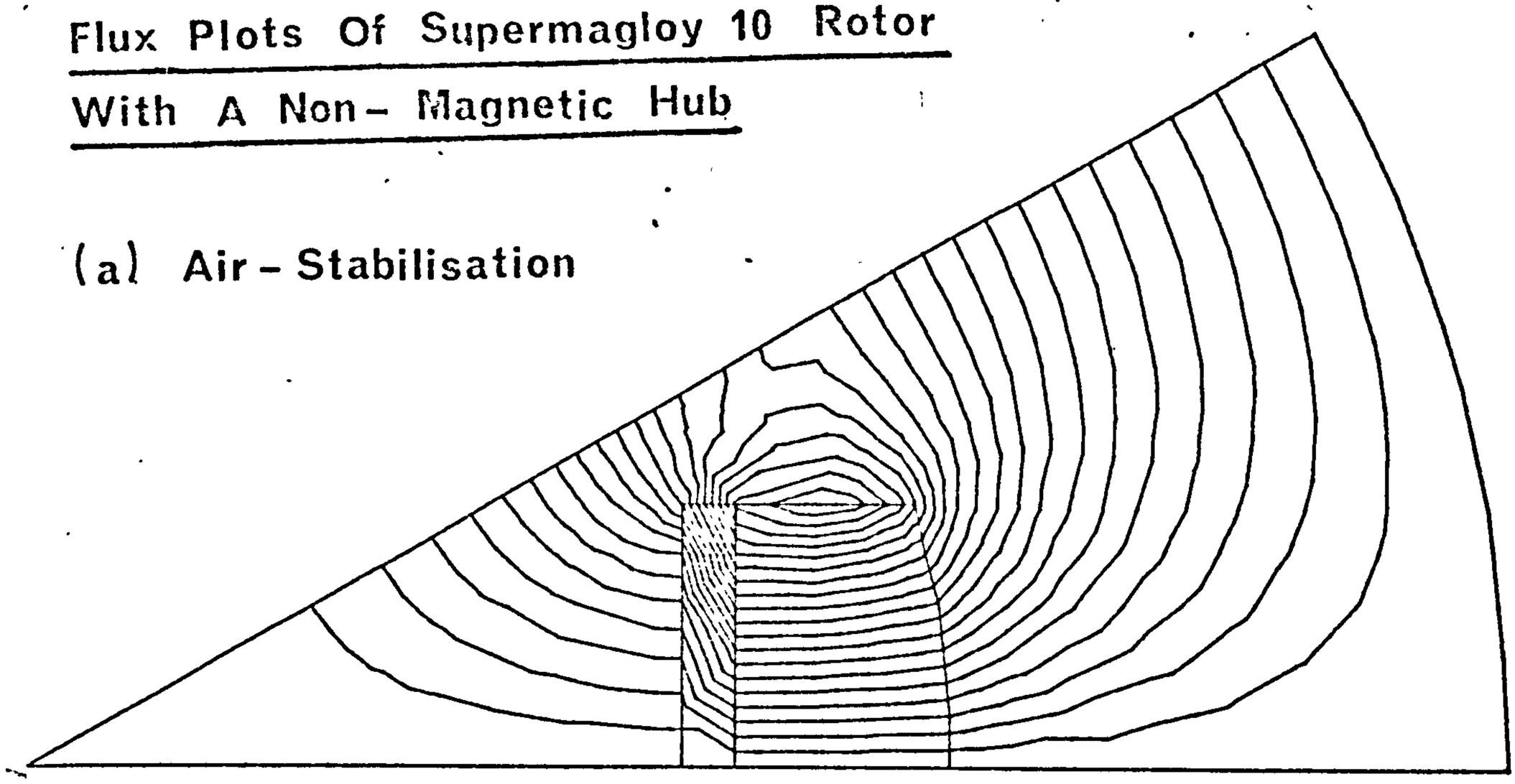

(b) Recoil Operation

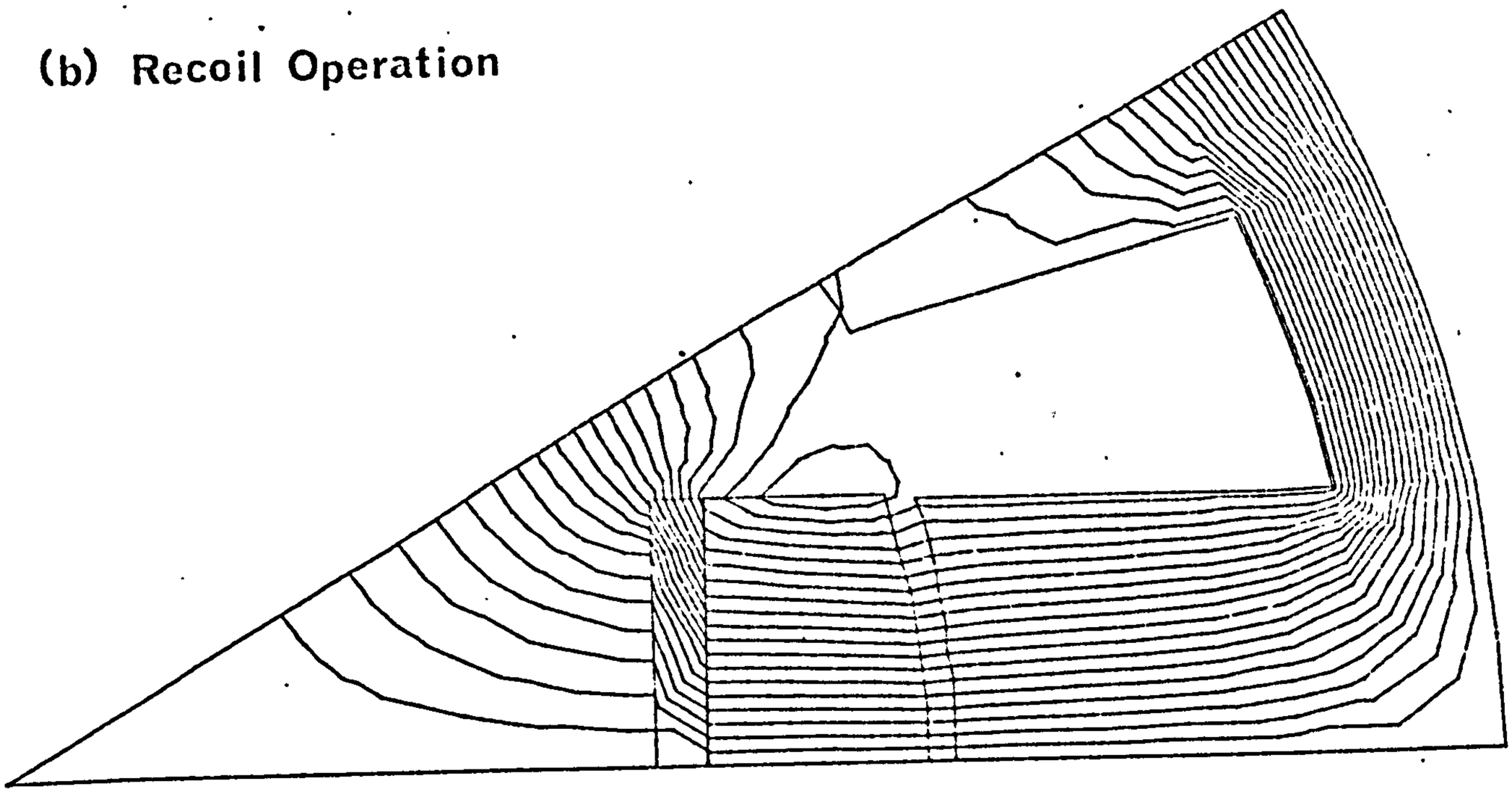

(c) Inductance Calculation

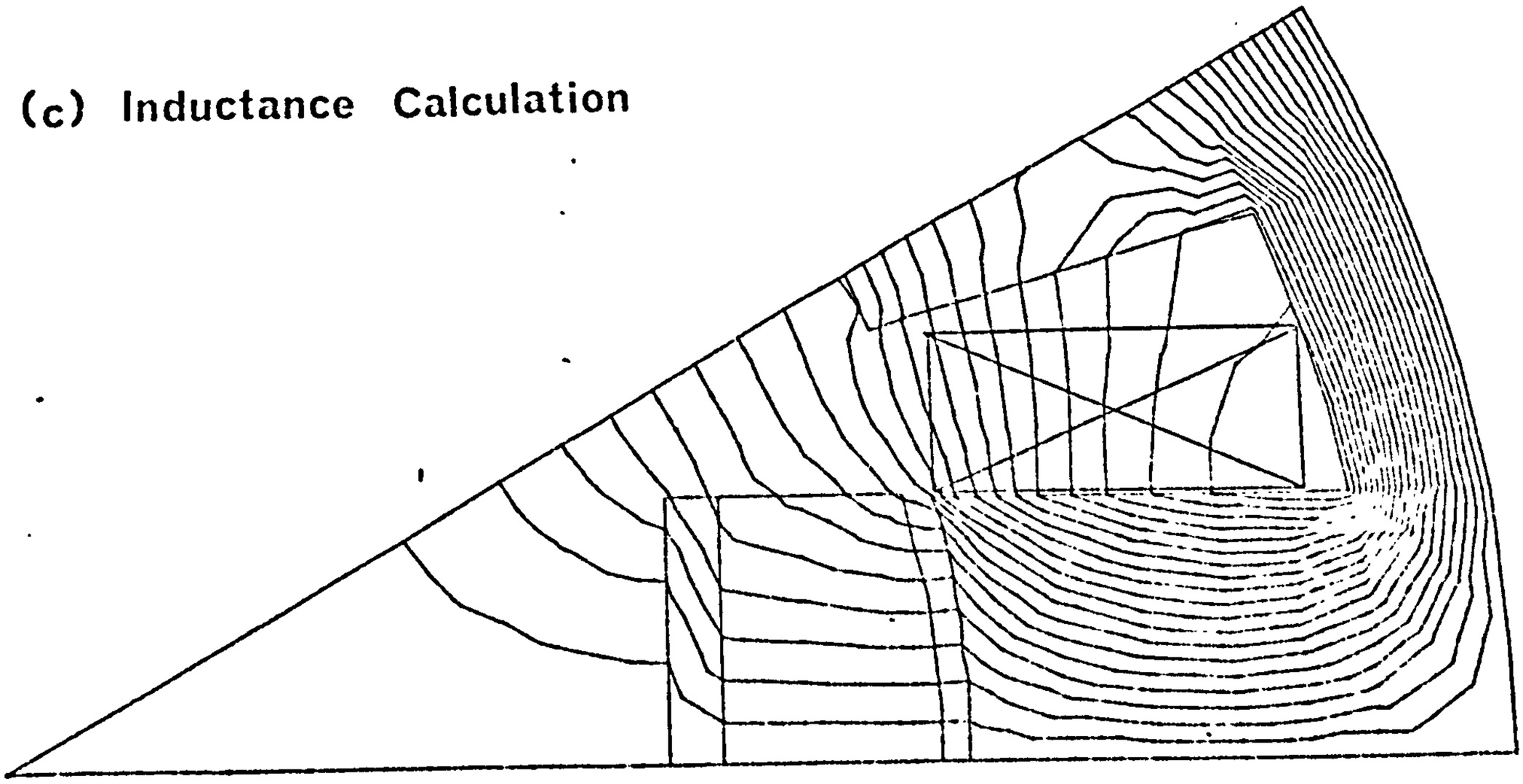

Fig 6·25

Fig 6·26

6·25 Location Of Hall Probes During Air Stabilisation

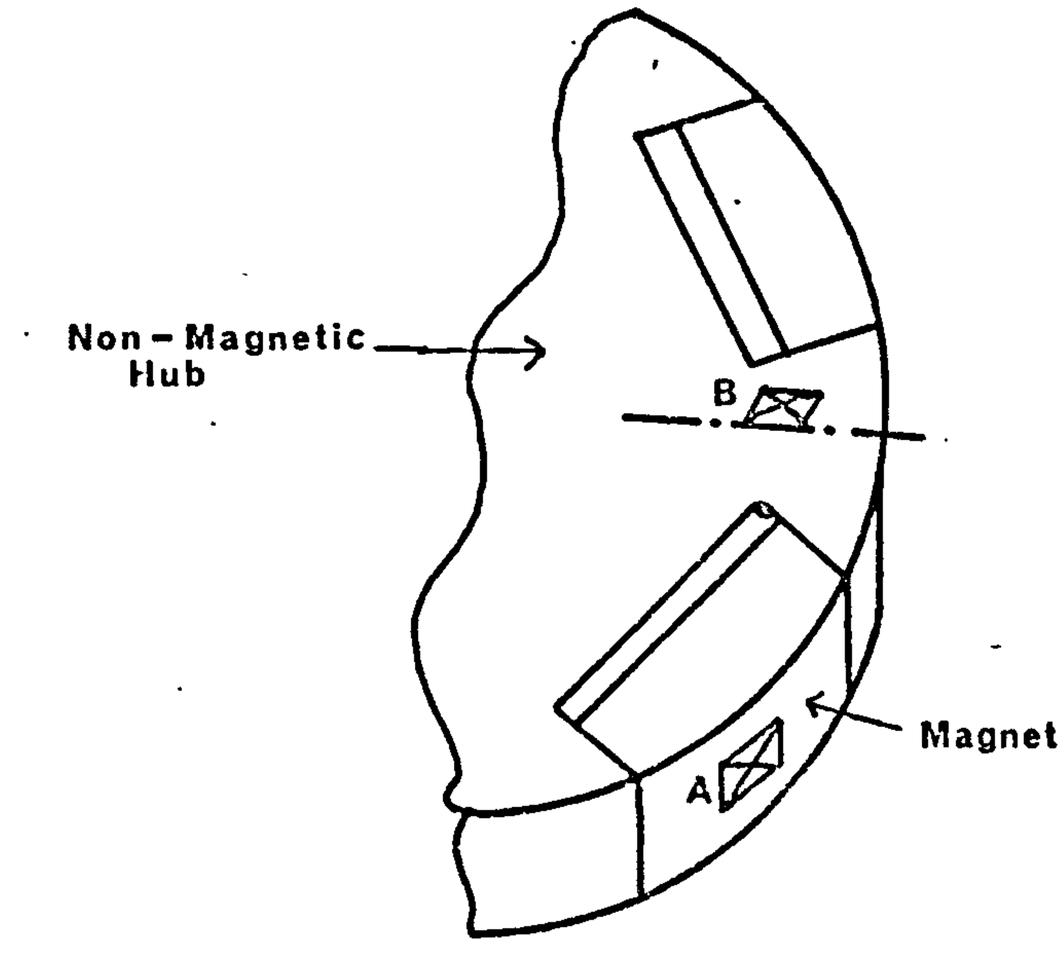

6·26 Flux Paths Of Rotor Poles

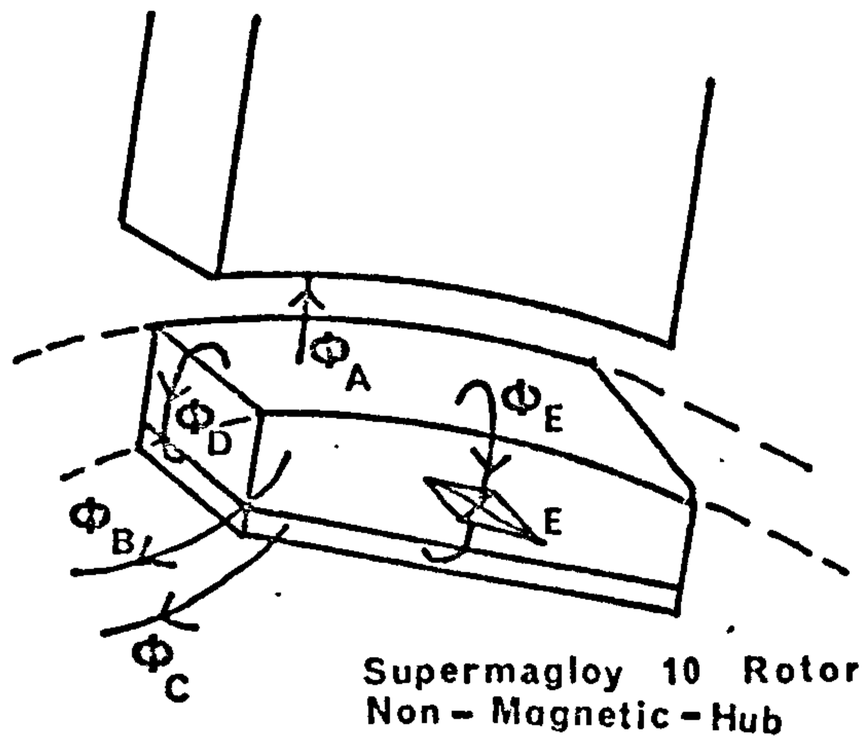

Supermagloy 10 Rotor With Non – Magnetic – Hub

Fig 6·27

Variations Of Operating Speed With Turns Factor

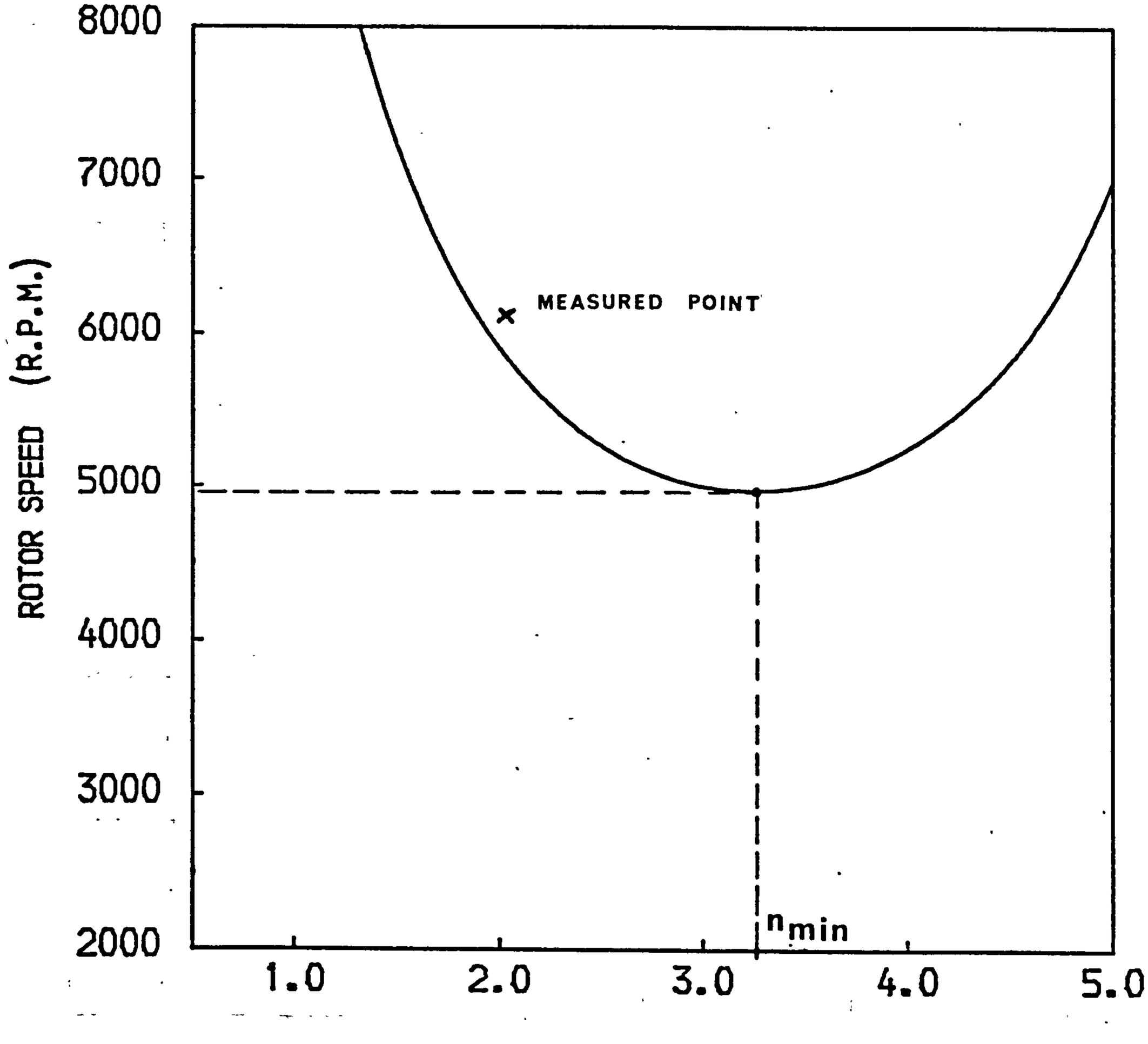

24V 250W Bulb
Supermagloy 10 Rotor With Non-Magnetic Hub

Fig 6·28

Measured Loss Torque

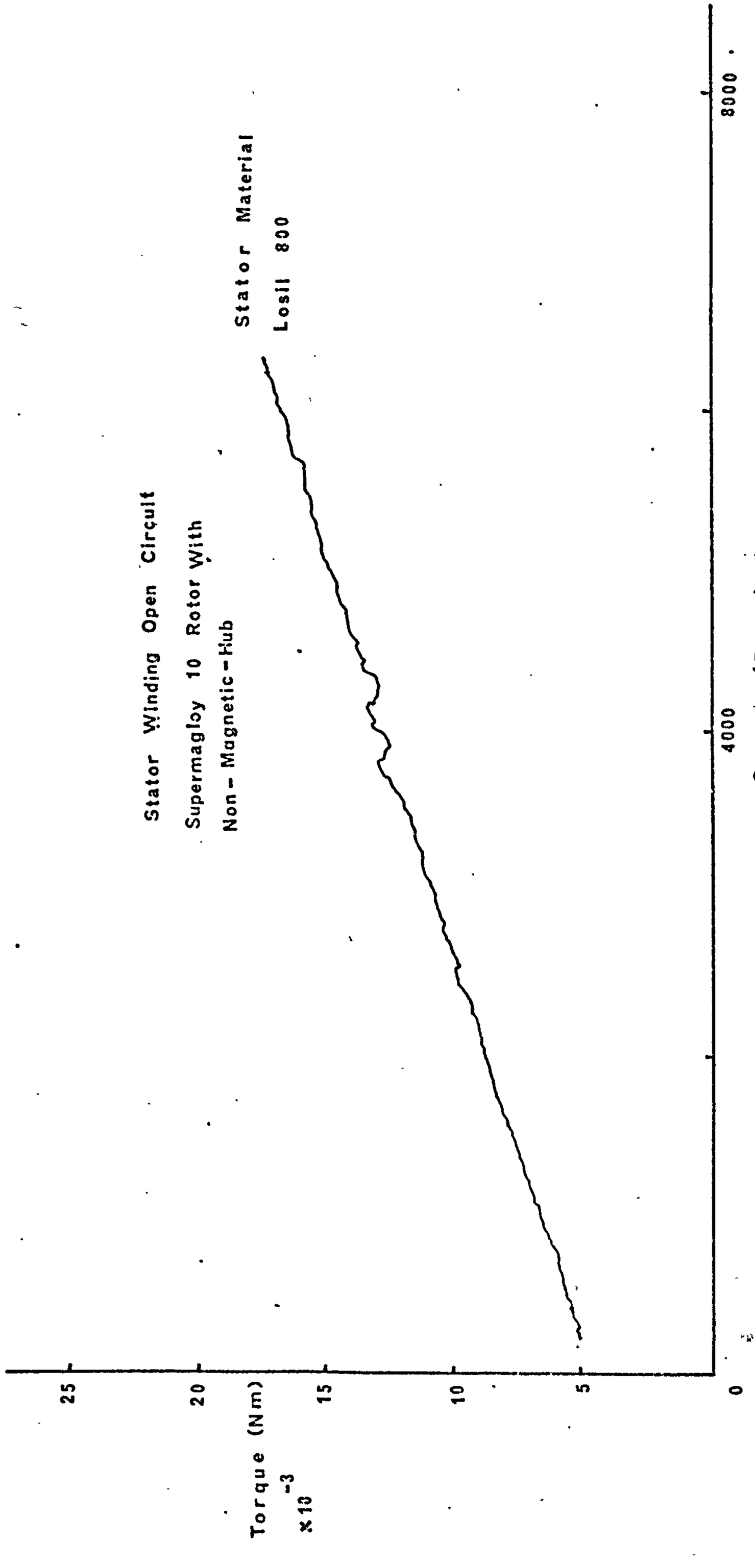

Torque-Speed Curve Of A 250W Generator

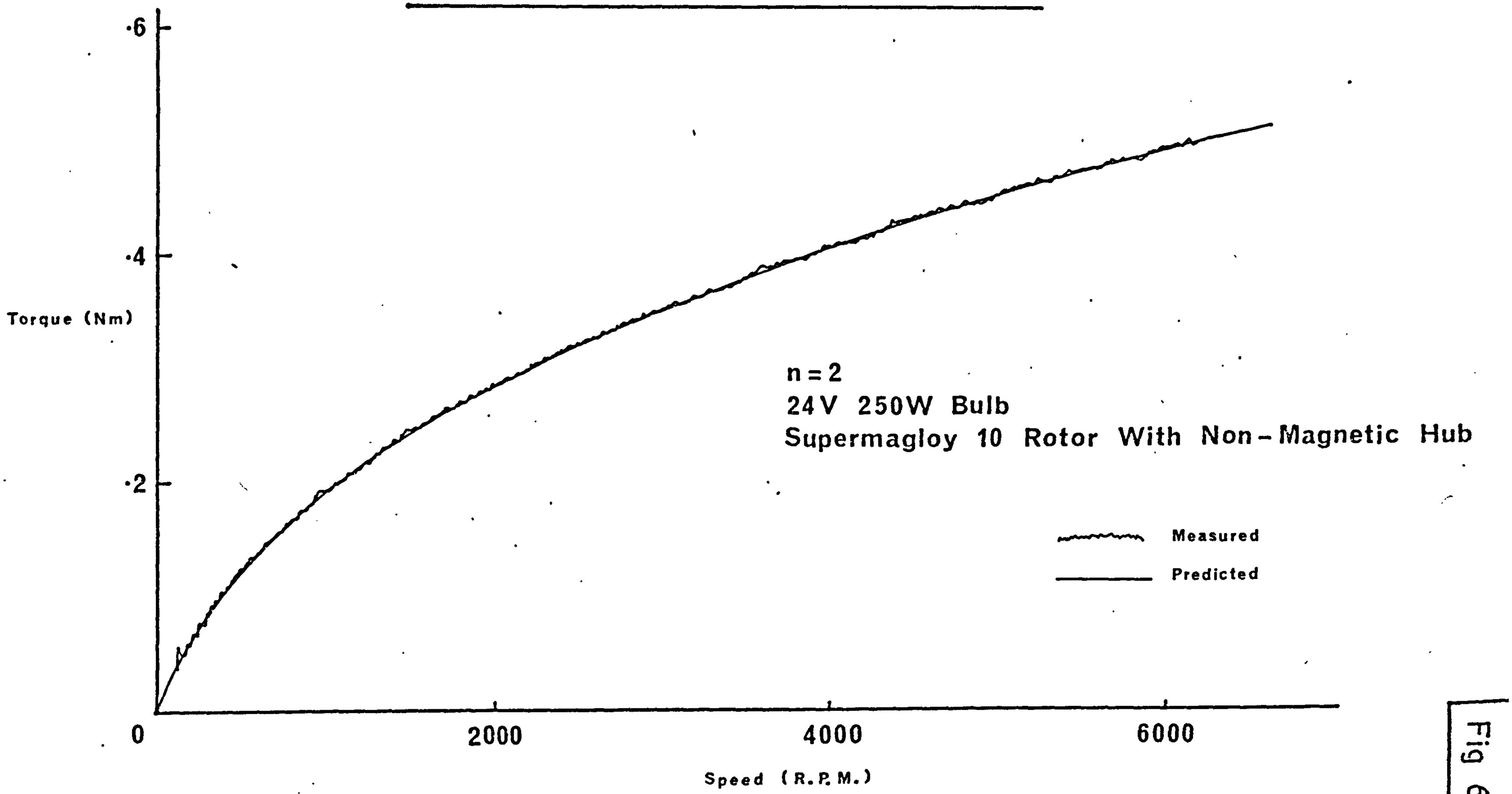

Fig 6.29

Fig 6·30

Flux Plots Of Supermagloy 10 Rotor With Magnetic Hub

(a) Air-Stabilisation

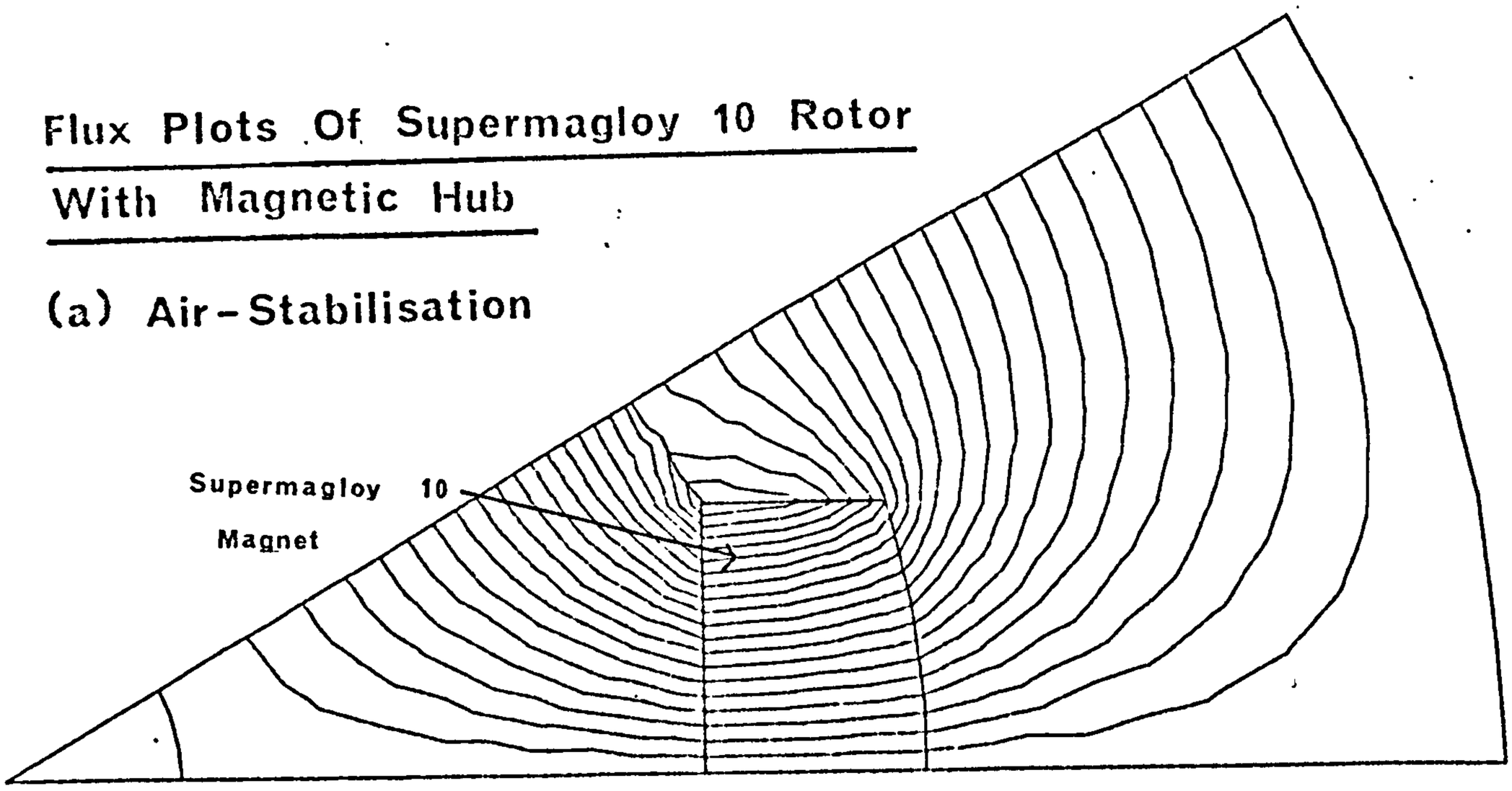

(b) Recoil Operation

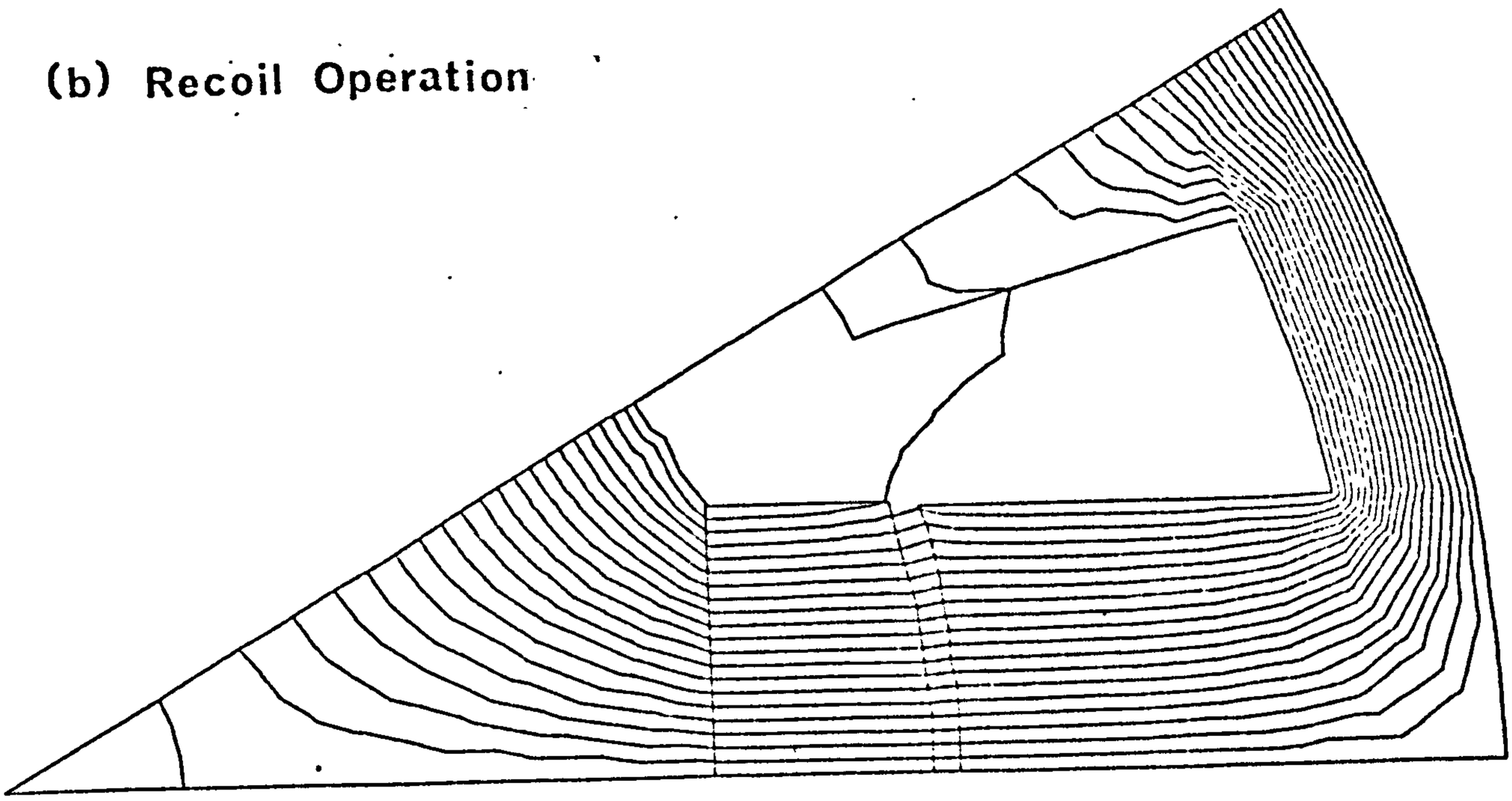

(c) Inductance Calculation

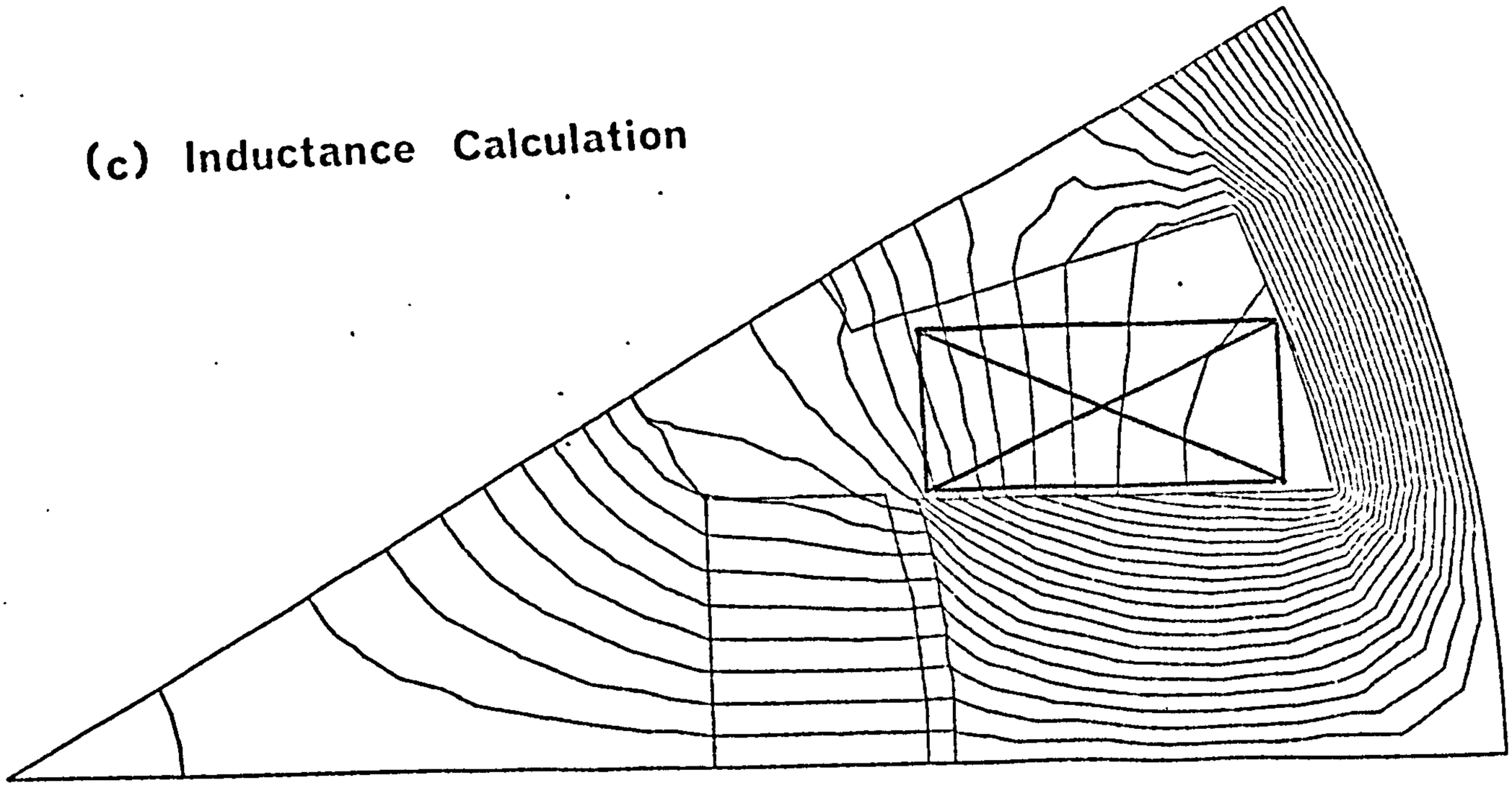

Fig 6·31
Fig 6·32

6·31 Location Of Hall Probes During Air Stabilisation

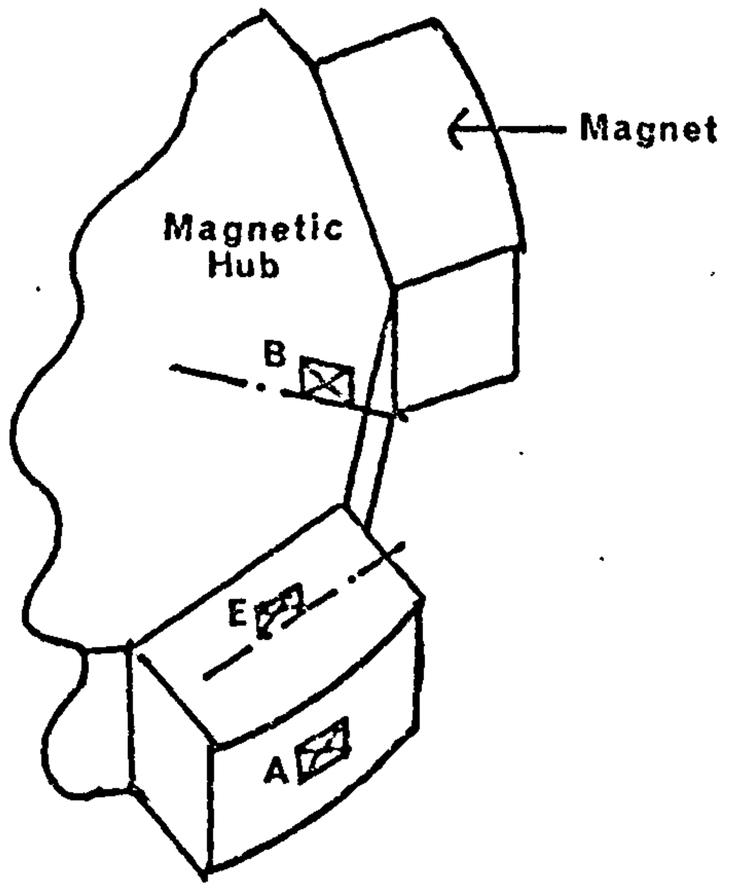

Supermagloy 10 Rotor With Magnetic-Hub

6·32 Alternative Rotor Geometry

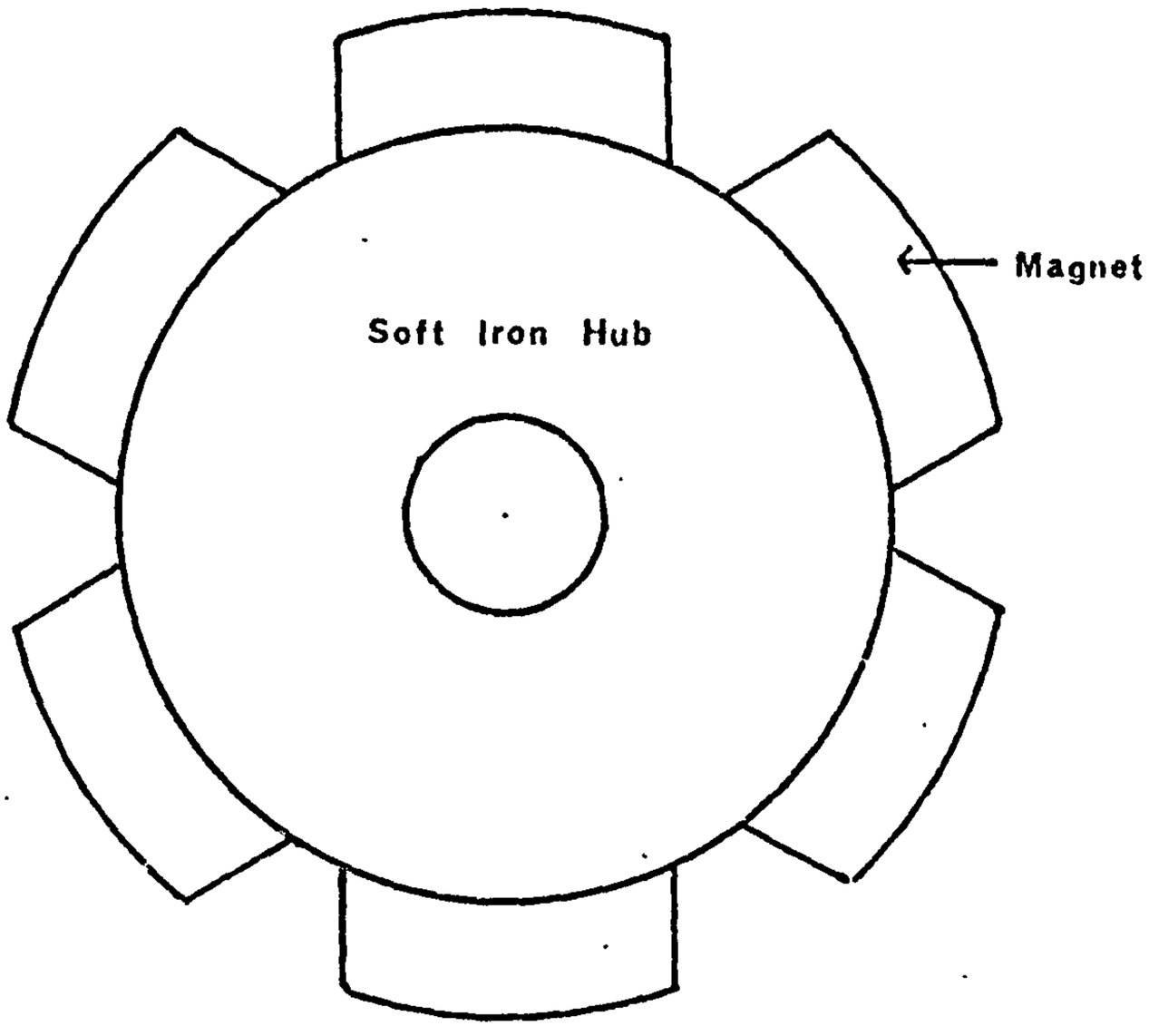

Fig 6·33

Measured And Computed Saliency Torques At Various Displacement Angles

Supermagloy 10 Rotor With Magnetic-Hub
Airgap = 1mm
Magnet Radial Depth = 8 mm

Measured Point	Computed Point	Stator Core
o	⊕	Without Interpoles
x	▲	With Interpoles

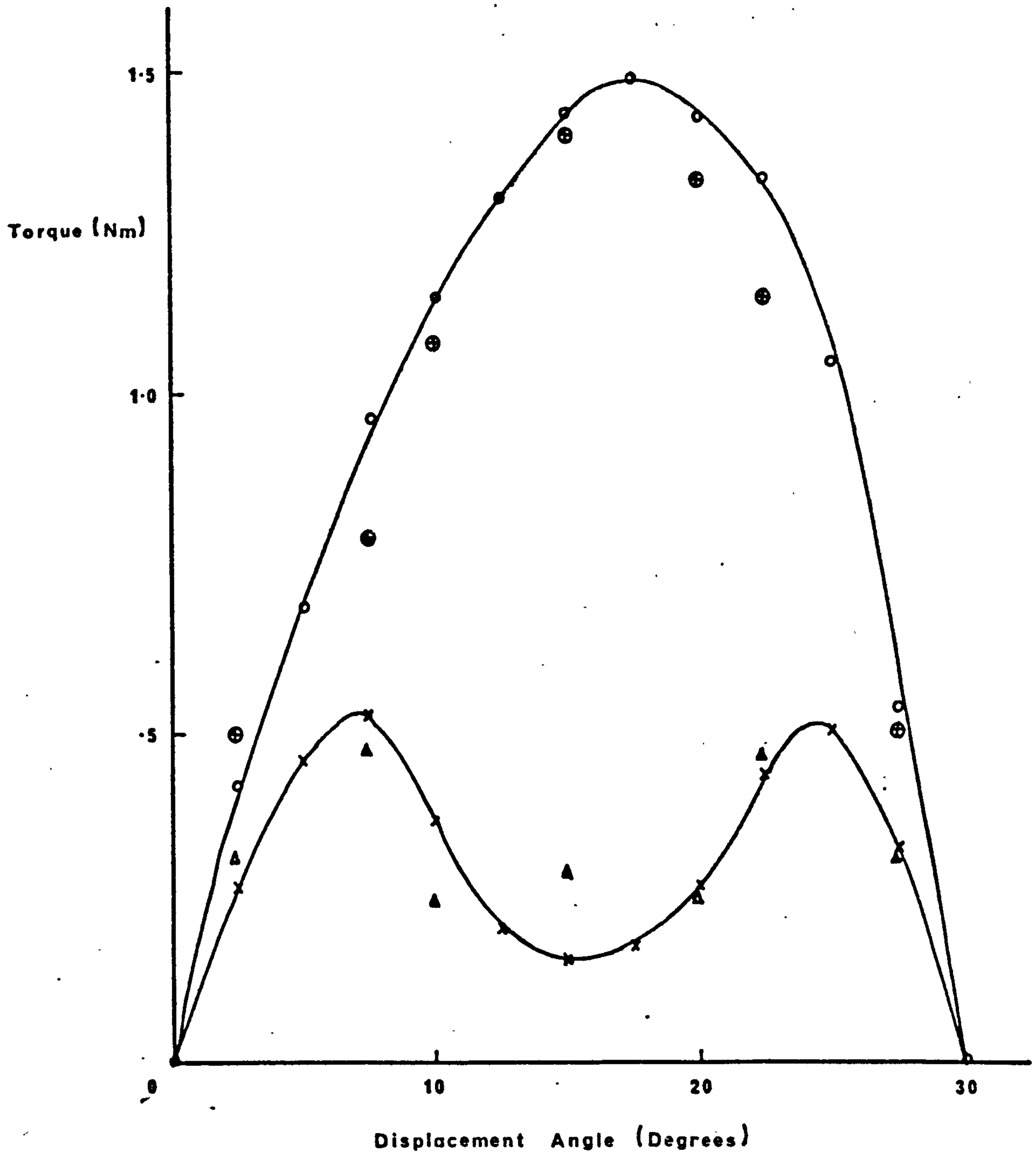

Fig 6·34

Flux Plots For The Calculation Of Saliency Torque

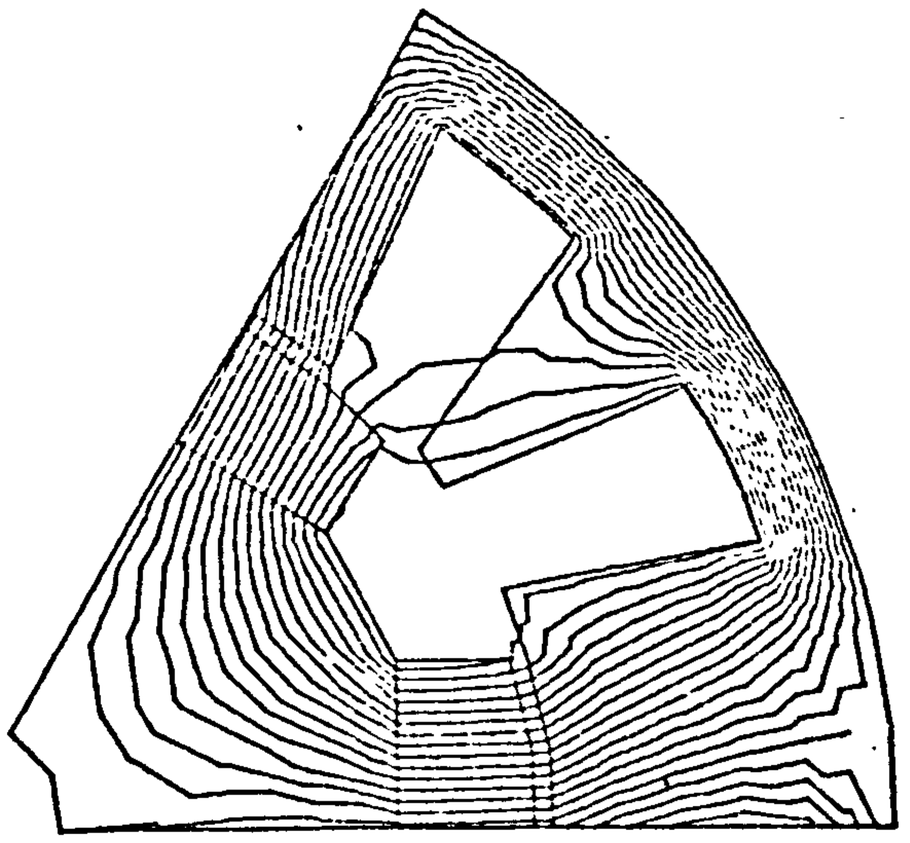

7·5°

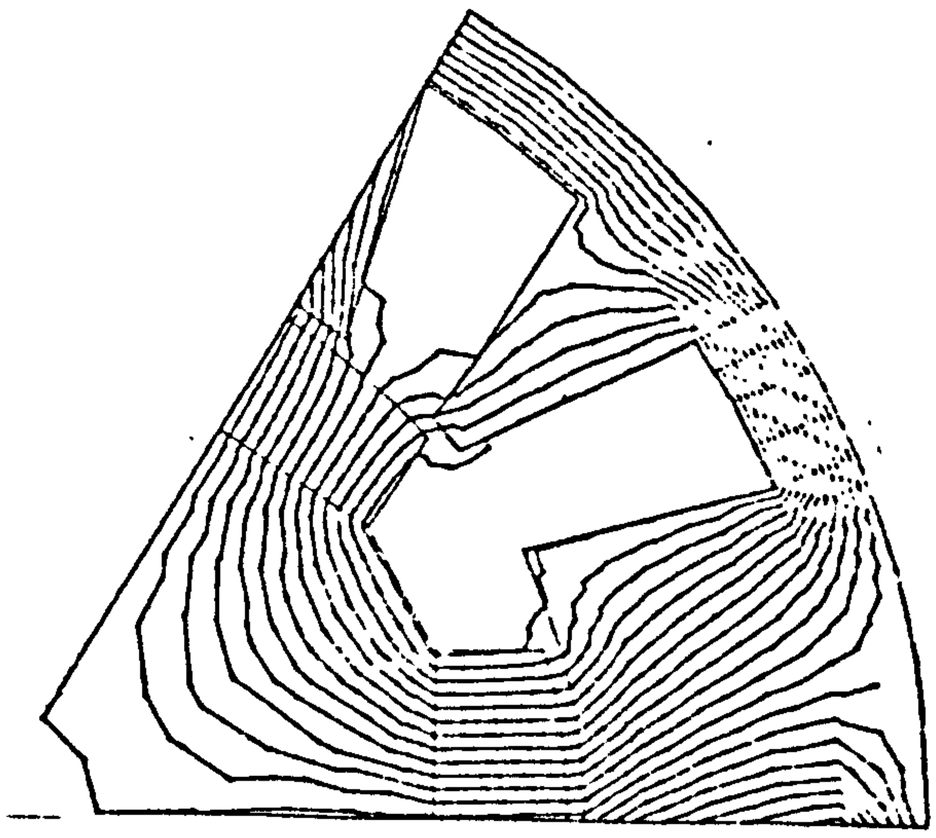

10°

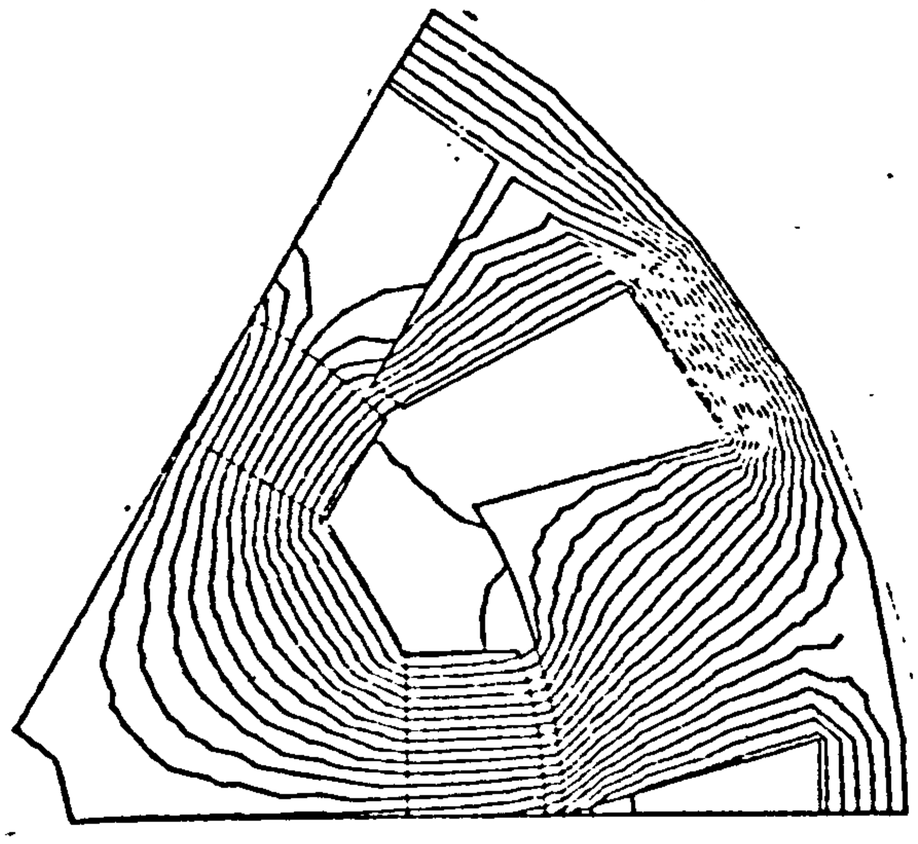

15°

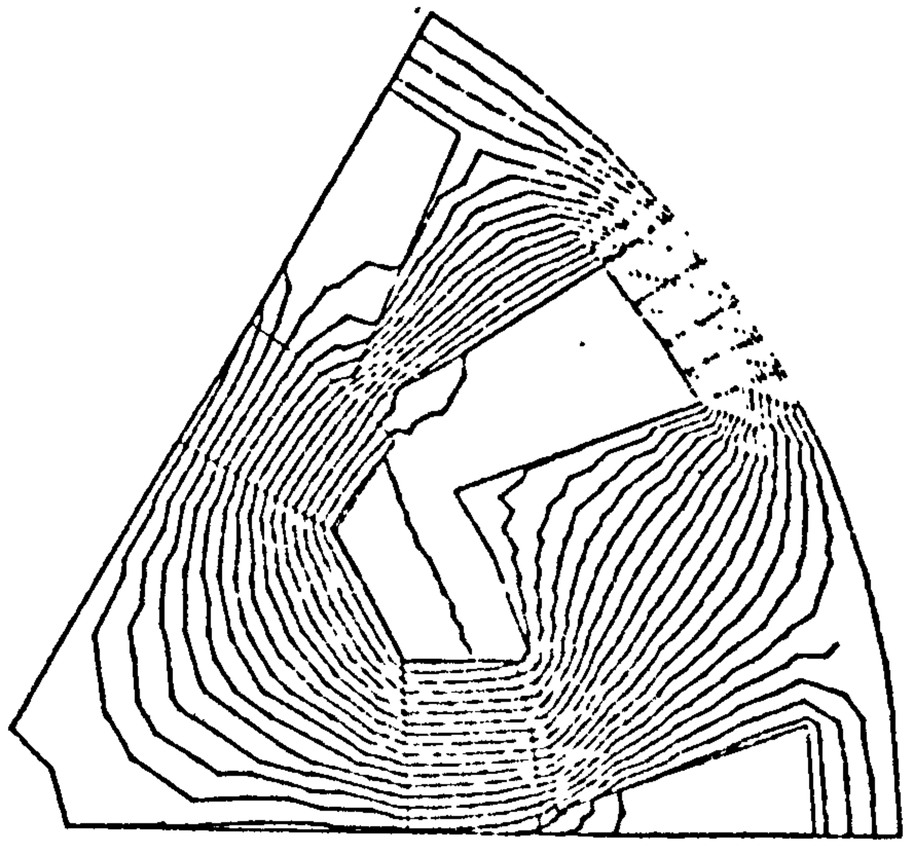

20°

22·5°

27·5°

Fig 6·35

Geometries Of Stator Cores With And Without Interpoles

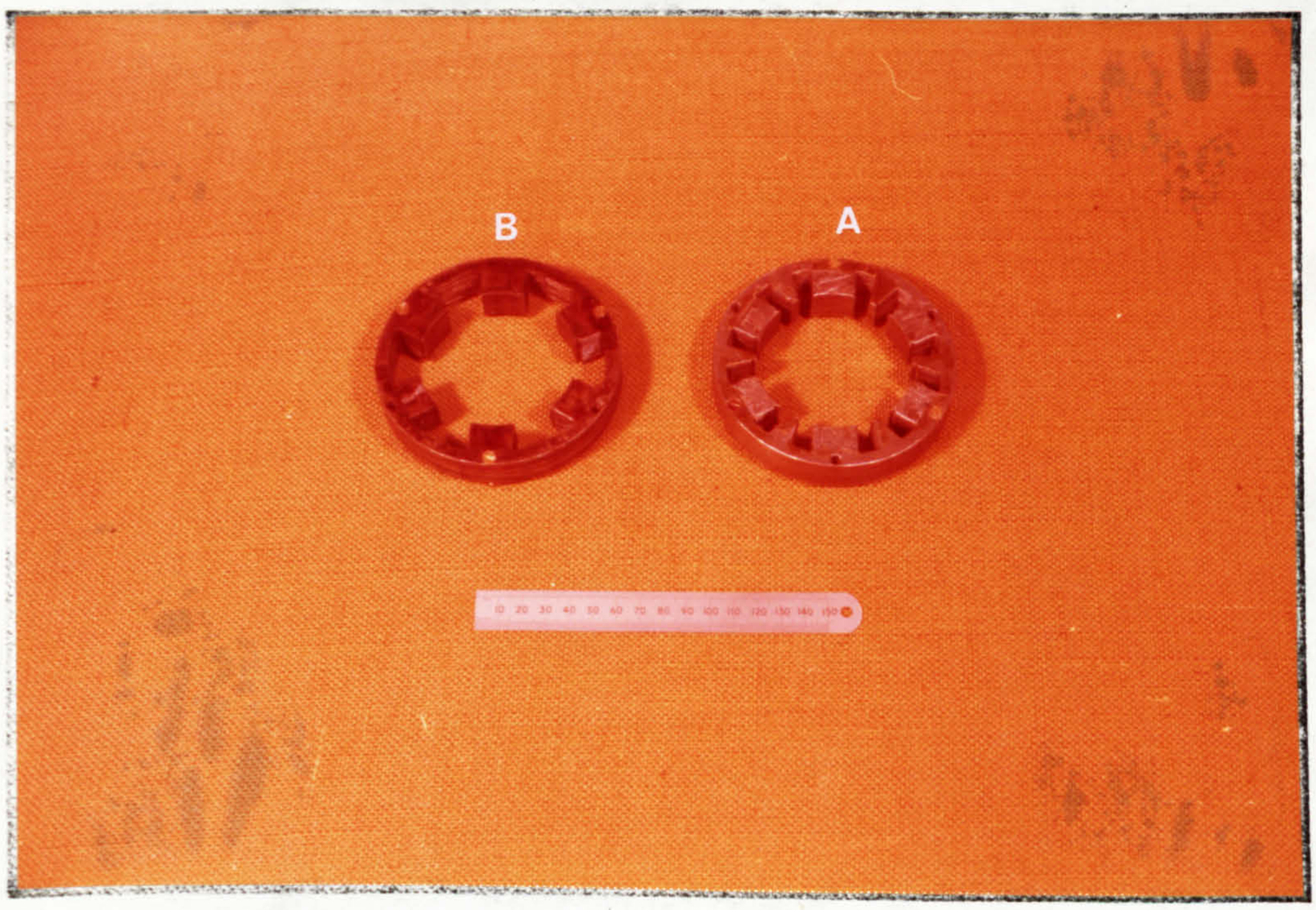

A : With Interpoles

B : Without Interpoles

Fig 6·36

Flux Plots For The Calculation Of Saliency Torque

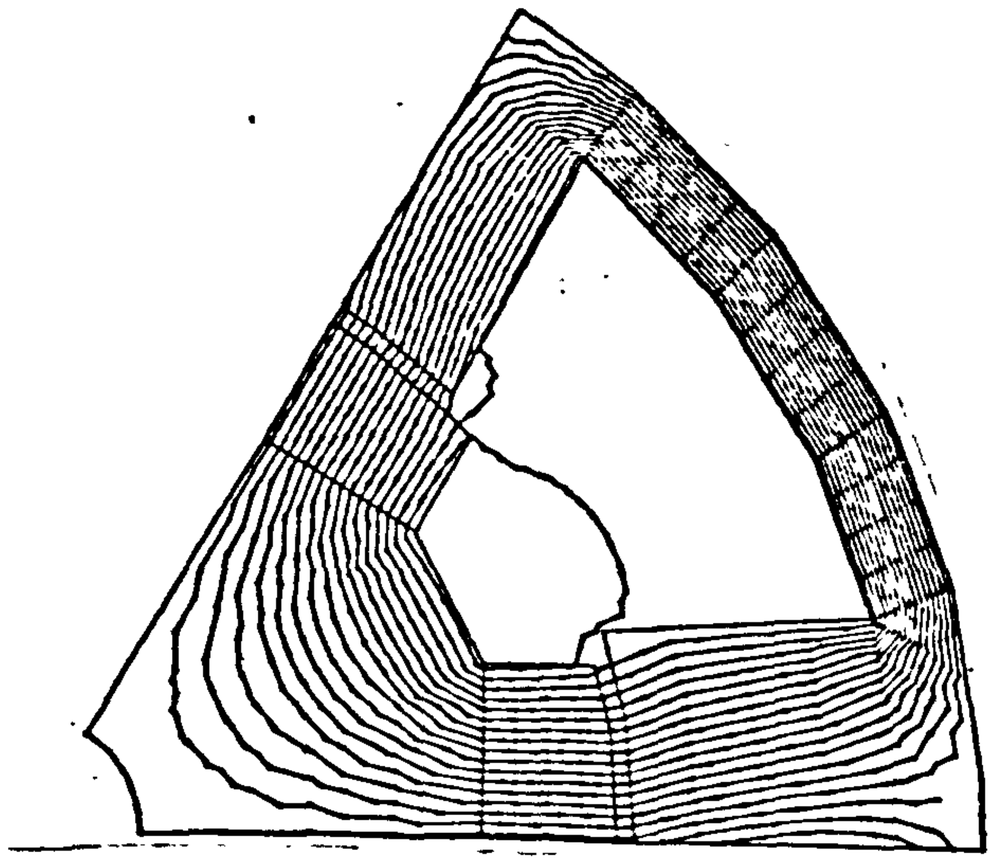

2·5°

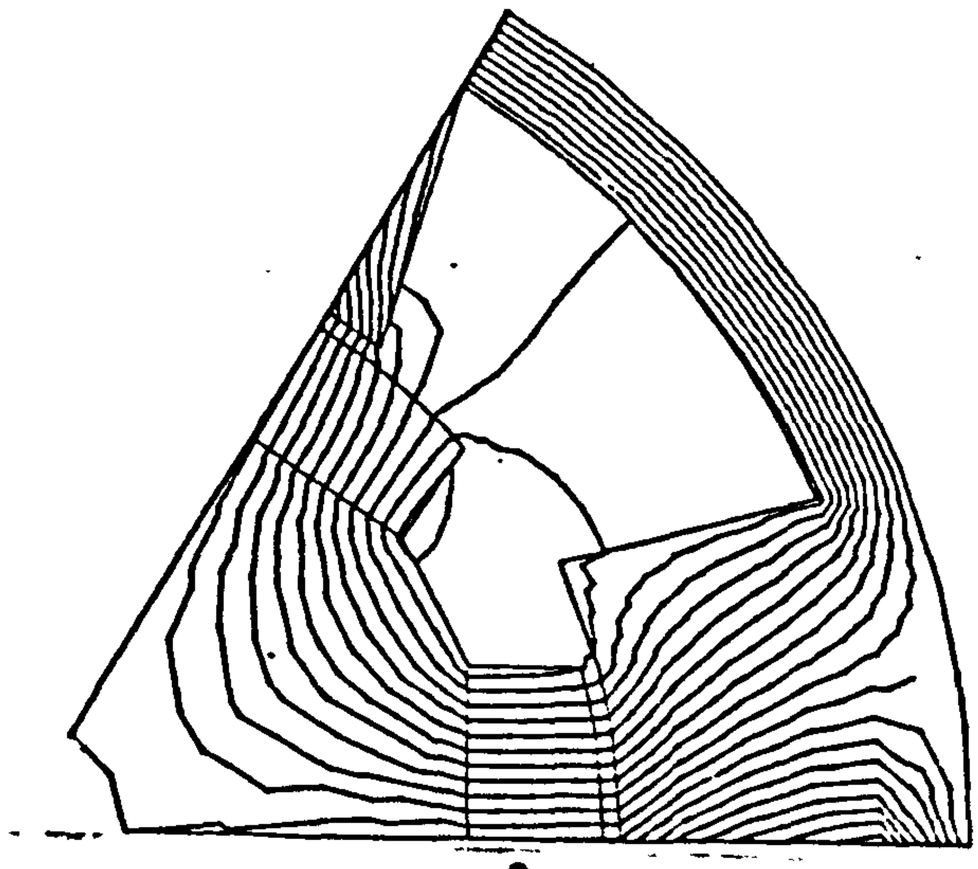

10°

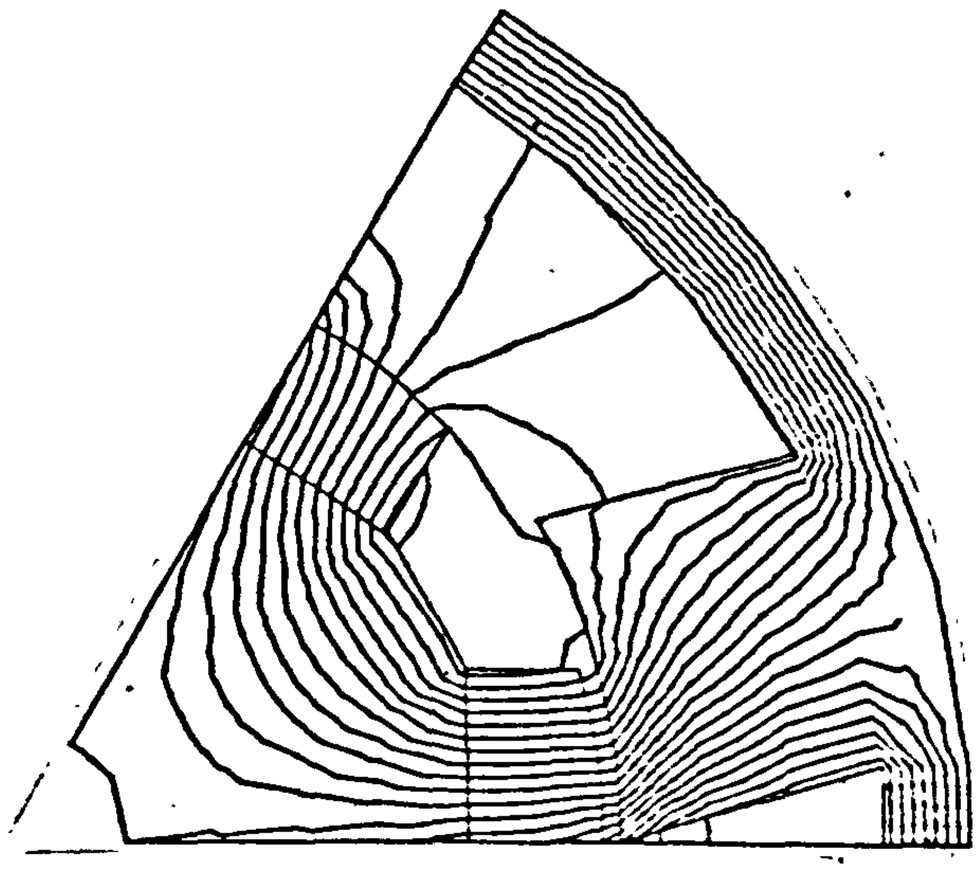

15°

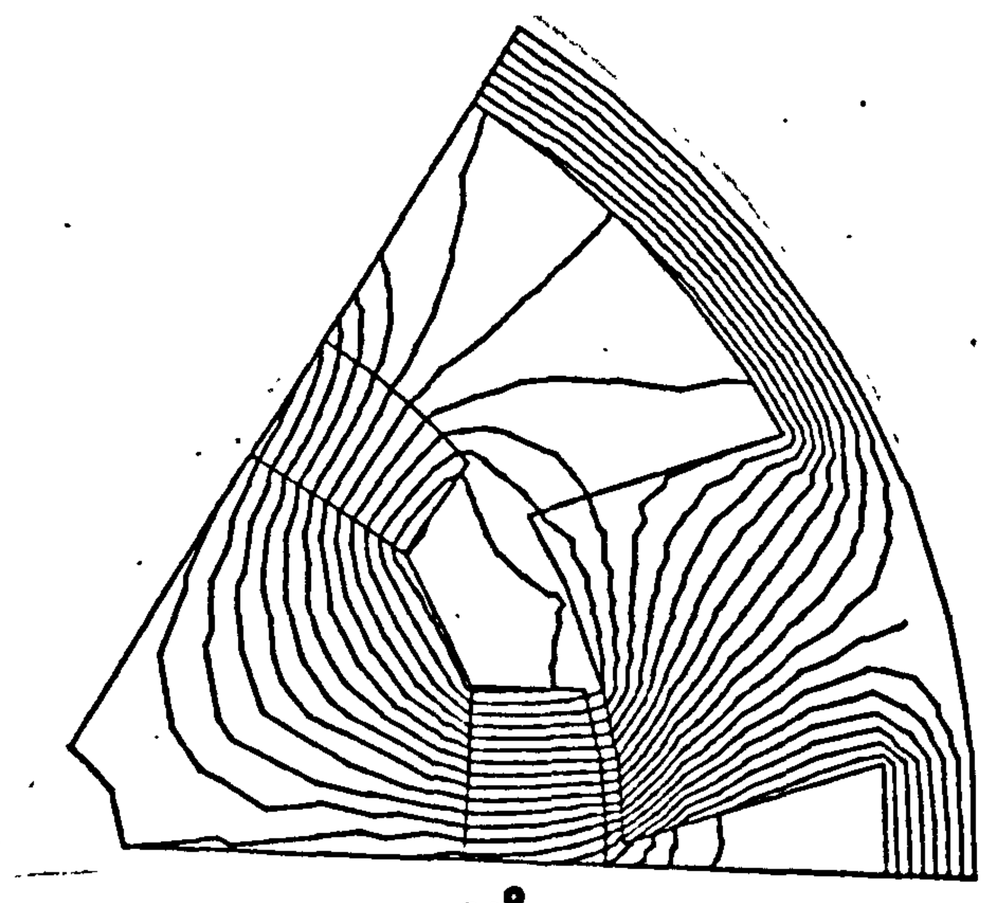

20°

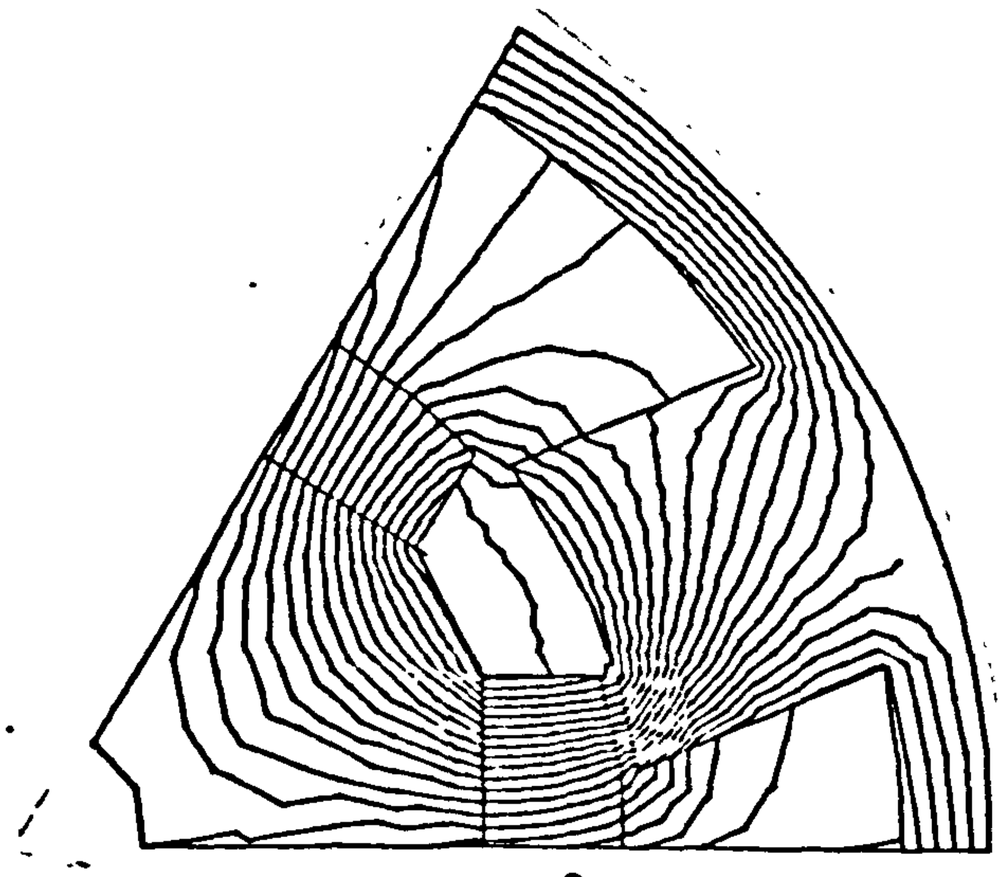

22·5°

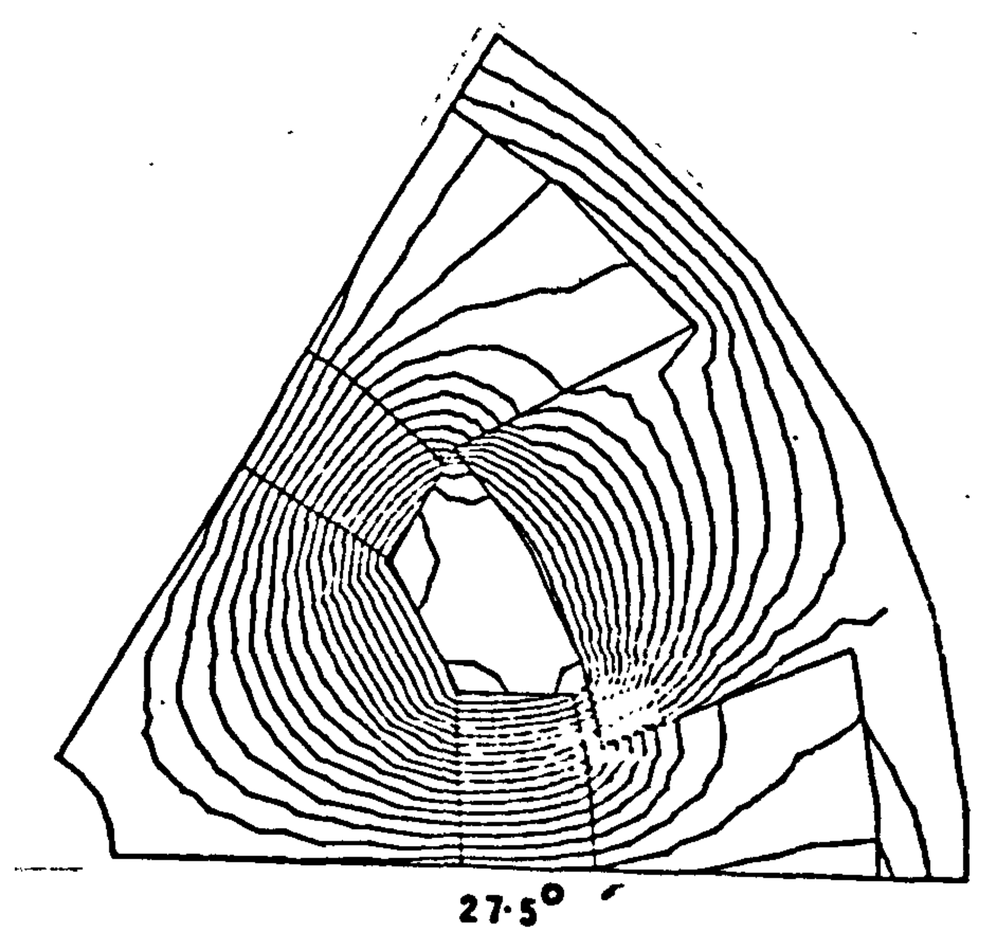

27·5°

Fig 6·37

Variations Of Operating Speed With Turns Factor

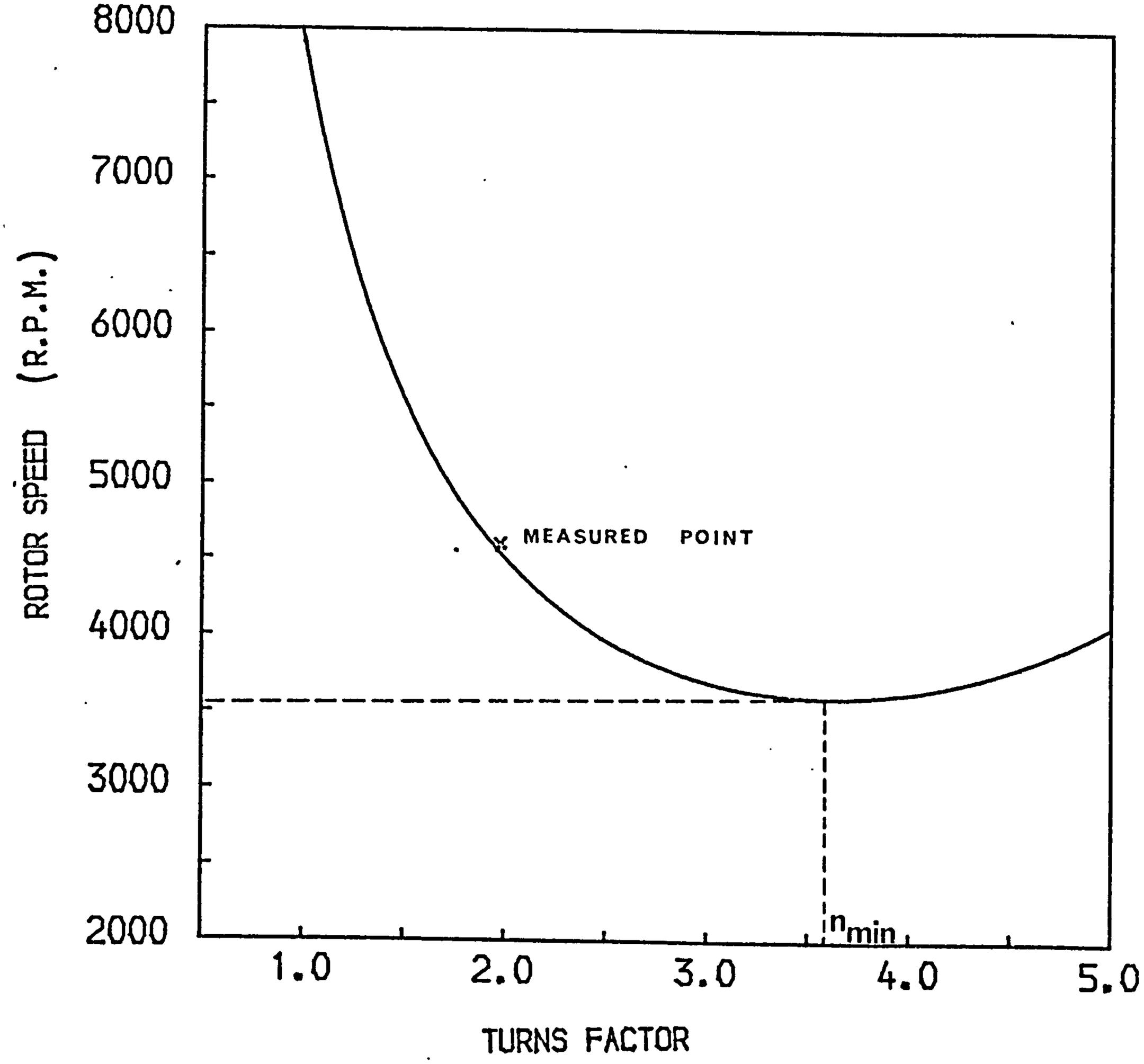

24V 250W Bulb
Supermagloy 10 Rotor With Magnetic Hub

Measured Loss Torque

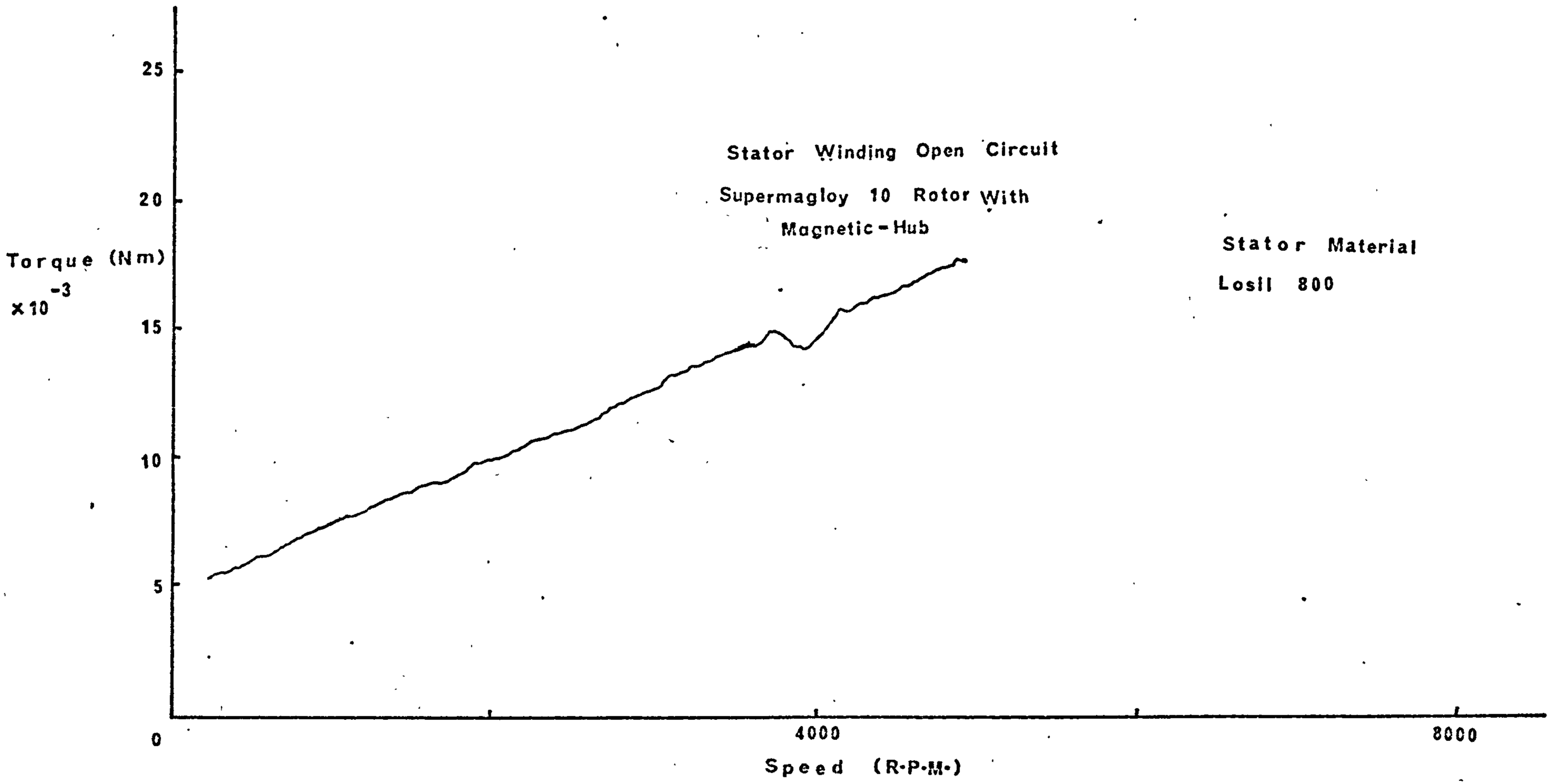

Fig 6.38

Fig 6·39

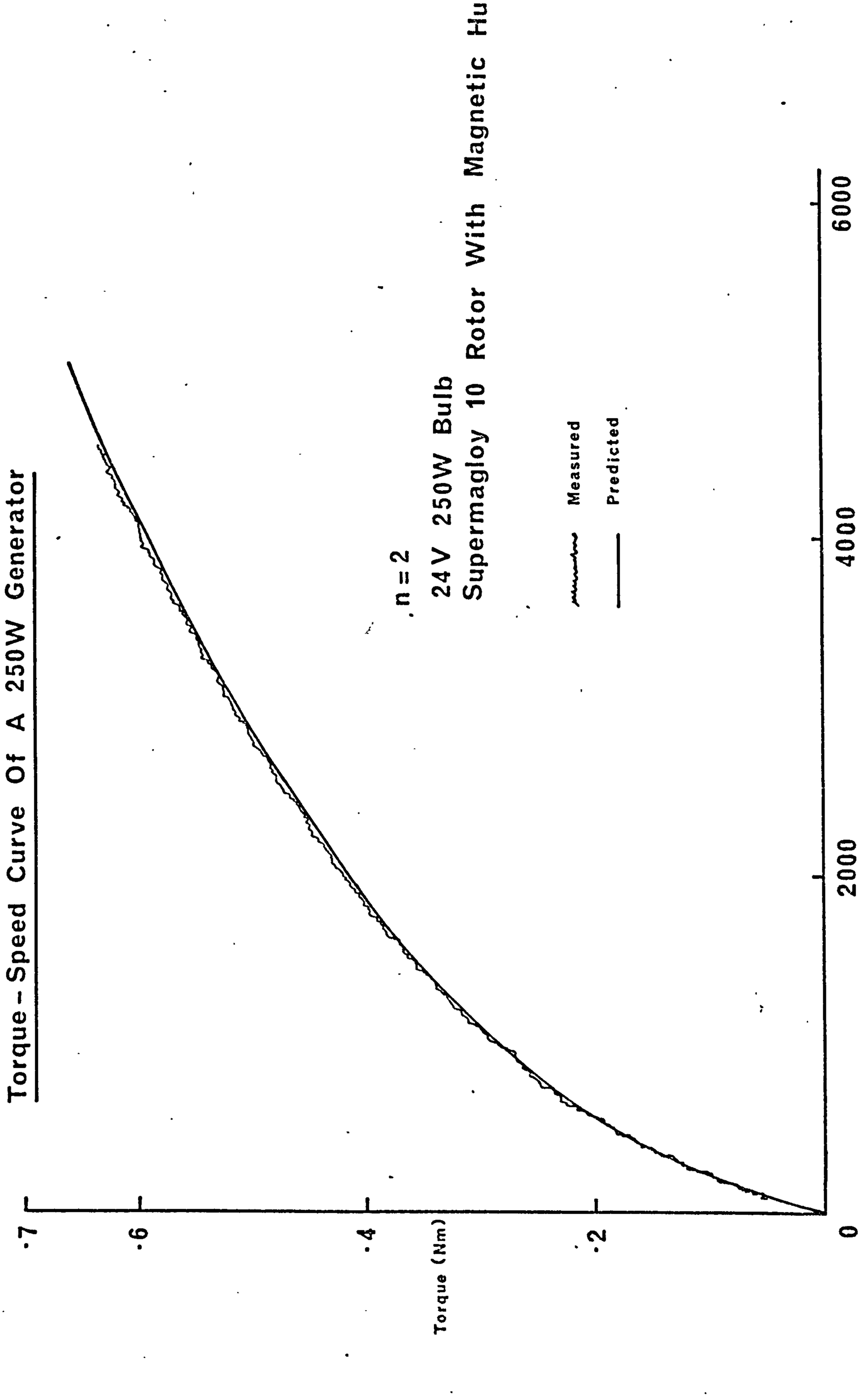
Torque - Speed Curve Of A 250W Generator
n = 2
24V 250W Bulb
Supermagloy 10 Rotor With Magnetic Hub
Measured
Predicted
Torque (Nm)
.7
.6
.4
.2
0
2000
4000
6000
Speed (R.P.M.)

6·40 Coordinates Of A Node

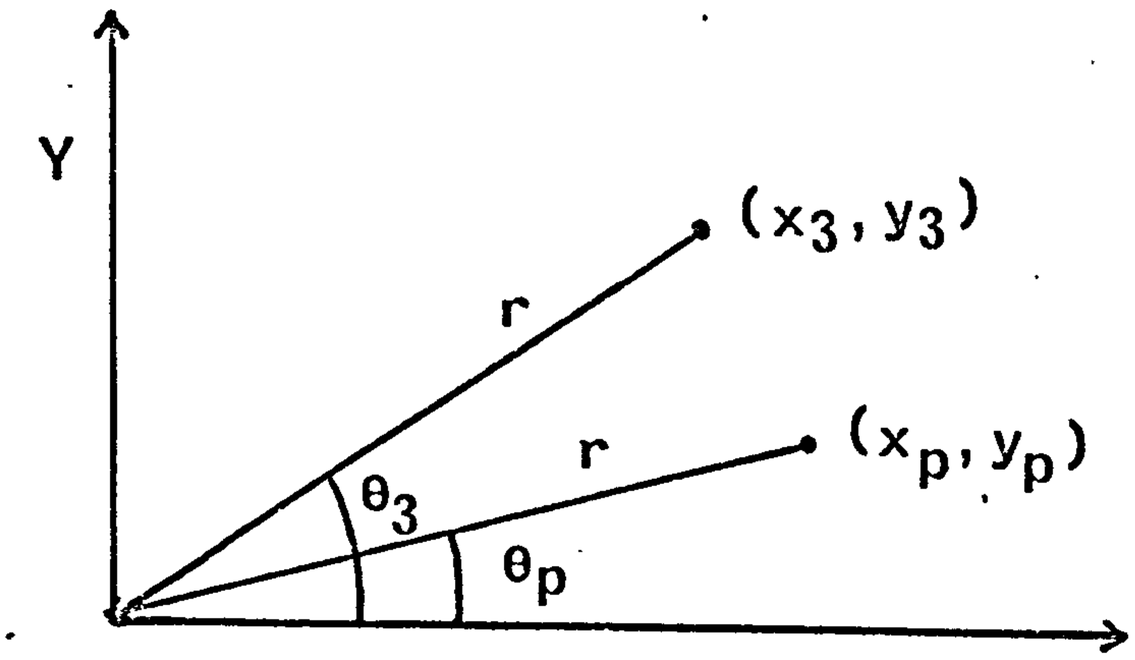

6·41 Finite Element Mesh For p= 6

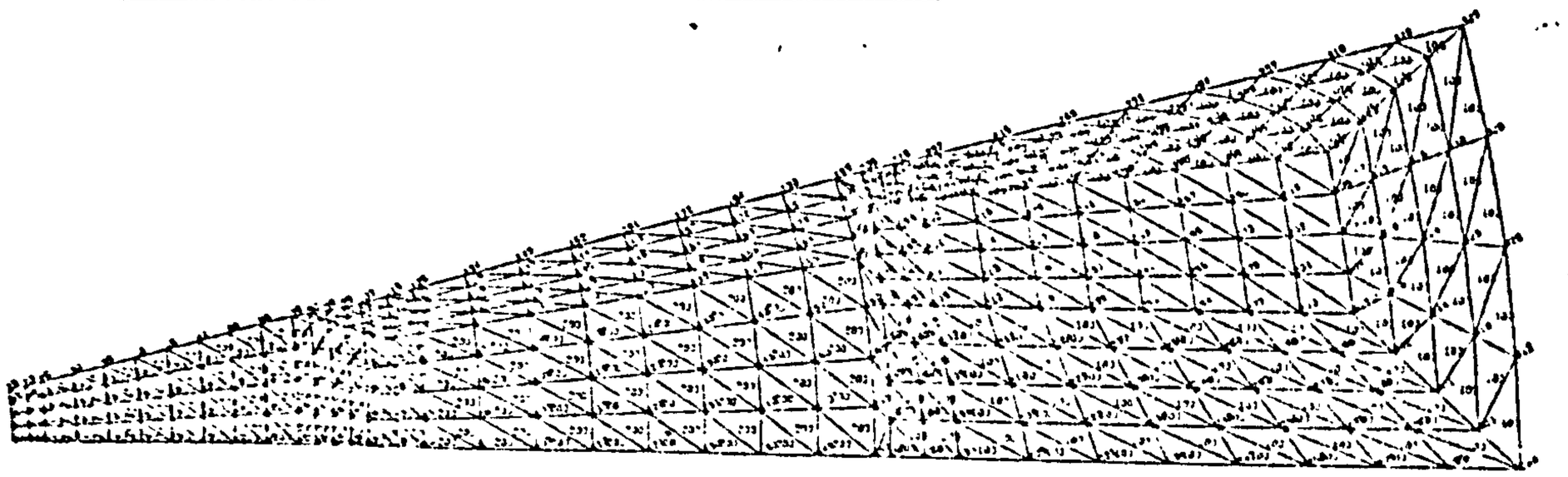

6·42 Variation Of Resistance With Pole Pairs

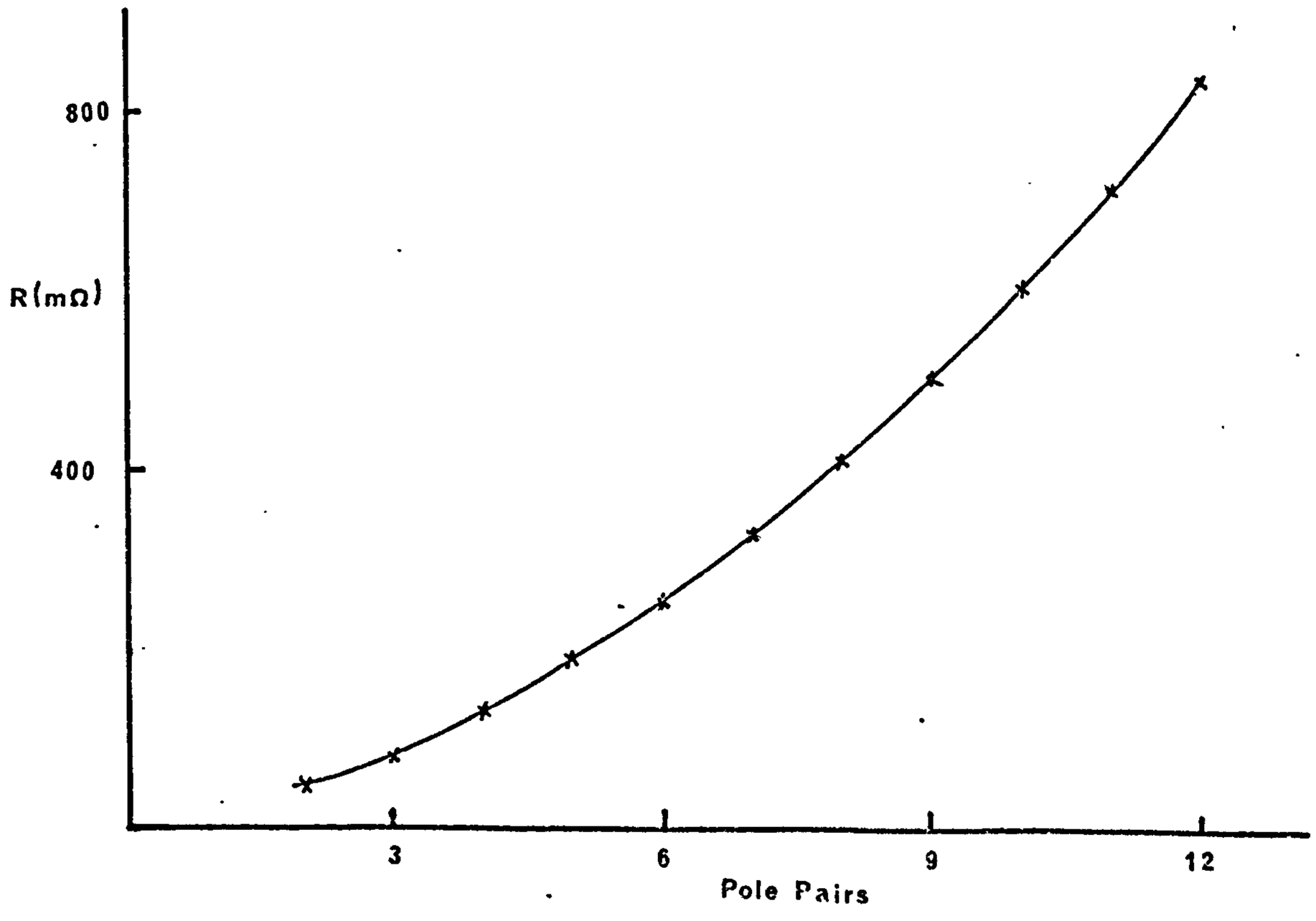

Fig 6·43

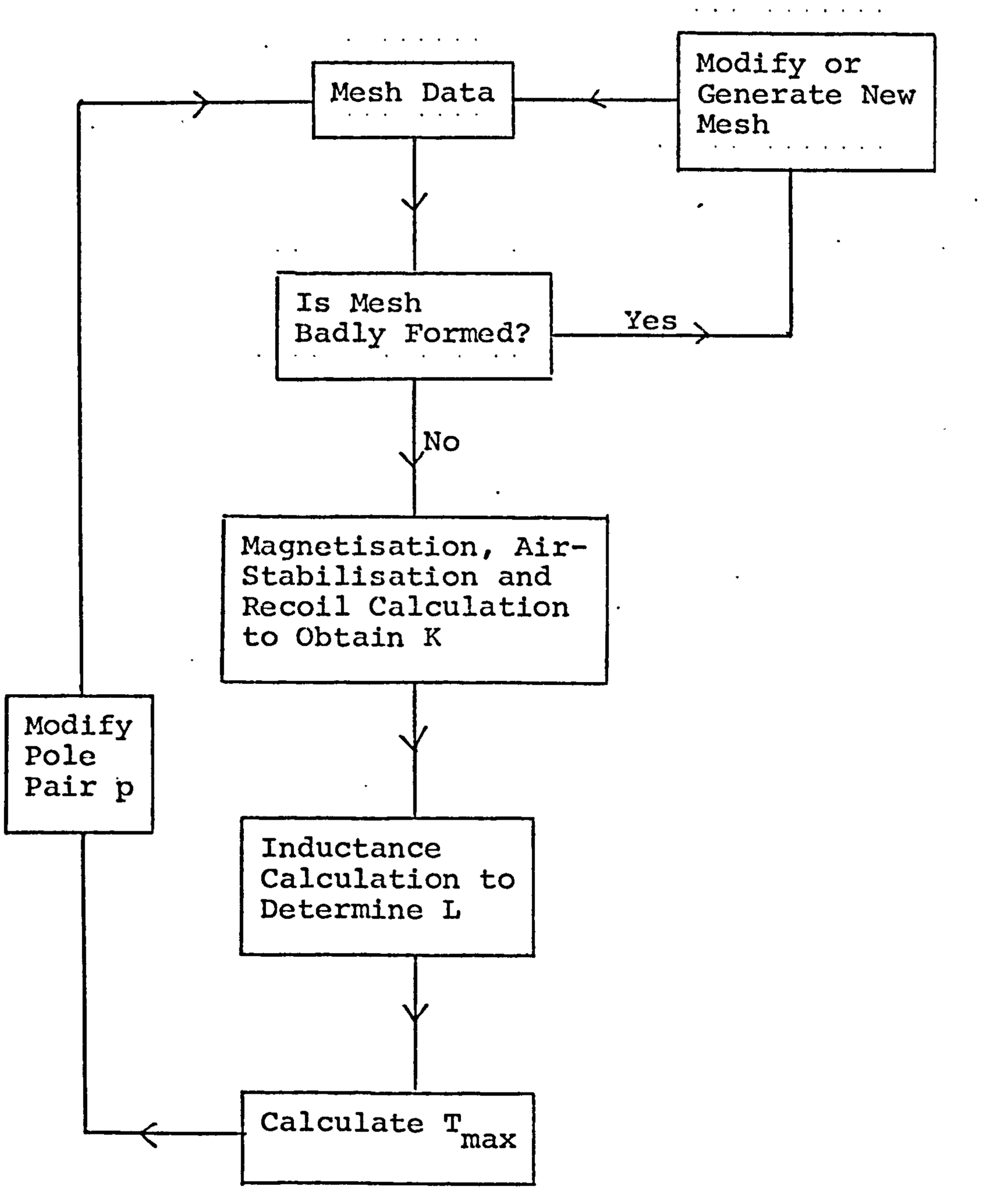

Organization of computer programs to investigate the variations of T_{max} with p

Fig 6·44

Parameters Of Cobalt Generator Having Different Pole Pairs

(a)

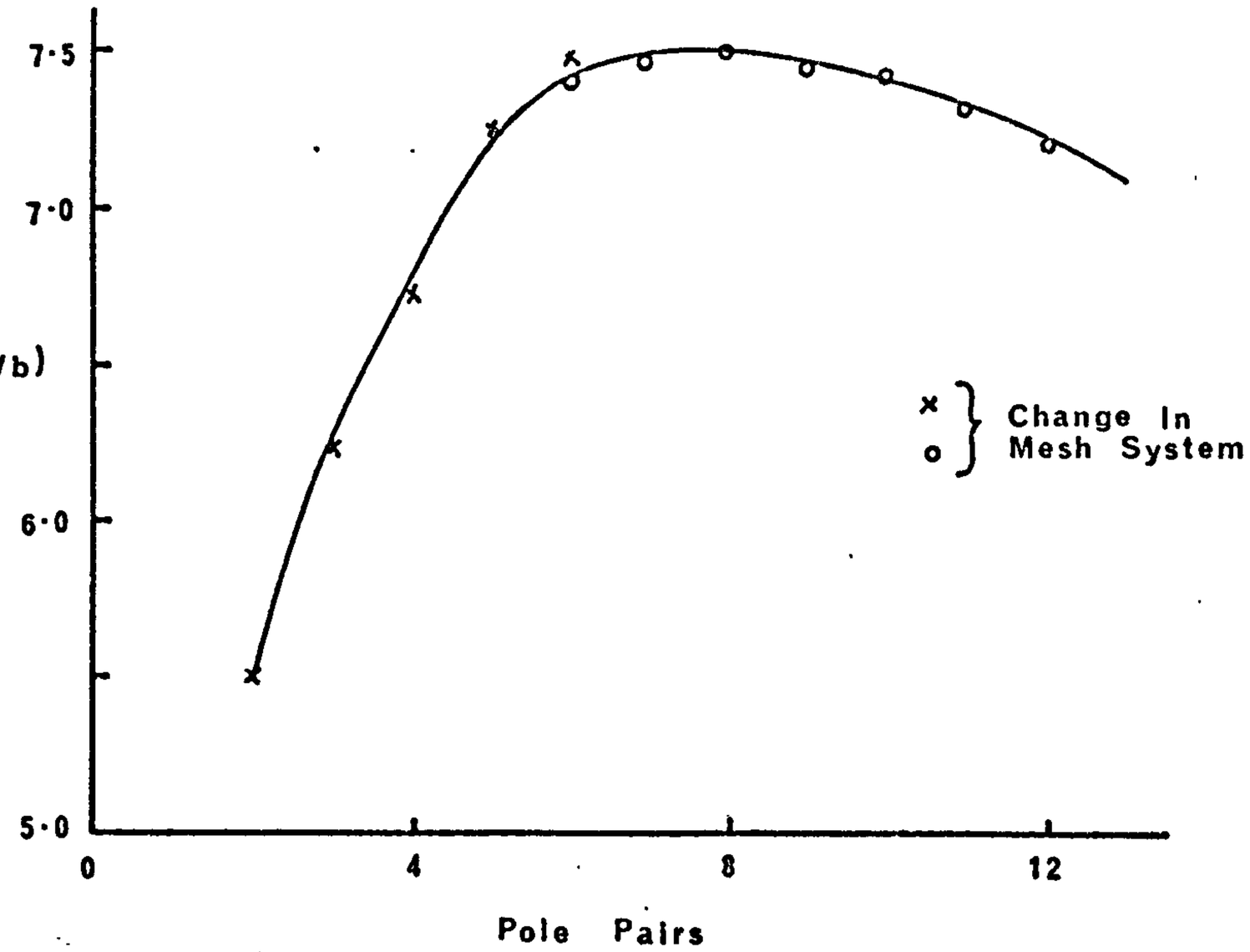

(b)

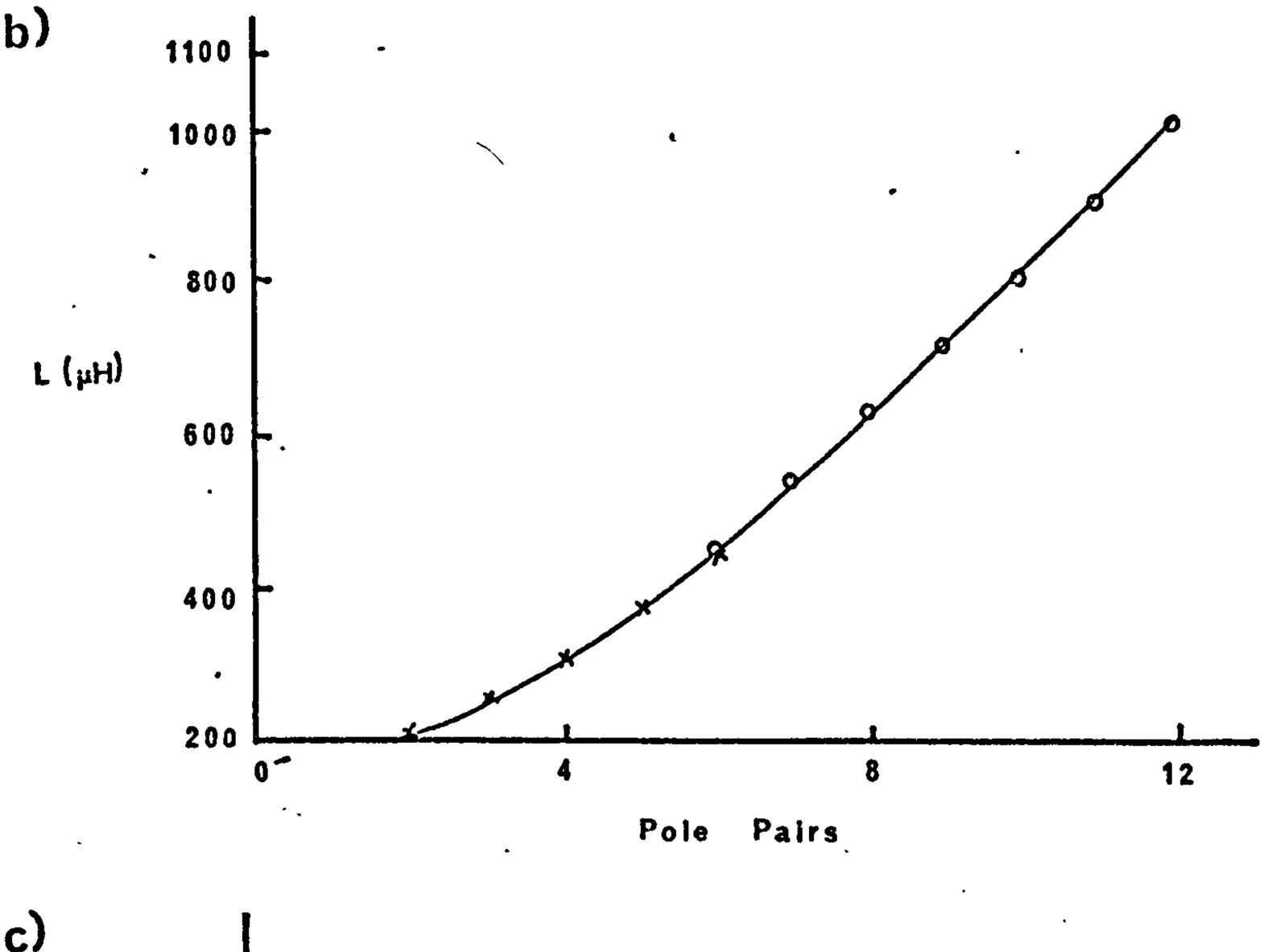

(c)

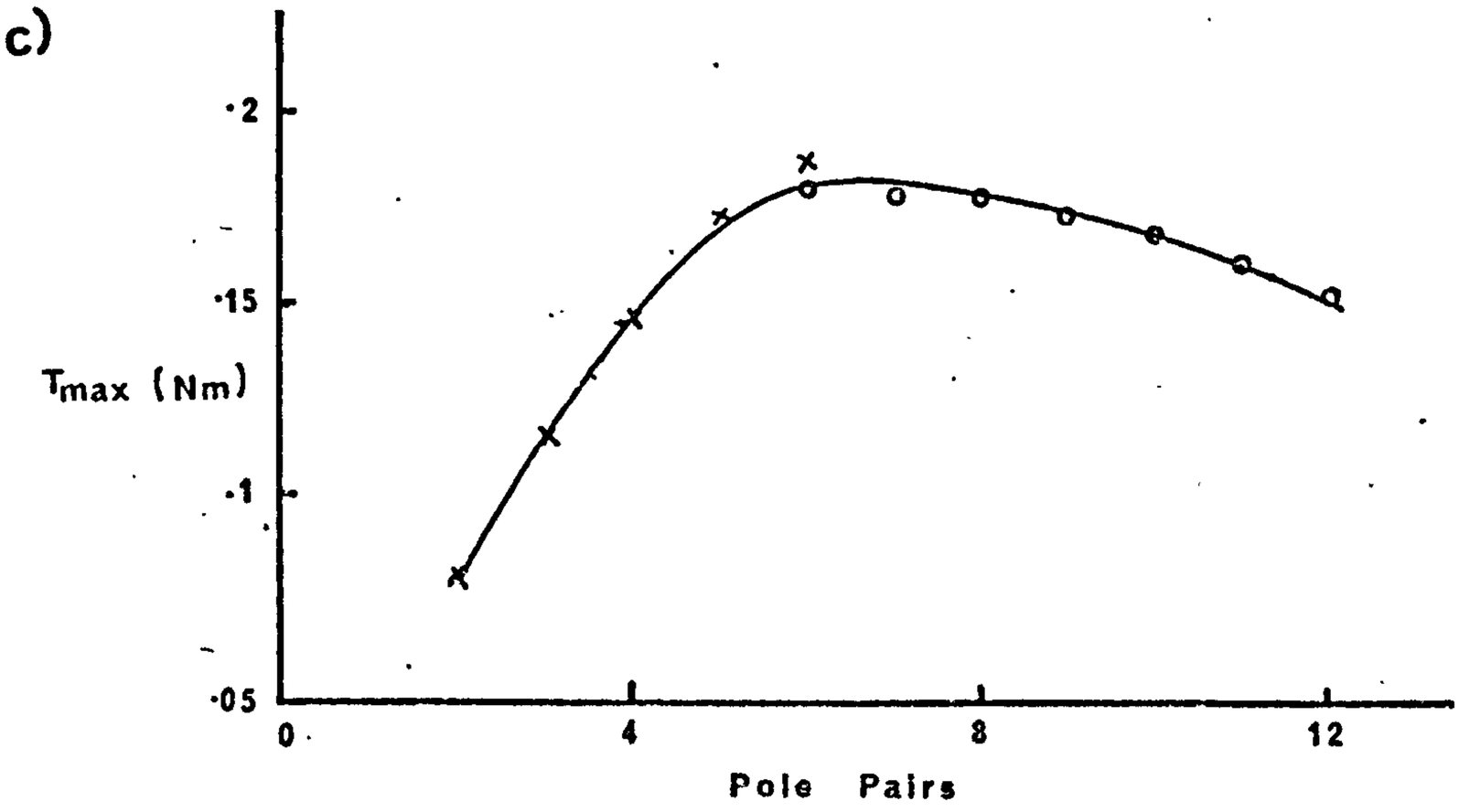

Fig 6·45

Flux Plots Of Cobalt Generator Having Different Pole Numbers

(a) p= 6

Magnetisation

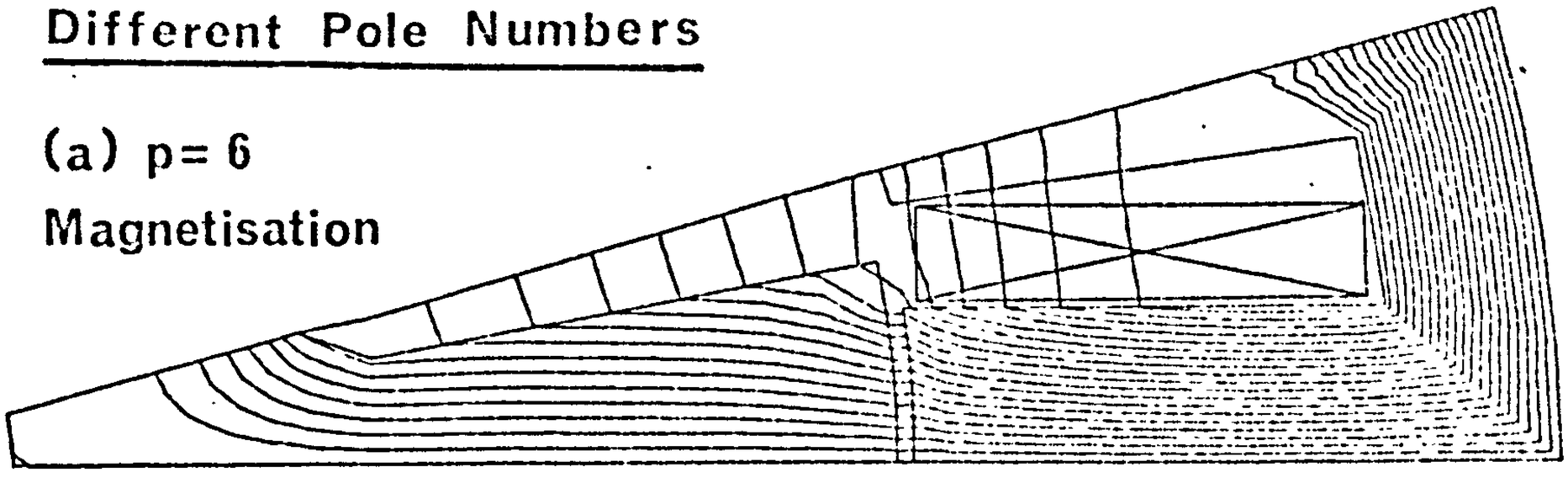

Air-Stabilisation

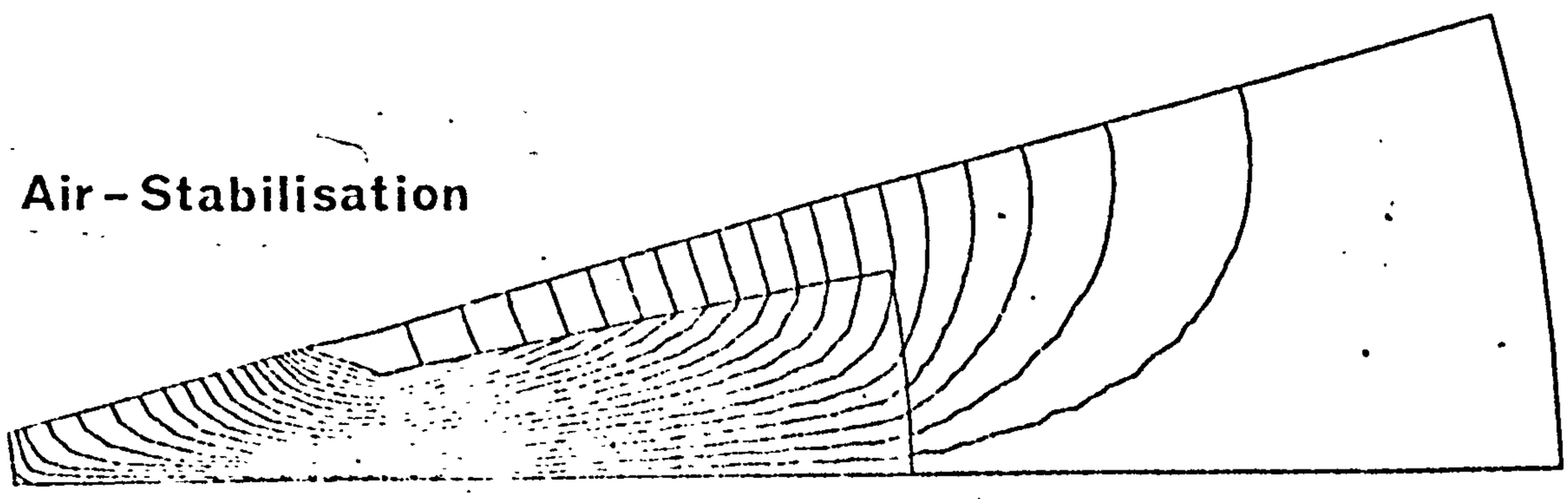

Recoil Operation

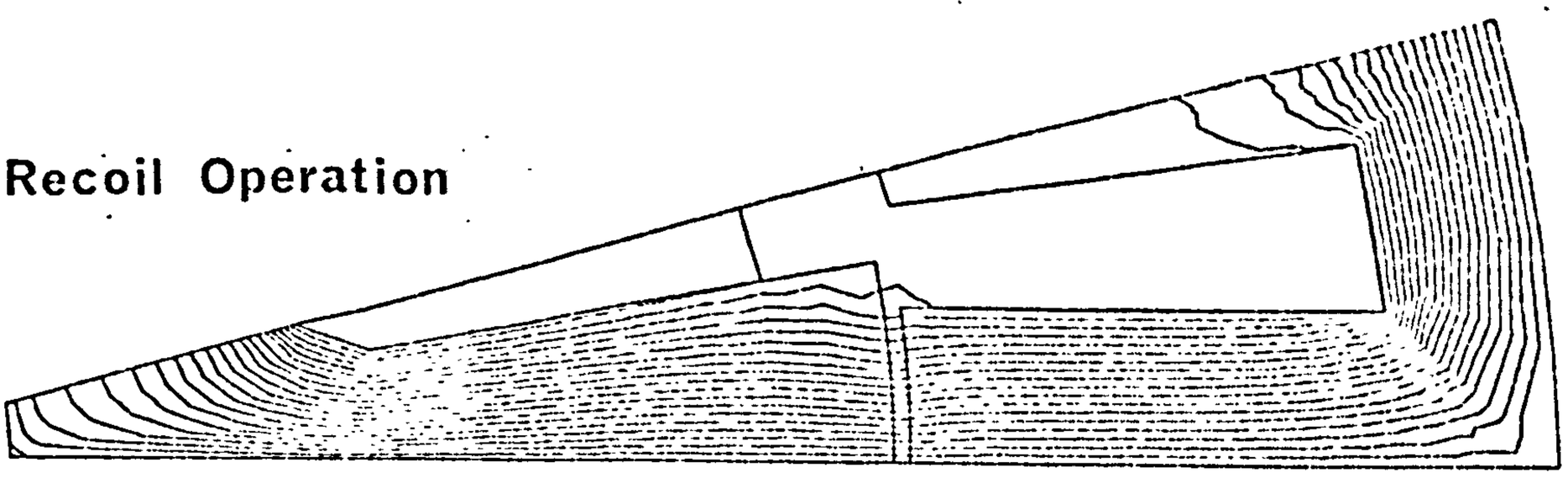

(b) p = 9

Magnetisation

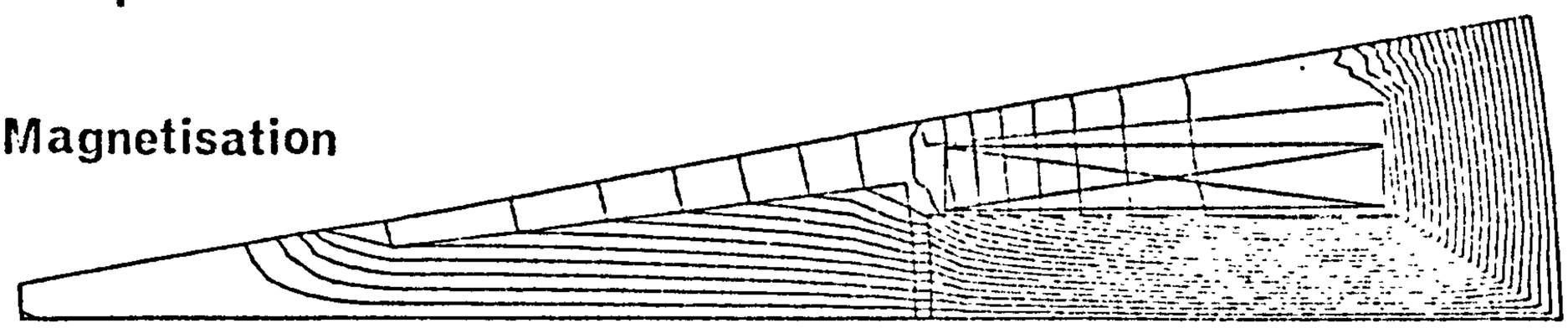

Air-Stabilisation

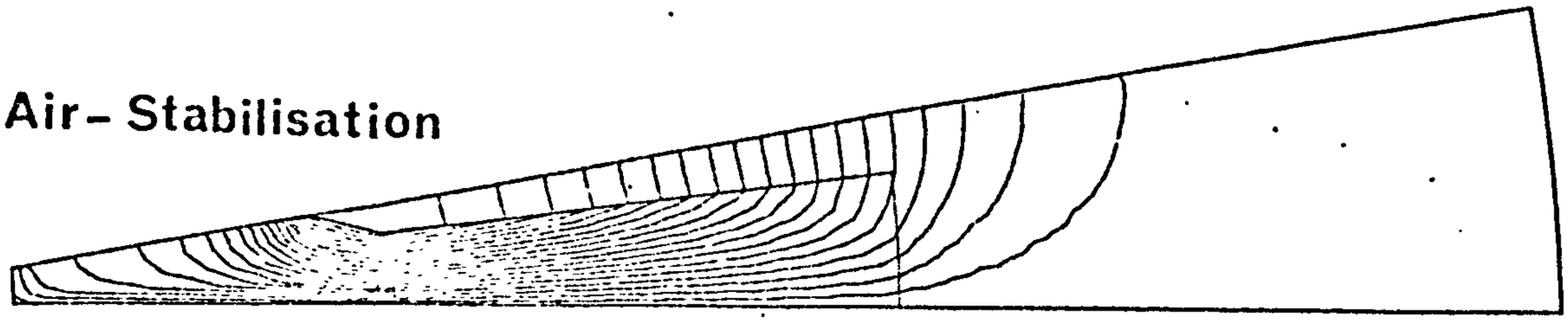

Recoil Operation

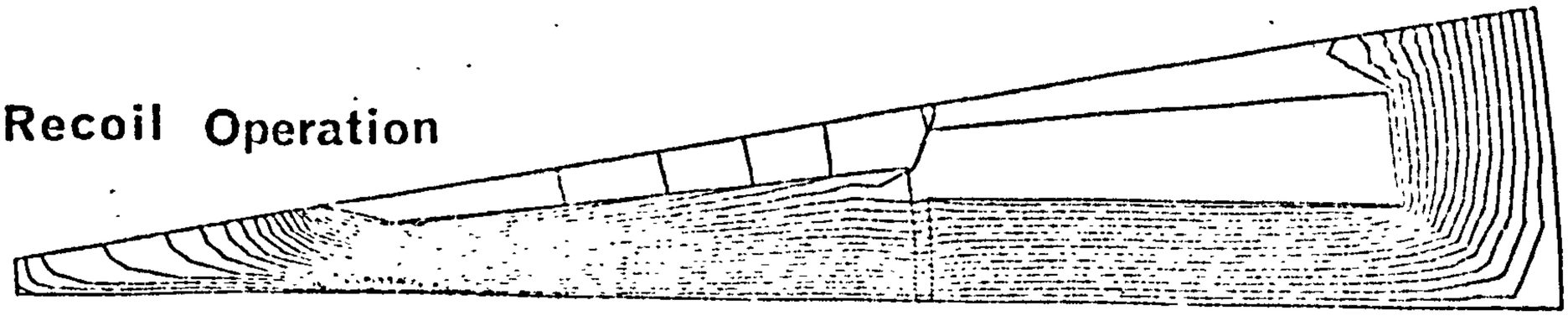

Fig 6·46

Variation Of N_{min} With Pole Pairs

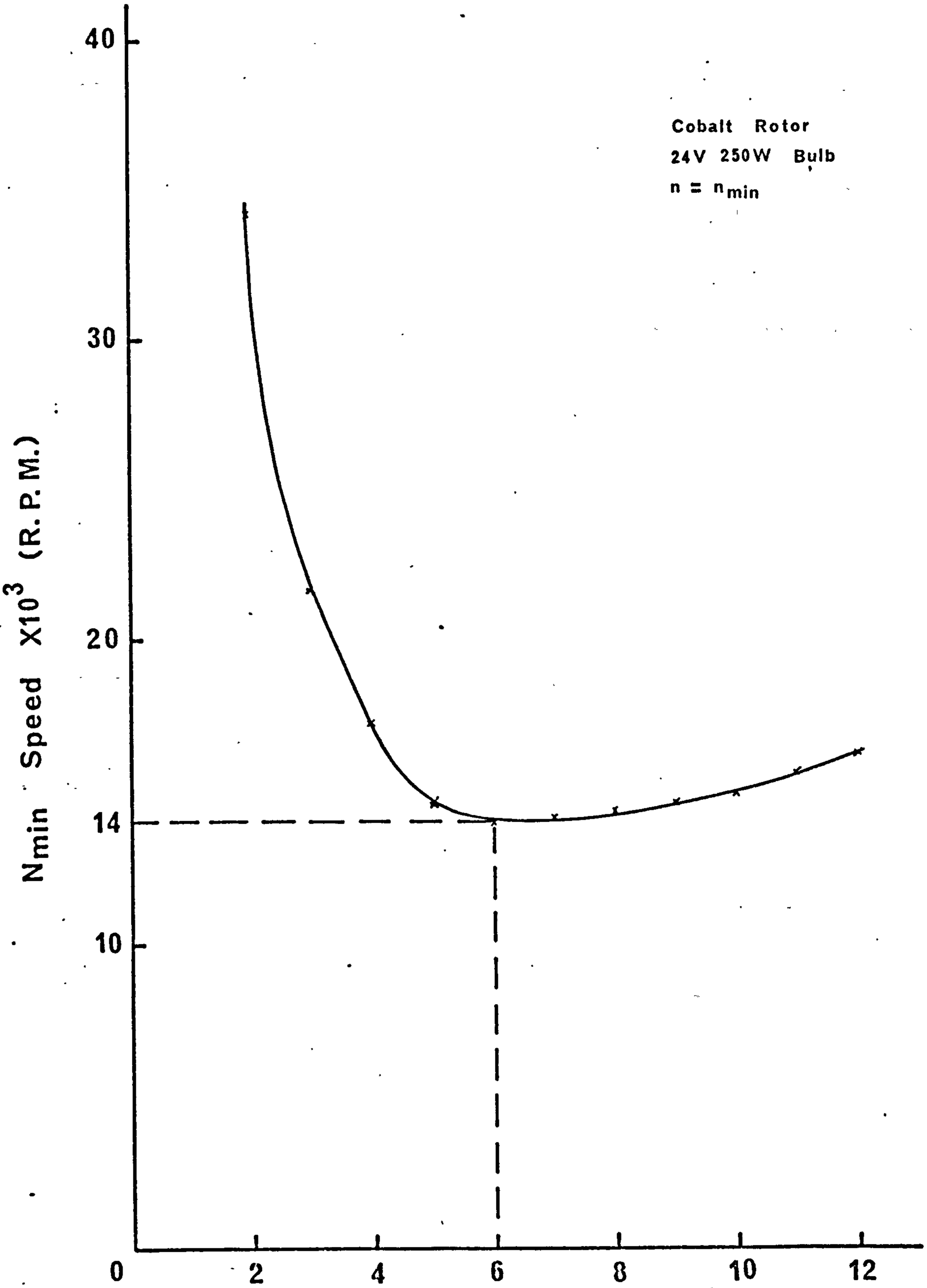

Parameters Of Supermagloy 10 Generator Having Different Pole Pairs

(a)

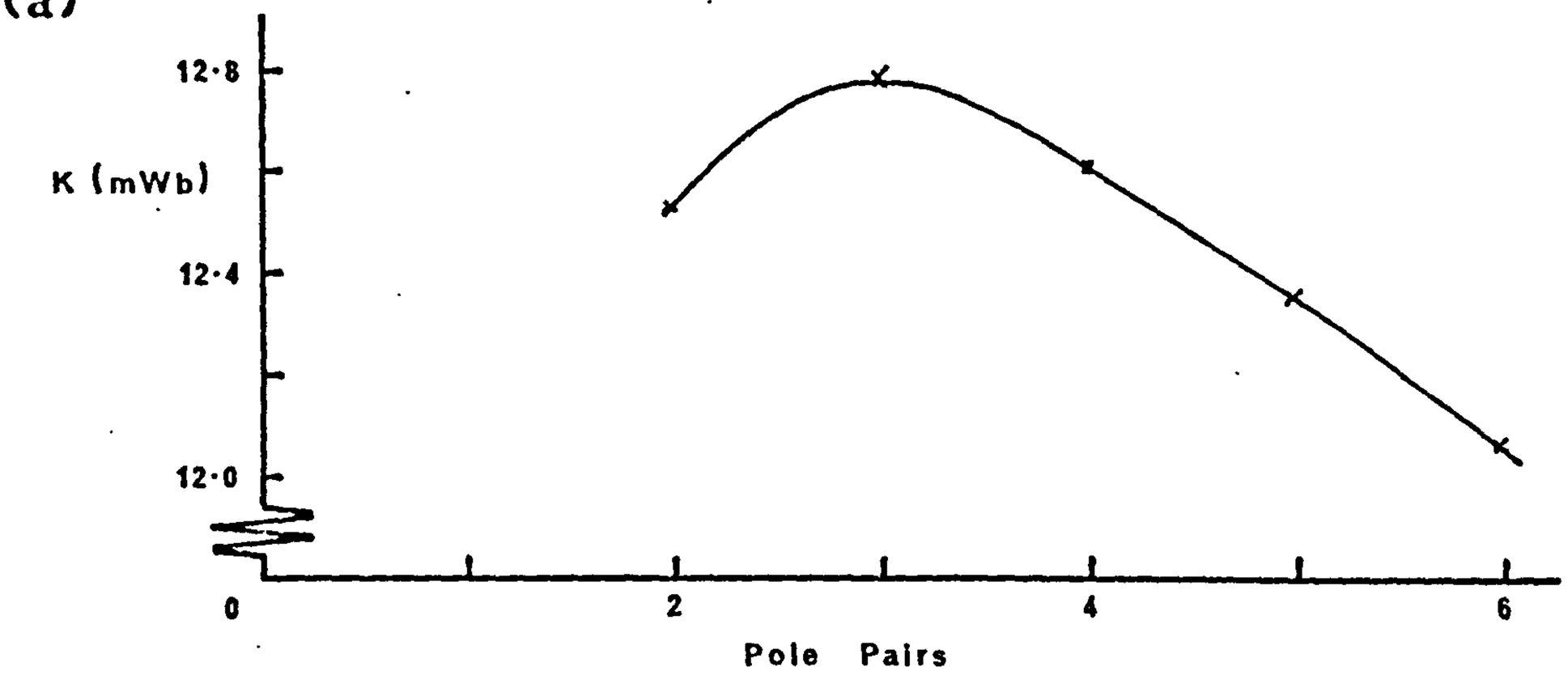

(b)

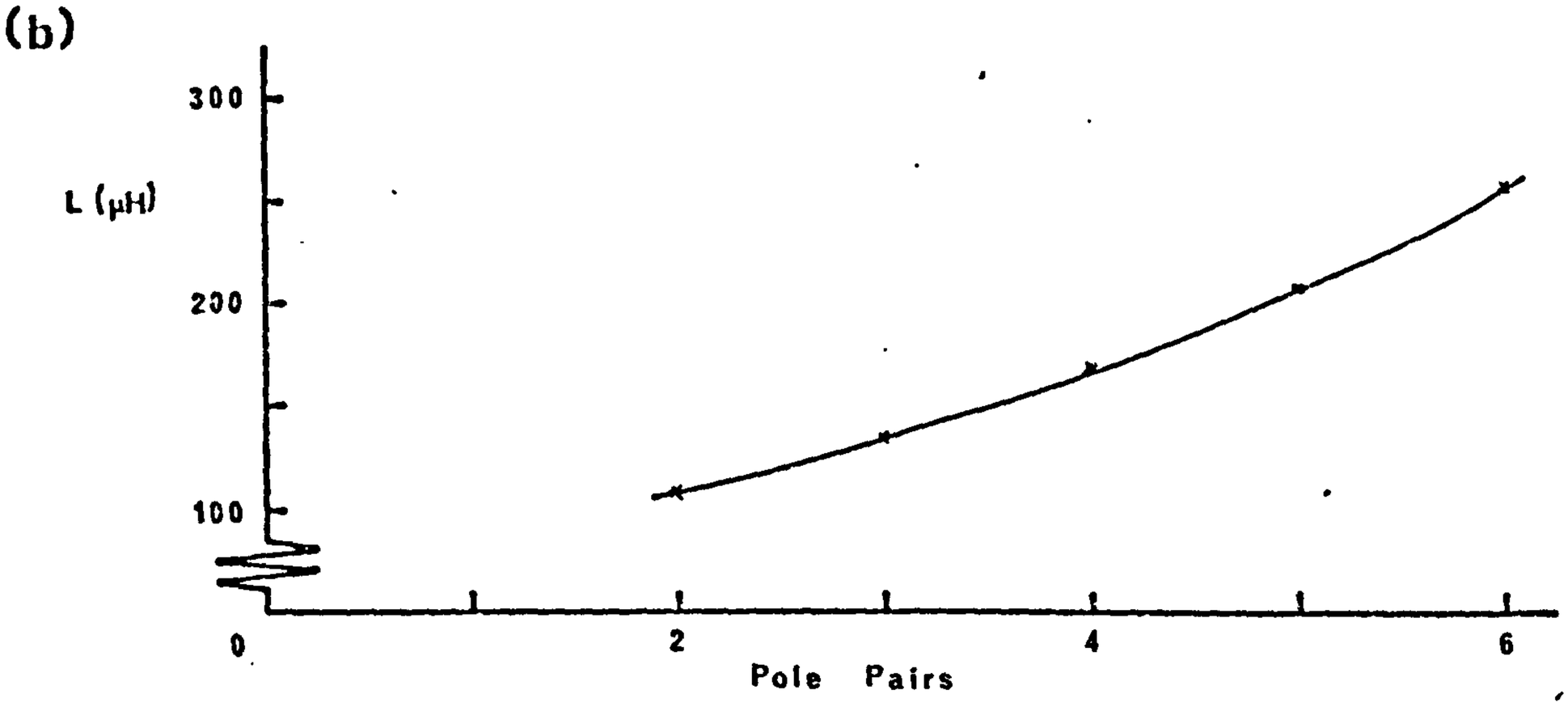

(c)

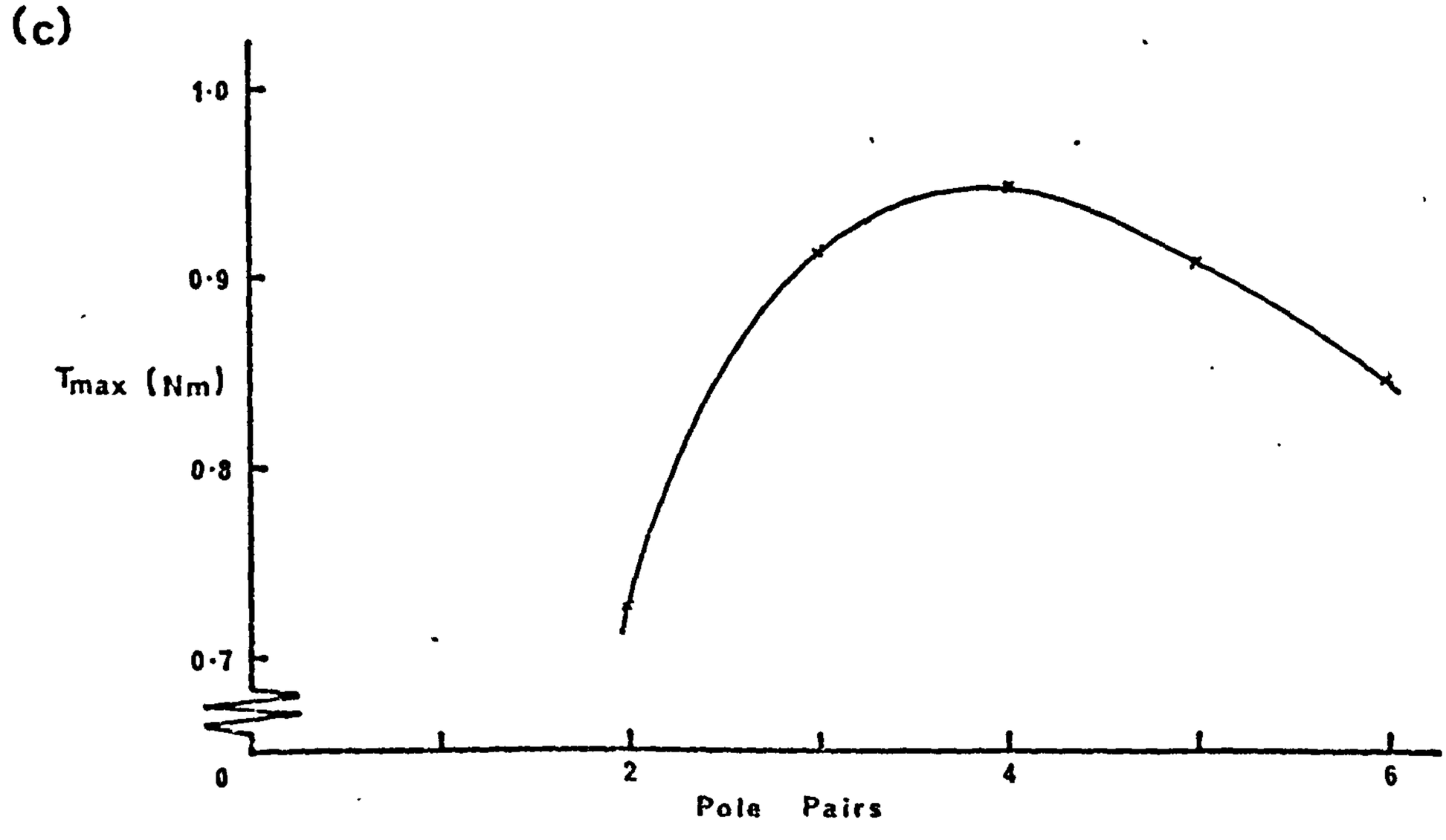

Flux Plots Of Supermagloy 10 Generator Having Different Pole Numbers

(a) p = 4

Air-Stabilisation

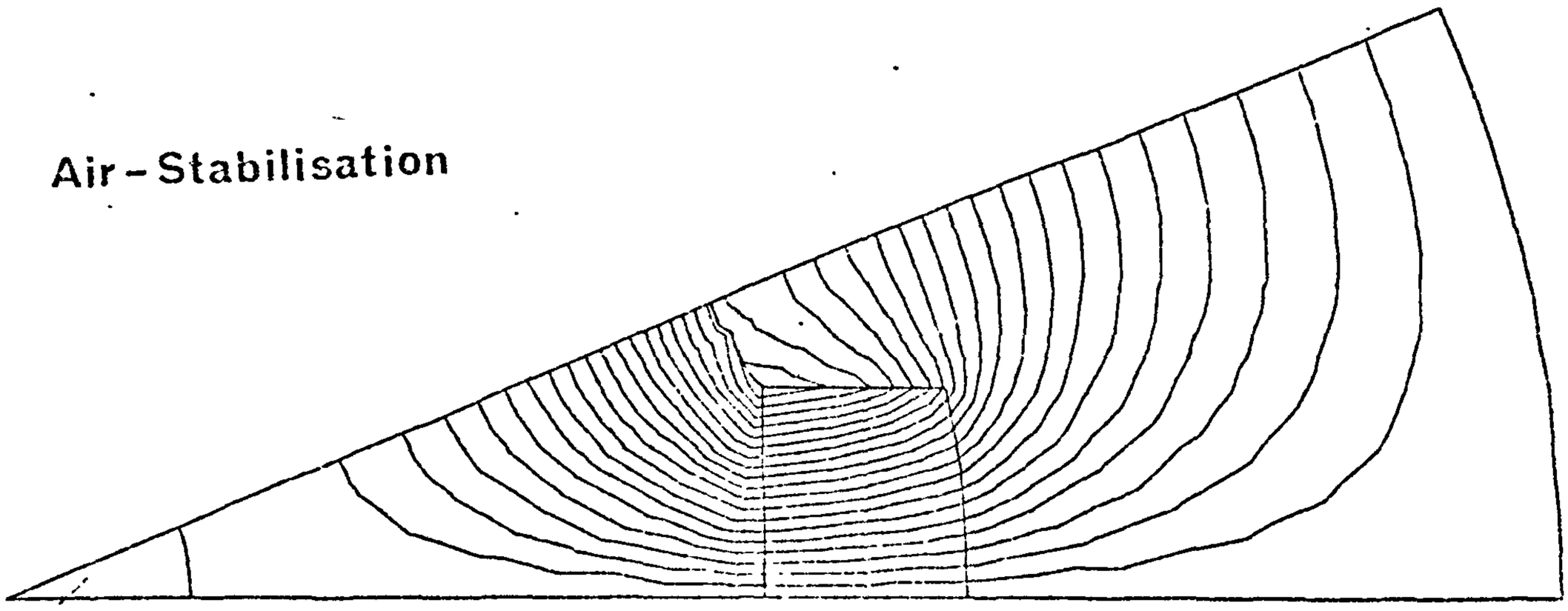

Recoil Operation

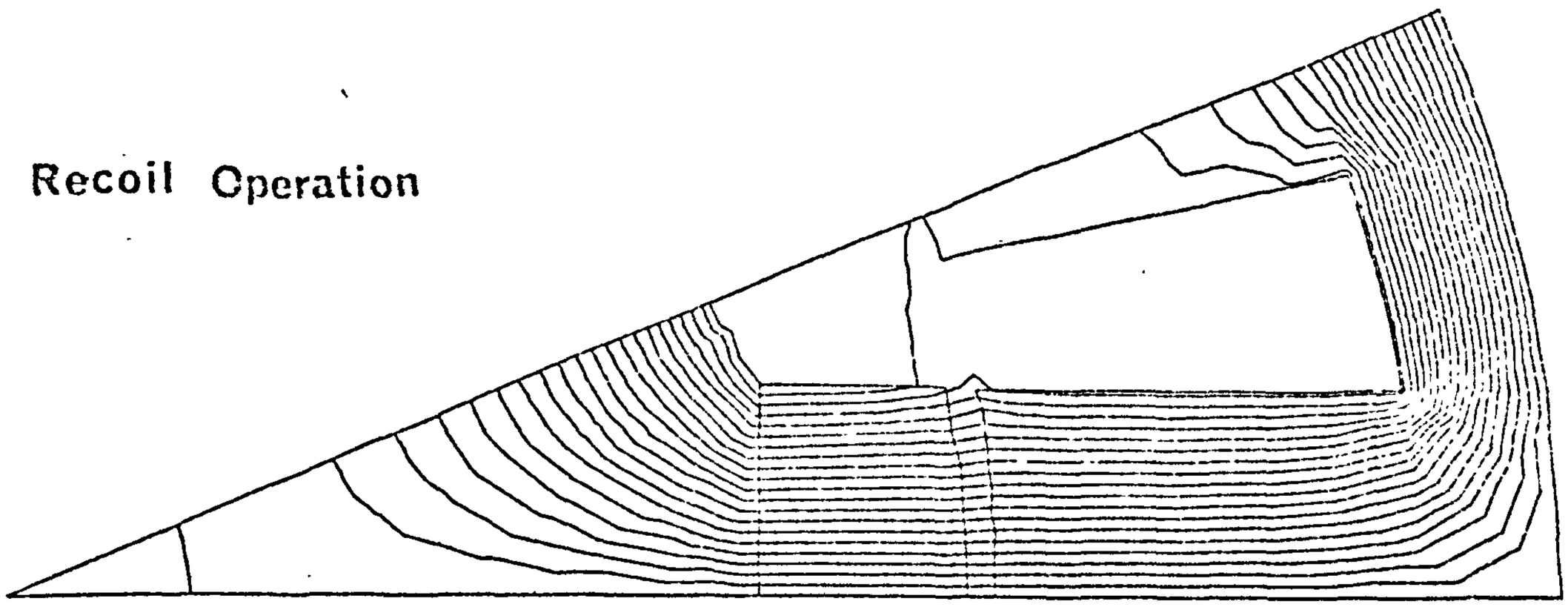

(b) p= 6

Air-Stabilisation

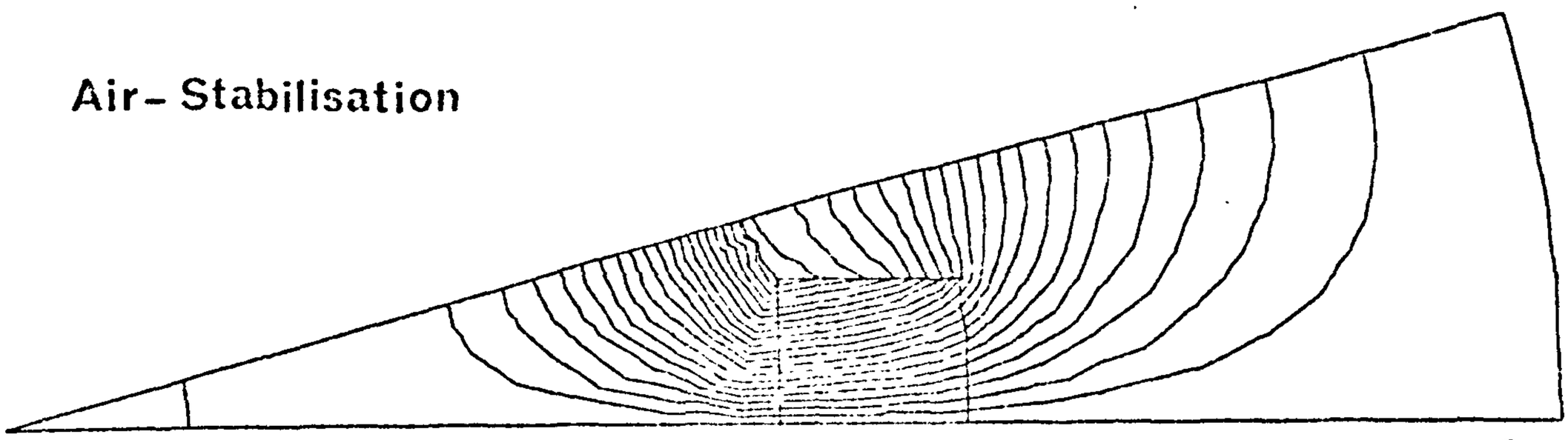

Recoil Operation

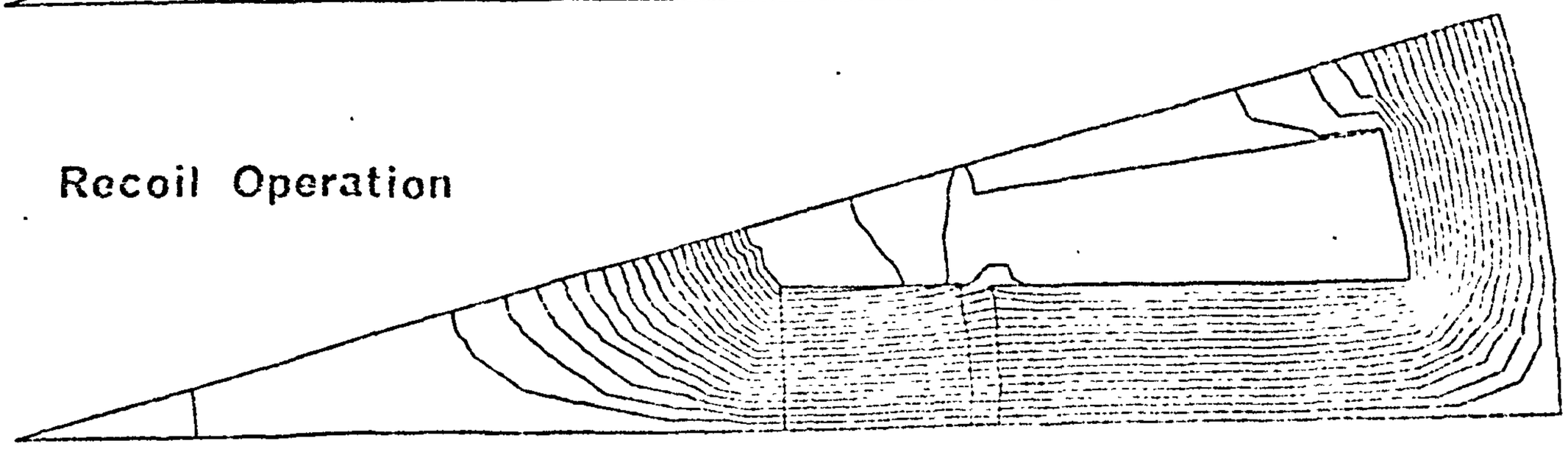

Fig 6·49

Variation Of N_{min} With Pole Pairs

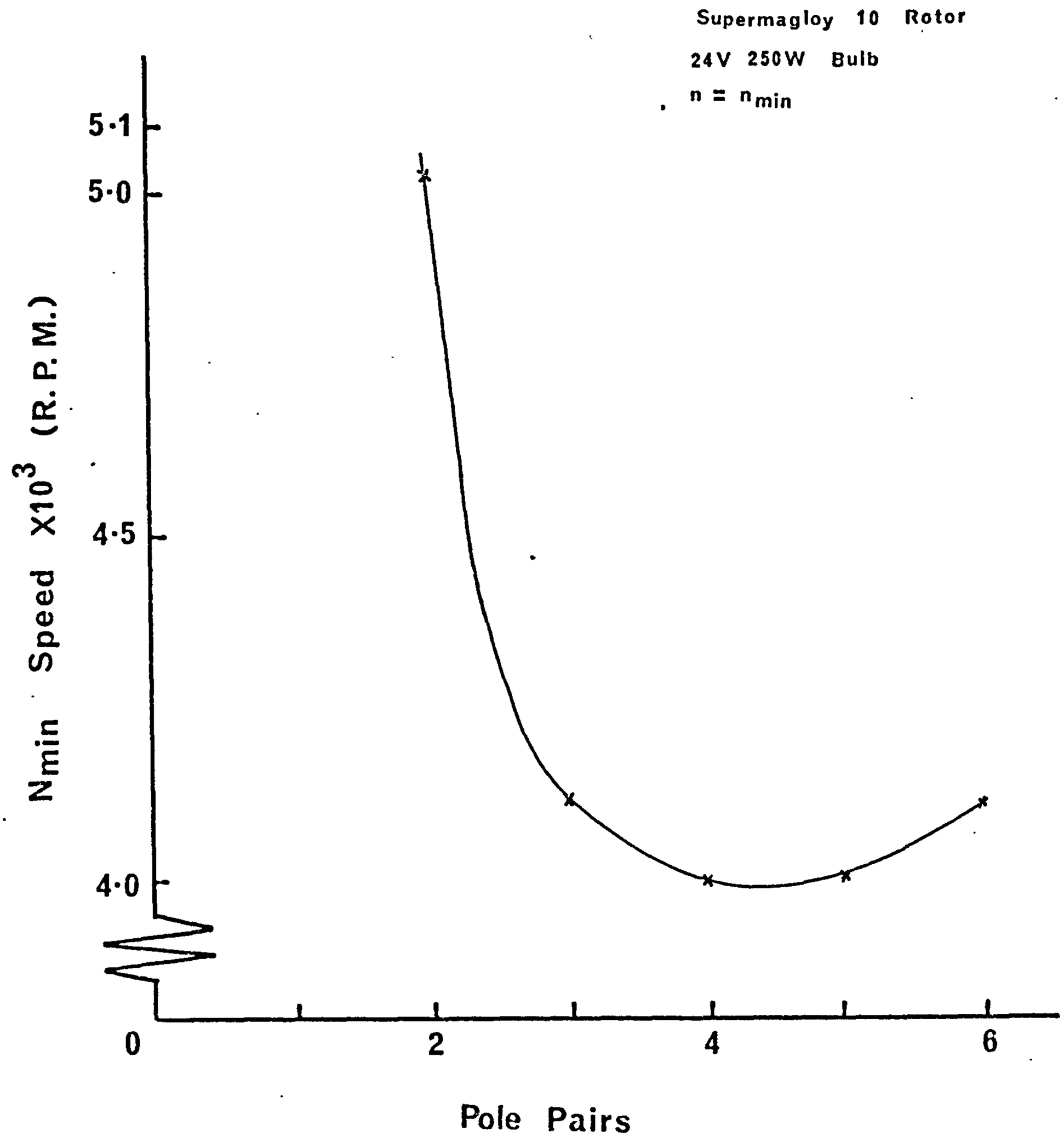

Torque-Speed Curve Of A 250W Generator Having A Supermagloy 10 Rotor With Magnetic Hub

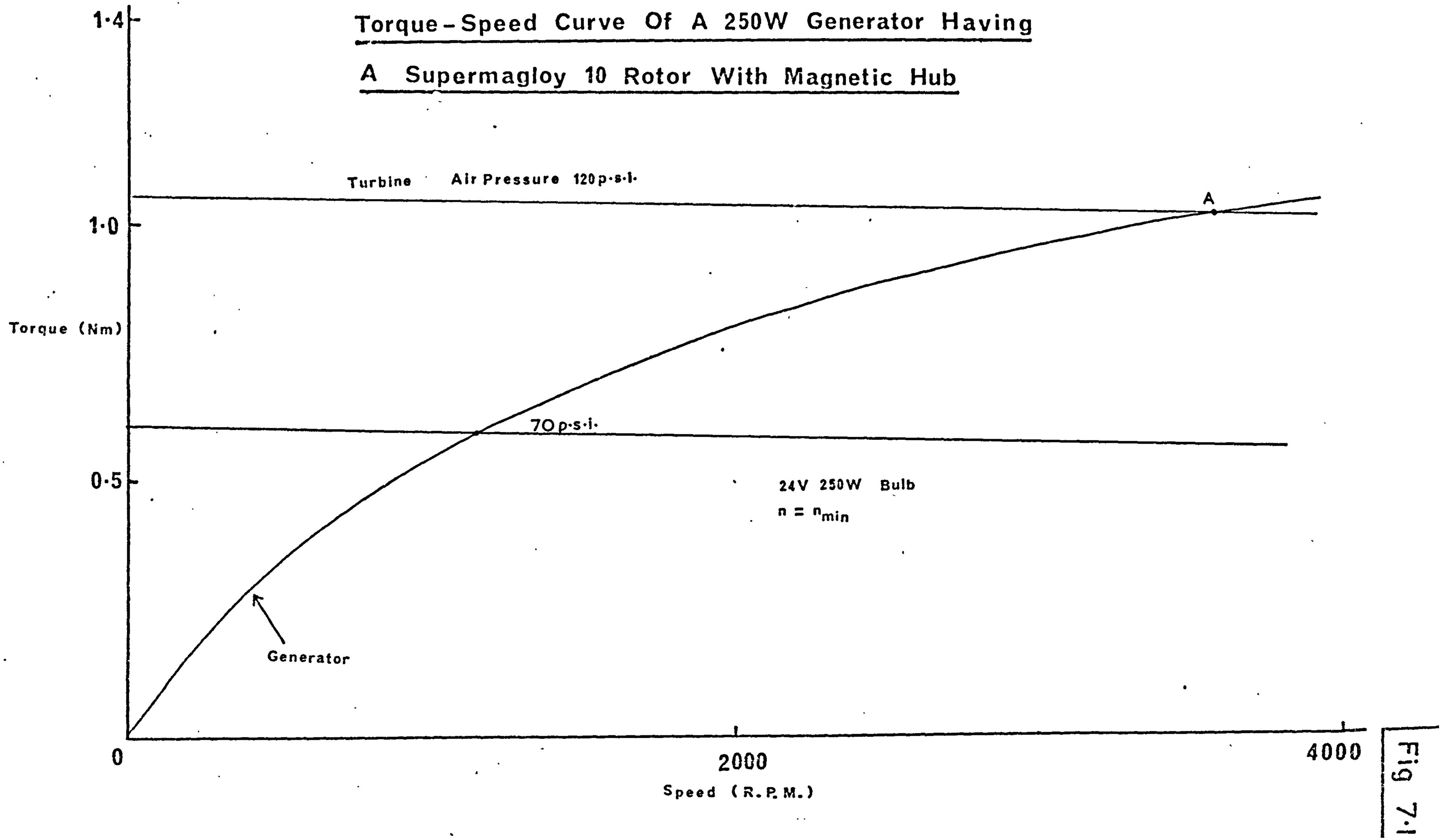

Fig 7.1

Turbine Torque-speed Characteristics

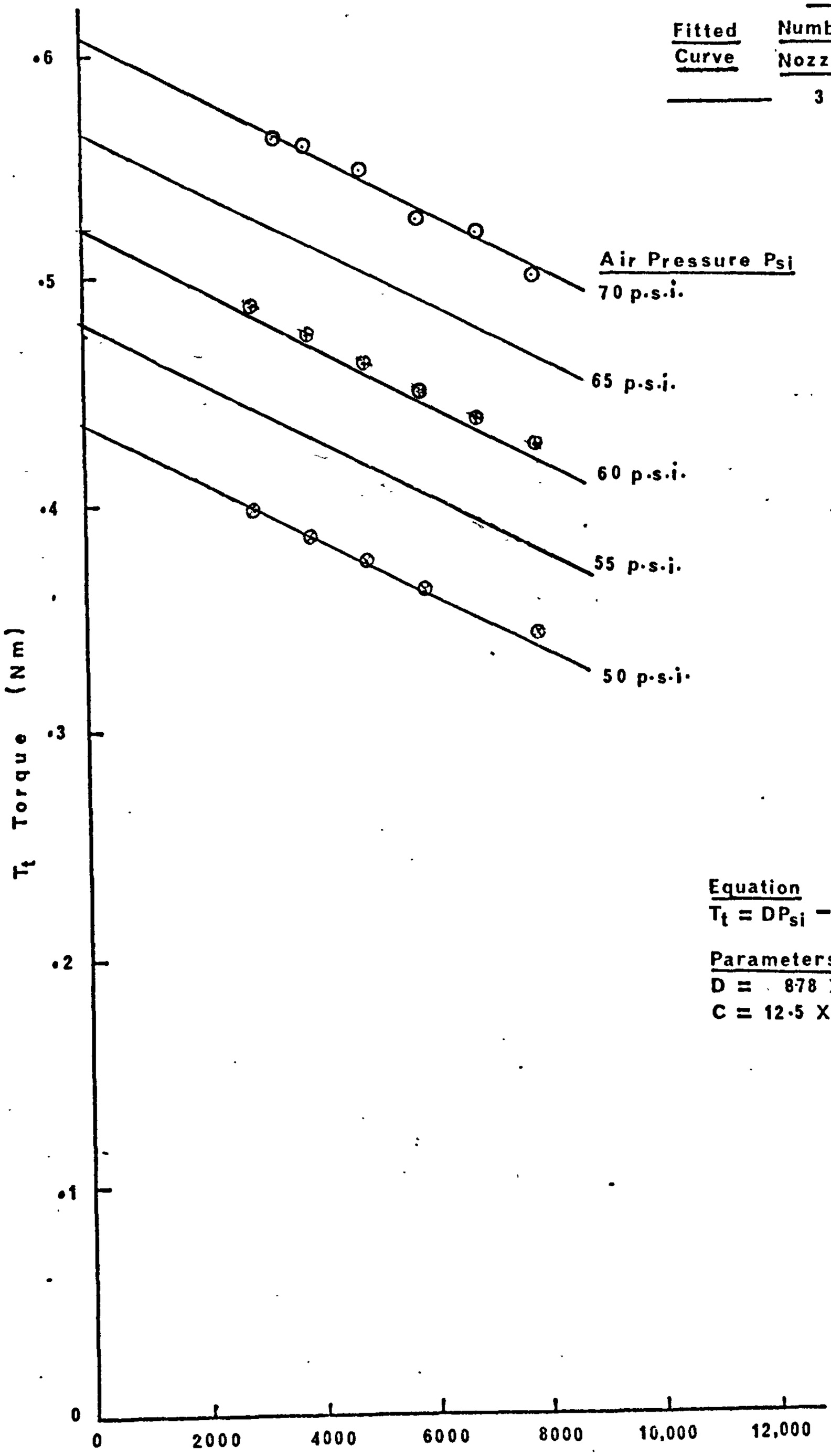

Power - Speed Characteristics Of Turbine

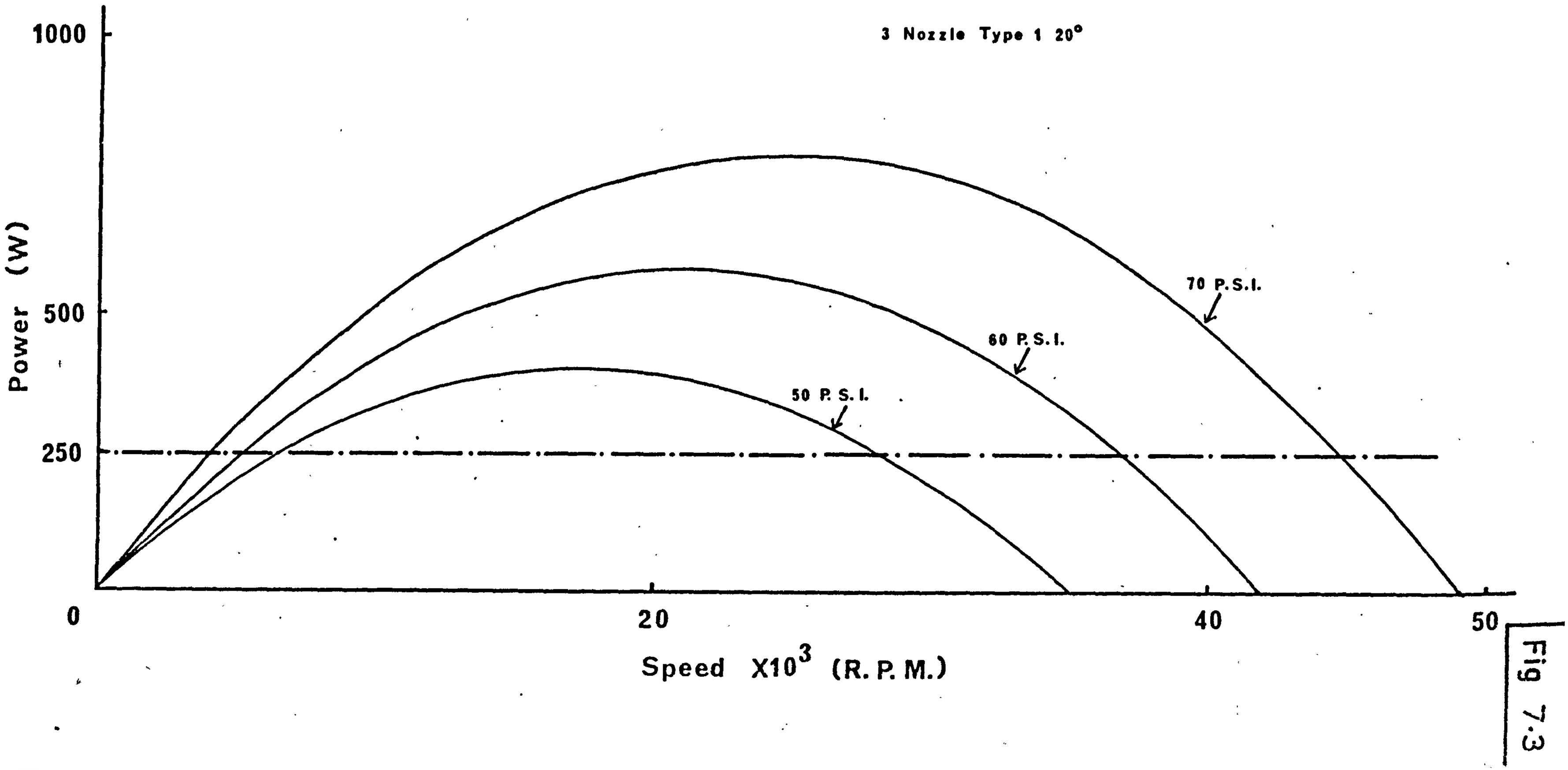

Fig 7.3

Fig 7·4

Variations Of Operating Speed With Turns Factor

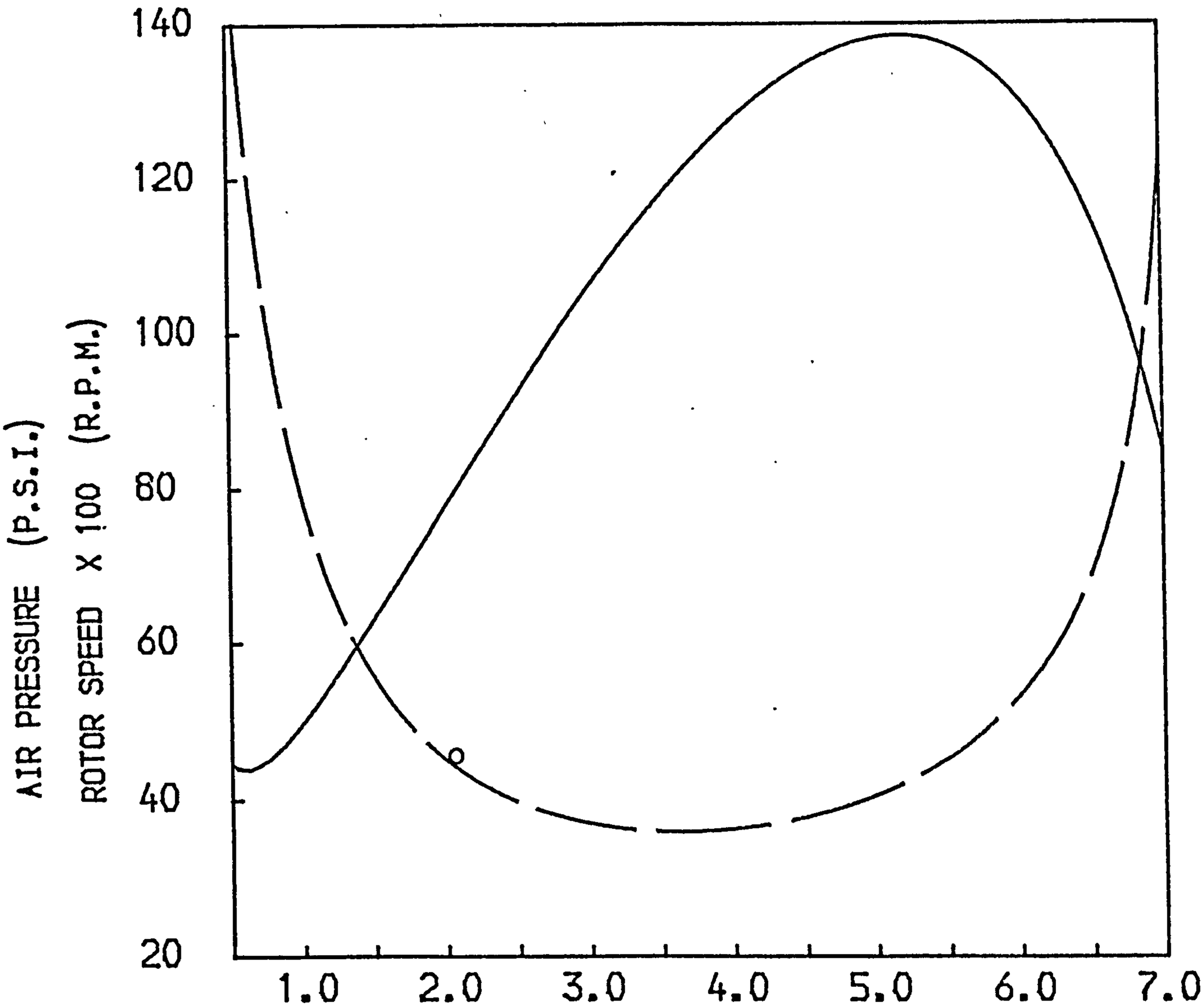

24V 250W Bulb

Supermagloy 10 Rotor With Magnetic Hub

	Predicted	Measured
Speed	— —	o
Air Pressure	———	

Fig 7·5(a)

Fig 7·5(b)

(a) Variations Of Turns Factor With Speed

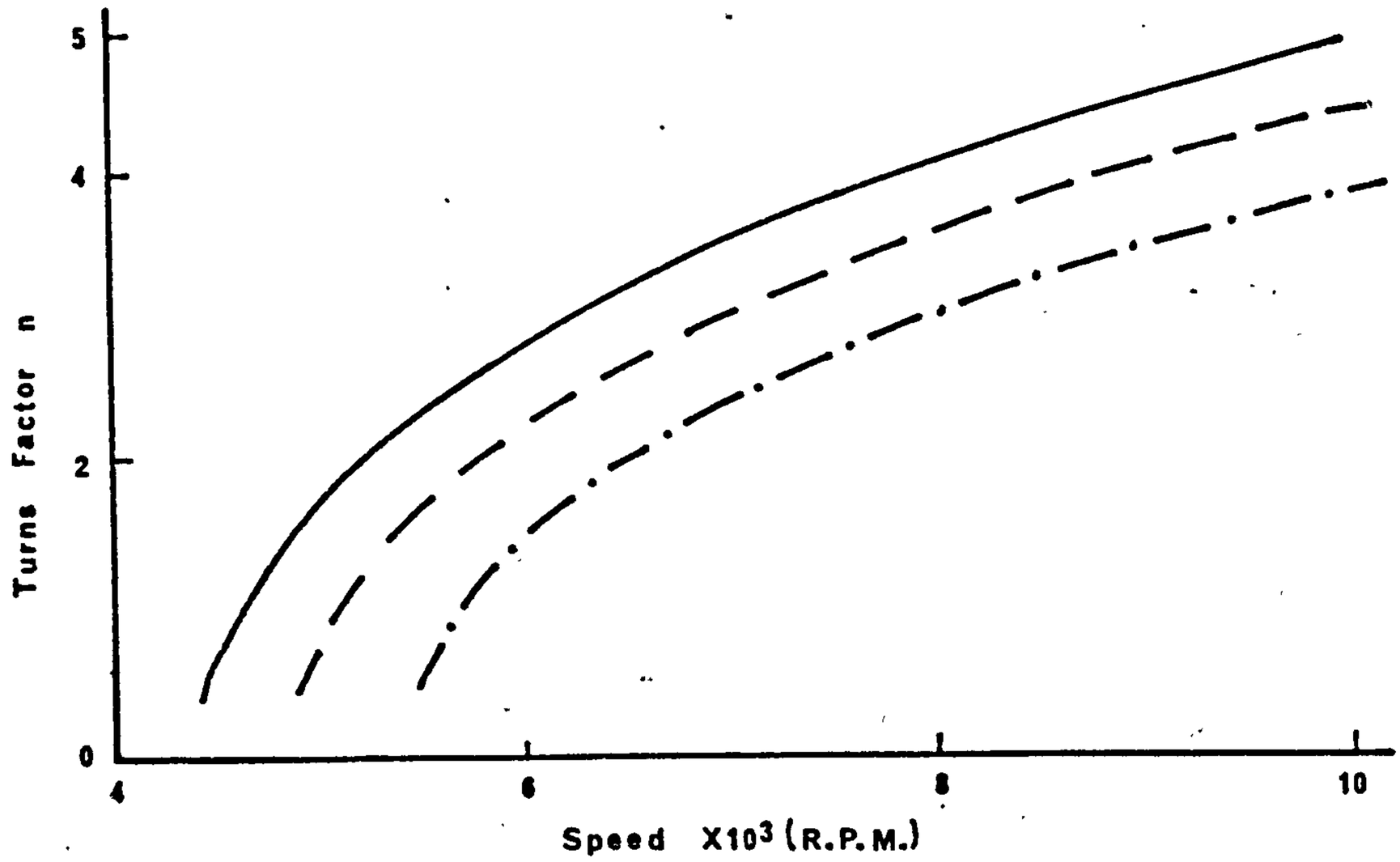

(b) Variations Of Peak Flux Linkage With Speed

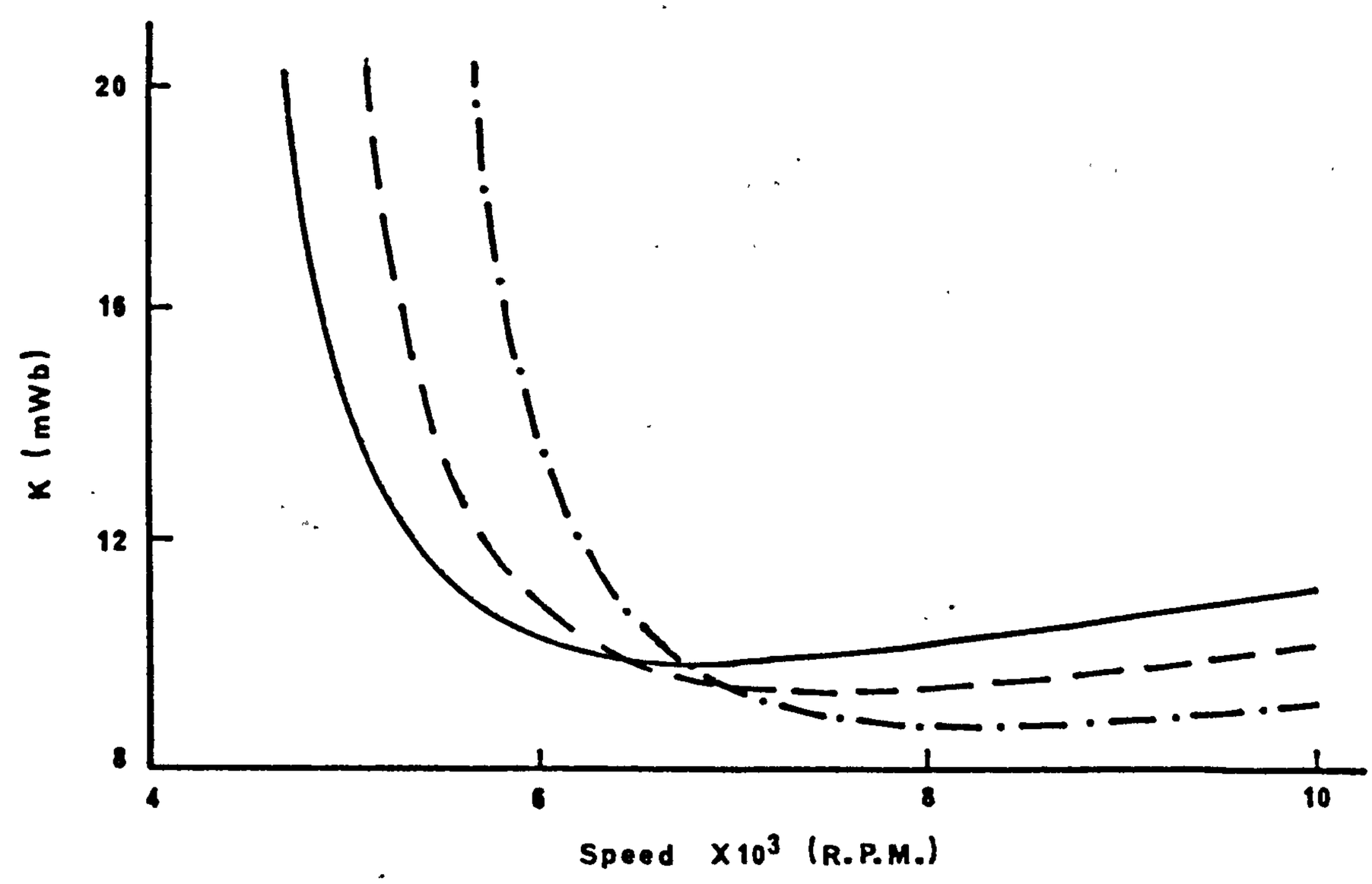

AIR PRESSURE (P.S.I.)

——— 70

— — 65

—·— 60

Parameter
L = 140 μH
R = 88 mΩ

Load
24V 250W Bulb

Fig 7·6

Fig 7·7

7·6 Typical Variations Of K With $\dot{e}$

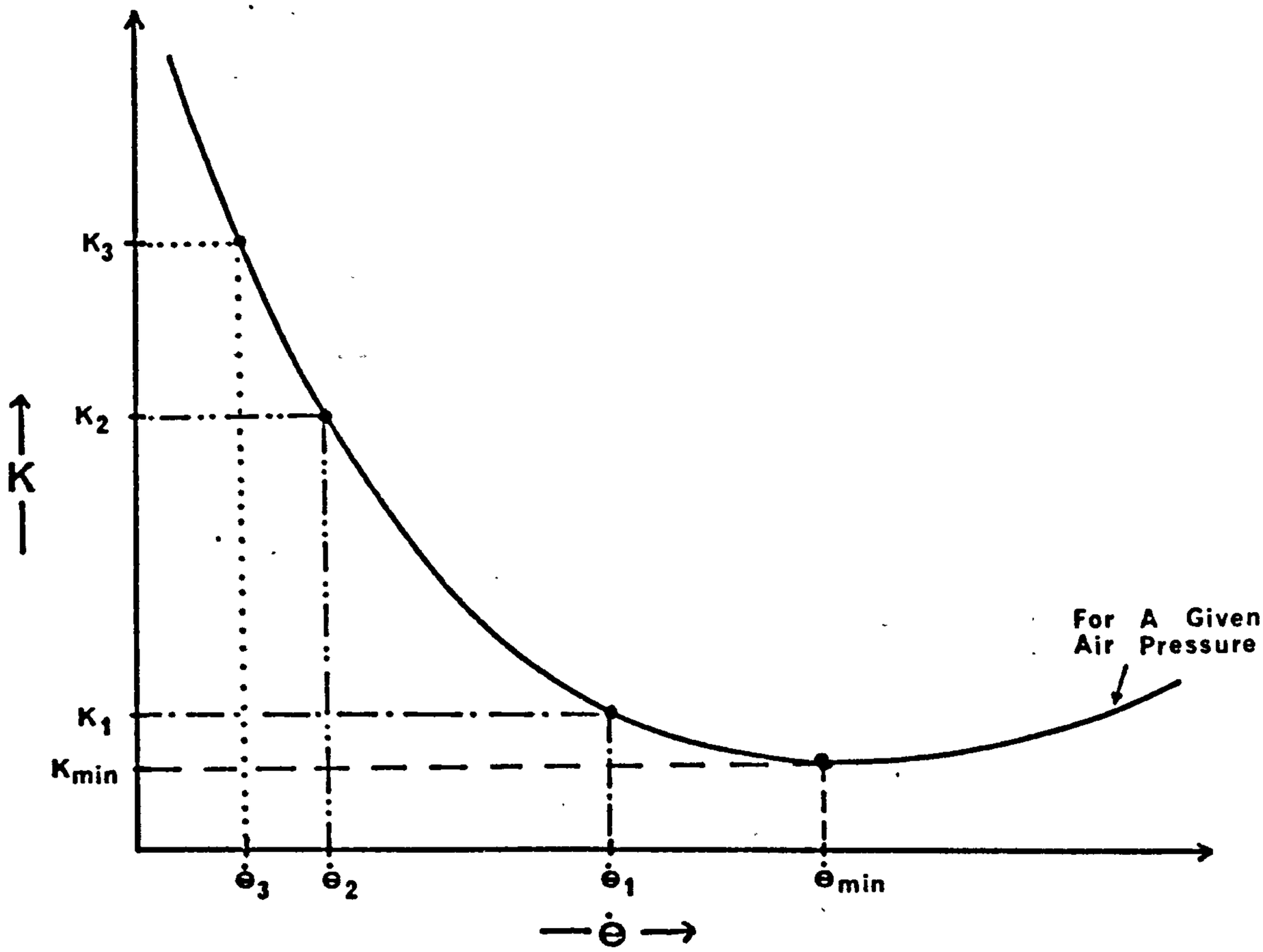

7·7 Rotor Geometry

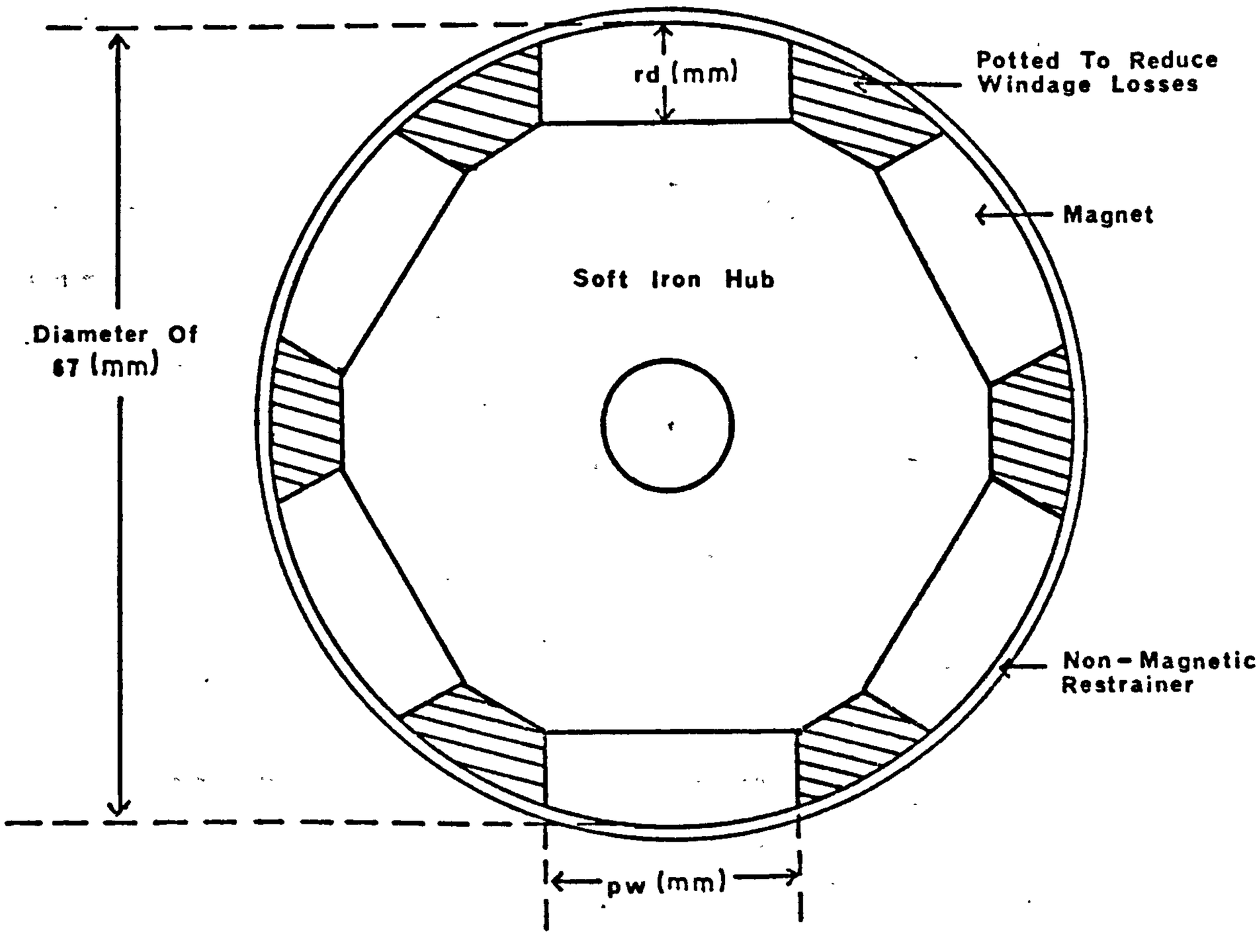

Fig 7·8

Fig 7·9

7·8 Computed Variations Of Peak Flux Linkage With Magnet Geometry

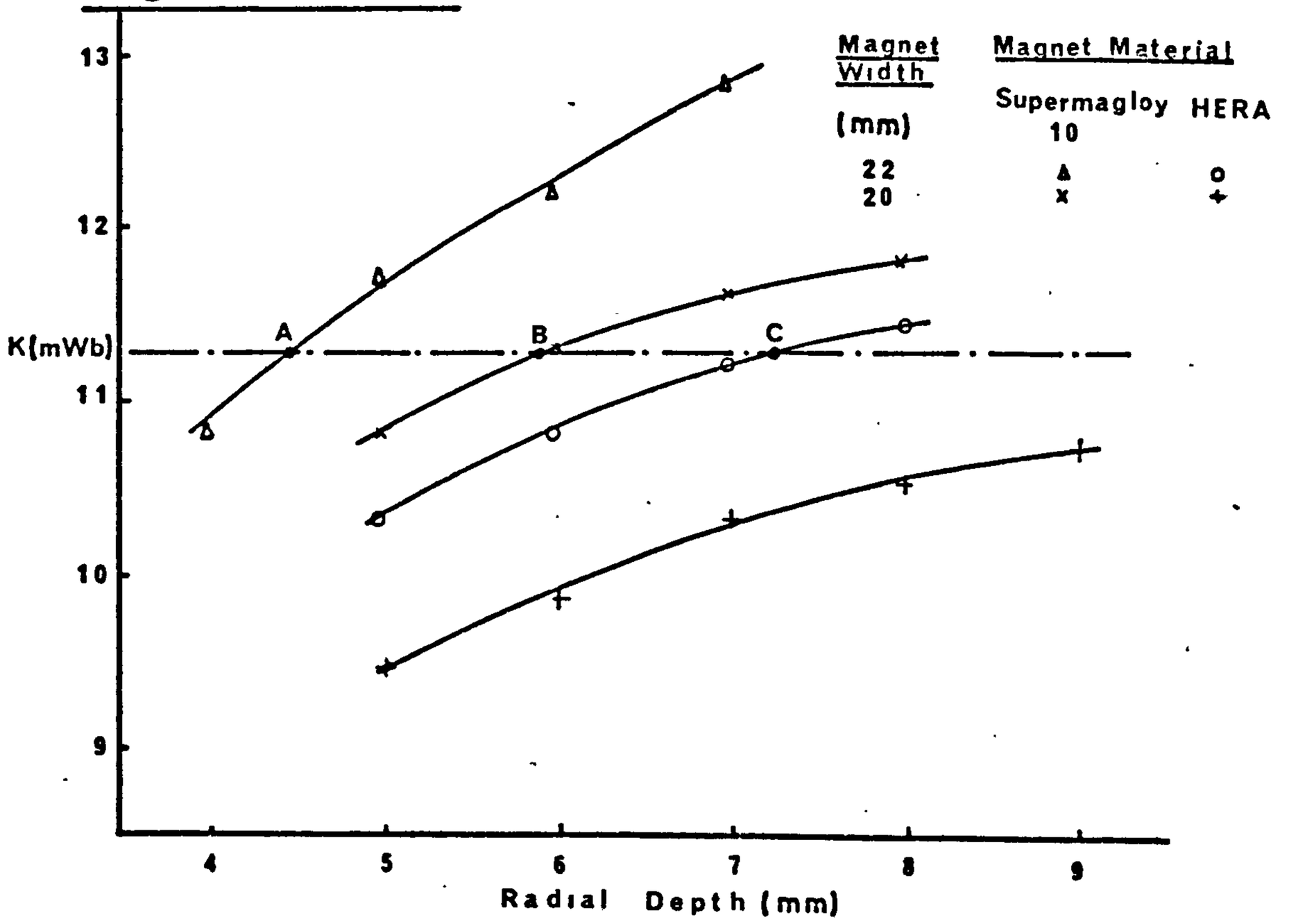

7·9 Computed Variations Of Stator Inductance With Magnet Geometry

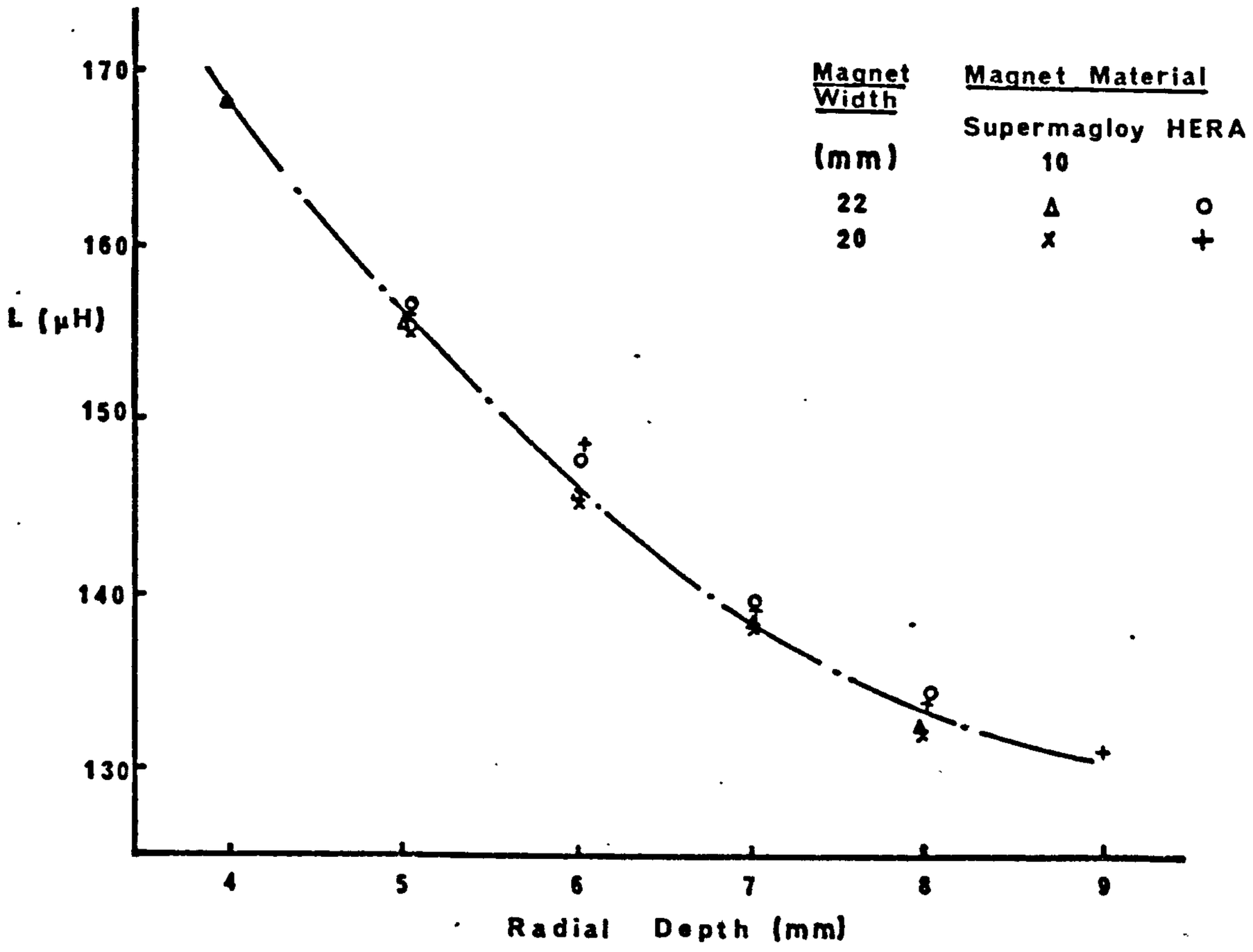

Fig 7·10

Rare Earth Rotors

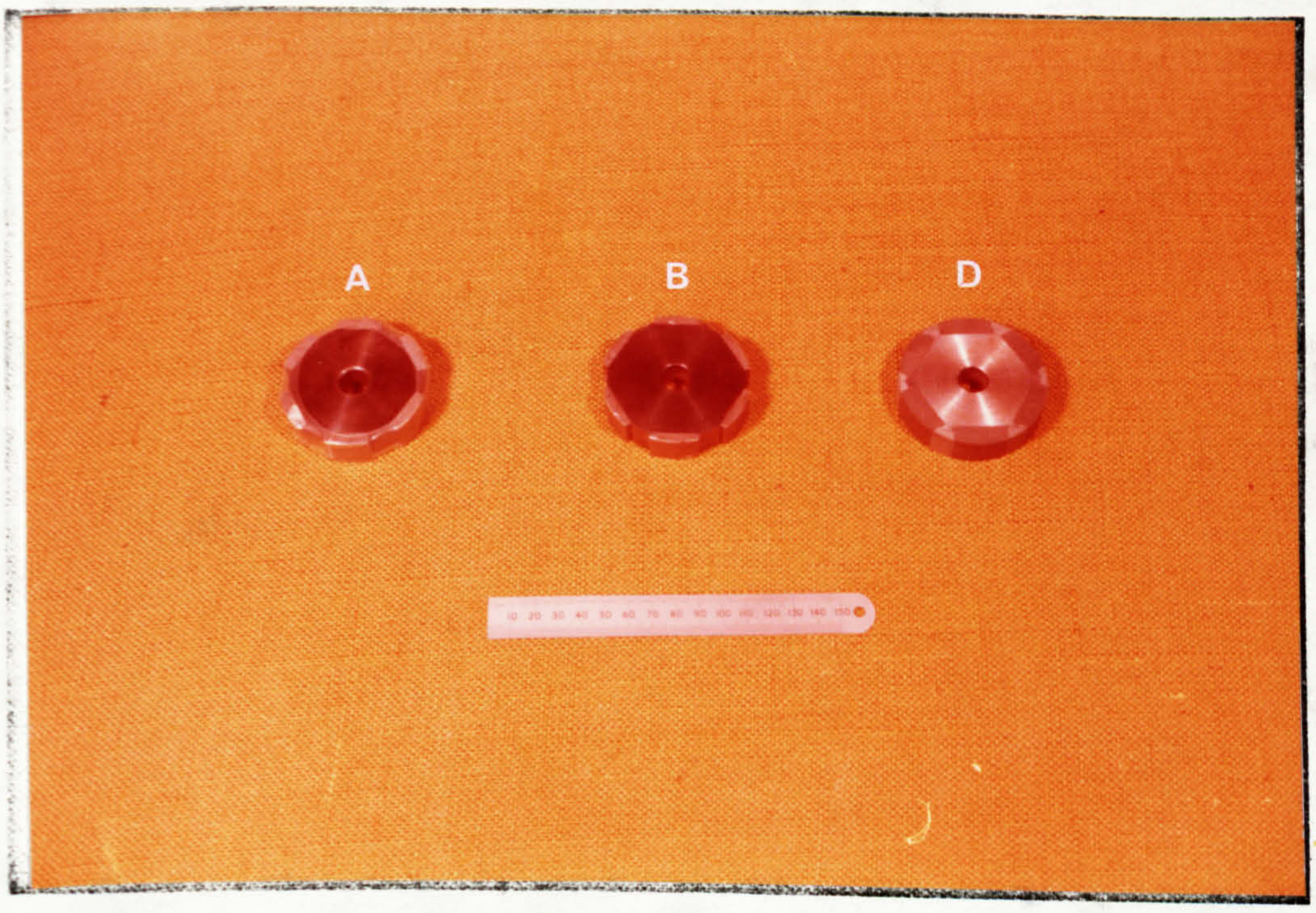

Fig 7·11

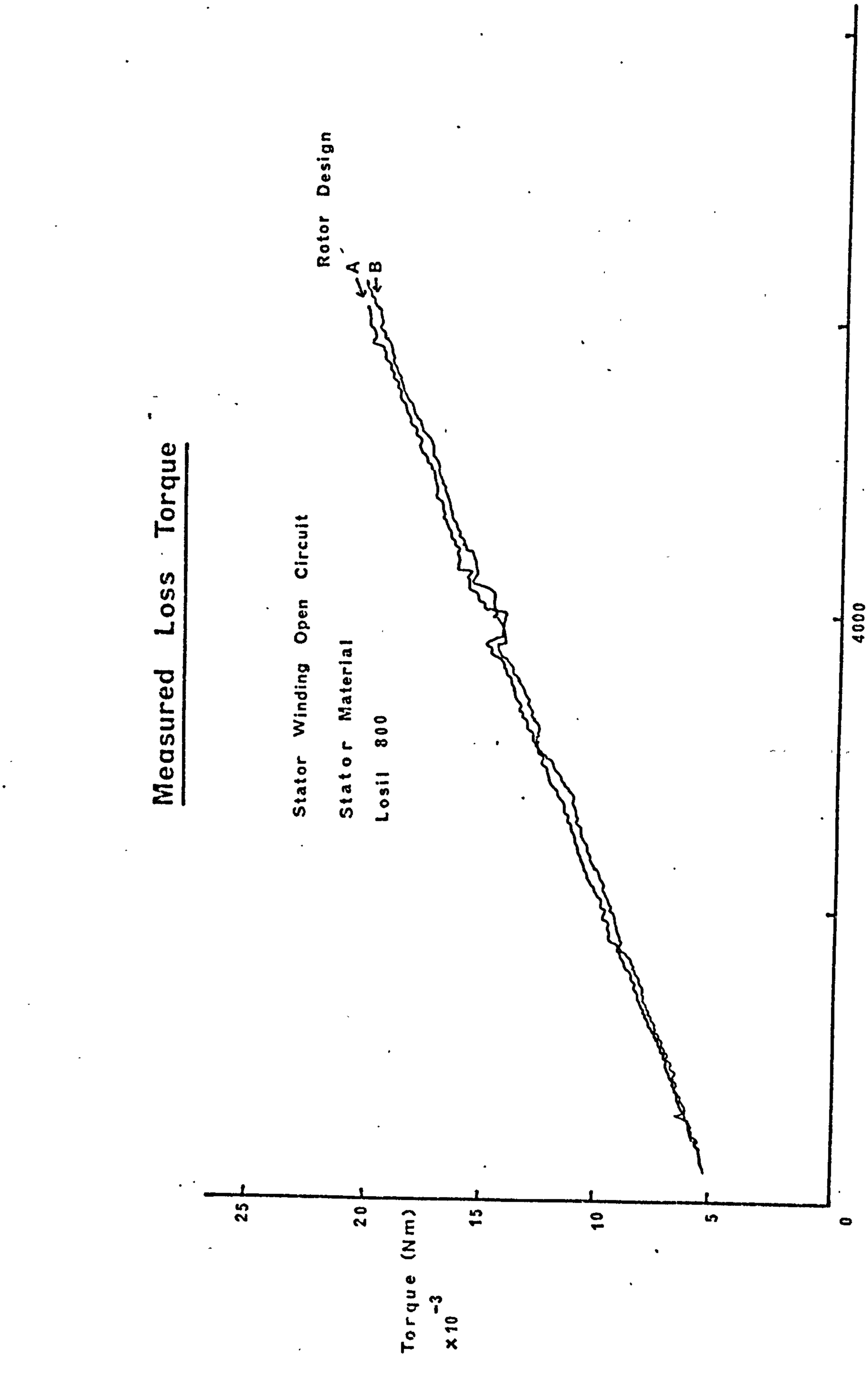
Measured Loss Torque
Stator Winding Open Circuit
Stator Material
Losil 800
Rotor Design
A
B
Torque (Nm)
x10 -3
25
20
15
10
5
0
4000
8000
Speed (R·P·M·)

Fig 7·12

Variations Of Operating Speed And Air Pressure With Turns Factor

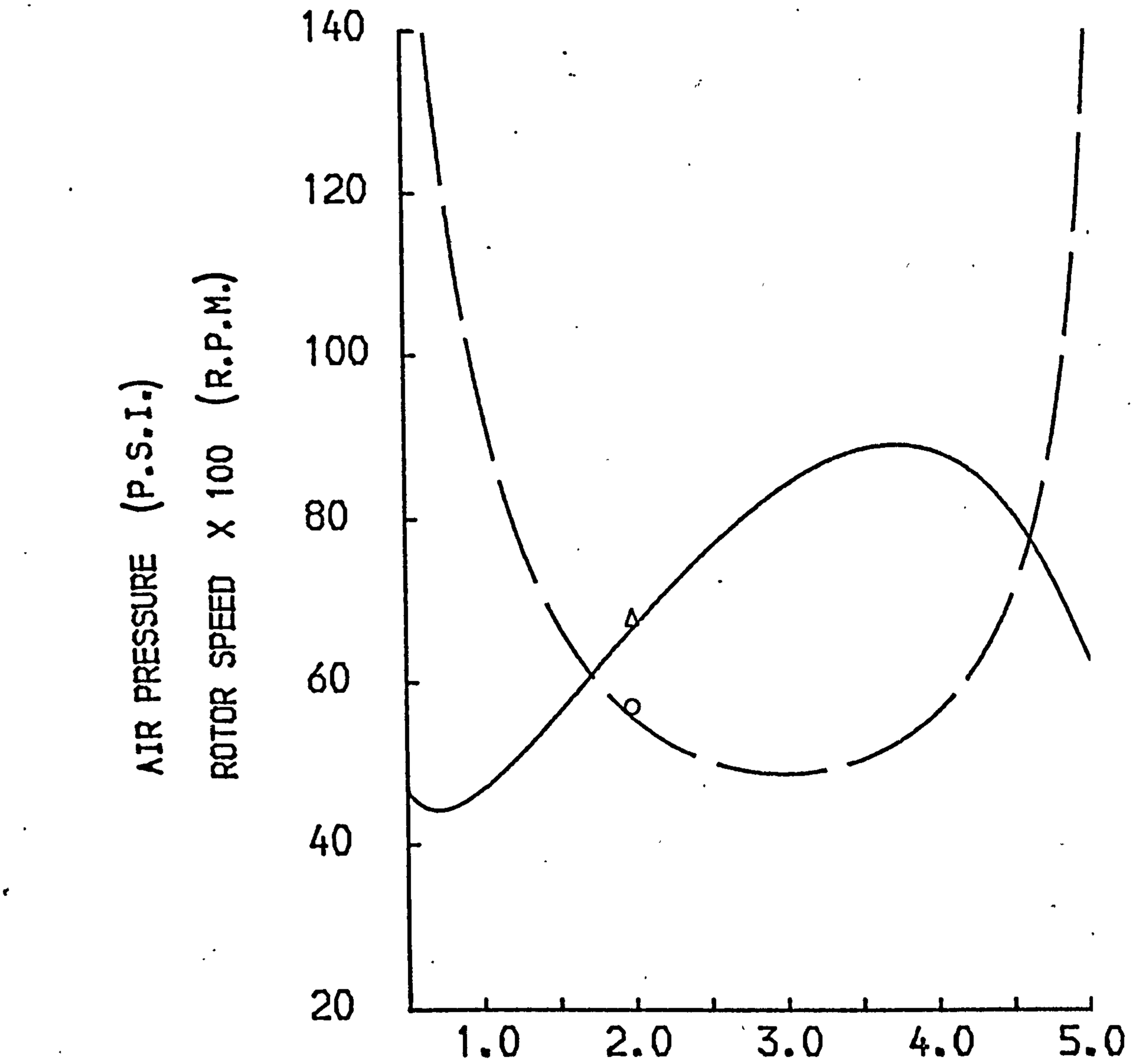

24V 250W Bulb
Rotor Design A

	Predicted	Measured
Speed	— —	O
Air Pressure	———	Δ

Fig 7·13

Torque - Speed Curve Of Generator With Rotor Design A

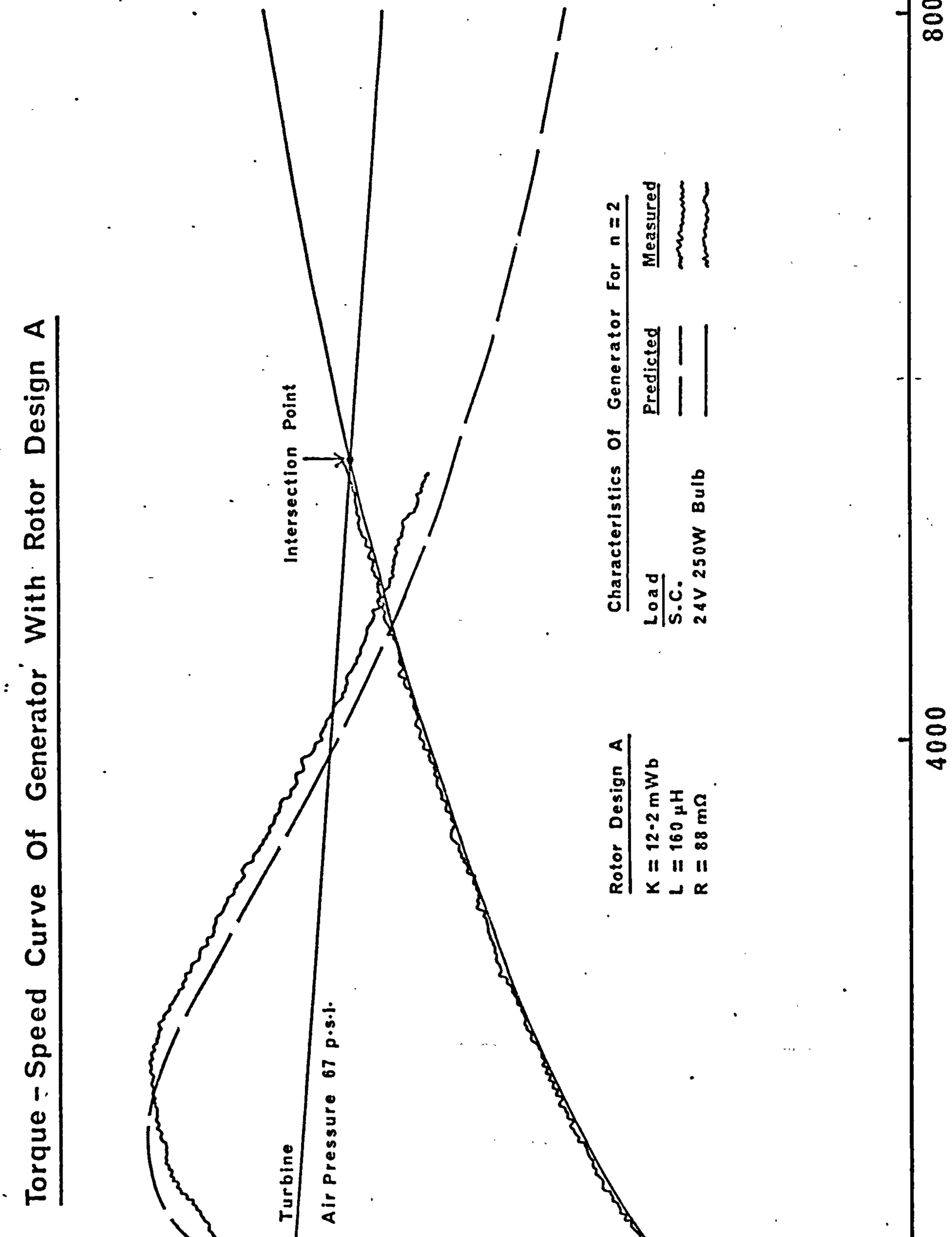

Measured And Computed Saliency Torques At Various Displacement Angles

Rotor Design A
Airgap = 1·5mm
Magnet Radial Depth = 4·5 mm
Pole Width = 22 mm

Measured Point	Computed Point	Stator Core
o	⊕	Without Interpoles
x	Δ	With Interpoles

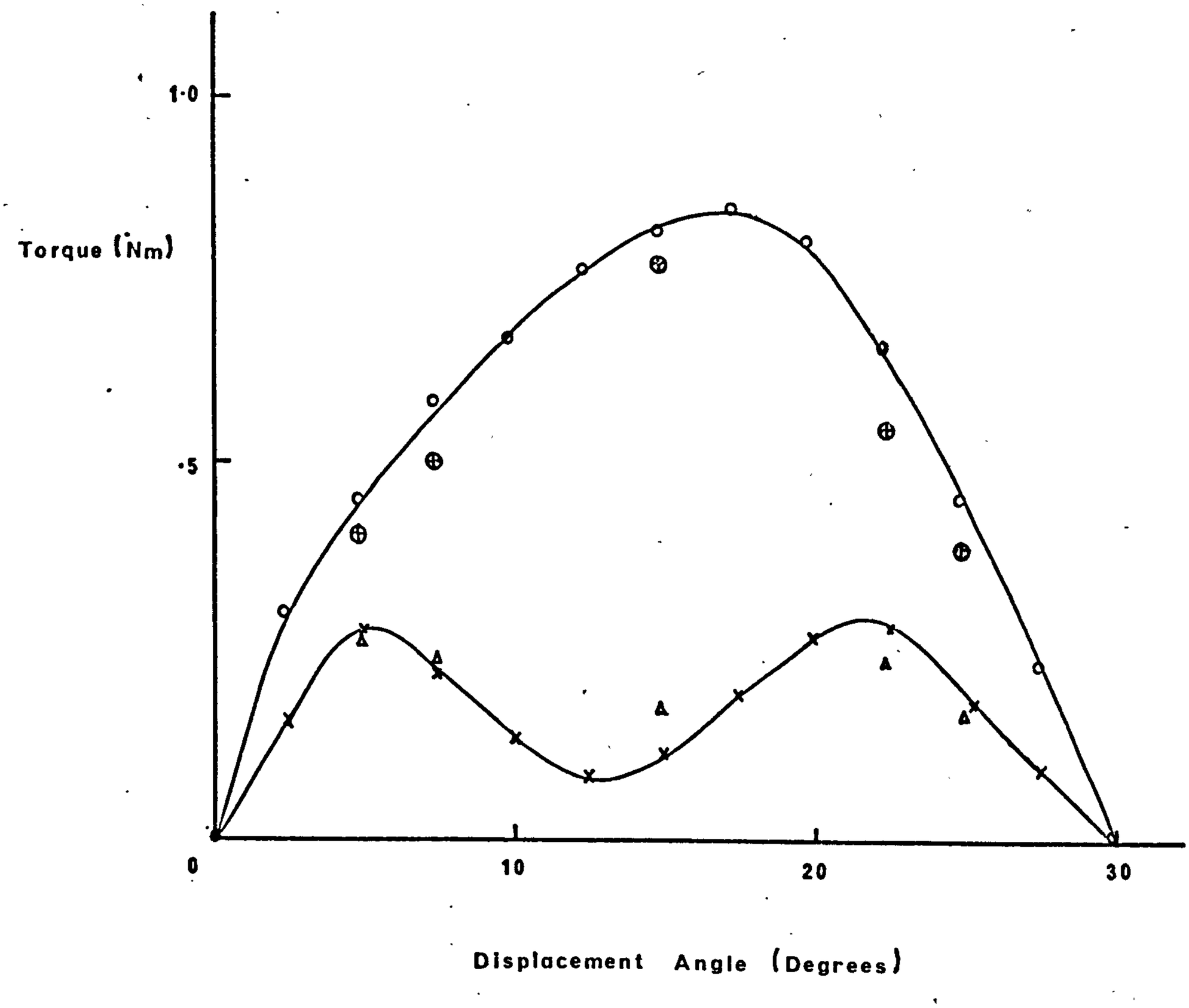

Variations Of Operating Speed And Air Pressure With Turns Factor

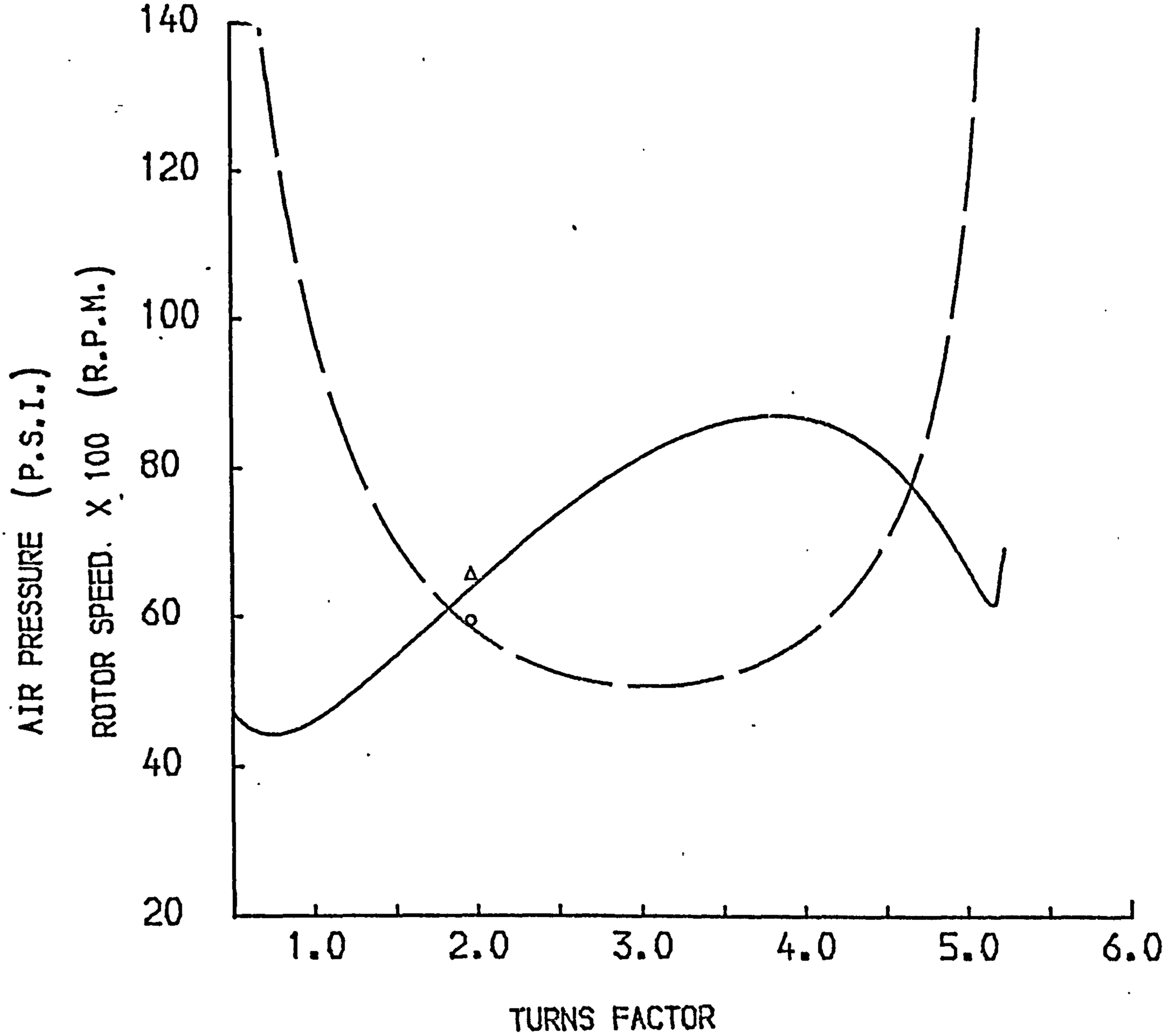

24V 250W Bulb
Rotor Design B

	Predicted	Measured
Speed	— —	O
Air Pressure	———	Δ

Torque – Speed Curve Of Generator With Rotor Design B

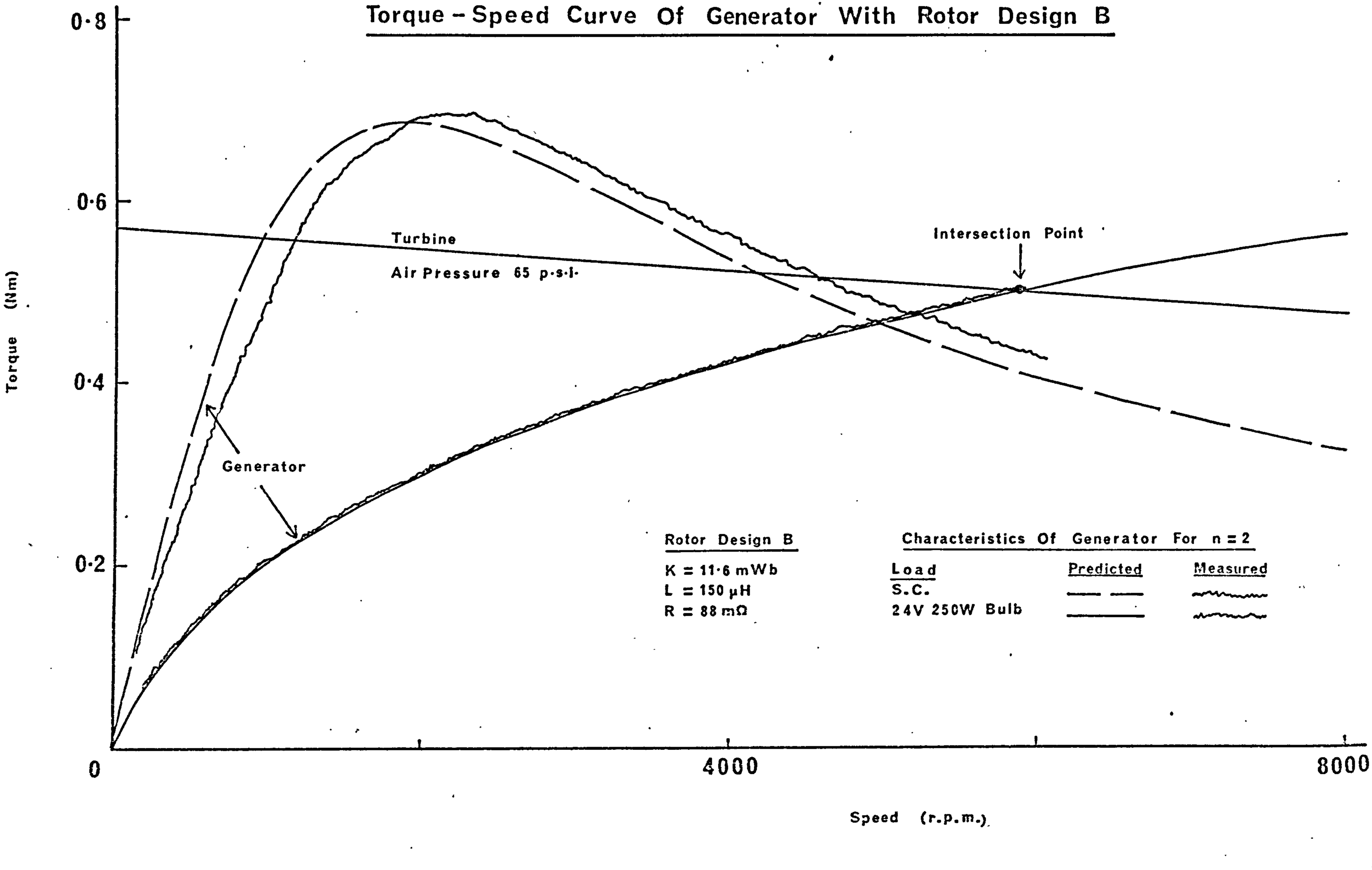

Fig 7.16

Fig 7·17

Measured And Computed Saliency Torques At Various Displacement Angles

Rotor Design B
Airgap = 1·5mm
Magnet Radial Depth = 6 mm
Pole Width = 20 mm

Measured Point	Computed Point	Stator Core
o	⊕	Without Interpoles
x	Δ	With Interpoles

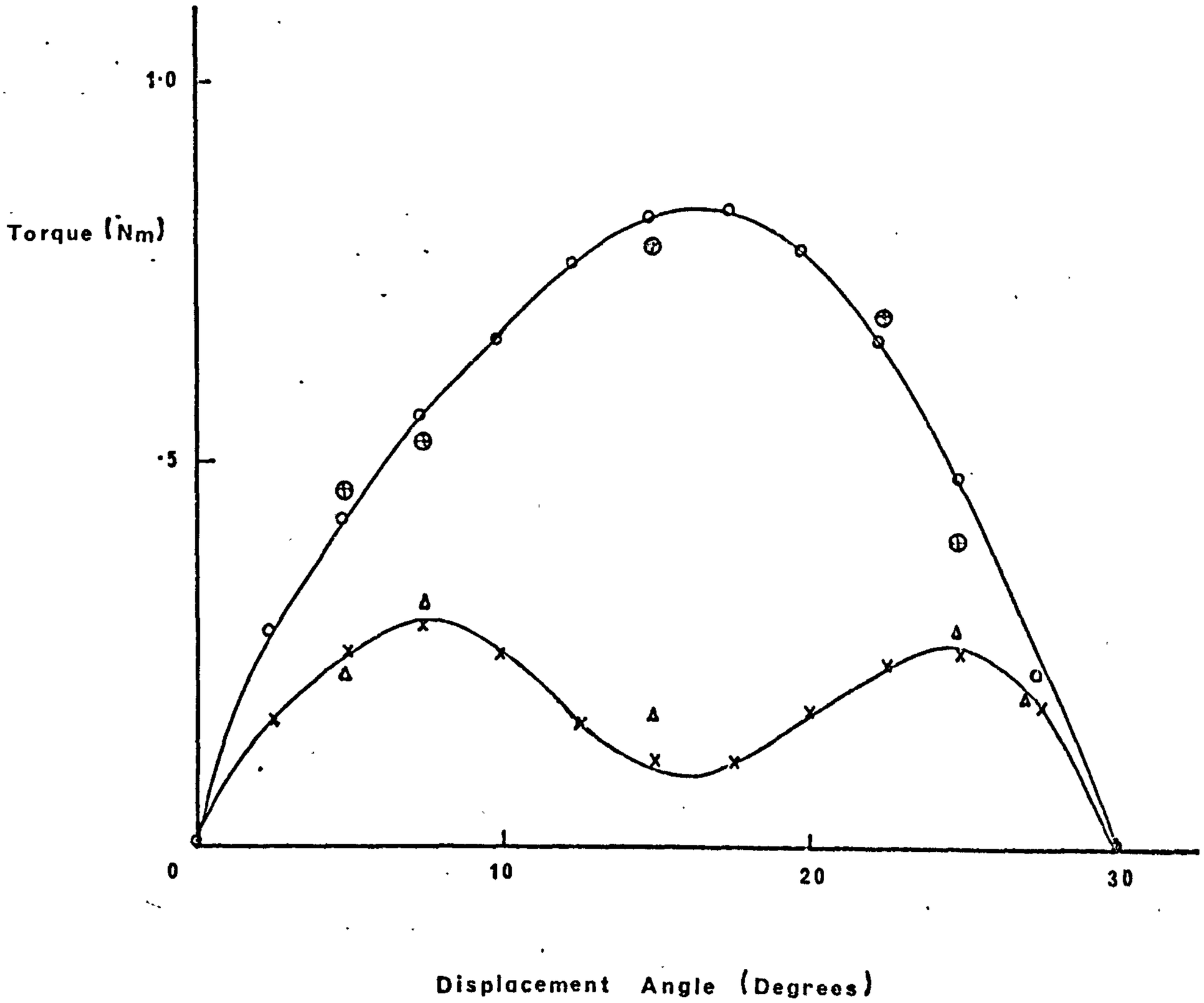

Measured And Computed Saliency Torques At Various Displacement Angles

Rotor Design C
Airgap = 1·5mm
Magnet Radial Depth = 7mm
Pole Width = 22 mm

Measured Point	Computed Point	Stator Core
o	⊕	Without Interpoles
x	Δ	With Interpoles

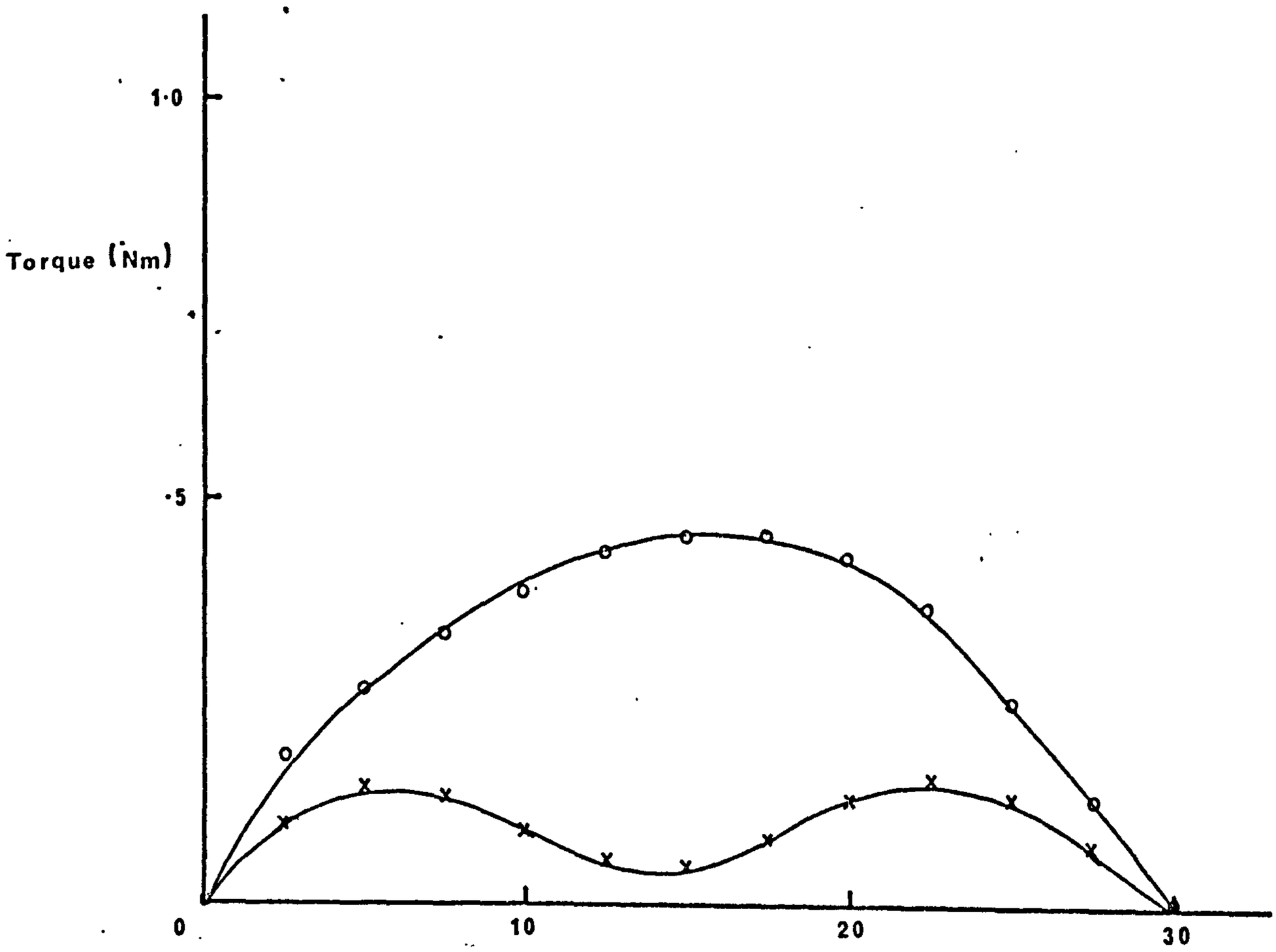

Variations Of Operating Speed And Air Pressure With Turns Factor

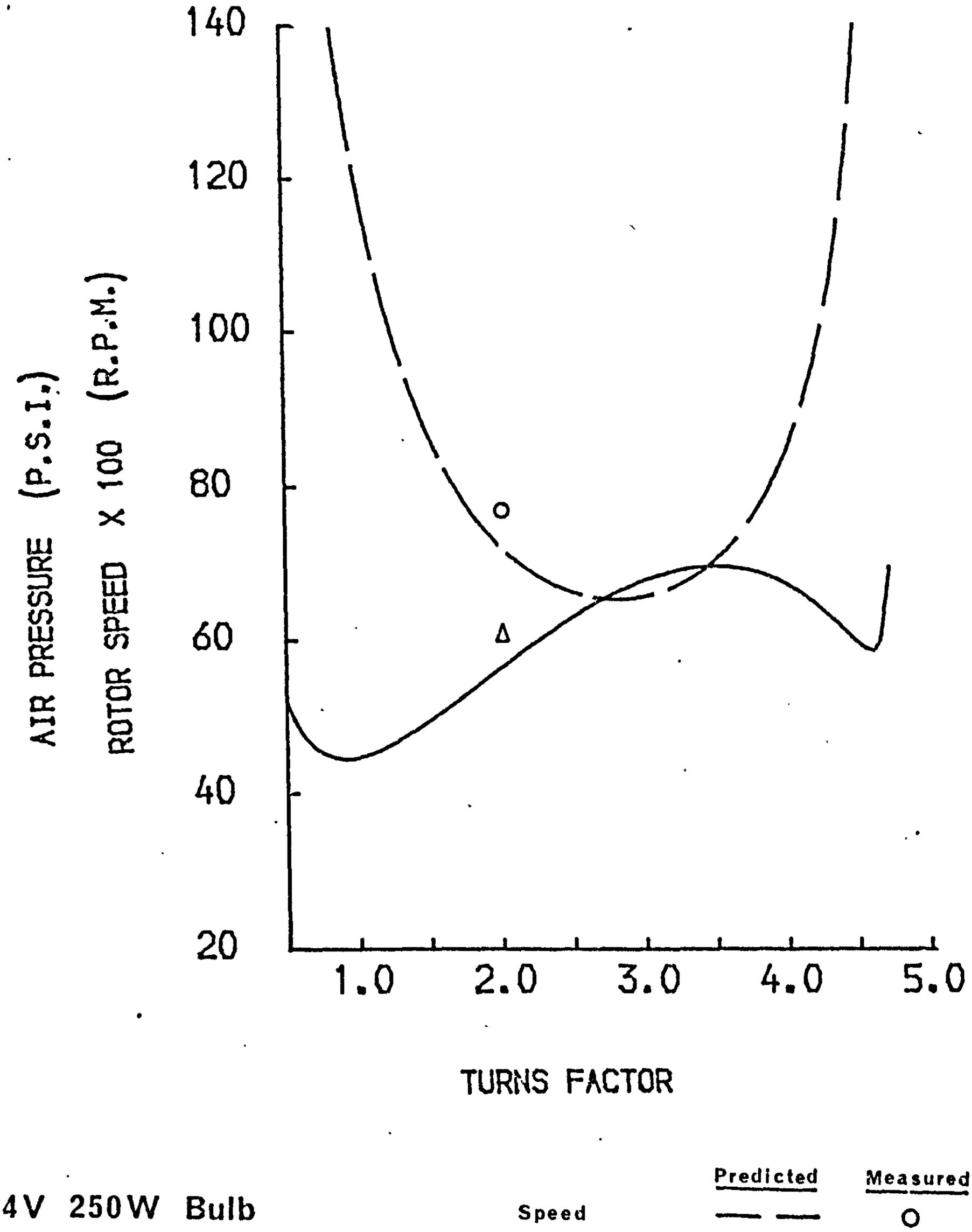

24V 250W Bulb
Rotor Design C

	Predicted	Measured
Speed	— —	o
Air Pressure	———	Δ

Fig 7·2C

Torque – Speed Curve Of Generator With Rotor Design C

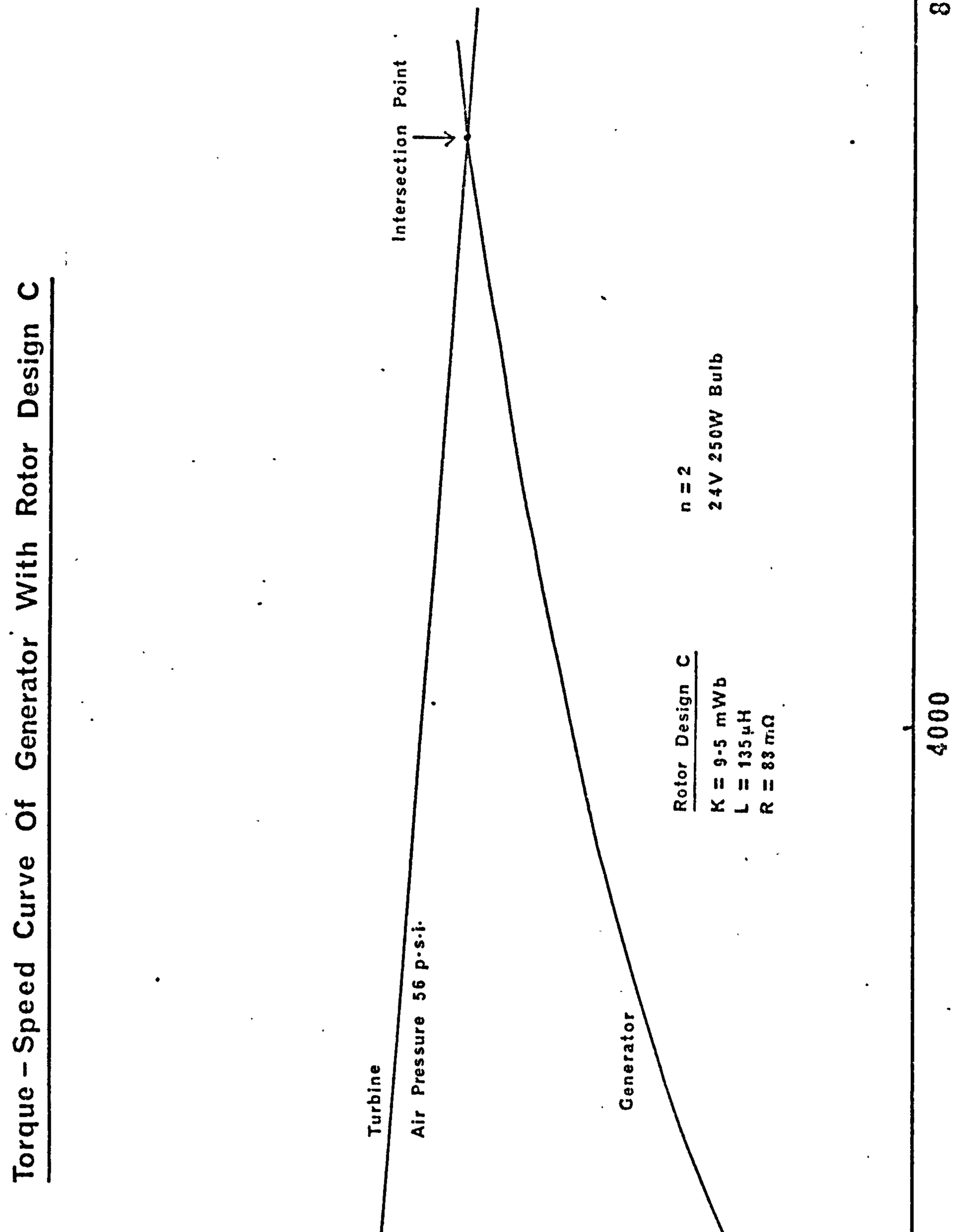

Fig 7·21

Fig 7·22

7·21 Computed Variations Of Peak Flux Linkage With Magnet Geometry

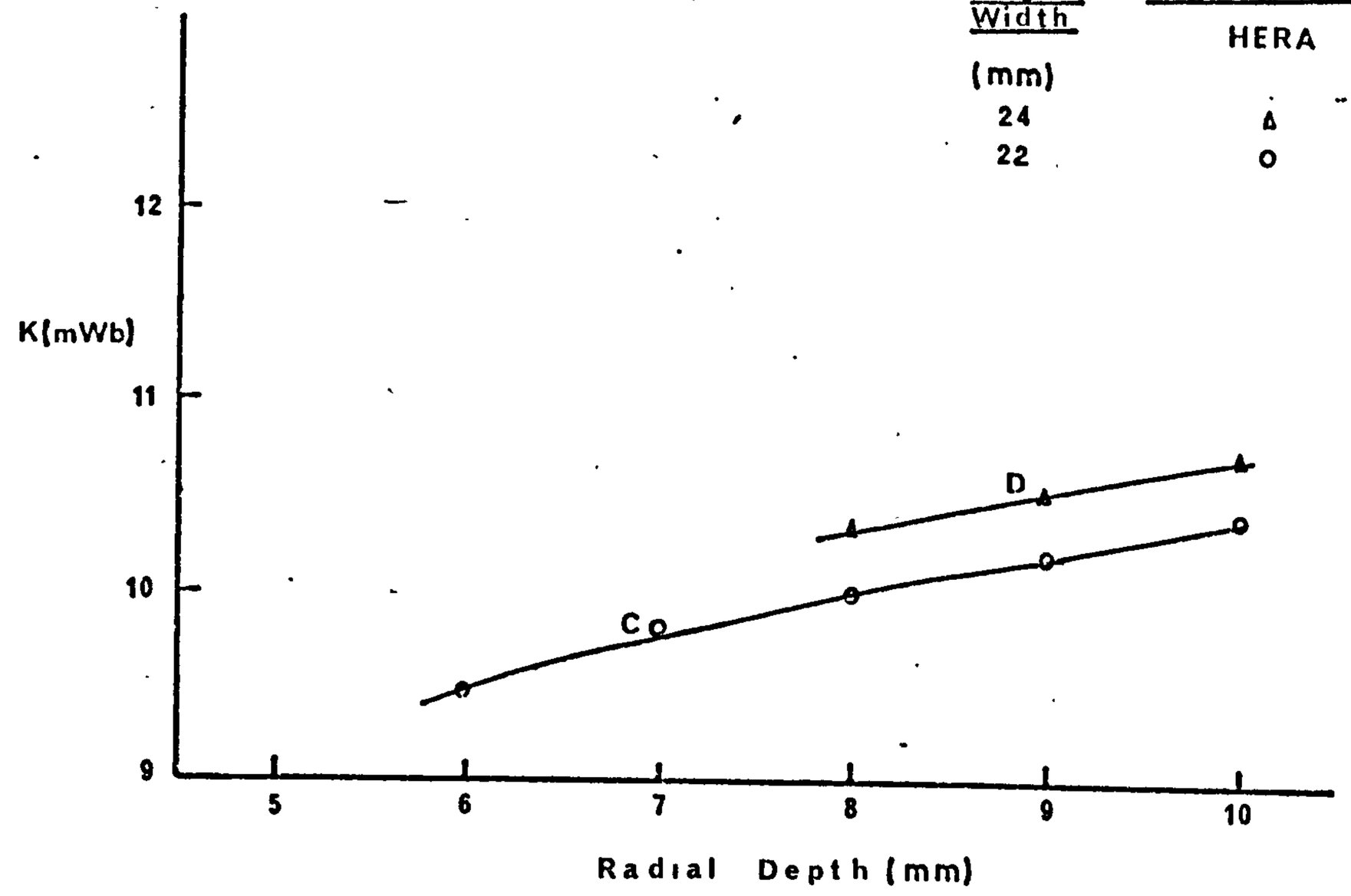

7·22 Computed Variations Of Stator Inductance With Magnet Geometry

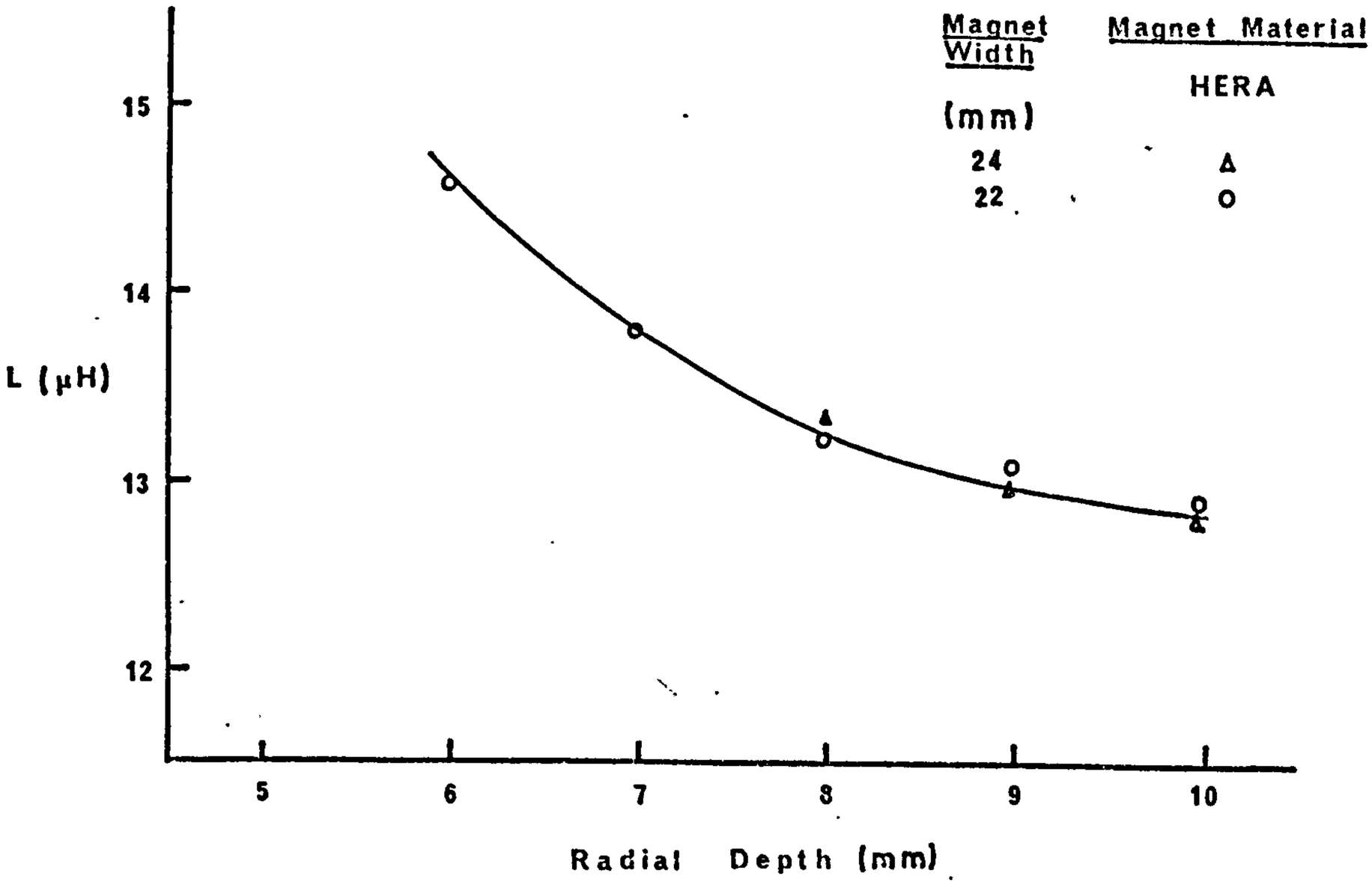

Fig 7·23

Variations Of Operating Speed And Air Pressure With Turns Factor

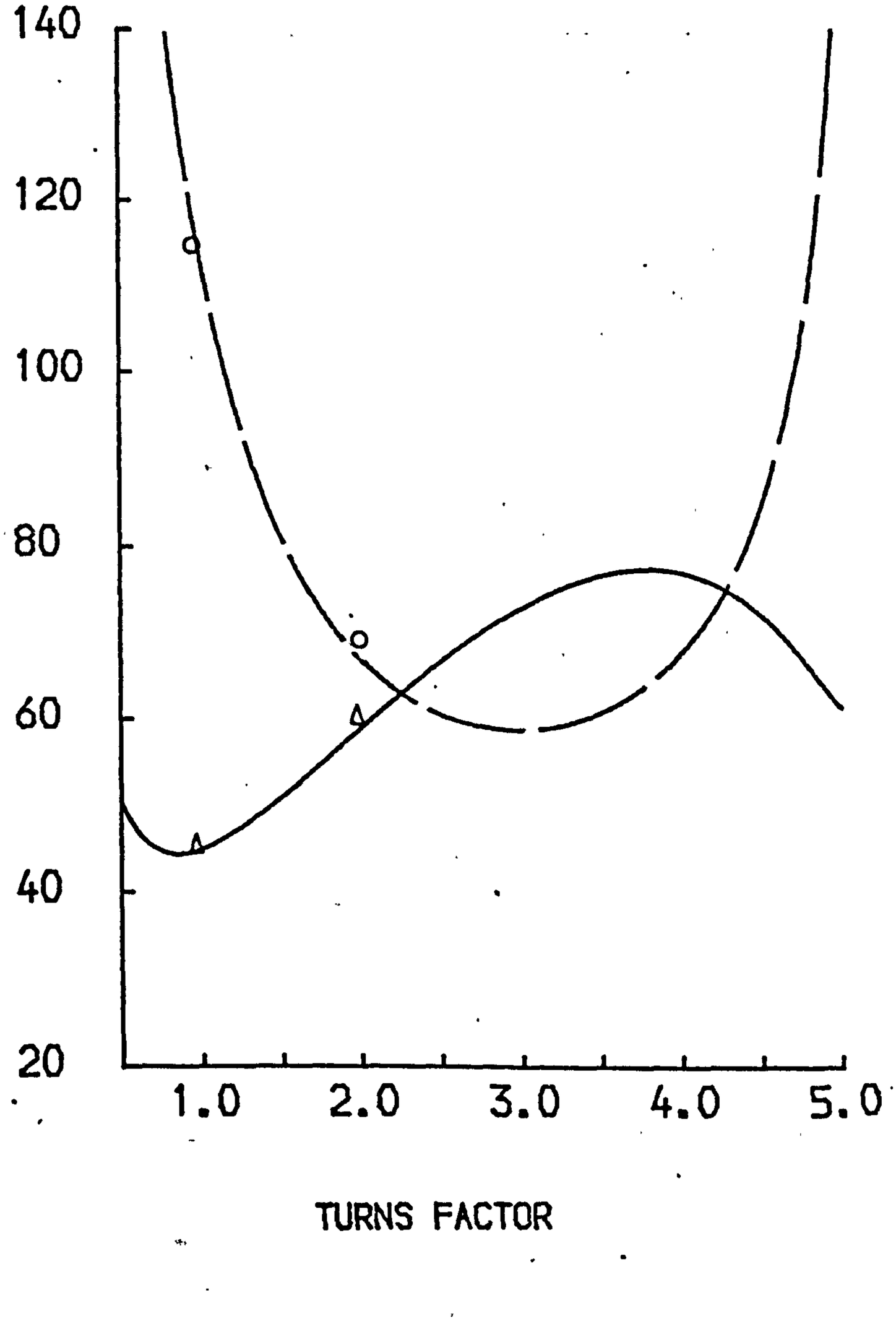

24V 250W Bulb
Rotor Design D

	Predicted	Measured
Speed	— —	O
Air Pressure	———	Δ

Variations Of Torque - Speed Curves Due To Changes In Turns Factor

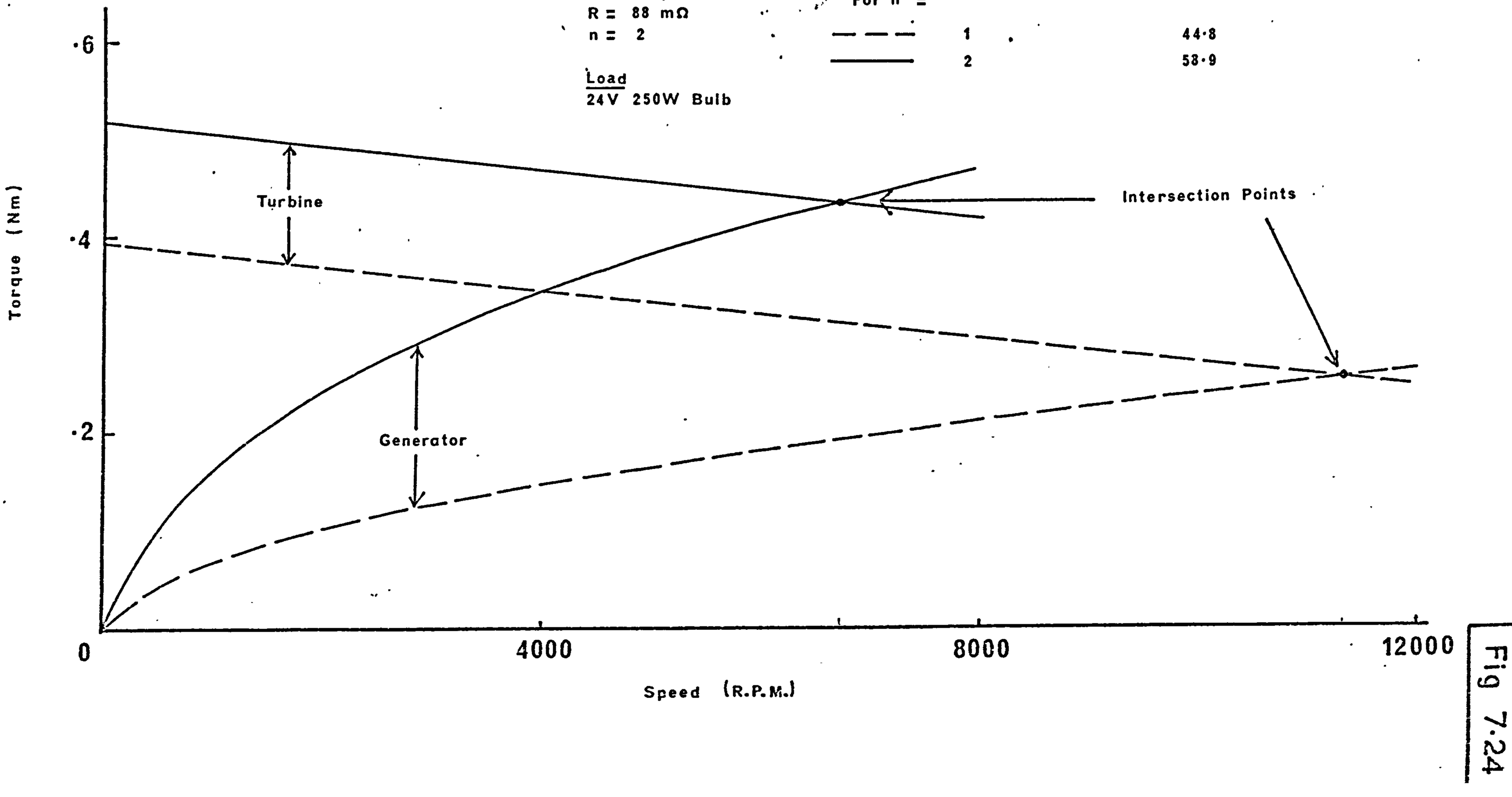

Fig 7.24

(a) Variations Of Torque - Speed Curves Due To Changes In K Values

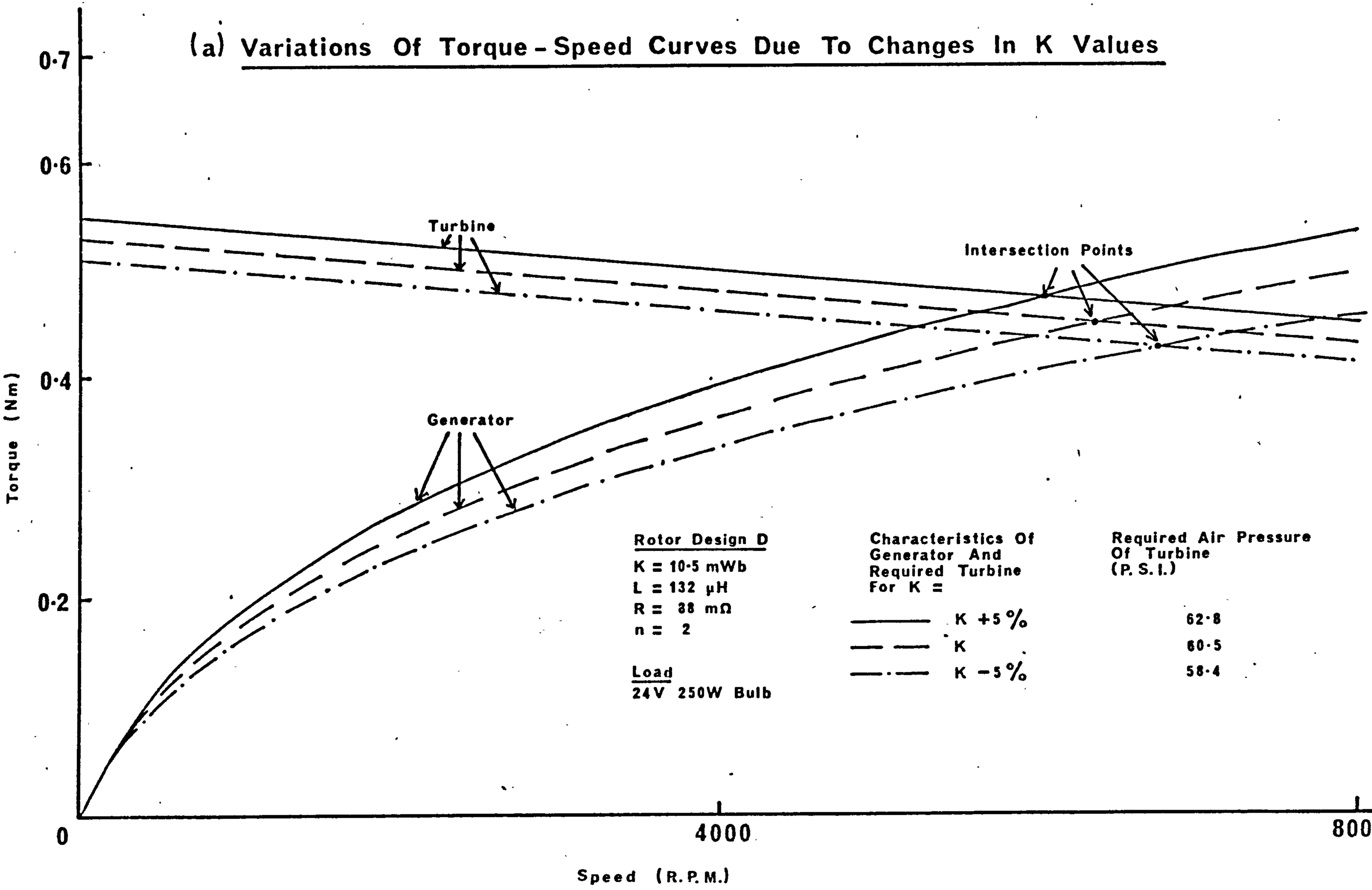

Fig 7·25(a)

(b) Variations Of Output Power Speed Curves Due To Changes In K Values

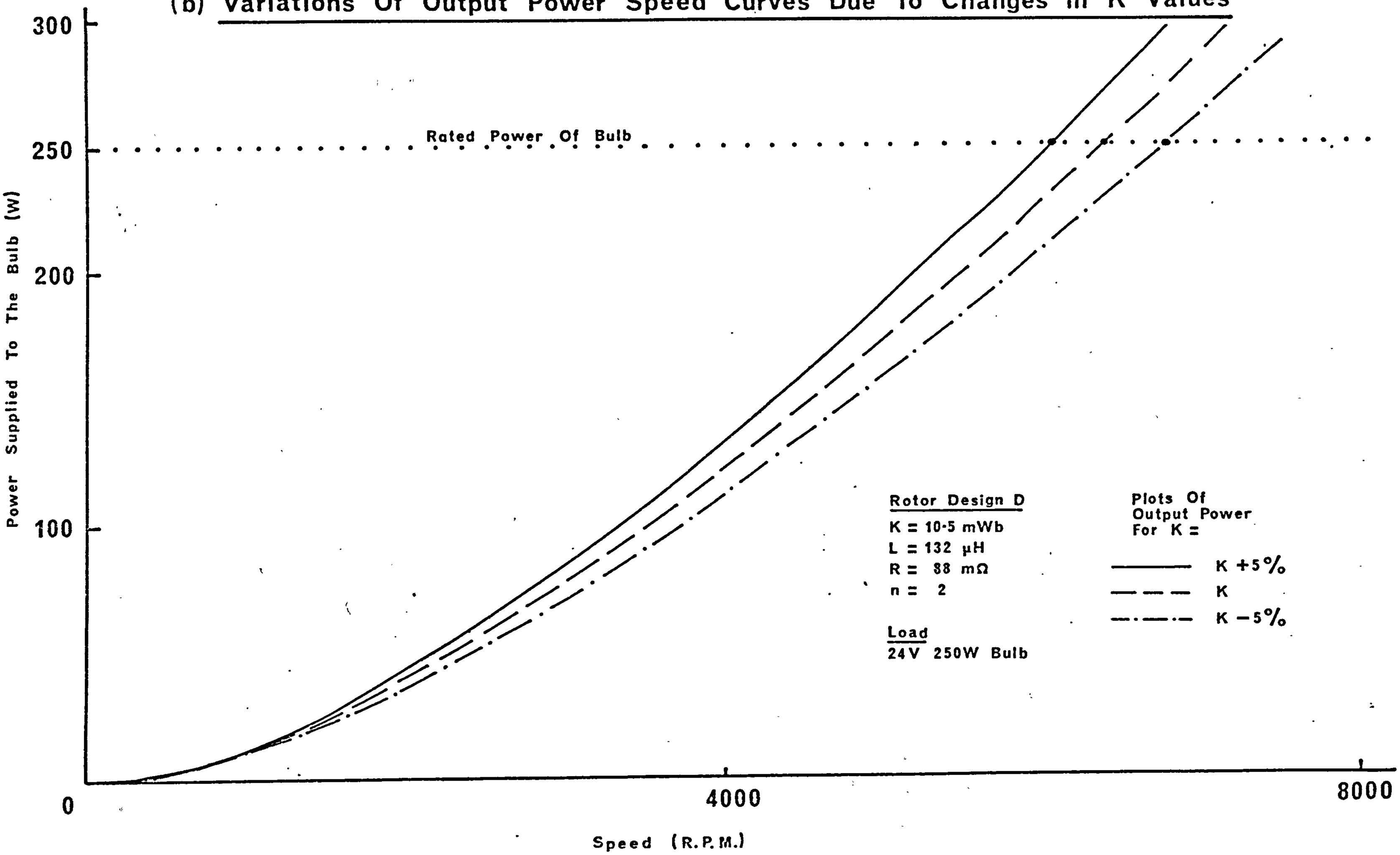

Fig 7.25(b)

Fig 7·26

Fig 7·27

7·26 Effect Of Generator Overspeeding

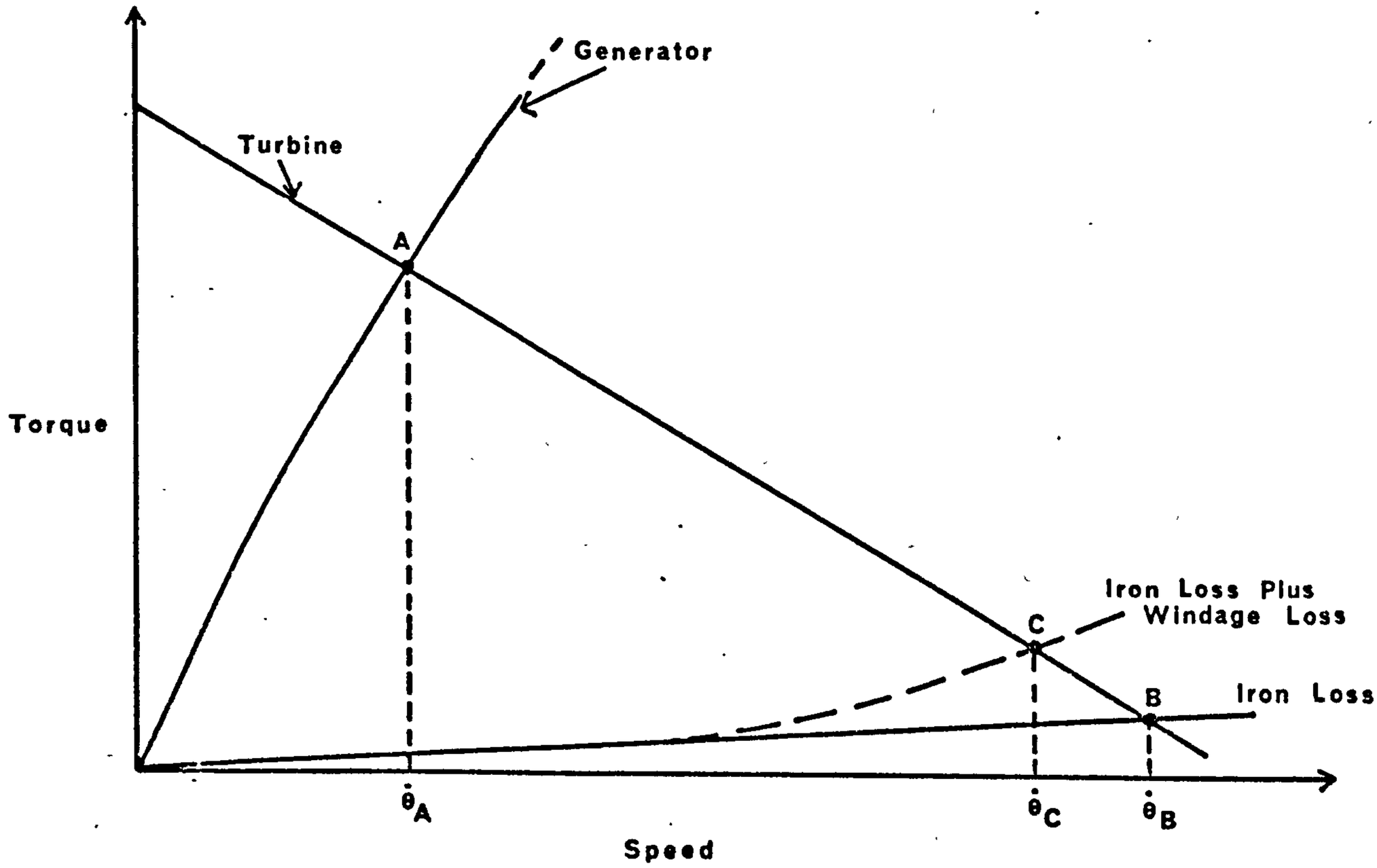

7·27 Overspeed Protection Approach

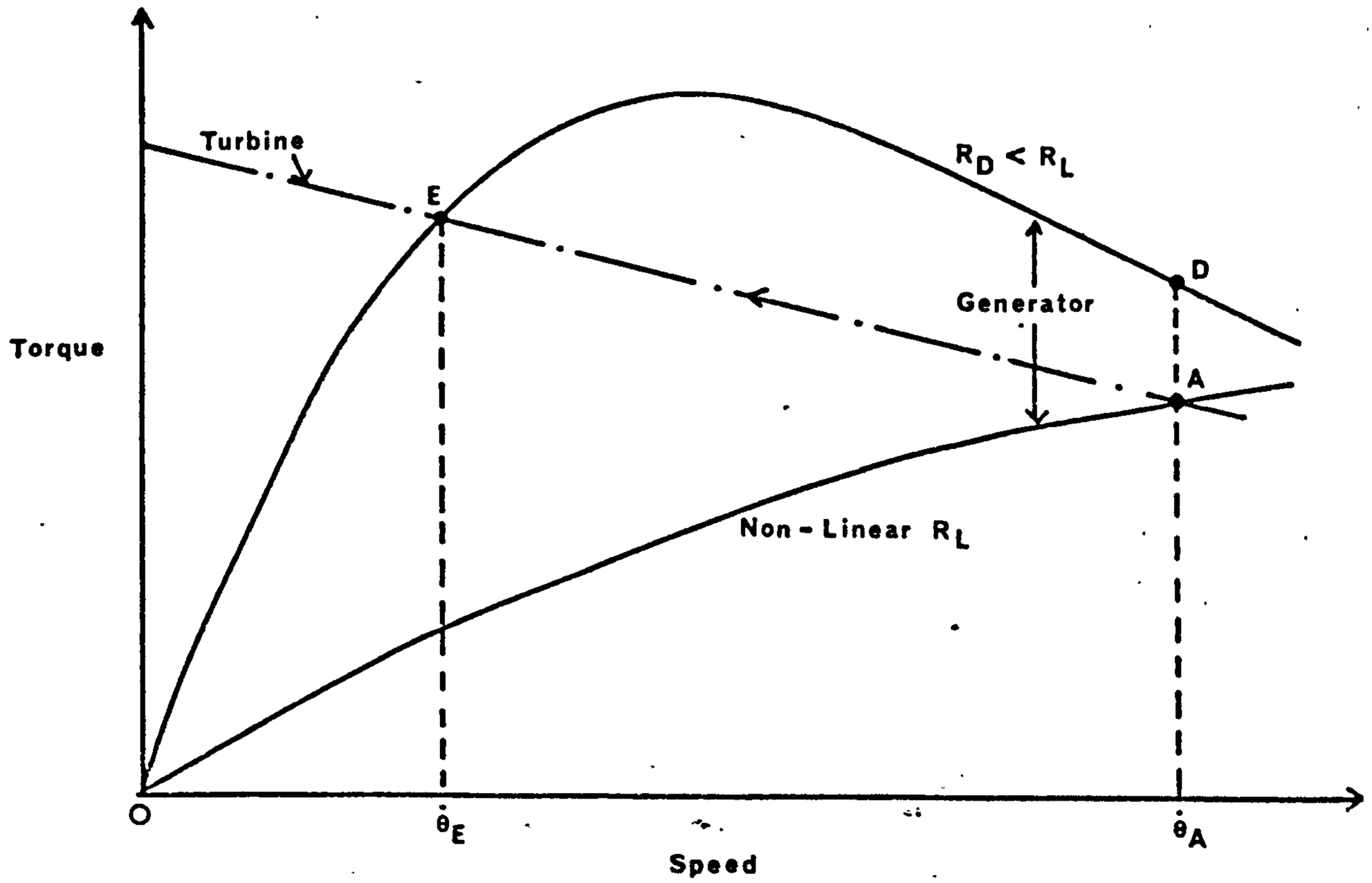

Fig. 7·28

Protection Circuit Arrangement

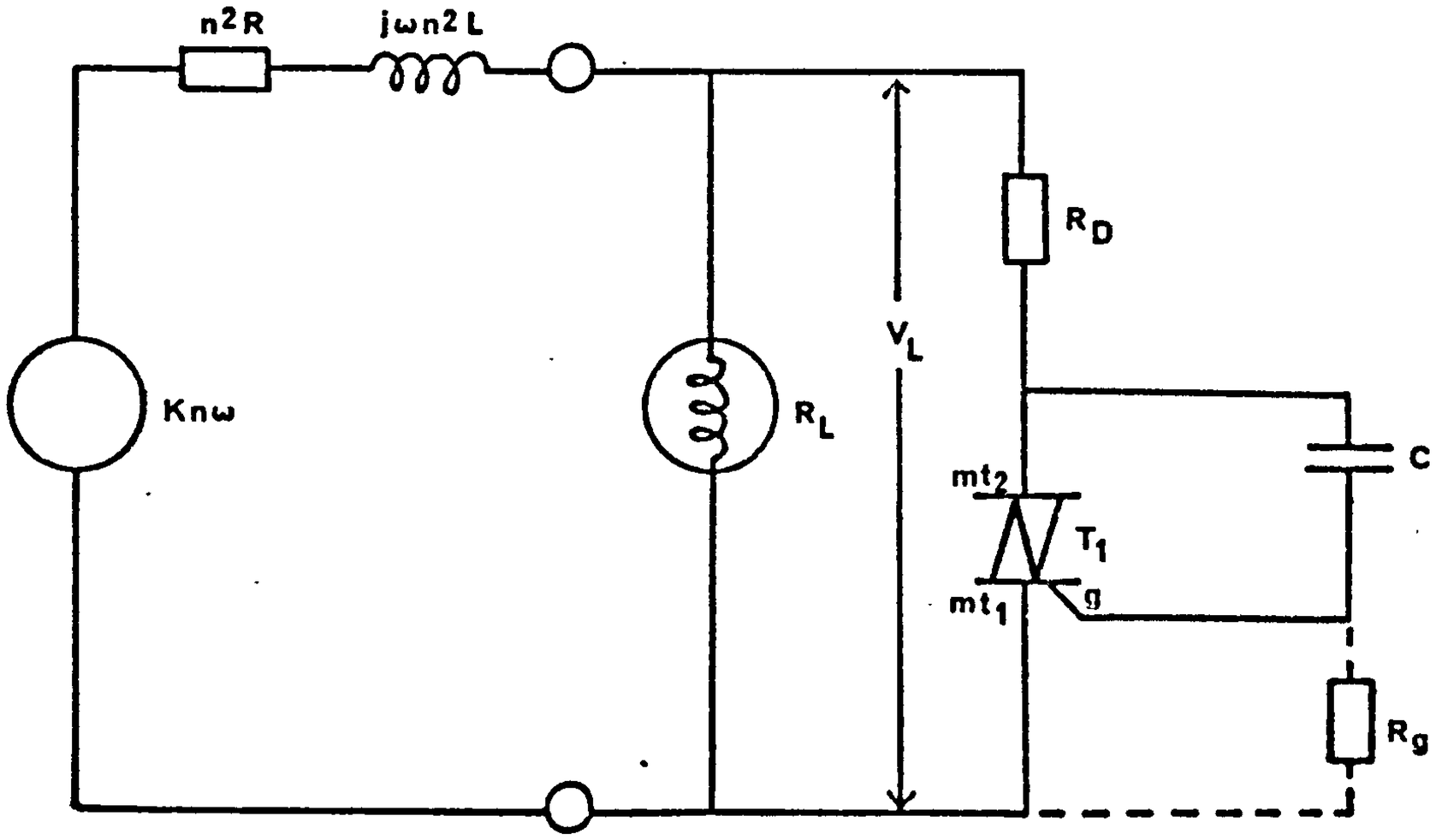

Fig 7·29

Torque - Speed Curves Of Generator For Various Loads

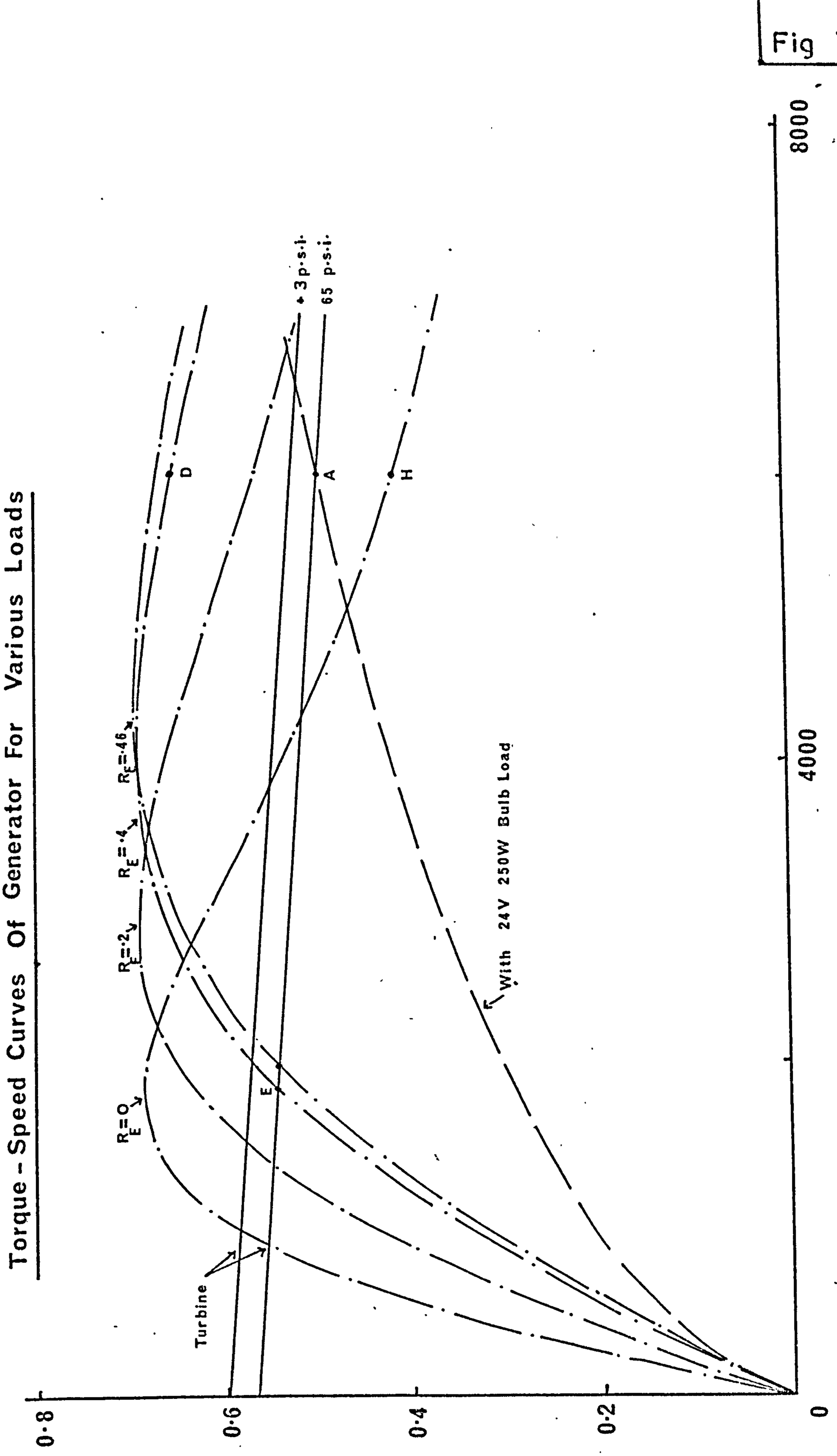

Fig 7·30

Equivalent Circuit Of Protection Circuit

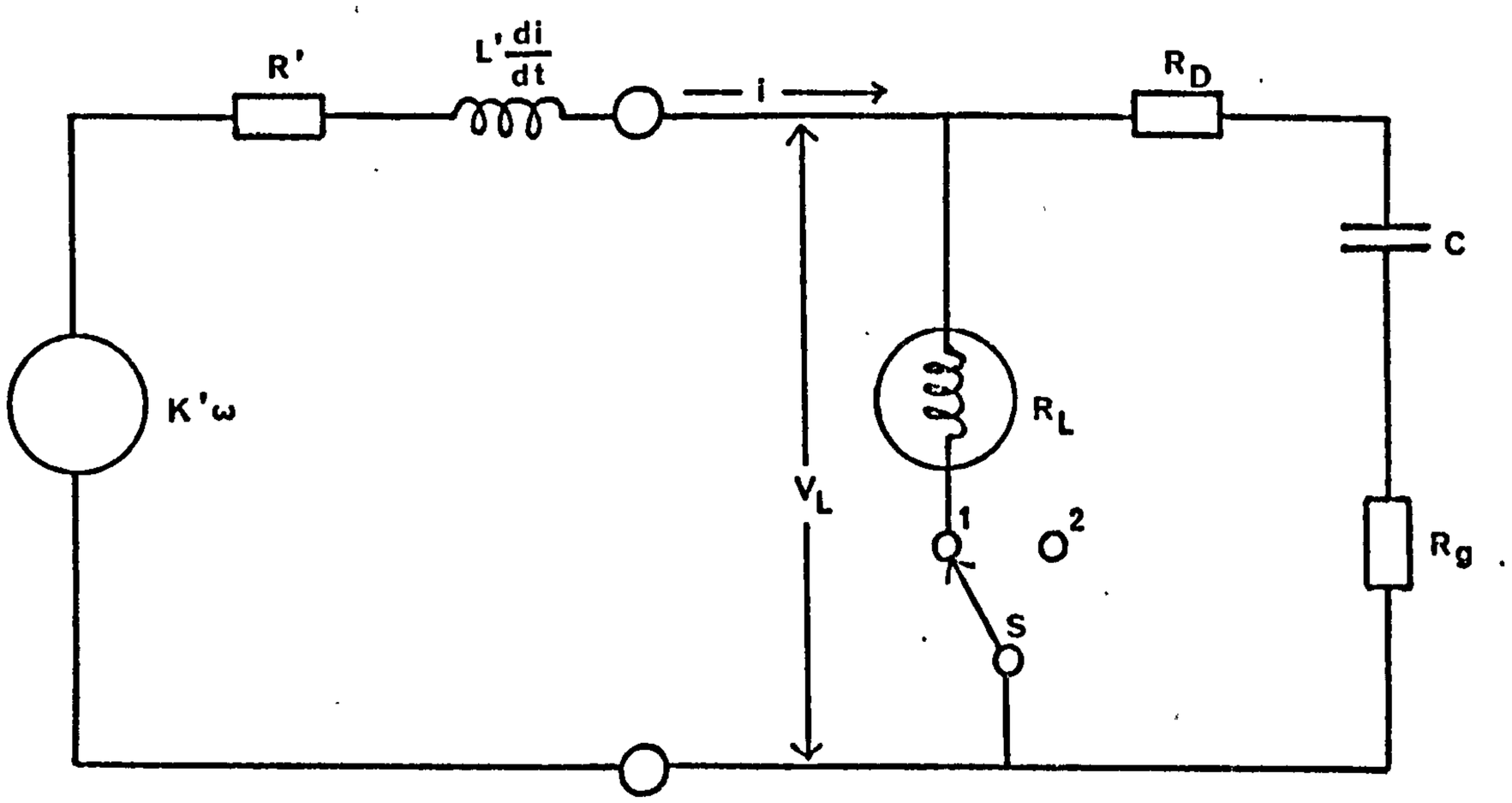

Fig 7·31
Fig 7·32

7·31 Transient Gate Voltage When Bulb Fails At i = 0

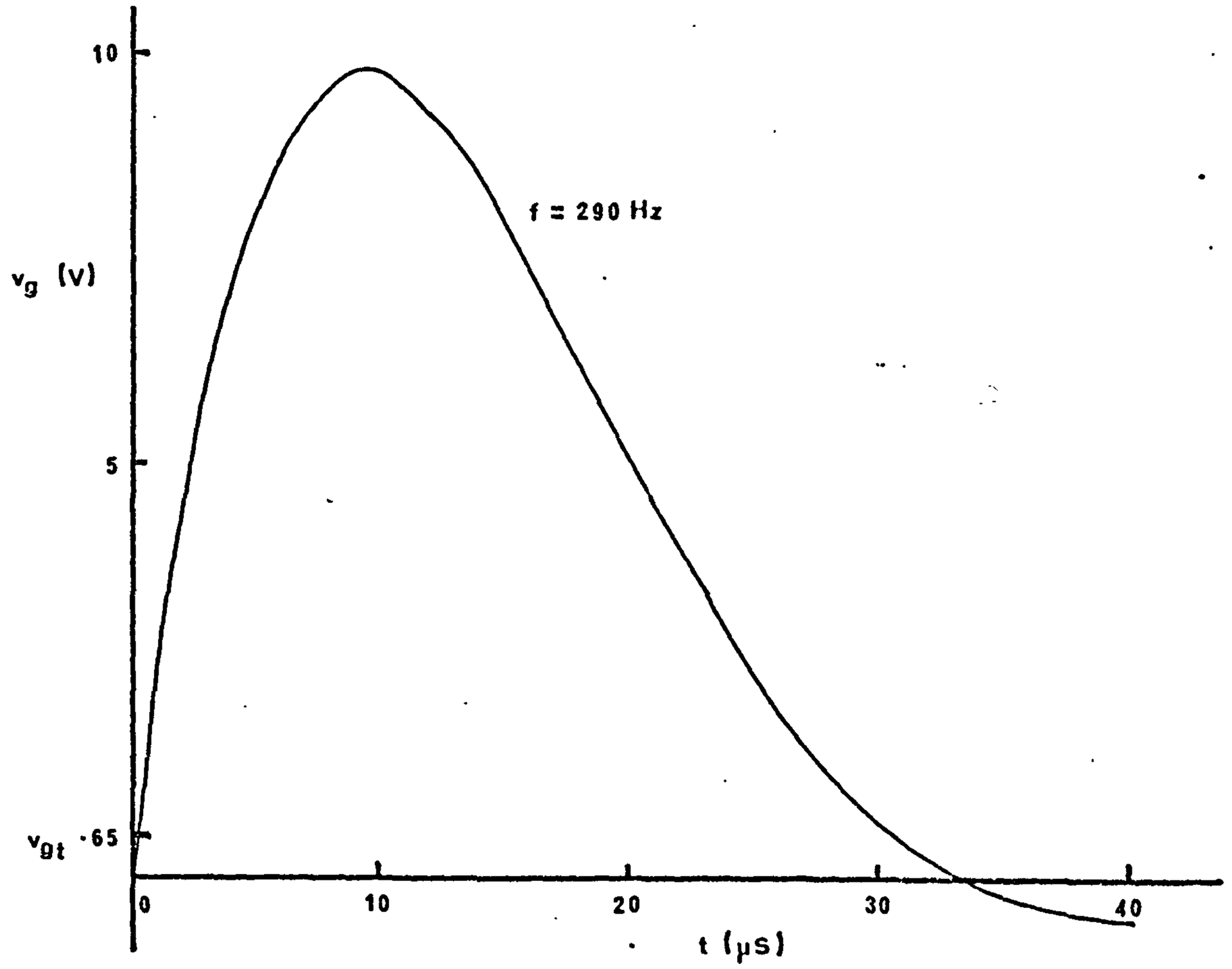

7·32 Transient Gate Voltage When Bulb Fails At $i = I_{max}$

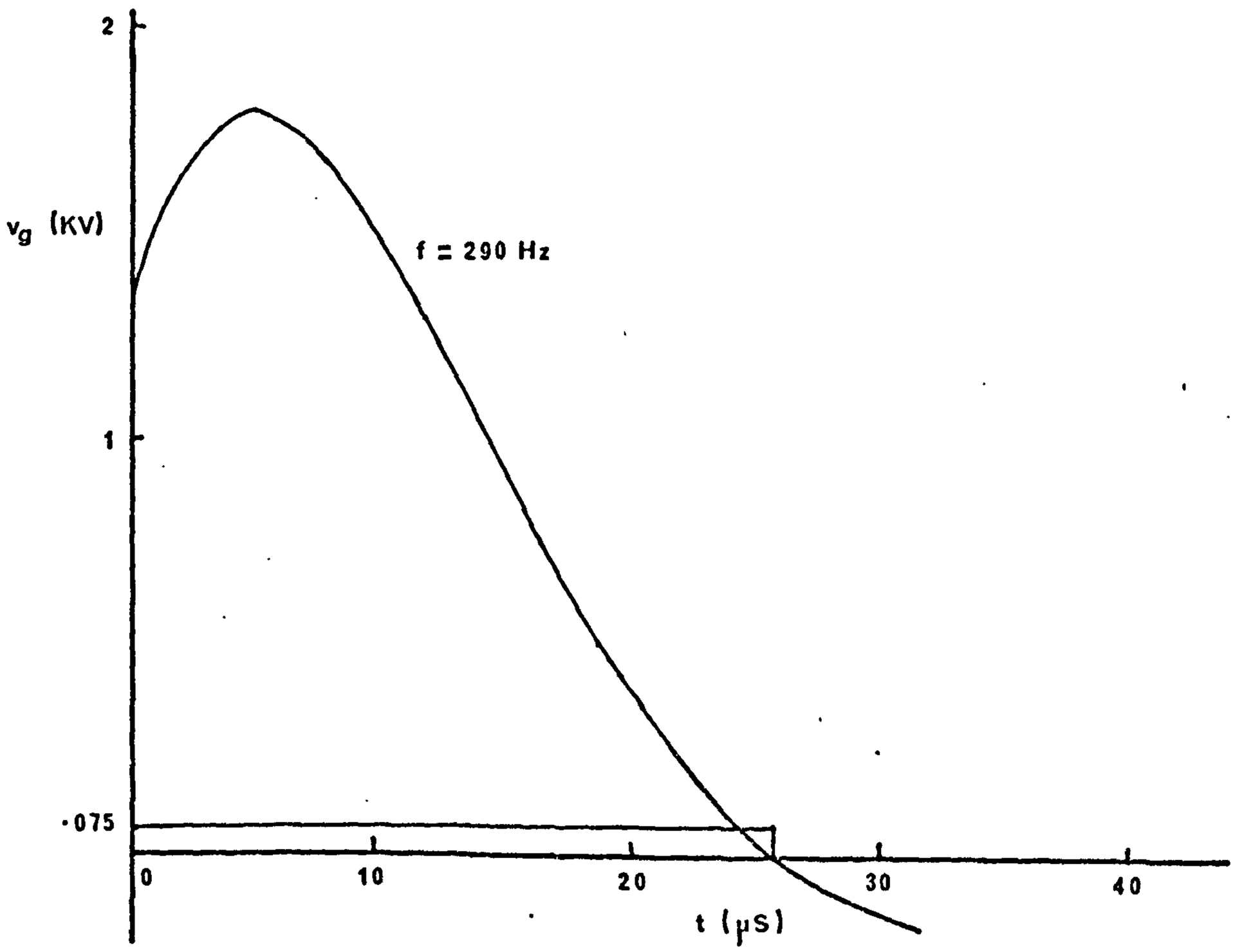

Fig 7·33

Transient Gate Voltage After Bulb Failure At i = 0

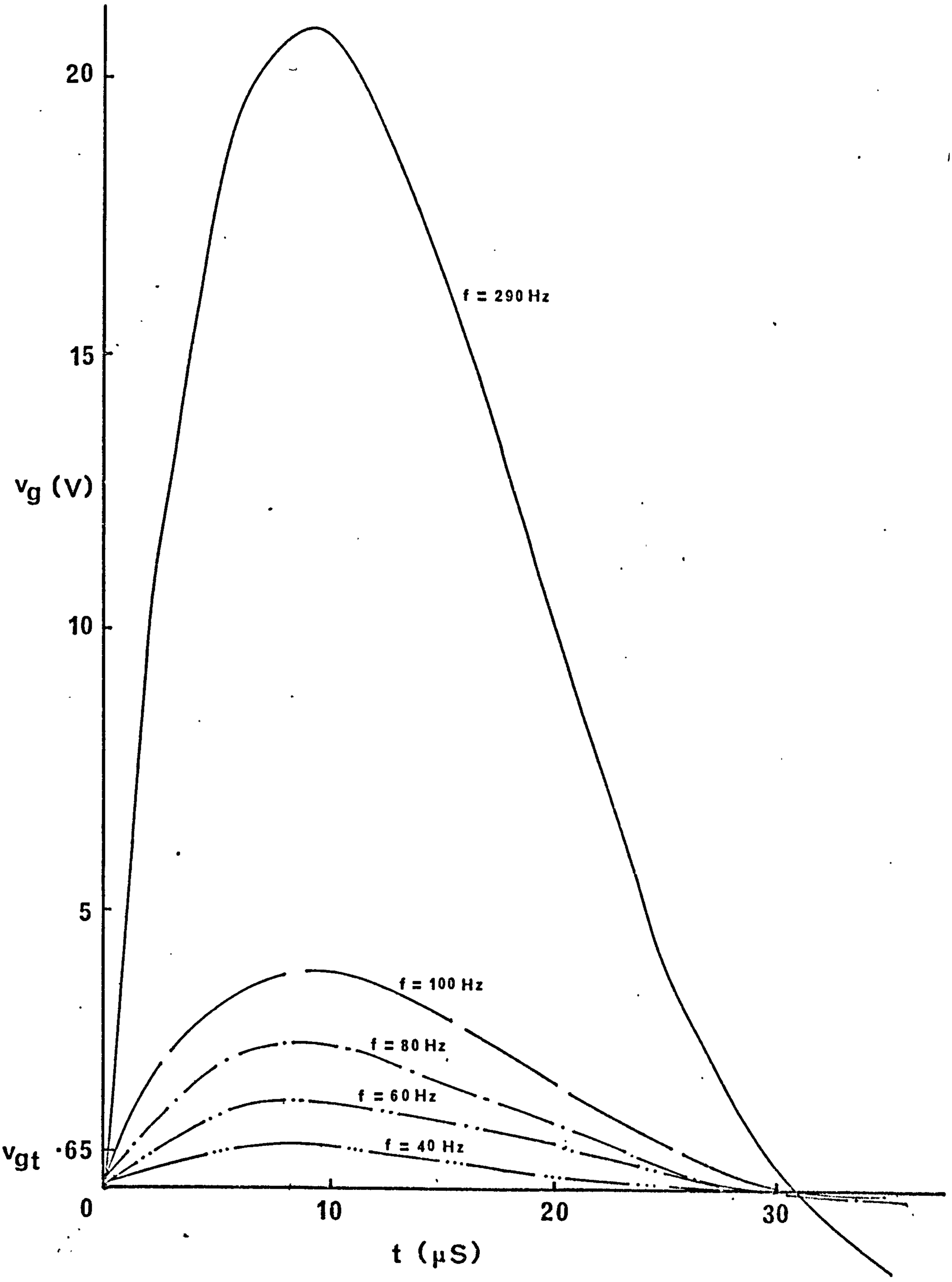

Fig 7·34

Open Circuit Overspeed Protection Approach

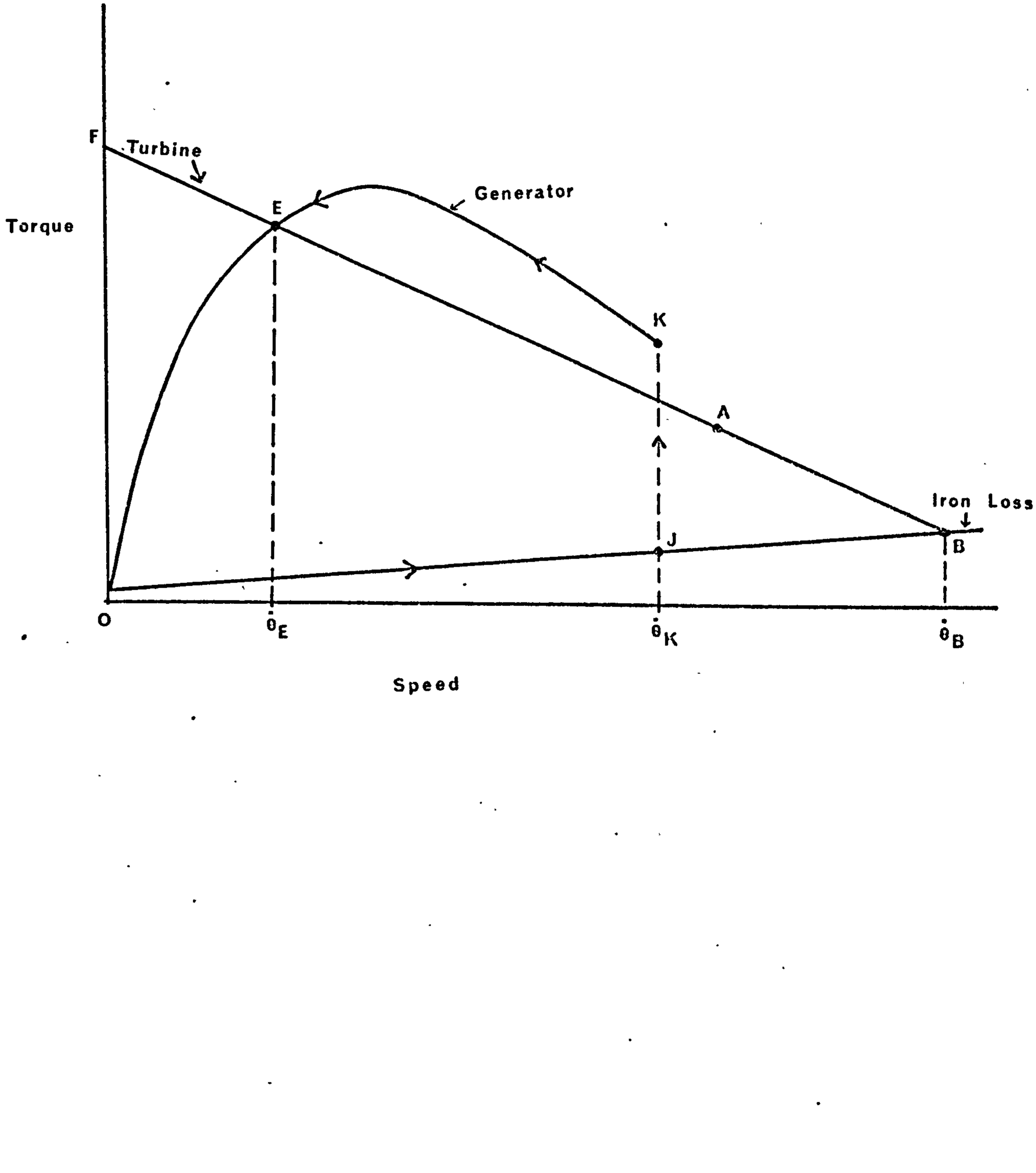

Fig 7·34

Open Circuit Overspeed Protection Approach

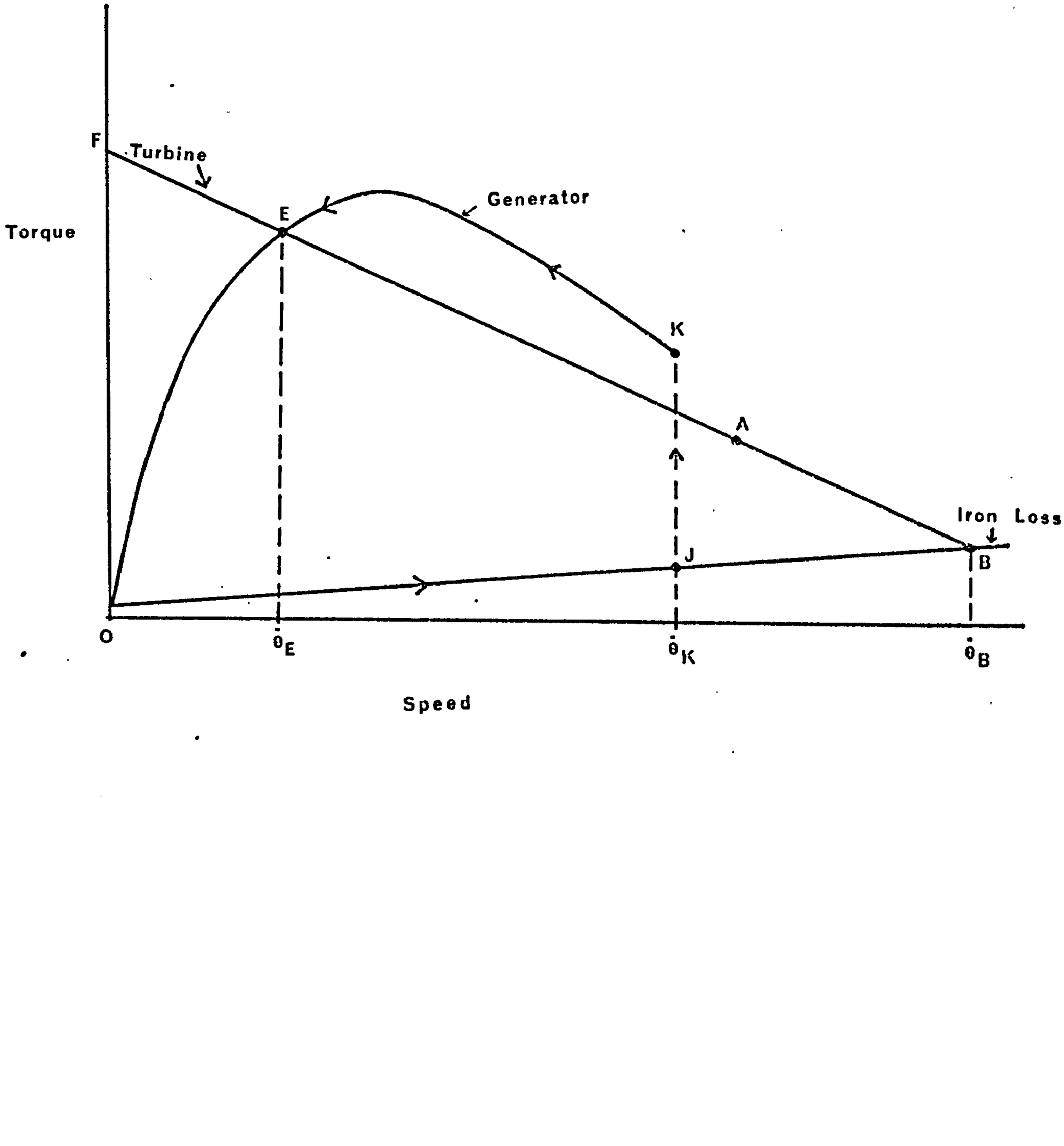

Fig 7·35

Power and Torque – Speed Curve Of Generator With Rotor Design B

Output Power (W)

Bulb Voltage x 0·1 (V)

Power Supplied To The Bulb (W)

Torque (Nm)

Speed (R.P.M.)

Air Pressure p.s.i.

68 +3
65 −3
62

24V 250W Bulb
n = 2

Rated Power Of Bulb

Rated Bulb Voltage

Turbine Torque

Generator Torque

Output Power

Bulb Voltage

300
250
200
100
0

·8
·6
·4
·2
0

2000
4000
6000
7000

Fig 7·36

Fig 7·37

7·36 The Final Protection Circuit

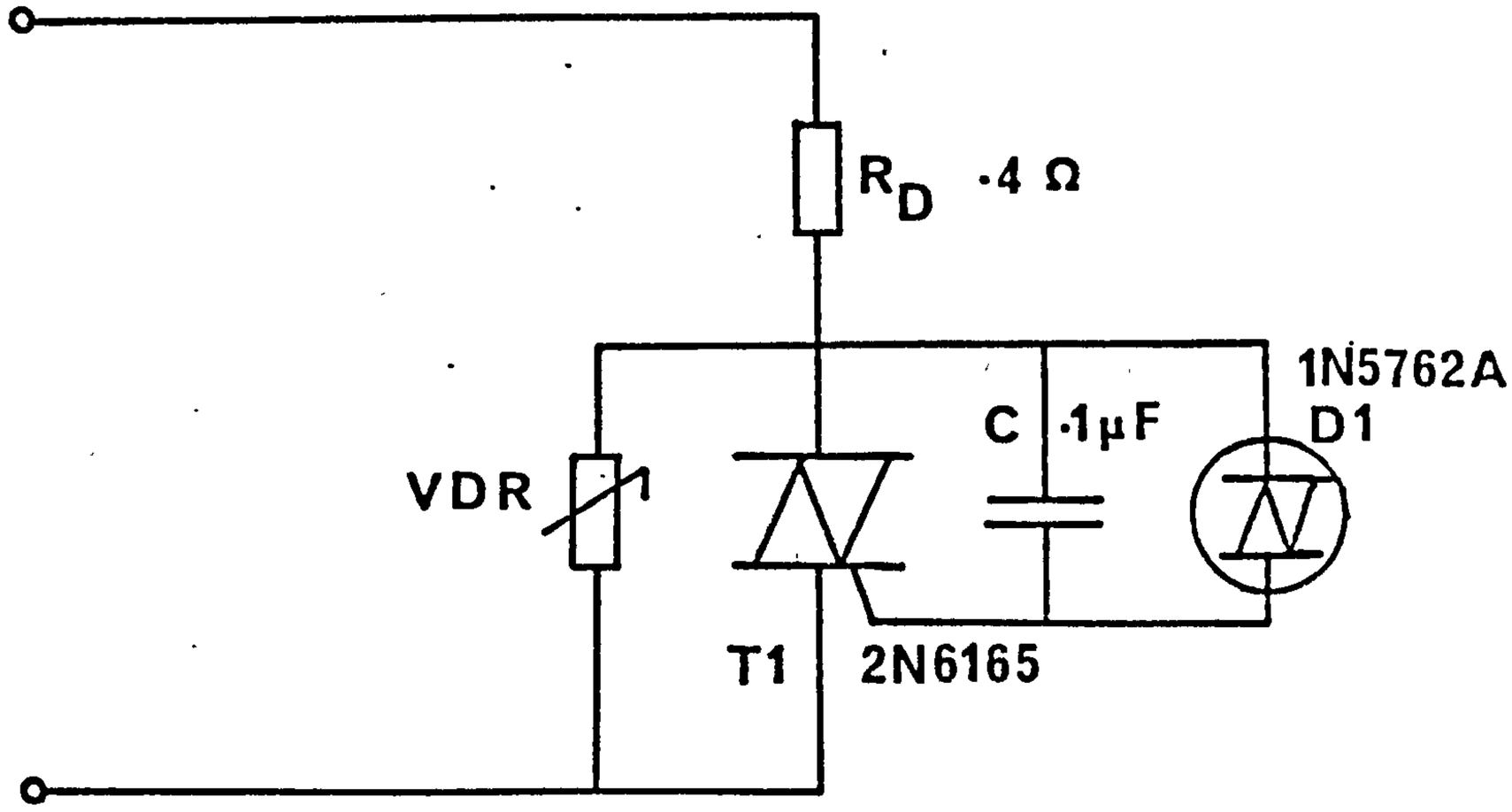

7·37 A Typical Transient Gate Voltage Waveform

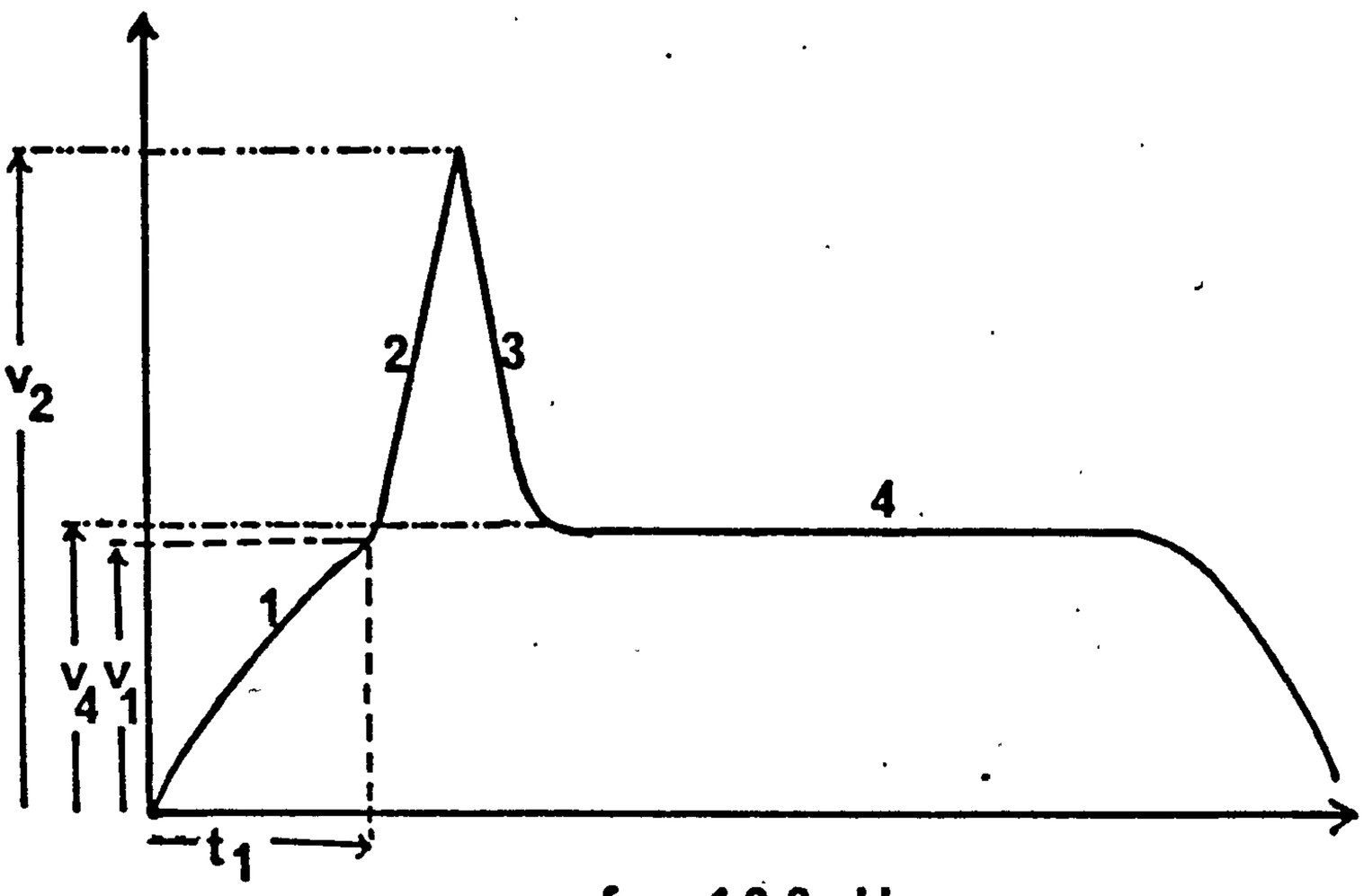

f = 100 Hz
t_1 = 6 μS
v_1 = ·65 V
v_2 = 1·4 V
v_4 = ·7 V

Turbine Torque-speed Characteristics

Equation

$T_t = DP_{si} - C\dot{\theta}$

A Type 1 Nozzle

Angle of Nozzle	Parameter D	Parameter C	Fitted Curve
32°	$2{\cdot}54 \times 10^{-3}$	$6{\cdot}17 \times 10^{-6}$	—— ——
20°	$2{\cdot}75 \times 10^{-3}$	$6{\cdot}6 \times 10^{-6}$	——·——

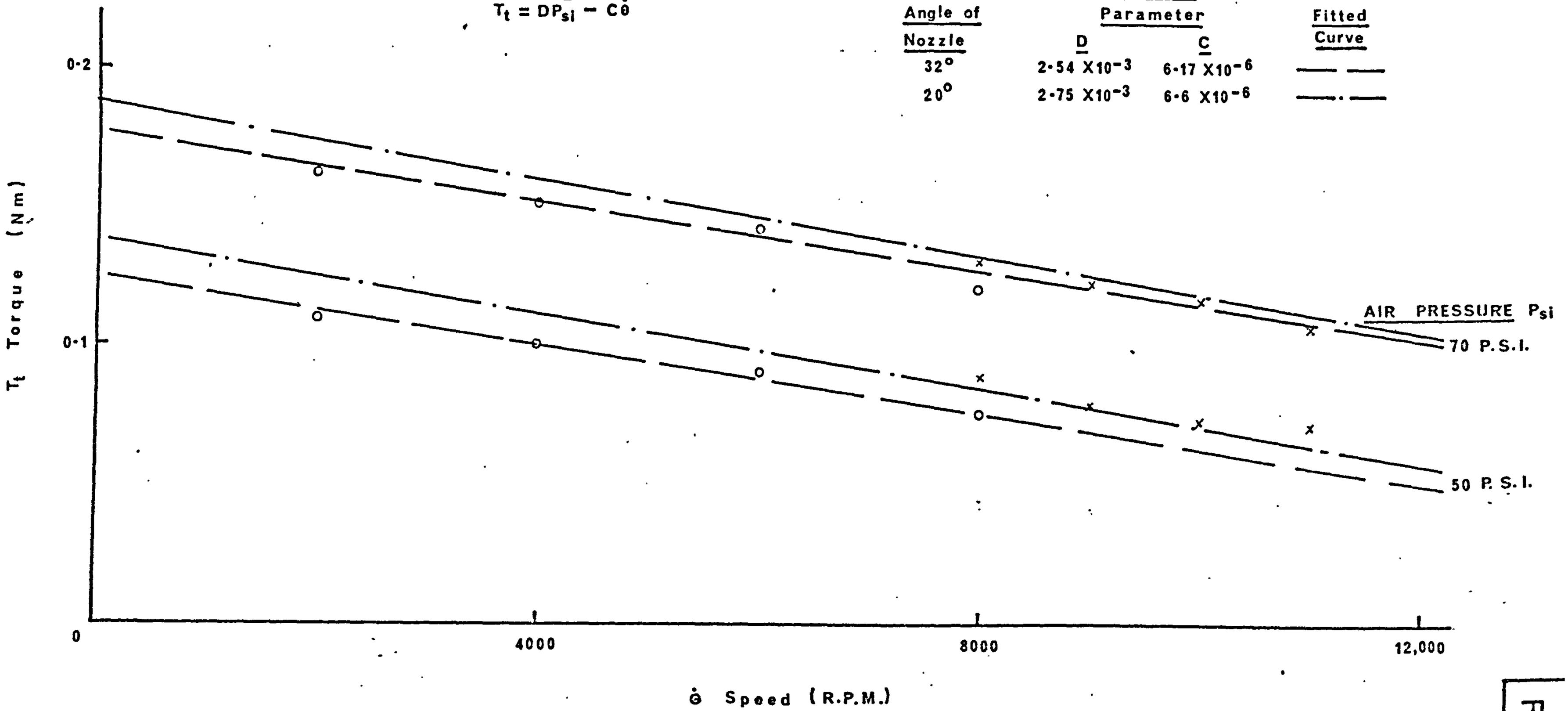

Fig 7.38

Fig 7·39

Variations Of Operating Speed And Air Pressure With Turns Factor

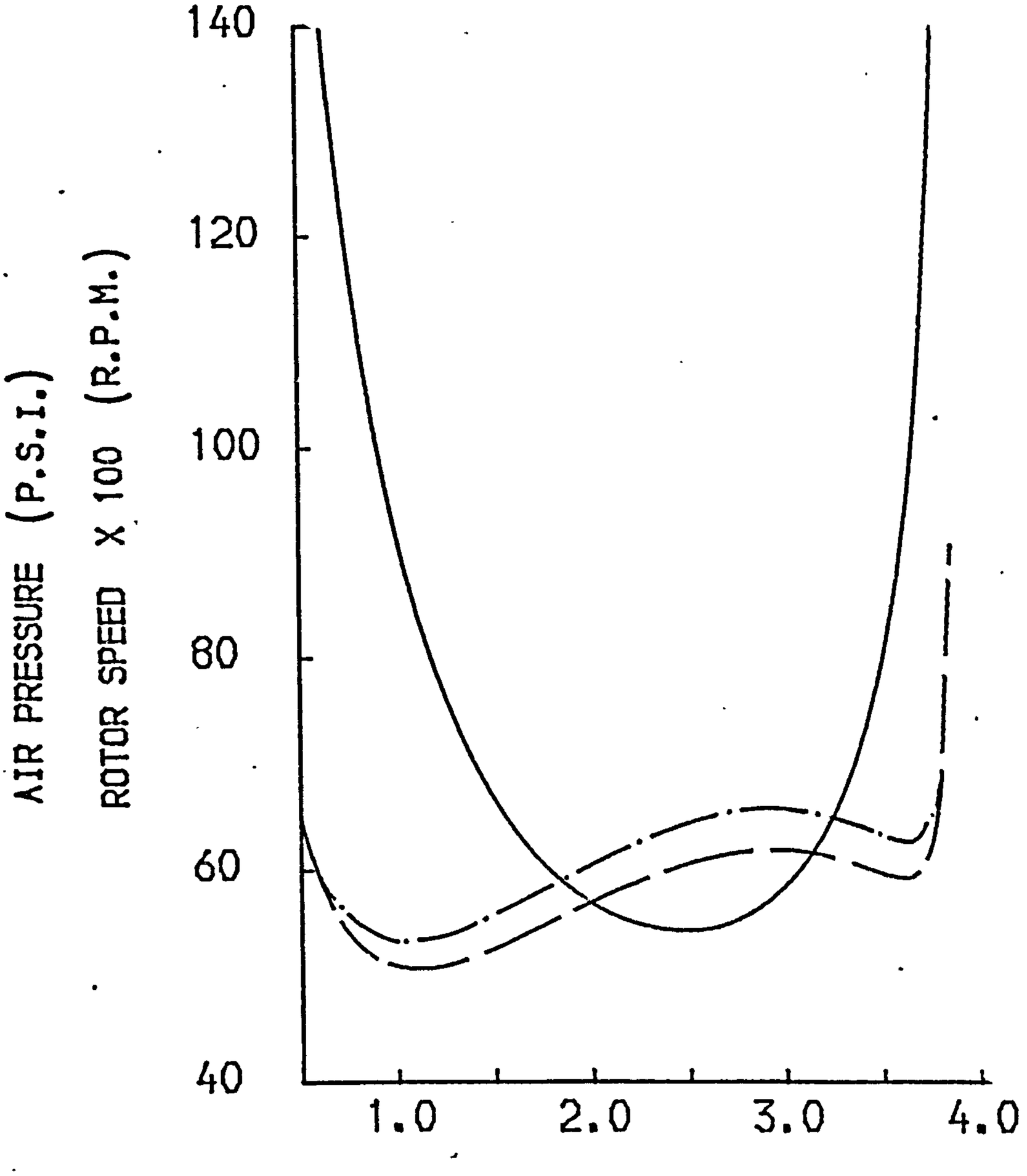

Cobalt Generator Powering A 12V 55W Bulb

A Type 1 Nozzle

Angle of Nozzle	Air Pressure
32°	— · —
20°	— —

Speed

Fig A·1

Picture Of Test Rig

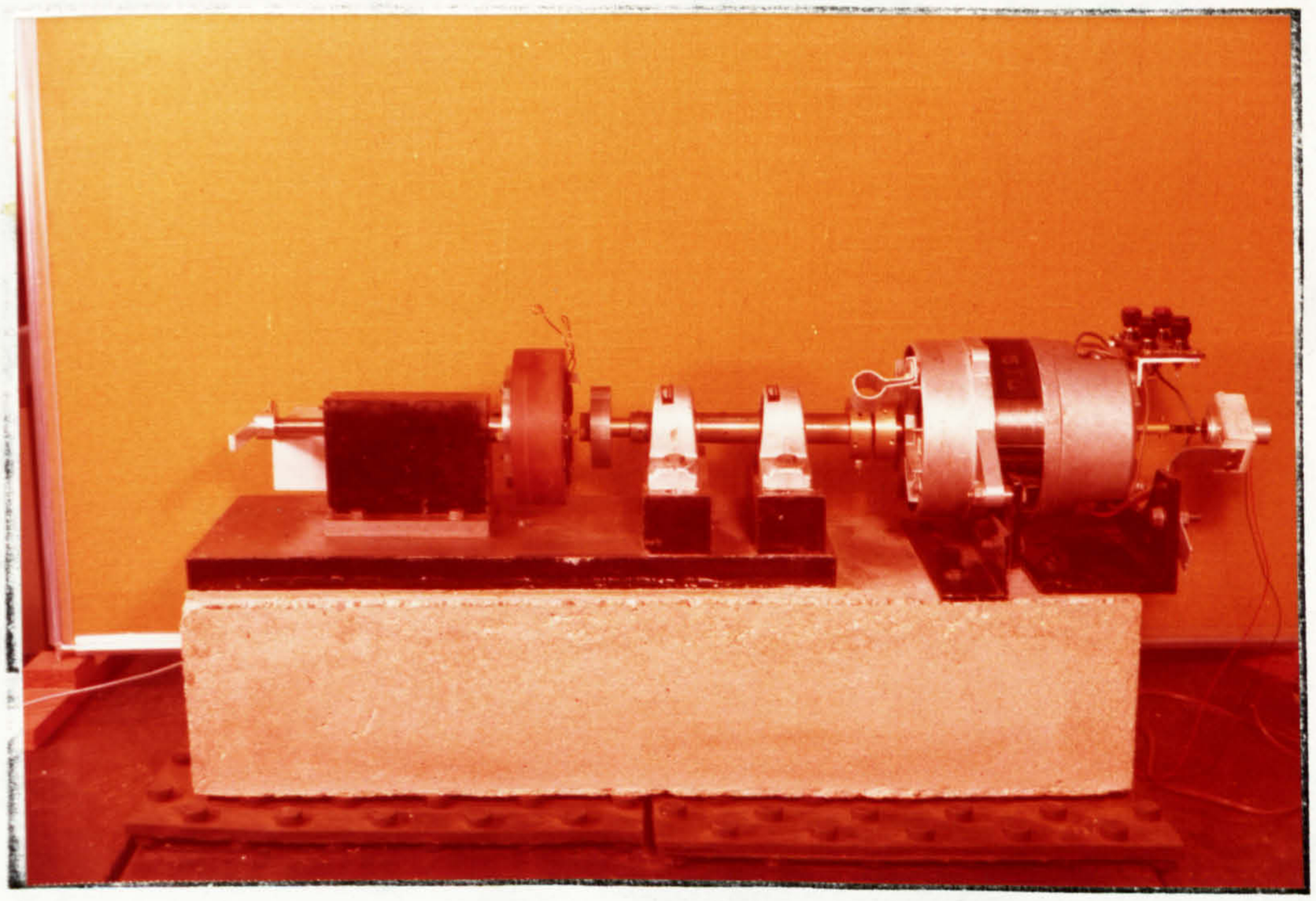

Fig A·2

Schematic Diagram Of Test Rig

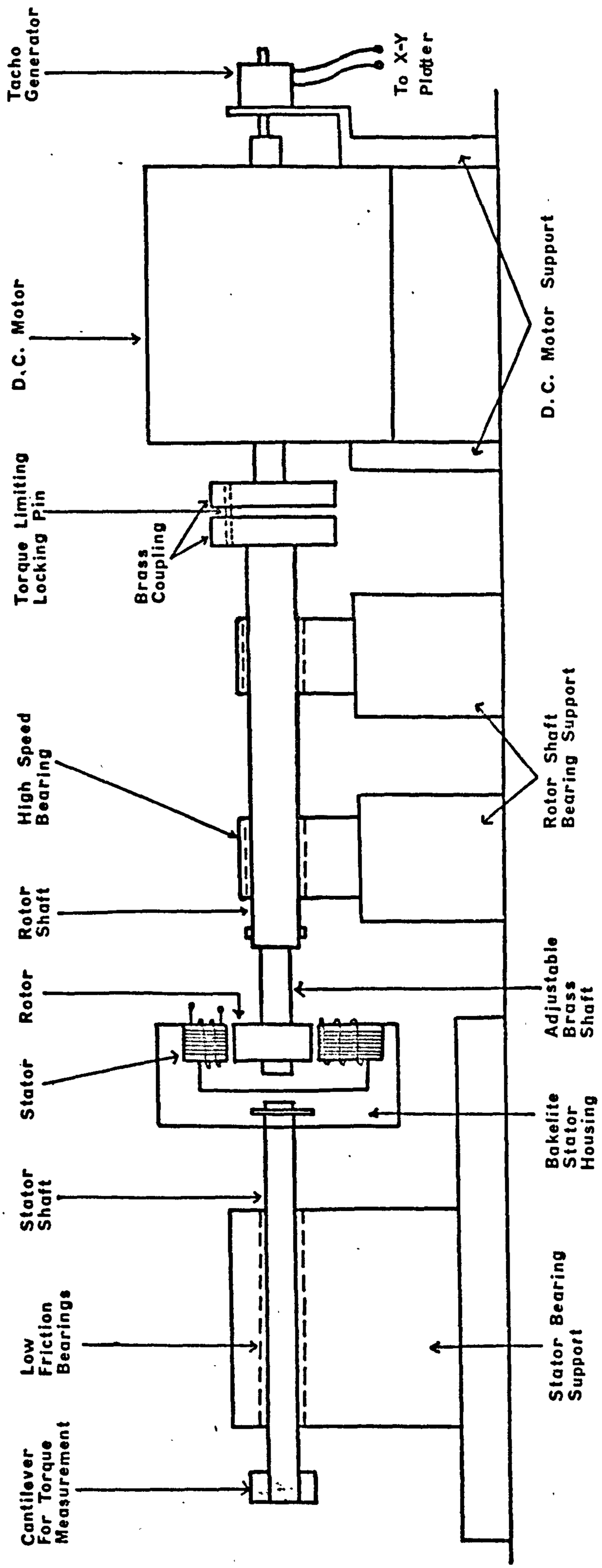

Fig A·3

Fig A·4

A·3 Stator-Rotor Arrangement

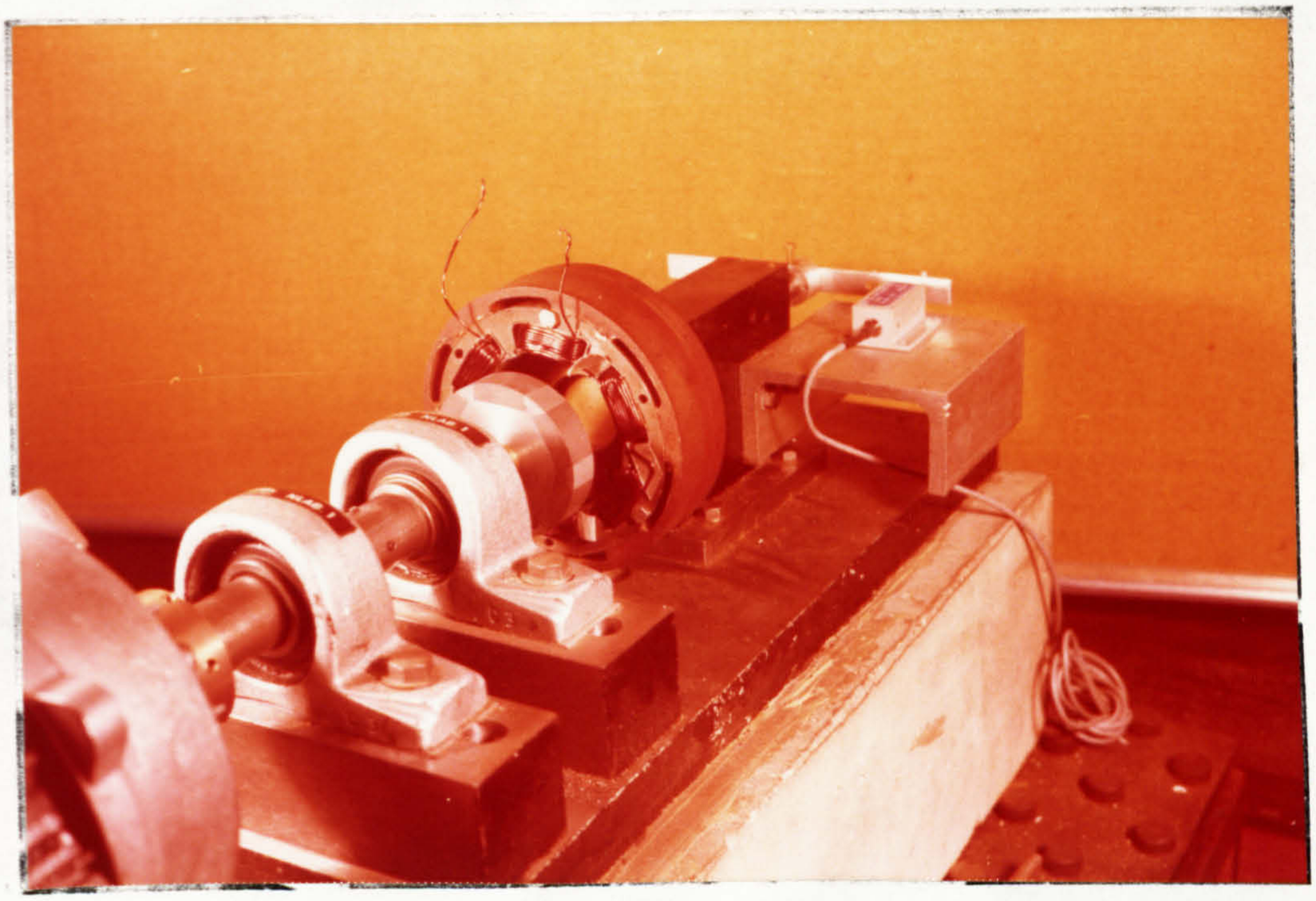

A·4 Torque Measuring Arrangement

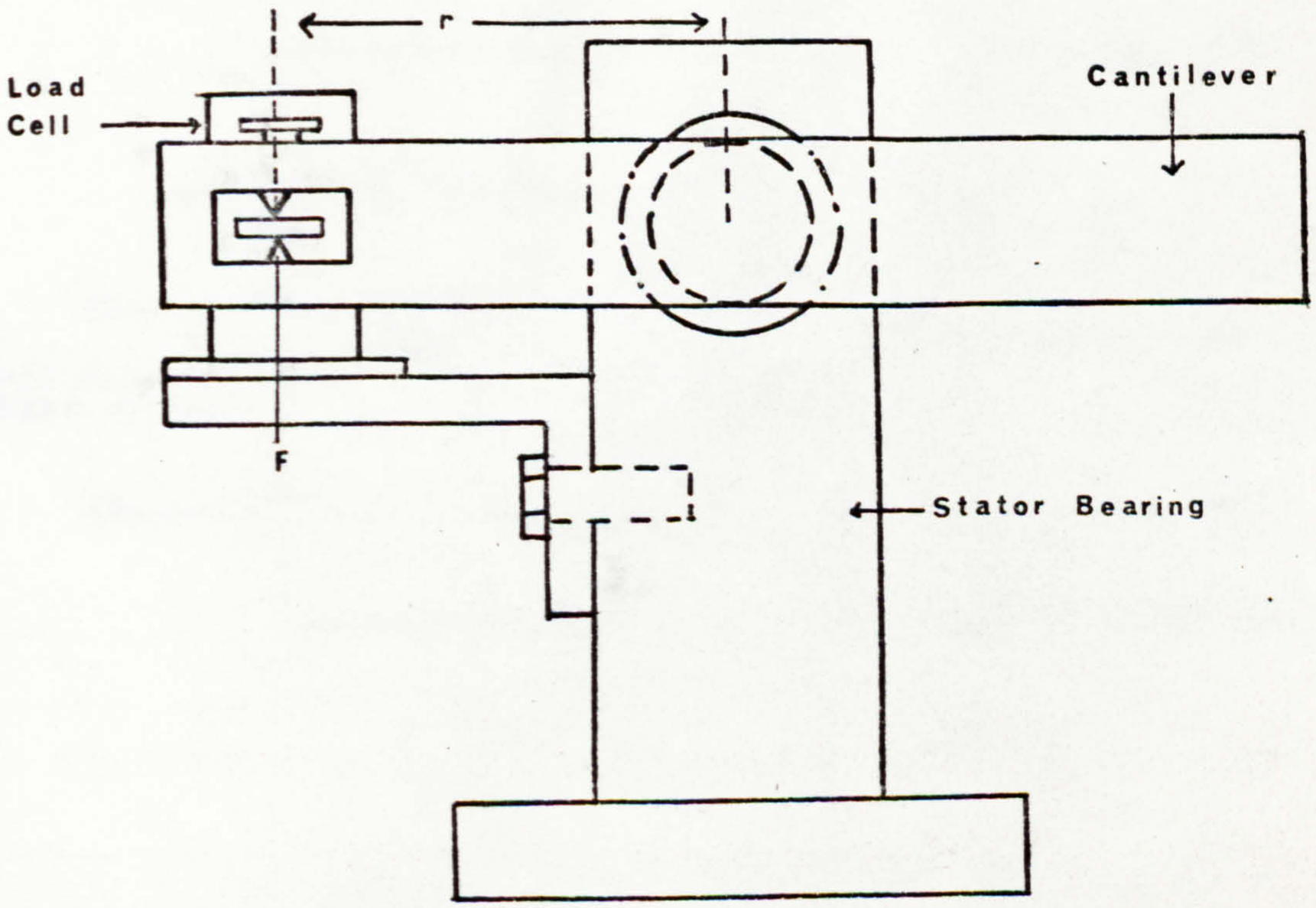

Fig A·5

Fig A·6

A.5 Picture Of Torque Measuring Equipment

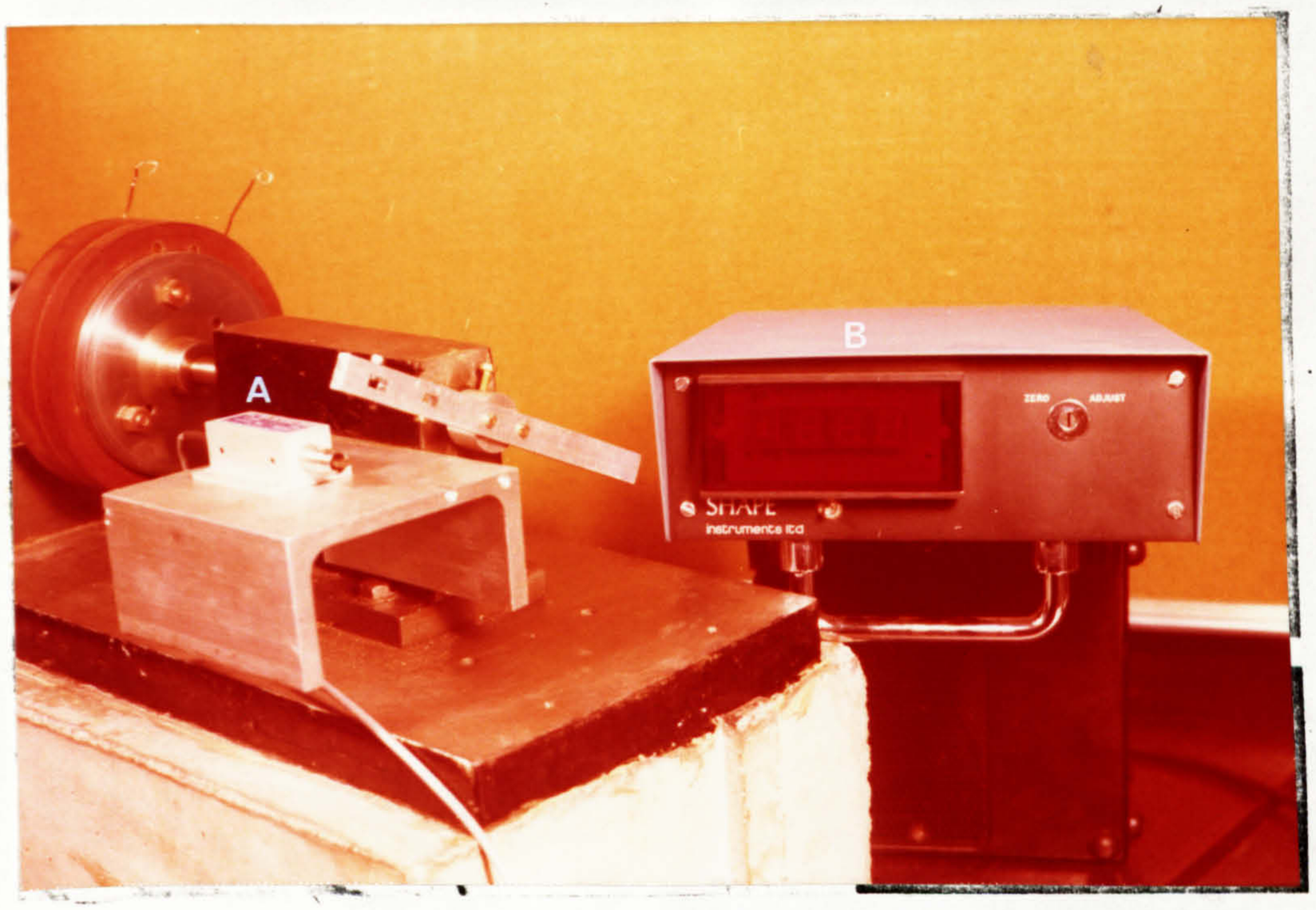

A·6 Offset Circuit

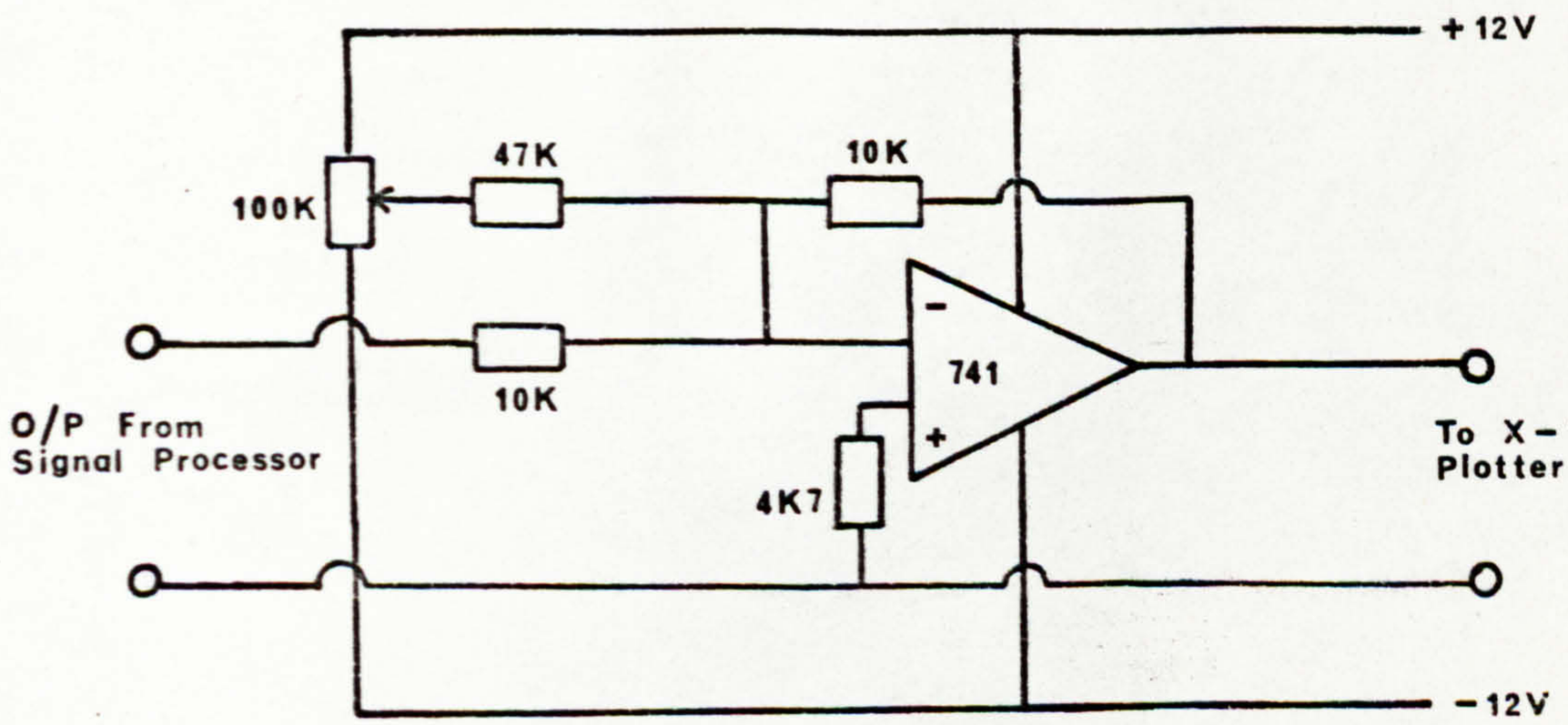

Fig A·7
Fig A·8

A·7 Saliency Torque Measuring Arrangement

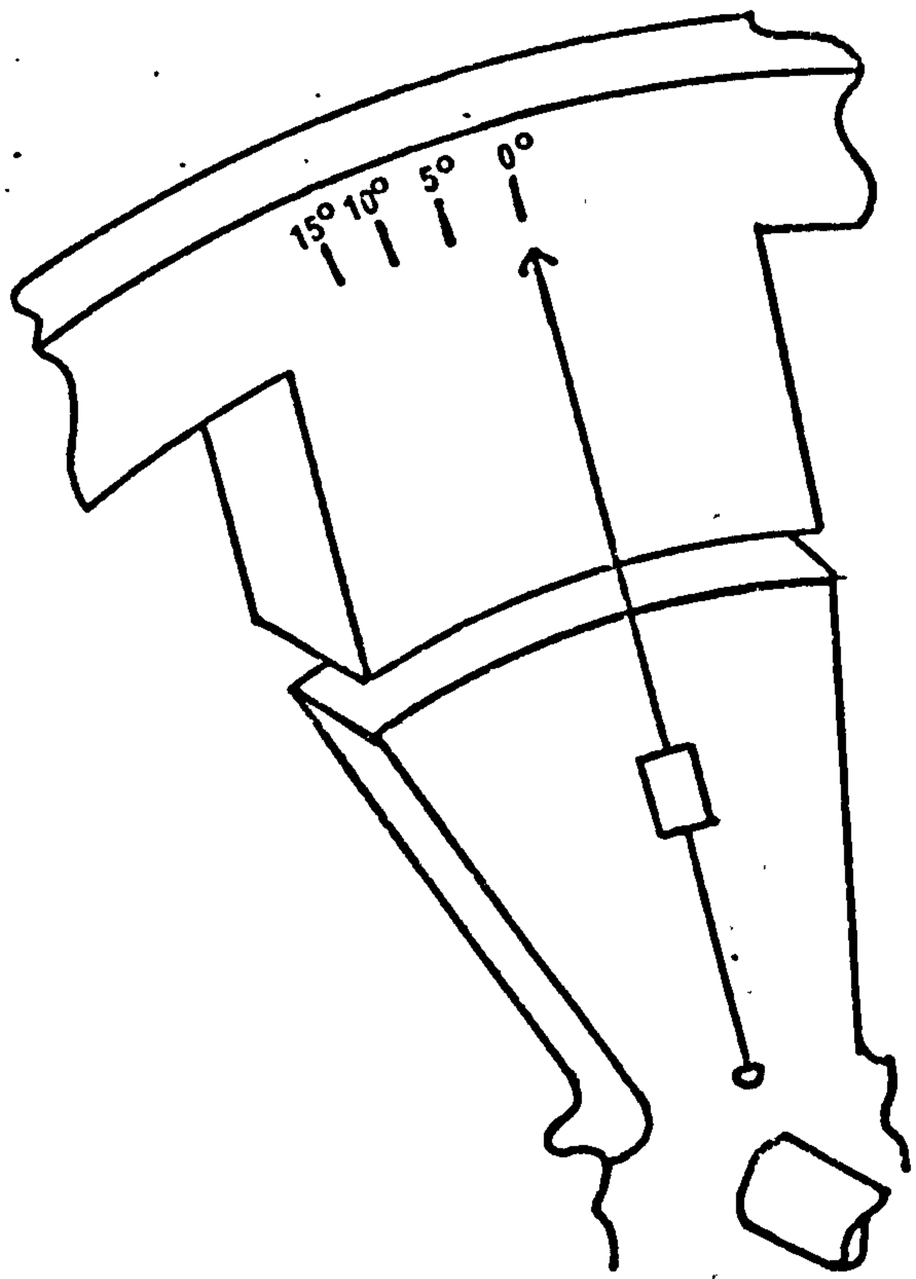

A·8 Circuit Arrangement

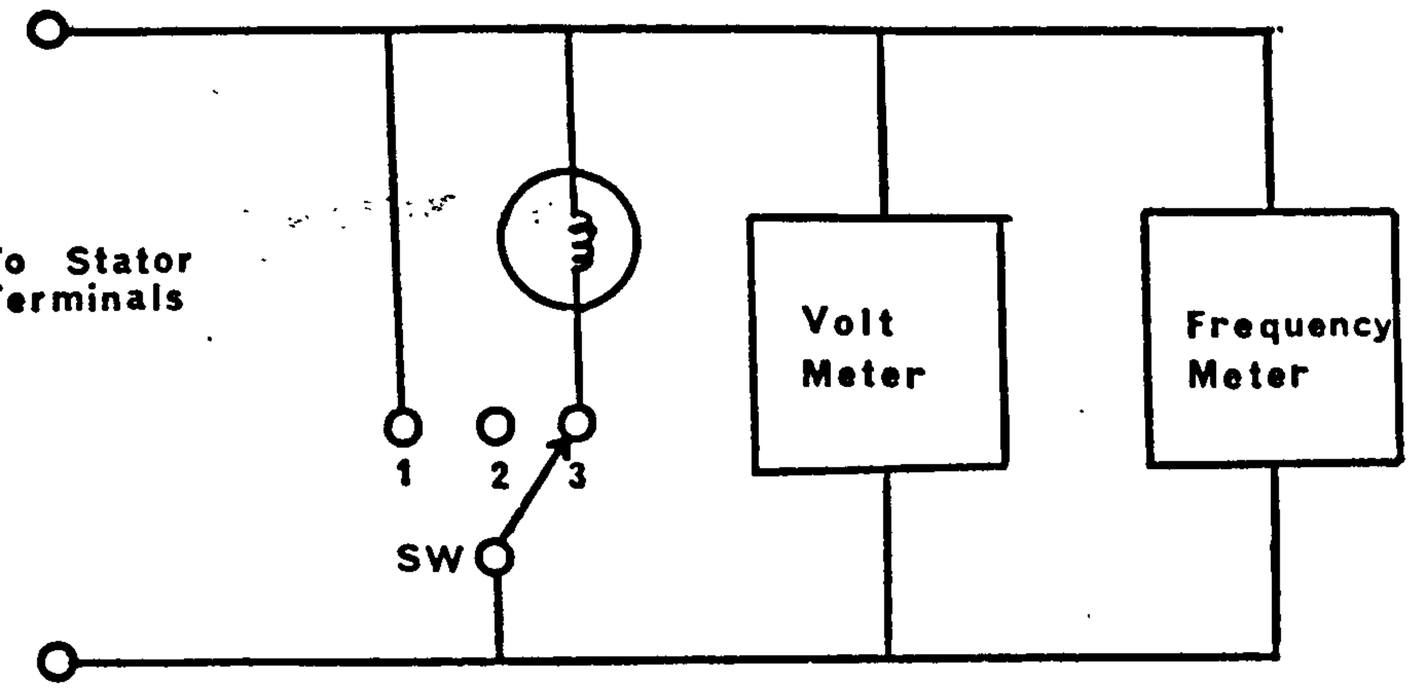

Fig A·9

A·9 Integrated Circuit

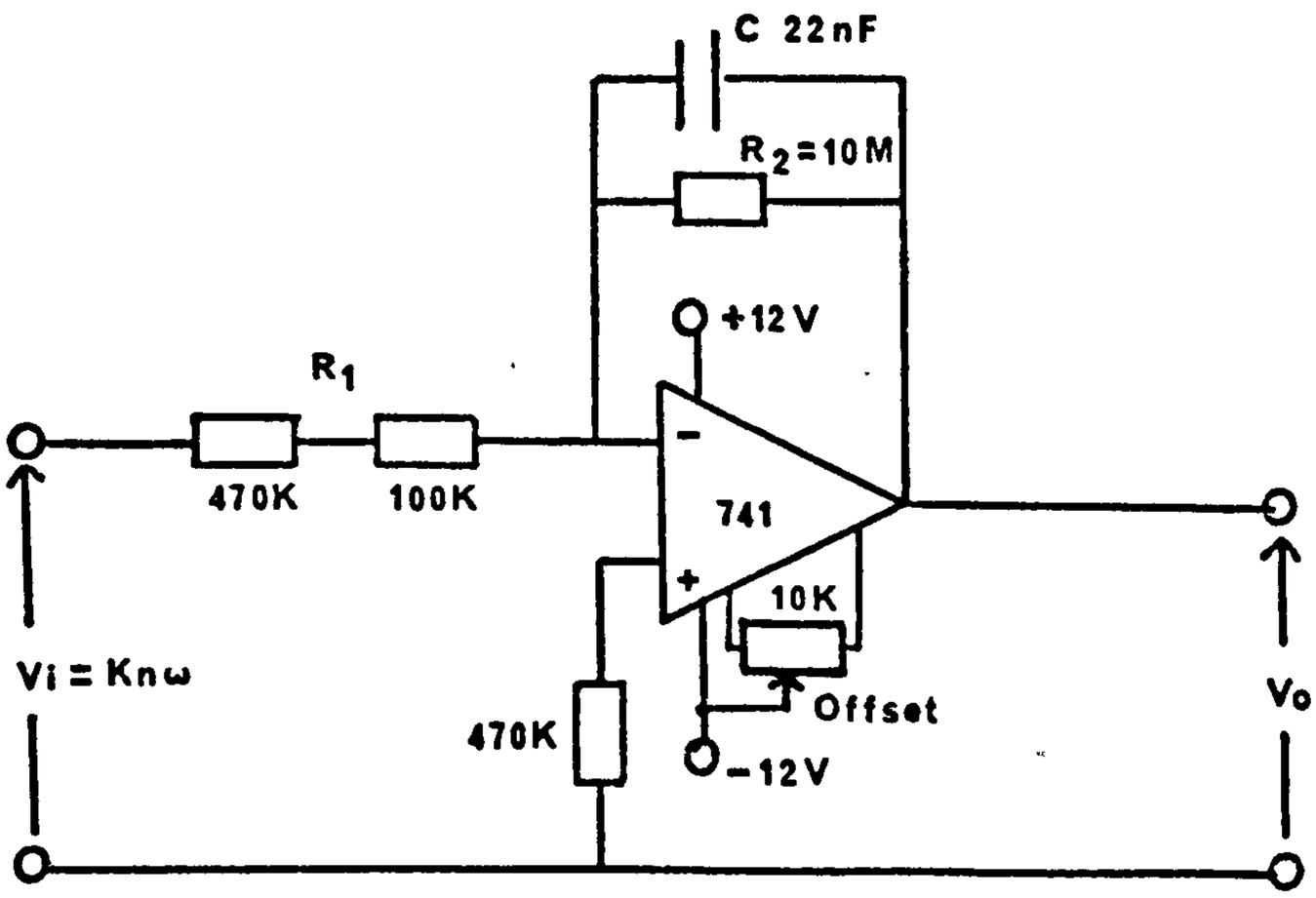

Fig A·IC

A·10 Speed Control Circuit

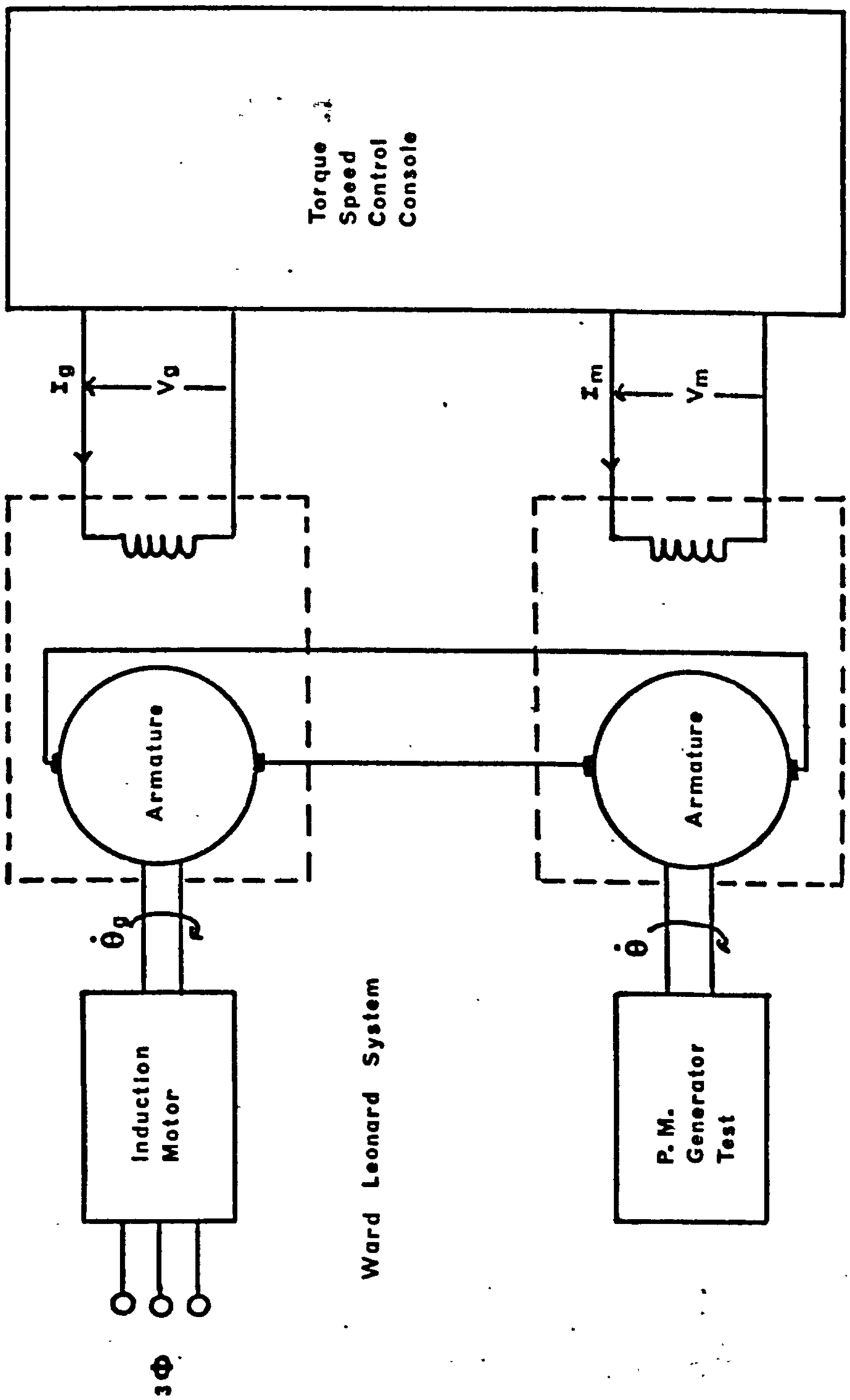

Fig B·1

Shape Of Short-Circuit Current Variation

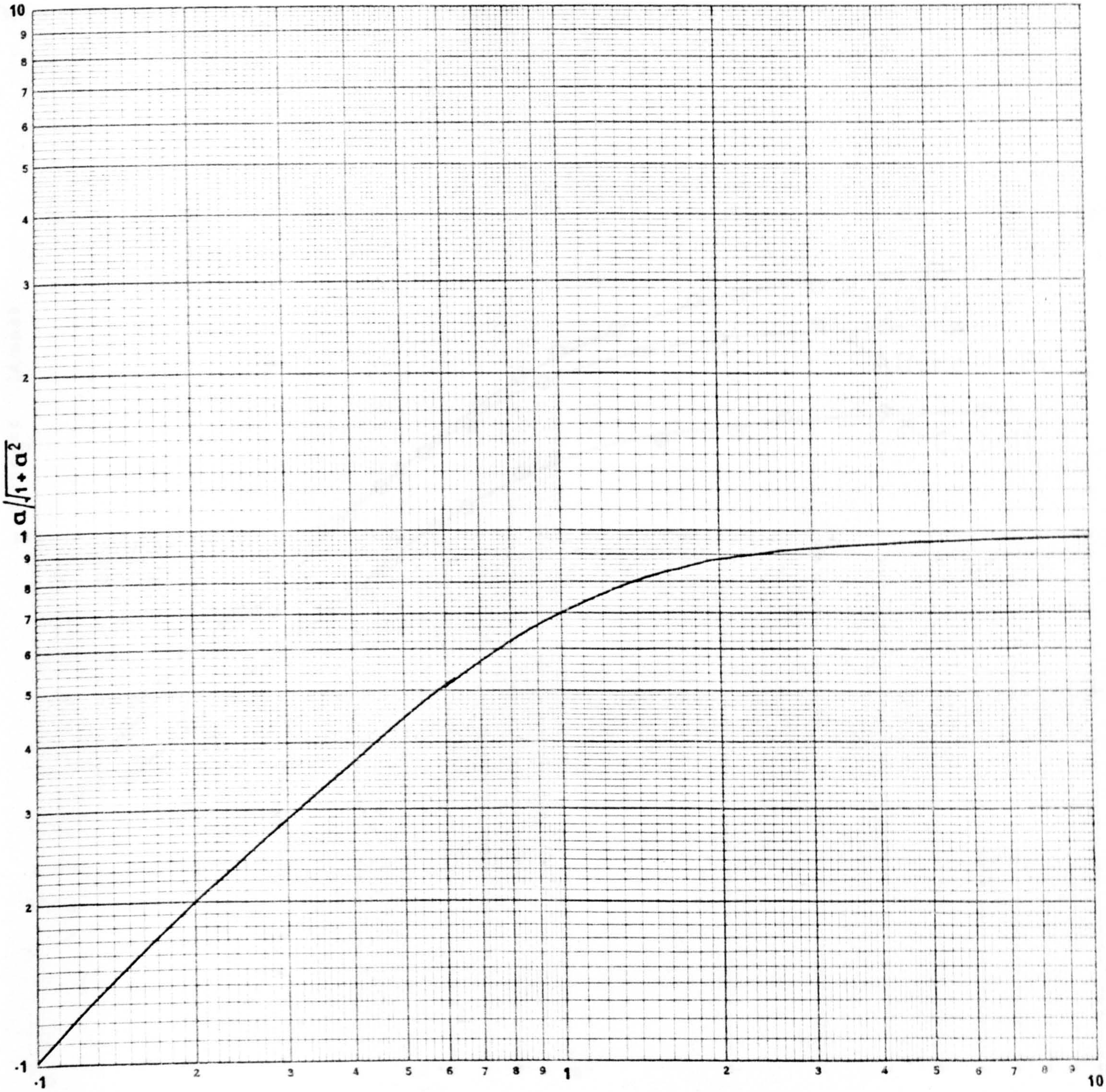

Fig B·2

VARIATION OF SHORT CIRCUIT CURRENT WITH FREQUENCY FOR DIFFERENT ROTOR MATERIALS

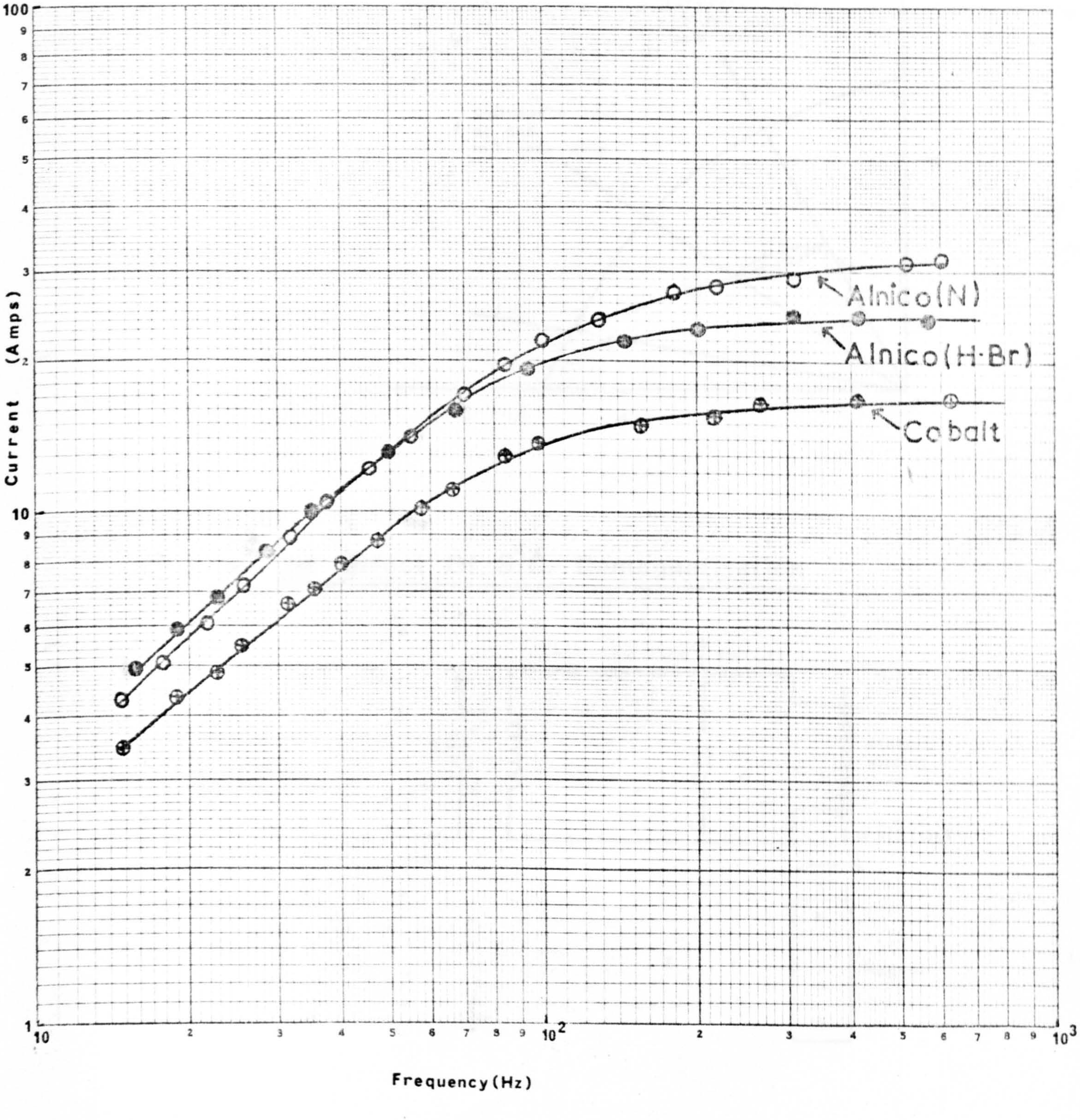

Fig C·1

Fig C·2

C·1 Effect Of Alternating Permeance Line

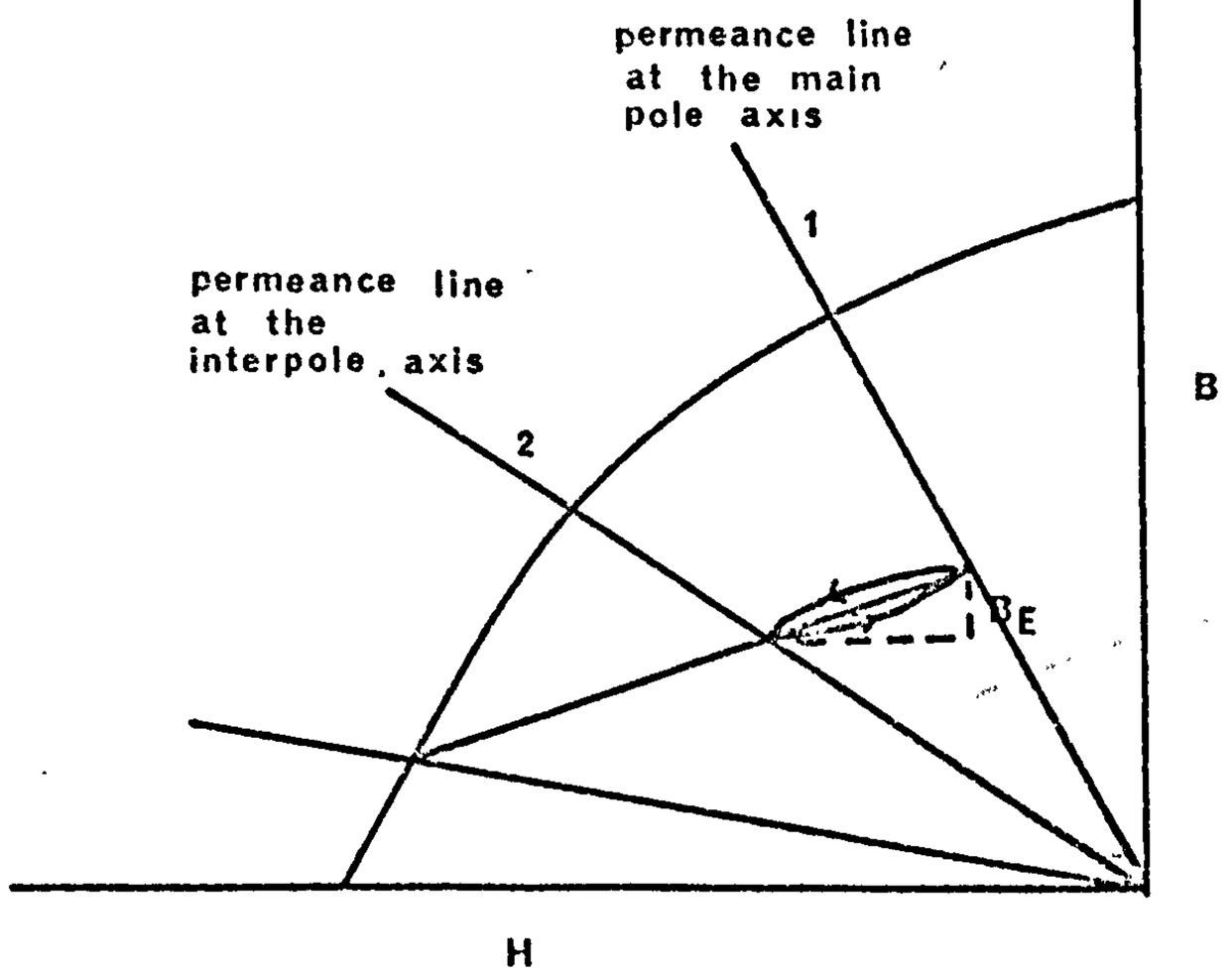

C·2 Effect Of S.C. Demagnetisation

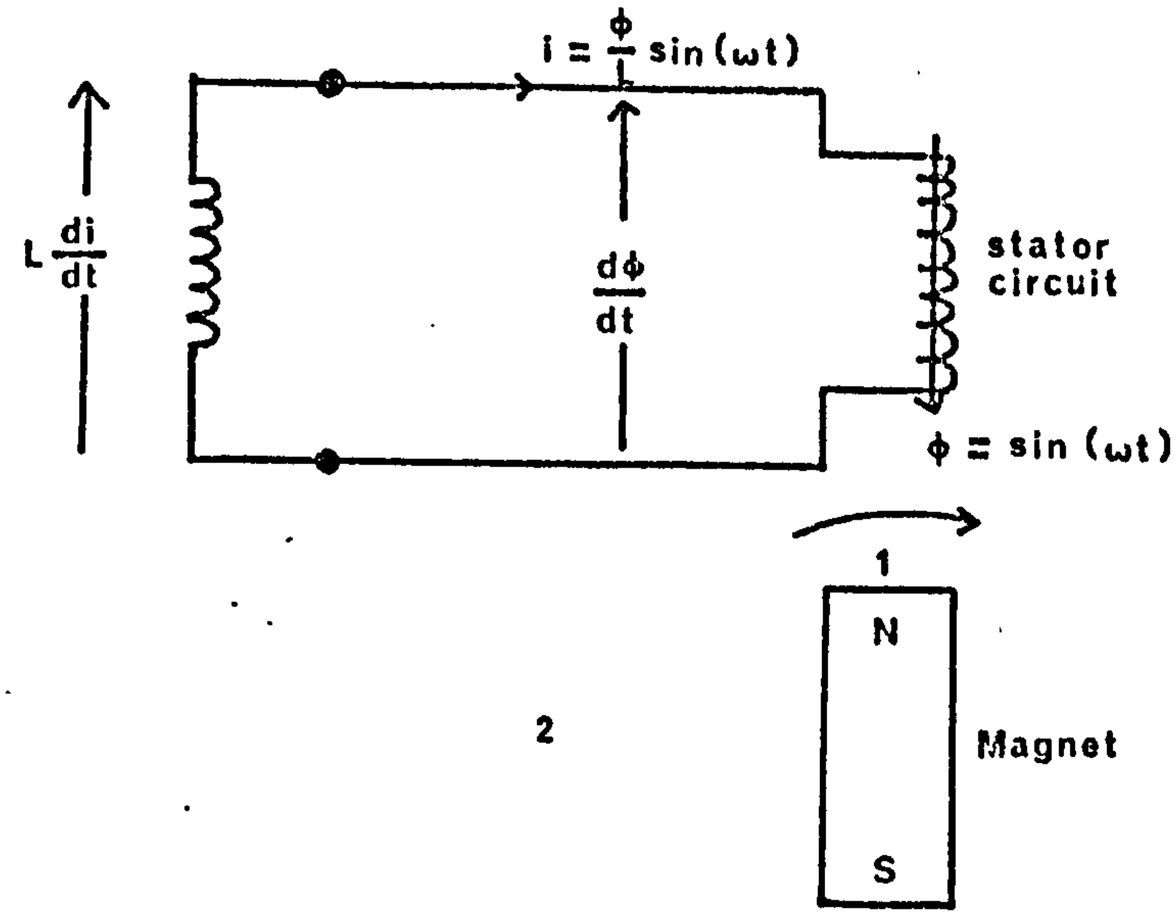

Fig C·3

Effect Of External Demagnetisation

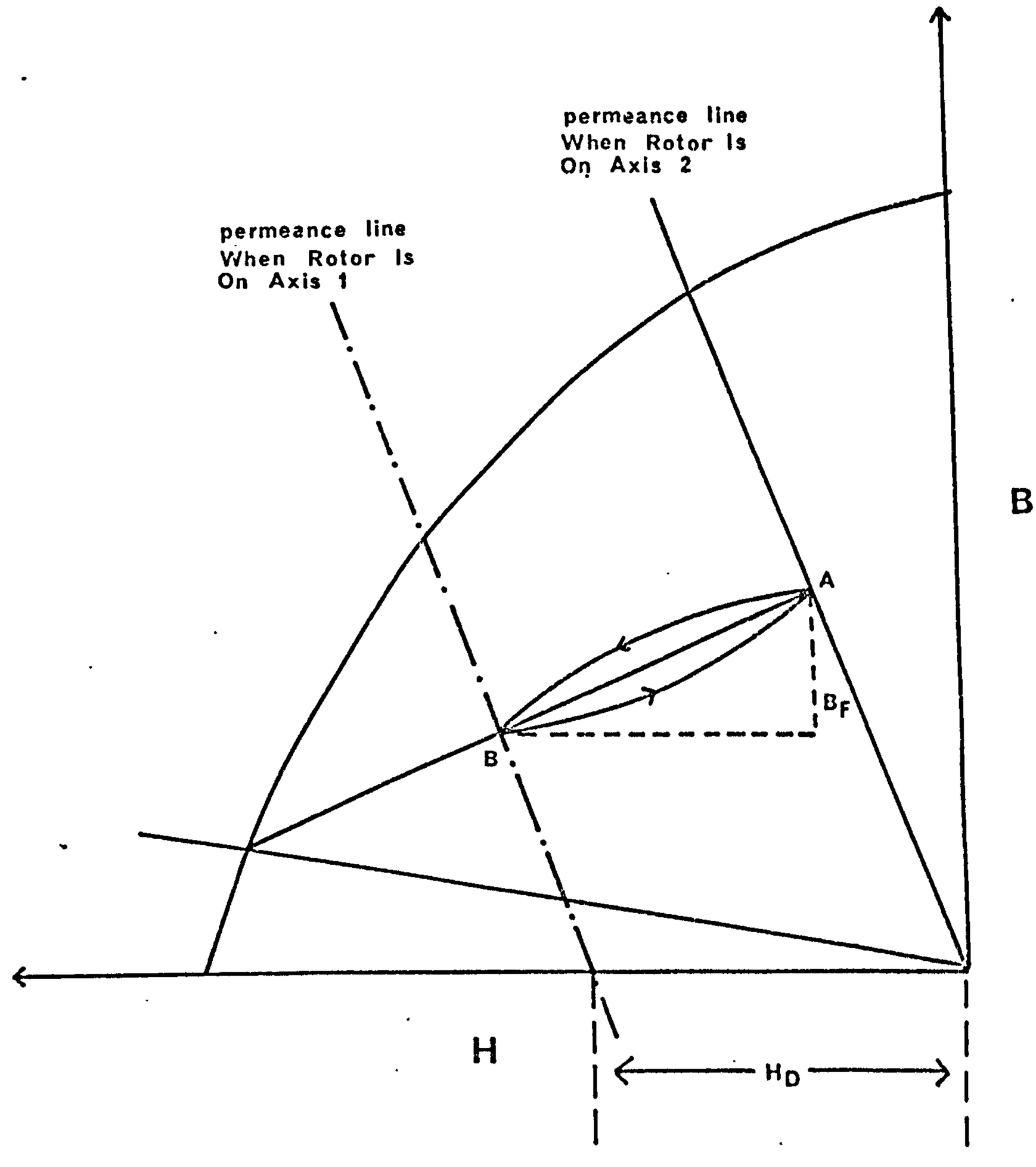

Measured Loss Torque

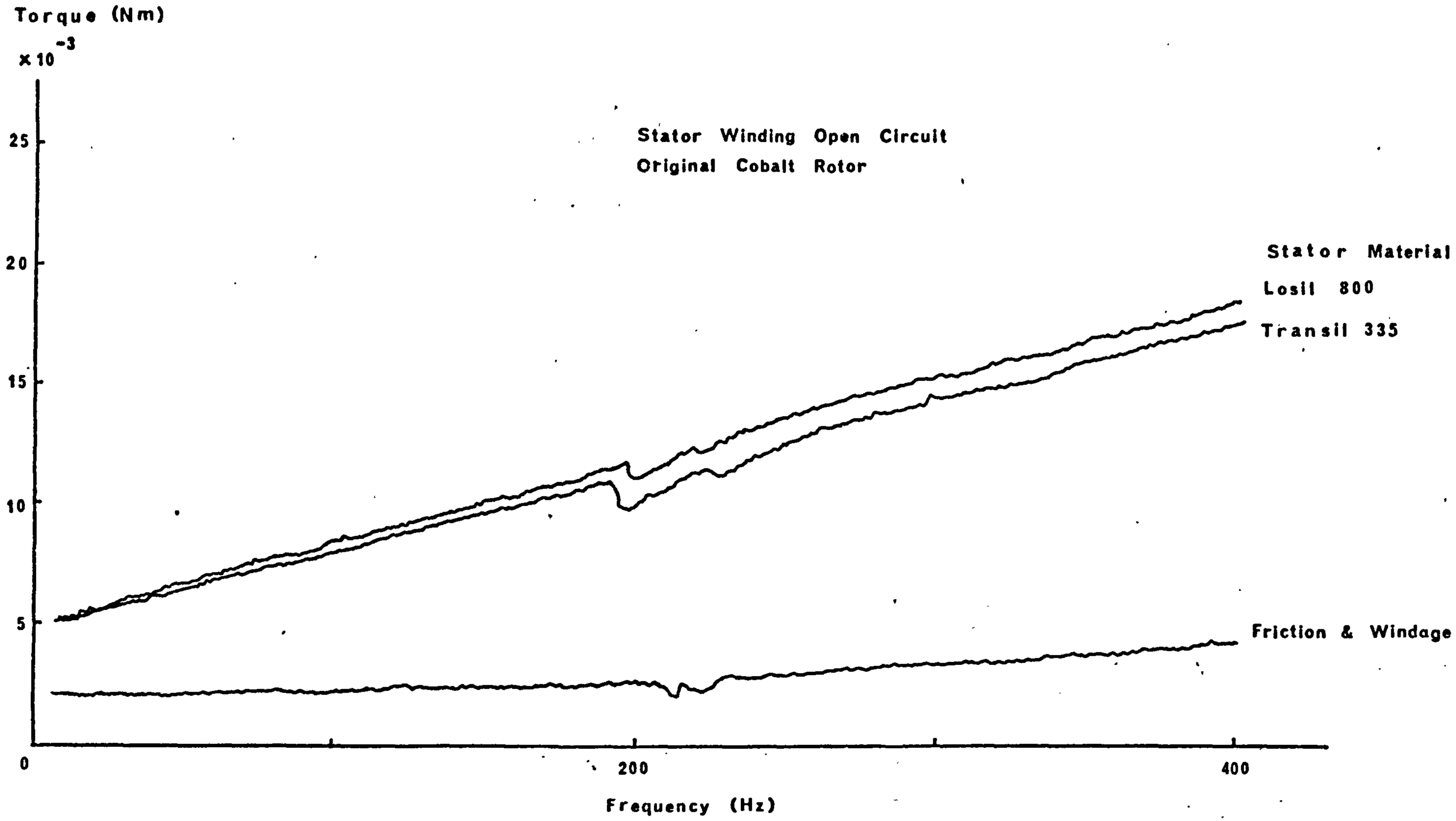

Fig C.4 -

Fig C·5

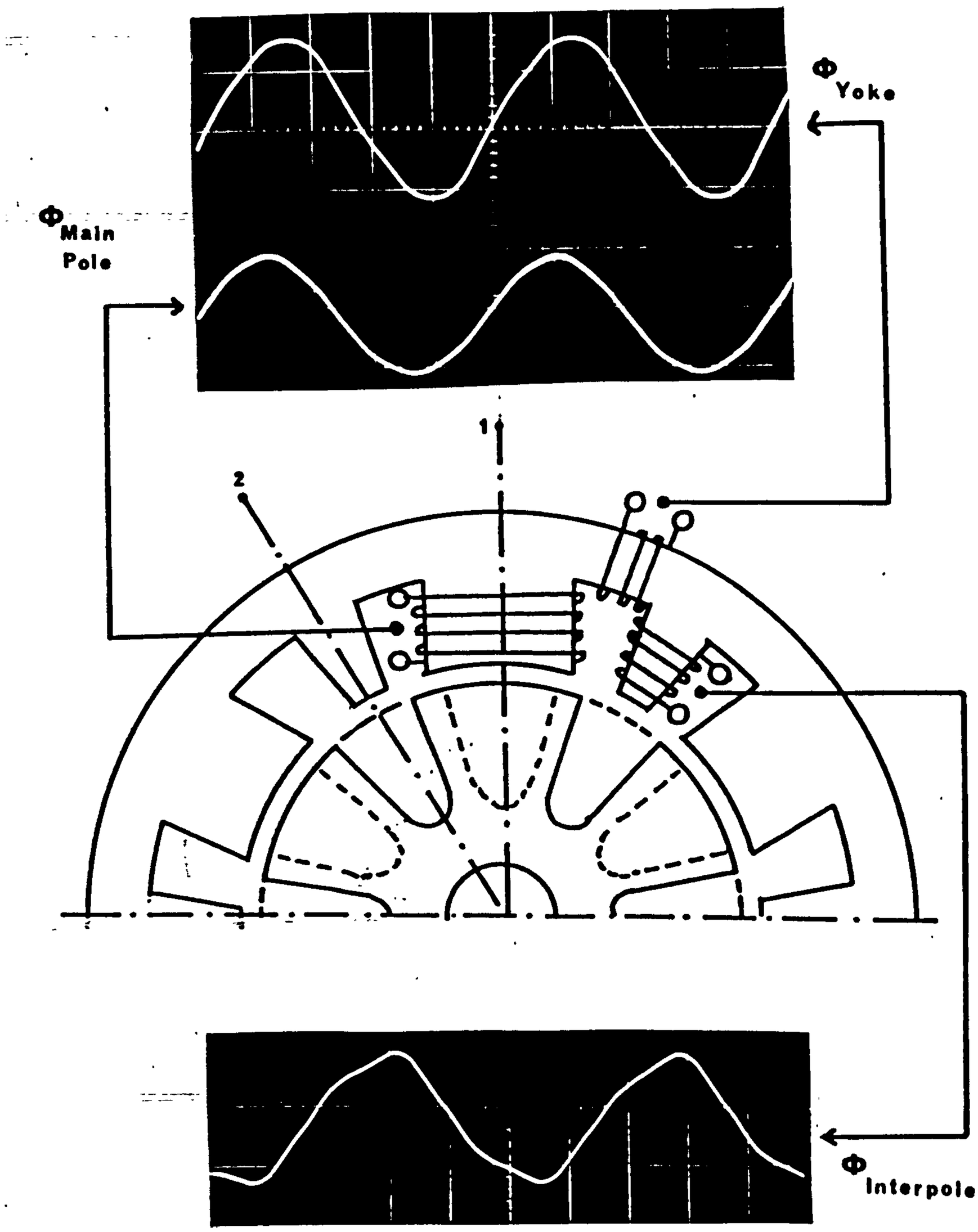

C·5 Waveforms Of Flux Linkages

Fig C·6(a)

Fig C·6(b)

C·6 Coil Arrangement For Loss Measurement

(a)

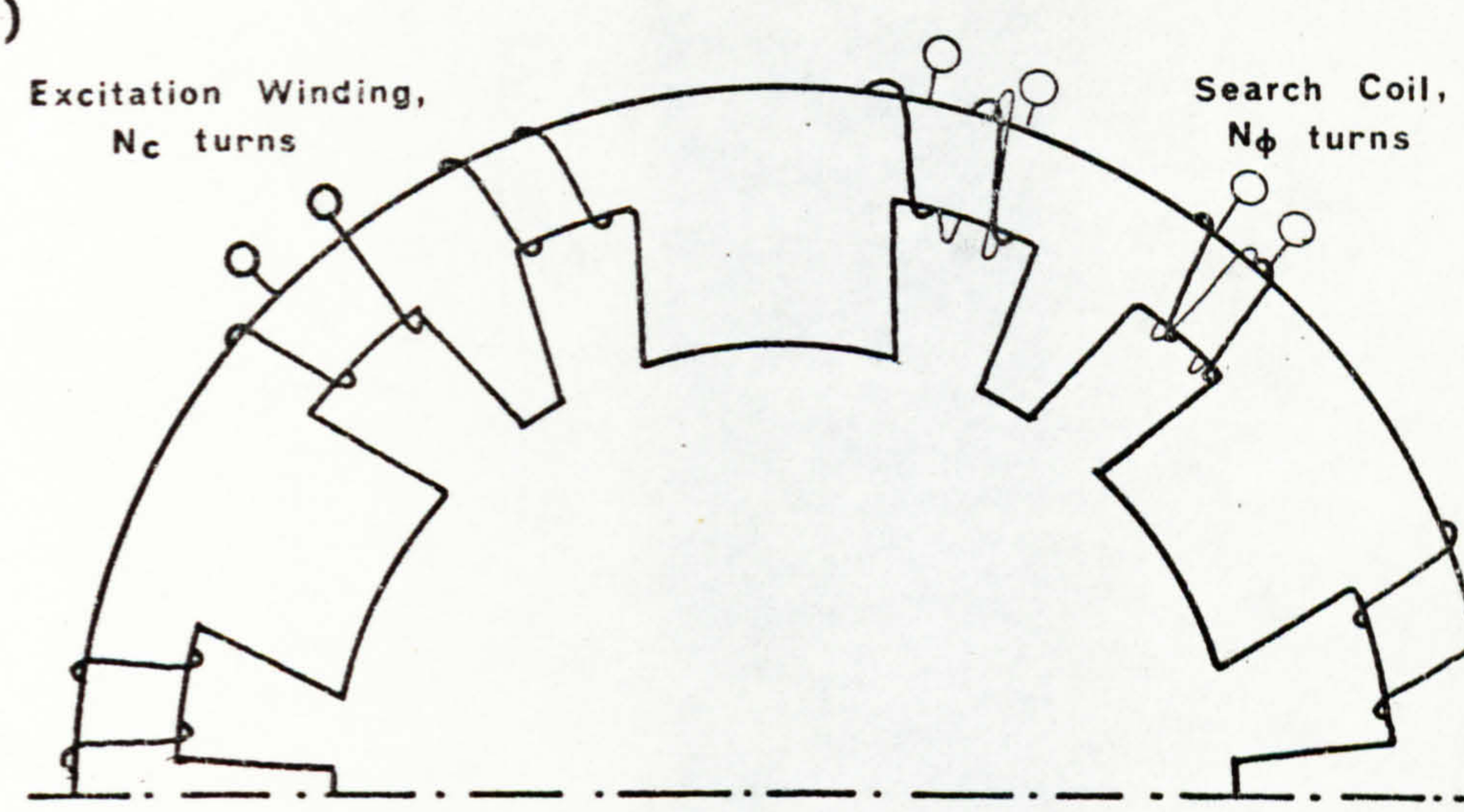

(b)

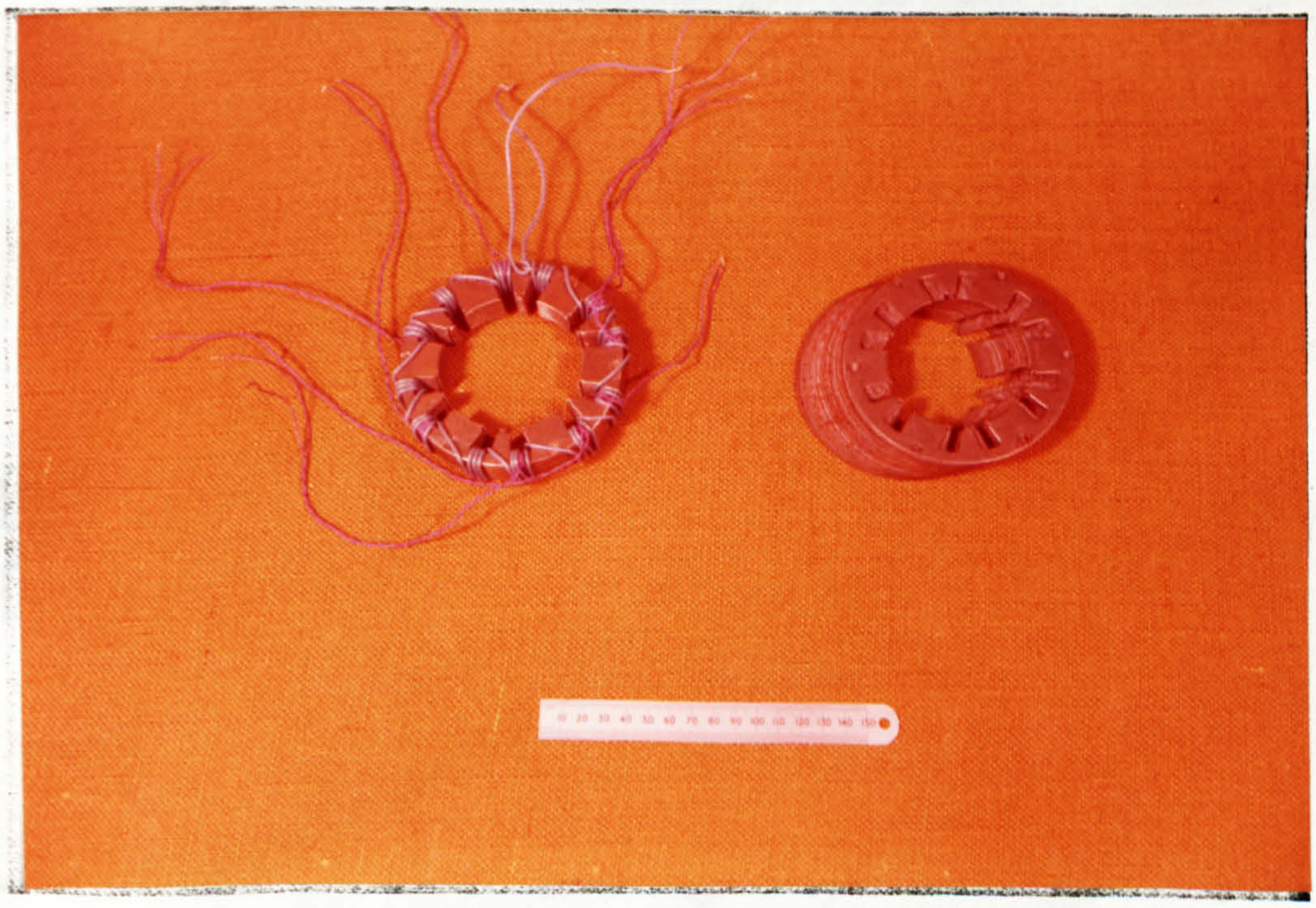

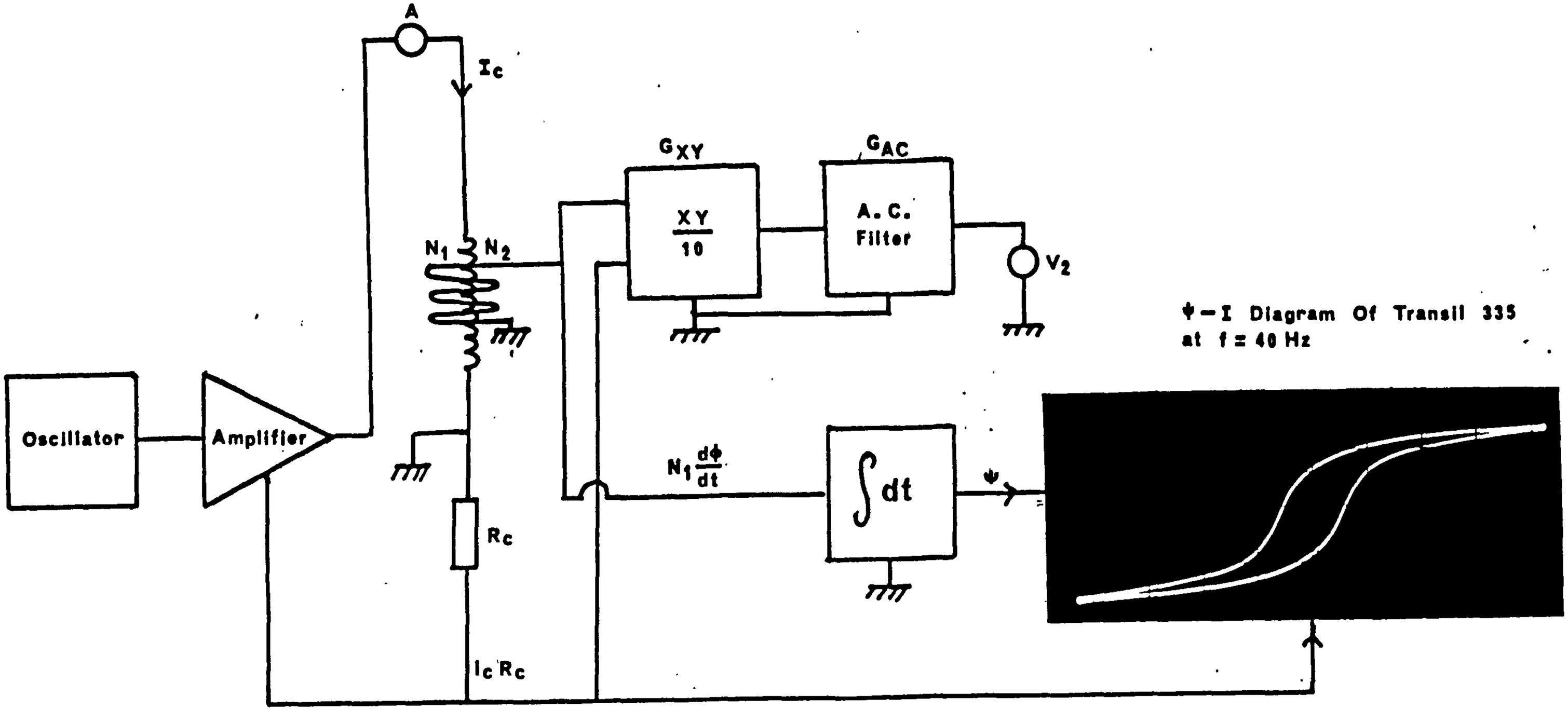

ψ – I Diagram Of Transil 335
at f = 40 Hz

Circuit Arrangement For Power Loss Measurement

Fig C.7

Fig C·8 (a)

Iron Loss For Losil 800

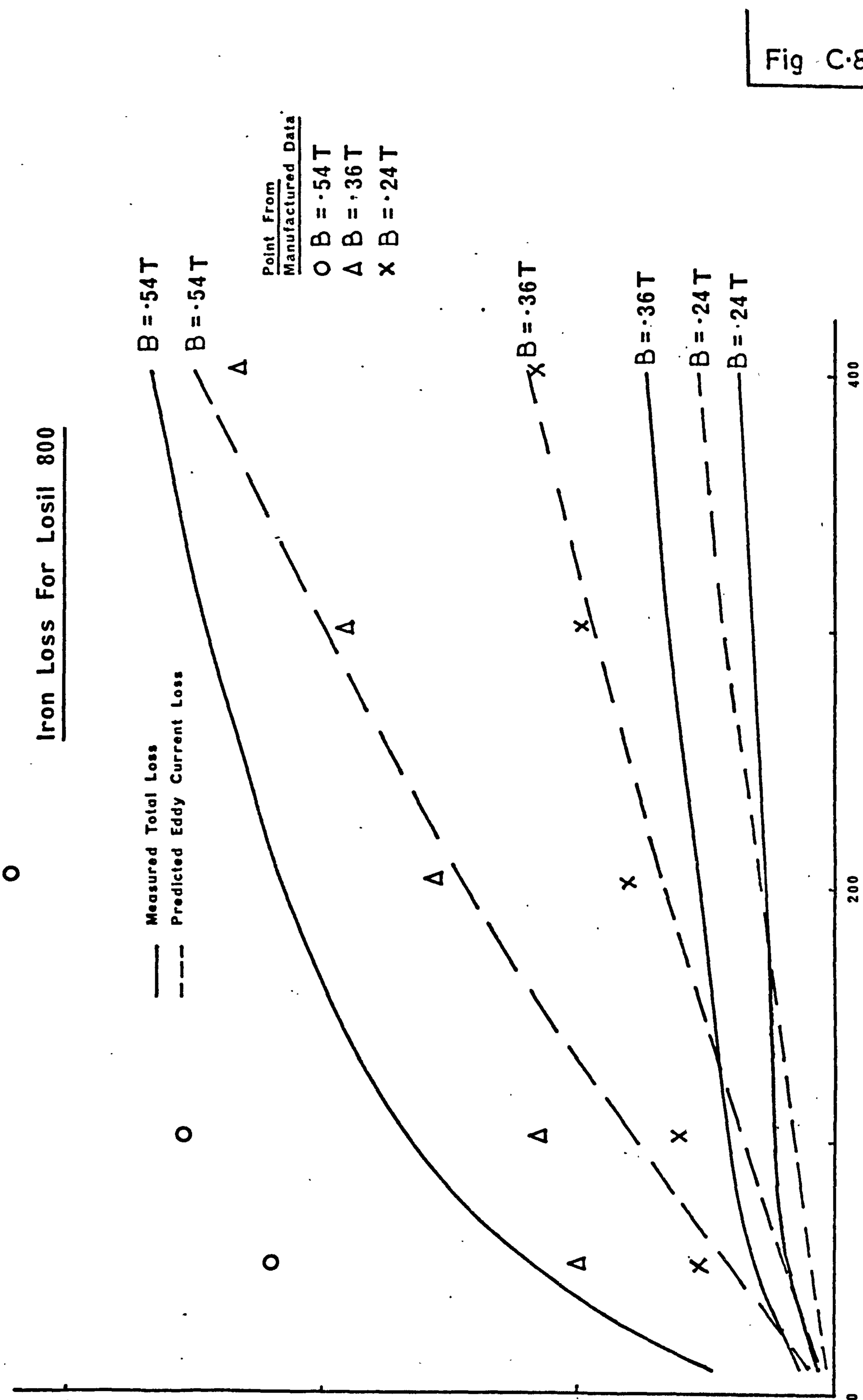

Iron Loss For Transil 335

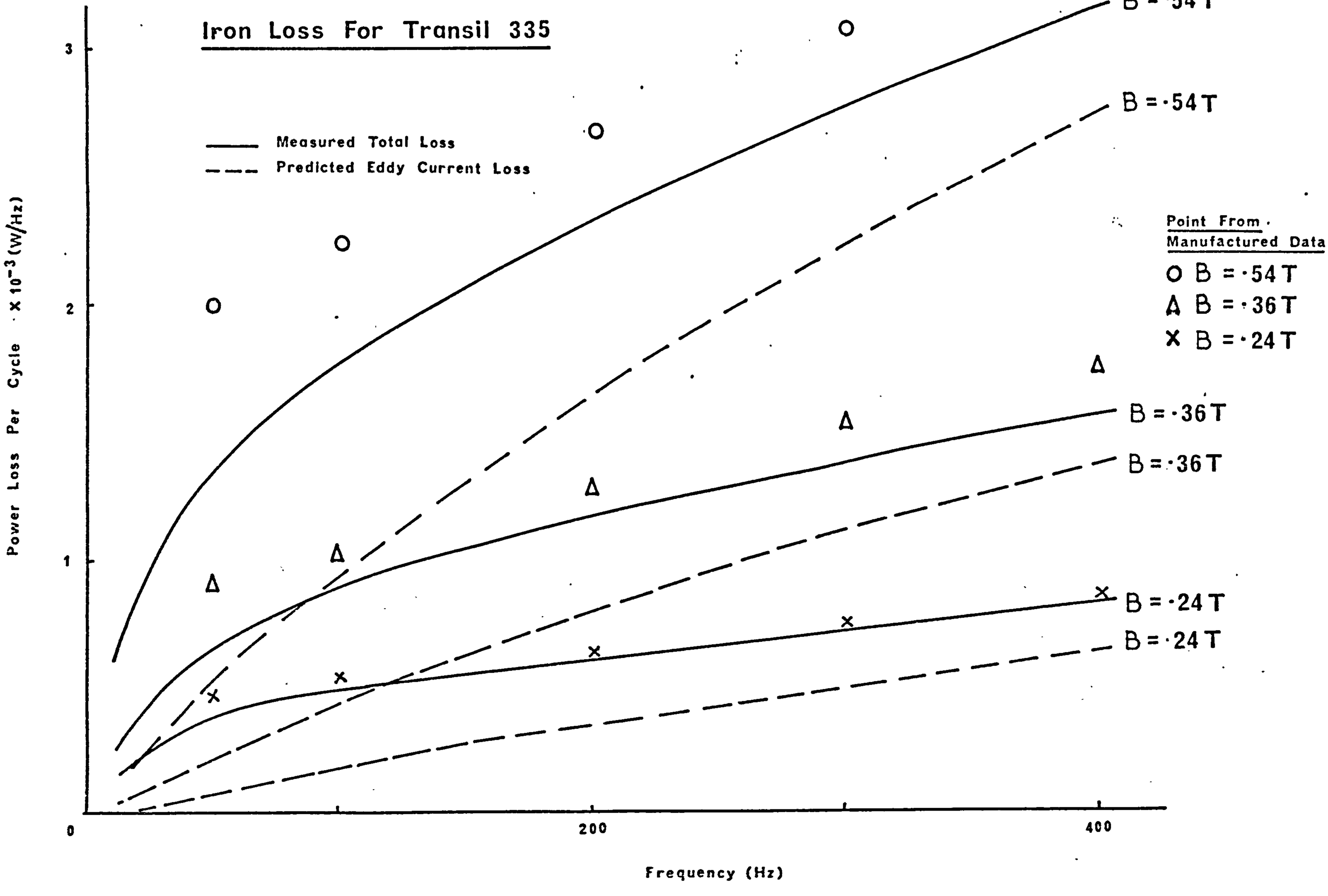

Fig C·8(b)

Fig C·9

Predicted And Measured Iron Loss

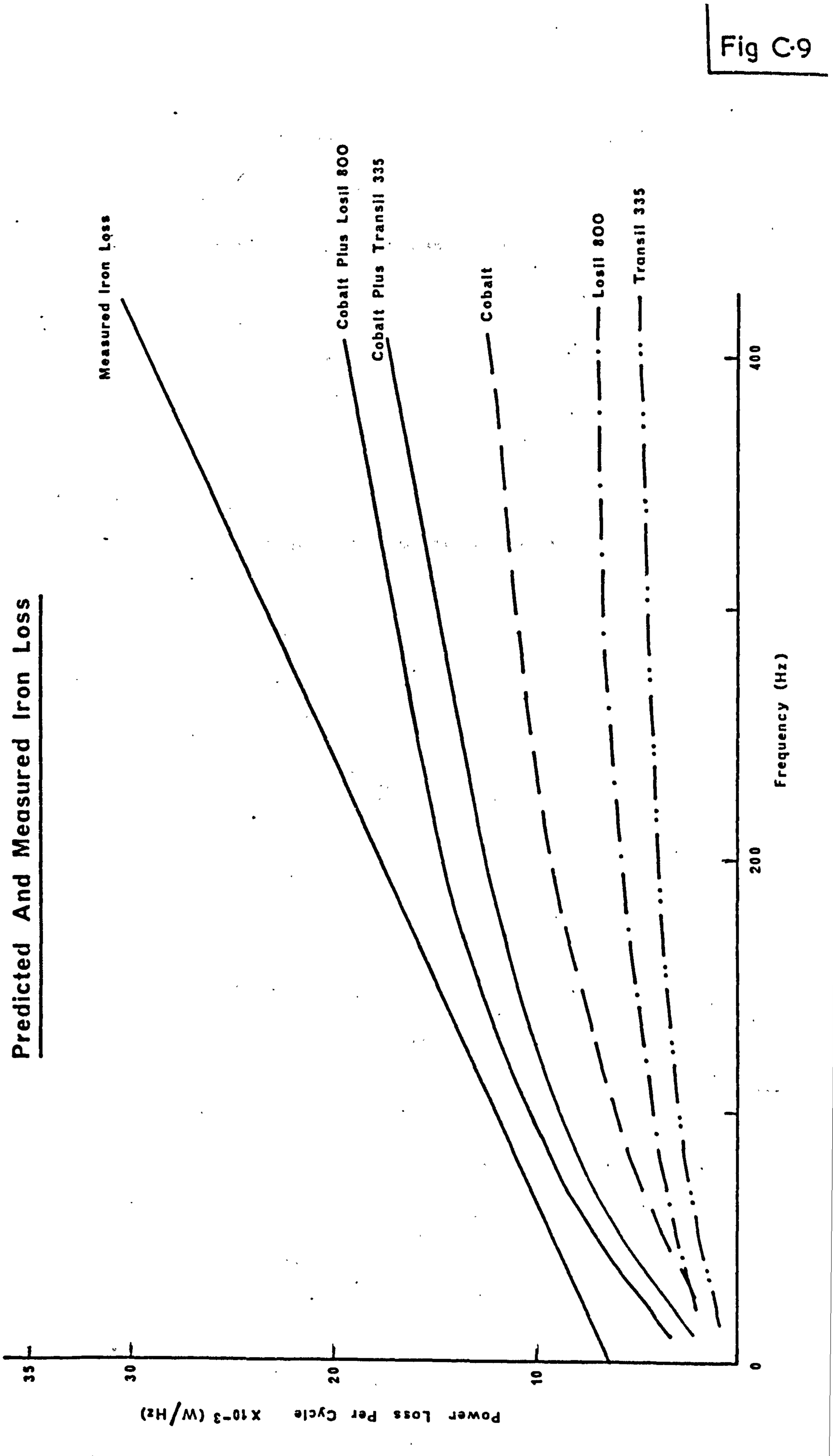

Fig C·10 (a)
Fig C·10 (b)
Fig C·11

C·10 Waveform Of Ψ In Rotor Pole

(a) Measured Waveform

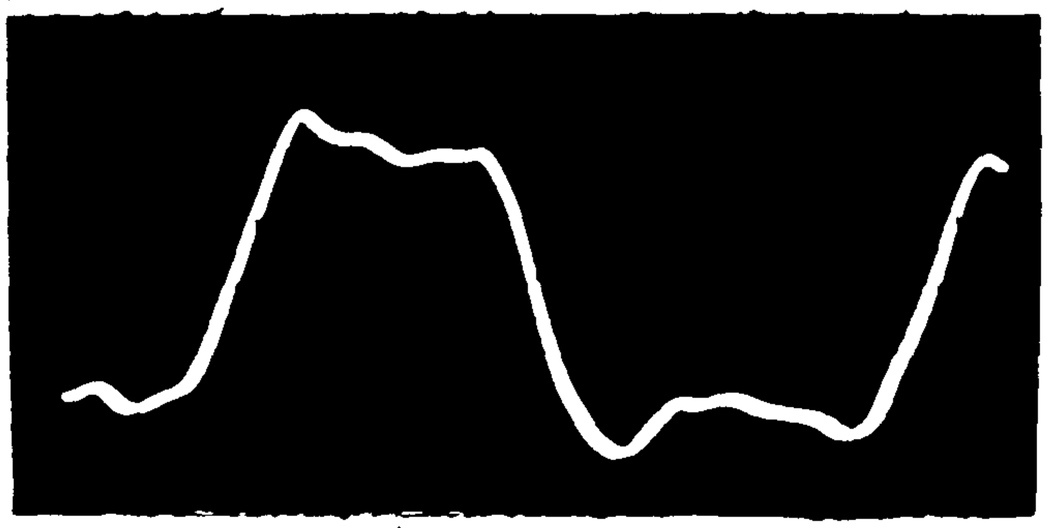

(b) Synthesized Waveform

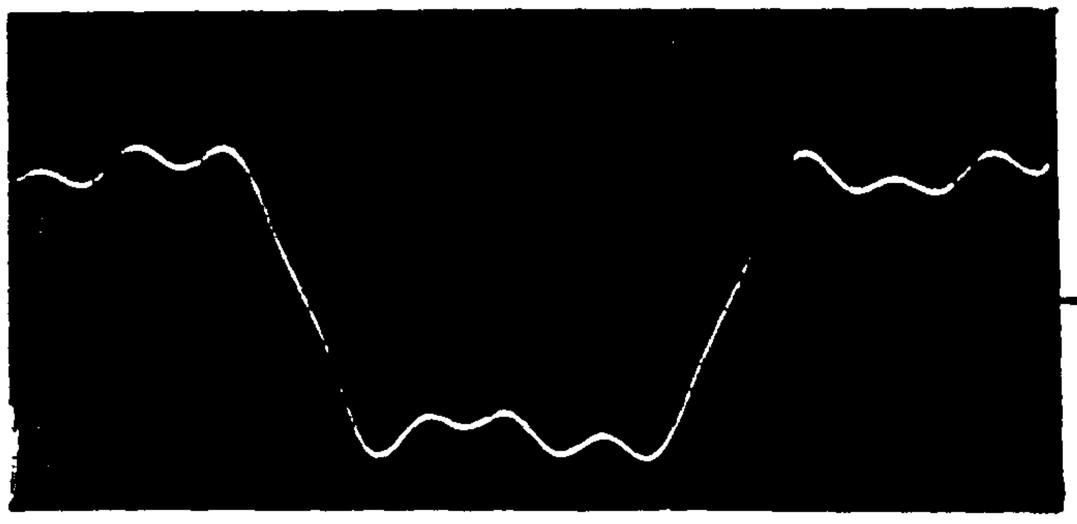

Harmonics		
Number	%	Phase
3	33	5
5	16	3
7	11	2
9	9	4

C·11 Flux Pulsation In Rotor

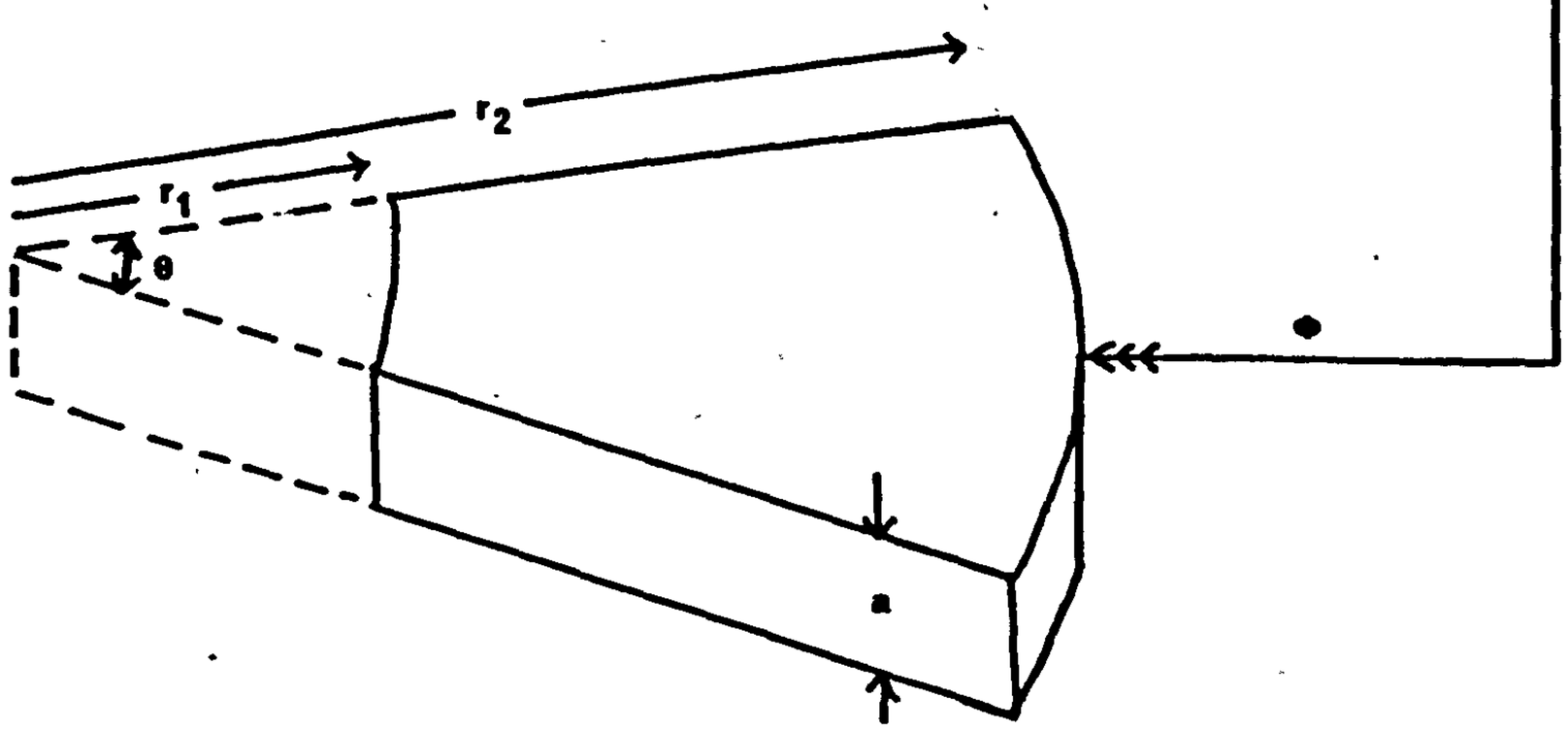

Fig D·1
Fig D·2
Fig D·3

D·1 Single Phase Machine

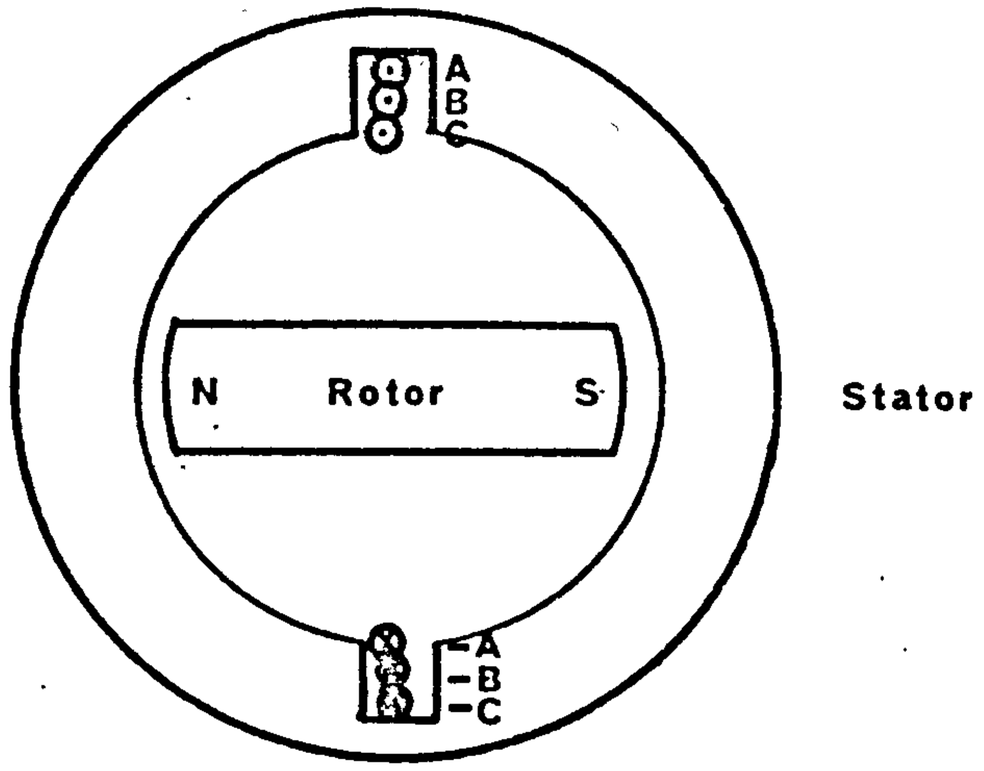

D·2 Three Phase Machine

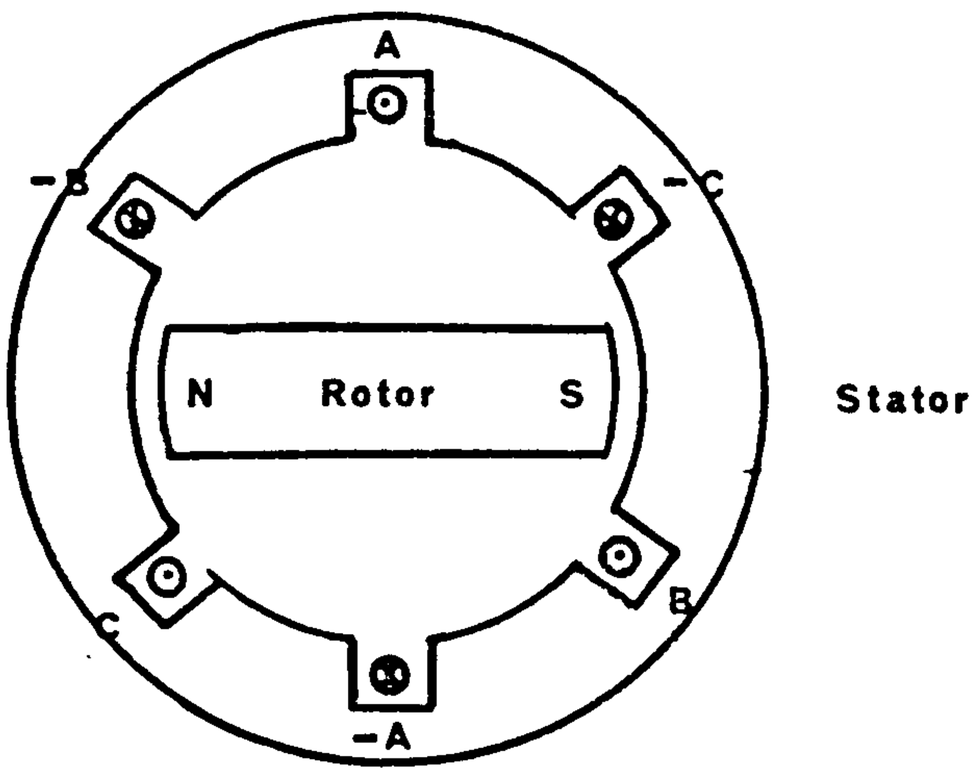

D·3 Full Wave Rectifier Circuit

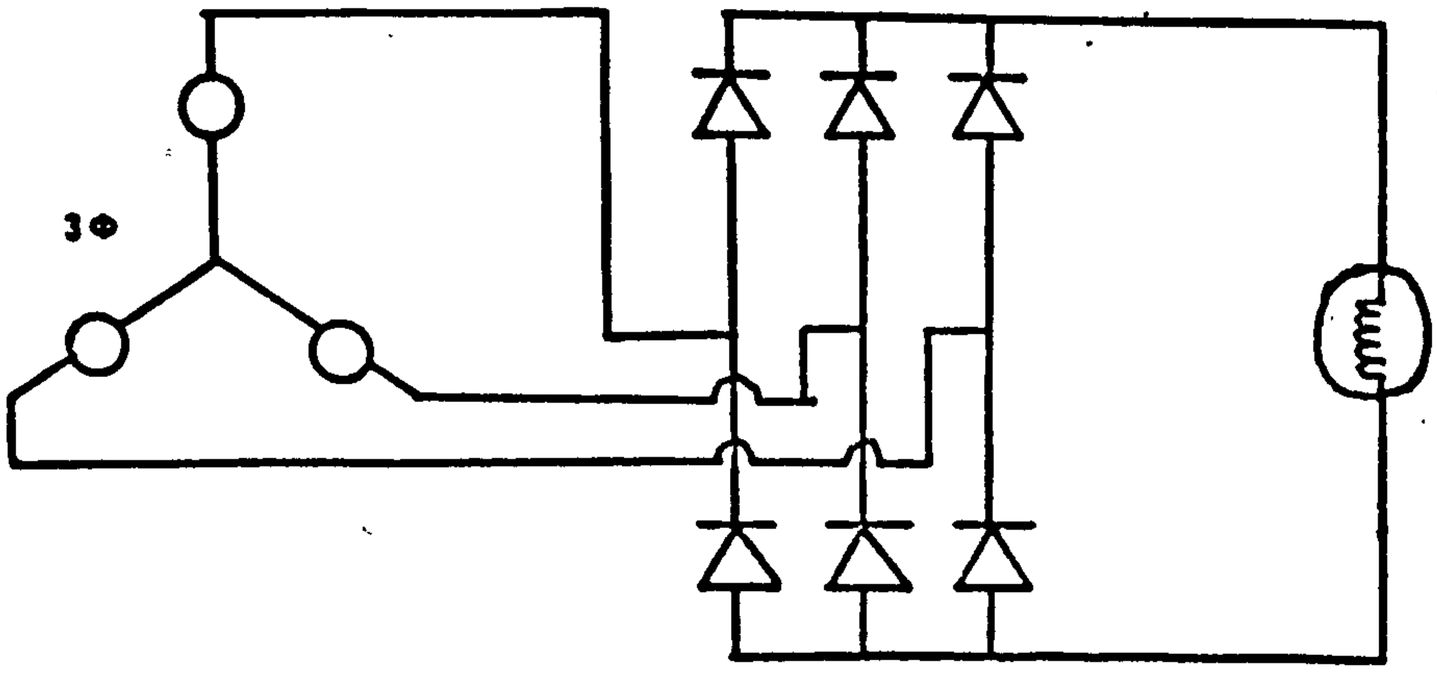

Fig E·1
Fig E·2(a)
Fig E·2(b)

E·1 Design 1

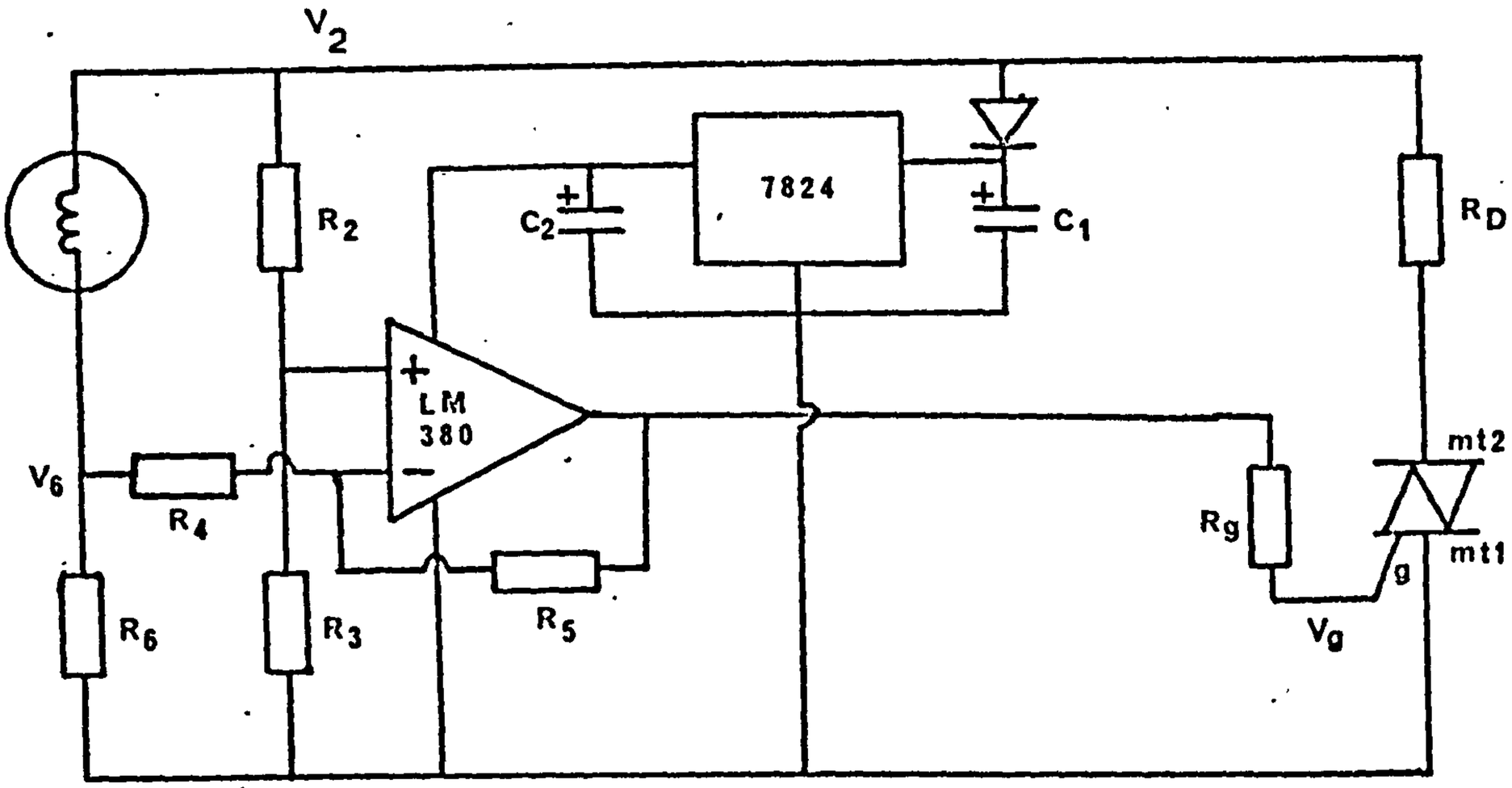

E·2 Design 2

(a) Flip Flop

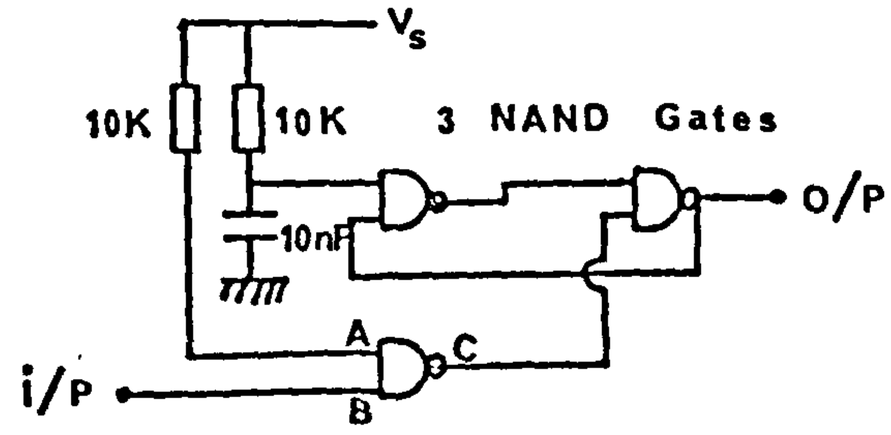

Truth Table		
A	B	C
0	0	1
1	0	1
0	1	1
1	1	0

(b) Circuit Design

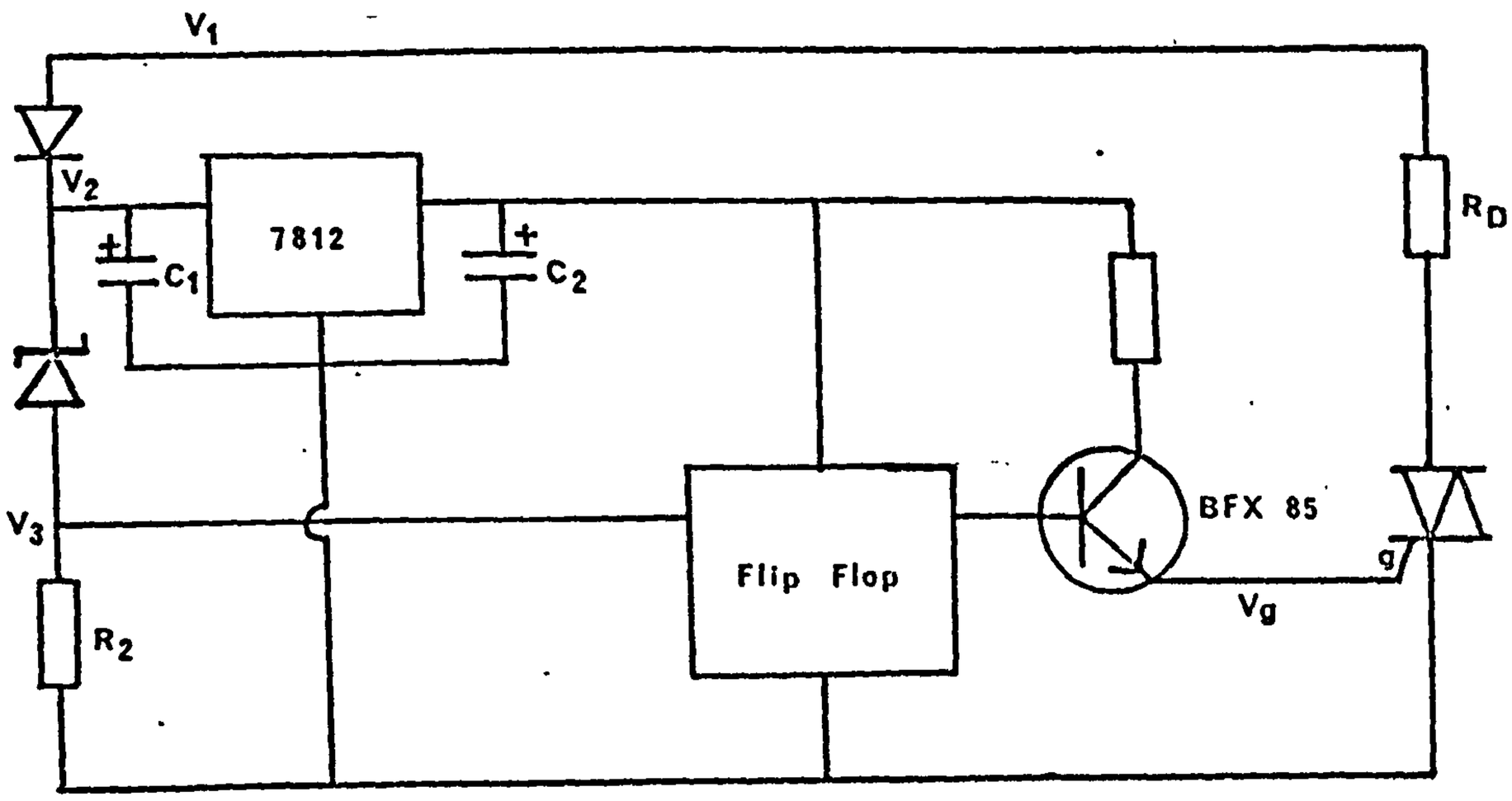

Fig E·3
Fig E·4

E·3 Design 3

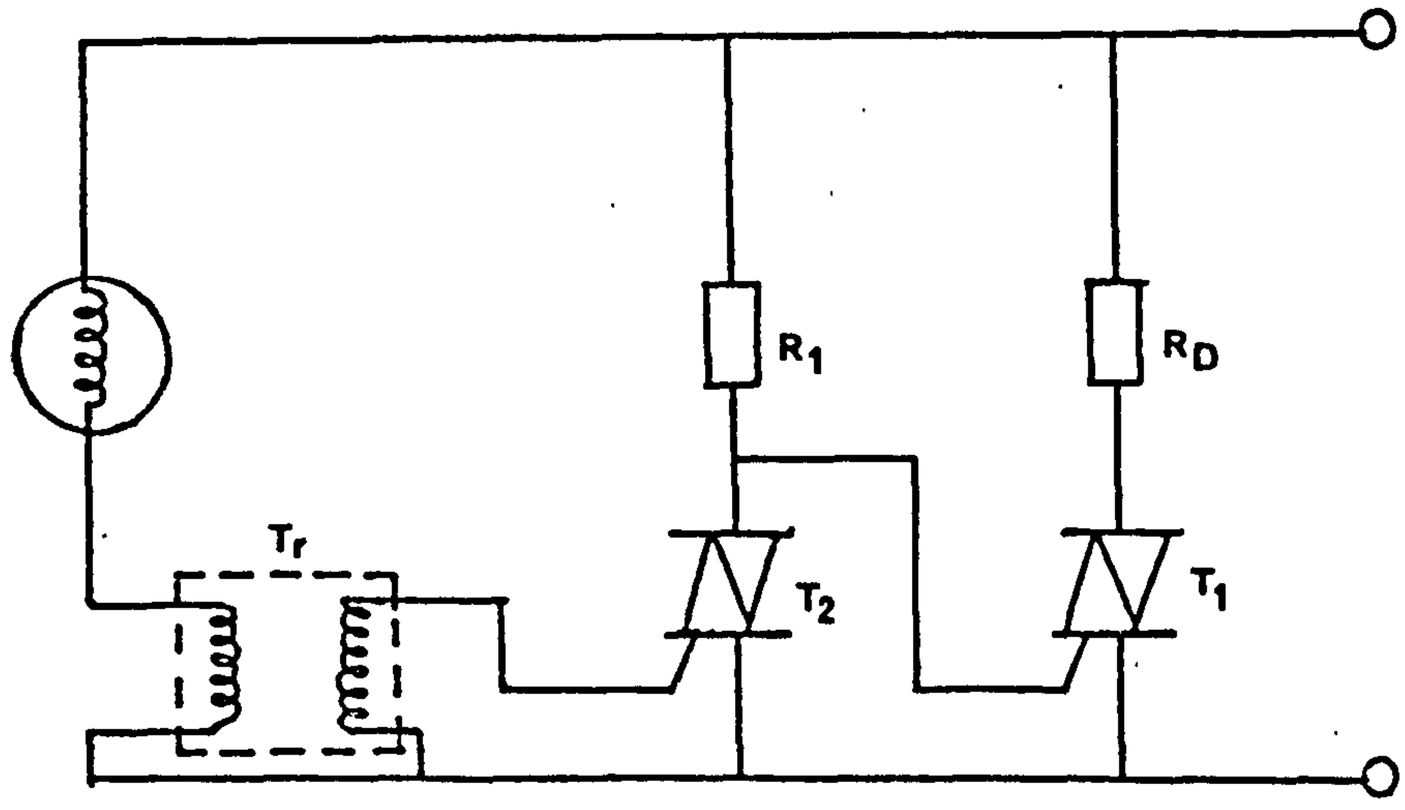

E·4 Design 4

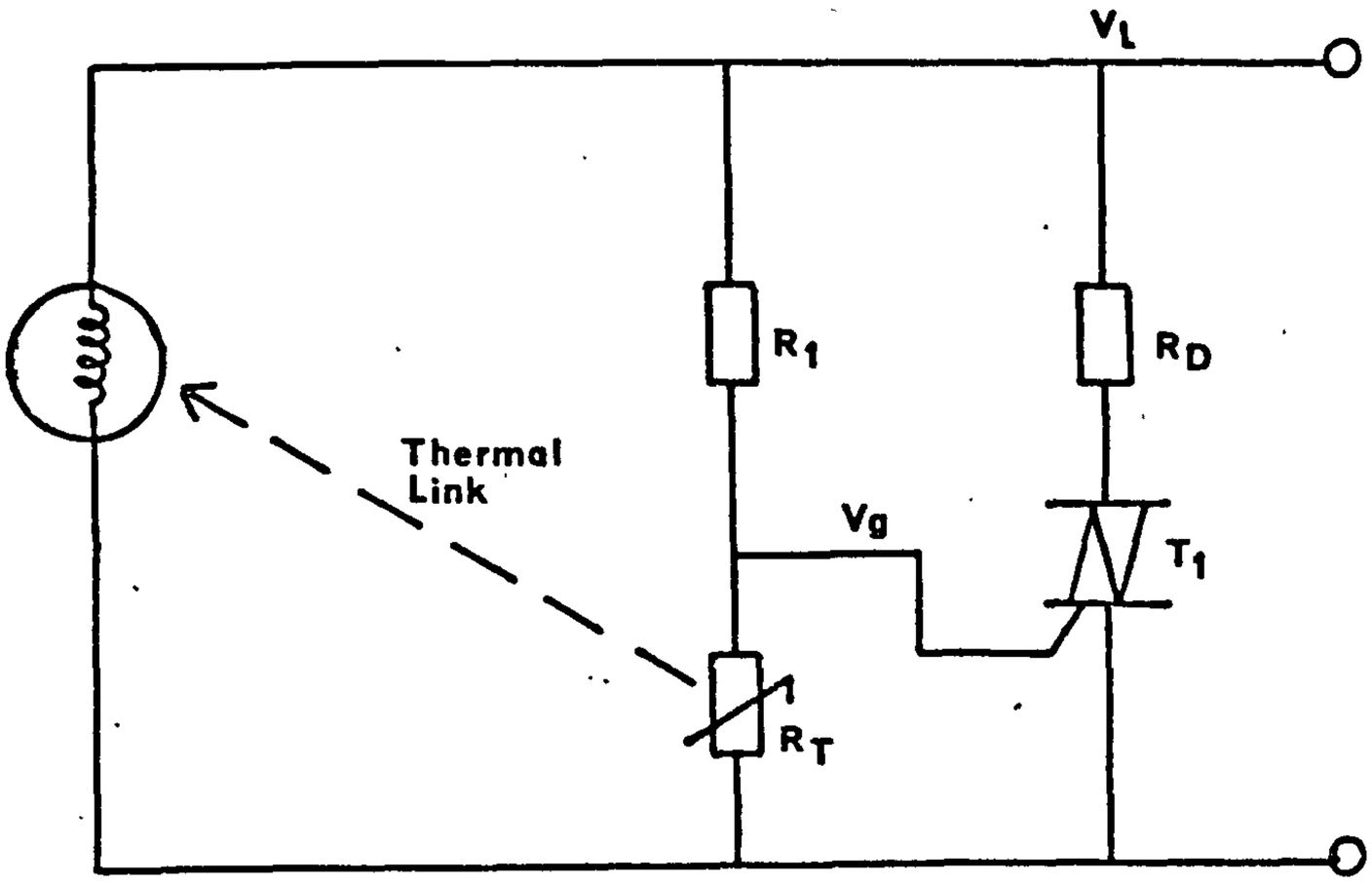

Fig E·5

Fig E·6

E·5 Design 5

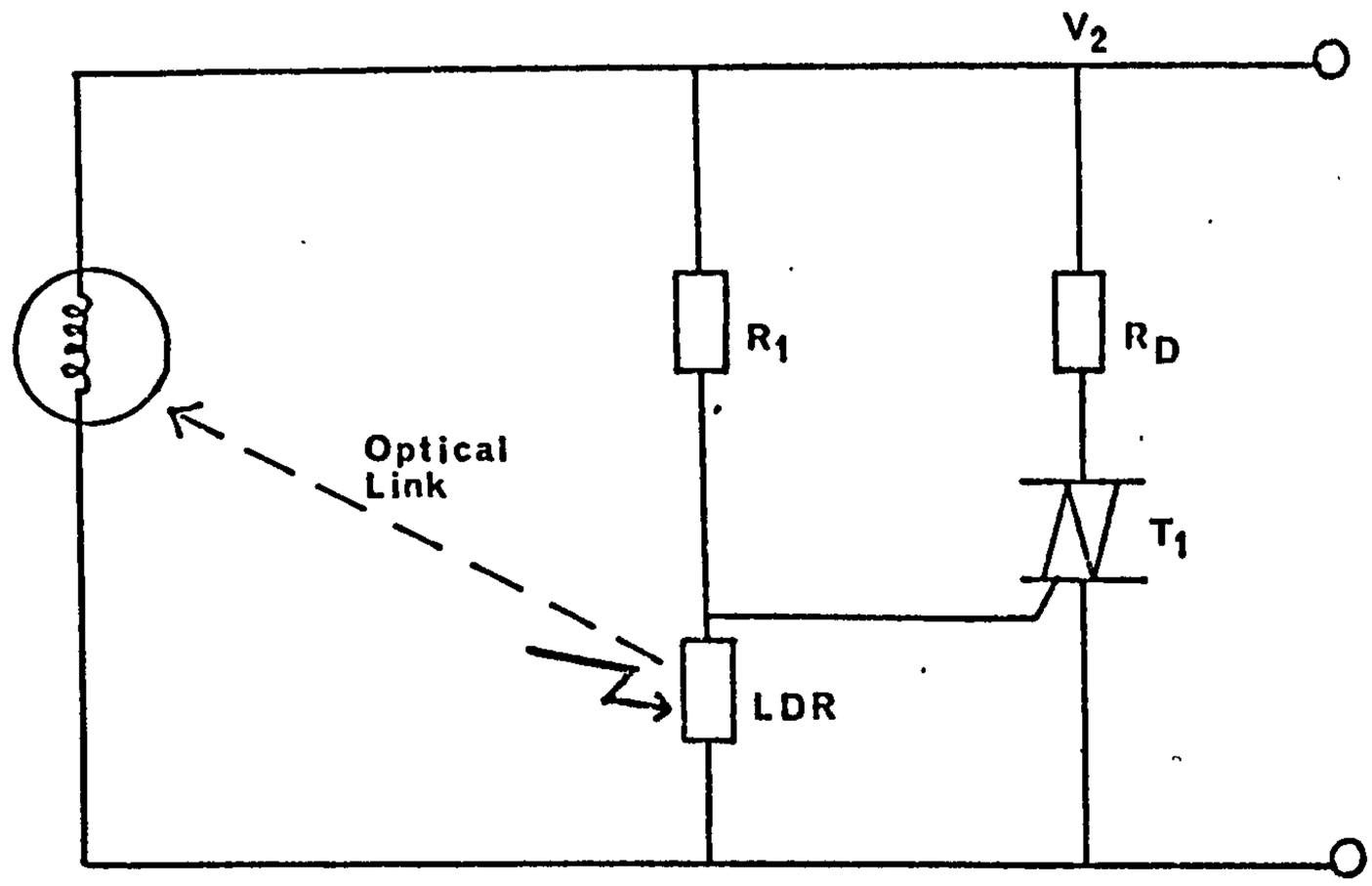

E·6 Design 6

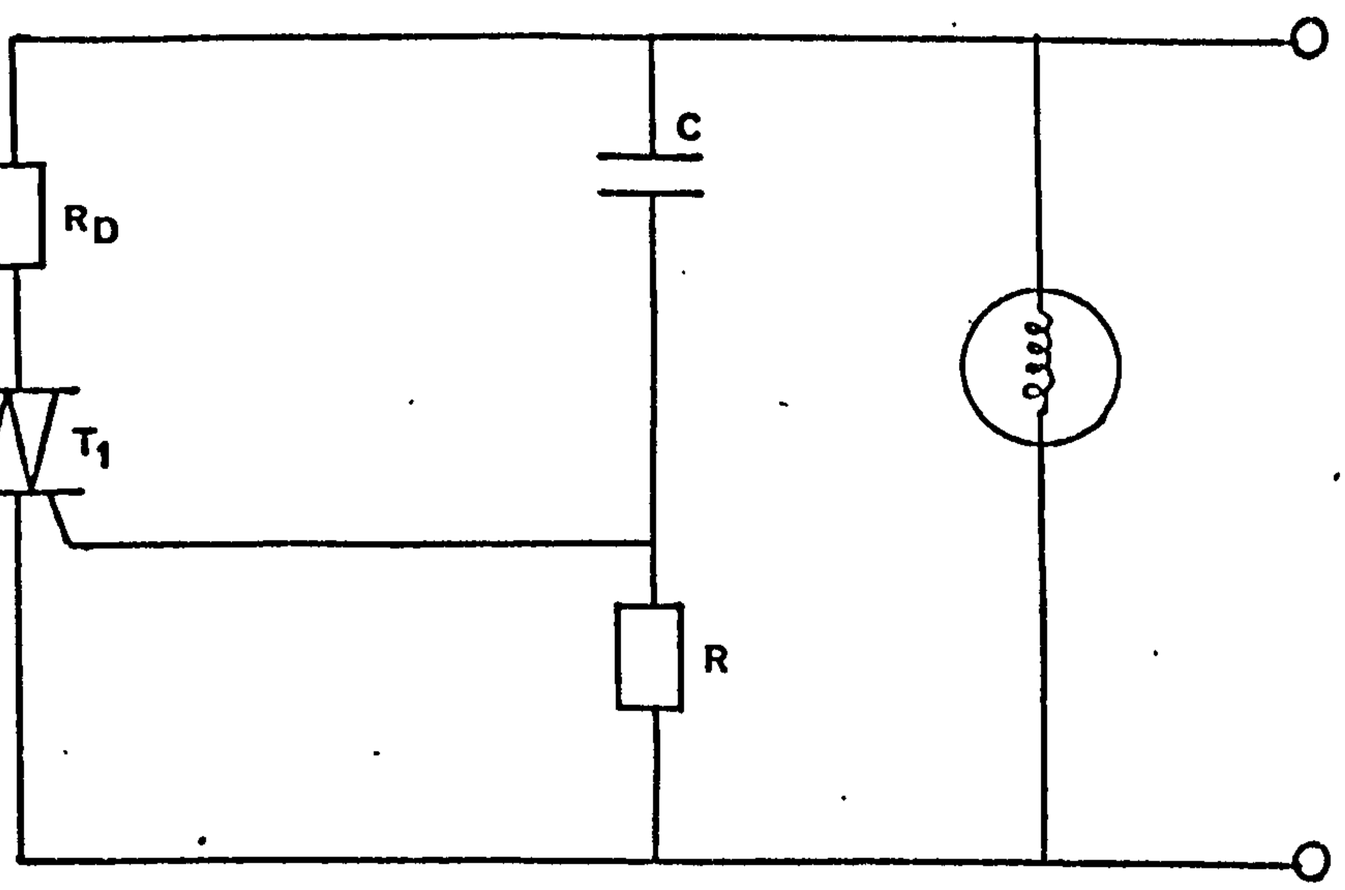

CONTENTS

PART 2: Oscillation Studies in Miniature Synchronous Motors

PART 2

SUMMARY

The work described in the second part of this thesis is concerned with studies of the dynamic oscillatory behaviour of miniature permanent-magnet synchronous motors.

A linear mathematical model previously developed for analysis of the constant speed performance of these motors has been extended to include the effects of speed oscillations about their mean synchronous speed. Whilst the model successfully predicted the peak torque available from the test motor for the non-oscillatory case, and provided magnetic saturation was avoided, it did not accurately model the motor at other operating conditions.

Experimental work has shown that iron-losses due to hysteresis in the stator magnetic material is significant in these motors and a new model including the effects of hysteresis has been developed. This latter model gives good agreement with test results.

A number of novel experimental techniques are described in the thesis.

LIST OF PRINCIPAL SYMBOLS

A	open loop gain
C	capacitor/amplitude of rotor oscillation
E_a	generated voltage of d.c. motor
$G_{a.c.}$	gain of a.c. filter
G_1	gain of laser instrument
G_i	gain of integrator
[G]	rotational inductance matrix
g	gravitational constant
I	stator current
I_m	equivalent magnet current
i, i_c	instantenous stator current
i_d	instantenous equivalent current in d-axis coil
i_q	instantenous equivalent current in q-axis coil
I_a	current to d.c. motor
[i]	current matrix
J	system inertia
K	coil constant
k	equivalent magnet flux linkage
k_g	equivalent flux linkage of reference generator
K_a	torque constant of d.c. motor
L	coil inductance
[L]	inductance matrix
L_d	inductance of the d-axis coil
L_q	inductance of the q-axis coil
L_c	inductance of the stator coil
l	length of suspension
M	mass/mutual inductance
$M_{dc}, M_{cd},$ M_{qc}	mutual inductance between stator and rotor coils
N_{sc}, N_c	number of turns of search coil and stator coil
P_i	total iron loss
p	pole pairs
R	coil resistance
R_a	resistance of d.c. motor
[R]	resistance matrix
S	reluctance of stator coil C
T	torque
T_D	drag torque
T_e	electromagnetic torque
T_f	friction torque
T_{fm}	friction torque of motor

T_{fr} friction torque of test rig

T_L load torque

T_{LS} stalling torque

T_i equivalent iron loss torque

T_r saliency torque per coil

$T_s, T_{\theta max}$ resultant peak saliency torque

T_+ peak torque of motor

v_f output voltage of a.c. filter

v_r reference signal

v_i input voltage of amplifier

v_R voltage across feedback resistor

v_a voltage across d.c. motor

$[v]$ voltage matrix

$v_{\dot{\theta}}$ speed signal

$v_{\dot{\theta}a.c.}$ a.c. speed signal

$v_{\dot{\theta}d.c.}$ d.c. speed signal

Z_L impedence

$[Z]$ impedence matrix

$J_o(C), J_1(C), J_{2(C)}, J_o(2C), J_1(2C), J_2(2C)$
Bessel functions of first order

α electrical phase shift between stator coils

α_g electrical phase shift between stator coil and reference generator coil

β phase of rotor oscillation

γ saliency angle

ψ flux linkage

ψ_{sc}, ψ_c flux linkage of search coil and coil C

ψ_g flux linkage of reference generator

ψ_q, ψ_d flux linkage in the q-axis and d-axis

ψ_{dc} flux linkage between coils in the d and C axis

ϕ_c angle which I_d lags I

θ mechanical angle

$\dot{\theta}$ rotor speed

$\ddot{\theta}$ rotor acceleration

ω angular frequency

ω_o oscillation frequency

load angle

Ⓗ hysteresis angle of motor

$Ⓗ_g$ hysteresis angle of reference generator

CHAPTER 1

INTRODUCTION

1.1 Miniature Synchronous Motors

Miniature synchronous motors are single-phase units having rotor speeds which are synchronous to the mains frequency. Their typical power ratings range from 0.05W to 5W. Due to their small size, high output torque per unit volume, synchronous running and low manufacturing cost, these miniature synchronous motors have found many applications, such as:

(i) Clocks and timing devices for industrial applications

(ii) Programmers in washing machines, cookers, etc.

(iii) Control devices and motor-driven valves in heating and air-conditioning systems

(iv) Registering instruments

(v) Cooling and extractor fans

(vi) Drive motors for cassette units and turntables

The annual consumption of these motors in the European market alone exceeds 10 million units[2].

The majority of these motors have a multi-polar permanent magnet rotor made of high coercivity ferrite material. The stator soft iron magnetic circuit generally consists of two end-plates from which the pole fingers are punched and bent perpendicularly inwards, and an annular cover to bridge the two end-plates as shown in Fig.1.1. The excitation is provided by a single coil wound around a plastic moulded bobbin. The stator pole fingers produce a multipolar radial field from the axial

coil mmf. The resultant pulsating field can be resolved into two constant-amplitude counter-rotating components termed the forward and backward fields of the motor. With the motor at rest, the forward and backward rotating fields produce no net unidirectional starting torque. Starting is achieved in many motors by relying on rotor oscillations at standstill being sufficiently large to eventually accelerate the motor to synchronous speed. However, such motors have no preferred starting direction and various mechanical devices are used to prevent rotation in the unwanted direction. Improved unidirectional starting and consequent elimination of these mechanical non-reversing devices can be achieved by using shading rings to produce a quasi two-phase excitation with a net resultant starting torque. Another, more expensive, method of producing a two-phase excitation is by using two axially displaced half stators having separate coils, a common rotor and pole fingers displaced in space by $\pi/2$ electrical degrees. One of the coils has a suitable capacitor connected either in series or parallel with it to create a phase shift in its excitation current with respect to that in the other coil. This method can be very effective in reducing the counter rotating backward field but because of manufacturing tolerances does not eliminate it. By switching the capacitor to the other coil a reversible drive can be achieved.

1.2 Oscillation Studies

When the motor is running synchronously with the forward field the backward field produces a pulsating torque. In addition the salient pole stator structure causes the rotor to

experience a pulsating saliency torque. This saliency torque combined with the backward field torque results in rotor speed fluctuations about the synchronous speed.

These speed oscillations can lead to reduced output power and also excessive noise and wear associated with coupled gear boxes, etc. The amplitude and frequency of the oscillations for a specific motor are a complex function of a number of variables such as load torque, coupled inertia, supply frequency and voltage.

Schemmann[3] has studied similar oscillatory behaviour in much larger and unshaded synchronous motors and has published work on an analogue simulation of them. Other work[6] undertaken in this Department has studied the steady-state non-oscillatory performance of the miniature synchronous motor but no analytical study of the oscillatory behaviour is known. Previous experimental work[7] and Schemmanns' results show that the nature of the oscillation is complex. Under certain combinations of load and supply the motor can exhibit unstable operation resulting in loss of synchronisation or sporadic motion with zero mean speed. During stable operation the rotor oscillation about synchronous speed can have different oscillation frequencies or combinations of frequencies, depending on such parameters as the supply current, load inertia and load torque. Schemmann has observed that for a supply frequency of 50Hz the oscillation frequency can contain 25Hz, 33⅓ Hz, 50Hz or 100Hz components. Previous work in the Department has verified the 50Hz and 100Hz components. With so many different possible modes of oscillation the analysis in this thesis has been restricted to the study of oscillation

at twice supply frequency since this can be the predominant component for many machines.

Initially the linearized steady-state model[6] was extended to cover the oscillatory behaviour of the motor. However, results suggested that even at low excitation levels, the effect of hysteresis in the stator iron was significant. A model based on the d-q axis theory but including hysteresis has shown that the performance of the motor can be predicted with good accuracy. Chapter 4 describes the experimental arrangements and the various techniques used for determining the machine parameters and performance.

1.3 Construction of Test Motor

The motor used in the study is manufactured by Impex Electrical Limited (model number 9904-111-04 series - AU5051). The specification of the motor is given in Table 1.1.

The motor is designed as a reversible capacitor motor. It has two stator coils and a capacitor. The coils and capacitor are connected either in series or parallel arrangement as shown in Fig.1.2.

Fig.1.3 shows the motor unit and its capacitor. Below the motor, from left to right, are the various components of the motor which are the stator coil, the end-plate separating the two stator coils, the permanent magnet rotor and the second stator coil.

This motor is chosen for the investigation because its pole structure is regular compared to that in shaded pole motors[6].

In addition the phase of the excitation current can be varied with respect to that in the other coil.

Table 1.1: Specification of test motor

Capacitor	4.7μF
Power rating	1.8VA
Rated current in each stator coil	38mA
Voltage rating of motor for stator coils in:-	
series arrangement	24V
parallel arrangement	48V
Permanent magnet material	Barrium ferrite
Number of pole pairs	12

CHAPTER 2

LINEARIZED MODEL

2.1 Analysis of Non-Oscillatory Case

The following analysis in miniature synchronous motors is based on previous work undertaken in the Department[6,7] and the following assumptions are made:

(i) Spatial flux harmonics are negligible

(ii) Hysteresis and eddy current effects are neglected

(iii) Excitation current in the stator coil is sinusoidal

(iv) Saturation effects are neglected

The analysis is limited to the case of a single coil (single-phase) excitation of the two-coil motor, the second coil remaining open-circuited.

2.1.1 Equivalent circuit model

Based on the above assumptions the motor is modelled as an equivalent circuit given in Fig.2.1. From the equivalent circuit, the voltage equation is written as:

$$v = iR + \frac{d}{dt}(Li+\psi) \qquad (2.1)$$

where i is the current in the stator coil

R is the coil resistance

L is the self-inductance of the coil and it can be assumed to be independent of rotor position because the effective permeability of the ferrite rotor is almost unity

ψ is the flux linkage between the rotor magnet and the stator coil.

Fig.2.2 shows the difference between the waveforms of the current in the stator coil when the motor is excited from either a voltage source or a current source. From the figure it can be seen that with a voltage source, the current waveform is distorted. This distortion is caused by non-linearities in L due to saturation of the stator iron and hysteresis. Hence to avoid these non-linearities, as well as have a sinusoidal excitation current i to simplify the analysis, the motor is supplied from an a.c. current source. Using the current as the reference phasor, it is expressed as

$$i = I\cos(\omega t) \tag{2.2}$$

where I is the peak current

ω is the angular frequency and equals $2\pi f$

f is the supply frequency

With the rotor running at a steady speed this can be expressed as

$$\dot{\theta} = \frac{d\theta}{dt} = \frac{\omega}{p} \tag{2.3}$$

where the instantaneous position is

$$p\theta = \omega t+\lambda \tag{2.4}$$

and λ is the relative angle between the rotor and stator reference axes.

Neglecting space harmonics, the magnet flux linkage for a p pole-pair motor can be expressed as

$$\psi = \frac{k}{p}\sin(p\theta) \tag{2.5}$$

$$= \frac{k}{p}\sin(\omega t+\lambda) = \frac{k}{p}\cos(\omega t+\lambda-\frac{\pi}{2}) \tag{2.6}$$

and the induced emf is then

$$\frac{d\psi}{dt} = \frac{k}{p}\omega \cos(\omega t+\lambda) \qquad (2.7)$$

Fig.2.3 shows the phasor diagram of $d\psi/dt$ and ψ w.r.t. the reference phasor I. The angle λ is defined as the load angle and is the angle by which $d\psi/dt$ leads I.

2.1.2 Torque expressions

With the stator coils open-circuited and the rotor free to rotate, the rotor will align itself at a position relative to the stator where the reluctance of the magnet flux path is a minimum. If the rotor is displaced slightly from that position a saliency torque will develop and return the rotor to the initial 'rest' position. The saliency torque is proportional to the airgap flux density squared and the displacement angle[11].

With the rotor rotating at a constant speed $\dot{\theta}$ the saliency torque will be zero at positions of minimum and maximum reluctance, as shown in Fig.2.4. These two positions correspond to the positions where the magnet flux linkage ψ is maximum and zero respectively. From equation (2.5), $\psi=0$ when $p\theta=n\pi$ and will be maximum when $p\theta=n\pi/2$, where n is an integer.

The saliency torque can therefore be expressed in the form

$$T_{r_1} = T_r \sin(2p\theta) \qquad (2.8)$$

With the second stator poles displaced by α the saliency torque of the second stator is then

$$T_{r_2} = T_r \sin 2(p\theta+\alpha) \qquad (2.9)$$

where the two stators are assumed to be identical.

Thus the total saliency torque of the motor is

$$T_{r_1}+T_{r_2} = T_r \sin(2p\theta)+T_r \sin 2(p\theta+\alpha)$$

$$= T_s \cos 2(p\theta+\gamma) \qquad (2.10)$$

where T_s is the resultant maximum saliency torque of the two stators and equals

$$2T_r \cos(\alpha) \qquad (2.11)$$

and

$$2\gamma = \alpha-\pi/2 \qquad (2.12)$$

If the poles of the two stators are displaced by exactly $\pi/2$, the saliency torque of one stator will be equal and opposite to that of the other stator such that, from equation (2.11),

$$T_s = 2T_r \cos(\pi/2) = 0 \qquad (2.13)$$

However, because of manufacturing tolerances, it is unlikely that α can be exactly $\pi/2$. For example for a p=12 motor a tolerance of $\pm 1^{o}$ electrical will demand a production system capable of assembly to $\pm 1/12^{o}$ or $\pm 0.08^{o}$ mechanical displacement between the two stator halves.

The electromagnetic torque produced can be expressed as[1,8,9]

$$T_e = i\frac{d\psi}{d\theta} \qquad (2.14)$$

and thus the total torque acting on the rotor is then

$$T = T_s \cos 2(p\theta+\gamma)+i\frac{d\psi}{d\theta} \qquad (2.15)$$

Substituting equations (2.2),(2.4) and (2.5) into equation (2.15), it can be shown that

$$T = T_s \cos 2(\omega t+\lambda+\gamma) + \frac{kI}{2} \cos(2\omega t+\lambda) + \frac{kI}{2} \cos(\lambda) \qquad (2.16)$$

Equation (2.16) shows that there is an oscillatory torque, at twice the supply frequency, superimposed on the average torque which is

$$T = \frac{kI}{2} \cos(\lambda) \qquad (2.17)$$

For a given motor the parameter k is fixed by the magnet mmf and the number of turns in the stator coil. At a given excitation current I the load angle λ is determined by the load torque applied to the motor. From equation (2.17) $\lambda=\pi/2$ corresponds to zero applied torque and the maximum theoretical torque available occurs when $\lambda=0$. This torque is termed the peak torque T^+ which is given as

$$T^+ \doteq \frac{kI}{2} \cos(\lambda) = \frac{kI}{2} \qquad (2.18)$$

for $\lambda=0$

If the load torque exceeds T^+ then the rotor will drop out of synchronism and stall.

2.2 Extension of Analysis to Include Oscillations

Assuming that the rotor has a single oscillation frequency of amplitude C and an angular frequency ω_o about its mean synchronous speed then the instantaneous angular position is

$$p\theta = \omega t+\lambda+C \cos(\omega_o t+\beta) \qquad (2.19)$$

giving a speed of

$$\dot{\theta} = \frac{d\theta}{dt} = \frac{\omega}{p} - C\frac{\omega_o}{p} \sin(\omega_o t+\beta) \qquad (2.20)$$

and an acceleration of

$$\ddot{\theta} = \frac{d^2\theta}{dt^2} = -C\frac{\omega_o^2}{p} \cos(\omega_o t+\beta) \qquad (2.21)$$

Substituting equations (2.2), (2.19) and (2.5) into equation (2.15), the electrical torque acting on the rotor is rewritten as

$$T = I\cos(\omega t)k\cos(\omega t+\lambda+C\cos(\omega_o t+\beta))$$
$$+T_s\cos 2(\omega t+\lambda+\gamma+C\cos(\omega_o t+\beta)) \qquad (2.22)$$

This torque must be balanced by a mechanical torque which in general will take the form,

$$T_L + D\frac{d\theta}{dt} + J\frac{d^2\theta}{dt^2} \qquad (2.23)$$

where T_L is the load torque of the system

D is the damping torque coefficient of the system

J is the inertia of the system

With a smooth cylindrical rotor there is negligible windage loss. The damping torque coefficient D will therefore be small and has been assumed to be zero in order to simplify the analysis. By substituting equation (2.21) into equation (2.23), the mechanical torque is then

$$T_L + J\left(-C\frac{\omega_o^2}{p}\cos(\omega_o t+\beta)\right) \qquad (2.24)$$

2.2.1 Prediction of oscillation frequencies

To predict the oscillation frequency ω_o the electrical torque expression given in equation (2.22) is solved analytically and equated to the mechanical torque given in equation (2.24). To simplify the electrical torque analysis C is assumed to be small but still finite. Using Bessel functions of first order[5] given in Appendix A, and neglecting terms higher than second order Bessel functions, the electrical torque is

expressed as

$$T = kI\cos(\omega t)\left[\cos(\omega t+\lambda)\{J_o(C)-2J_2(C)\cos(2\omega_o t+2\beta)\}\right.$$
$$\left.-\sin(\omega t+\lambda)\{2J_1(C)\cos(\omega_o t+\beta)\}\right]$$
$$+T_s\left[\cos(2\omega t+2\lambda+2\gamma)\{J_o(2C)-2J_2(2C)\cos(2\omega_o t+2\beta)\}\right.$$
$$\left.-\sin(2\omega t+2\lambda+2\gamma)\{2J_1(2C)\cos(\omega_o t+\beta)\}\right] \qquad (2.25)$$

$$= T^+J_o(C)\{\cos(2\omega t+\lambda)+\cos(\lambda)\}$$
$$-T^+J_2(C)\{\cos(2\omega_o t+2\omega t+2\beta+\lambda)+\cos(2\omega_o t-2\omega t+2\beta-\lambda)$$
$$+2\cos(\lambda)\cos(2\omega_o t+2\beta)\}$$
$$-T^+J_1(C)\{\sin(2\omega t+\omega_o t+\lambda+\beta)-\sin(\omega_o t-2\omega t+\beta-\lambda)$$
$$+2\sin(\lambda)\cos(\omega_o t+\beta)\}$$
$$+T_sJ_o(2C)\cos(2\omega t+2\lambda+2\gamma)$$
$$-T_sJ_2(2C)\{\cos(2\omega_o t+2\omega t+2\beta+2\lambda+2\gamma)$$
$$+\cos(2\omega_o t-2\omega t+2\beta-2\lambda-2\gamma)\}$$
$$-T_sJ_1(2C)\{\sin(\omega_o t+2\omega t+\beta+2\lambda+2\gamma)$$
$$-\sin(\omega_o t-2\omega t+\beta-2\lambda-2\gamma)\} \qquad (2.26)$$

From equation (2.26) the electrical oscillatory torques have oscillation frequencies of

(i) 2ω
(ii) $2\omega_o+2\omega$
(iii) $2\omega_o-2\omega$ or $2\omega-2\omega_o$
(iv) $2\omega_o$
(v) $\omega_o+2\omega$
(vi) $\omega_o-2\omega$ or $2\omega-\omega_o$
(vii) ω_o
(viii) 2ω (2.27)

By equating the various oscillation frequencies given in equation (2.27) to the oscillation frequency of the mechanical torque ω_o in sequence, it can be shown that the predicted oscillation frequencies are

$$\omega_o = \frac{2}{3}\omega, \ \omega \text{ or } 2\omega \qquad (2.28)$$

In equation (2.26) the oscillatory torques with the terms $J_o(C)$ and $J_o(2C)$ have the largest amplitudes and are likely to predominate. Hence the predominant oscillation frequency is then $\omega_o = 2\omega$.

2.2.2 Torque analysis for an oscillation frequency of twice supply frequency ($\omega_o = 2\omega$)

Analysis given in the previous section has shown that the predominant oscillation frequency is likely to be $\omega_o = 2\omega$ and substituting for $\omega_o = 2\omega$ in equations (2.24) and (2.26) gives

$$\begin{aligned} T_L - JC\frac{4\omega^2}{p}\cos(2\omega t+\beta) \\ = \quad & T^+J_o(C)(\cos(2\omega t+\lambda)+\cos(\lambda)) - T^+J_2(C)\cos(2\omega t+2\beta-\lambda) \\ & + T^+J_1(C)\sin(\beta-\lambda) - 2T^+J_1(C)\sin\lambda\cos(2\omega t+\beta) \\ & +T_sJ_o(2C)\cos(2\omega t+2\lambda+2\gamma)-T_sJ_2(2C)\cos(2\omega t+2\beta-2\lambda-2\gamma) \\ & +T_sJ_1(2C)\sin(\beta-2\lambda-2\gamma)+\ldots(\text{other terms related to} \\ & \text{frequencies of } 4\omega \text{ and } 6\omega) \end{aligned} \qquad (2.29)$$

Neglecting the terms having frequencies of 4ω and 6ω the R.H.S. and L.H.S. of equation (2.29) can be compared. The time invariant term gives the average torque, thus

$$T_L = T^+J_o(C)\cos(\lambda) - T^+J_1(C)\sin(\lambda-\beta)-T_sJ_1(2C)\sin(2\lambda+2\gamma-\beta) \qquad (2.30)$$

Similarly the $\sin(2\omega t+\beta)$ and $\cos(2\omega t+\beta)$ terms can be equated on both sides to give

$$-T^+(J_o(C)+J_2(C))\sin(\lambda-\beta) - T_s(J_o(2C)+J_2(2C))\sin(2\lambda+2\gamma-\beta) = 0 \qquad (2.31)$$

for the former while those with the term $\cos(2\omega t+\beta)$ give

$$-JC\frac{4\omega^2}{p} = T^+(J_o(C)-J_2(C))\cos(\lambda-\beta) - 2T^+J_1(C)\sin(\lambda)$$

$$+ T_s(J_o(2C)-J_2(2C))\cos(2\lambda-2\gamma-\beta) \qquad (2.32)$$

Substituting for $T_s \sin(2\lambda+2\gamma-\beta)$ from equation (2.31) into equation (2.30) gives

$$T_L = T^+J_o(C)\cos(\lambda) - T^+J_1(C)\sin(\lambda-\beta)$$

$$+ J_1(2C)T^+\frac{(J_o(C)+J_2(C))}{(J_o(2C)+J_2(2C))}\sin(\lambda-\beta) \qquad (2.33)$$

$$= T^+(J_o(C)\cos(\lambda) + J_1(C)\sin(\lambda-\beta)) \qquad (2.34)$$

where $J_1(2C)(J_o(C)+J_2(C))/(J_o(2C)+J_2(2C)) = 2J_1(C)$ as shown in Appendix A.

Equation (2.34) shows that the average torque is related to rotor oscillations via $J_o(C)$ and $J_1(C)$ and this explains analytically how the average torque is affected by rotor oscillations. For small oscillations where the first term of equation (2.34) predominates, it is likely that the torque decreases as rotor oscillation increases, provided λ and β are unchanged.

2.3 Measurement and Prediction of Maximum Torque Obtainable From the Rotor

Analysis in section 2.2.2 has shown that the average torque is affected by oscillation. Hence a high coupled inertia was used to reduce rotor oscillation so that the maximum average torque obtainable could be measured using the experimental set-up described in section 4.1. A D.C. generator with a constant

current output was used to load the motor with a torque T_L. The load torque T_L was increased via the constant current control of the D.C. generator with the rotor stalled. At the point when the rotor just stalls it can be assumed that the average torque acting on the rotor has a magnitude approaching its peak value and the load angle λ is near zero such that

$$\lim_{\lambda \to 0} \frac{kI}{2} \cos(\lambda) = \frac{kI}{2} = T^{+} = T_{LS} \qquad (2.35)$$

where T_{LS} is the minimum load torque required to just stall the rotor.

With an inertia of $J = 200 \times 10^{-7}$ kgm^2 which is 19 times the rotor inertia, tests were undertaken to measure the value of T_{LS} for different excitation currents I at a supply frequency of 50Hz. Fig.2.5 shows the variation of T_{LS} with I. From the graph it can be seen that for the case of $T_{LS} = 0$, i.e. when the D.C. generator is not loading the motor, the rotor stalls at excitation currents less than I = 11mA. This suggests that there is a self-imposed load or drag torque due to friction, windage and iron losses acting on the rotor. By extrapolating the curve to the I = 0 axis this drag torque T_D is estimated as 12×10^{-4}Nm. Further investigations on the loss components which cause the drag torque are undertaken in section 2.4. Referring to Fig.2.5, at high excitation currents saturation in the magnetic circuit takes place and causes the gradient of the graph to decrease. Studies in section 3.5 have confirmed that for I > 60mA, the magnetic circuit of the stator iron begins to saturate.

Measurements of T_{LS} against I were repeated at supply frequencies of 30, 40 and 60Hz. The results, also plotted in Fig.2.5, show that changes in supply frequency have negligible effect on the values of T_{LS}. By extrapolating the test results for each supply frequency to the I = 0 axis the drag torque is again estimated as 12 x 10^{-4}Nm for all the cases. Since the estimated drag torque is constant over the supply frequency range of 30 to 60Hz, it verifies that the mechanical damping torque $D\dot{\theta}$ can be assumed to be negligible. Tests have shown that the values of T_{LS} were the same in both directions of rotation over the test frequency range. This is expected since the forward and backward rotating fields should have equal amplitudes.

From equation (2.35) it can be seen that with a known value of k, the variation of T_{LS} with I can be predicted. Using the experimental procedure described in section 4.8 the values of k for the two stators were measured. Test results show that k values of both stators have equal magnitudes of 218 x 10^{-3} Nm/A. This confirms that because of symmetry in the two halves of the motor the k values are the same.

Since the tests above have shown that there is a drag torque T_D acting on the rotor, this suggests that the torque expression should be modified such that

$$T_L + T_D = \frac{kI}{2} \cos(\lambda) \qquad (2.36)$$

Assuming that at the point when the rotor stalls the load angle λ is zero, the load torque required to stall the rotor is then

$$T_{LS} = \frac{kI}{2} - T_D \qquad (2.37)$$

By using the measured k value and estimated value of T_D in equation (2.37), the variation of T_{LS} with I is predicted and plotted in Fig.2.5. At low current levels, the predicted and measured values of T_{LS} show close agreement, and obviously at high current levels the predicted values are higher than the measured values because saturation in the stator iron has reduced the value of k. Thus to avoid saturation and hence satisfy assumption (iv) in section 2.1, future motor tests were confined to excitation levels of I < 60mA.

2.4 Investigations Of Drag Torque To Identify Its Components

In the torque analysis of section 2.1.2 both the hysteresis and eddy current losses were neglected. However due to the rotating magnet there will be iron-losses in the stator resulting in a drag torque T_i acting on the rotor.

Since eddy current power loss is caused by the induction of circulating currents within the magnetic material and hysteresis power loss results from the cycling of its hysteresis loop, the total iron loss can be represented[12,13] as

$$P_i = a_1 f + b_1 f^2$$

and the equivalent iron-loss torque loading the rotor is then

$$T_i = P_i \frac{p}{\omega} = a_2 + b_2 f \qquad (2.38)$$

where a and b are constants for a given material and specified working flux density.

In addition to the iron-loss torque there is a frictional component of the drag torque. The friction component has been subdivided into a component T_{fm} due to the motor alone and a

component T_{fr} due to the rest of the test rig. Thus the total friction torque is given by

$$T_f = T_{fm} + T_{fr} \qquad (2.39)$$

2.4.1 Measurement of the open-circuit drag torques of the motor ($T_i + T_{fm}$)

The drag torque was measured using the 'swinging frame' technique[6] by measuring the torque required to restrain the stator. The shaft of the test motor was coupled to a d.c. motor and its other end supported by a pedestal bearing so that the stator, with open-circuit coils, was free to rotate. The rotor was coupled to a large inertia disc and driven at a constant speed by the d.c. motor. The stator reaction torque was then measured by a gramme-gauge attached to the stator casing.

The total frictional drag torque in the motor T_{fm} is caused by friction in the two end bearings of the motor and two end-springs which hold the rotor in its correct axial location. For the measurement of T_{fm}, T_i was eliminated by replacing the permanent magnet rotor with an identical axial length perspex rotor so that the two end-springs were kept in their respective positions as in the test motor. The values of T_{fm} were measured at different speeds. The results plotted in Fig.2.6 show that the frictional torque T_{fm} is a constant of 3×10^{-4}Nm. The experiment was repeated with the perspex rotor and two end-springs removed to determine the friction torque in the two bearings. The results also plotted in Fig.2.6 show that the bearing friction is only 0.5×10^{-4}Nm and the difference between this curve and that of T_{fm} represents the frictional torque due to the two end-springs.

With the permanent magnet rotor reinserted and the two end-springs assembled into their respective places in the test motor, the drag torque measurements were repeated. The results are plotted in Fig.2.6 for comparison purposes. Assuming that the frictional torque T_{fm} remains the same at 3×10^{-4}Nm, then the iron-loss torques can be calculated by subtracting the drag torques for the case with the permanent magnet rotor from that with the perspex rotor as shown in the figure. This 'measured' iron-loss torque frequency curve in Fig.2.6 fits the typical iron-loss torque frequency variation expressed in equation (2.38). The results show that the iron-loss due to eddy-currents is much smaller than that due to hysteresis and hence the eddy current iron-loss component can be neglected. Thus the drag torque due to iron-loss T_i is estimated as 6×10^{-4}Nm and can be assumed to be independent of speed. Since the rotor is made from powdered barium ferrite having a high resistivity, and since the recoil hysteresis loop of the material is very small, it can be assumed that all the iron-losses are confined to the stator iron only.

2.4.2 Measurement of friction torque of the test rig plus the motor ($T_f = T_{fr} + T_{fm}$)

The friction torque of the test rig was measured using the same experimental system as used to measure T_{LS} in section 2.3. To eliminate the iron losses in the test motor, the permanent magnet rotor was replaced with the perspex rotor as described in section 2.4.1. The D.C. machine was used as a motor to drive the test motor and coupled inertia disc. With the rotor rotating, the current to the D.C. drive motor was

reduced until it stalled. At the point where it stalls, the rotating friction torque equals the torque produced by the D.C. motor. Results show that the rotating friction torque T_f of the test rig is 6.5×10^{-4}Nm. The large inertia disc adds an excessive force to the motor bearings and the test was repeated with the disc removed in order to check on the magnitude of the additional friction torque. With the disc removed, the friction torque T_f was reduced to 6×10^{-4}Nm.

2.5 Verification Of Oscillation Analysis

2.5.1 Frequency and amplitude of rotor oscillation

With the motor mounted on the experimental rig described in section 4.1 tests were carried out to determine the modes of rotor oscillations about synchronous speed at different current I, supply frequency f and inertia J. Results showed that there were mainly two possible modes of rotor oscillation.

The most predominant mode of rotor oscillation observed was oscillations at twice the supply frequency ($\omega_o = 2\omega$) as predicted in section 2.2.1. The second mode consisted of two component frequencies of twice supply frequency and supply frequency. This more complex oscillation can be expressed as

$$\dot{\theta} = \frac{\omega}{p} + A_1\cos(\omega t+\beta_1) + A_2\cos(2\omega t+\beta_2) \qquad (2.40)$$

This mode of oscillation only occurs at regions of low supply frequencies and low inertias, and analysis of this mode of oscillation is not covered in this thesis.

Fig.2.7 gives the oscillograms of current I and speed $\dot{\theta}$ for the two different modes of rotor oscillation. The change

in oscillation mode from that of Fig.2.7(a) to that of Fig. 2.7(b) was quite abrupt with no intermediate stage. This is probably caused by the change in the stability of rotor oscillation due to the interacting torque expressions of equations (2.15) and (2.23).

For the case when the rotor oscillation is $\omega_o = 2\omega$, the amplitude of oscillation C has been measured at various excitation currents, supply frequencies and inertias. Fig.2.8 shows the plots of C against I. In the graphs there are upper limits of C for each case because above these points the mode of rotor oscillation changes to that described by equation (2.40). At I > 60mA, the gradient of the curves decrease, suggesting that C is affected by saturation in the stator iron. The results of Fig.2.8 show that C is always less than 0.23 radians, hence verifying the assumption in section 2.2.1 that C is small.

2.5.2 Comparison of predicted and measured electromechanical torque components

Studies in the previous section have verified that the amplitude of rotor oscillation is small and the predominant oscillation frequency is $\omega_o = 2\omega$. The next stage was to verify the oscillatory and average torque expressions given in equations (2.30), (2.31) and (2.32).

By rearranging equations (2.31) and (2.32), the saliency torque is given as

$$T_s = \{ \left[-T^+ \frac{(J_o(C)+J_2(C))}{(J_o(2C)+J_2(2C))} \sin(\lambda-\beta)\right]^2 + \left[\frac{-JC4\omega^2/p - T^+(J_o(C)-J_2(C))\cos(\lambda-\beta)+2T^+J_1(C)\sin(\lambda)}{(J_o(2C)-J_2(2C))}\right]^2 \}^{\frac{1}{2}} \quad (2.41)$$

Investigations in section 2.3 suggested that the drag torque T_D could be included in the torque analysis by considering it as a constant extra load torque acting on the rotor, as shown in equation (2.36).

By including the drag torque into equation (2.34), the average torque equation is rewritten as

$$T_L+T_D = T^+(J_o(C)\cos(\lambda) + J_1(C)\sin(\lambda-\beta)) \quad (2.42)$$

In equation (2.41), the terms on both sides of the equation can be measured or calculated from measured values. Hence by checking that the L.H.S. of the equation equals the R.H.S., the accuracy of the oscillatory torque analysis can be established. Similarly the measured value of T_L+T_D in equation (2.42) should equal the value obtained by substituting for measured values of the variables in the R.H.S. of the equation.

With known values of k and I, T^+ can be calculated. The measurements of J and C are straightforward and their details are given in sections 4.4 and 4.6 respectively. The value of λ is measured using a reference generator and details of the experimental procedure are described in section 4.9. Since the oscillation frequency is twice the supply frequency, the measurement of β necessitates electronic circuitries to synthesize a reference signal having a frequency of 2ω from the current signal which has a frequency of ω. With this synthesizing technique to determine β, there is an instrumentation limitation because there are two possible values of β such that

$$\beta_1 = \beta \qquad (2.43)$$

and $$\beta_2 = \beta - 180^{o} \qquad (2.44)$$

Further details on the measurement of β are given in section 4.7. Using the measurement set-up described in section 4.1 and with the permanent magnet rotor in the motor, the saliency torque T_s was measured. The torque required to start the rotor at standstill has to overcome the torque T_s+T_f. Measurement has shown that $T_s+T_f = 14 \times 10^{-4}$Nm and since T_f has been measured as 6×10^{-4}Nm, the value of T_s is then 8×10^{-4}Nm.

For fixed values of f = 50Hz and J = 15.5×10^{-7}kgm^2, the motor was tested at different excitation currents I for various values of load torque T_L. Typical results of the test are shown in Table 2.1. Fig.2.9 shows the variations of predicted T_L+T_D and T_s with I for $\beta = \beta_1$ while Fig.2.10 shows the corresponding plots for $\beta = \beta_2$. In Figs.2.9 and 2.10 for a fixed applied torque $T_L + T_D$ the predicted torque $T_L + T_D$ is not constant but increases linearly with I. Similarly the values of predicted T_s for the cases of β_1 and β_2, shown in Figs.2.9 and 2.10, vary with current I and do not correspond to the expected constant measured value of $T_s = 8 \times 10^{-4}$Nm. The measurements were repeated at f = 40Hz and 60Hz for T_L = 0 and 14×10^{-4}Nm. Again the predicted $T_L + T_D$ values shown in Fig. 2.11 increase with current and do not remain constant as expected. Clearly therefore this mathematical model is incorrect.

TABLE 2.1

Measured parameters

T_L	$\bar{I}$(mA)	C (radians)	λ (degrees)	β degrees	
				β_1	β_2
$T_L = 0$	20.5	.041	16.3	15.7	-164.3
	28.3	.062	33.8	30.2	-149.8
	34.0	.075	43	38.4	-141.6
	42.4	.093	48.6	44.4	-135.6
	56.6	.122	52.2	53.2	-126.8
$T_L = 14 \times 10^{-4}$Nm	31	.064	5	5	-175
	36.8	.079	20.8	17.4	-162.6
	42.4	.092	28.6	27.1	-152.9
	48.1	.102	33.6	31.9	-148.1
	56.6	.117	38.6	40.9	-139.1
$T_L = 28 \times 10^{-4}$Nm	45.3	.093	4.4	3	-177
	48.1	.099	11.1	9.2	-170.8
	50.9	.107	15.9	15.2	-164.8
	53.7	.113	19.6	19.4	-160.6
	56.6	.119	22.5	23.4	-156.6

To check whether the discrepancy occurred only in the presence of oscillations, the inertia J was increased from 15.5×10^{-7} to 200×10^{-7} kgm^2 such that $C \to 0$. The average torque is then given approximately as

$$T_L + T_D = T^+ \cos(\lambda) \qquad (2.45)$$

The experiments were repeated for the same f and T_L values as those shown in Figs.2.10 and 2.11. The values of $T_L + T_D$ were predicted from the L.H.S. of equation (2.45) and plotted in their respective figures. The results show that the predicted average torque still varies linearly with current and thus eliminating the oscillations as the cause of the discrepancy.

Tests in section 2.3 have shown that below saturation T^+ varies linearly with I and hence the only possible error in equation (2.45) is in the effective value of λ used to predict the magnitude of the R.H.S. of the expression. However, assumptions regarding the sinusoidal waveform of ψ were made previously in establishing equation (2.45). A check was made on these assumptions to show that flux harmonics did not contribute to the errors in the model. The results are given in Appendix B.

Clearly therefore the linearized model is inadequate and further consideration of the torque mechanisms was undertaken. Analogue simulation studies by Bassyouni[6] had shown that for the non-oscillatory case a more accurate modelling of the machines could be achieved by inclusion of the effects of hysteresis loops of the magnetic circuit on the torque mechanism. It was decided therefore to attempt to develop an analytical model to include the hysteresis characteristic of the magnetic circuit.

CHAPTER 3

MODEL INCLUDING HYSTERESIS EFFECT

3.1 Introduction

Studies in Chapter 2 have shown that the hysteresis effect in the stator iron is significant and this causes the linearized model to be inaccurate. In this Chapter a model based on the d-q axis theory but including hysteresis is developed. The hysteresis effect is taken into account by assuming the stator flux linkage lags its mmf by a hysteresis angle Ⓗ.

3.2 Equivalent Circuit Model

Assuming that the permanent magnet rotor can be modelled as an equivalent coil carrying a constant d.c. current I_m, then the equivalent circuit model for a 2-pole (p=1) machine is as shown in Fig.3.1. With the rotor coil rotating at a constant speed $\dot{\theta}(=\omega/p)$, the rotor sets up a rotating mmf. It is well known[12,13] that a rotating mmf can be produced by stationary coils carrying polyphase currents and thus the permanent magnet rotor is represented by a two-phase system carrying a.c. currents producing an identical rotating mmf to the original single rotating coil, as shown in Fig.3.2. For equivalent mmfs,

$$i_d = I_m \cos(p\theta) \qquad (3.1)$$

$$i_q = I_m \sin(p\theta) \qquad (3.2)$$

where $p\theta$ is the instantaneous angular position of the rotor and the rotor coils d and q are assumed to be identical with the same number of turns as the stator coil C.

In order to have stationary coil axes on a rotating rotor the d and q coils must be assumed to be supplied via commutators, as in the case of d.c. machines. The d-q transformation is therefore often referred to as the commutator transformation. As in d.c. machines, the emf induced in the rotor or stator coils due to rotation is proportional to the flux on an axis normal to the coil axis, however in a.c. machines there is an additional emf induced by transformer action between coils on the same axis.

Assuming that each winding produces a sinusoidal flux density distribution and the armature is symmetrical the voltage equations of the d-q axis model are given as

$$v_d = (R_d+L_dS)i_d+L_q\dot{\theta}i_q+M_{dc}Si_c \qquad (3.3)$$

$$v_q = -L_d\dot{\theta}i_d+(R_q+L_qS)i_q-M_{qc}\dot{\theta}i_c \qquad (3.4)$$

$$v_c = M_{cd}Si_d+O+(R_c+L_cS)i_c \qquad (3.5)$$

where S = d/dt operator

$M_{dc}=M_{qc}=M_{cd}=M$ are the mutual inductance between stator coil and rotor coils

It can be seen in equations (3.3)-(3.5) that the flux between the stator and rotor coils on the d-axis gives rise to a transformer emf ($M_{dc}Si_c$ amd $M_{cd}Si_d$) whilst the same flux gives rise to a speed emf between the stator and rotor q-axis coils ($-M_{qc}\dot{\theta}i_c$).

In matrix form, equations (3.3)-(3.5) become:

$$[v] = [Z][i] \qquad (3.6)$$

The impedance matrix $[Z]$ can be divided into parts separating the resistive terms into an $[R]$ matrix, the inductance terms into an $[L]$ matrix and the motional voltage terms, which may be related to the inductance terms, in an array usually called the $[G]$ matrix. Hence the impedance matrix can be written as

$$[Z] = [R] + [L]s + [G]\dot{\theta} \tag{3.7}$$

where

$$[R] = \begin{bmatrix} R_d & 0 & 0 \\ 0 & R_q & 0 \\ 0 & 0 & R_c \end{bmatrix} \tag{3.8}$$

$$[L] = \begin{bmatrix} L_d & 0 & M \\ 0 & L_q & 0 \\ M & 0 & L_c \end{bmatrix} \tag{3.9}$$

and

$$[G] = \begin{bmatrix} 0 & L_q & 0 \\ -L_q & 0 & -M \\ 0 & 0 & 0 \end{bmatrix} \tag{3.10}$$

3.3 Torque Analysis Using the Model

The total instantaneous power input to the windings is

$$P = i_d v_d + i_q v_q + i_c v_c \tag{3.11}$$

$$= [i]^T [v] \tag{3.12}$$

Substituting equations (3.6) and (3.7) into equation (3.12) gives

$$P = [i]^T [R] [i] + [i]^T [L] s [i] + [i]^T [G] \dot{\theta} [i] \tag{3.13}$$

where $[i]^T [R] [i]$ represents the total copper loss in the machine and is of the form $\sum Ri^2$ since $[R]$ is a diagonal matrix

$[i]^T[L]s[i]$ represents the rate of change of stored magnetic energy

$[i]^T[G]\dot{\theta}[i]$ is the difference between the input power and the other two terms and represents the mechanical output power

For a p-pole pair machine, the torque acting on the rotor is then given as

$$T = p[i]^T[G][i] = p[i_d i_q i_c]\begin{bmatrix} 0 & L_q & 0 \\ -L_d & & -M \\ 0 & 0 & 0 \end{bmatrix}\begin{bmatrix} i_d \\ i_q \\ i_c \end{bmatrix} \quad (3.14)$$

$$= pi_d(i_q L_q) - pi_q(i_d L_d + i_c M) \quad (3.15)$$

$$= pi_d\psi_q - pi_q(\psi_d + \psi_{dc}) \quad (3.16)$$

where $\psi_q = i_q L_q$

$\psi_d = i_d L_d$

$\psi_{dc} = i_c M$

As the q-axis coincides with the interpolar axis, i.e. the axis having maximum reluctance, then it is assumed that $\psi_q \to 0$ and thus

$$T = -pi_q\psi \quad (3.17)$$

where $$\psi = \psi_d + \psi_{dc} \quad (3.18)$$

With the motor supplied from an a.c. current source and using the current in the stator coil C as the reference phasor, the current is expressed as

$$i_c = I\cos\omega t \quad (3.19)$$

Neglecting the effect of saturation and assuming that the flux linkage ψ lags the vector sum of the stator and rotor mmfs (I and I_d) by $\textcircled{H}^\circ$, then the phasor diagram of I, I_s, I_d, I_q and ψ is that given in Fig.3.3. It can be shown that the flux linkage is expressed as

$$\psi = K(I\cos(\omega t-\textcircled{H})+I_m\cos(p\theta-\textcircled{H})) \qquad (3.20)$$

where $K = N^2/S$

N is the number of turns in the stator coil C

S is the reluctance of the stator coil C

and

$$p\theta = \omega t-\phi_c \qquad (3.21)$$

Substituting equations (3.2) and (3.20) into equation (3.17) gives the torque as

$$T = -pI_m\sin(p\theta)K(I\cos(\omega t-\textcircled{H})+I_m\cos(p\theta-\textcircled{H})) \qquad (3.22)$$

As mentioned in Section 2.5 the load angle λ is measured using a reference generator which is coupled mechanically to the test motor. With both stators of the reference generator and test motor open-circuit, and their rotors driven at constant speed $\dot{\theta}(=w/p)$ by a d.c. motor, the o.c. emf of the reference generator is

$$\frac{d\psi_g}{dt} = -K_gI_{mg}\omega\sin(\omega t-\textcircled{H}_g-\alpha_g) \qquad (3.23)$$

while that of the test motor is

$$\frac{d\psi}{dt} = -KI_m\omega\sin(\omega t-\textcircled{H}) \qquad (3.24)$$

where K_g, I_{mg} and $\textcircled{H}_g$ are the parameters of the reference generator

α_g is the electrical phase difference between the test motor and reference generator

The stator of the reference generator is aligned w.r.t. the stator of the test motor such that $d\psi_g/dt$ and $d\psi/dt$ are in phase and hence, from equations (3.23) and (3.24), the angle of the reference generator ($\alpha_g+Ⓗ_g$) equals the hysteresis angle Ⓗ of the test motor.

Under normal operation of the motor when I_d lags I by ϕ_c, as shown in Fig.3.4, the angle ϕ_c is expressed as

$$\phi_c = \frac{\pi}{2} - Ⓗ - \lambda \qquad (3.25)$$

and ϕ_c can be determined by measuring the value of λ with the reference generator.

Taking into account the second stator, which is displaced by α^o and left open-circuit, the total torque acting on the rotor is

$$T = -pKI_m \sin(p\theta)\ (I\cos(\omega t-Ⓗ)+I_m\cos(p\theta-Ⓗ)) \\ -pKI_m^2 \sin(p\theta+\alpha)\cos(p\theta-Ⓗ+\alpha) \qquad (3.26)$$

By substituting equations (3.21) and (3.25) into equation (3.26), it can be shown that the average torque is

$$T = p\frac{KI_mI}{2}\cos(\lambda+2Ⓗ)-pKI_m^2\sin Ⓗ \qquad (3.27)$$

In equation (3.27), the last term is equivalent to the hysteresis iron-loss drag torque T_i discussed in Section 2.4. However the effect of hysteresis also modifies the load angle from λ to $(\lambda+2Ⓗ)$, thus verifying the observations made at the end of Section 2.5.2.

3.3.1 Torque analysis with stator coil open-circuit

With the stator windings open-circuit and neglecting friction torques, the torque required to rotate the rotor is

given as

$$T_\theta = -pKI_m^2 \sin(p\theta)\ \cos(p\theta-Ⓗ) - pKI_m^2 \sin(p\theta+\alpha)\ \cos(p\theta+\alpha-Ⓗ) \quad (3.28)$$

$$= -pKI_m^2 [\cos(\alpha)\sin(2p\theta+\alpha-Ⓗ)+\sin Ⓗ] \quad (3.29)$$

The first term of equation (3.29) is the saliency torque and is an alternating torque while the second term is the drag torque due to hysteresis. If hysteresis is neglected, i.e. Ⓗ=0, equation (3.29) is of the same form as equation (2.10).

3.4 Oscillation Analysis

Assuming that the rotor oscillates at $\omega_o=2\omega$ with an amplitude C about its mean synchronous speed then the instantaneous angular position is

$$p\theta = \omega t-\phi_c+C\ \cos(2\omega t+\beta) = \omega t-\frac{\pi}{2}+Ⓗ+\lambda+C\cos(2\omega t+\beta) \quad (3.30)$$

By substituting equation (3.30) into equation (3.26) and assuming C<<1, it can be shown that the instantaneous torque is given as

$$\begin{aligned} T = p\frac{KI_mI}{2}\ & [J_o(C)\cos(\lambda+2Ⓗ)-J_1(C)\sin(\lambda-\beta)+J_o(C)\cos(2\omega t+\lambda) \\ & -2J_1(C)\sin(\lambda+2Ⓗ)\cos(2\omega t+\beta)-J_2(C)\cos(2\omega t+2\beta-\lambda)] \\ +p\frac{KI_m^2}{2}\ & [J_o(2C)\{\sin(2\omega t+2\lambda+Ⓗ)+\sin(2\omega t+2\lambda+Ⓗ+2\alpha)\} \\ & +J_2(2C)\{\sin(2\omega t+2\beta-2\lambda-Ⓗ)+\sin(2\omega t+2\beta-2\lambda-2\alpha-Ⓗ)\} \\ & +J_1(2C)\{\cos(2\lambda+Ⓗ-\beta)+\cos(2\lambda+2\alpha+Ⓗ-\beta\}-2\sin Ⓗ] \end{aligned} \quad (3.31)$$

This torque must equal the mechanical torque which is generally given as

$$T_L+T_f+D\dot{\theta}+J\ddot{\theta} \qquad (3.32)$$

Since $D\dot{\theta} \to 0$ as shown in Section 2.3, the mechanical torque is then

$$T_L+T_f-JC\frac{4\omega^2}{p}\cos(2\omega t+\beta) \qquad (3.33)$$

By equating equations (3.31) and (3.33), the average torque is given as

$$\begin{aligned} T_L+T_f = {} & p\frac{KI_mI}{2}\left[J_o(C)\cos(\lambda+2\textcircled{H})-J_1(C)\sin(\lambda-\beta)\right] \\ & +p\frac{KI_m^2}{2}\left[J_1(2C)\{\cos(2\lambda+\textcircled{H}-\beta)+\cos(2\lambda+2\alpha+\textcircled{H}-\beta)\}\right. \\ & \left.-2\sin\textcircled{H}\right] \end{aligned} \qquad (3.34)$$

The oscillatory torque consists of two components, the $\cos(2\omega t+\beta)$ terms giving the expression

$$\begin{aligned} -JC\frac{4\omega^2}{p} = {} & p\frac{KI_mI}{2}\left[(J_o(C)-J_2(C))\cos(\lambda-\beta)-2J_1(C)\sin(\lambda+2\textcircled{H})\right] \\ & +p\frac{KI_m^2}{2}(J_o(2C)-J_2(2C))\left[\sin(2\lambda+2\alpha+\textcircled{H}-\beta)+\sin(2\lambda+\textcircled{H}-\beta)\right] \end{aligned} \qquad (3.35)$$

while the $\sin(2\omega t+\beta)$ terms give

$$\begin{aligned} 0 = {} & -p\frac{KI_mI}{2}(J_o(C)+J_2(C))\sin(\lambda-\beta) \\ & +p\frac{KI_m^2}{2}(J_o(2C)+J_2(2C))\left[\cos(2\lambda+\textcircled{H}-\beta)+\cos(2\lambda+2\alpha+\textcircled{H}-\beta)\right] \end{aligned} \qquad (3.36)$$

3.5 Comparisons of Average Electrical and Mechanical Torques for the Case of Negligible Rotor Oscillation

The accuracy of the model was established by comparing the average mechanical and electrical torques acting on the rotor. Initially the comparison was restricted to the case when rotor oscillations were negligible, i.e. $C \to 0$. The mechanical torque consists of the friction torque of the test rig and motor

T_f(=6.5x10^{-4}Nm), and the load torque T_L from the d.c. generator. The electrical torque is predicted using measured values of p, K, I_m, Ⓗ, I and λ in equation (3.27).

The measurements of K, I_m and Ⓗ are straightforward and are as described in Section 4.10. The measured values of K, I_m and Ⓗ are given in Table 3.1. The measurements were repeated on the second stator and the results showed that the parameters are identical for the two halves of the test motor.

With the stators of the reference generator and test motor aligned such that $Ⓗ_g+\alpha_g$ equals Ⓗ as described in Section 3.3, the experimental technique for measuring λ remains the same in the presence of hysteresis and is as described in Section 4.9.

Using a high coupled inertia of J=200x10^{-7}kgm^2 to reduce rotor oscillation, such that C$\rightarrow$0, experiments were undertaken to measure the values of λ at different levels of current I for a fixed supply frequency of f=50Hz. The experiments were repeated for different load torques T_L. The electrical torques acting on the rotor are calculated and plotted in Fig.3.5(a) together with the known applied mechanical torques (T_L+T_f). The plots show that the agreement between the electrical and mechanical torques is reasonable, hence verifying the model for the case of negligible rotor oscillation. The measurements were repeated at supply frequencies of f=40Hz and 60Hz. The calculated electrical torques plotted in Figs.3.5(b) and 3.5(c) again show good agreement with the mechanical torques.

Table 3.1: Parameters of the stators

I_m	17.8mA
K	1.02Wb/A
(H)	10.6°

Table 3.2: Typical values of the steady-state experiment

f=50Hz, J=200x10^{-7}kgm^2, T_f=6.5x10^{-4}Nm

Load torque T_Lx10^{-4}Nm	Measured		Calculated electrical torque x10^{-4}Nm	Mechanical torque $T_L + T_f$ x10^{-4}Nm
	I(mA)	λ°		
0	19.8	20	9.2	6.5
	26.9	35	9.2	
	31.1	41	8.8	
	36.8	46	8.5	
	42.4	48.5	9.0	
14	31.1	5	23.5	20.5
	36.8	20.5	23	
	42.4	28.5	23	
	48.1	33.5	23.4	
	56.5	38.5	24.1	
28	45.2	4.4	37.6	34.5
	48.1	11.1	37.5	
	50.9	15.9	37.4	
	53.7	19.6	37.5	
	56.5	22.5	37.7	

There appears to be a constant error of approximately 2.5×10^{-4}Nm between the calculated and applied torques. It is thought likely that this is an experimental error in determining the friction torque T_f. Table 3.2 shows some typical values of measured λ and I at different values of T_L together with their corresponding calculated electrical torques.

Using the experimental set-up described in Section 4.10, the ψ-i loops of the stator at various excitation currents can then be displayed as shown in Fig.3.6. The loops were displayed with the rotor at standstill and thus the permanent magnet rotor can be considered as a d.c. mmf which biases the ψ-i loop on the i axis. Tests showed however that the ψ-i loops are insensitive to rotor position and this is because the mmf due to the stator current is much larger than that due to the rotor. In Fig.3.6 the ψ-i loops saturate at I > 60mA, thus confirming the experimental deduction made in Section 2.3. To avoid saturation in the stator iron, the motor was tested at currents less than 60mA.

3.6 Comparison of Calculated and Measured Torques with Stator Coil Open-Circuit

From equation (3.29), the maximum value of T_θ is given as

$$T_{\theta max} = -pKI_m^2 (\cos(\alpha)+\sin\textcircled{H}) \qquad (3.37)$$

By substituting the measured values of K, I_m, $\textcircled{H}$ and α into equation (3.37), the saliency torque (first term in the equation) is calculated as 3.4×10^{-4}Nm and the hysteresis drag torque (second term) is 7.1×10^{-4}Nm. Thus the value of

$T_{\theta max}$ is $10.5x10^{-4}$Nm.

The result given in Section 2.5.2, for the case neglecting hysteresis effect, suggested that the saliency torque T_s was $8x10^{-4}$Nm. However analysis given in Section 3.3.1, which takes account of hysteresis in the stator iron has showed that there is also a hysteresis drag torque together with the saliency torque. Hence the apparent measured value of T_s is actually a measure of saliency torque plus the hysteresis drag torque T_i. From this it can be seen that the measured value of

$$T_s+T_i = 8x10^{-4}Nm$$

is in reasonable agreement with the calculated value of $T_{\theta max} = 10.5x10^{-4}$Nm.

3.7 Verification of Model when the Rotor has Oscillations about its Mean Synchronous Speed

3.7.1 Comparison of the instantaneous mechnical and electrical torque values

The verification of the model when the rotor has oscillations about its mean synchronous speed is based on a comparison of the instantaneous mechanical and electrical torques. The instantaneous mechanical torque is calculated by using t as an independent variable in equation (3.33) for known values of T_L, T_f, J, C, ω, p and β. Similarly with known values of α, ω, Ⓗ, λ, C, β, p, K, I_m and I in equations (3.26) and (3.30), the instantaneous electrical torque can also be calculated.

For fixed values of f=50Hz and $J=15.5x10^{-7}kgm^2$ experiments were undertaken to measure λ, C and β at different

current levels I and load torques T_L. Table 3.3 shows some of the experimental results.

Because of experimental limitations there are two alternative values of β i.e. $\beta_1=\beta$ and $\beta_2=\beta-180^o$ and this results in two plots of mechanical torques as well as two plots of electrical torques. Figs.3.7 to 3.12 show some typical plots of instantaneous electrical and mechanical torques for the measured points indicated in Table 3.3. From the plots it can be seen that good agreement between the electrical and mechanical torques is only achieved for $\beta=\beta_2$. This value of $\beta=\beta_2$ has therefore been used for all subsequent calculations.

3.7.2 Comparison of average and oscillatory torque magnitudes

The previous Section 3.7.1 has verified the instantaneous torque expressions, equations (3.22) and (3.33) by taking time as the independent variable. A better understanding of the effects of oscillation on the magnitude of the average and oscillatory torques can be obtained by comparing the various components of torque magnitudes related to the time invariant terms, $\cos(2\omega t+\beta)$ terms and $\sin(2\omega t+\beta)$ terms given by equations (3.34), (3.35) and (3.36) respectively. Again verification is based on a comparison of the experimental values of the L.H.S. and R.H.S. of each equation.

By substituting the measured terms p, K, I_m, Ⓗ, λ, C, I and $\beta(=\beta_2)$ into the L.H.S. of equations (3.34), (3.35) and (3.36), the average and oscillatory electrical torques are calculated and plotted in Fig.3.13. For comparison purposes

the average and oscillatory mechanical torques (R.H.S. of equations (3.34), (3.35) and (3.36)) are also plotted in Fig.3.13. The plots of the electrical and mechanical average torques given in Fig.3.13(a) show close agreement, hence verifying the average torque analysis given in equation (3.34). The electrical and mechanical oscillatory torques related to $\cos(2\omega t+\beta)$ are compared in Fig.3.13(b) while those related to $\sin(2\omega t+\beta)$ are in Fig.3.13(c). From Figs.3.13(b) and 3.13(c) it can be seen that the electrical oscillatory torques related to $\cos(2\omega t+\beta)$ are much larger than those related to $\sin(2\omega t+\beta)$. This confirms that the oscillatory torques of $D\dot{\theta}$ are smaller than those of $J\ddot{\theta}$ and can be neglected. In Fig.3.13(b) the electrical and mechanical oscillatory torques show good agreement and this verifies the oscillatory torque analysis given in equation (3.35).

The experiment was repeated for larger oscillation amplitudes by testing the motor at f=40Hz. The results are shown in Fig.3.14. Again close agreement is achieved between the electrical and mechanical torques, for both average and oscillatory values.

These tests verify that the model including hysteresis give reasonable prediction of the motor performance.

Table 3.3 Experimental results

f=50Hz, J=15.5x10^{-7}kgm^2, T_f=6x10^{-4} Nm					Instantaneous mechanical and electrical torques plotted in fig.
Load torque T_Lx10^{-4}Nm	Measured variables				
	I(mA)	C (radians)	β°	λ°	
0	20.5	.0415	15	20	
	28.0	.0622	30.2	36.	3.7
	56.6	.122	53.2	52.2	3.8
14	31.1	.064	5	5	3.9
	42.4	.0914	27.1	28.6	
	56.6	.1173	41	38.6	3.10
28	45.3	.093	3	4	3.11
	50.9	.1067	15.2	15.9	
	56.6	.1189	23.4	22.5	3.12

CHAPTER 4

EXPERIMENTAL ARRANGEMENTS AND PROCEDURES USED IN THE INVESTIGATION

4.1 Test Rig

A schematic diagram of the rig used for testing the synchronous motor is shown in Fig.4.1. The test motor is mounted on a non-magnetic aluminium test bed and is supplied by an a.c. current source described in section 4.2. A d.c. machine coupled to the rotor shaft of the test motor is used to either drive or load the test motor, depending on its selected mode of operation i.e. motoring or generating. Since test results given in Fig. 2.8 have shown that higher system inertias reduce rotor oscillations, the D.C. machine used must have a very low inertia. For this reason the Escap motor (No.:23D21-213) was chosen. Table 4.1 gives the specifications of the Escap motor.

Coupled to the other end of the test motor is a synchronous motor having the same number of poles as the test motor. This motor is used for measuring the load angle λ and is termed the reference generator. Again, the reference generator must have a very low inertia and a sub-miniature synchronous motor, the SA1A AMY6 motor, was chosen. The specifications of the AMY6 motor are summarized in Table 4.1. This synchronous motor is designed as a shaded pole motor and to minimise the eddy current effects in the shading rings, the shading plates around the stator poles were removed. The reference generator is mounted on a perspex frame such that its stator can be rotated in space

and aligned with that of the test motor. Fig.4.2 shows the reference generator on its mounting frame.

The reference generator and D.C. motor are connected to both ends of the test motor by a three-section universal coupling (HUCO No. :2100) as shown in Fig.4.1. The HUCO couplings are essential to minimise any friction torques due to slight misalignments in the shafts of the three coupled machines. Table 4.1 shows the specifications of the HUCO couplings. Assuming that the drag torque acting on the O.C. reference generator is 6×10^{-4}Nm, the torsional angle between the rotors of the test motor and reference generator is $71.3 \times 6 \times 10^{-4} = 0.043^{o}$, or $0.043 \times 12^{o} = 0.5^{o}$ electrical if referred to the p = 12 reference generator. This means that the error in measuring λ caused by the torsional twist in the HUCO coupling is negligible.

TABLE 4.1

Specifications of D.C. motor (Escap 23D21-213)

Voltage rating	15V
Stall torque (20^{o}C)	245×14^{-4}Nm
Back-emf constant	2.8×10^{-3} V/r.p.m.
Rotor inertia	4.7×10^{-7} kgm^2
Torque constant	$.270 \times 10^{-4}$ Nm/A

Specifications of reference generator (AMY6)

Power rating	0.2W
Voltage rating	24V
Permanent magnet material	Barrium ferrite
Number of pole pairs	12

Specifications of HUCO coupling (2100 series)

Torsional twist constant	71.3^{o} per Nm

4.2 The A.C. Current Source For The Test Motor

During the initial stage of the experiment the test motor was supplied from a voltage amplifier (Savage Mk II Star 1 kilowatt amplifier)[14]. To ensure that the motor current was sinusoidal, the test motor having an impedance of 230 +j0.7ω was connected in series with a 2KΩ wirewound resistor. This method of producing constant current in the test motor is identical to that used by Bassayouni[6]. However it has been found that the voltage amplifier used produces an unwanted beat frequency of f -50Hz where f is the frequency of the oscillator. This beat frequency generation is inherent in the design of the Savage amplifier and hence could not be eliminated.

It is well known[15] that the current across an impedance Z_L can be made independent of Z_L by connecting Z_L in the feedback loop of an amplifier. Fig.4.3 shows the current feedback circuit. The output voltage of the amplifier is given as

$$v_o = (v_i - v_R)/A \qquad (4.1)$$

where A is the open loop gain of the amplifier.

Assuming A >> 1, then the input voltage is

$$v_i = v_R = iR \qquad (4.2)$$

and the current is

$$i = v_i/R \qquad (4.3)$$

From equation (4.3) it can be seen that this current feedback arrangement makes the current i independent of Z_L. By replacing Z_L with the test motor, the circuit arrangement

shown in Fig.4.3 is used as an a.c. current source for the test motor.

A commercially available audio power amplifier, the JPS 150L, was chosen for the modification of its conventional voltage feedback to current feedback arrangement because it has the suitable voltage and current ratings of 56V peak and 10A peak respectively. The schematic diagram of the power amplifier sub-divided into its voltage and current amplification stages is shown in Fig.4.4. With the switch S in position 1, the power amplifier is in its normal voltage feedback arrangement via R_1, R_2 and C_1. The power amplifier is switched to current feedback when switch S in in position 2. The capacitors C_3 and C_4 are used to block d.c. voltages and R_3 provides a unity transfer function for d.c. signals, with R being the a.c. current feed-back resistor. It has been found that in practice the power amplifier can be unstable under current feedback mode and C_2 must be used as a compensating capacitor[15] such that it inserts an extra pole into the transfer function at a lower frequency than the existing poles and introduces a phase lag in the transfer function.

Tests with the modified power amplifier switched to current feedback mode have shown that the voltage waveform across R, i.e. the signal representing the current of the motor, is identical to that of the input voltage v_i. Oscillograms in Fig. 4.5 show the current waveforms of the test motor for different input voltage waveforms to the amplifier. From these it can be seen that the amplifier is a voltage-to-current converter, i.e. it gives an a.c. output current for an input voltage signal.

4.3 The D.C. Machine And Its Power Supply

In the chosen d.c. machine (Escap motor), the magnetic field is provided by a permanent magnet. The armature coils are wound on an ironless former and supplied with current via a commutator. Fig.4.6 shows the equivalent circuit of the d.c. machine with the armature circuit (conductors, commutator and brushes) represented by R_a. If generated voltage E_a is less than the supply voltage V_a, the source will supply power to the machine, which therefore acts as a motor. Then the voltage equation is given as

$$V_a = E_a + I_a R_a \tag{4.4}$$

If $E_a > V_a$, the source will absorb power from the machine which therefore behaves as a generator. With opposite direction for positive I_a, the generated voltage is

$$E_a = V_a + I_a R_a \tag{4.5}$$

With steady state conditions, the generated voltage is expressed as

$$E_a = K_a \dot{\theta} \tag{4.6}$$

and the torque produced is

$$T_L = \frac{E_a I_a}{\dot{\theta}} = K_a I_a \tag{4.7}$$

where K_a is the torque constant and is proportional to n and B_g

n is the number of conductors in series between the brushes

B_g is the airgap flux density.

Referring to equation (4.7), the torque of the d.c.

machine T_L is directly proportional to the armature current I_a. Hence with a d.c. current source supplying the armature circuit, the torque of the d.c. machine can be controlled by varying the current I_a and is independent of speed.

With the armature winding open-circuit (I_a = 0) and the d.c. machine driven at synchronous speed $\dot{\theta}$ (=ω/p) by the test motor, the generated emf E_a was measured at different supply frequency f (= $\omega/2\pi$) of the test motor. Fig.4.7 shows the variation of E_a with f. From the results, the torque constant is calculated as

$$K_a = \frac{E_a}{\dot{\theta}} = p\,\frac{E_a}{\omega} = \frac{p}{2\pi}\;\frac{E_a}{f} = 280 \times 10^{-4}\ \text{Nm/A} \qquad (4.8)$$

which is in close agreement with the value specified by the manufacturer.

4.3.1 The d.c. current source for the d.c. machine

Using the same current feedback arrangement described in section 4.2, the circuit design used for the d.c. current source is as shown in Fig.4.8. The power op-amp used is the LM379S[16] having a voltage and current rating of 14V peak and 1A peak. The current I_a is controlled by the potentiometer R which is supplied by a constant voltage v_z. The resistor network R_2 and R_3 is used for adjusting the output offset-voltage since no such facility is provided within the op-amp. In the diagram, S is a 2 pole- 2 way centre off switch for selecting the mode of operation, i.e. motoring, off or generating.

4.4 Measurement Of Inertia J

The inertia of the permanent magnet rotor is measured

using a bifilar suspension technique[17]. The rotor is suspended by two thin threads fastened to its circumference and rotated by an angle θ. Assuming system damping is negligible, the motion equation of the system is given as

$$J \frac{d^2\theta}{dt^2} + Mg\,x \sin\left(\frac{x}{\ell}\,\theta\right) = 0 \qquad (4.9)$$

where J is the inertia

M is the mass

x is the radius of the rotor

ℓ is the length of the thread

g is the gravitational constant ($9.81 ms^{-2}$)

For a small angular rotation $\sin(x\theta/\ell) \rightarrow (x\theta/\ell)$ and equation (4.9) is now rewritten as

$$J \frac{d^2\theta}{dt^2} + Mg \frac{x^2}{\ell}\,\theta = 0 \qquad (4.10)$$

Equation (4.10) describes a typical simple harmonic motion equation with a period of

$$T = 2\pi \sqrt{\frac{J\ell}{Mgx^2}} \qquad (4.11)$$

By rearranging equation (4.11), the inertia is given as

$$J = \frac{Mg}{\ell} \left(\frac{Tx}{2\pi}\right)^2 \qquad (4.12)$$

With the rotor suspended by two 150mm threads and twisted to oscillate, the period T was timed with a 0.2 second resolution stop watch over 50 cycles. The experiment was repeated for different thread lengths and cycles. Using equation (4.12), the average 'measured' inertia of the rotor plus its steel shaft

is given as 10.5×10^{-7} kgm^2.

Using the above experimental technique, the inertia of the rotor, steel shaft and a HUCO coupling was measured as 10.65×10^{-7} kgm^2 and hence the inertia of the HUCO coupling is estimated as 0.15×10^{-7} kgm^2. The same technique was used to determine the inertia of the brass disc which was used to reduce oscillations such that $C \rightarrow 0$.

Since the rotor of the reference generator was small, it was assumed that its inertia was negligible compared to that of the test motor. Table 4.2 gives the inertia of each component on the test rig.

TABLE 4.2

Component	Inertia $\times 10^{-7}$ kgm^2
Test motor	10.5
D.C. motor	4.7
HUCO coupling	0.15
Brass disc	190
Reference generator	negligible

4.5 Measurement of Instantaneous Rotor Speed $\dot{\theta}$

A Laser Doppler Velocimeter[18] was used for measuring the instantaneous speed of the rotor $\dot{\theta}$. Since the instrument uses a laser beam to track the rotor movement, this method of measuring speed does not increase the inertia of the system. The instrument consists of a laser, a signal processing filter, a compatible frequency counter and an integral power supply.

The rotor speed signal is obtained from the 'Frequency Analogue Output' socket of the instrument. Some typical rotor speed signals measured with the instrument are shown in Fig.2.7. The speed signal obtained with the instrument is expressed as

$$v_{\dot{\theta}} = G_{\ell}\,\dot{\theta} \qquad (4.13)$$

where G_{ℓ} is the gain of the instrument.

With stator coils of the test motor open-circuited and the d.c. motor driving the test motor at a constant speed $\dot{\theta}$(=2πf/p, where f is the frequency of the induced emf in the stator coil), tests were undertaken to measure the variations of $v_{\dot{\theta}}$ with f. Fig.4.10 shows the plot of $v_{\dot{\theta}}$ against f (= $p\dot{\theta}/2\pi$). From the figure it can be seen that $v_{\dot{\theta}}$ varies linearly with f and hence verifying that G_{ℓ} is a constant.

The speed of the rotor can also be measured with a tacho-generator. However this method of measuring speed was not used in the investigation because it would increase the inertia of the system. To check that the laser can measure rotor oscillations accurately, tests were undertaken to compare the oscillatory speed signals measured with the laser and with the O.C. output voltage of the d.c. machine operating as a tacho-generator. Fig.4.11 compares the rotor speed oscillations measured with the laser and the d.c. machine. The signals which contain high noise levels were those measured with the laser instrument. In Fig.4.11(a) it can be seen that the agreement between the measured speed signals is good. However if the direction of rotation is reversed, the oscillograms given in

Fig.4.11(b) show that the oscillatory speed signal from the laser is 180^{o} out of phase with that of the d.c. machine. Although facility on the laser exists which eliminates this ambiguity unfortunately this was not appreciated at the time. The correct phase of the oscillations was therefore ascertained by comparison of the results for both values of β, as described in section 3.7.1.

4.6 Measurement Of The Amplitude Of The Rotor Oscillation C

From equation (4.13), the speed signal from the laser instrument is given as

$$v_{\dot{\theta}} = G_{\ell}\left[\frac{\omega}{p} - \frac{2\omega C}{p}\sin(2\omega t+\beta)\right] \qquad (4.14)$$

$$= v_{\dot{\theta}d.c.} - v_{\dot{\theta}a.c.} \qquad (4.15)$$

where the d.c. voltage $v_{\dot{\theta}d.c.} = G_{\ell}\frac{\omega}{p}$ (4.16)

and the a.c. voltage $v_{\dot{\theta}a.c.} = G_{\ell}\frac{2\omega}{p}C$ (4.17)

Since the speed signal from the laser instrument contained noise, as seen in Fig.4.11, and to minimise instrumentation error due to noise, the r.m.s. value of $v_{\dot{\theta}a.c.}$ was measured with a Wave Analyser, the Marconi TF2330, which has a bandwidth of 7Hz. The magnitude of $v_{\dot{\theta}d.c.}$ was measured after filtering out the a.c. component of the speed signal using an a.c. filter circuit shown in Fig.4.12. Using equations (4.16) and (4.17), it can be shown that the amplitude of rotor oscillations is given as

$$C = \frac{v_{\dot{\theta}a.c.}}{v_{\dot{\theta}d.c.}}\frac{1}{\sqrt{2}} \qquad (4.18)$$

4.7 Measurement Of The Phase Of The Rotor Oscillation β

4.7.1 Synthesizing a reference signal having a frequency of 2ω

From equation (4.14), the phase of the rotor oscillation β can be measured w.r.t. a reference signal having an angular frequency of 2ω. Hence this necessitates a reference signal of frequency 2ω to be synthesized from the reference signal of I cos(ωt) as defined in section 2.1.1. By wiring the analogue multiplier circuit[20] shown in Fig.4.13 as a squaring circuit, a signal of 2ω can be synthesized from an input signal of ω. For a given input signal of $v_R \cos(\omega t)$, the voltage across the feedback resistor R of the a.c. current source, the output voltage of the squaring circuit is given as

$$v_o = \frac{XY}{10} = \frac{v_R^2 \cos^2(\omega t)}{10} = \frac{v_R^2}{20}\left[1 + \cos(2\omega t)\right] \qquad (4.19)$$

The oscillogram in Fig.4.14 shows the input signal ($v_R \cos(\omega t)$) and the a.c. output signal from the squaring circuit ($v_R^2/20 \cos(2\omega t)$). The synthesized output signal of the squaring circuit is referred to as the reference signal for the measurement of β.

4.7.2 Technique used for measuring β

Because the speed signal from the laser output contains a high noise level, the phase of rotor oscillation β cannot be measured with great accuracy using conventional phase measuring equipment because the Schmitt trigger circuits used in the equipment are sensitive to noise. Integrators having π/2 phase shifts were tried as a first attempt to reduce the noise level in the speed signal. But they were not successful because the

low frequency speed signal due to the concentric movement in the rotor shaft was amplified and it modulated the speed signal. Third order low pass filters having Butterworth characteristics[19] were also tried, but this method was rejected because the phase shift is a function of frequency. Hence a phase measurement technique using an analogue multiplier was developed. Assuming the a.c. speed signal can be expressed as

$$v_{\dot{\theta}a.c.} = v_2\cos(2\omega t+\beta) + \sum_{n\neq 2} v_n\cos(n\omega t+\beta_n) \qquad (4.20)$$

and the reference signal is

$$v_r = v\cos(2\omega t) \qquad (4.21)$$

By multiplying $v_{\dot{\theta}a.c.}$ and v_r via an analogue multiplier (Fig.4.13) and filtering the a.c. component via an a.c. filter (Fig.4.12), the d.c. output voltage from the a.c. filter is given as

$$v_f = G_{a.c.}\frac{v_2 v}{20}\cos(\beta) \qquad (4.22)$$

where $G_{a.c.}$ is the d.c. gain of the a.c. filter.

The analysis above shows that the method of measuring β is independent of noise and harmonics. However it must be emphasised that this technique of measuring β has high error as $|\cos(\beta)| \to 1$. This is due to the lack of sensitivity in the cosine function as $\beta \to 0$ or 180^{o}. To overcome this lack of sensitivity near this region the reference signal is integrated such that

$$v_r = G_i v \sin(\omega t) \qquad (4.23)$$

and the d.c. component after multiplying v_r with $v_{\dot{\theta}a.c.}$ is then

given as

$$v_f = -G_i G_{a.c.} \frac{V_2 V}{20} \sin(\beta) \qquad (4.24)$$

where G_i is the gain of the integrator.

For higher measurement accuracy of β it was decided that the integrator should be used only when $|\cos(\beta)| > 0.7071$.

Using the experimental arrangement in Fig.4.15, test results have shown that this technique of measuring β is independent of any added distortion or noise, and β can be measured within $\pm 3^{o}$ over the range 0 to 360^{o}. Fig.4.16 shows some of the distorted waveforms used to verify that the phase measuring technique is insensitive to unwanted signals.

Test results given in section 4.5 have shown that the laser instrument cannot sense the direction of rotation, and therefore there are two alternative values of $v_{\theta a.c.}$ such that

$$v_{\theta a.c.} = m v_2 \cos(2\omega t + \beta) \qquad (4.25)$$

where $m = \pm 1$.

By substituting m into equations (4.22) and (4.24), the phase of rotor oscillation is given as

$$\beta = \cos^{-1}\left[\frac{20\, v_f}{m G_{a.c.} V_2 V}\right] = \sin^{-1}\left[\frac{-20\, v_f}{m G_i G_{a.c.} V_2 V}\right] \qquad (4.26)$$

For $m = 1$ in equation (4.26), the angle of β can be determined since the polarities of $\cos(\beta)$ and $\sin(\beta)$ define the quadrant in which β operates, and similarly for the case of $m = -1$. This gives rise to two alternative values of β i.e.

$$\beta_1 = \beta \quad \text{for } m = 1 \tag{4.27}$$

and

$$\beta_2 = \beta - 180^{o} \text{ for } m = -1 \tag{4.28}$$

4.8. Measurement Of Coil Constants k and k_g

By using the experimental rig, described in section 4.1, in which the test motor is driven at a constant speed $\dot{\theta}(=\omega/p)$ by a d.c. motor, the open-circuit induced emf of the stator has been measured. From equation (2.7) the emf equation is

$$E = \frac{d\psi}{dt} = \frac{k}{p}\omega\cos(\omega t) \tag{4.29}$$

and k can be determined from the measurement of E and ω. By integrating E with a calibrated integrator, having unity gain at 15Hz, the peak output voltage of the integrator is given as

$$v_o = G_i \frac{k}{p} \tag{4.30}$$

from which $$k = p\frac{v_o}{G_i} = \frac{12v_o}{2\pi 15} \tag{4.31}$$

where G_i is the gain of the integrator which equals $2\pi 15$.

Tests have shown that k is independent of frequency up to the maximum test frequency of 200Hz. Results show that the value of k is 218×10^{-3}Nm/A.

The test was repeated for the reference generator and the result showed that k_g is 10.3×10^{-3}Nm/A.

4.9 Measurement Of Load Angle λ

With the reference generator and test motor driven at a constant speed $\dot{\theta}(=\omega/p)$ by the D.C. motor, the stator of the reference generator was aligned with that of the test motor,

such that the O.C. emfs of the reference generator and test motcr were in phase. Alignment was checked using the phase measurement technique described in section 4.7.2. From section 3.3, the flux linkage of the reference generator is given as

$$\psi_g = K_g I_{mg} \cos(p\theta - \textcircled{H}) = \frac{k_g}{p} \cos(p\theta - \textcircled{H}) \qquad (4.32)$$

where k_g is the coil constant and was measured as 10.3×10^{-3} Nm/A using the technique described in section 4.8.

Substituting $p\theta$ from equation (3.30) into equation (4.32) gives

$$\psi_g = \frac{k_g}{p} \cos(\omega t + \lambda - \frac{\pi}{2} + C \cos(2\omega t + \beta)) \qquad (4.33)$$

Neglecting the harmonic content of $d\psi_g/dt$, the O.C. emf of the reference generator is

$$E_g = \frac{d\psi_g}{dt} = \frac{k_g \omega}{p} [J_o(C)\cos(\omega t + \lambda) - J_1(C)\sin(\omega t + \beta - \lambda)] \qquad (4.34)$$

Using the circuit arrangement shown in Fig.4.17, the output voltage of the a.c. filter is given as

$$V_f = \frac{G_{a.c.}(A_1 V_R)}{20} A_2 \frac{k_g}{p} \omega [J_o(C)\cos(\lambda) - J_1(C)\sin(\beta - \lambda)] \qquad (4.35)$$

In equation (4.35) the only unknown is the load angle λ and it is determined using an iterative method known as Newton-Raphson[21].

4.10 Measurement of K, I_m and Ⓗ Of Test Motor

Using the test results of section 4.8, the flux linkage of the main coil C produced by the magnet is given as

$$\psi_C = \frac{k}{p} = \frac{218 \times 10^{-3}}{12} = 18.2 \text{ mWb}$$

With a search coil wound on the stator concentric with the stator coil C and assuming no leakage, the flux linkage of the search coil is given as

$$\psi_{SC} = \frac{N_{SC}}{N_C} \psi_C \qquad (4.36)$$

where N_{SC}, N_C are the number of turns in the search coil and coil C respectively.

The flux linkage ψ_{SC} was measured by integrating the emf of the search coil. Measurements of ψ_{SC} were made with the rotor driven at constant speed and stator coil C open-circuited, and then repeated with the rotor stationary but with coil C excited to give the same magnitude and frequency of ψ_{SC}, then for these conditions

$$\psi_{SC} = \frac{N_{SC}}{N_C} K I_m \underline{/-\text{Ⓗ}} \qquad (4.37)$$

and from equation (4.36) therefore

$$K = \psi_C / I_m \qquad (4.38)$$

where I_m is the equivalent current in coil C required to produce flux linkage ψ_{SC}

Ⓗ is the angle which ψ_{SC} lags I_m

Using the experimental arrangement shown in Fig.4.18, the values of I_m and Ⓗ are measured at various test frequencies and the results together with the corresponding calculated values of K are given in Table 4.3.

The tests were repeated on the second stator coil in the motor and the results showed that the average values of K, I_m and Ⓗ were identical.

TABLE 4.3

Measured values of K, I_m and Ⓗ

Frequency f(Hz)	Equivalent current I(mA)	K value (H)	Ⓗ value (degrees)
30	17.7	1.028	10.3
40	17.7	1.028	10.4
50	17.8	1.022	10.5
60	17.8	1.022	10.6
70	17.9	1.017	10.8
80	17.9	1.017	11.0
Average value	17.8	1.02	10.6

4.11 Measurement Of The Electrical Shift Between The Two stator coils α^o

With both the stator coils in the test motor open-circuit and the rotor driven at a constant speed by the D.C. motor, the flux linkage of a stator coil produced by the magnet is given as

$$\psi = KI_m \cos(\omega t - Ⓗ) \qquad (4.39)$$

while that in the second stator is

$$\psi = KI_m \cos(\omega t - Ⓗ + \alpha) \qquad (4.40)$$

By using the phase measurement technique described in section 4.7.2, the phase shift between the flux linkages in the two stator coils was measured. The results showed that the angle α was measured as $85^{o} \pm 3^{o}$ over the test frequency range of 30 to 100Hz.

CHAPTER 5

CONCLUSIONS

Initially a linear mathematical model was used to predict the performance of the test motor. Under the non-oscillatory condition, test results showed that the peak torque obtainable from the test motor was predicted with reasonable accuracy when the drag torque due to friction and iron-losses was simply included as a lumped additional torque component. The model was then extended to cover the oscillatory behaviour of the motor. Experimental observations confirmed that the predicted oscillation frequency was twice the supply frequency. For this oscillation mode, the accuracy of the model was investigated by comparing the predicted average and oscillatory torques with known values of applied load torques. Results showed that the model did not accurately predict the torque values. The cause of the in-accuracy was thought to be the effects of hysteresis in the magnetic material of the stator since drag torque experiments showed that hysteresis iron-losses were significant. Analogue simulation studies by Bassyouni[6] had previously shown that, for the non-oscillatory case, a more accurate model for the motor could be achieved if the hysteresis effects were included in the form of a hysteresis loop in the simulation.

By representing the permanent magnet as an equivalent mmf source and characterising the effect of hysteresis as a phase lag between the flux linkages and the corresponding mmf,

a model based on the d-q axis theory was developed. Analysis has shown that the effect of hysteresis does introduce a drag torque but additionally it modifies the load angle in the torque expressions. The new model including hysteresis gave good agreement between predicted and known values of both the average and oscillatory torques. Following the completion of this work subsequent studies in the Department based on the model developed here have successfully analysed the full dynamic behaviour of these motors over a wide range of oscillation modes.

The small size of these motors has necessitated the development of novel experimental procedures. Constant current source systems have been designed and a number of important instrumentation techniques have been devised.

REFERENCES

1. FITZGERALD, A.E.: "Electrical machinery", McGraw-Hill Ltd., Kingsley, C.Jr. and Kusko, A., third edition, p.524-530.

2. GERBER, H.: "Miniature synchronous motors with permanent magnet rotor", Neue. Tech., Switzerland, Vol.15, Oct. 1973, p.382-392.

3. SCHEMMANN, H.: "Stability of small single-phase synchronous motors", Philips Tech. Rev. 33, 1973, No.8/9, p.235-243.

4. VEIONOTT, C.G.: "Fractional and subfractional horsepower electric motors", McGraw-Hill Ltd., 1970.

5. McLACHLAN, N.W.: "Bessel functions for engineers", Oxford University Press, 1934.

6. EL-BASSYOUNI, K.M.E.: "Torque and speed-emf characteristics of miniature synchronous motors", Ph.D. thesis, 1976, University of Sheffield.

7. BROWN, R. and BIRCH, T.S.: "Investigations carried out at the University of Sheffield, (unpublished notes).

8. O'KELLY, D. and SIMMONS, S.: "Instroduction to generalized conversion", p.40-67.

9. WHITE, D.C. and WOODSON, H.H.: "Electromagnetic energy conversion", p.12-24.

10. TAN, G.H.: Part 1 of Ph.D. thesis, Section 2.2.

11. TAN, G.H.: Part 1 of Ph.D. thesis, Section 4.5.

12. EDWARDS, J.D.: "Electrical machines", Int. Text Book Co. Ltd., 1973.

13. HINDMARSH, J.: "Electrical machines and their applications", Pergamon Press, 1970.

14. Handbook of the Savage Mk.II star kilowatt amplifier, Brian W. Savage.

15. MILLMAN, J. and HALKIAS, C.C.: "Integrated electronics: analogue and digital circuits and systems", McGraw-Hill 1972.

16. N.S. ELECTRONICS: Data leaflet for LM379S dual channel 6W op-amp, Jan. 1976.

17. SPIEGEL, M.R.: "Theoretical mechanics"

18. Handbook of the Laser Doppler Velocimeter, Cambridge Consultant Ltd.

19. CLAYTON, G.B.: "Linear intergrated circuit applications", Unwin Bros. Ltd., 1977.

20. INTERSIL 8013: Technical leaflets on four quadrant analogue multiplier, Dec. 1971, June 1972.

21. STEPHENSON, G.: "Mathematical methods for science students", Longman Group Ltd.

APPENDIX A

BESSEL FUNCTIONS OF FIRST ORDER

Using the Bessel functions the following terms are expressed as,

$$\cos(C\ \sin\theta) = J_o(C) + 2\sum_{p=1}^{\infty} J_{2p}(C)\cos(2p\theta) \qquad (A.1)$$

$$\sin(C\ \sin\theta) = 2\sum_{p=1}^{\infty} J_{2p-1}(C)\sin(2p-1)\theta \qquad (A.2)$$

$$\cos(C\ \cos\theta) = J_o(C) + 2\sum_{p=1}^{\infty} J_{2p}(C)\,(-1)^p\cos(2p\theta) \qquad (A.3)$$

$$\sin(C\ \cos\theta) = -2\sum_{p=1}^{\infty} J_{2p-1}(C)\,(-1)^p\cos(2p-1)\theta \qquad (A.4)$$

where

$$J_n(C) = \sum_{r=0}^{\infty} \frac{(-1)^r \left(\frac{C}{2}\right)^{n+2r}}{r!\,(n+r)!} \qquad (A.5)$$

For small C values and neglecting higher order terms,

$$J_o(C) = 1 - \frac{\left(\frac{C}{2}\right)^2}{(1!)^2} + \frac{\left(\frac{C}{2}\right)^4}{(2!)^2} - \frac{\left(\frac{C}{2}\right)^6}{(3!)^2} \qquad (A.6)$$

$$J_1(C) = \frac{C}{2} - \frac{\left(\frac{C}{2}\right)^3}{1!2!} + \frac{\left(\frac{C}{2}\right)^5}{2!3!} - \frac{\left(\frac{C}{2}\right)^7}{3!4!} \qquad (A.7)$$

$$J_2(C) = \frac{\left(\frac{C}{2}\right)^2}{0!2!} - \frac{\left(\frac{C}{2}\right)^4}{1!3!} + \frac{\left(\frac{C}{2}\right)^6}{2!4!} - \frac{\left(\frac{C}{2}\right)^8}{3!5!} \qquad (A.8)$$

Fig.A.1 shows the variations of $J_o(C)$, $J_1(C)$ and $J_2(C)$ with C.

Similarly for terms relating to 2C are

$$J_o(2C) = 1 - \frac{C^2}{(1!)^2} + \frac{C^4}{(2!)^2} - \frac{C^6}{(3!)^2}$$

$$J_1(2C) = C - \frac{C^3}{1!2!} + \frac{C^5}{2!3!} - \frac{C^7}{3!4!} \qquad \text{(A.10)}$$

$$J_2(2C) = \frac{C^2}{0!2!} - \frac{C^4}{1!3!} + \frac{C^6}{2!4!} - \frac{C^8}{3!5!} \qquad \text{(A.11)}$$

(a) Proving

$$J_1(2C)\ \frac{(J_o(C)+J_2(C))}{(J_o(2C)+J_2(2C))} = 2J_1(C)$$

$$J_o(C)+J_2(C) = \sum_{r=0}^{\infty} \frac{(-1)^r (\frac{C}{2})^{2r}}{(r!)^2} + \sum_{r=0}^{\infty} \frac{(-1)^r (\frac{C}{2})^{2+2r}}{r!(2+r)!}$$

$$= 1 + \sum_{r=1}^{\infty} \frac{(-1)^r (\frac{C}{2})^{2r}}{(r!)^2} - \sum_{r=1}^{\infty} \frac{(-1)^r (\frac{C}{2})^{2+2(r-1)}}{(r-1)!(r+1)!}$$

$$= 1 + \sum_{r=1}^{\infty} (-1)^r (\frac{C}{2})^{2r} \left[\frac{1}{(r!)^2} - \frac{1}{(r-1)!(r+1)!}\right]$$

$$= 1 + \sum_{r=1}^{\infty} (-1)^r (\frac{C}{2})^{2r} \left[\frac{1}{(r!)^2} - \frac{1}{(\frac{r!}{r})(r+1)r!}\right]$$

$$= 1 + \sum_{r=1}^{\infty} \frac{(-1)^r (\frac{C}{2})^{2r}}{(r!)^2} \left[\frac{1}{r+1}\right]$$

$$= 1 + \sum_{r=1}^{\infty} \frac{(-1)^r (\frac{C}{2})^{2r}}{r!(r+1)!}$$

$$= 1 + \frac{1}{(\frac{C}{2})} \sum_{r=1}^{\infty} \frac{(-1)^r (\frac{C}{2})^{2r+1}}{r!(r+1)!}$$

$$= \frac{2}{C} \sum_{r=0}^{\infty} \frac{(-1)^r (\frac{C}{2})^{2r+1}}{r!(r+1)!} = \frac{2}{C} J_1(C) \qquad \text{(A.12)}$$

Similarly,

$$J_o(2C)+J_2(2C) = 1 + \sum_{r=1}^{\infty} \frac{(-1)^r (C)^{2r}}{r!(r+1)!}$$

$$= \frac{1}{C} J_1(2C) \qquad \text{(A.13)}$$

$$\therefore \quad \frac{J_o(C)+J_2(C)}{J_o(2C)+J_2(2C)} = \frac{2J_1(C)}{J_1(2C)}$$

$$\therefore \quad J_1(2C)\frac{(J_o(C)+J_2(C))}{(J_o(2C)+J_2(2C))} = 2J_1(C) \quad \text{QED} \qquad \text{(A.14)}$$

APPENDIX B

INVESTIGATION ON THE HARMONIC CONTENT OF THE FLUX LINKAGE ψ AND ITS EFFECT ON THE TORQUE EXPRESSION

With the stator winding open-circuited and the rotor driven by a d.c. motor at a constant speed (w/p), the harmonic content of the magnet flux linkage ψ was measured by analysing the integrated O.C. output voltage with a wave analyser. The results normalised to the fundamental are shown in Table B.1

Table B.1 Spectrum analysis of ψ

f = 30 to 100Hz	
Fundamental	100%
Harmonic:	
3rd	2%
5th	1.5%
7th	0.3%
>9th	0.2%

By including the harmonic terms of ψ, ψ can be represented as

$$\psi = \psi_t = \psi_1 \sin(p\theta) + \psi_3 \sin(3p\theta + \Omega_3) + \ldots + \psi_n \sin(np\theta + \Omega_n) \qquad (B.1)$$

where $\psi_n = k_n/p$

Ω_n is the phase of harmonic

n is the harmonic number

From equation (2.14), the electromagnetic torque is

$$T_e = i\frac{d\psi}{d\theta} \qquad (B.2)$$

the power is then

$$P_e = i\frac{d\psi}{d\theta}\frac{d\theta}{dt} = i\frac{d\psi}{dt} \qquad (B.3)$$

Assuming the current i is distorted also, the total average power including the harmonic power terms is then

$$\sum_{n=1}^{\infty} P_{en} = \sum_{n=1}^{\infty} \frac{nk_n i_n}{2} \cos(\varepsilon_n) \qquad (B.4)$$

where ε_n is the phase shift between k_n and i_n.

However, since the measured distortion of the current i is less than 0.2% for all harmonics and assuming the worst case when k_n and i_n are in phase, the total harmonic power

$$\sum_{n>1}^{\infty} \frac{nk_n i_n}{2} \qquad (B.5)$$

is small and negligible when compared to the fundamental component. The approximation that the harmonic content of P_e can be neglected still holds even if the harmonic distortion of ψ is increased due to saturation in the magnetic circuit. However if the harmonics of ψ increase, the eddy current losses in the stator magnetic circuit, due to induced emf, will also increase.

Fig 1-1
Fig 1-2

1-1 Exploded View Of Motor

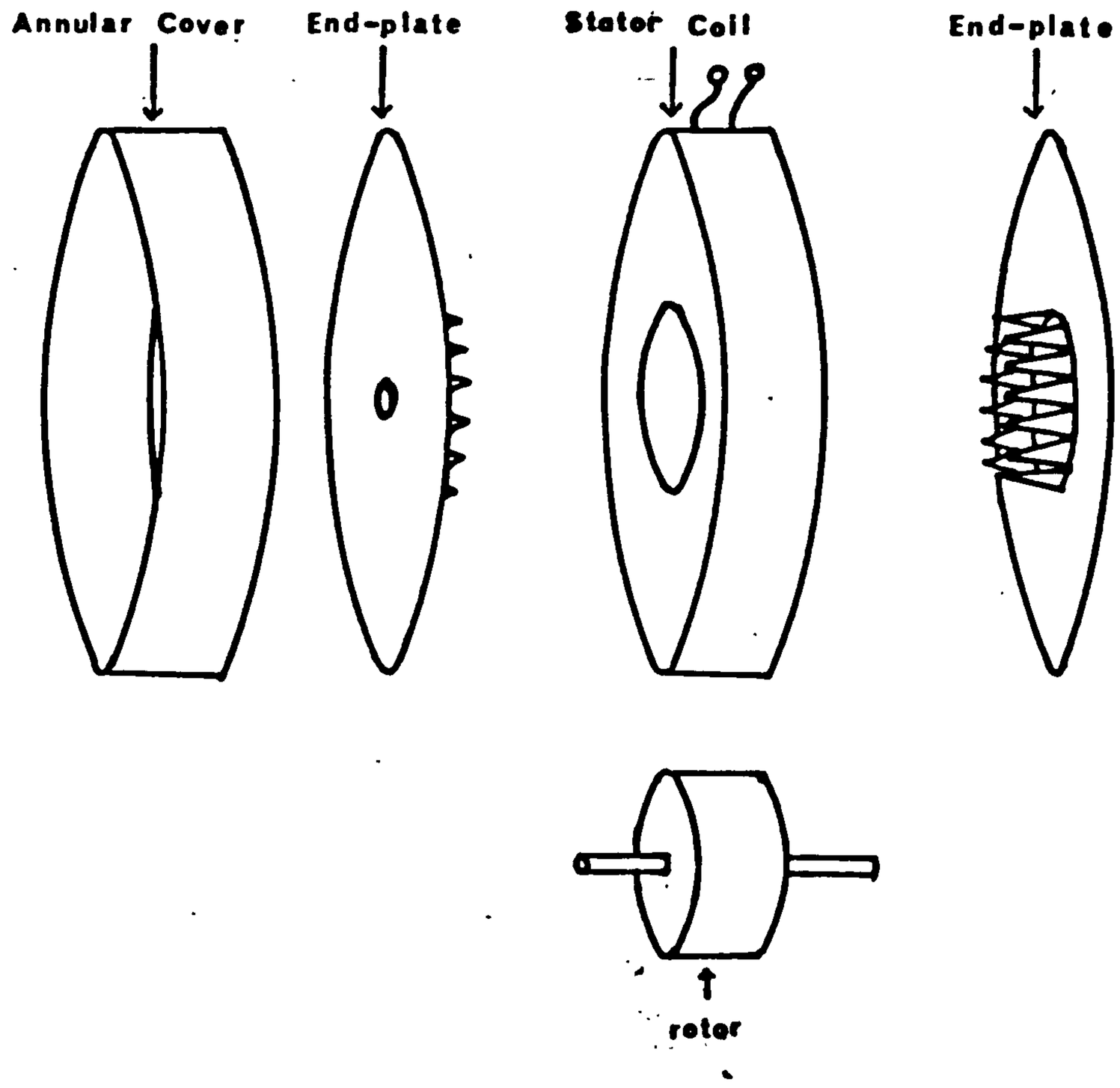

1-2 Circuit Connection Of Capacitor Motor

(a) In parallel

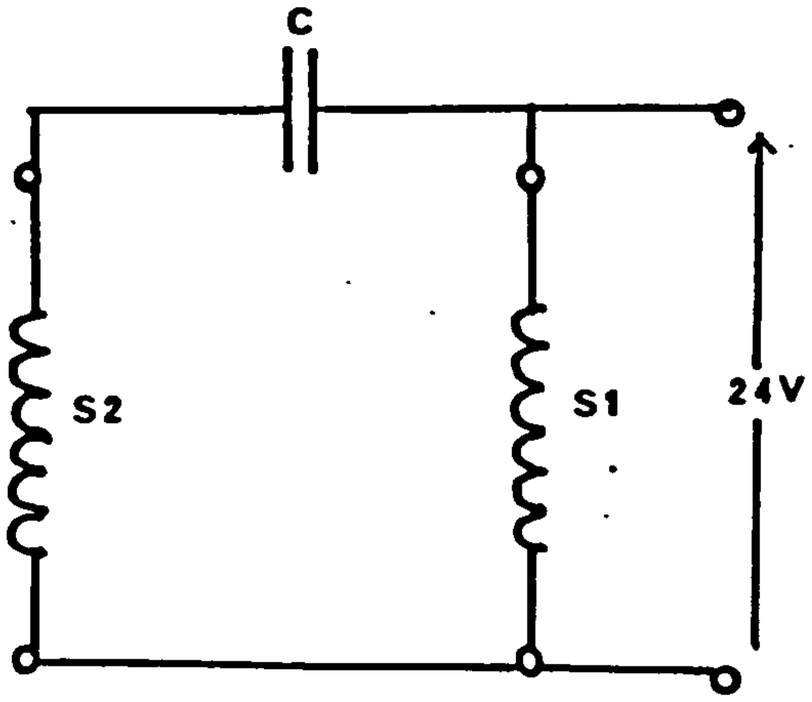

(b) In series

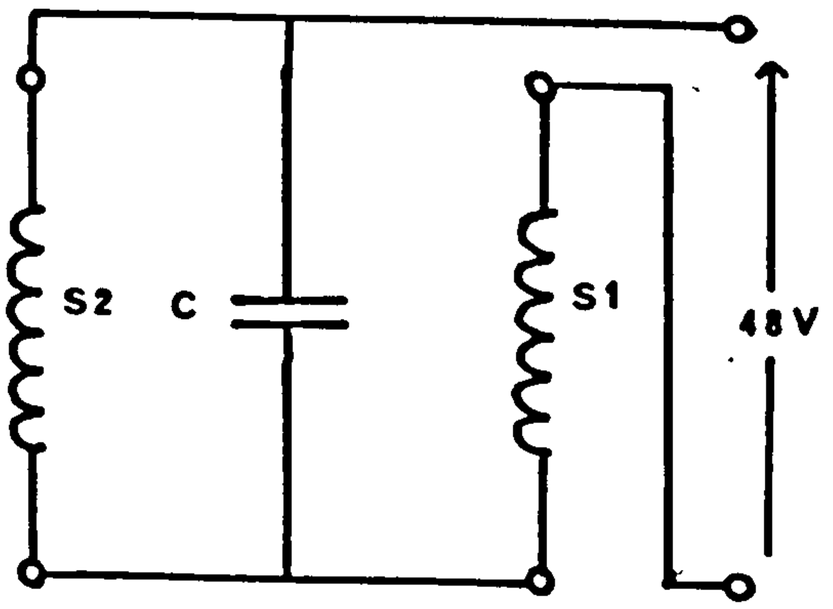

Fig 1·3

Test Motor

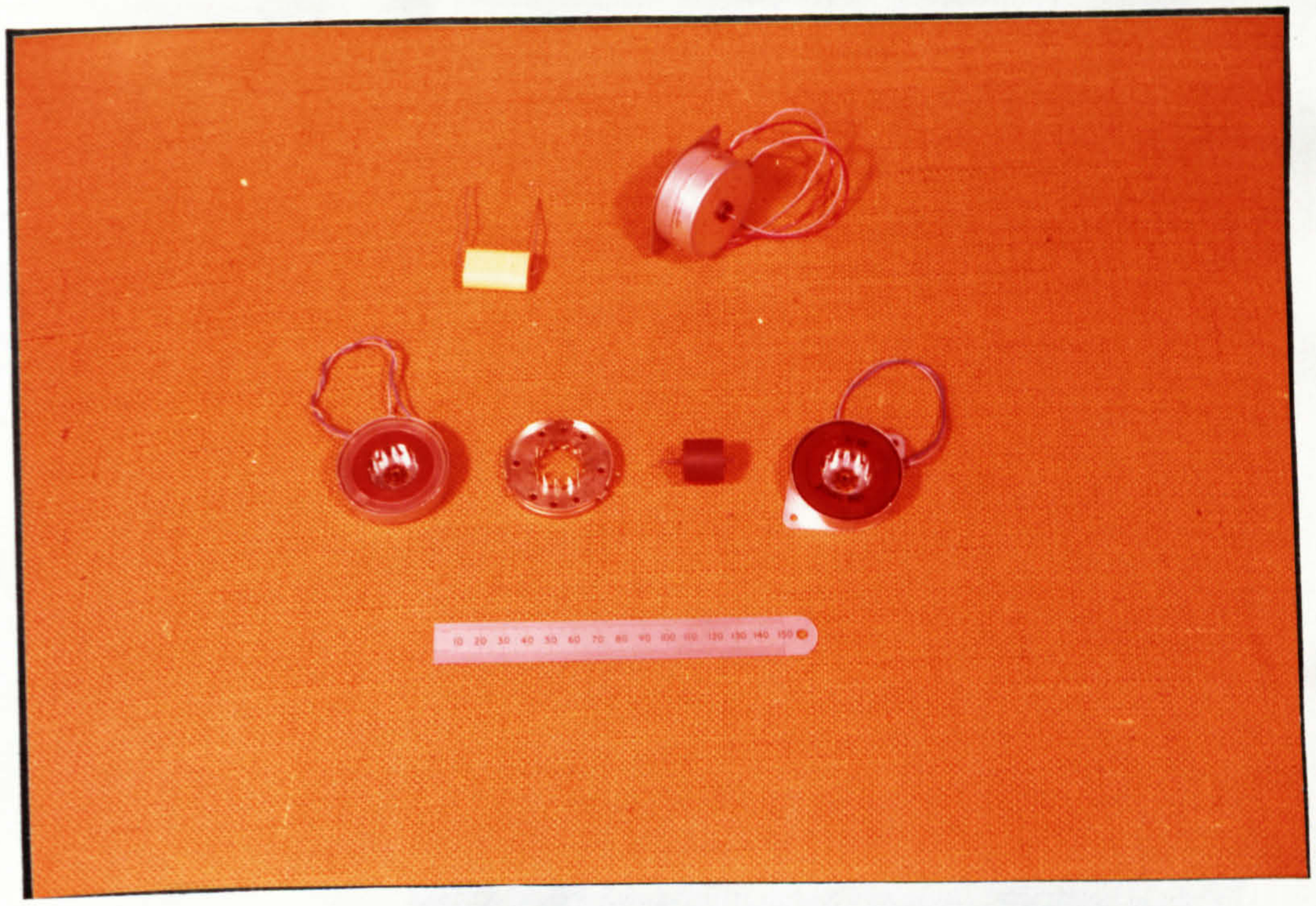

Fig 2·1
Fig 2·2

2·1 Equivalent Circuit Model

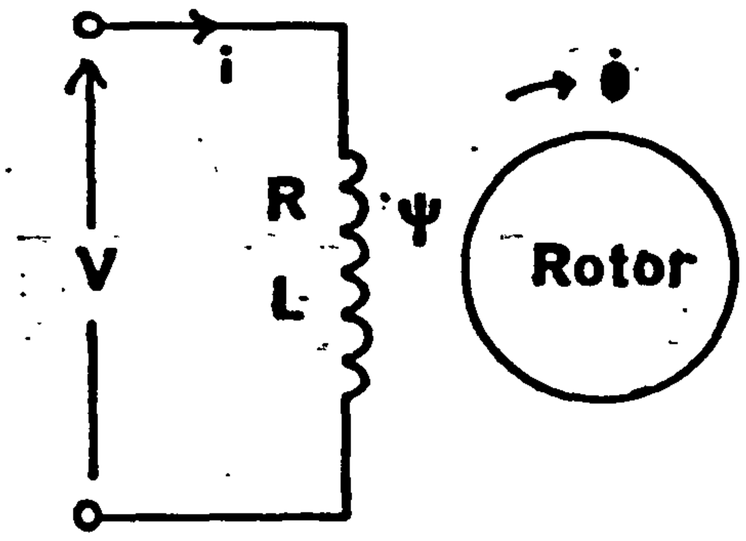

2·2 Current Waveforms at f= 30 Hz

(a) Voltage Fed Motor

Input Voltage

Current

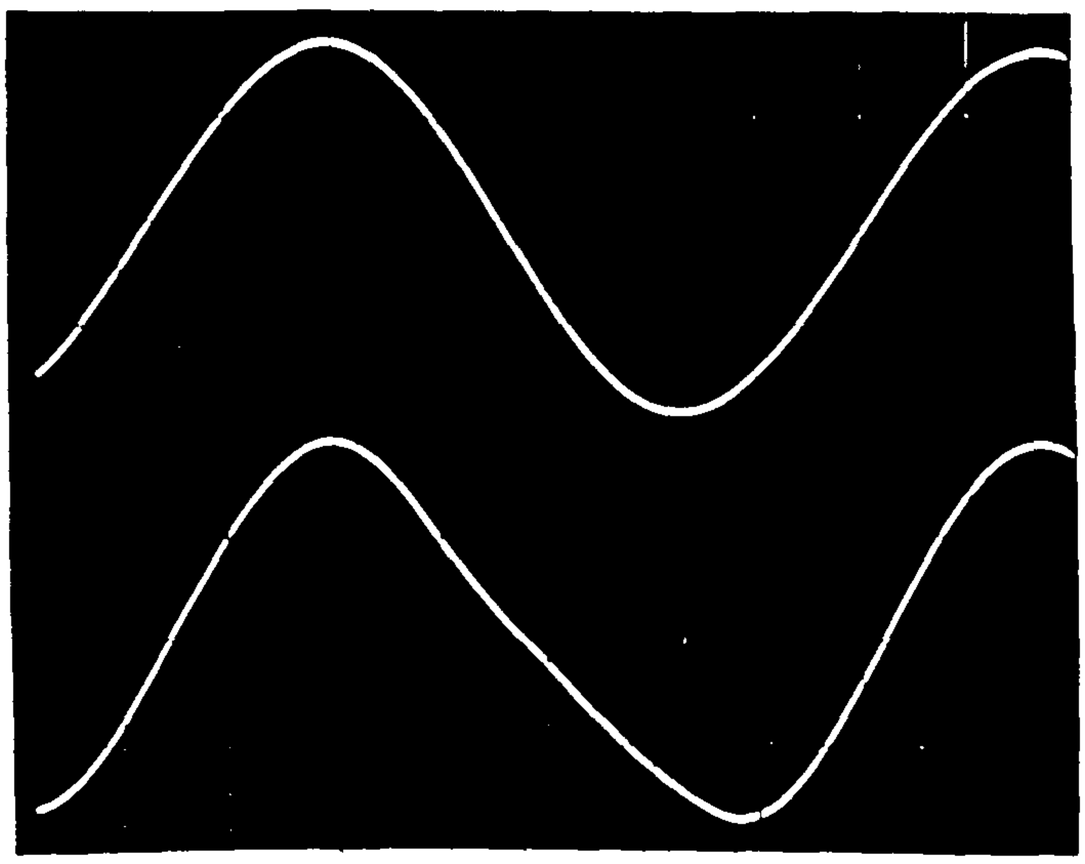

(b) Current Fed Motor

Input Voltage

Current

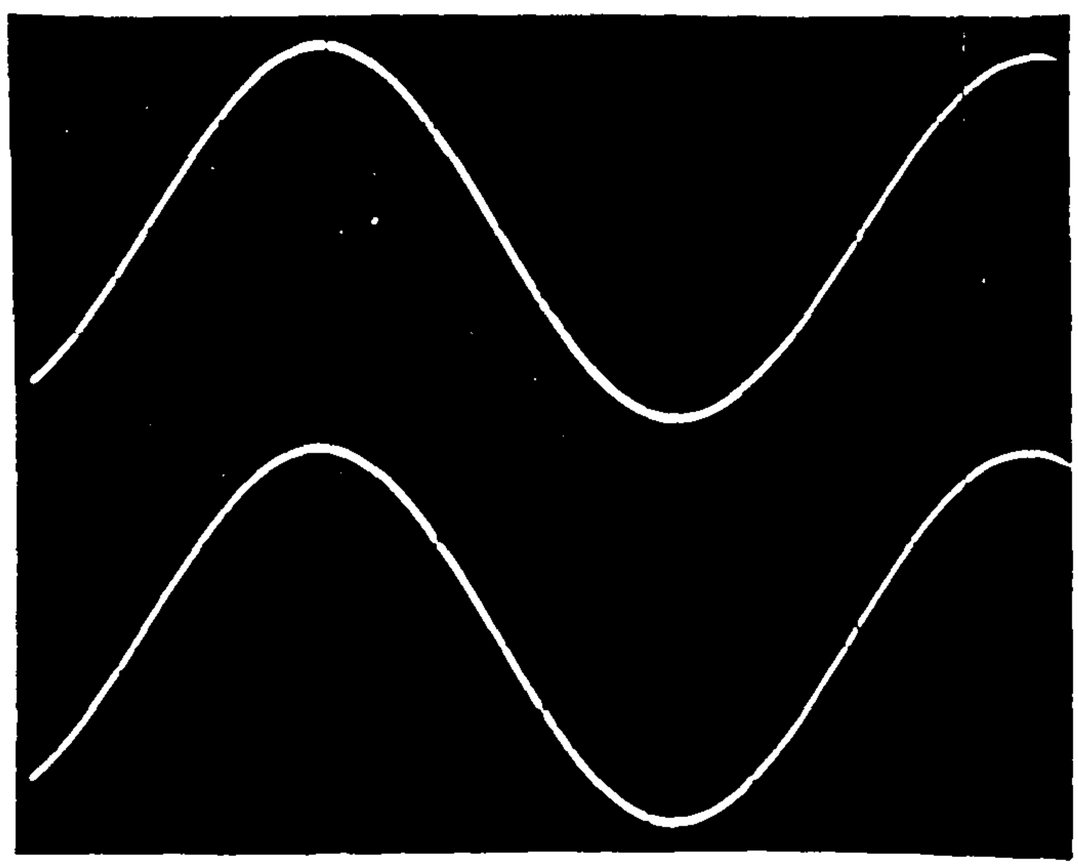

Fig 2·3
Fig 2·4

2·3 Phasor Diagram

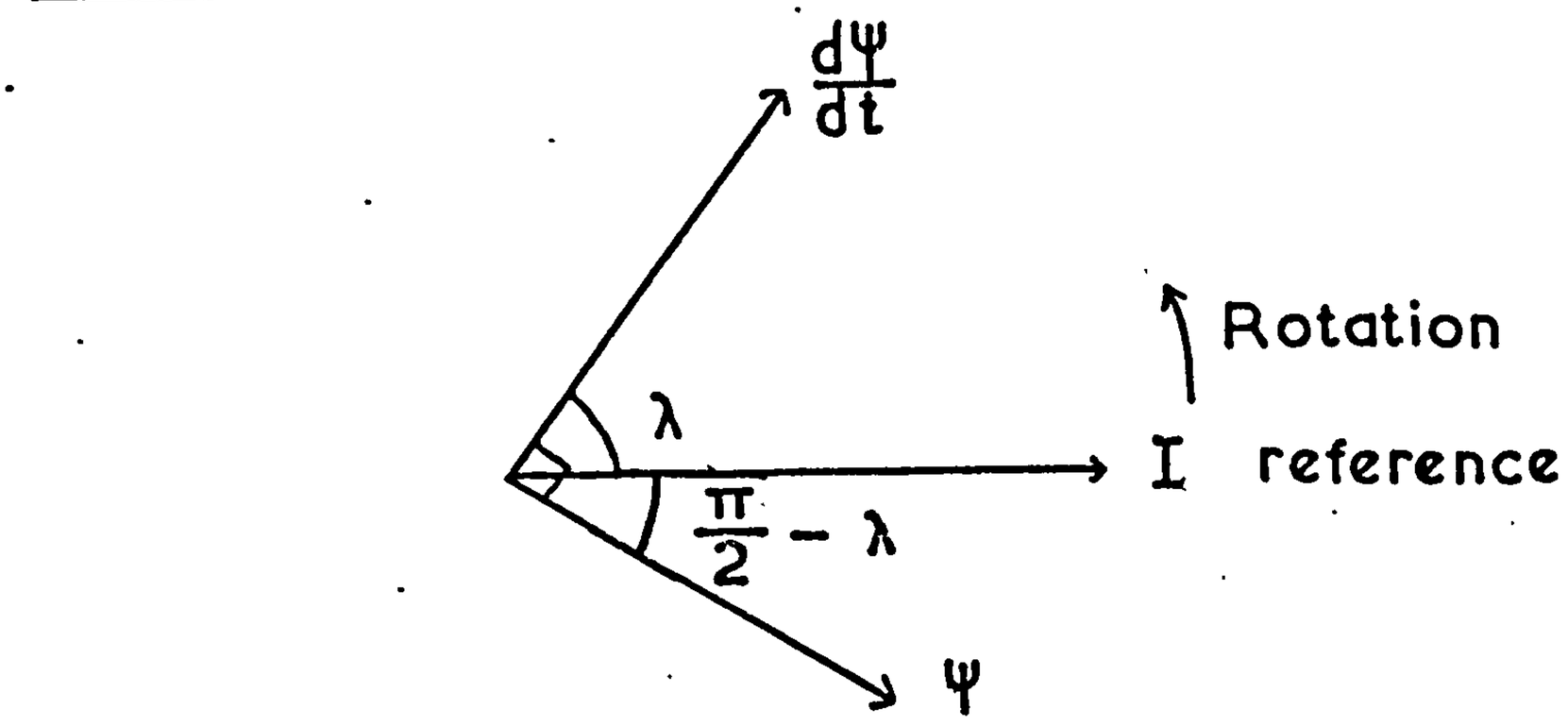

2·4 Stator Rotor Relative Positions

(a) $p\Theta = n\pi/2$

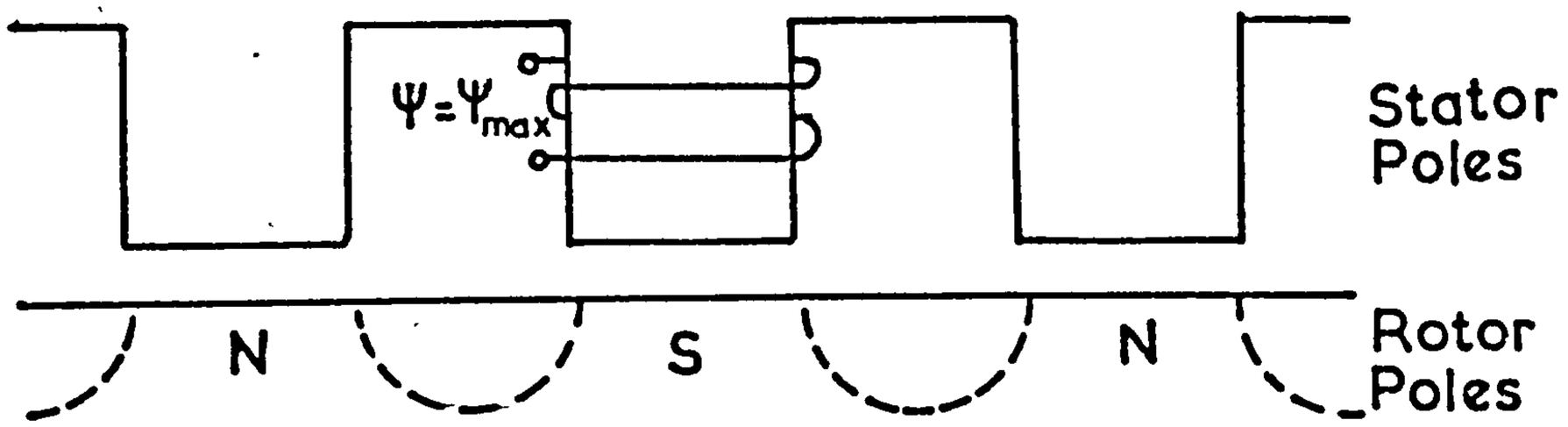

(b) $p\Theta = 0$ or $n\pi$

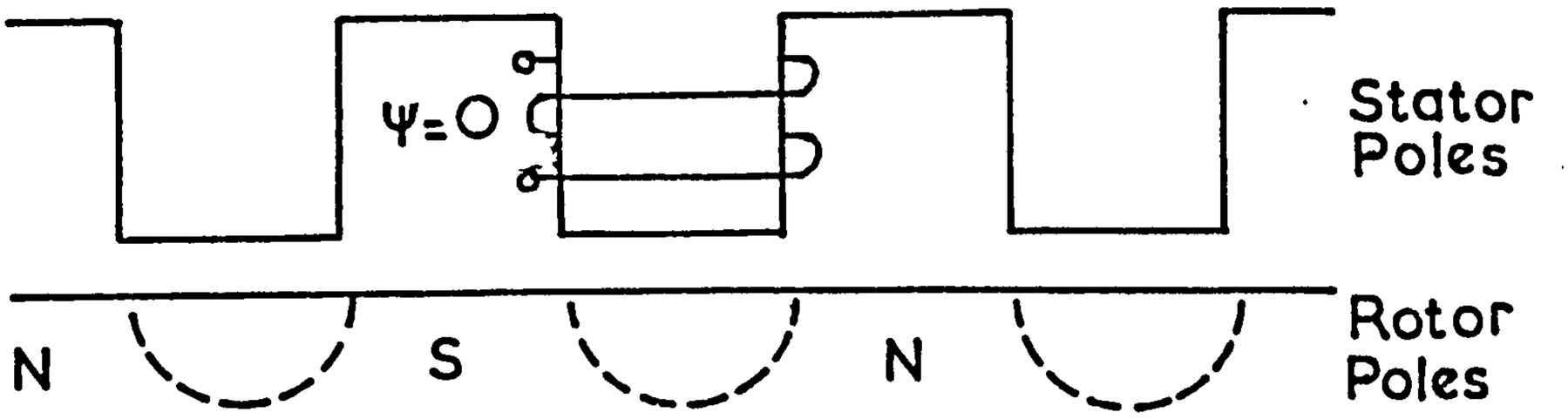

Fig 2·5

Variation Of Peak Torque With Current

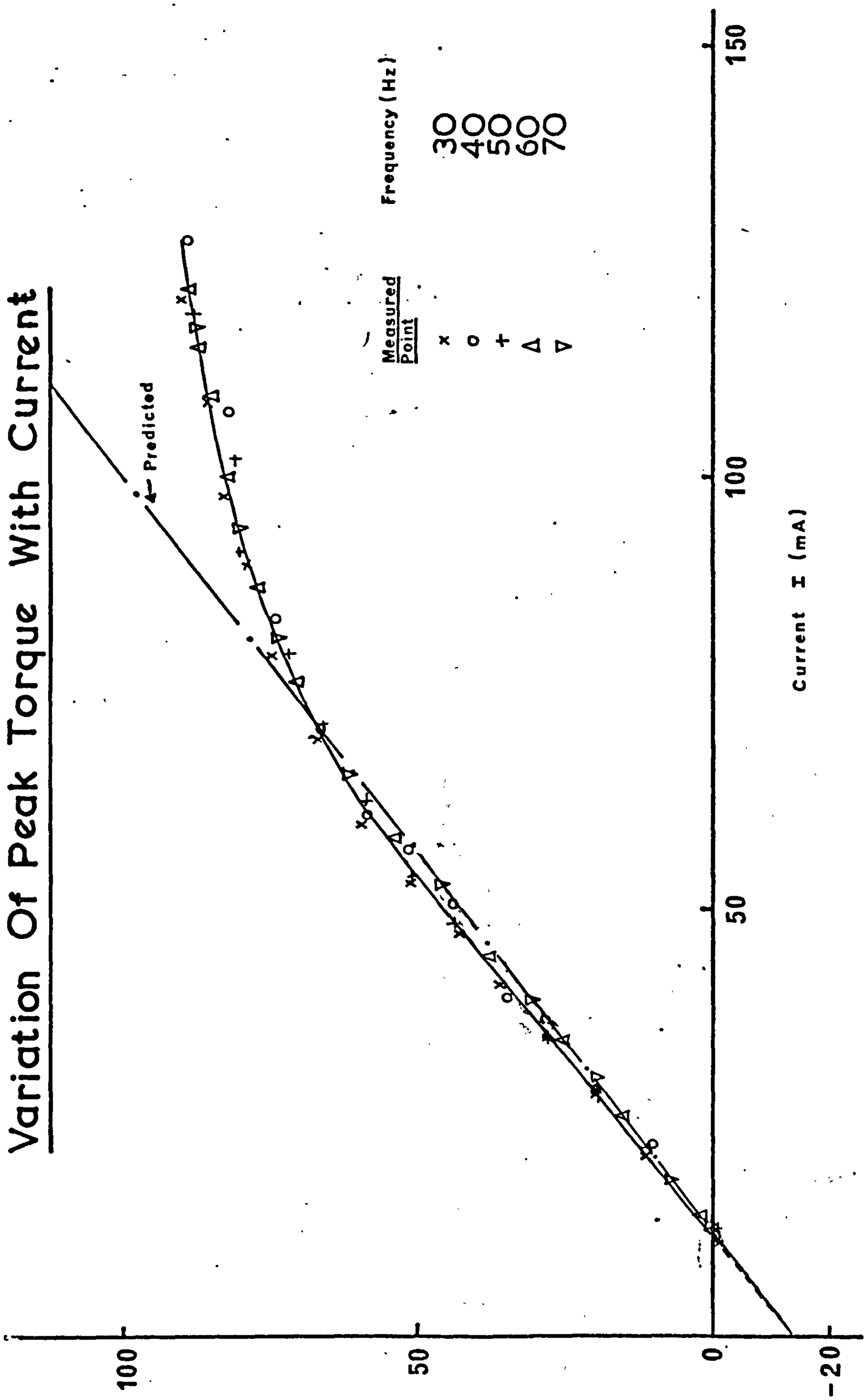

Fig 2·6
Fig 2·7

2·6 O·C· Drag Torques

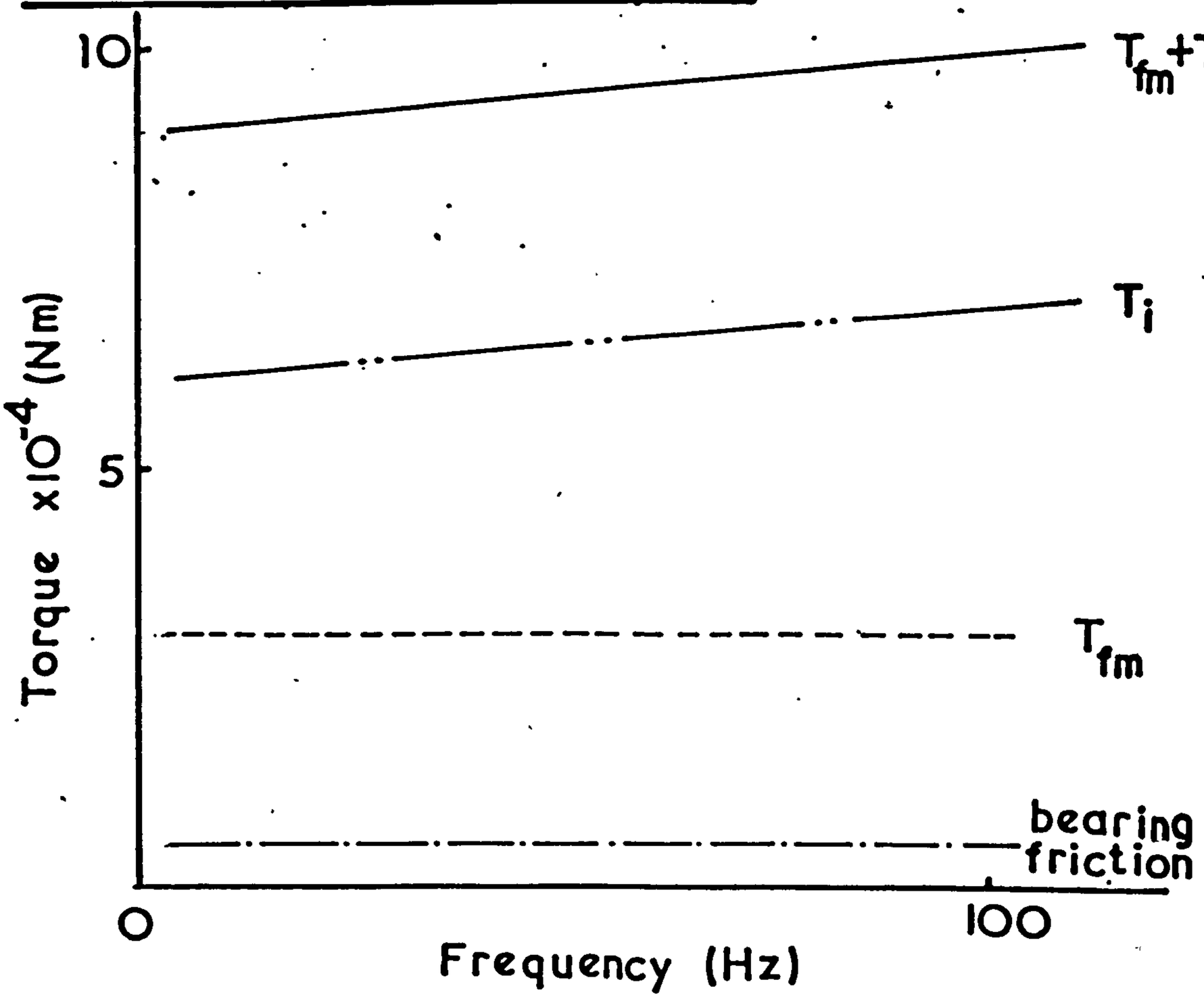

2·7 Speed Oscillations

f = 40Hz, J = 15·5x10⁻⁷ kg m²

(a) I = 45 mA

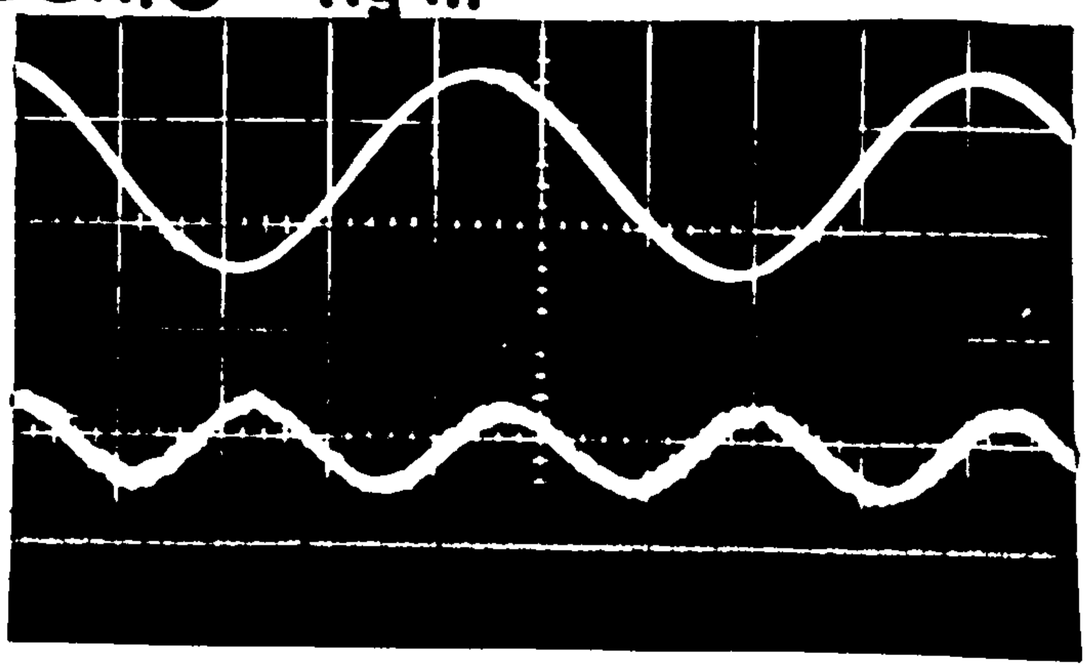

(b) I = 60mA

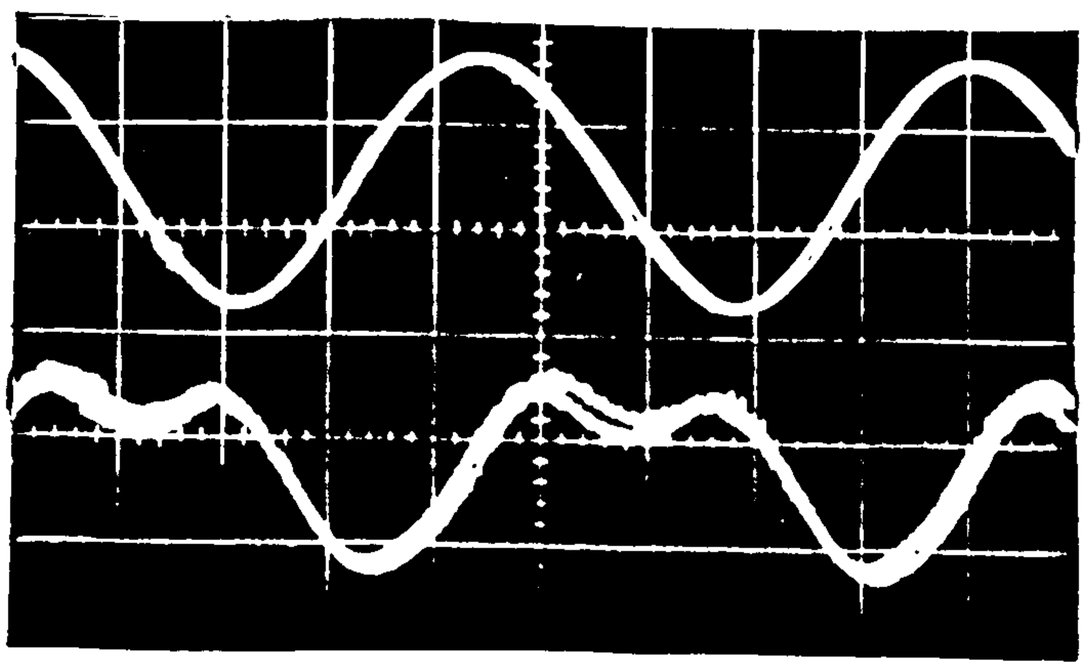

Fig 2·8a
Fig 2·8b

Variations Of Amplitude Of Rotor Oscillation With Current

(a) Case Of $J = 10{\cdot}5 \times 10^{-7}$ kg m^2

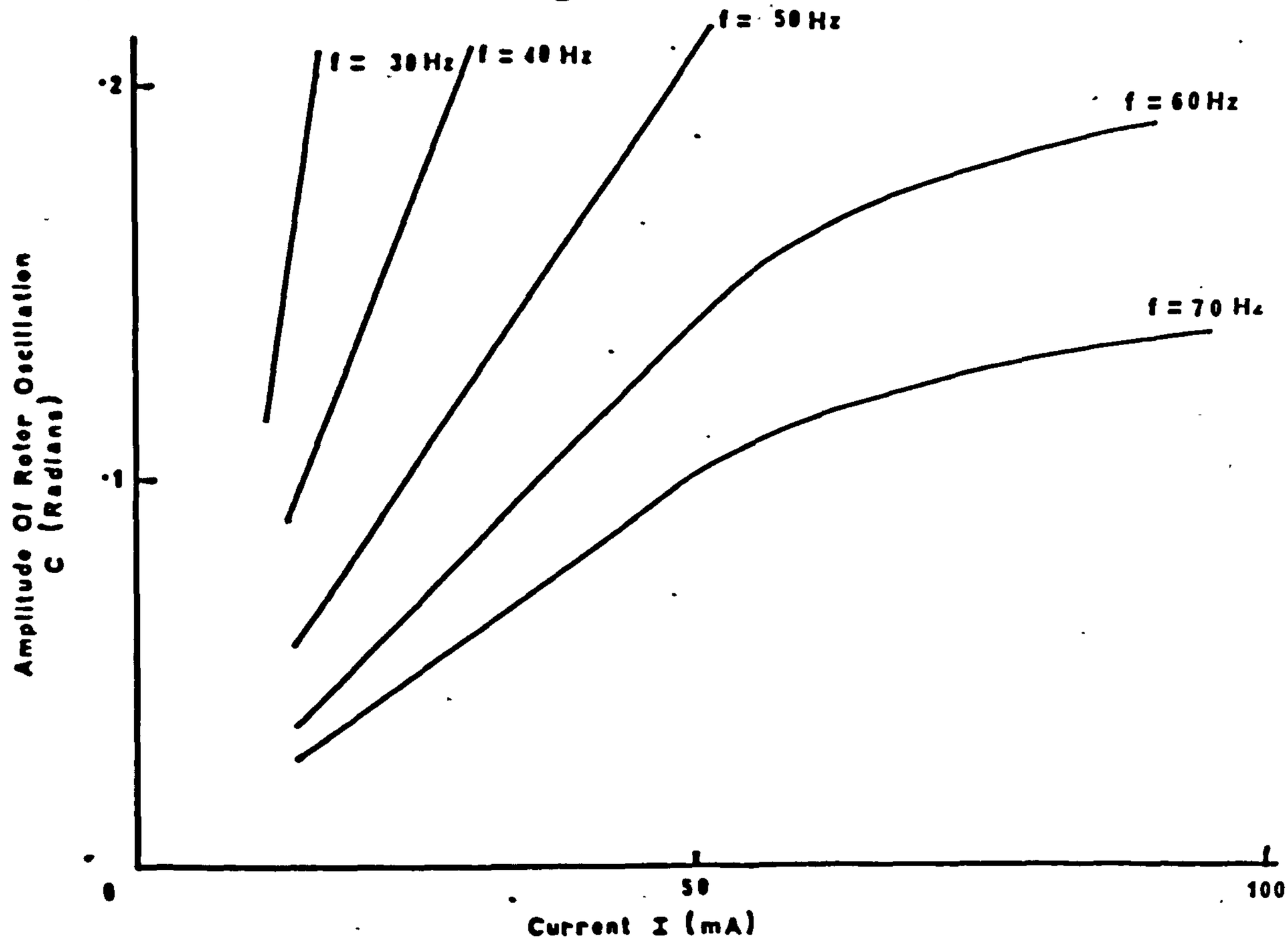

(b) Case Of $J = 15{\cdot}5 \times 10^{-7}$ kg m^2

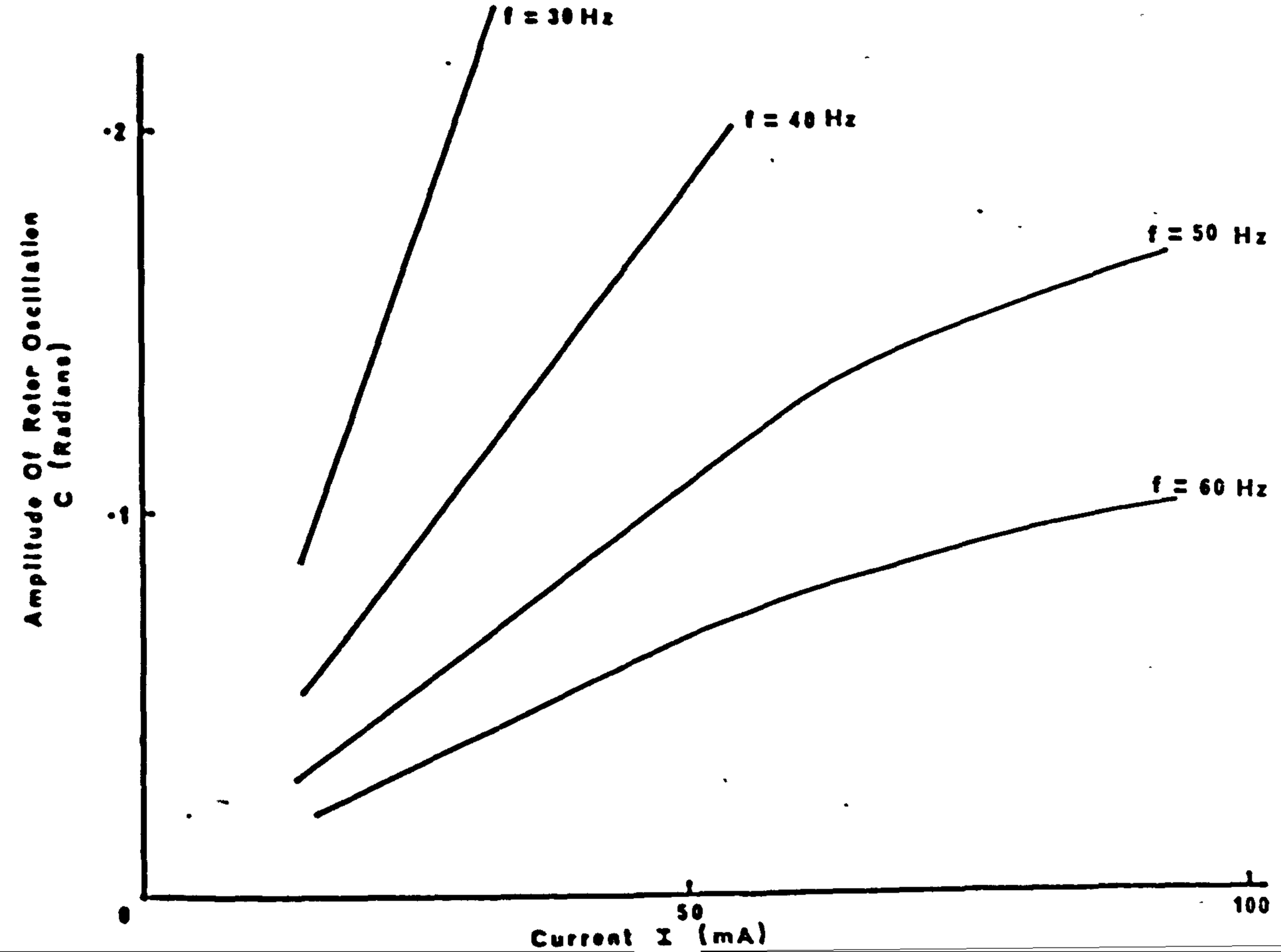

Fig 2·8c
Fig 2·8d

Variations Of Amplitude Of Rotor Oscillation With Current

(c) Case Of $J = 22 \times 10^{-7}$ kg m^2

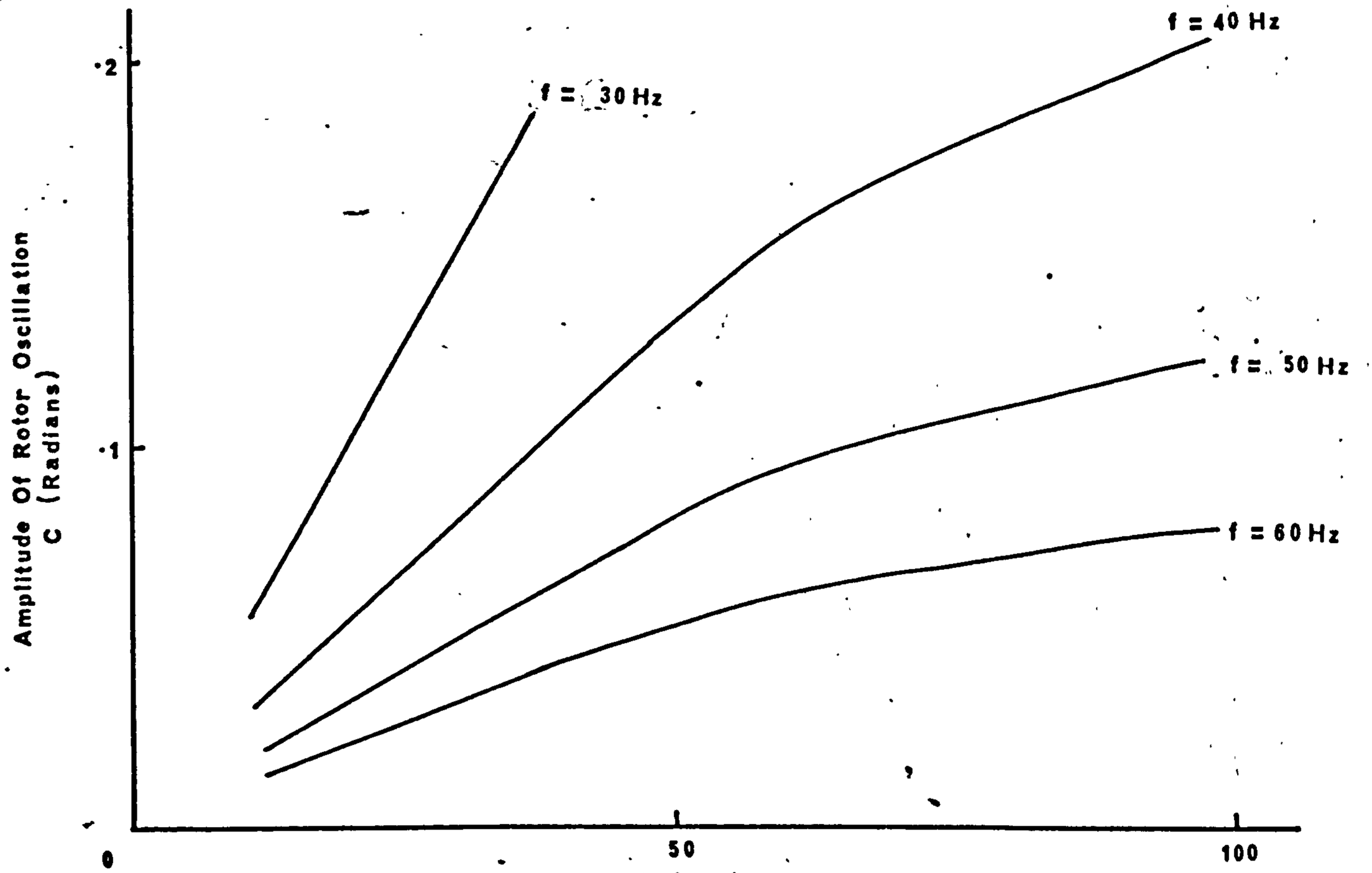

(d) Case Of $J = 40 \times 10^{-7}$ kg m^2

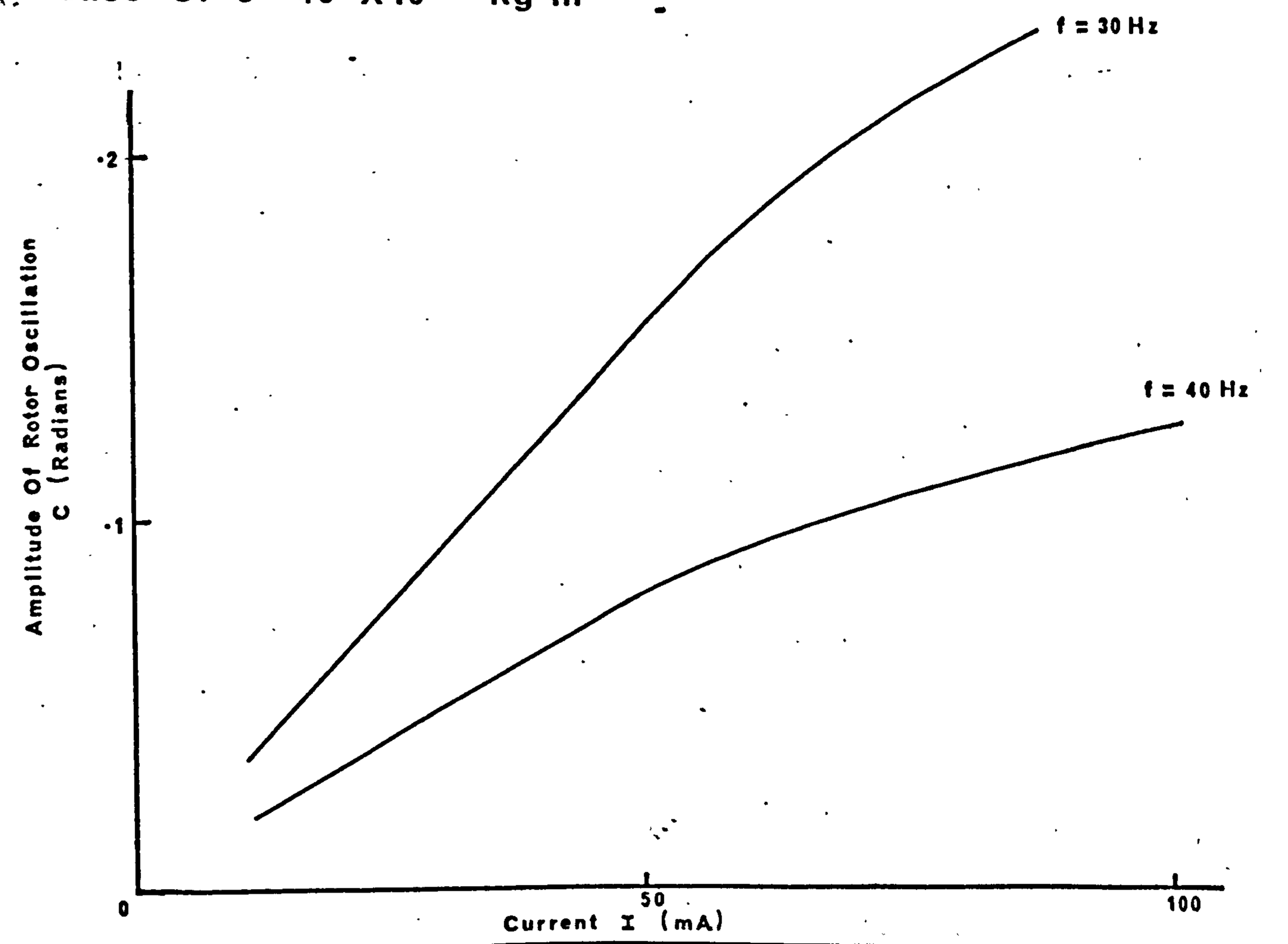

Comparison Of Predicted and Measured Torques

Case : $\beta=\beta_1$

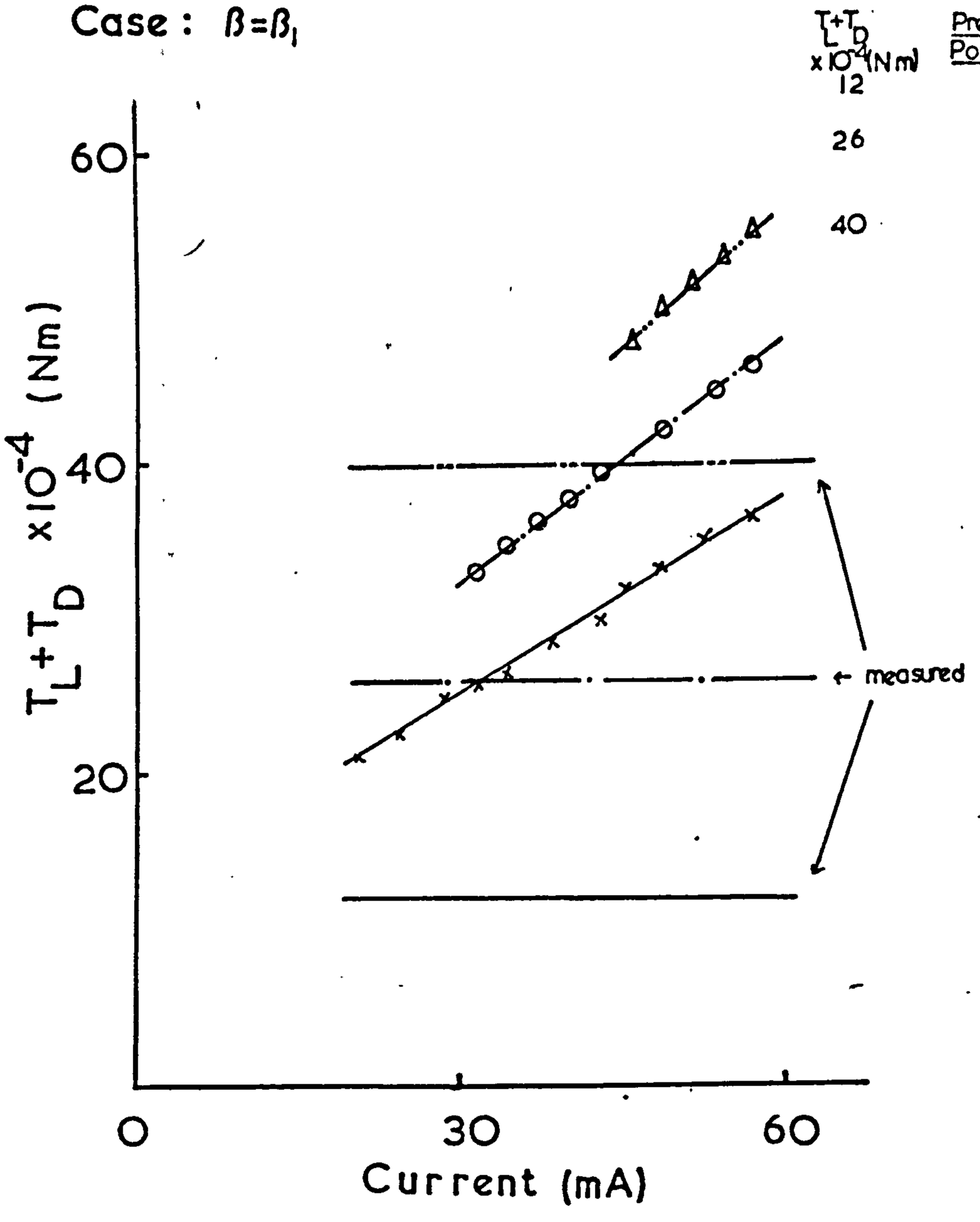

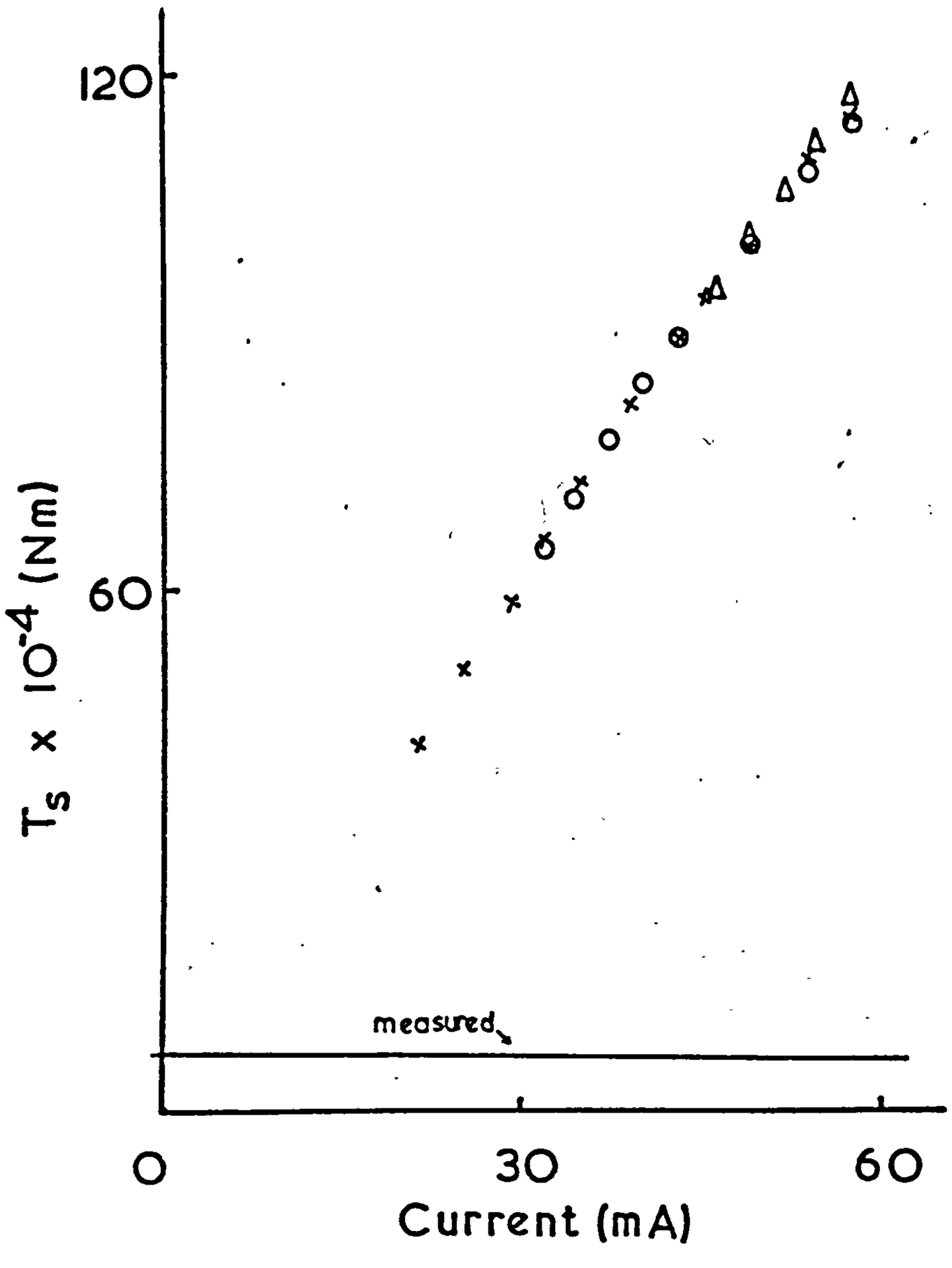

Fig 2.9

Comparison of Predicted and Measured Torques

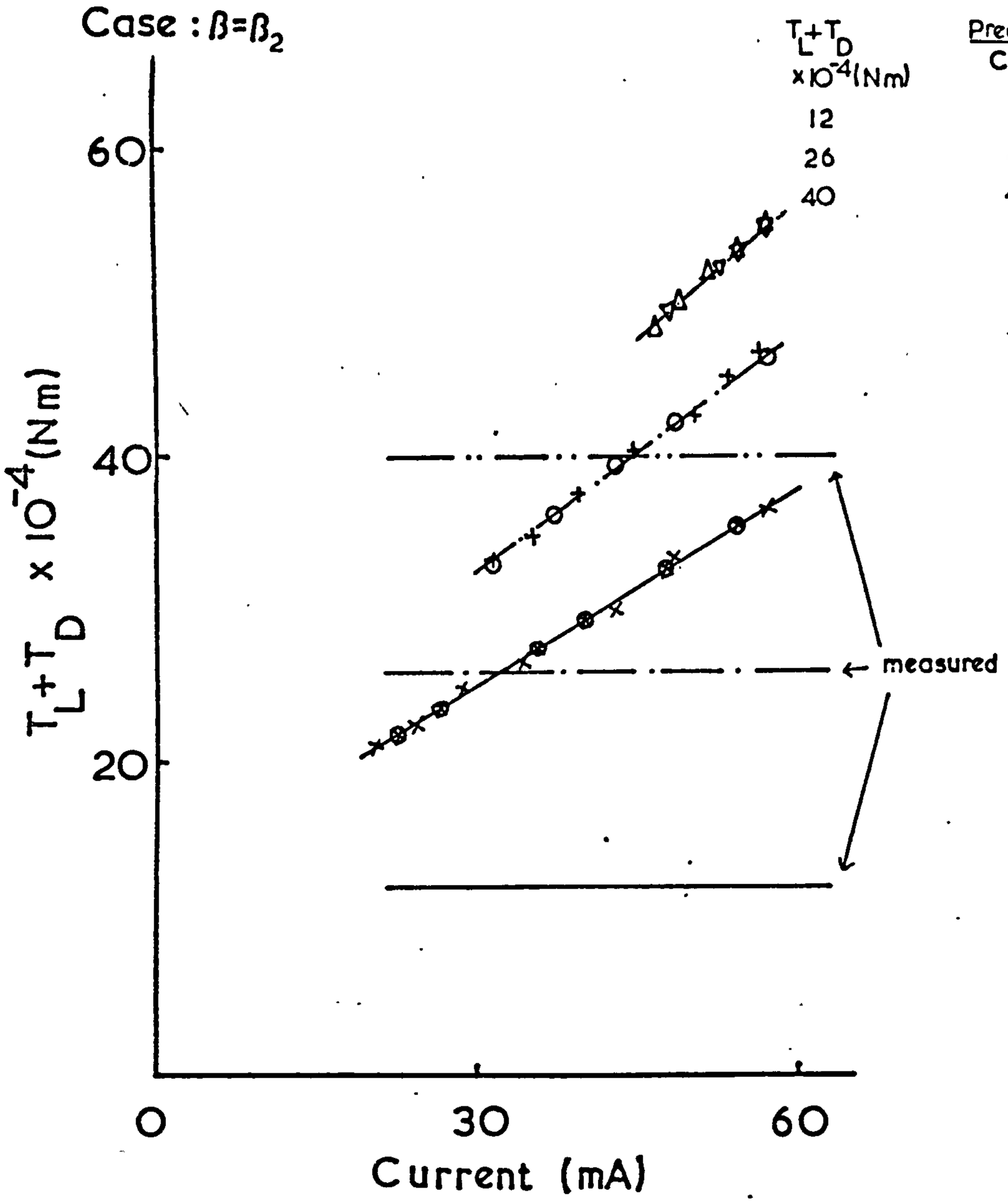

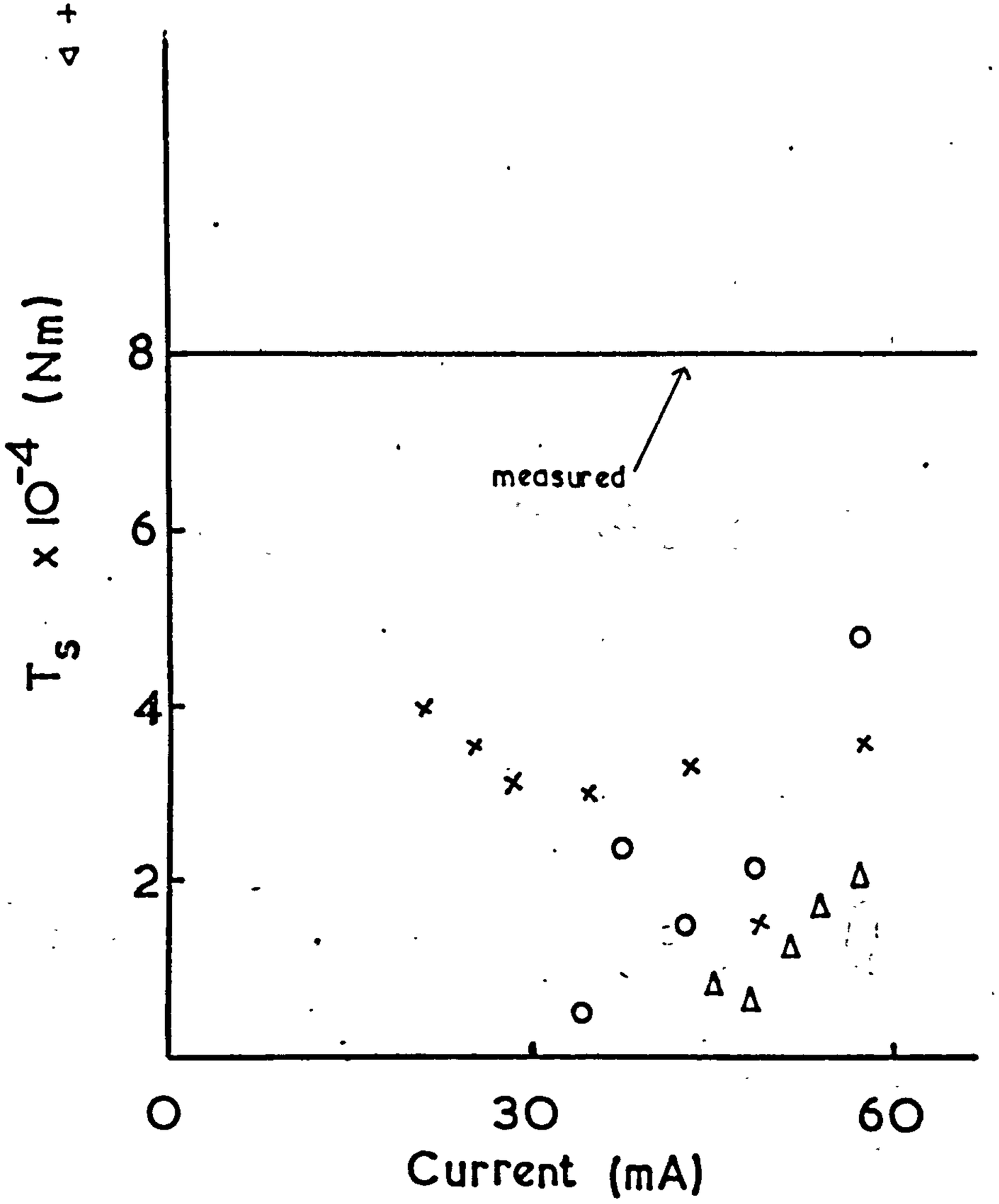

Fig 2.10

Comparsion Of Predicted and Measured Torques

T_L+T_D $\times 10^{-4}$(Nm)	Predicted C finite	Predicted C→O
12	x	⊗
26	o	+
40	Δ	▽

f = 40 Hz

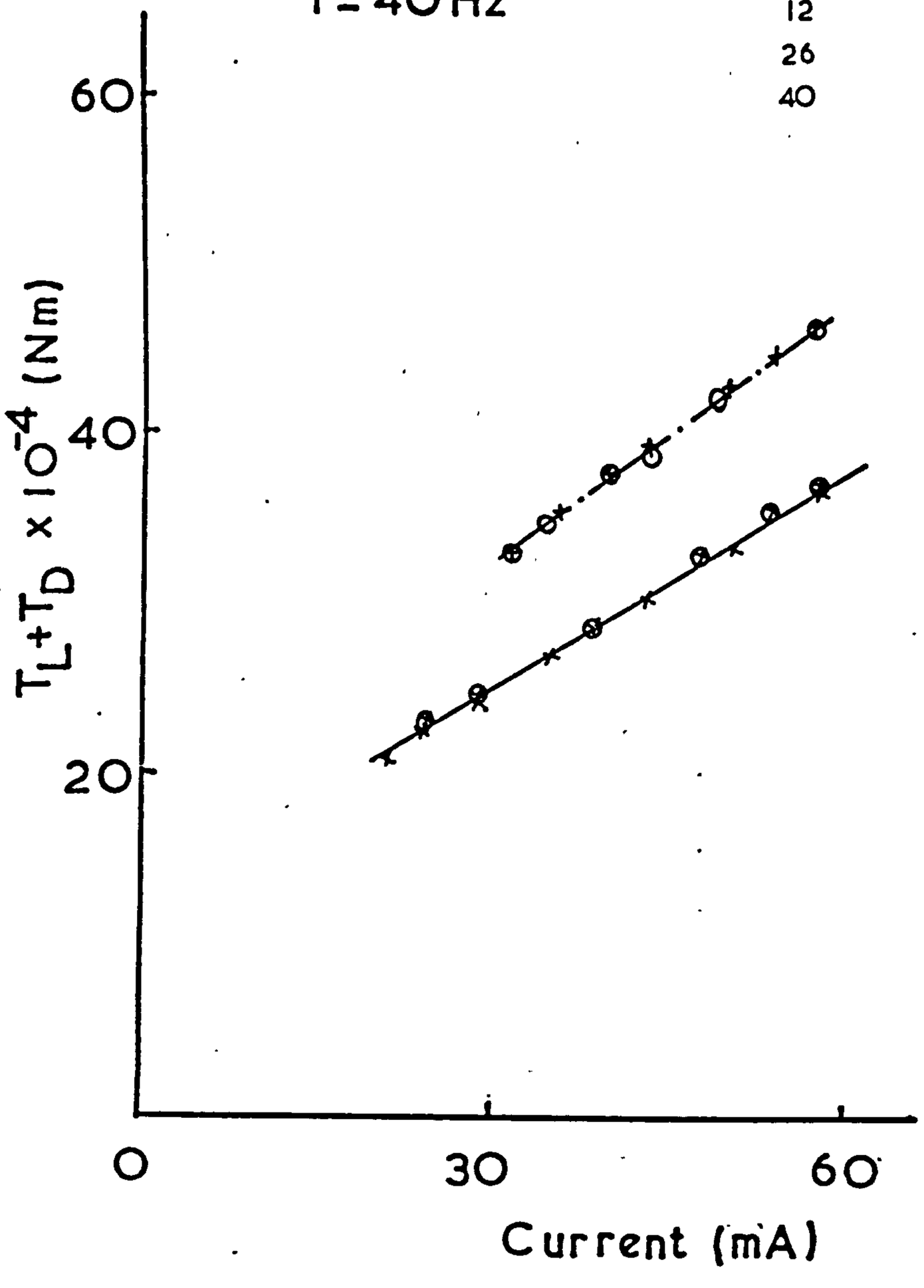

f = 60 Hz

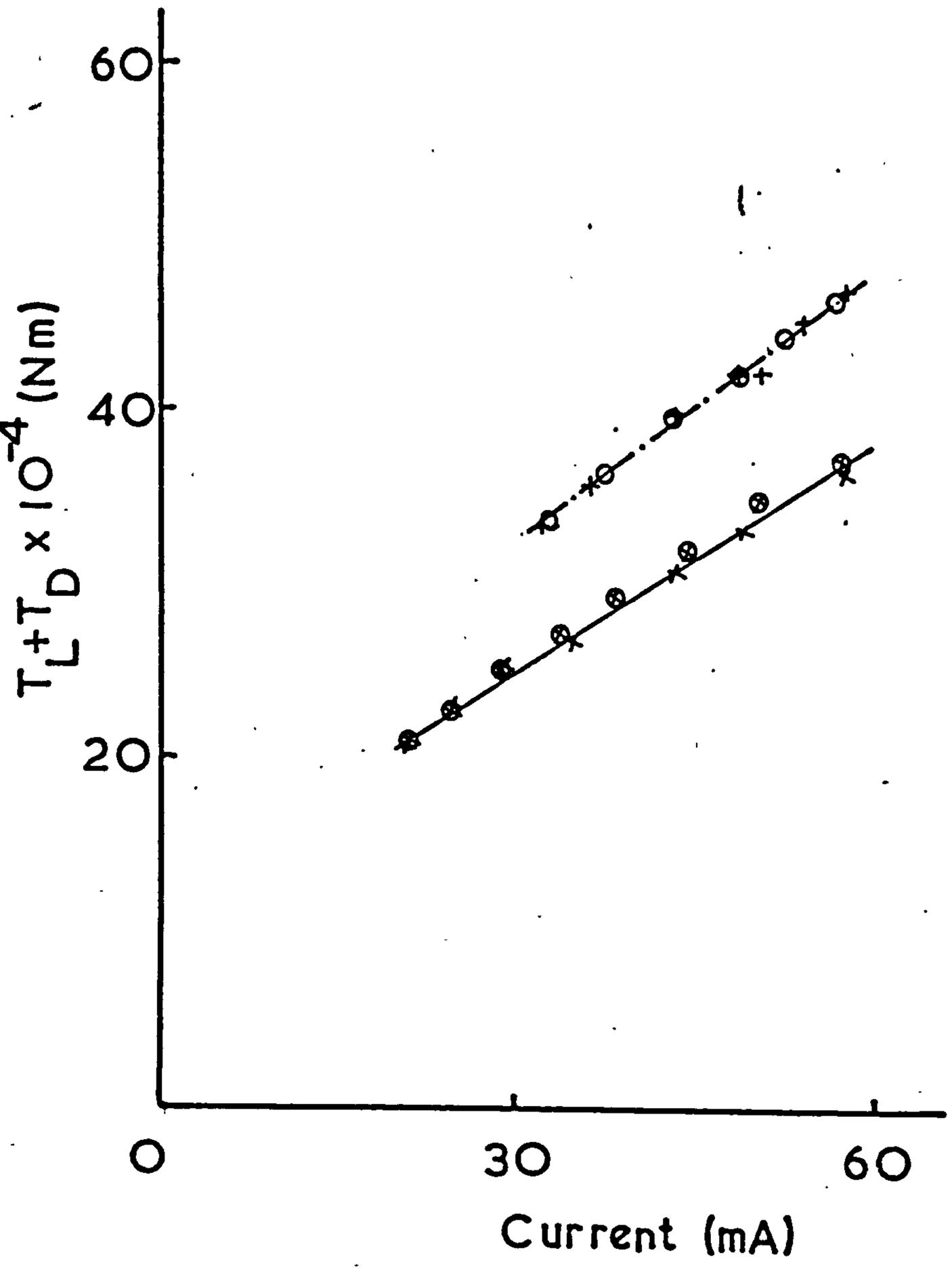

Fig 2.11

Fig 3·1
Fig 3·2
Fig 3·3

3·1 Equivalent Circuit Model

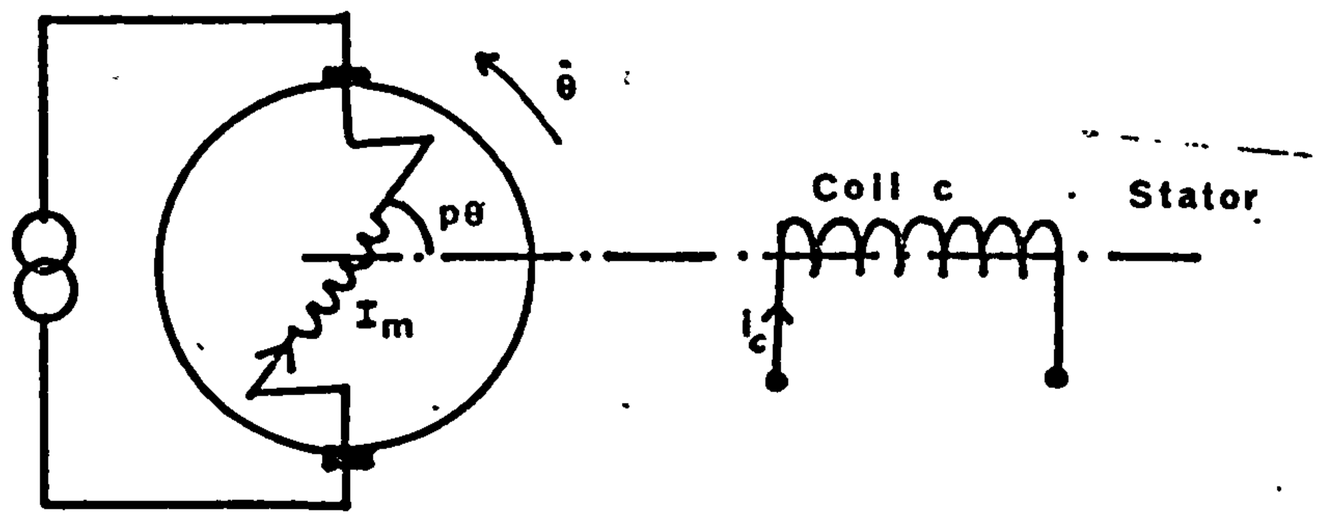

Equivalent
Rotor Coil

3·2 d – q Axis Model

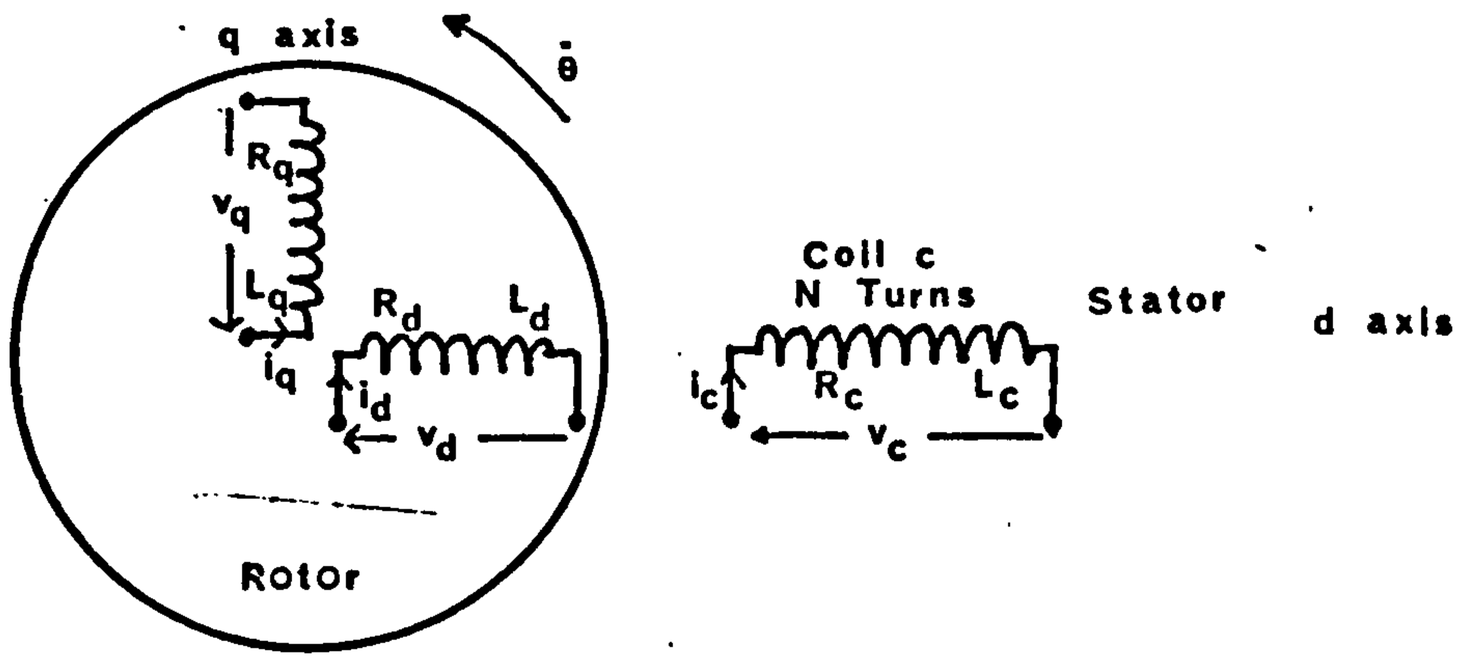

3·3 Phasor Diagram Of Flux Linkage And Currents

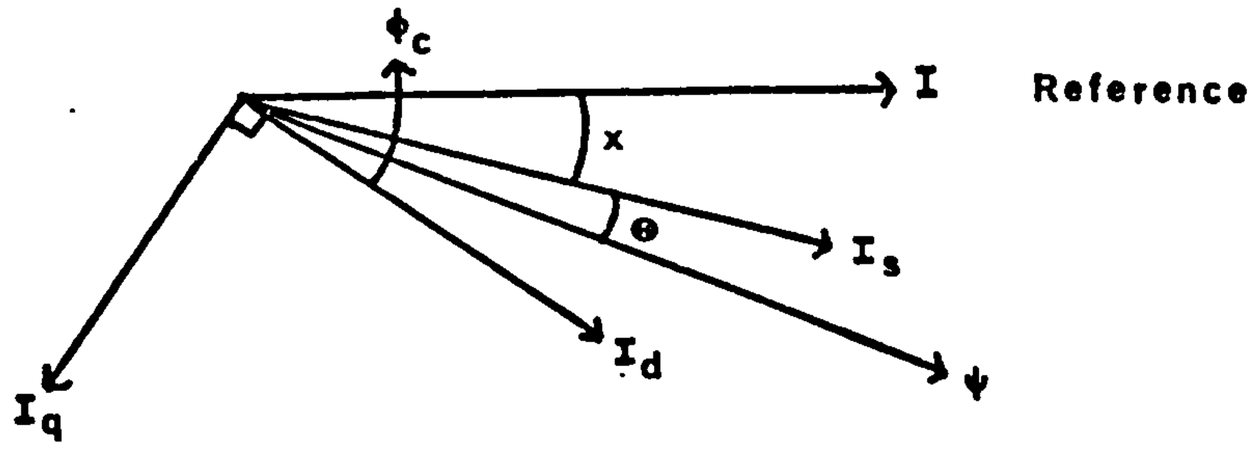

Fig 3.4

Phasor Diagram

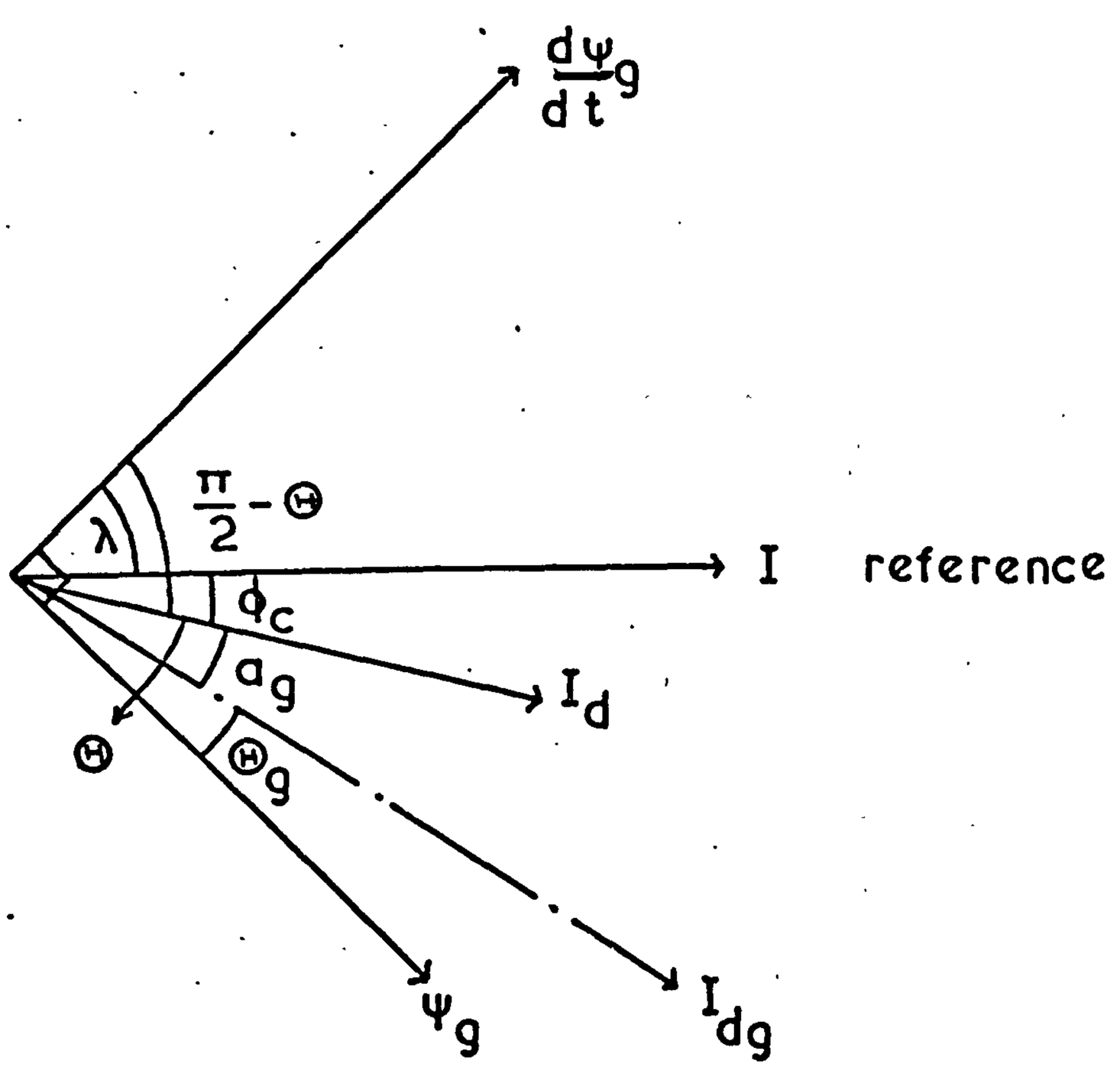

Fig 3·5

Comparison of Predicted and Measured Torques

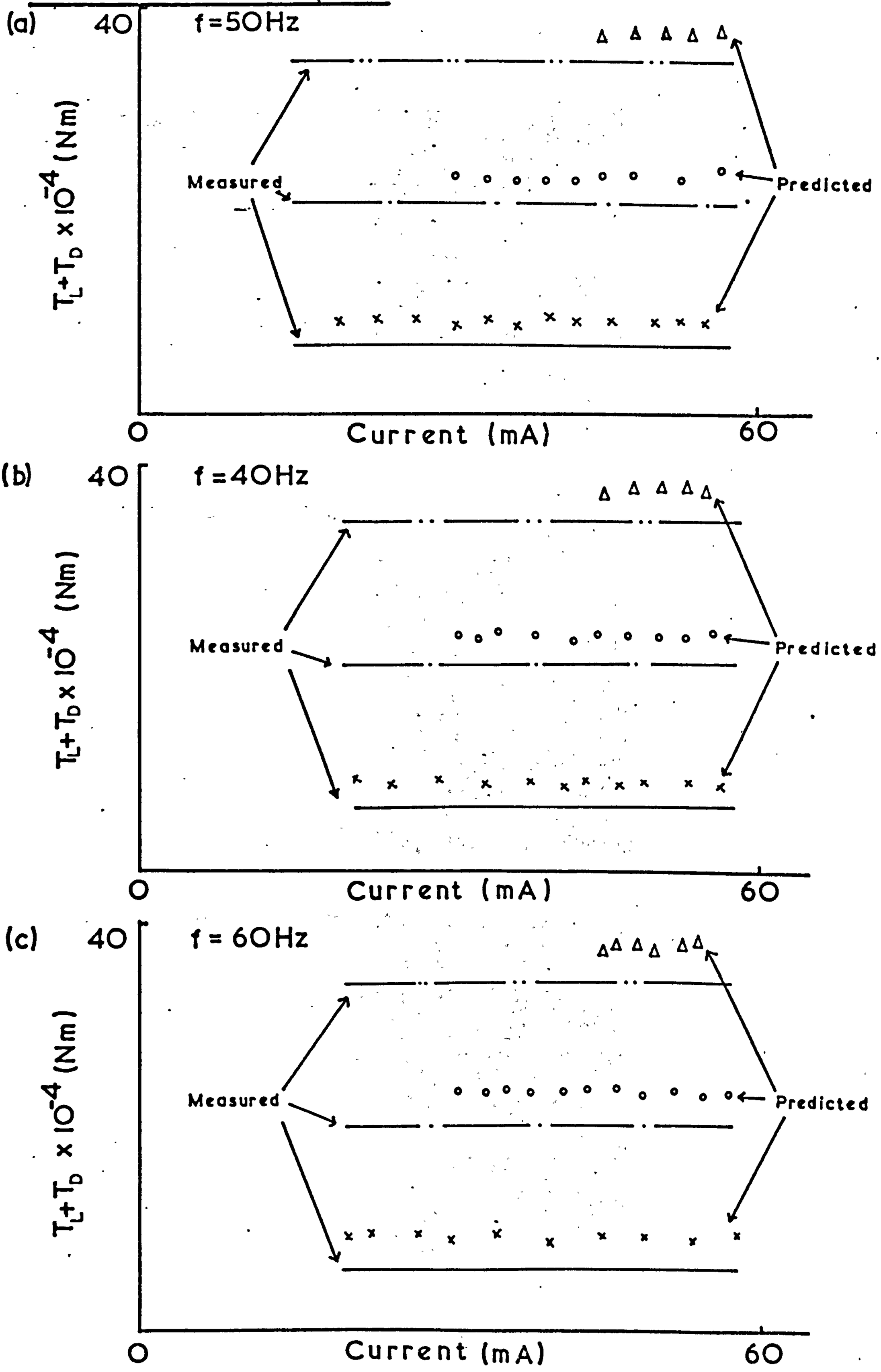

Fig 3·6

Ψ-i Loops of Stator

a) I=55mA

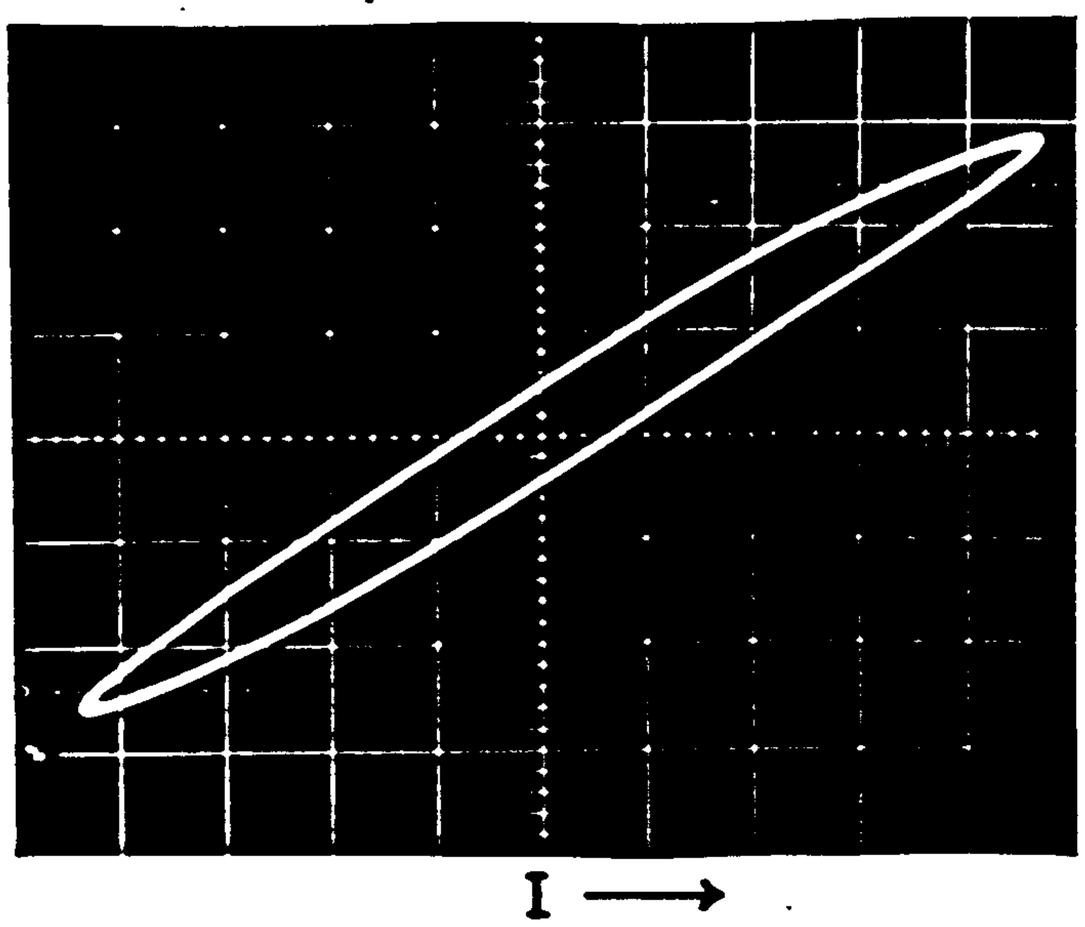

b) I=100mA

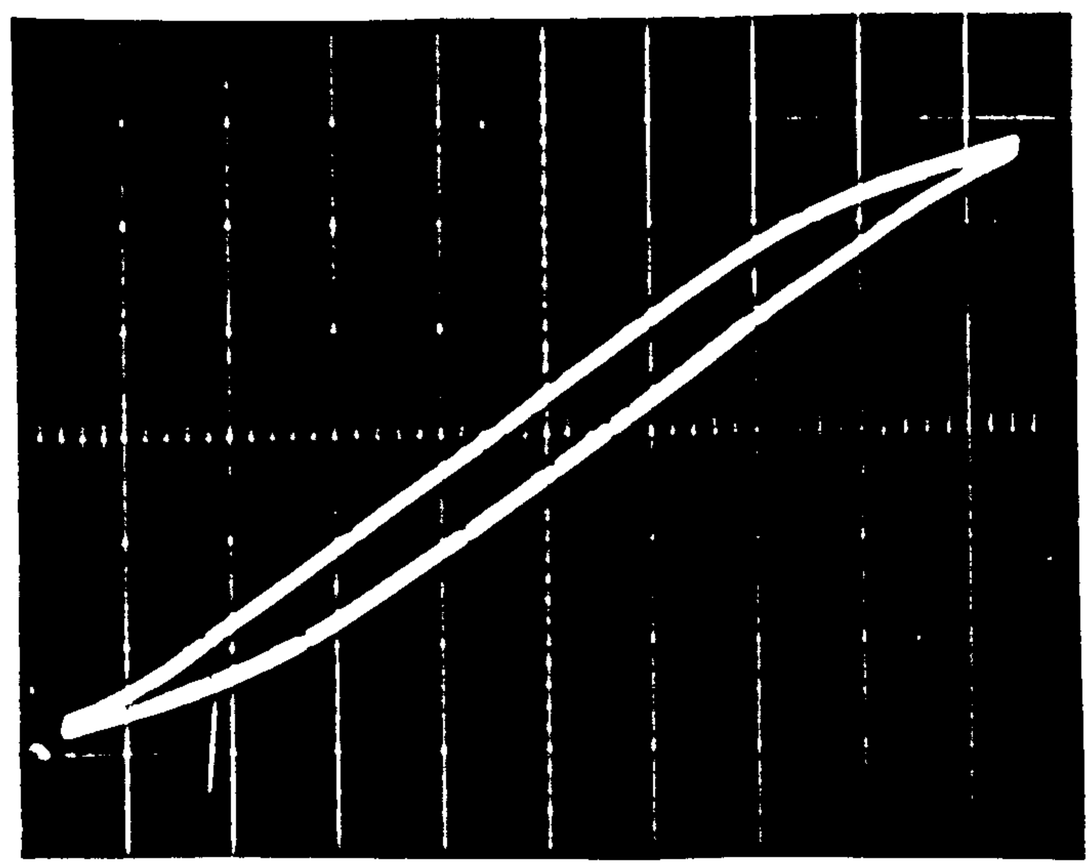

c) I=150mA

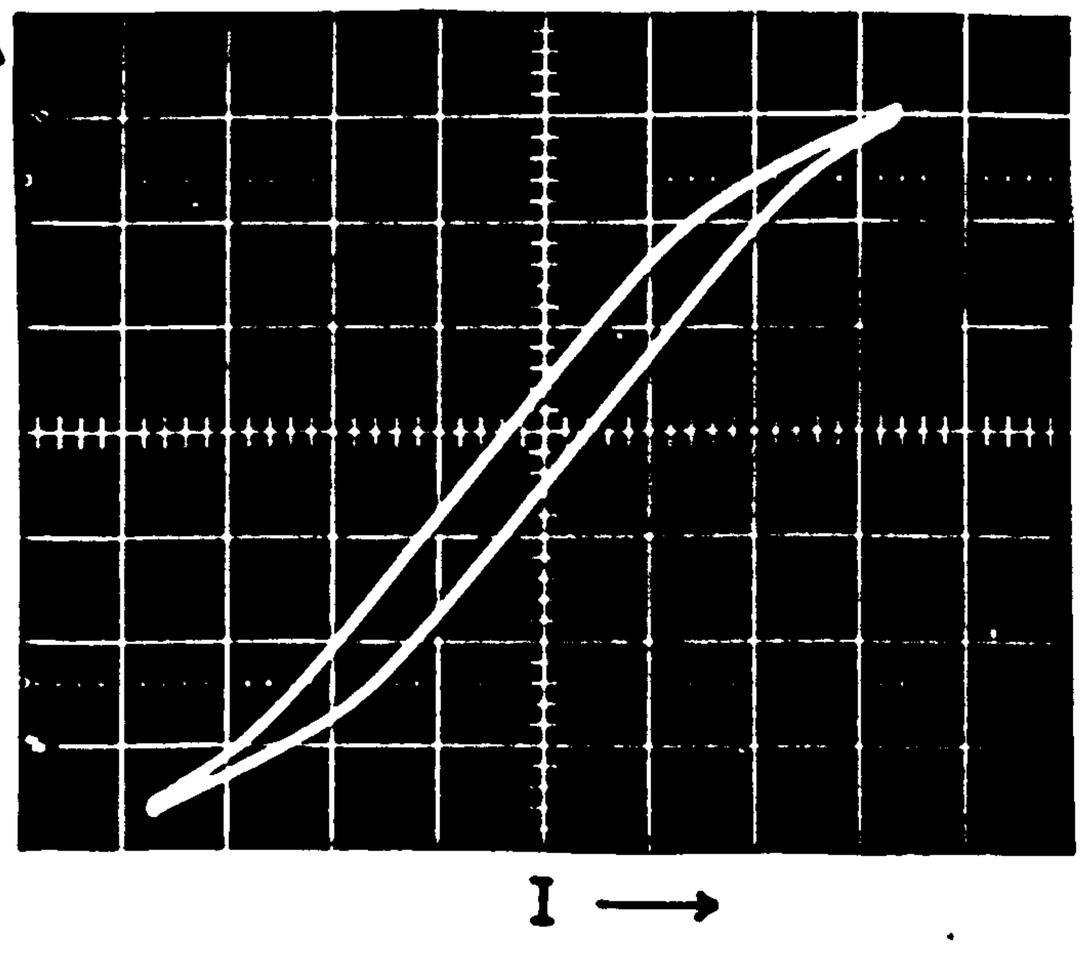

Fig 3.7

Comparison Of Instantaneous Torques

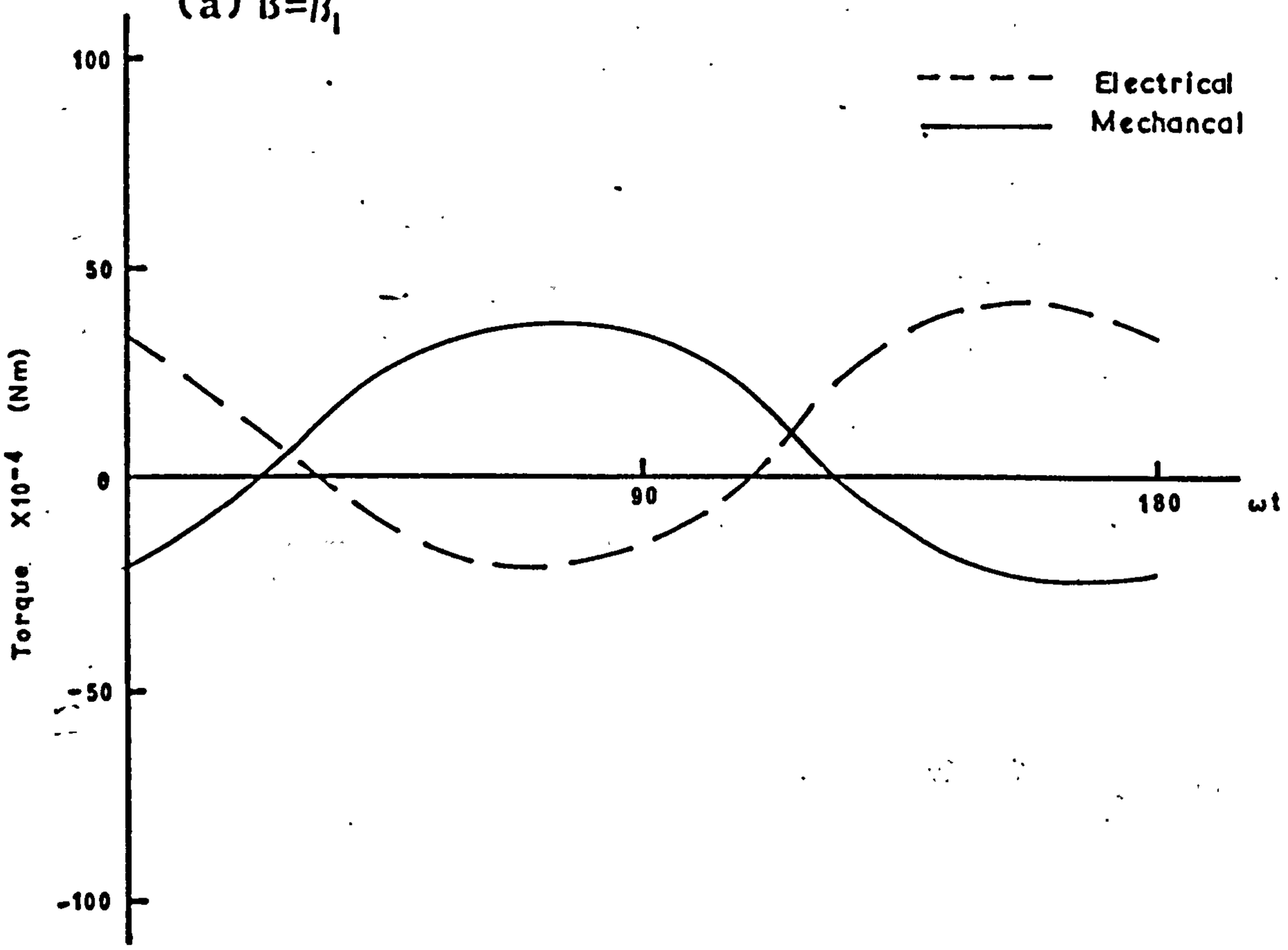

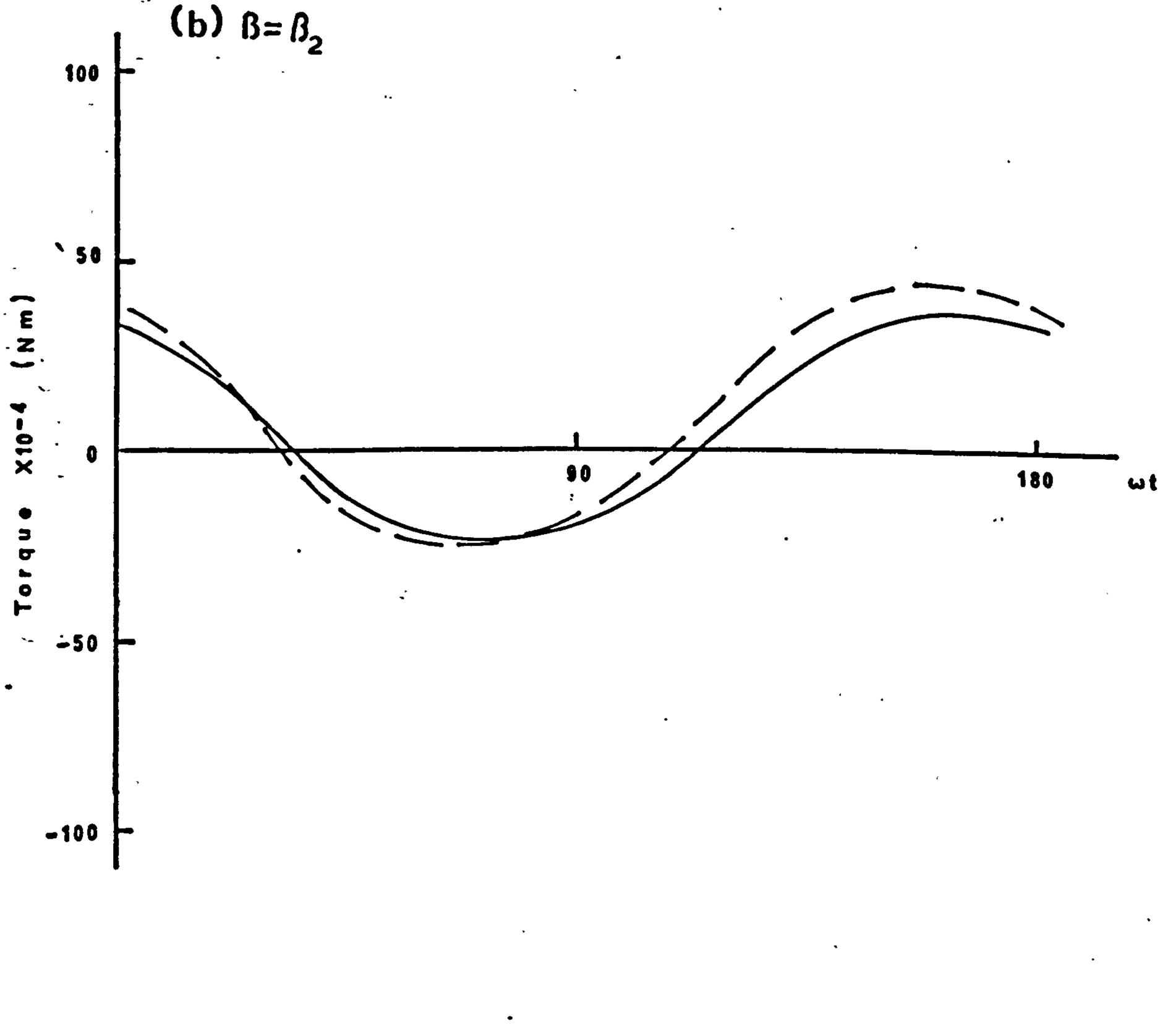

Fig 3·8

Comparison Of Instantaneous Torques

a) $\beta = \beta_1$

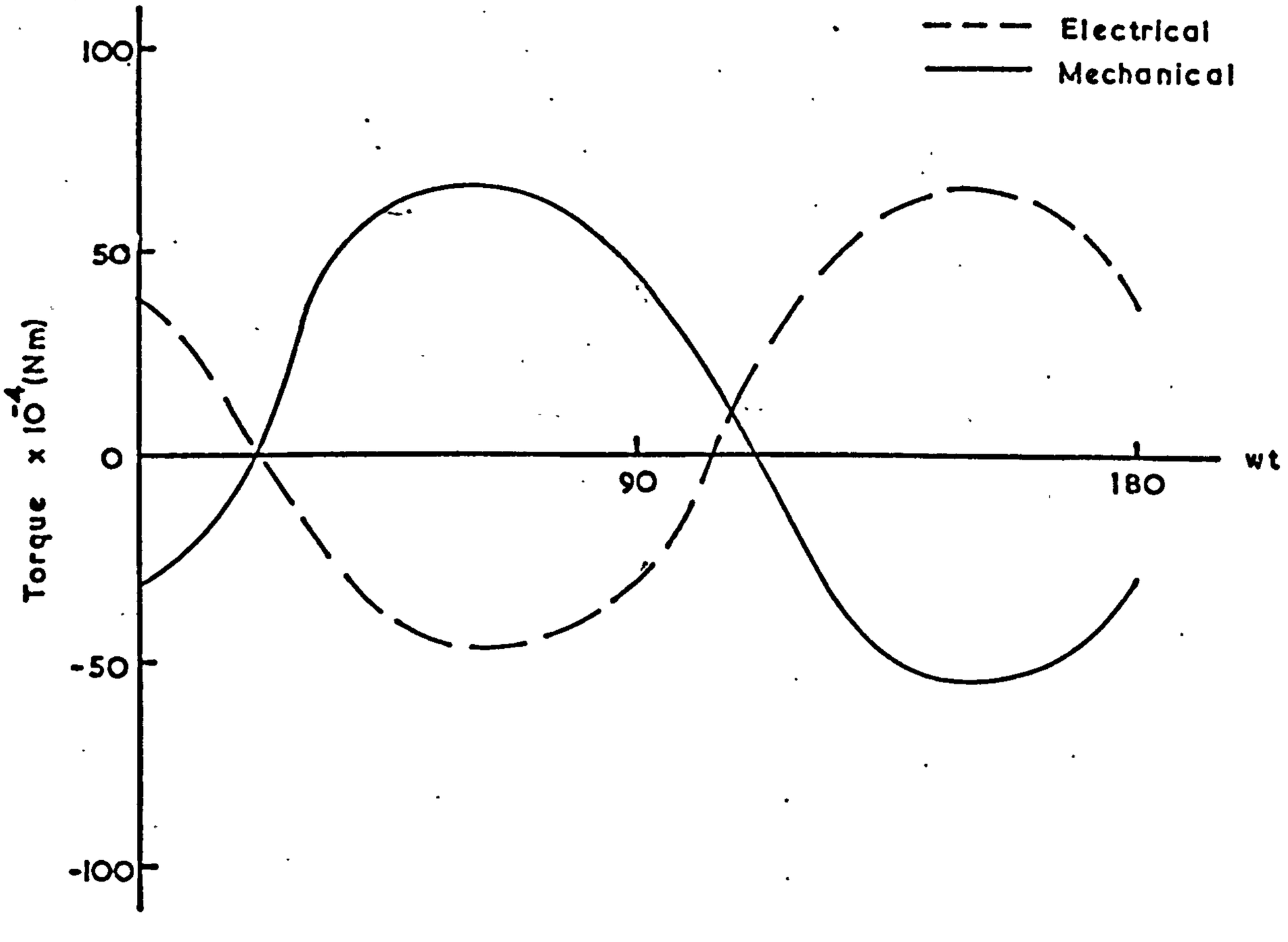

b) $\beta = \beta_2$

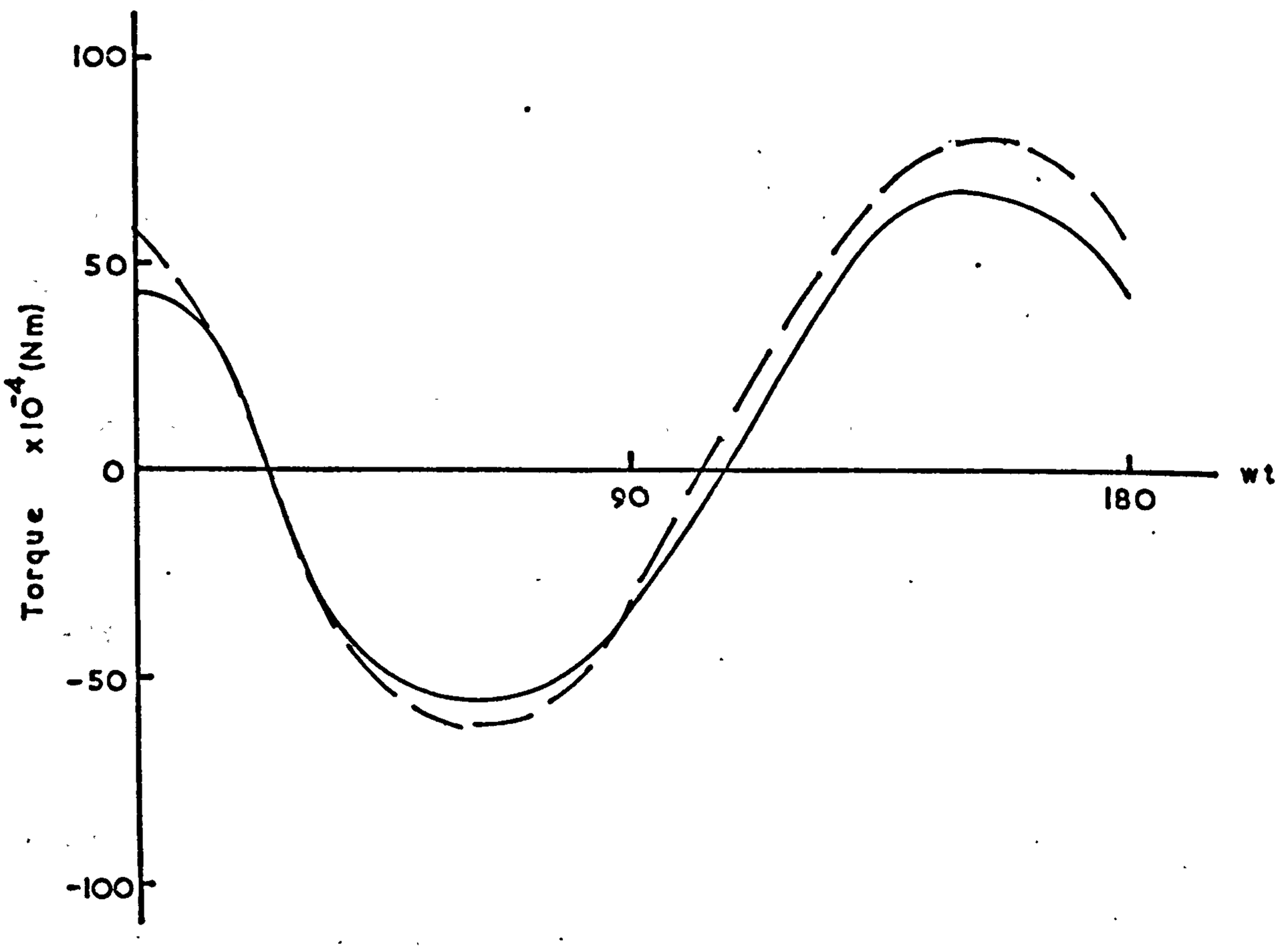

Fig 3·9

Comparison Of Instantaneous Torques

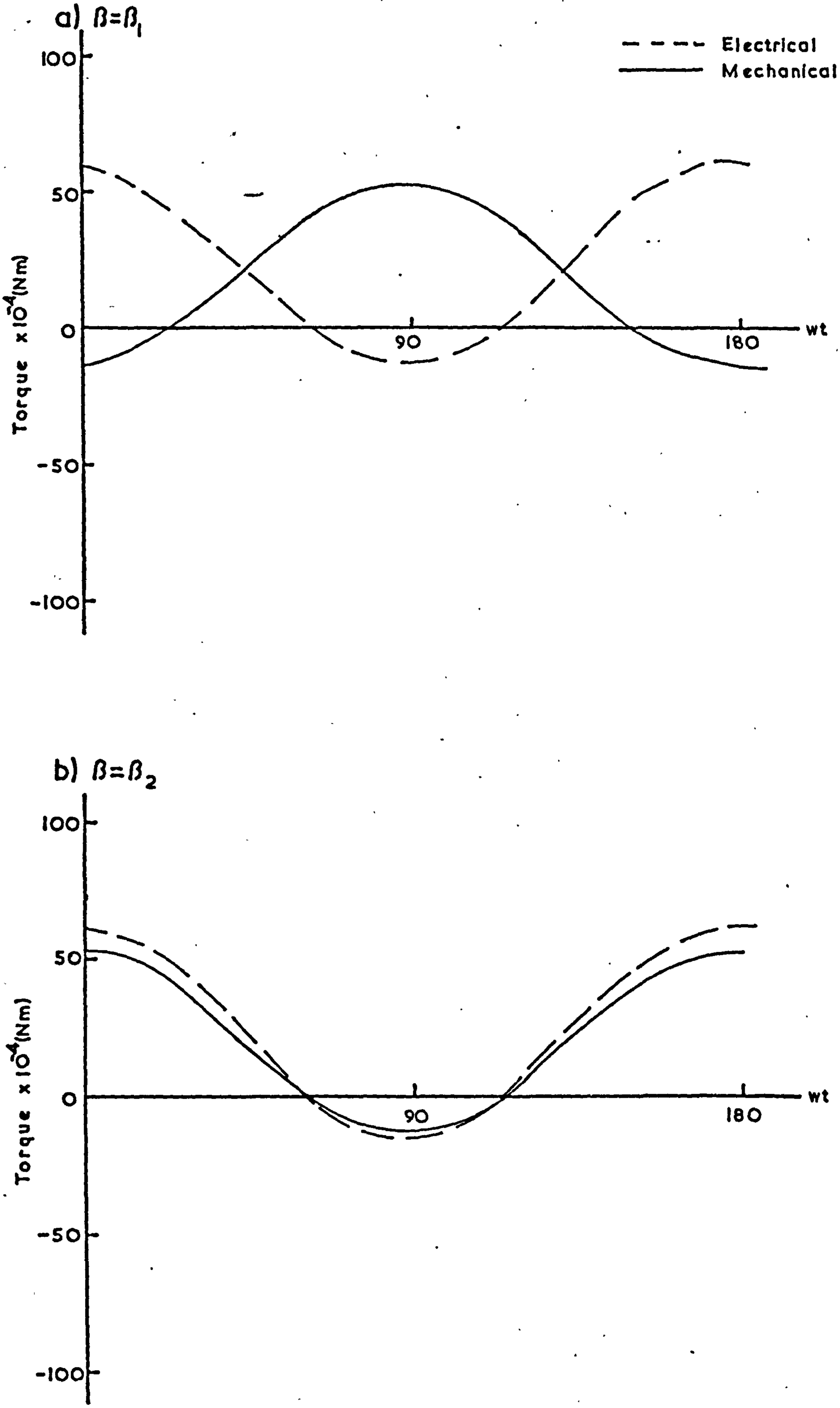

Fig 3·10

Comparison Of Instantaneous Torques

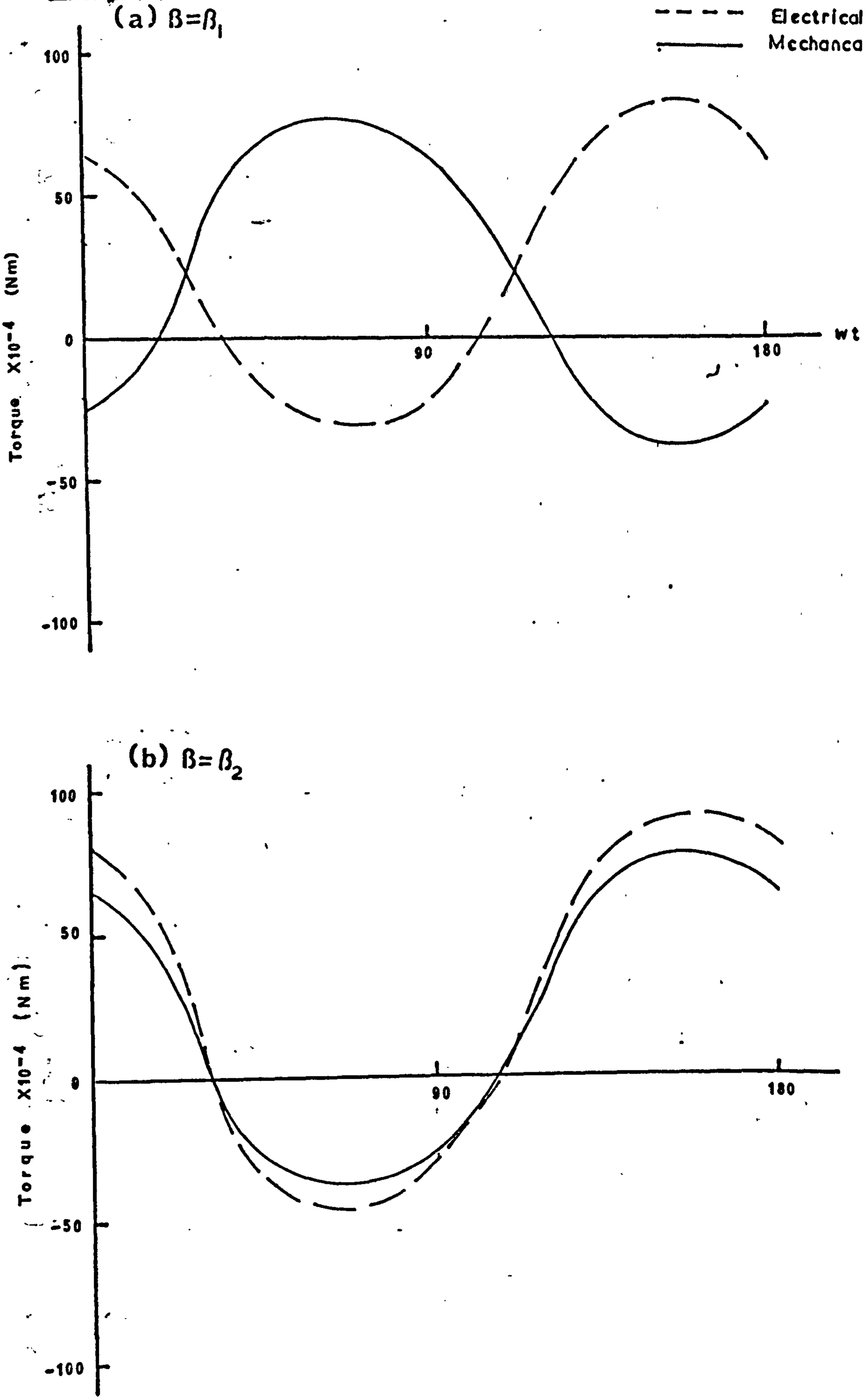

Fig 3·11

Comparison Of Instantaneous Torques

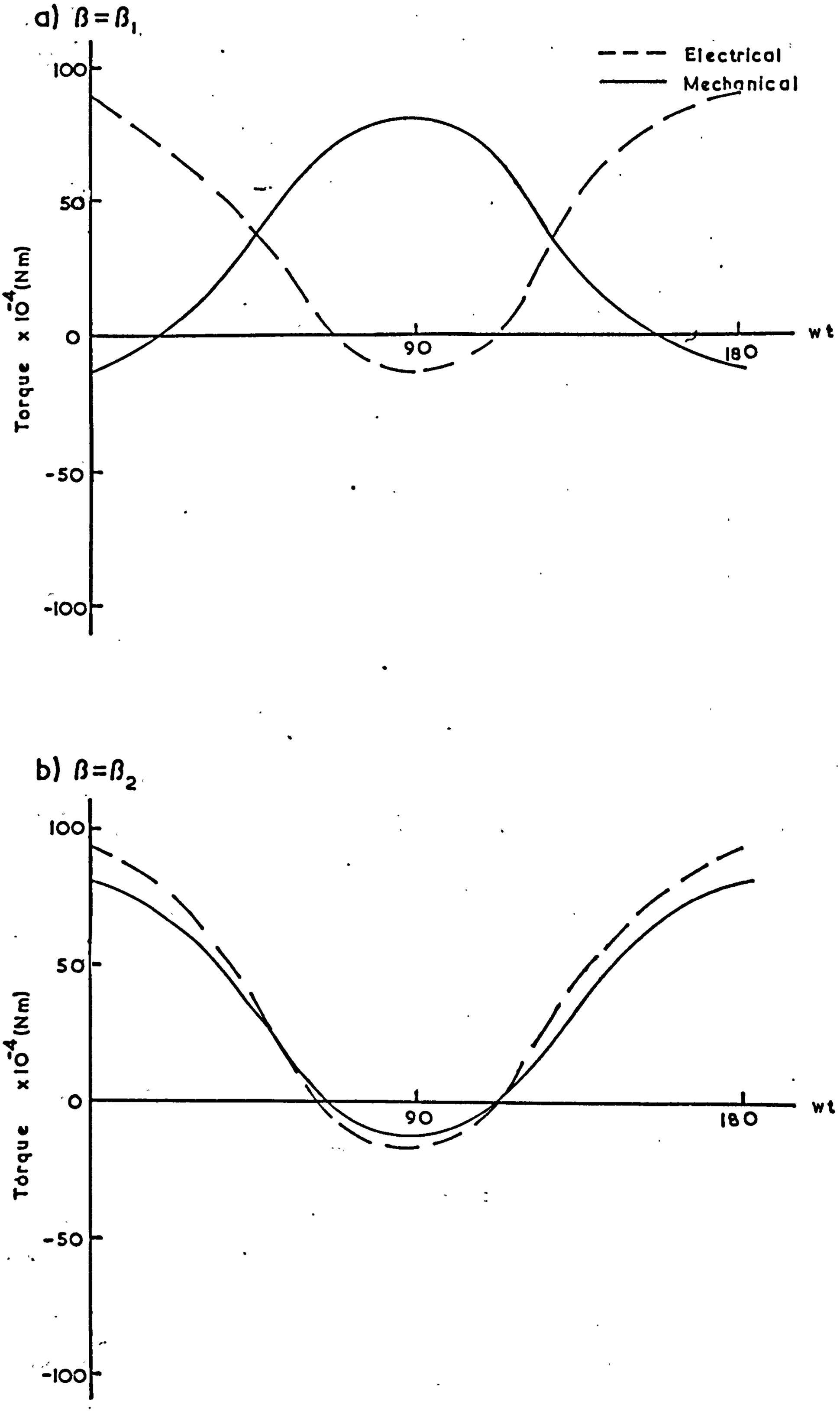

Fig 3·12

Comparison Of Instantaneous Torques

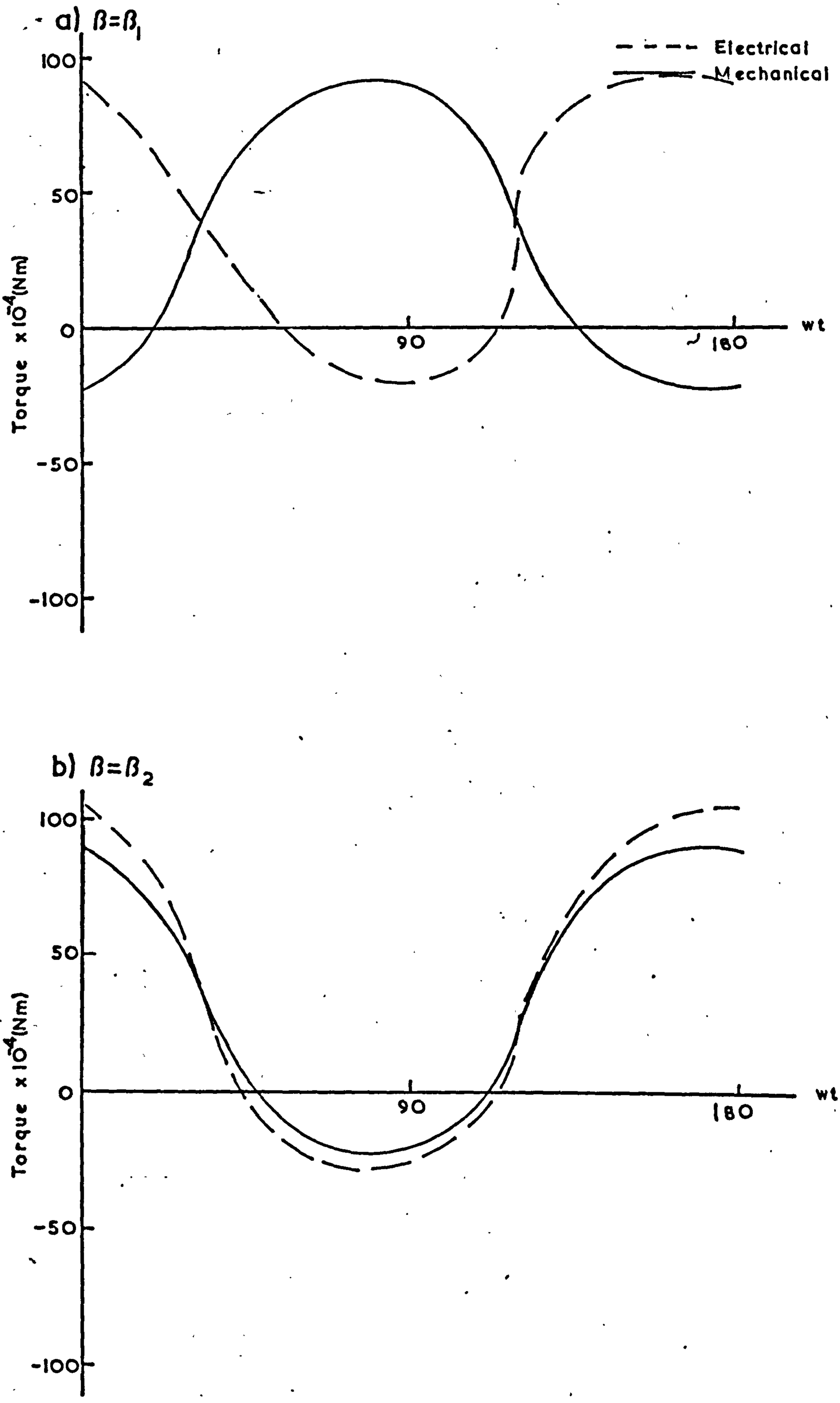

Comparison Of Torque Values

Fig 3·13

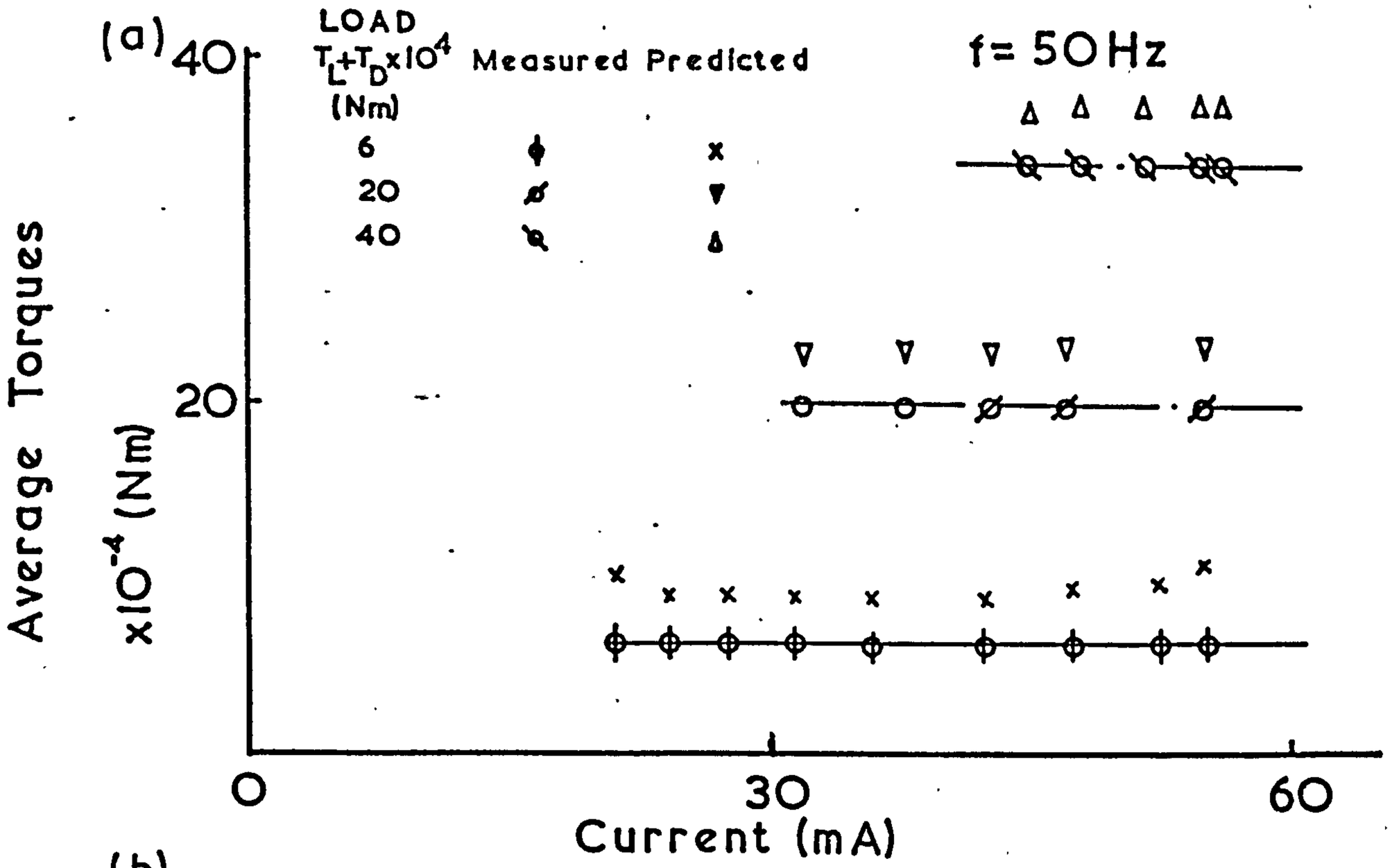

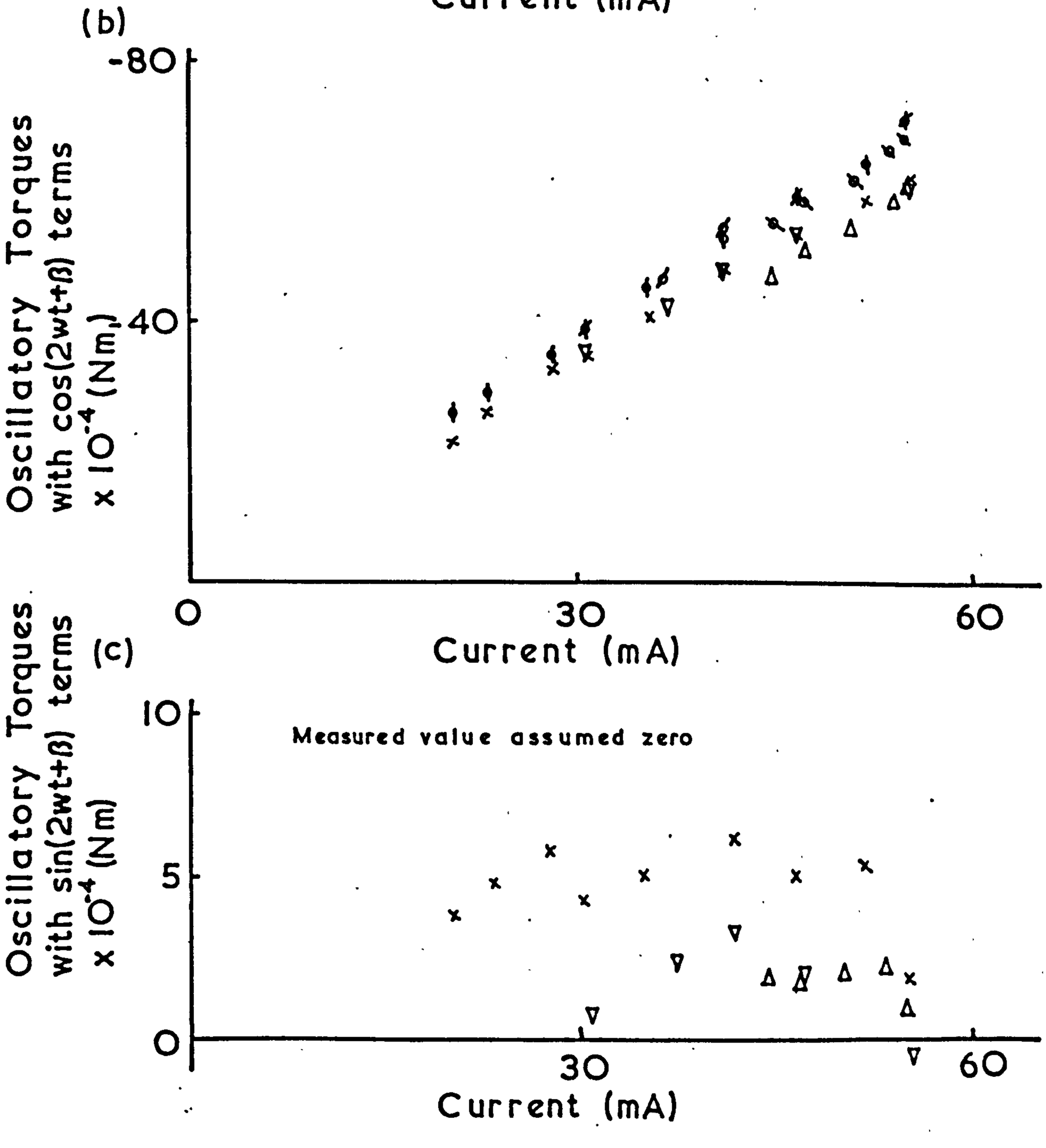

Comparison Of Torque Values

Fig 3.14

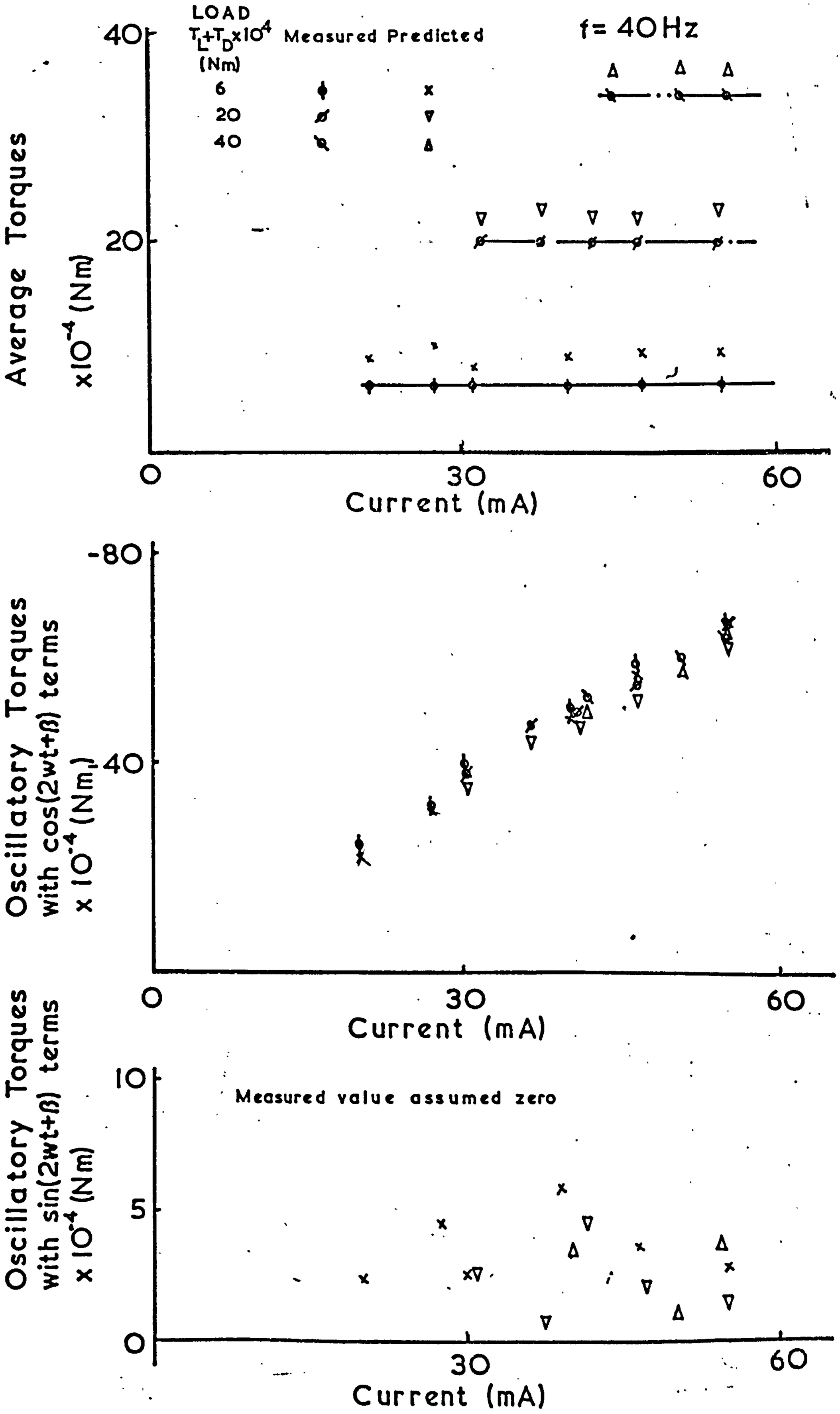

Fig 4·1

Experimental Arrangement

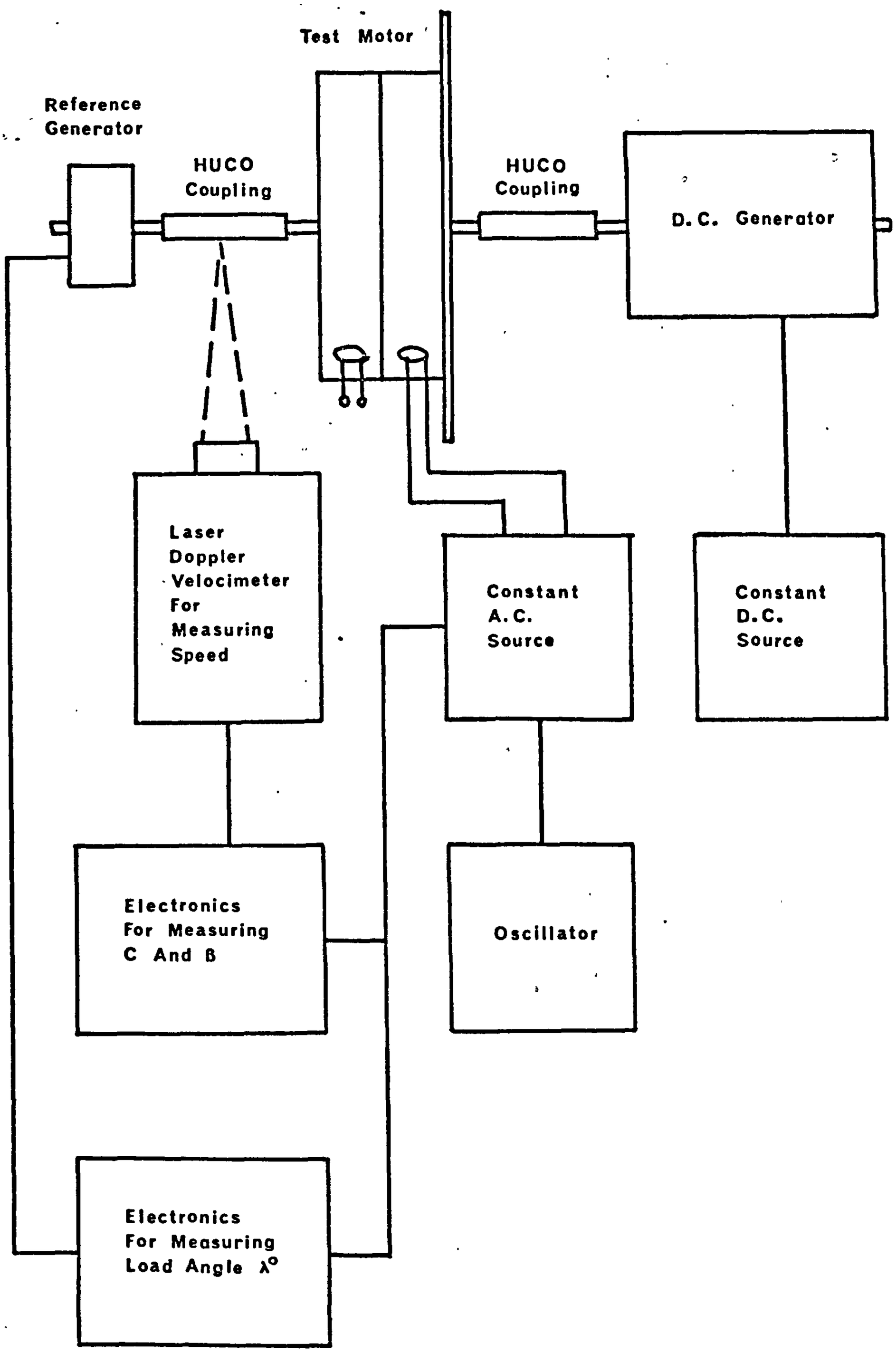

Fig 4·2
Fig 4·3

4·2 Reference Generator

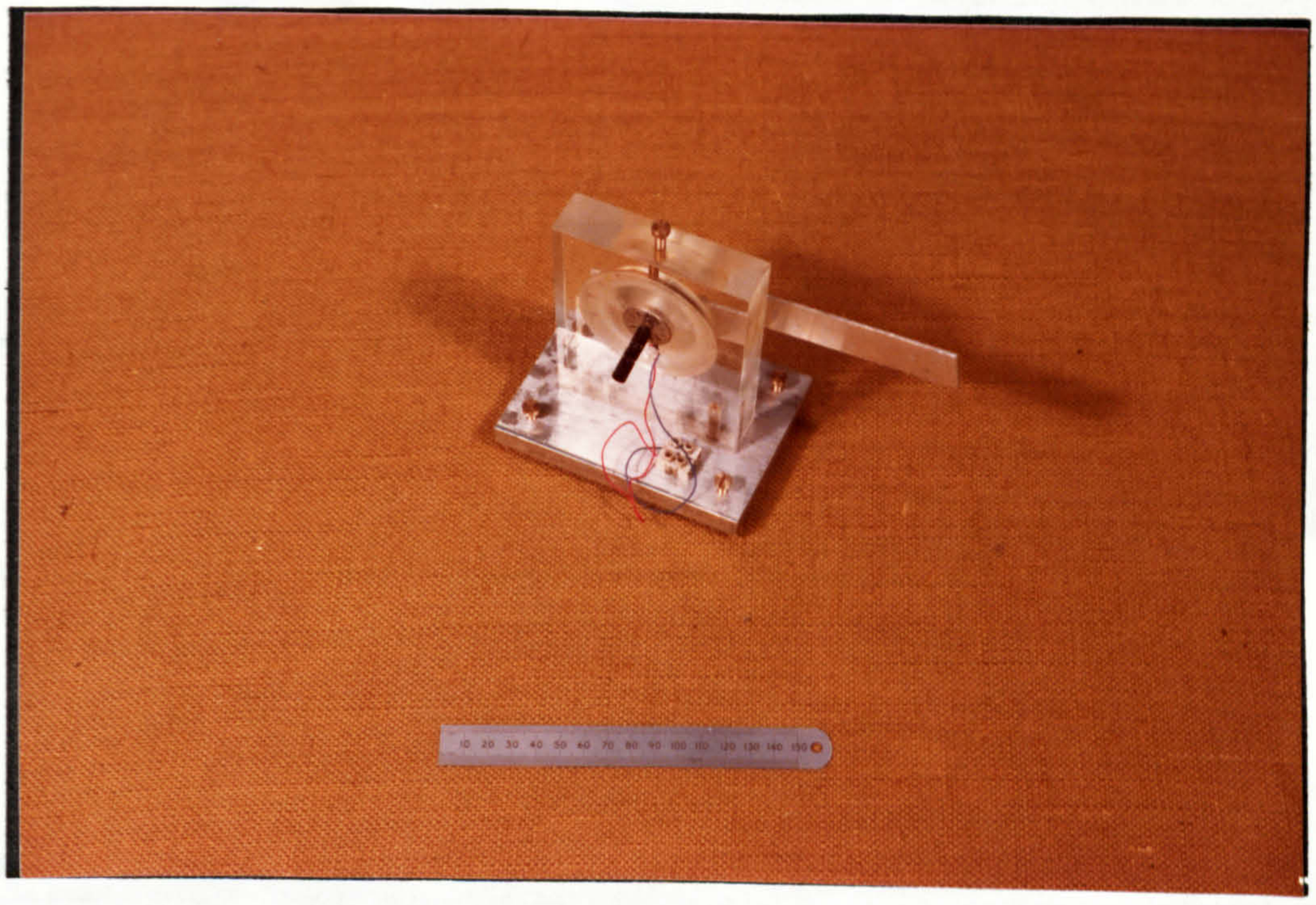

4·3 Current Feedback Arrangement

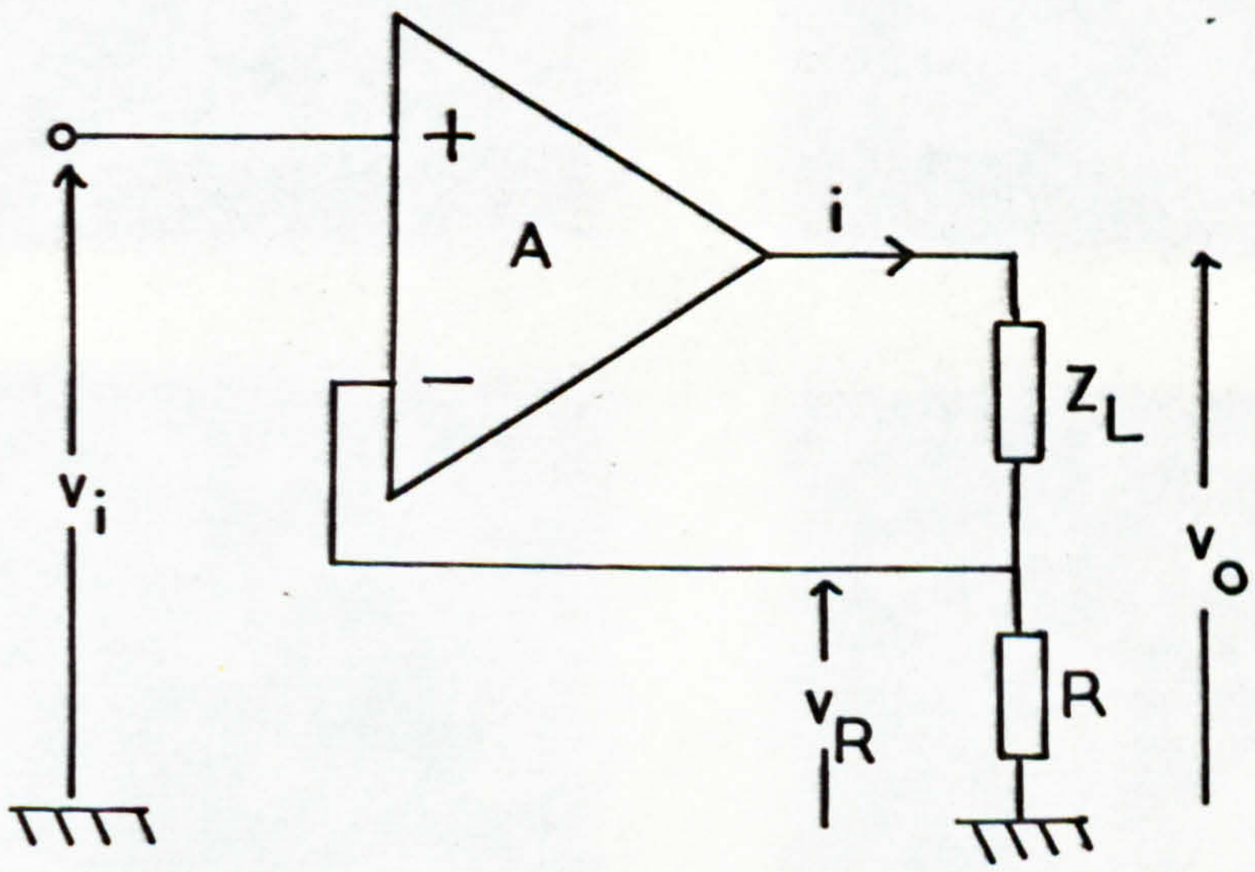

Fig 4·4
Fig 4·5

4·4 A·C· Current Source Circuit

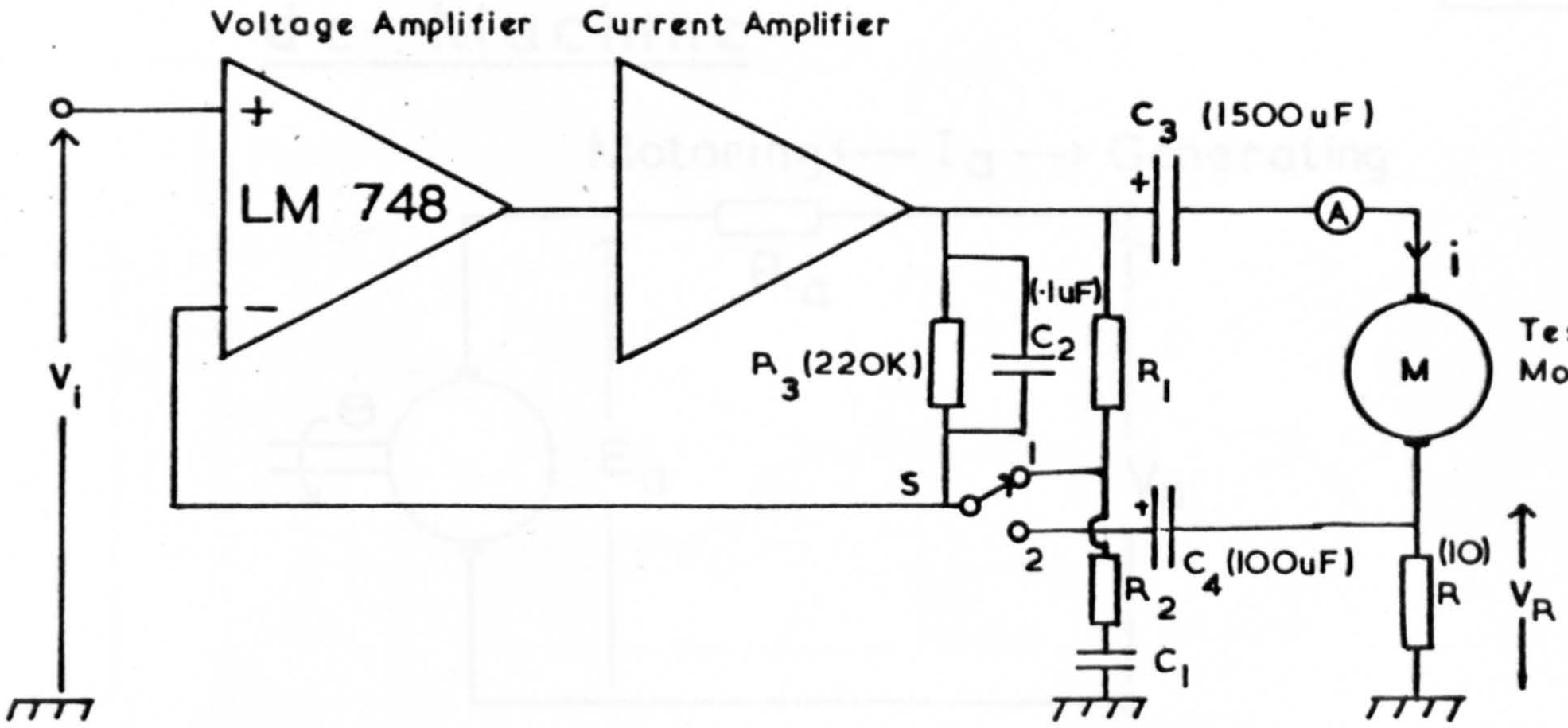

4·5 Performance Of A·C· Current Source

Oscillograms

Top:
V_i
Bottom:
i

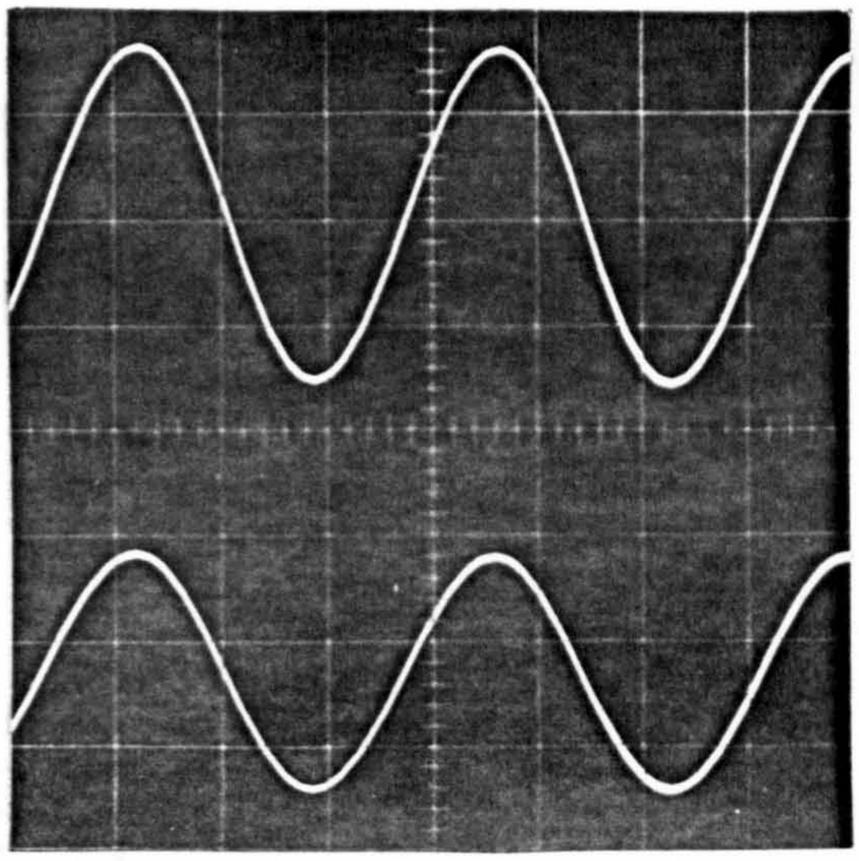

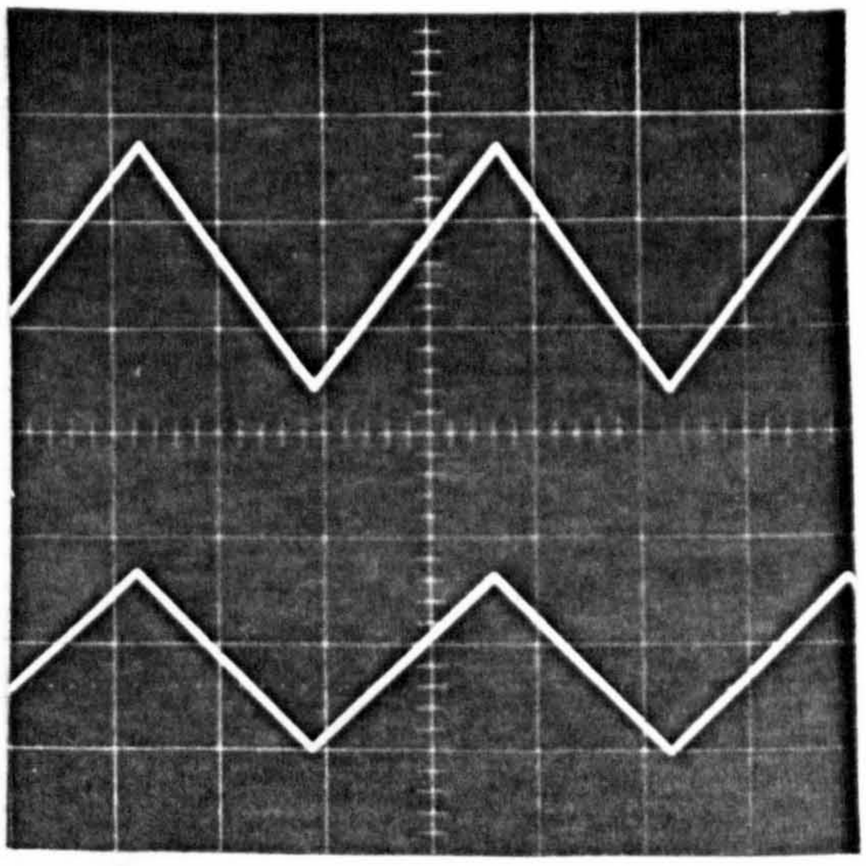

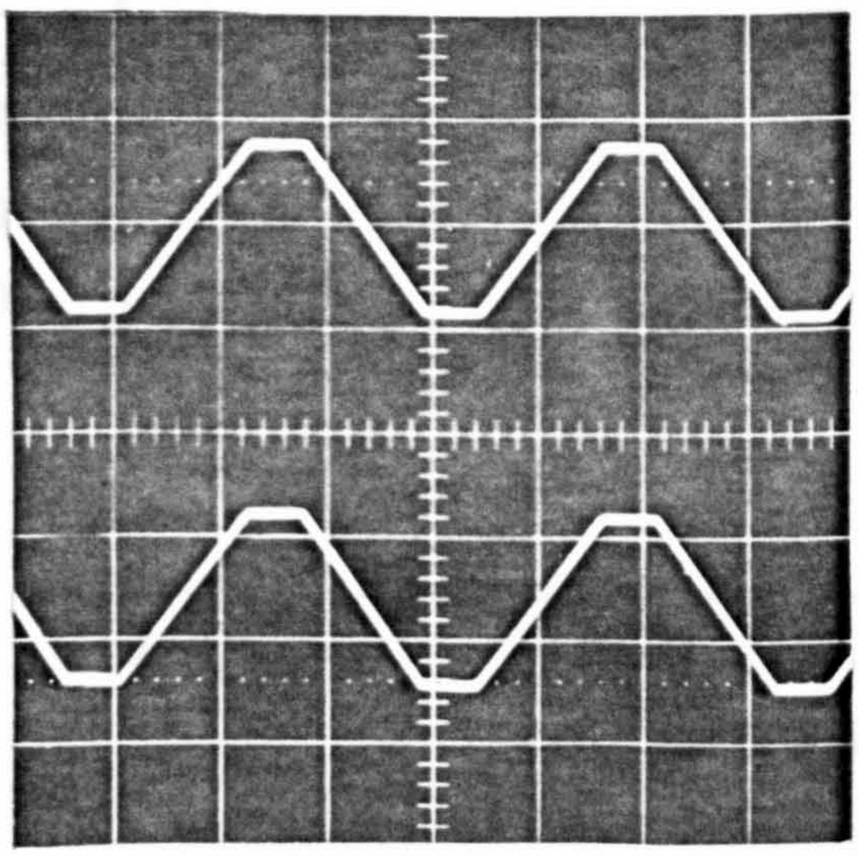

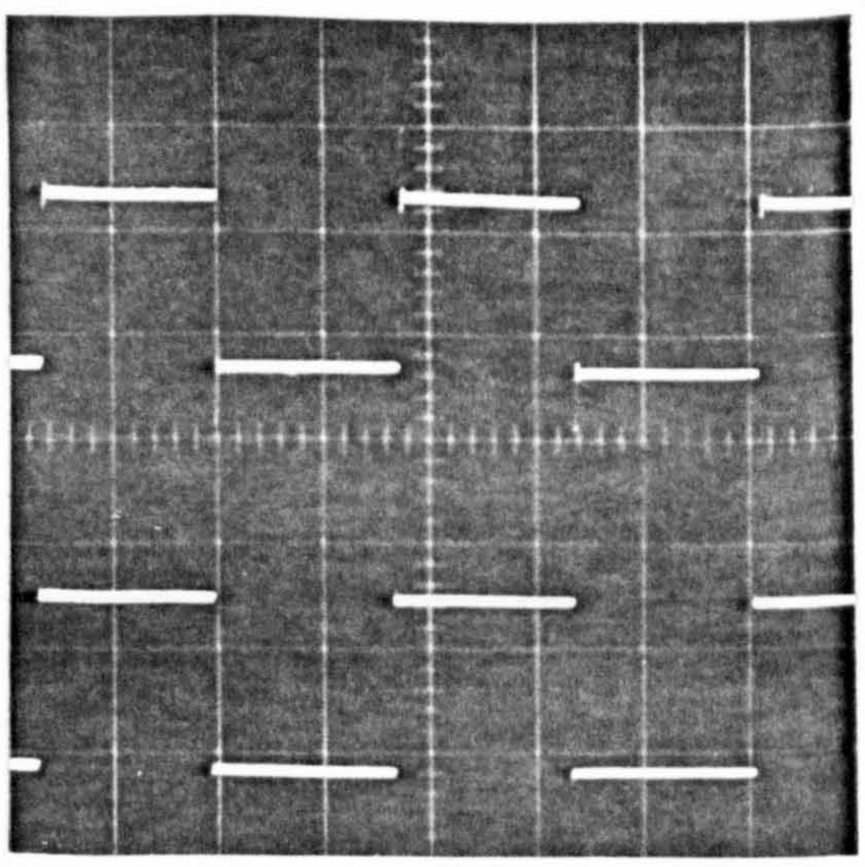

Fig 4·6
Fig 4·7

4·6 Equivalent Circuit Of The d·c· Machine

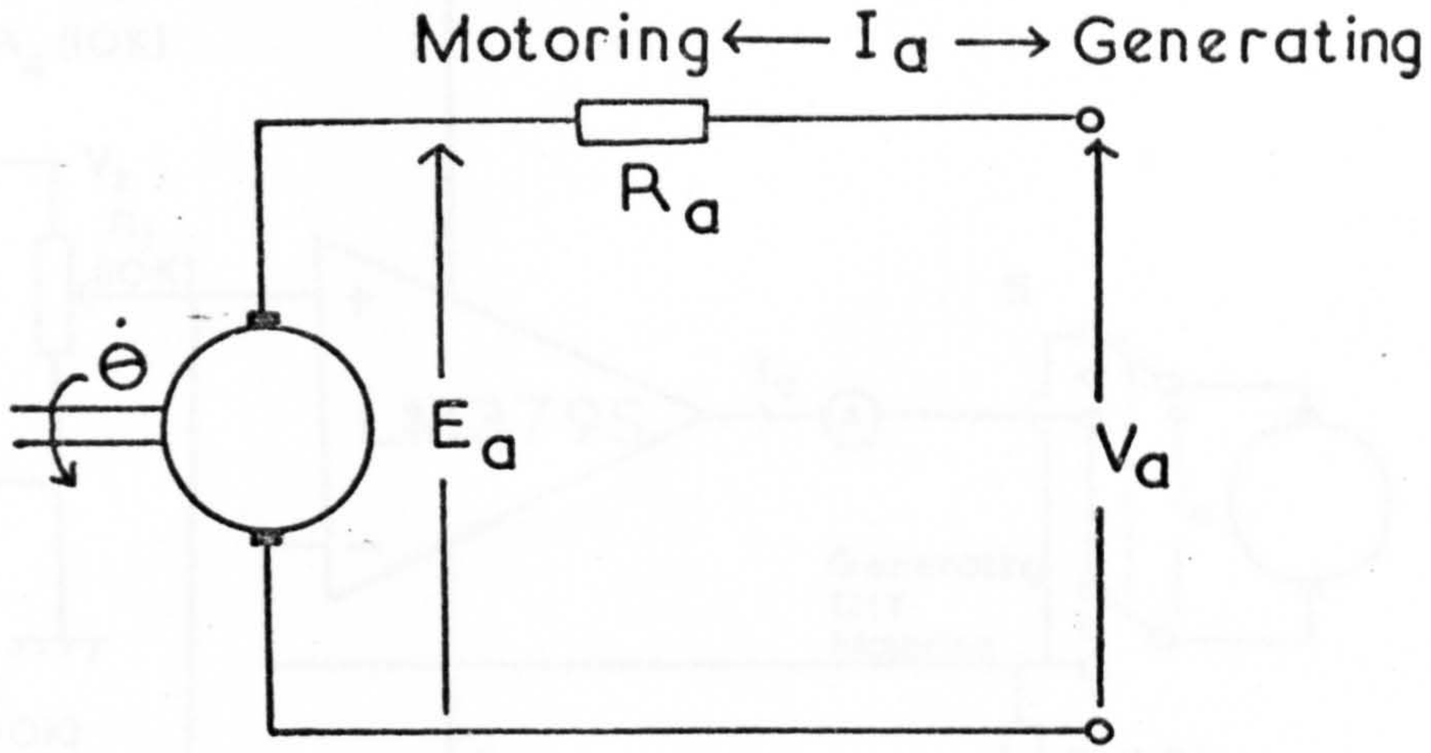

4·7 O·C· Emf Characteristic Of d·c· Machine

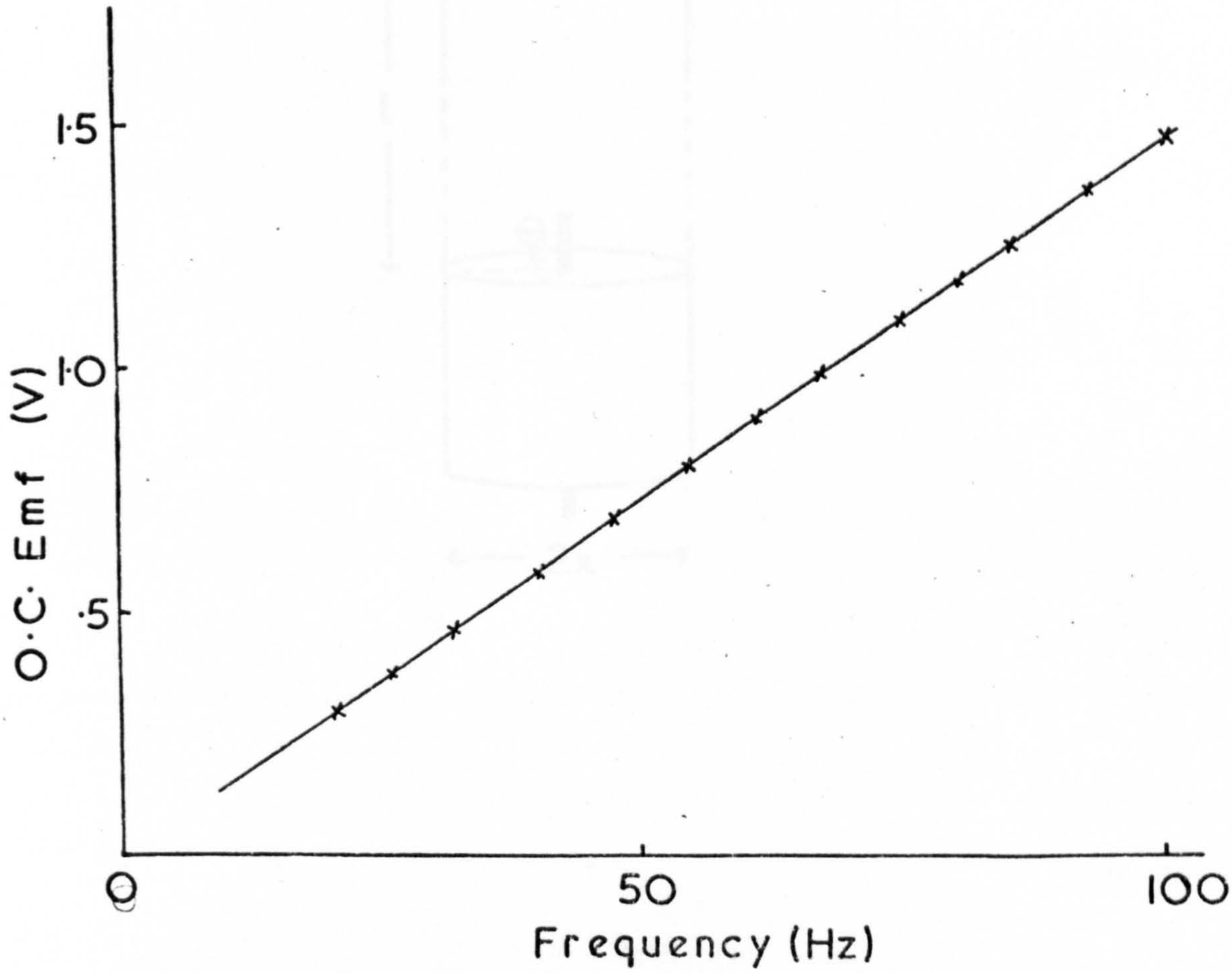

Fig 4·8
Fig 4·9

4·8 D·C· Current Source Curcuit

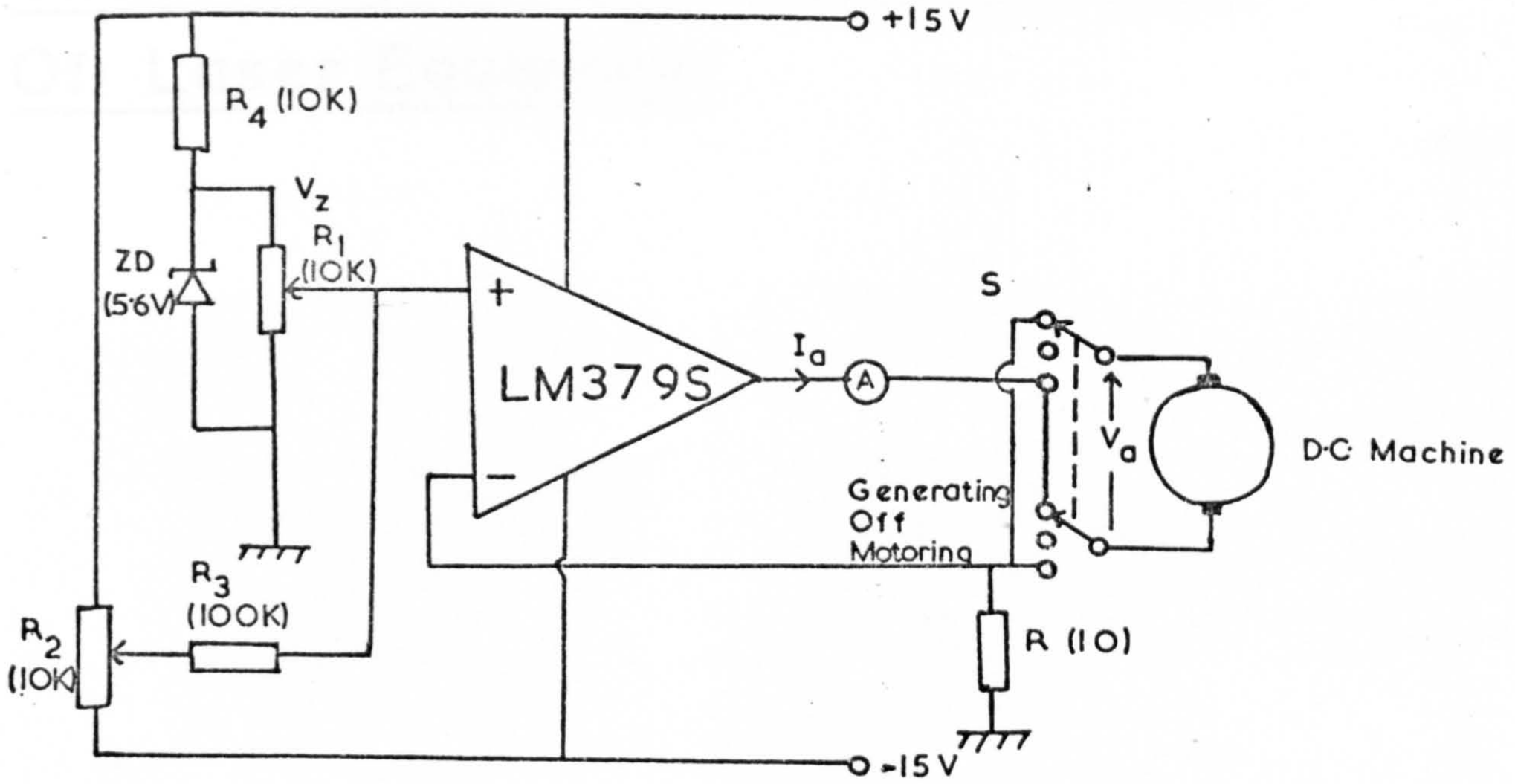

4·9 Bifilar Suspension Arrangement

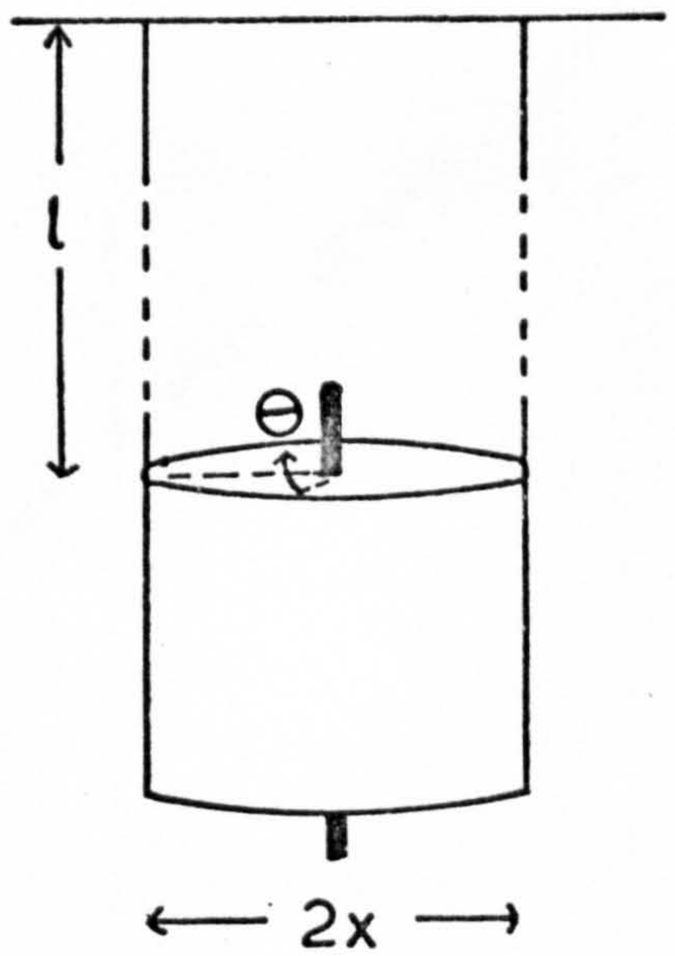

Fig 4·K

The Voltage Speed Characteristics Of Laser Equipment

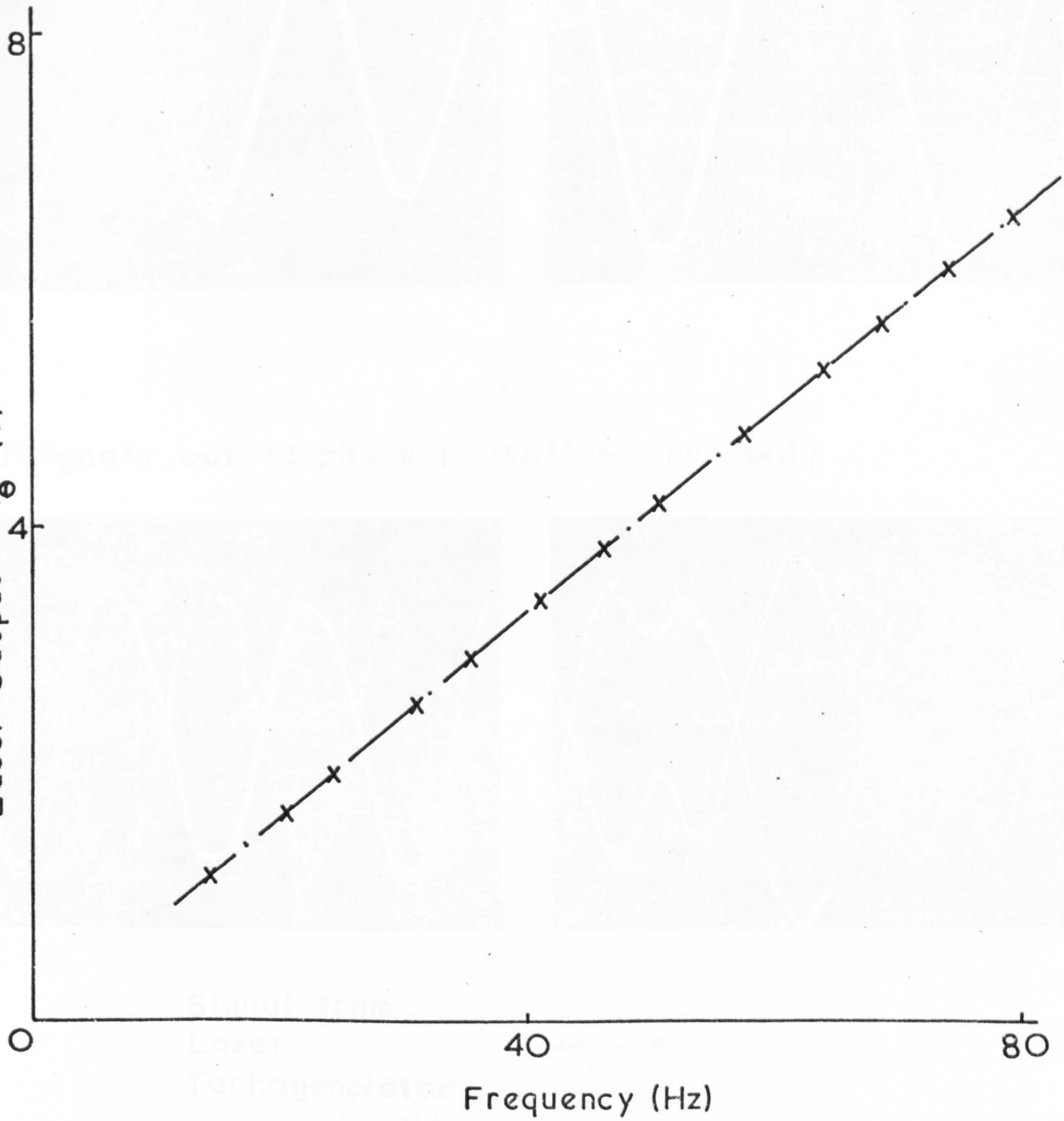

Fig 4·11

Comparison Of Oscillatory Speed Signals Measured With The Laser And Tachogenerator

a) Signals in phase

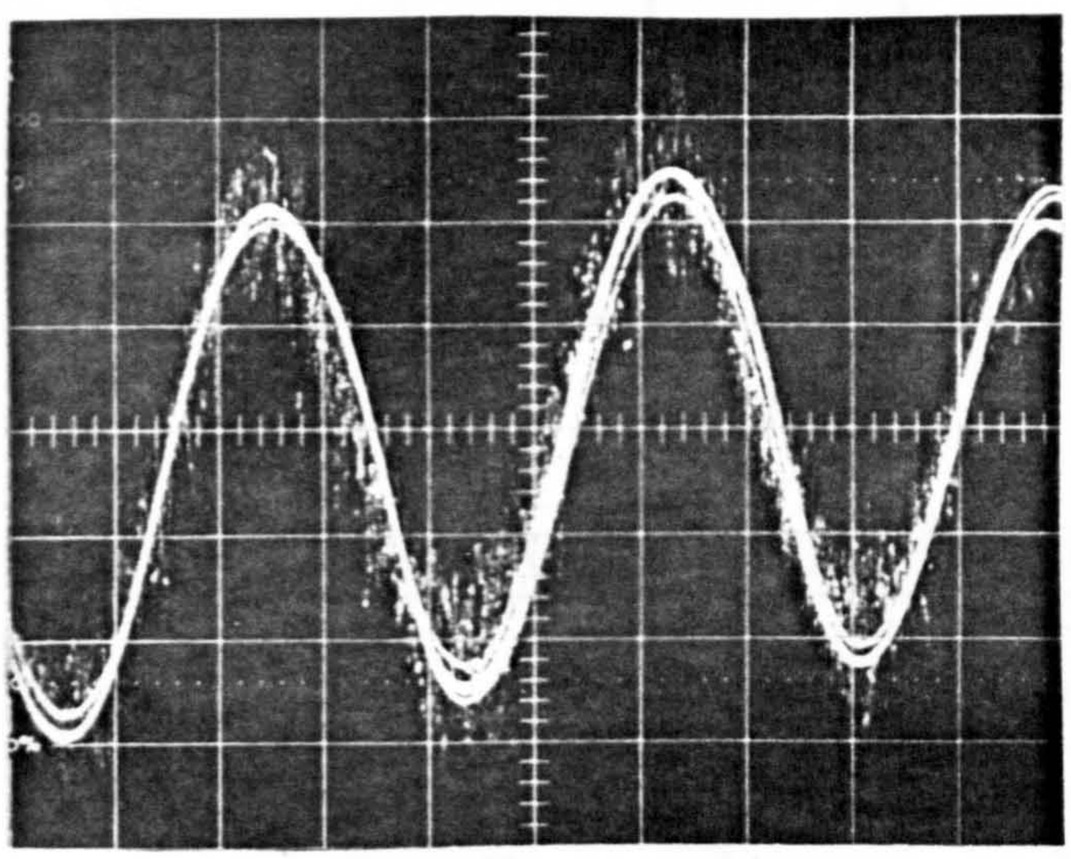

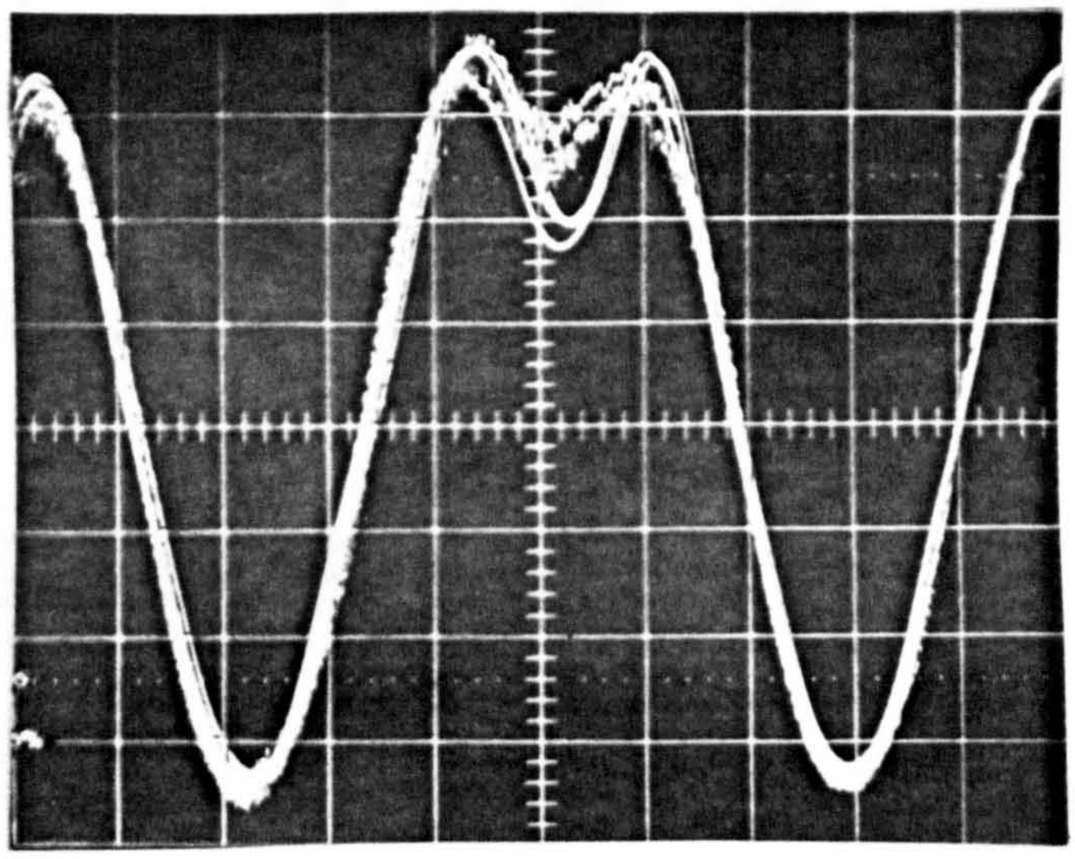

b) Signals out of phase (Rotation reversed)

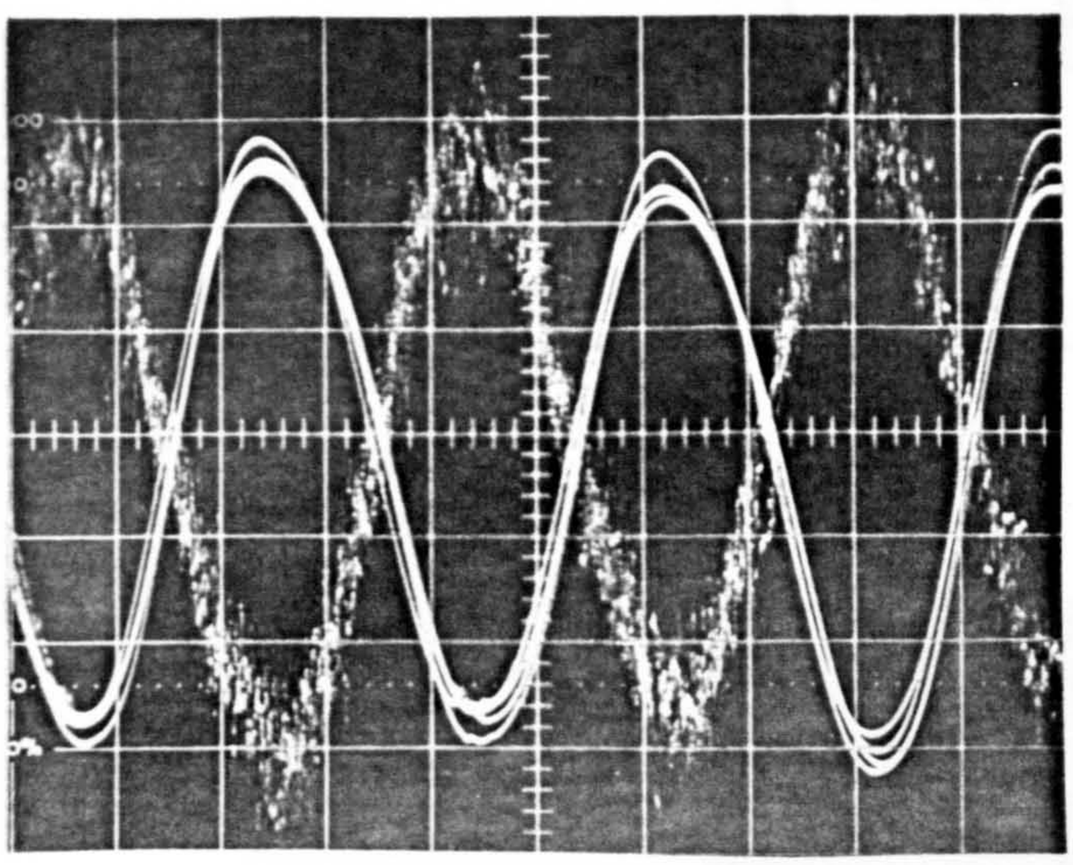

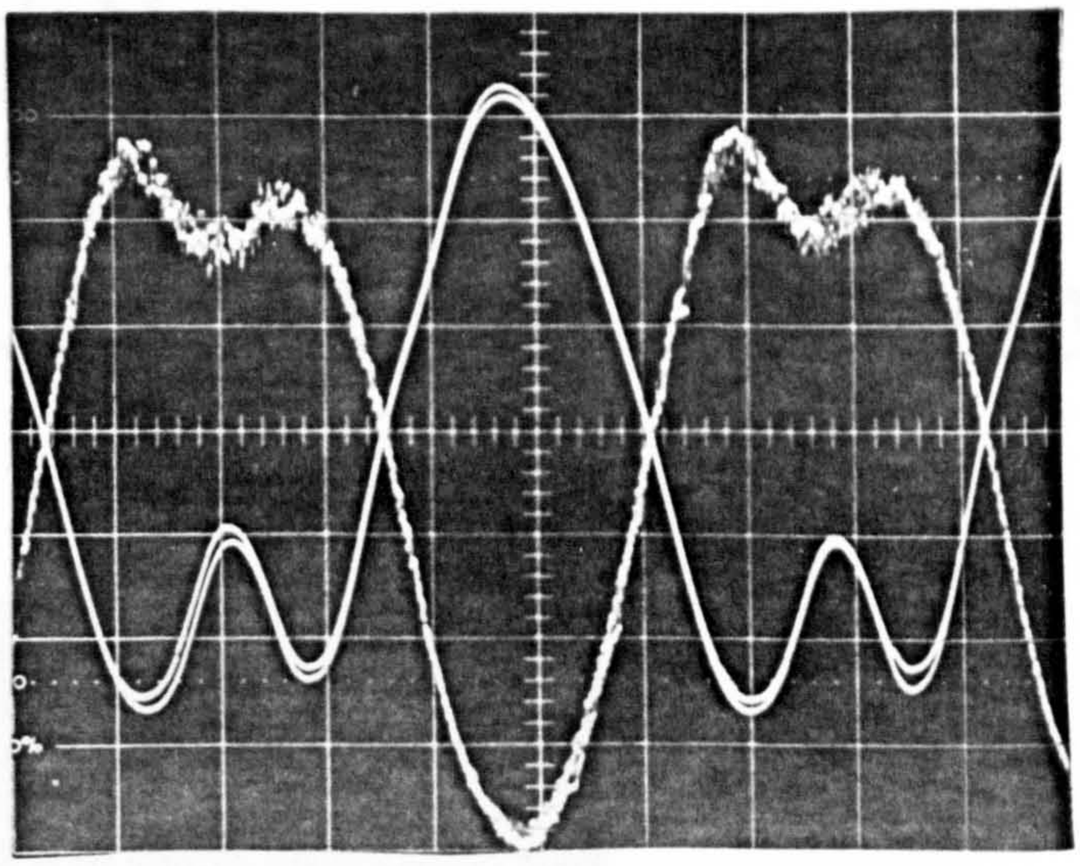

Signal from :
Laser
Tachogenerator

Fig 4·12
Fig 4·13
Fig 4·14

4·12 A·C· Filter Circuit

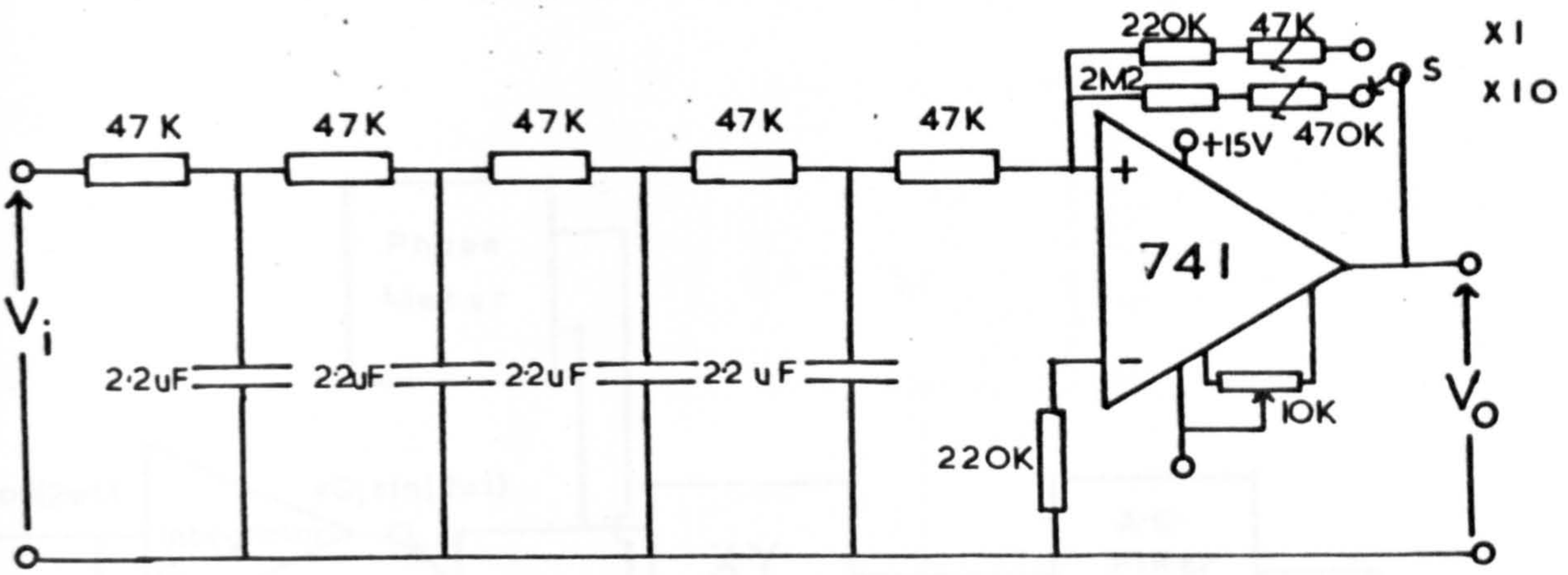

4·13 Analog Multiplier Circuit

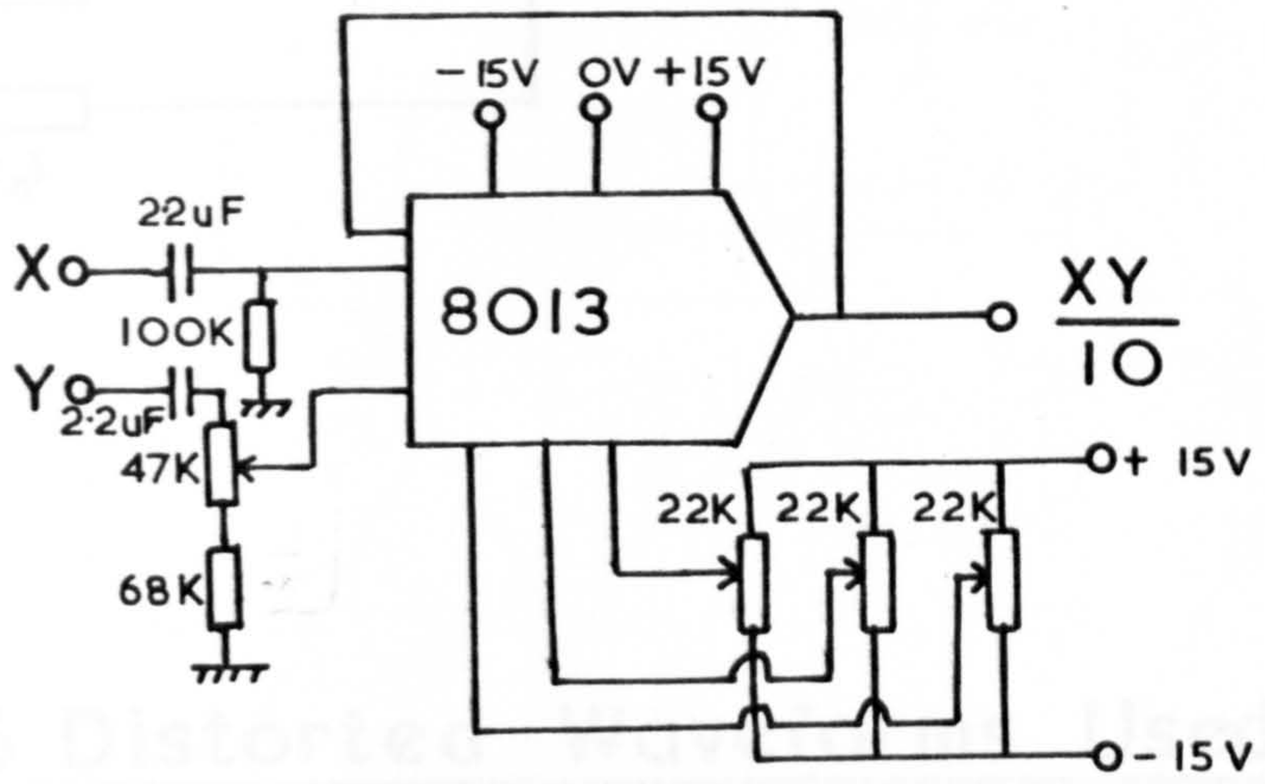

4·14 Synthesized Double Frequency Waveform

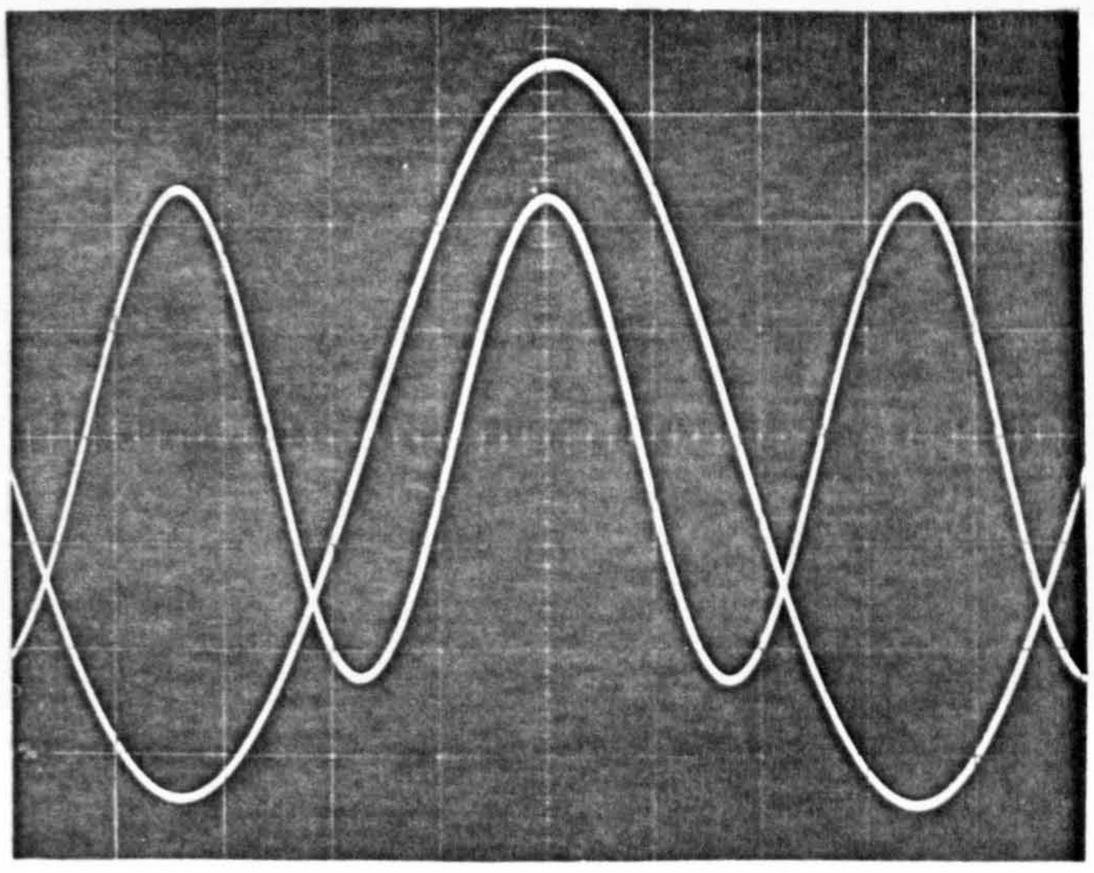

Fig 4·15

Fig 4·16

4·15 Circuit Arrangement Used Testing Phase Measuring Technique

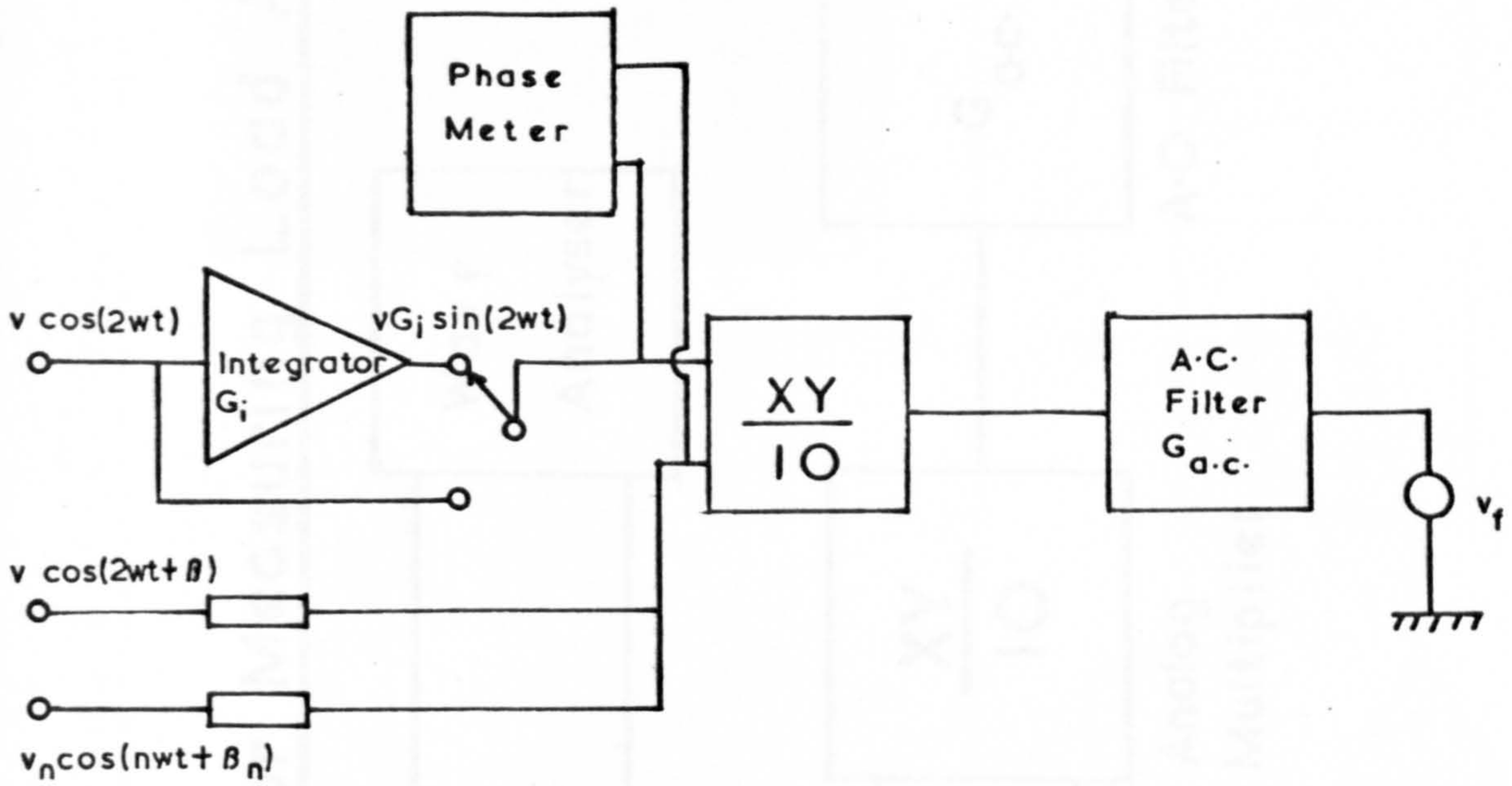

4·16 Distorted Waveforms Used In Test

Oscillograms
Top: reference signal
Bottom: distorted signal

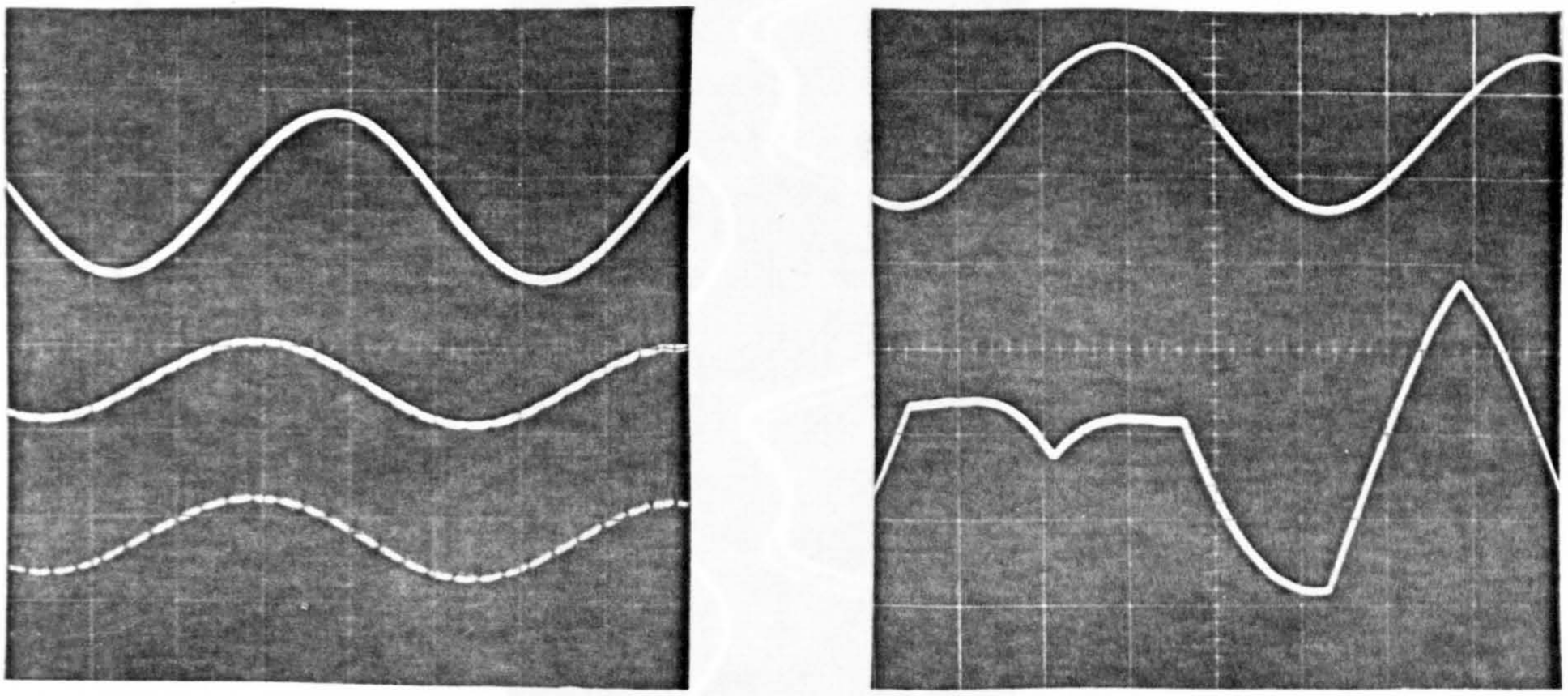

Circuit Arrangement Used For Measuring Load Angle λ

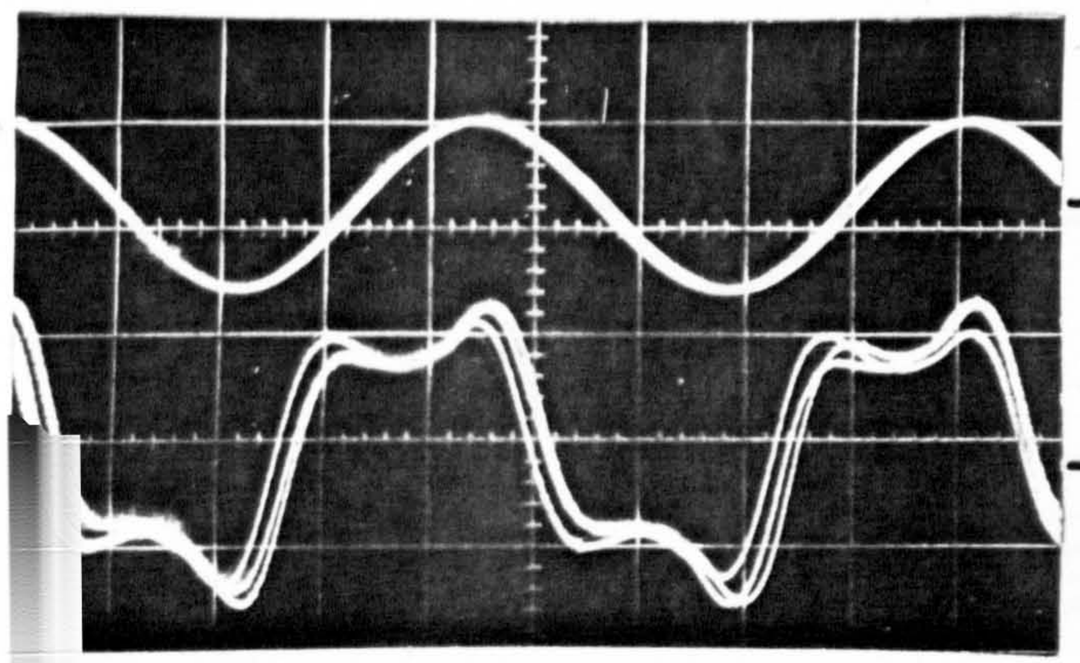

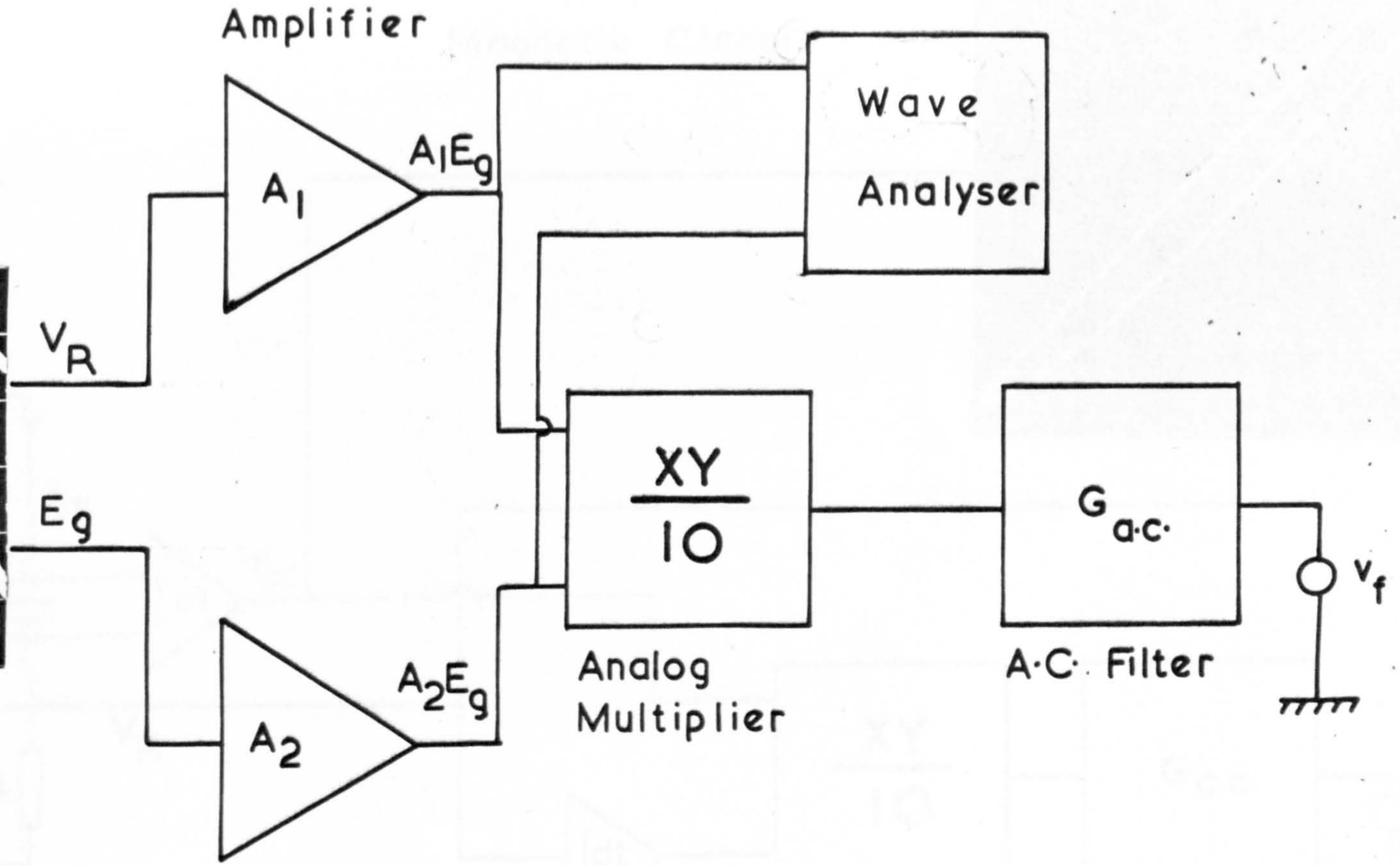

Fig 4.17

Circuit Arrangement Used For Measuring Ψ-i Characteristics

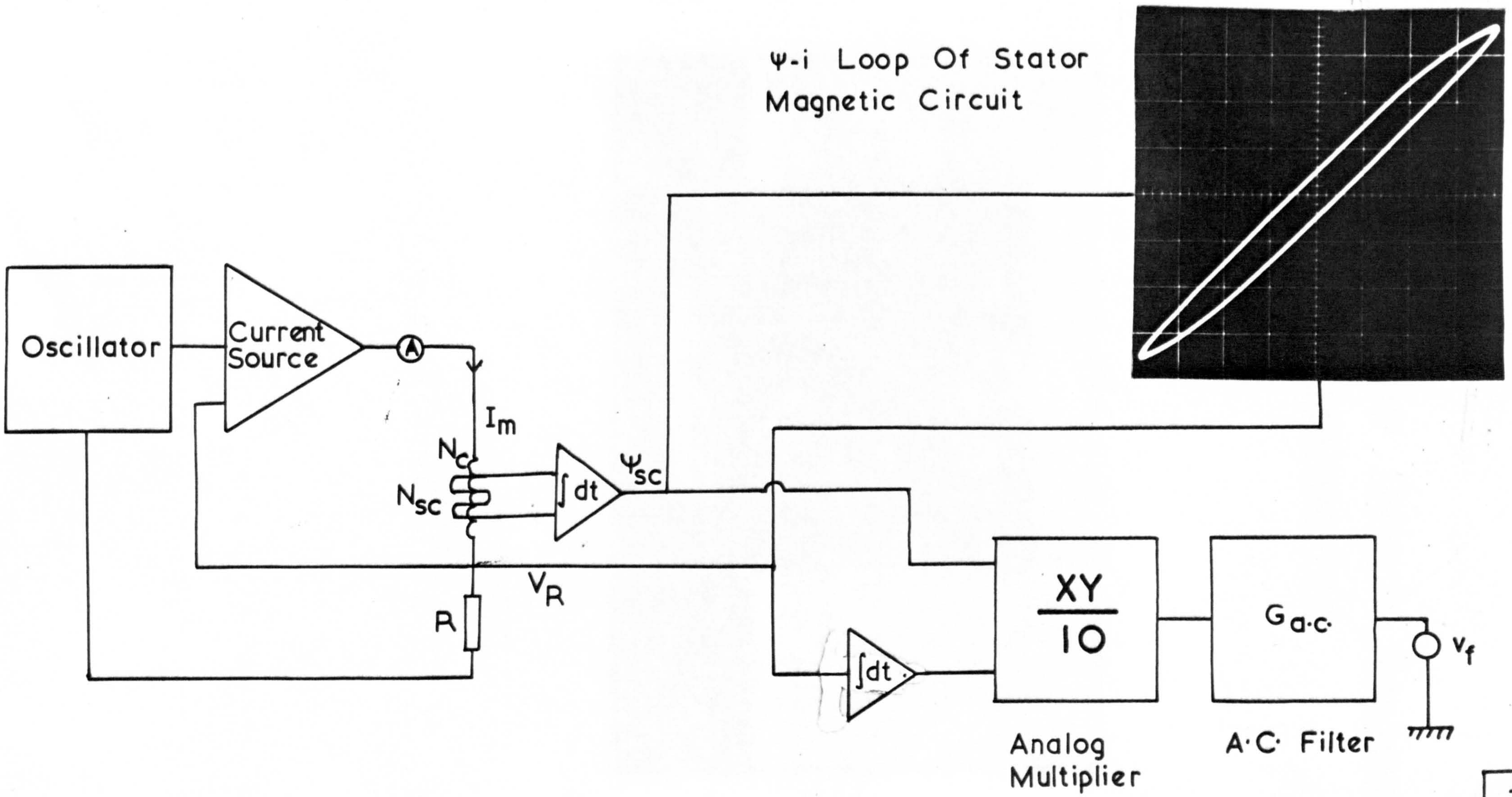

Fig 4·18

Fig 4.19

Instrumentation Console Designed For The Investigation

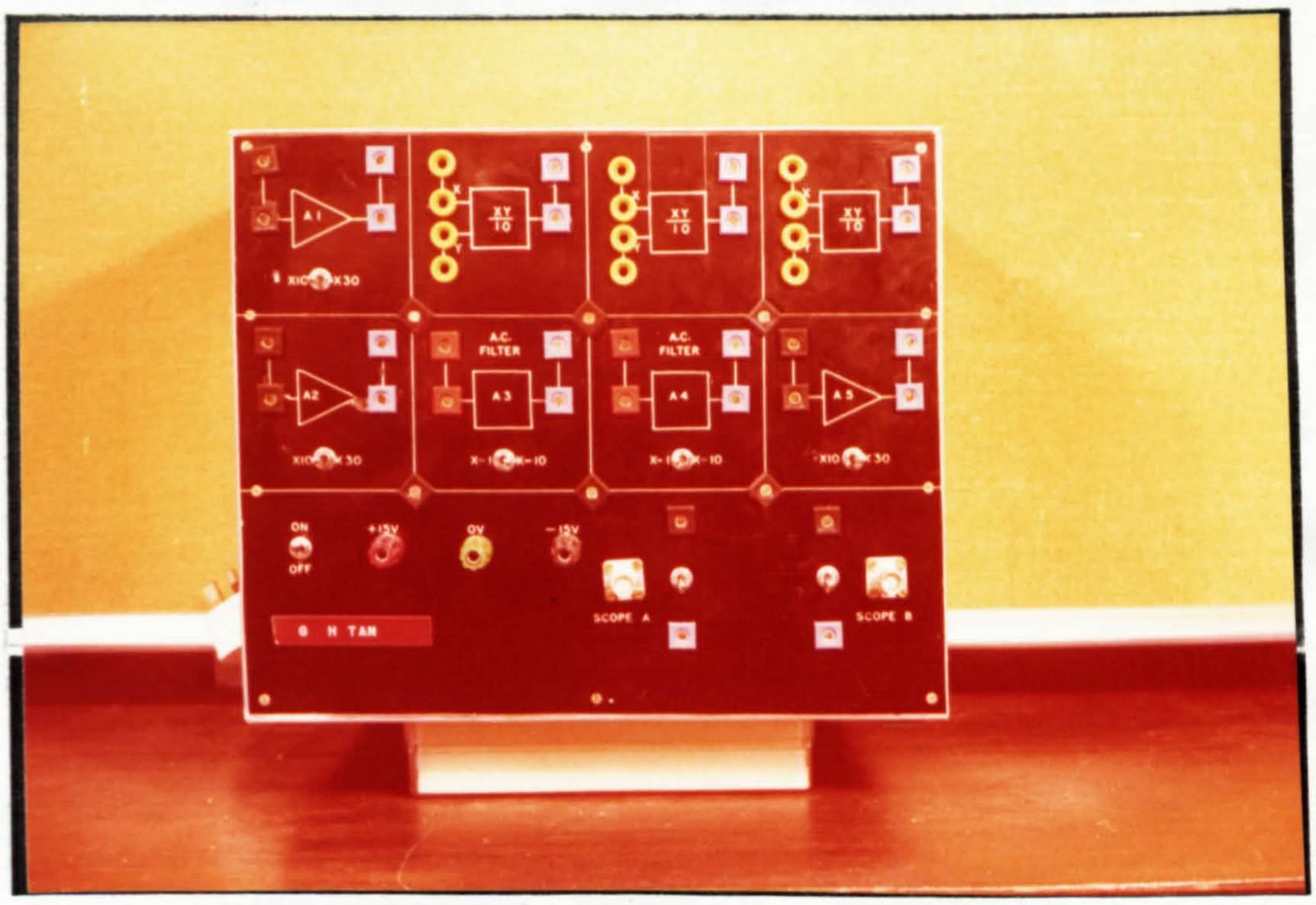

Fig A·1

Bessel Function Characteristics